Sociedad Mexicana del Hidrógeno A. C.

JOURNAL OF
NEW MATERIALS FOR
ELECTROCHEMICAL SYSTEMS

CICY

CINVESTAV
Unidad Mérida

CONACYT

9th International Symposium on New Materials and Nano-Materials for Electrochemical Systems

XII International Congress of the Mexican Hydrogen Society

Mérida, Yucatán, México

July 9-13, 2012

BOOK OF PROCEEDINGS

LENERSE

Metrohm
México

Calle 43 # 130, Col. Chuburná de Hidalgo,
C.P. 97200, Mérida, Yucatán, México.

Centro Público de Investigación del Sistema Conacyt.

ISBN:

Primera edición: Julio 2012.

Edición y diseño editorial: Mascha A. Smit
Diseño de portada: Norma Marmolejo Quintero
Desarrollo web: Fernely Aguilar Cruz, Rosaura Martín Caro

Hecho en México.

TABLE OF CONTENTS

9th International Symposium on New Materials and Nano-Materials for Electrochemical Systems
XII International Congress of the Mexican Hydrogen Society
Merida, Mexico, 2012

Electron Microscopy and Electrochemical Characterization of Pt/C and Pt-Au/C Catalysts Synthesized by Surface Redox Reactions

P. del Angel[1,*], R. G. González-Huerta[2], M. L. Hernández-Pichardo[3], E. Palacios-González[1], J. A. Montoya[1], J. Lara-Peralta[2]

[1]Instituto Mexicano del Petróleo, Dirección de Investigación y Posgrado, Eje Central L. Cárdenas 152, 07730, México, D. F.
[2]Instituto Politécnico Nacional-ESIQIE, Laboratorio de Electrocatálisis, UPALM, 07738 D.F. México, D.F.
[3]Instituto Politécnico Nacional-ESIQIE, Laboratorio de Investigación de Fisicoquímica y Materiales, UPALM, 07738 México, D.F.
[*]Tel (5255)9175-8405, pangel@imp.mx

ABSTRACT

Pt-M/C systems (M= metal from groups VIII or IB) are potential electrocatalysts for the fuel cells technology. This work aims to study the oxygen reduction reaction over Pt-Au/C catalysts. The preparation of the monometallic Pt/C catalysts was carried out by means of the impregnation of platinum over graphite. The bimetallic catalyst Pt-Au/C was prepared by selectively depositing Au on supported monometallic Pt/C catalysts by means of the reduction "in-situ" of $AuCl_4^-$. Redox method used was the Refilling method, which consisted in adsorbing hydrogen first on the metal (Pt), and subsequently reducing the $AuCl_4^-$ species by contact with the Pt-H interface at low temperature. The catalysts were characterized by X-ray diffraction (XRD), Scanning Electron Microscopy (SEM) and Transmission Electron Microscopy (TEM), whereas for the electrochemical tests the catalysts were supported on Vulcan XC-72 carbon and they were evaluated by linear and cyclic voltammetry. The composition of the individual metal particles of the solids indicated the presence of both metals, Pt and Au. A partial Au coating of certain Pt facets is possible, which indicates that the coating mechanism is selective and could influence the catalytic properties of the bimetallic Pt-Au/C catalysts. The electrochemical characterization showed a Tafel slope of - 94 mV dec^{-1} for the Pt-Au/C sample, with a 0.62 transfer coefficient, that means a catalytic activity towards the Oxygen Reduction Reaction (ORR).

1. Introduction

During the past decades much effort has been done in the study of mono and multimetallic supported catalysts used in the oil refining industry, and electrocatalysts for the fuel cells technology. A fundamental issue on bimetallic catalysts is the interaction between both metals that is not always achieved during the synthesis, but the formation of undesirable non-homogeneous bimetallic aggregates might occur [1], which produces deleterious effects on the catalytic properties of those bimetallic systems. In that case, compositional and structural variations might occur, for example the crystal overgrowths of one metal phase over another, multiple twinning or asymmetric metals aggregation [2]. Indeed, these structural variations may provoke important effects on the activity and selectivity of the supported bimetallic catalysts.

This situation has motivated the search of alternative methods that could offer better control of the metals interaction. Surface redox reactions [3-12] have a great potential for controlling the deposit and location of the second metal over specific crystallographic faces of metal particles [11-12]. For example, graphite supported Pt-Au catalysts [13-14] have been synthesized by surface redox reactions using $AuCl_4^-$ precursors in aqueous solutions, which are reduced by the Pt phase itself or by pre-adsorbed hydrogen acting as reducing agents. The present work explores the use of short-chain low alcohols, for substituting aqueous solutions in the surface redox reactions, i.e. Refilling (RE) method, which was used for selectively depositing a second metal (Au) onto specific crystallographic faces of graphite supported Pt particles on the Pt/C systems. The control of the metal deposits at the nanometric scale could lead to significant applications in catalytic technologies such as fuel cells, fine chemicals production and carbon monoxide oxidation [15-17]. The aggregation state of Pt and Au in the Pt-Au/C bimetallic catalysts synthesized by RE method has been studied at the single particle level and the influence of short-chain solvents was evaluated. Some advanced techniques were used for characterizing the compositional and structural features at the single particle level, such as X-ray Diffraction (XRD), Scanning Electron Microscopy (SEM), Energy Dispersive Spectroscopy (EDS), High Resolution Electron Microscopy (HREM) was studied.

2. Experimental

A monometallic 5 wt % Pt/C catalyst (MC) was used as the basis for synthesizing bimetallic catalysts by surface redox reactions (RE). The monometallic solid was prepared by impregnating a graphite support LONZA LT10 with hexachloroplatinic acid (i.e., H_2PtCl_6, Aldrich 99.9 %) in absolute ethanol (Merck 99.9 %). After drying at 70°C and reducing the solids at 300°C under H_2, the presence of small Pt particles having typical diameters between 1 and 10 nm was verified by electron microscopy techniques. These particles spread out on the top surface and edges of the graphite layer stacks, which in turn have a particle distribution between 2 and 20 μm. The metal Pt concentration of the monometallic solids was determined by atomic absorption spectroscopy (AAS), leading to 4.3 % wt. Pt^o (i.e., MC in Table 1). The metal (Pt) dispersion was determined by H_2 adsorption techniques, which indicated the metal dispersion of the Pt/C catalysts being about 8 %.

The parent catalyst Pt/C (MC) described above was modified by adding a second metal close to the electrochemical series of Pt, i.e., Au. The "Refilling" method (RE) was used, which consisted of using a reducing agent like hydrogen, which was pre-adsorbed on the metallic surface (Pt) of the parent catalyst (13). In the present case C_2H_5OH was used as the solvent media. Therefore, Table 1 summarizes the preparation conditions used as well as the compositional data determined by atomic absorption spectroscopy. Also, Table 1 shows the chemical composition data of bimetallic Pt-Au catalysts. The solid RE-70 was obtained by deposition of the second metal (Au) followed by drying at 70°C, without any further treatment.

Table 1. Metal concentration of the catalysts Pt/C and Pt-Au/C (Atomic Absorption Spectroscopy, AAS).

Catalyst	Pt wt %	Au wt %	Preparation conditions (H_2)
MC	4.3%	-	300°C, 3h
RE-70	4.4%	0.42%	drying at 70°C

The X-ray diffraction (XRD) patterns were obtained in a Siemens D-500 diffractometer fitted with a Cu tube (35 kV, 25 mA) and a graphite monochromator, for eliminating the Kβ lines. The Au^o and Pt^o phases were identified after the JCPDS database.

The samples were performed using a Scanning Electron Microscope (SEM) Nova-200 Dual-Beam with Schottky type field emission gun and a resolution of 1.1 nm. It has coupled an energy dispersive spectrometer (EDS) from EDAX, to detect elements from the beryllium onwards. The samples were fixed onto a sample holder using carbon tape. SEM images and EDS were obtained in order to determine the morphology of the nanoparticles and their composition. Furthermore, the samples were studied by high-resolution transmission electron microscopy (HRTEM), the micrographs were obtained in a TITAN 80-300 with Schottky type field emission gun operating at 300 kV. The point resolution and the information limit were better than 0.085 nm. HRTEM digital images were obtained using a CCD camera and Digital Micrograph Software from GATAN. The elemental composition was determined by Energy dispersive X-ray spectroscopy (EDS) with an EDAX spectrometer fitted to the TEM. In order to prepare the materials for observation, the powder samples were ultrasonically dispersed in ethanol and supported on holey carbon coated copper grids.

A conventional single three-electrode test electrochemical cell was used in the electrochemical experiments. All of the electrode potentials in this work are related to a normal hydrogen electrode (NHE) in a 0.5 M H_2SO_4 aqueous solution electrolyte. The electrochemical measurements were performed using a Potentiostat AUTOLAB. All electrochemical experiments were conducted at room temperature. The working electrode was a glassy carbon disk with a 5 mm diameter (0.19 cm^2). Glassy carbon and reference hydrogen electrodes were used as the counter and the reference electrode. The catalytic ink was prepared by dispersing 1 mg of catalyst in 8µL of Nafion® and 60 µL of

ethyl alcohol in an ultrasound bath for 15 min. A drop containing 8 µL of catalyst ink was deposited onto the working electrode surface and dried at atmospheric conditions. The electrodes were activated in an oxygen free electrolyte, by scanning the potential in a region between 1.2V/NHE to 0.0 V/NHE at 50 mV /s for 10 cycles, until a steady state voltamperogram was reached. Thereafter, the electrolyte was saturated with pure oxygen for 30 min and maintained on the electrolyte surface during rotating disk electrode (RDE) experiments. Hydrodynamic experiments were recorded in the range of rotation rate of 100 to 1600 rpm at 5 mV/s.

3. Results and discussion

The X-ray diffraction patterns corresponding to the Pt/C (MC) and Pt-Au/C (RE-70) bimetallic catalysts prepared by RE method are reported in Figure 1. The vertical line around 38.18° (2Θ) indicates the theoretical position of the Au(111) peak. For the bimetallic catalyst, RE-70, the XRD peaks do not change of position, this means that Au^o and Pt^o is not an alloy.

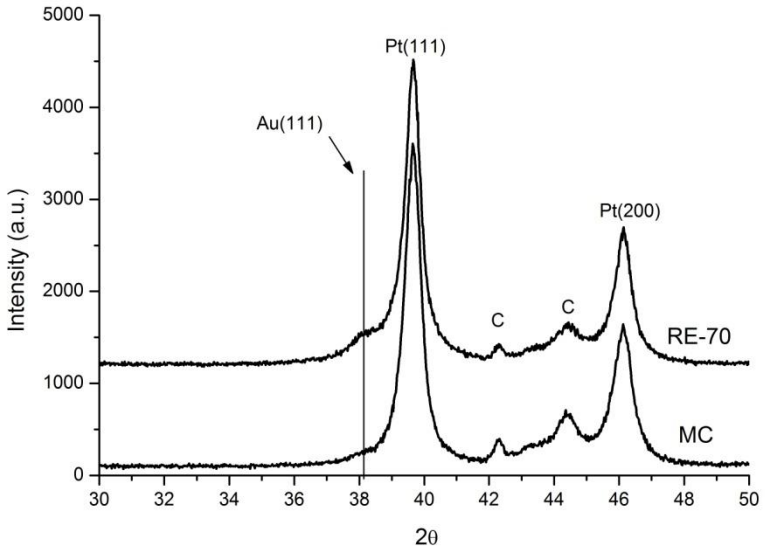

Figure 1. XRD patterns of the monometallic Pt/C (MC) and bimetallic Pt-Au/C (RE-70) catalysts.

Table 2 shows a comparison between the mean particle diameters determined by X-ray diffraction and TEM. The difference might be due to overestimation of the crystallite diameters by XRD arising from instrumental artifacts [18-19].

Table 2. Mean particle diameters determined by TEM and XRD.

Catalyst	MET	XRD	
	Ds (Å)	Dv Pt (Å)	Dv Au (Å)
MC	110	140	--
RE-70	100	170	70

SEM image and EDS of RE-70 bimetallic catalyst are shown in Figure 2. White spots correspond to Pt-Au bimetallic nanoparticles, the corresponding EDS was obtained from all the region of the SEM image (global analysis). The quantification of gold and platinum is a little lower compared with the AAS analysis.

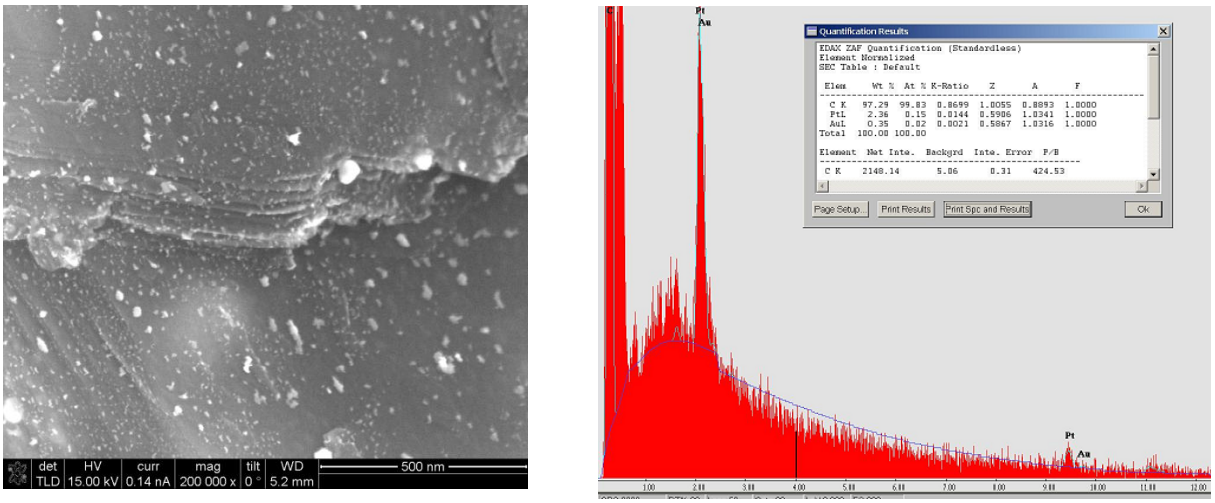

Figure 2. SEM image and EDS analysis of Pt-Au/graphite bimetallic catalyst.

The chemical composition of the single metal particles was determined by Energy Dispersive Spectroscopy (EDS) in a TEM in two modes. The first consisted of using a narrow electron beam probe ($\varphi \sim 1 - 2$ nm) for microanalysis of single particles, while the second mode was performed using large beam probe diameters, i.e., 1 to 10 μm, for the global analysis of sample regions containing hundreds of metal particles to obtain the average composition. As expected, the global analyses indicated a concentration of Pt higher than Au (similar to the EDS obtained by SEM), while the point analyses indicate a mixed situation, where single particles may be either richer in Au or Pt. Although particles containing only Au were not found, about 5 % of the particles analyzed contained only Pt, thus indicating a close contact of the Au phase with the Pt phase at the nanometric scale. These results might be explained

considering the formation of a layer of Au on top of the metal particles, which is detected only by EDS methods, because the conventional chemical analysis (AAS) gives only "bulk composition", without taking account of the metal phase distribution.

The interaction between both metals at the single-particle level was studied by direct lattice resolution imaging, using high resolution electron microscopy techniques. Thus, Figure 3 displays the lattice image of a metal particle after the deposit of the second metal (Au). Here, one observes a metal particle consisting of two parts, one located in the center of the particle with a lattice spacing of about 0.22 nm, while the other located outer of the particle with a lattice spacing of about 0.235 nm. This was confirmed by the EDS obtained from this single Pt-Au nanoparticle.

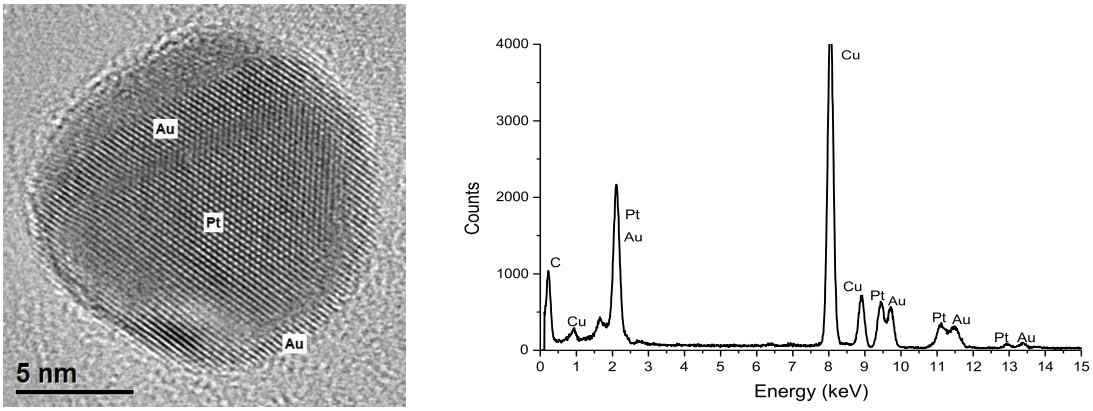

Figure 3. HRTEM and EDS analysis of a single Pt-Au nanoparticle on the RE-70 bimetallic catalyst.

Figure 4 shows RDE experiments. The polarization curves on Pt-Au/C, incorporated into a Nafion® film electrode, were performed at different rotation rates, in an oxygen-saturated 0.5M H_2SO_4 solution at 25°C. The polarization curves show three well defined potential zones: charge transfer, mixed and mass transport. It was considered that defined limiting currents are associated with the high diffusion of oxygen through the electrode surface and the uniform distribution of active sites. A similar polarization curve was observed on the Pt/C electrode. In these electro-catalysts, the oxygen reduction is fast enough that, at high overpotentials, a flat limiting plateau is observed. This phenomenon can be associated to a good distribution of the electrocatalytic sites on the electrode surfaces. On a film-coated electrode surface, the overall measured density current (j), is related to the kinetic density current (j_k) and the boundary layer diffusion-limited current density (j_L). Thus, the overall measured current of the oxygen reduction can be written as being dependent on the kinetic current and the diffusion-limited current, as shown on the left side of the equation 1.

$$\frac{1}{j} = \frac{1}{j_k} + \frac{1}{j_L} = \frac{1}{j_k} + \frac{1}{B\omega^{1/2}}, \qquad (1)$$

The kinetic current density is proportional to the intrinsic activity of the catalyst, and the diffusion-limited current density is proportional to electrode rotation rate (ω). The constant B is $0.2nFCD^{2/3}v^{-1/6}$, where 0.2 is a constant used when ω is expressed in revolutions per minute, C is the bulk concentration of oxygen (1.1×10-6 mol cm^{-3}), D is the diffusion coefficient of oxygen in the sulfuric acid solution (1.4×10-5 cm^2 s^{-1}), and v is the kinematic viscosity of the sulfuric acid (1.0×10-2 cm^{-2} s^{-1}).

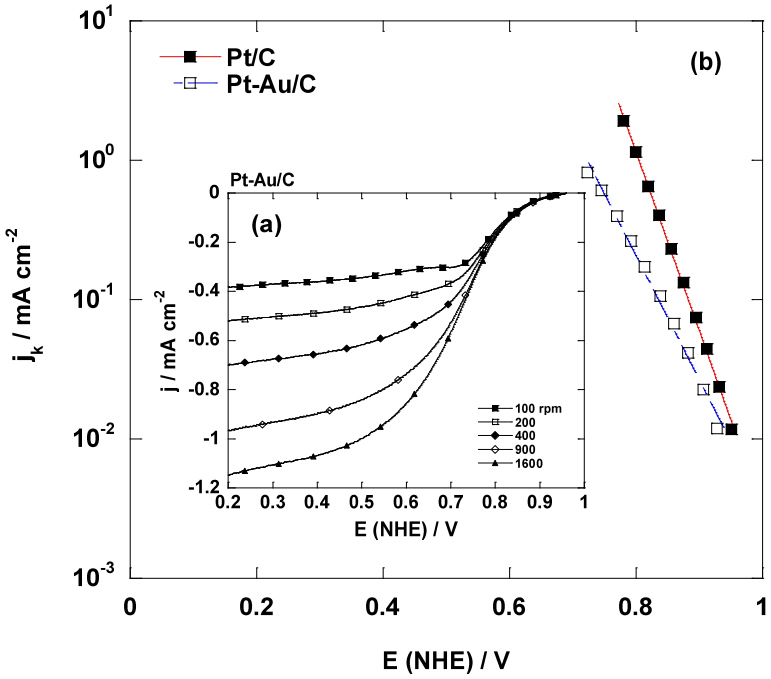

Figure 4. RDE responses on supporting Pt/C and Pt-Au/C electrodes in O2 saturated 0.5 M H2SO4: a) Linear Voltammetry, b) Tafel plots.

The Figure 4(b) shows the mass-transfer-corrected Tafel plots for the Pt/C and Pt-Au/C electro-catalysts. Tafel slopes at low current density have a value of 80 mV dec^{-1} and 94 mV dec^{-1} in the Pt/C and Pt-Au/C respectively, which indicate that the first electron transfer on the adsorbed oxygen molecule is the rate-determining step. This behavior is in agreement with results reported by other authors for Pt/C and Pt-Au/C catalysts prepared by other methods [20-21].

4. Conclusions

The application of surface redox methods using alcohol led to the reduction "in-situ" of $AuCl_4^-$ species and the selective deposit of Au^o onto the (111) faces of Pt small particles. At room temperature most of the small metal particles analyzed showed the presence of both metals, Pt and Au. The aggregation state of the small metal particles was sensitive to the preparation method. Also, the preferential decoration of Pt(111) particle facets with Au was verified by high resolution electron microscopy techniques.

The electrochemical characterization showed a Tafel slope of - 94 mV dec^{-1} for the Pt-Au/C, which indicates that the first electron transfer on the adsorbed oxygen molecule is the rate-determining step. The Pt-Au/C catalyst shows catalytic activity towards the Oxygen Reduction Reaction (ORR).

5. Akcnowledgements

The authors thank the facilities of the Electron Microscopy Laboratory of the Instituto Mexicano del Petróleo. This work has been supported by the IPN project SIP- 20120486, SIP-20120475, multidisciplinary project IPN-SIP 1338 and project ICYTDF PIEMP11-31.

6. References

[1] Nagy, J. B., Barette, D., Fonseca, A., Jeuniecu, L., Monnoyer, Ph., Piedrigross, P., Ravet-Bodart, I., Verfuillie, J. P., and Wathelet, A., In Nanoparticles in Solids and Solutions; J.H. Fendler and I.Dékány, Eds.; Kluwer Academic Publishers: Dordrecht, 18, 71, (1996)

[2] Chandler, B.D., Schabel, A. B., and Pignolet, L. H., J. Phys. Chem. B 105, 149 (2001)

[3] Barbier, J., Advances in Catalyst Preparation, Study Number 4191 CP, Catalytica Studies Division. Mountain View, (1992)

[4] Menezo, J. C., Denanot, M. F., Peyrovi, S., and Barbier, J., Appl. Catal. 15, 353 (1985)

[5] Barbier, J., Menezo, J. C., Montassier, C., Naja, J., Del Angel, G., and Domínguez, J. M., Catal. Lett. 14, 37 (1992)

[6] Barbier, J., Boitiaux, J. P., Chaumette, P., Leporq, S., Menezo, J.C., and Montassier, C., Eur. Patent 380 402, assigned to Institut Français du Pétrole, (1990)

[7] Marecot, P., Barbier, J., Mabilon, G., Durand D., and Prigent, M. Eur. Patent 92 90516-2, assigned to Institut Français du Pétrole, (1992)

[8] Dumas, J. M., Geron, C., Hadrane, H., Marecot, P., and Barbier, J., J. Mol. Catal. 77, 87 (1992)

[9] Menezo, J. C., Hoang, L. C., Montassier, C., and Barbier, J. React. Kinet. Catal. Lett. 46 (1), 1 (1992)

[10] Barbier, J., Dumas, J. M., Geron, C., and Hadrane, H., Appl. Catal. 1990, 67, L1.

[11] Barbier, J., Marécot, P., Del Angel, G., Bosch, P., Boitiaux, J. P., Didillon, B., Dominguez, J. M., Schifter, I., and Espinosa, G., Appl. Catal. A: Gral. 1994,116, 179.

[12] Espinosa G, Del Angel G, Barbier J, Bosch P, Lara V, and Acosta D, J. Mol. Cat. A: Chem., 164, 253 (2000).

[13] Del Angel, P., Dominguez, J. M., Del Angel, G., Montoya, J. A., Lamy-Pitara, E., Labruquere, S., and Barbier, J., Langmuir, 16, 7210 (2000).

[14] Del Angel, P., Domínguez, J. M., Del Angel, G., Montoya, J. A., Capilla, J., Lamy-Pitara, E., and Barbier, J., Topics in Cataysis, 18, 183 (2002).

[15] Haruta, M., Yamada, N., Kobayashi, T., and Iijima, S., J. Catal., 115, 301 (1989).

[16] Haruta, M., Tsubota, S., Kobayashi, T., Kageyama, H., Genet, M. J., and Delmon, B., J. Catal. 144, 175 (1993).

[17] Haruta, M., Catal. Today, 36, 153.L. Vegard, Z. Phys. 5, 17 (1997)

[18] Thorpe, M. F., and Garboczi, E. J., Phys. Rev. B 42, 8405-8417 (1990).

[19] Domínguez, J. M., Simmons, G. W., and Klier, K., J. Molec. Catal. 20, 369 (1983).

[20] B. Ruiz Camacho, M. Torres Rodríguezand O. Solorza-Feria, J. New Mat. Electrochem. Systems12, 043-047 (2009).

[21] G. Vázquez-Huerta, G. Ramos-Sánchez, A. Rodríguez-Castellanos, D. Meza-Calderón, R. Antaño-López, O. Solorza-Feria, Journal of Electroanalytical Chemistry 645, 35–40 (2010)

Design and Manufacture of a PEMFC Stack Using Pd_5Cu_4Pt/C as Cathodic Electrocatalyst

D.C. Martínez-Casillas[1], O.A. Gil-Esquivel[1], J.L. Díaz-Bernabé[1], A. Rodríguez-Castellanos[1], O. Solorza-Feria[1,*]

[1]Depto. Química, Centro de Investigación y de Estudios Avanzados del IPN,
A. Postal 14-740, 07360 México D.F., México.
[*]Tel: 57473715, fax 57473389, mail: osolorza@cinvestav.mx

ABSTRACT

This work presents the design, manufacture and performance evaluation of a PEMFC stack. The Pd_5Cu_4Pt/C cathodic electrocatalyst was synthesized by chemical reduction of $PdCl_2$, $CuCl_2$ and H_2Cl_6Pt with $NaBH_4$ in THF and supported on Vulcan Carbon by ultrasound assistance. The electrocatalyst was physically characterized by X-ray diffraction (XRD) and transmission electron microscopy (TEM). The design of the fuel cell stack was done using AutoCad software. Manufacture of the fuel cell was carried out by CNC router and CNC laser cutter. 8 membrane-electrode assemblies (MEAs) were prepared by spraying the Pd_5Cu_4Pt/C ink on the cathodic side of Nafion® NR 212 membranes. Then gas diffusion layer (carbon cloth) at the cathodic side and commercial electrode (Pt/C E-tek) at the anodic side of the Nafion membrane were placed, followed by hot-pressing of the assembly at 120ºC and 11 kg cm^{-2} for 1.5 min. The PEMFC stack characterization was performed by potenciostatic polarization test. The operation conditions of the stack were: feeding the fuel (H_2) and oxidant (O_2) at room temperature and a pressure of 1 atm, operation temperature varied from 25 to 42 ºC. Open circuit voltage (E_{OCV}) of the stack was around 7 V, obtaining a maximum power density of W_{max}=527 mW cm^{-2}.

1. Introduction

Decreasing of oil reserves as source of energy generation has caused the investigation of alternative energy sources, mainly those from renewable origin. A Polymer electrolyte membrane fuel cell (PEMFC) offers several advantages such as improved energy efficiency and environmentally friendly power source. The main areas of application include transportation, distribution of energy and portable power systems [1]. In a hydrogen-fuelled PEM fuel cell the cathodic oxygen reduction reaction (ORR) is several orders slower than the anodic reaction. Therefore, the ORR dominates the overall performance of such fuel cells. The ORR has been extensively studied and discussed. However this reaction continues being of great interest. Thus, finding a good ORR catalyst is a subject in PEMFC electrocatalysis.

Up to now, Pt and its alloys are the most active and stable electrocatalysts used for the ORR [2]. However, the high price of platinum and its availability on the planet show us the direction that we should follow, i.e. search new catalyst without Pt or with the least possible content of this metal. A recent study shows that Pd_5Cu_4Pt presents a good electrochemical activity towards ORR as well as performance as cathode in a PEMFC [3].

The aim of this work is the design and manufactures a PEMFC stack using Pd_5Cu_4Pt/C as cathodic electrocatalyst and coupling it to a MP4 multimedia player.

2. Experimental

2.1 Electrocatalyst synthesis

The trimetallic electrocatalyst was produced by a $NaBH_4$ reduction of $PdCl_2$, $CuCl_2$ and H_2PtCl_6 in a THF solution as reported in literature [3]. Briefly, a chemical reactor was charged with the metals precursors and THF, maintaining the solution was under stirring. Then, the reducing agent $NaBH_4$ was slowly added. Afterwards, reaction products were washed and then dried at 60 ºC. An ultrasonic probe was used to support the electrocatalyst on Vulcan carbon XRC-72 at 40 wt%. The Pd_5Cu_4Pt, Vulcan carbon and a water-ethylene solution was charged on a reactor where the solution was bubbled during 15 min with N_2. Then, it was sonicated with high intensity ultrasound for 1 hour. Finally, the obtained black powder was washed, dried and kept in a closed vessel prior to physical characterization.

2.2 Physical Characterization

The Pd_5Cu_4Pt/C was physically characterized by X-ray diffraction (XRD) using an X'Pert PRO PW3040 (PANalytical) with monochromatic Cu $K\alpha_1$ radiation (λ = 1.5406 Angstroms) in a 2θ range from 30º to 90º with a step width of 0.2° min^{-1}. Diffraction pattern was analyzed with MDI Jade 5.0 software to determine the average

crystallite size. The electron transmission microscopy (TEM) was used to determine the morphology and particle size. The TEM images were obtained using a Philips CM-200 microscope, operated at 200 kV, equipped with energy-dispersive X-ray (EDX) spectroscopy used to obtain an average local chemical compositions of the sample.

2.3 Design, manufacture and evaluation of the PEMFC stack

The PEMFC stack consists of 8 cells plus an electronic converter to coupling it to the MP4 multimedia player. The design of the stack was executed by AutoCAD software, considering designs previously used in our research group [4-5]. Construction of monopolar, bipolar and end plates were carried out by milling machine through CNC controller. Gaskets, membranes and acrylic pieces were cut by a CNC laser cutter.

Fuel cells are constituted by plates of high density carbon with a thickness of 5 mm, 50 mm wide and 50 mm long. The flow field design of gas to the cathode and anode is shaped cross straight channels. Copper sheets were used as current collector and acrylic plates act as input and output channels for fuel and oxidant. Aluminum end plates, silicone gaskets and stainless steel studs were used. Between each carbon plate there is a membrane-electrode assembly (MEA), a three layered structure, diffusion, catalyst and monomer layers, was used to prepare the MEAs. Figure 1 shows an outline of the stack elements mentioned above from a side view.

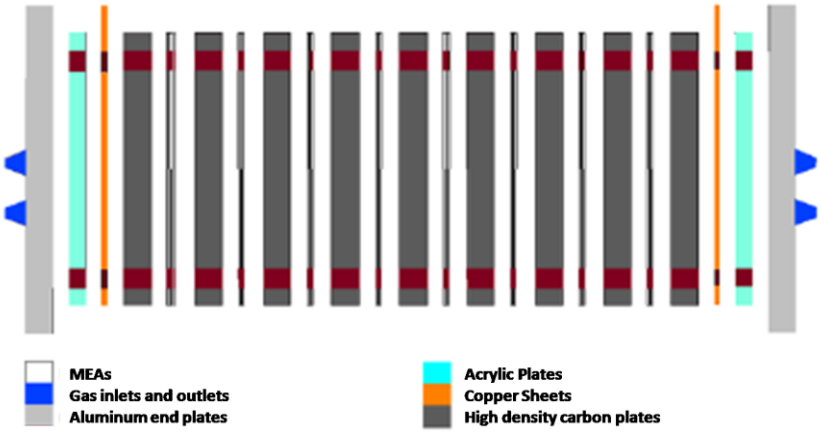

Figure 1. Side view of the PEMFC stack.

Each MEA was prepared by spraying the catalyst ink (Pd_5Cu_4Pt/C 40 wt%) on the cathodic side of the Nafion® NRE-212 (Dupont Fluoro Products) membrane, geometrical electrocatalyst area of 9 cm^2. Then, the gas diffusion layer (porous carbon cloth) at the cathodic side and the commercial platinum carbon cloth (Pt/C, E-TEK, 20 wt% with a loading of 0.5 mg cm^{-2}) at the anodic side of the membrane were placed, followed by hot-pressing of the

assembly at 120 ºC and 11 kg cm^{-2} for 1.5 min. MEAs were inserted into the stack for testing. The performances of fuel cells were determined by potentiostatic polarization in a commercial fuel cell system (Compucell GT, Electrochem 890B). The gas pressures at the anode and cathode side were kept at 1 atm for H_2 and O_2. The fuel cell test station was operated with high purity H_2 and O_2 at 50 cm^3 min^{-1}. Humidification of reactant gases was kept at 25 ºC. Operation temperature varied in the range of 25-42ºC.

2.4 Electronic converter

An electronic DC/DC converter was designed and built in order to regulate the electrical energy generated in the PEMFC stack by a low-drop regulator. The lineal buck converter can operates with input voltages from 5 to 8 V and produce an output voltage of 3.8 V with a variation of ± 0.5 V. Figure 2 shows the power electronics, DC/DC converter.

Figure 2. Power electronics DC/DC converter.

3. Results and discussion

3.1 Physical characterization

The X-ray diffraction of the electrocatalyst synthesized is shown in Figure 3 also the crystalline planes of each metal are indicated. Is observable that the diffraction pattern is shifted from the fcc crystalline phase of palladium (JCPDC card 00-065-2867). A peak at 25 2θ degree indicates the carbon present in the compound. The crystallite size was determined by fitting the diffraction pattern using the software MDI jade 5.0. Estimated average crystallite size of about 9.5 nm.

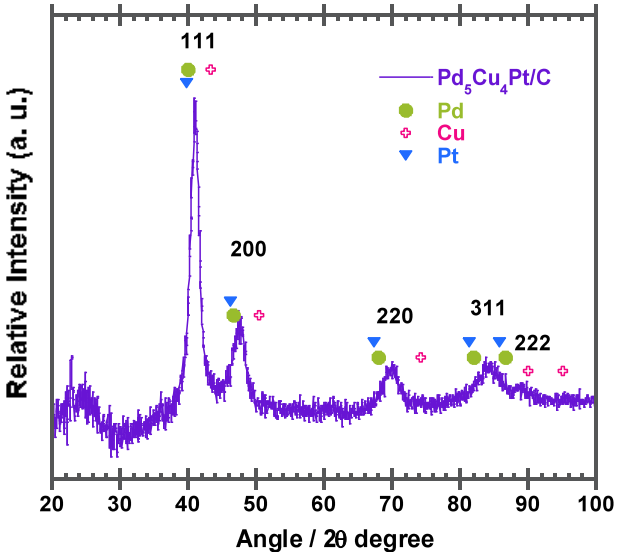

Figure 3. XRD spectra of Pd_5Cu_4Pt/C electrocatalyst.

Figure 4 shows a TEM image of agglomerated particles in nanometric size. It is appreciated that the particles are below 10 nm in size which is in agreement with results obtained from XRD data of Fig. 3. The inset in Fig. 4 shows the corresponding selected area of diffraction patterns. The average composition of the as-synthesized powders, as determined by EDS, was approximately 58 wt% C, 24 wt% Pd, 14wt% Cu and 4wt% Pt, this is in agreement with the expected 40 wt% for the Pd_5Cu_4Pt/C during the supporting technique. Focus on the electrocatalyst average composition was 57 at% Pd, 34 at% Cu and 9 at% Pt, in concordance with the started estimated composition of synthesis.

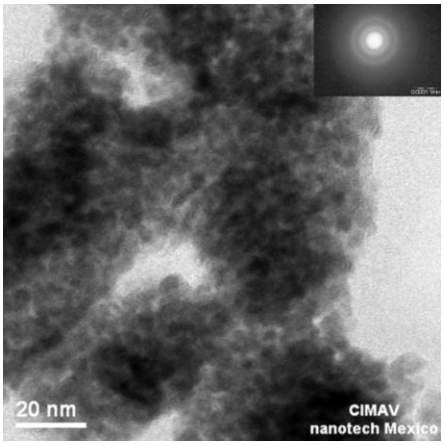

Figure 4. TEM image of the synthesized electrocatalyst. Inset electron diffraction pattern.

TEM mapping images for the Pd_5Cu_4Pt/C electrocatalyst, Fig. 5, shows a uniform elemental Pd, Cu, Pt and C distribution in the particles of the mapped area. Therefore these results agree with those reported for typical electrocatalyst analysis, and suggest that that the Pd_5Cu_4Pt/C nanocrystallite synthesis method is suitable for a cathode catalyst material. The next step was prepared the MEAs as previously reported [3], then assemble the PEMFC stack and characterize its performance.

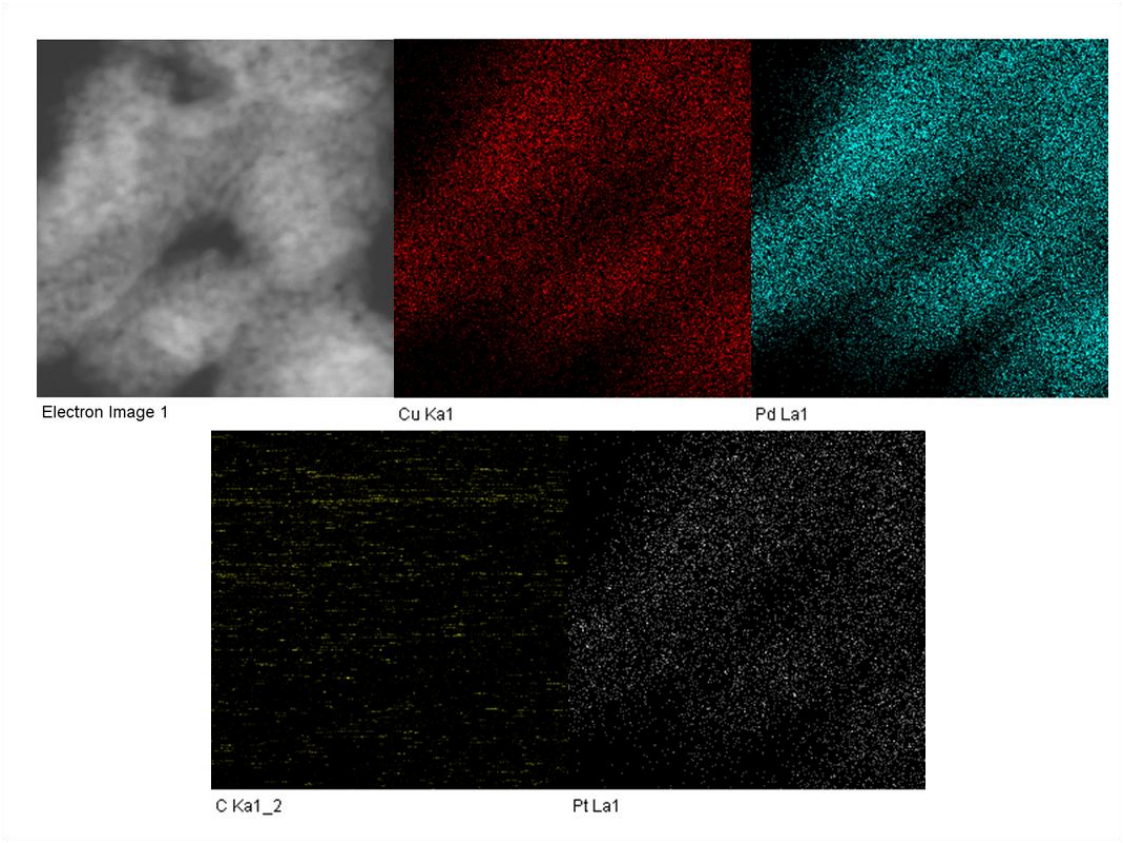

Figure 5. Mapping images of the components of the Pd_5Cu_4Pt/C electrocatalyst.

3.2 Performance of the PEMFC stack

Figure 6 shows the voltage-current response of the fuel cell stack, obtained as described in the experimental section. Can be appreciated an open circuit voltage (E_{OCV}) of the stack was 6.9 V, obtaining a maximum power density of W_{max}=527 mW cm^{-2}. The stack is able to provide the necessary energy to a MP4 multimedia player. In order to test current variations in the stack a curve of current versus time was recorded fixing the voltage at 5 V (maximum voltage required by the MP4). Figure 7 shows a stable response to that voltage for about 1200 min. These results indicate that the stack can be coupled to the electronic converter and finally connected to MP4 multimedia player.

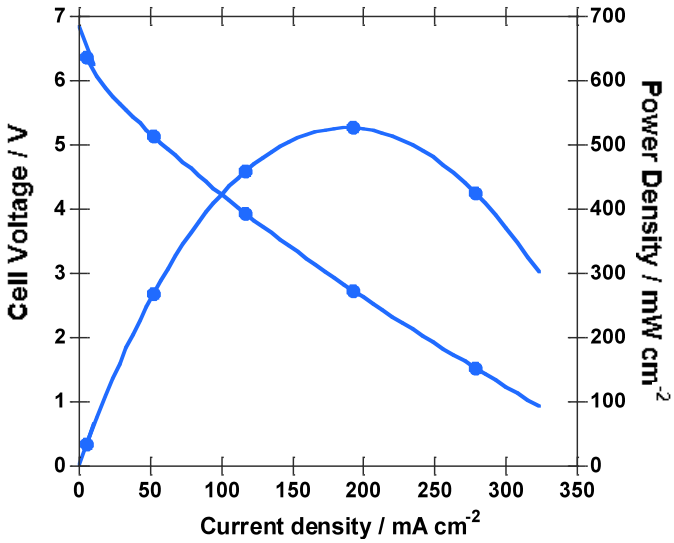

Figure 6. PEMFC stack performance.

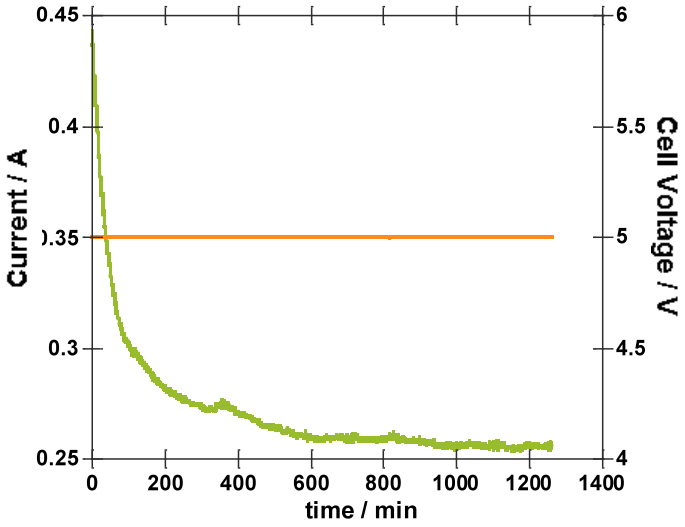

Figure 7. PEMFC stack stability.

3.3 Implementation of the prototype

Figure 8 shows a block diagram of the prototype coupled to the MP4 media player. For the implementation of the prototype two small gas containers were coupled to the cell for H_2 and O_2 storage. Then the gases are feed to the stack by two pumps working at 3V (that voltage can be obtained from the cell) the flows are 200 cc per minute. The

stack is connected to the DC/DC converter in order to regulate the electrical energy obtained. Finally from the converter the MP4 multimedia player is connected to be charged. The final working prototype is shown in Figure 9.

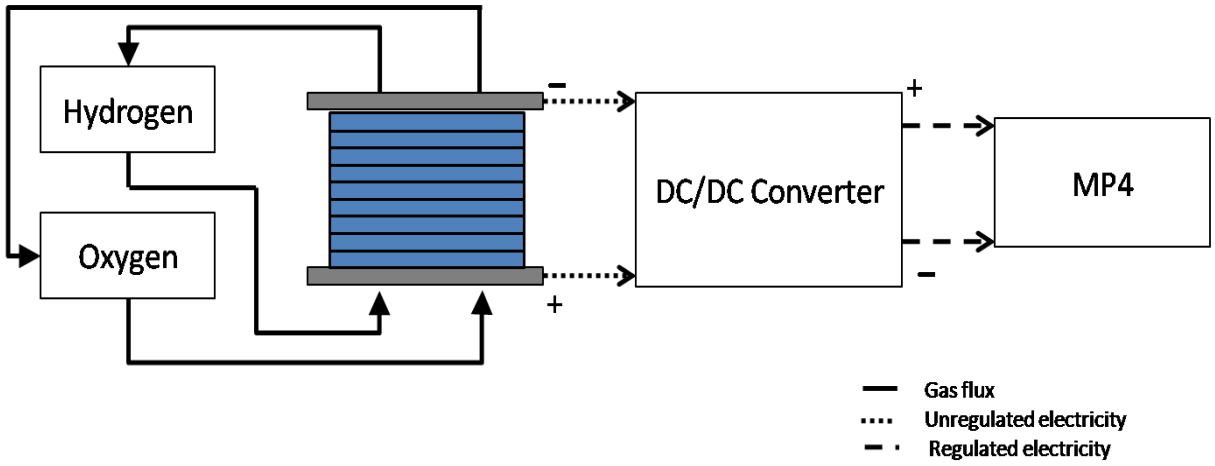

Figure 8. Block diagram of prototype.

Figure 9. Final prototype of PEMFC stack to charge a MP4 media player.

4. Conclusions

The present work shows an easy and effective method of synthesis employed for the preparation of nanometric trimetallic electrocatalyst. Physical characterization indicates the formation of particles with average crystallites around 10 nm in size.

Using the Pd_5Cu_4Pt/C as cathodic electrocatalyst a PEMFC stack was designed constructed. Feeding the stack with high purity hydrogen and oxygen a voltage of 6.9V and a maximum power density of W_{max}=527 mW cm^{-2} were achieved.

The stack was adapted in order to provide the necessary energy to a MP4 multimedia player. This demonstrative prototype is portable and shows that a new electrocatalyst can be used as cathodic electrocatalyst in a real device.

5. Akcnowledgements

We gratefully acknowledge the support of the Mexico's National Council of Science and Technology, CONACyT, under grants 83247 and 101537. DCMC thanks CONACyT for the doctoral fellowship and OAGE for the bachelor fellowship. The authors acknowledge Dra. Virginia Collins Martínez from CIMAV for the TEM measurements.

6. References

[1] A.A. Gewirth and M.S. Thorum, Inorg. Chem., 49, 3557 (2011).
[2] M. Shao, J. Power Sources, 196, 2433 (2011).
[3] D.C. Martínez-Casillas, O.A. Gil-Esquivel and O. Solorza-Feria, J. New Mat. Electrochem. Systems, in press (2012).
[4] A. Rodríguez Castellanos, E. López Torres and O. Solorza Feria, J. Mex. Chem. Soc., 50, 97 (2007).
[5] E. Fuentes Quezada, A. Rodríguez Castellanos and O. Solorza Feria, Proceedings of X Congreso Internacional de la Sociedad Mexicana del Hidrógeno: "Energías Renovables", XSMNH056, ISBN: 978-607-95325-1-2, Toluca México (2010).

Platinum Reduction Study on Pt/C as Electro-Catalysts for PEMFC

L. M. Leal Gámez[1], M. L. Hernández-Pichardo[2,*], R. G. González-Huerta[1], S. P. Paredes-Carrera[2], Jesús Franco-Cruz[2]

[1]IPN-ESIQIE, Laboratorio de Electrocatálisis, UPALM, 07738 D.F. México, D.F.
[2]IPN-ESIQIE, Laboratorio de Investigación de Fisicoquímica y Materiales, UPALM, 07738 México, D.F.
[*]Tel: 57296000, Fax 55862957, mail: mhernandezp@ipn.mx

ABSTRACT

In this work different methods of the platinum reduction were tested, modifying the preparation parameters such as: Pt precursor, reducing agent, and synthesis conditions, in order to find the higher dispersion of the platinum nanoparticles over the support, as well as the optimal particle size. The catalysts were characterized by X-Ray Diffraction (XRD), Scanning Electron Microscopy (SEM), X-ray photoelectron spectroscopy (XPS) and lineal and cyclic voltammetry. The results show that by using NaBH4 as reducing agent the total reduction of the platinum precursor is not possible, and the electrocatalytic activity diminishes significantly, probably due to the formation of NaBO2; whereas the higher activity was found by the reduction with hydrogen at 400 °C. The results of characterization by cyclic voltammetry show that catalyst prepared by photochemical deposition using hexachloroplatinic acid as like precursor of platinum has a high electrochemical activity, stability in acidic medium and a high distribution of the actives sites on the electrode surface. This means that this catalyst is considered as a possible candidate to be used as a cathode in the Membrane-Electrode Assembly (MEA) in a Proton Exchange Membrane Fuel cell (PEMFC).

Keywords: Photochemical deposition , chemical reduction, platinum catalysts.

1. Introduction

Many research efforts on proton exchange membrane fuel cells (PEMFCs) are aiming at the development of catalysts with enhanced electrocatalytic activity and low cost. The most widely used catalysts in PEMFCs are Pt-based nanocomposites, in which Pt nanoparticles are incorporated into carbon support materials. Due to the ease of preparation, impregnation is one of the most commonly used techniques to fabricate catalysts. High-surface-area carbon black can be impregnated with catalyst precursors by mixing the two in an aqueous solution. Following the impregnation step, a reduction step is required to reduce the catalyst precursor to its metallic state. As reduction occurs after the impregnation step, the nature of the support plays a crucial role in controlling particle size [1].

The deposit of the metallic phase on the catalyst surface is a critical step in the synthesis of the catalytic materials. Thus, the development of improved electrocatalysts with higher platinum dispersion is still a challenging issue [1]. It is well known that the catalytic activity of metal nanoparticles depends on their shape and size among others parameters such as the support [2]. Several methods have been employed to obtain Pt/C nanocomposites [1-4], by using different reducing agents such as ethylene glycol [1,3], formic acid [2], hydrazine hydrate [4] and sodium borohydrade solutions [5], among others. In general, it has been found that Pt nanoparticles were uniformly dispersed on the different supports by using this methods of reduction, however, a comparative study of the different reducing agent is lacking. Thus, in this work different methods of the platinum reduction over Vulcan XC-72 were tested, modifying the preparation parameters such as: Pt precursor, reducing agent, and synthesis conditions, in order to find the higher dispersion of the platinum nanoparticles over the support.

2. Experimental

2.1 Electrocatalysts synthesis

The Pt/C electrocatalysts were prepared by the impregnation method using two different precursors, platinum (II) acetylacetonate $Pt(C_5H_7O_2)_2$ and hexachloroplatinic acid $H_2PtCl_6xH_2O$. The platinum solutions were impregnated over Vulcan XC-72 carbon, with a nominal content of 10% wt. Pt. Three reduction methods were used: photochemical deposition (FD), chemical reduction with ethanol (RE) and chemical reduction with sodium borohydride (RQ).

The Pt/C-FD catalysts were prepared by the photochemical deposition of Pt using a UV-vis lamp of 80 W during 3 h. The carbon was dispersed into an ethanol solution of the platinum precursor; the suspension was ultrasonically irradiated with 25 KHz of power during 15 min at room temperature and stirred vigorously by a magnetic stirrer during 1 h. The suspension was poured into the photo-reactor and the sample was irradiated for 3 h. Finally the product was washed and dried at 70 °C by about 2 h.

The catalysts prepared by chemical reduction were synthesized by Pt impregnation by mixing the Pt precursor with the reducing agent (sodium borohydride or ethanol). The solution was stirred with the respective portion of Vulcan

XC-72 carbon during 1 h at room temperature; afterwards the product was washed. Finally, the slurry was filtered and dried at 110 °C for about 2 h.

2.2. Electrochemical measurements

A conventional single three-electrode test electrochemical cell was used in the electrochemical experiments. All of the electrode potentials in this work are related to a normal hydrogen electrode (NHE) in a 0.5 M H_2SO_4 aqueous solution electrolyte. The electrochemical measurements were performed using a Potentiostat (EG&G PAR 263A). All electrochemical experiments were conducted at room temperature. The working electrode was a glassy carbon disk with a 5 mm diameter (0.19 cm^2). Glassy carbon and reference hydrogen electrodes were used as the counter and the reference electrode. The catalytic ink was prepared by dispersing 1 mg of catalyst in 8µL of Nafion® and 60 µL of ethyl alcohol in an ultrasound bath for 15 min. A drop containing 8 µL of catalyst ink was deposited onto the working electrode surface and dried at atmospheric conditions. Cyclic voltammetry (CV) was used to activate the electrodes. The CV measurements were developed in a nitrogen-saturated electrolyte from 0.0 to 1.2 V (NHE) at 50 mV s^{-1} until a steady state voltamperogram was reached; approximately 20 cycles were necessary.

2.3 Physicochemical characterization

Pt and tungsten dispersion and local contents were studied by SEM using a QuantaTM 650 FEG Dual Beam Microscope, Field Emission Scanning Electron Beam. The X-ray diffraction patterns were obtained in a PANalytical X Pert PRO diffractometer fitted with a Cu tube. And the XPS spectra of the catalysts were recorded on a K-Alpha Thermo Scientific 180 apparatus after excitation with a monochromatic Al K radiation. Calibration of the energy position of an XPS peak was performed by using the binding energy of adventitious carbon 1s peak at 284.8 eV.

3. Results and discussion

The synthesized catalysts are described in Table 1. Cyclic Voltammetry (CV) has become a very popular technique for initial electrochemical studies of new system and has proved be very useful in obtaining information about stability in the reaction media and distribution of the actives sites on the electrode surfaces. The cyclic voltammetry characterization of the platinum electrodes was performed in a nitrogen-purged 0.5 M H_2SO_4 solution, at a 50 mV s^{-1} scan rate. In this experiment, the electrodes were submitted to 20 cycles in order to obtain reproducible voltammograms.

Table 1. Catalysts synthesized by different methods.

Catalyst	Pt Precursor	Synthesis Method
Pt/C-FD-AA	$Pt(C_5H_7O_2)_2$	Photochemical deposition (FD)
Pt/C-FD-AH	$H_2PtCl_6xH_2O$	Photochemical deposition (FD)
Pt/C-RE-AH	$H_2PtCl_6xH_2O$	Chemical reduction with ethanol (RE)
Pt/C-RQ-AA	$Pt(C_5H_7O_2)_2$	Chemical reduction with sodium borohydride (RQ)

Figure 1 shows cyclic voltammograms of the samples prepared by photochemical deposition using acetylacetonate (Pt/C-FD-AA) and hexachloroplatinic acid (Pt/C-FD-AH) for comparison purposes. The Pt/C-FD-AH electrode presents definition in adsorption-desorption hydrogen region, which is characteristic in polycrystalline noble metals. Analysis at a more positive potential, corresponding to the anodic region, shows a well-defined hydroxide-adsorbed peak. Cathodic scan shows a reduction potential of the oxides formed during anodic sweep at 0.8 V. On the other hand, the Pt/C-FD-AA catalyst, Figure 1, shows a striking difference in the current magnitude in all potential scan. The Pt/C-FD-AA presents an expected low electrochemically active area in the hydrogen region as well as low oxygen reduction activity. The reduction peak of the oxides formed during anodic sweep shows a high displacement to cathodic potential at 0.65 V. In both catalysts we can observed the shoulder current at around 1V; it is presumably due to the solvent or precursor present into the samples.

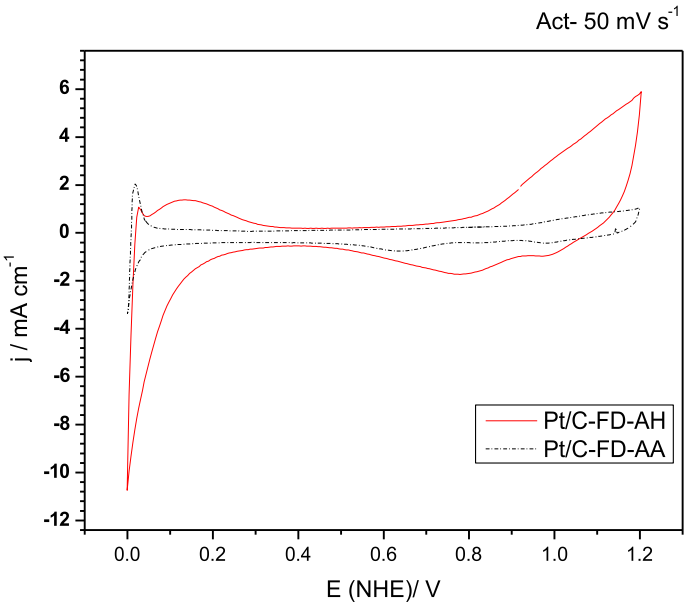

Figure 1. Cyclic voltammetry of Pt/C catalysts prepared by photodeposit using two different precursors, in O_2 free 0.5 M H_2SO_4 solution. Scan rate potential of 50 mVs^{-1}.

Figure 2 presents cyclic voltammograms of the Pt/C-RE-AH catalysts prepared by chemical reduction with ethanol, using hexachloroplatinic acid as like precursor of platinum; the Pt/C-RQ-AA catalysts prepared by chemical reduction with sodium borohydride using acetylacetonate like platinum precursor. The /C-RE-AH catalyst presents low definition in adsorption-desorption hydrogen region, but it shows a hydroxide-adsorbed region. Cathodic scan shows a reduction potential of the oxides formed during anodic sweep at 0.65 V. Pt/C-RQ-AA electrode has no catalytic activity, the current density is low, this electrode not show platinum electrochemical behavior. These catalysts show lower catalytic activity than catalysts synthesized by photo-chemical deposition.

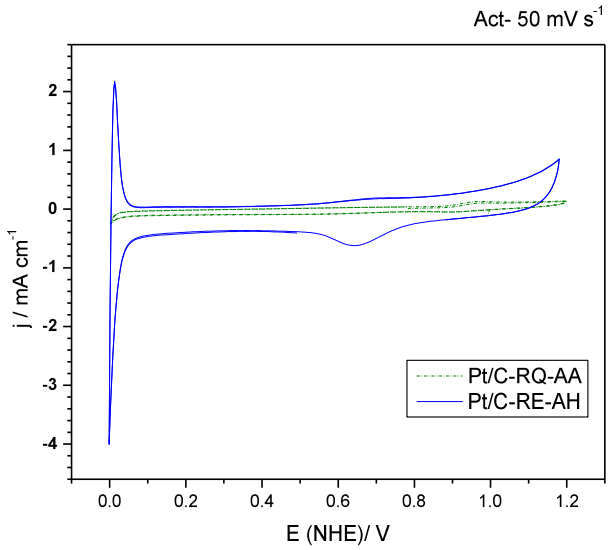

Figure 2. Cyclic voltammetry of Pt/C catalysts prepared by chemical reduction, with ethanol (RE) and with $NaBH_4$ (RQ), in O_2 free 0.5 M H_2SO_4 solution.

The characterization results by XRD are shown in Figures 3 and 4. It is observed that the catalysts prepared by photochemical deposition using hexachloroplatinic acid as well as the catalysts prepared by chemical reduction with ethanol generates a higher reduction of the platinum precursor; while the photochemical deposition with acetylacetonate is not sufficient for the total reduction of the platinum and the signals corresponding to the precursor are still obtained, which could indicates that the reduction of the acetylacetonate probably requires a higher time of irradiation. No picks corresponding to the platinum oxides were observed.

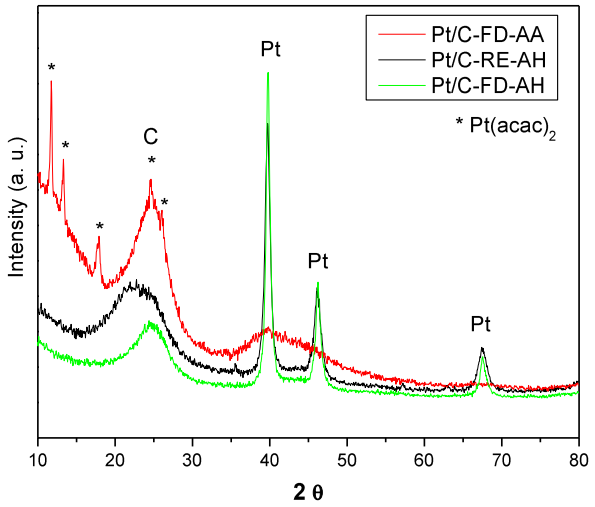

Figure 3. XRD patterns of the catalysts prepared by photochemical deposition (FD) and Chemical reduction with ethanol (RE).

On the other hand, Figure 4 shows the diffractogram of sample prepared by chemical reduction with sodium borohydride (RQ). It is observed that this is the more inefficient method since the only signals observed correspond to the precursor, as well as the reducing agent used ($NaBH_4$).

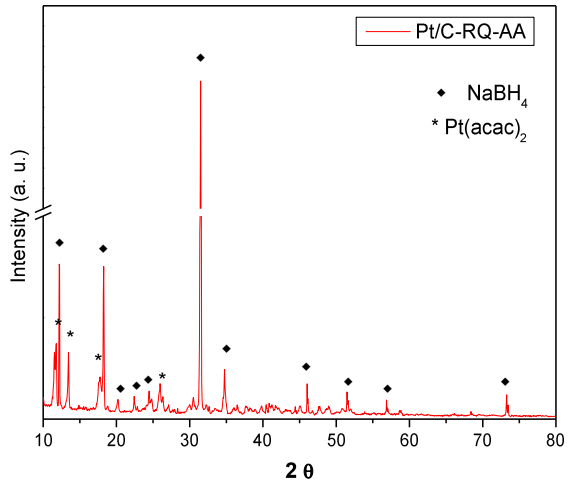

Figure 4. XRD patterns of the catalyst prepared by chemical reduction with sodium borohydride (RQ).

The results of the XPS are shown in Figures 5 and 6. Figure 5 shows a comparison of the three spectra of the samples prepared by the three synthesis methods. It is confirmed that the catalysts prepared by photochemical deposition using hexachloroplatinic acid as well as the catalysts synthesized by chemical reduction with ethanol generates a higher reduction of the platinum precursor as it was observed by XRD, since the peak fitting of the Pt 4f band yielded three components, which centered at 78.6 eV, 76.5 eV, 74.8 eV and 71.2 eV corresponding to platinum (IV), (II) an metallic platinum respectively [1].

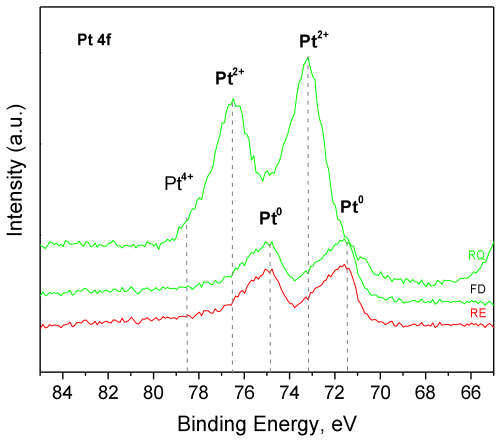

Figure 5. Comparison of the XP spectra of the Pt 4f region of the different catalysts.

Figure 6 shows the individual study of the XP spectra of the three methods. It is observed that all the samples present the three oxidation states indicating an incomplete Pt reduction; however the sample prepared by chemical reduction present a higher concentration of Pt(II) which could correspond to PtO as well as to the not reduced platinum (II) acetylacetonate.

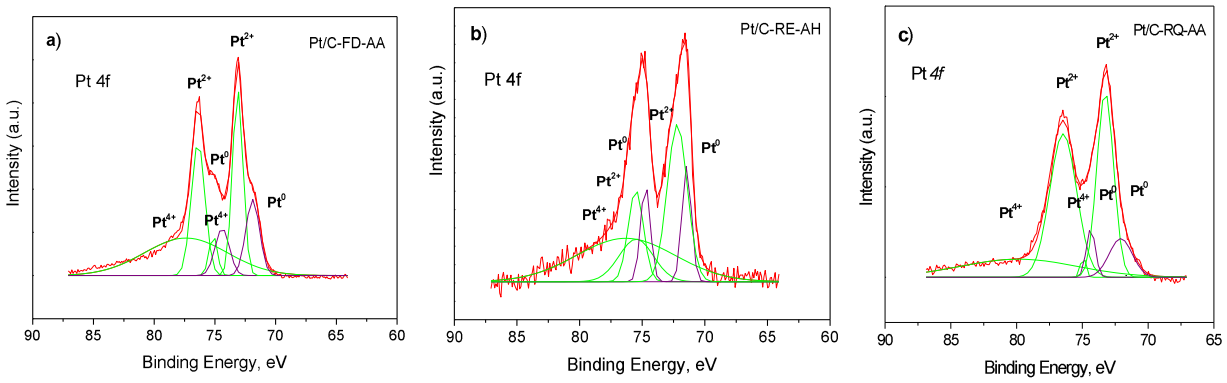

Figure 6. XP spectra of the Pt 4f region of the different catalysts: a) Pt/C-FD-AA, b) Pt/C-RE-AH and c) Pt/C-RQ-AA.

The reduction of platinum is reflected in the $(Pt^{4+}+Pt^{2+})/Pt^{0}$ ratio, it means that a lower ratio indicates a higher content of metallic platinum. Table 2 shows the results of the proportion and evolution of platinum surface nanostructures. It was found that the Pt/C-RE-AH catalyst presented the lower ratio confirming the higher Pt reduction by using this synthesis method.

Table 2. Proportion and evolution of platinum surface species.

Catalizador	Pt(IV)				Pt (II)				Pt^0				Pt^{2+}/Pt^0
	BE* (eV)	%	BE* (eV)	%	BE* (eV)	%	BE* (eV)	%	BE* (eV)	%	BE* (eV)	%	
Pt/C-FD-AA	--	--	--	--	76.3	49.9	73.2	29.6	74.5	5.4	71.9	15.1	3.87
Pt/C-RE-AH	76.3	34.6	75.5	11.3	75.4	11.9	72.2	25.6	74.7	7.6	71.5	8.9	2.27
Pt/C-RQ-AA	--	--	--	--	76.5	51.2	73.2	36.3	74.4	4.2	71.9	8.3	7.00

BE*: Bending Energy (eV).

Finally, Figure 7 shows the SEM study and mapping images for the Pt/C-FD-AH sample, it shows a uniform distribution of elemental platinum. The platinum powder morphology shows a rough surface with agglomerates of well-defined spherical cluster with dimensions of about 50 to100 nm.

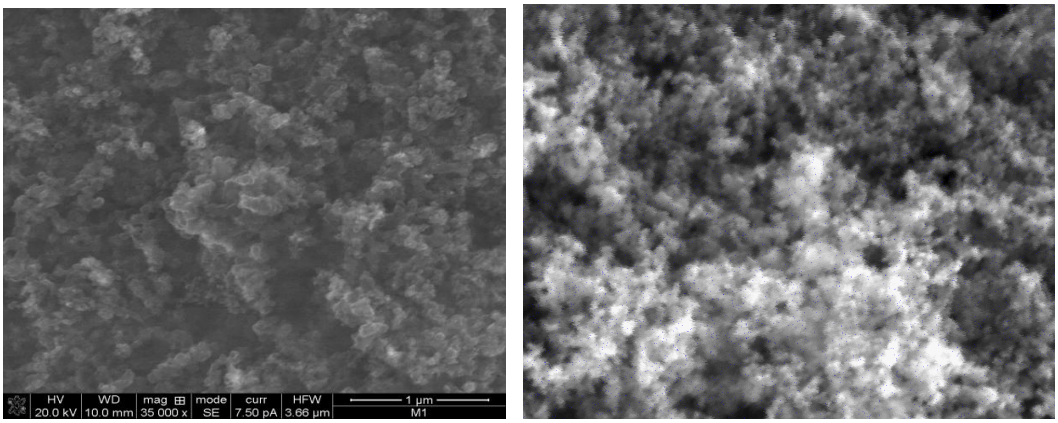

Figure 7. SEM micrographs of Pt/C- AH- FD- catalyst synthesized by the reduction method with ethanol and EDS analysis.

4. Conclusions

By changing the reducing agent and the platinum precursor, four Pt/C catalysts with different Pt morphologies were obtained. The electrocatalytic activities of the Pt/C nanocomposites were studied. It was found that the catalysts prepared by photochemical deposition shows higher catalytic activity than the other catalysts, which can be attributed to the high concentration of metallic platinum and uniform dispersion of the Pt nanoparticles on the carbon surface.

5. Akcnowledgements

This work has been supported by the IPN project SIP- 20120486, SIP-20120475 and multidisciplinary project IPN-SIP 1338. The authors also acknowledge the experimental support of the CNMC-IPN for this work.

6. References

[1] H. Huang, H. Chen, D. Sun and X. Wang, J. Power Sources, 204, 46 (2012).

[2] D.Wang, Y. Liu, J. Huang and T. You, J. Colloid Interf. Sci., 367, 199 (2012).

[3] M. Wang, F. Xu, H. Sun, Q. Liu, K. Artyushkova, E. A. Stach and J. Xie, Electrochim. Acta, 56, 2566 (2011).

[4] E. Yoo, T. Okada, T.Akita, M. Kohyama, I. Honma and J. Nakamura, J. Power Sources, 196, 110 (2011).

[5] J. J. Salvador-Pascual, V. Collins-Martínez, A. López-Ortíz and O. Solorza-Feria, J. Power Sources, 195, 3374 (2010).

Application of $Ru_xmo_ySe_z$ for Oxygen Reduction Reaction in Cathode and Two Anodic Material on the Performance of Two Single Chamber Microbial Fuel Cells

Vázquez-Larios, A.L.[1], Solorza-Feria, O.[2], Ríos-Leal, E[1]., González-Huerta, R. de G.[3], Poggi-Varaldo, H.M. [1,*]

[1] Environmental Biotechnology and Renewable Energy R&D Group, Depto. Biotecnología y Bioingeniería, Centro de Investigación y de Estudios Avanzados del IPN, Apdo. Postal 14-740, 07000 México D.F., México.
[2] Depto. Química, Centro de Investigación y de Estudios Avanzados del IPN, México D.F., México.
[3] ESIQIE del IPN, México D.F., México
*Author for all correspondence: hectorpoggi2001@gmail.com

Key words: anodic material; graphite; internal resistance; microbial fuel cell

Abstract

The objectives of our work were to evaluate *(i)* the application of calcogenide catalyst of the type $Ru_xMo_ySe_z$ for oxygen reduction reaction (ORR) in the cathode, and *(ii)* the effect of the type of the two anodic materials on the performance of two microbial fuel cells (MFCs). A new design of a single chamber MFC-A was built with a plexiglass cylinder, the two extreme circular faces were fitted with PEM-cathode assemblage, *i.e.*, left and right faces. The anode consisted of 65 triangular pieces of graphite filling the anodic chamber. The single chamber MFC-B had a 'sandwich' arrangement anode-PEM-cathode. The cathodes were made of flexible carbon-cloth containing 1mg/cm^2 $Ru_xMo_ySe_z$ catalyst. The cell was loaded with a sulfate-reducing inoculum and a mixed organic substrate. The MFC was characterized by linear sweep potential method. First, each face (left and right) of the MFCs was characterized by separate. The $P_{V\text{-}max}$ values for MFC-A were 1 200 and 1 125 mW/m^3 and those of MFC-B were 43 mW/m^3 for both separate faces. The values of R_{int} obtained were 146 and 167 Ω for MFC-A and MFC-B were 1 612 and 1 397 Ω, respectively. The MFC-A showed higher values of $P_{V\text{-}max}$ by a factor of 22.6 and 18.7. The R_{int} decreased by a factor of 11 and 8 for MFC-A. Parallel connection significantly decreased the internal resistance of the cell and almost doubled volumetric power for both cells. Power derived by cell A with cathode calcogenide catalyst was slightly inferior to that of a similar cell with Pt although the cost of the first catalyst is significantly lower than that of Pt, 90% lower. Finally, application of graphite anode made of small triangular pieces significantly improved the performance of a MFC-A that used $Ru_xMo_ySe_z$ as a cathodic catalyst for ORR.

1. Introduction

Microbial fuel cells (MFC) constitute a promising technology for sustainable production of alternative energy and waste treatment [1]. Platinum has been commonly used as a catalyst of oxygen reduction reaction (ORR) in MFCs. Yet the high cost of an MFC is mainly due to the high price of Pt. This, in turn, deters the commercial MFC applications. So, the development of new materials with high catalytic properties to perform oxygen reduction is presently a task of great importance [2]. One of the actual challenges in microbial fuel cells research consists of the application of new electrochemically active catalytic materials ($Ru_xMo_ySe_z$) [3,4], such as alternate electrocatalysts to replace the extensive use of the more expensive platinum. On the other hand anode materials have been, watch

later in microbial fuel cells in attempts to increase the power output per unit volume of reactor. Several types of materials and shapes have been used, such as carbon paper, graphite plate, carbon cloth, carbon mesh, granular graphite, granular activated carbon, carbon felt, reticulated vitrified carbon, carbon brush, stainless steel mesh [5,6].
The objectives of our work were to evaluate *(i)* the application of calcogenide catalyst of the type $Ru_xMo_ySe_z$ for oxygen reduction reaction (ORR) in the cathode, and *(ii)* the effect of the type of the two anodic materials on the performance of two microbial fuel cells (MFCs).

2. Experimental section

2.1. Microbial fuel cell architecture

A new design of a single chamber MFC-A was based on extended electrode surface (larger ξ, ratio of electrode surface to cell volume) and the arrangement of the anode-PEM-cathode. The cell was built with a plexiglass cylinder, the two extreme circular faces were fitted with PEM-cathod assemblage, i.e., left and right faces. The anode consisted of 65 triangular pieces of graphite (1.4 x 1.8 x 0.5 cm, side x height x thickness) filling the anodic chamber. The single chamber MFC-B had an assemblage or 'sandwich' arrangement of the anode-PEM-cathode [7] The cathodes were made of flexible carbon-cloth containing 1mg/cm^2 $Ru_xMo_ySe_z$ catalyst [3].
On the other hand, the design of a single chamber MFC-C was similar to the MFC-A except that the cathode was made with Toray flexible carbon-cloth that contained 0.5mg/cm^2 platinum catalyst (Pt 10 wt%/C-ETEK), instead of the calcogenide. All the cathodes in both cells MFC-A and MFC-B were in direct contact with atmospheric air on the perforated metallic plate side.

2.2. Model Extract and Biocatalyst

The cells were loaded with 7 ml from a model extract similar to the produced metabolites profile found in the biological hydrogen production from the organic fraction of the municipal solid wastes [8], [9], [10]. The model extract was concocted with a mixture of the following substances (in g/L): acetic acid (1.4), propionic acid (0.3) and butyric acid (0.2) as well as acetone (0.04) and ethanol (0.08) and mineral salts such as $NaHCO_3$ and Na_2CO_3 (3 each) and K_2HPO_4 and NH_4Cl (0.6 each). Organic matter concentration of model extract was ca. 35 g COD/L. The cells were loaded with 143 mL of mixed liquor from a sulphate-reducing, mesophilic, complete mixed, continuous bioreactor. The bioreactor had an operation volume of 3 L and was operated at 35°C in a constant temperature room. The bioreactor was fed at a flow rate of 120 mL/d with an influent whose composition was (in g/L): sucrose (5.0), acetic acid (1.5), $NaHCO_3$ (3.0), K_2HPO_4 (0.6), Na_2CO_3 (3.0), NH_4Cl (0.6), plus sodium sulphate (13.0).

2.3. Electrochemical technical and analytical methods

Potential sweep experiments were carried out at a scan rate of 0.1mV/s from open-circuit cell voltage (E_{OCP}), to the potential final 0.02mV, the potential sweep were performed in a potentiostat/galvanostat Voltalab model PGZ402 [15, 16].

The current (I_{MFC}), power (P_{MFC}), power density (P_{An}), volumetric power (P_V) and coulombic efficiency (η_{Coul}) were calculated as previously described [7].

The COD and VSS of the liquors of sulphate-reducing seed bioreactor and cells were determined according to the Standard Methods [11]. In addition, the individual concentrations of volatile organic acids and solvents in the model extract were analyzed by gas chromatography in a chromatograph Perkin Elmer Autosystem equipped with a flame ionization detector as described elsewhere [12].

3. Results and discussion

First, each face (I and II) of the MFC-A and MFC-B was characterized by separate (Figure 1a,b). Values of $E_{MFC, OCP}$ obtained were 0.591 and 0.593 V for the left and right face (MFC-A), and 0.332 and 0.311 V for the left and right face the cell B, respectively (Table 1). The $P_{V\text{-}max}$ values for MFC-A were 1 200 and 1 125 mW/m^3, the corresponding values in MFC-B were 53 and 60 mW/m^3 for both separate faces, that is, much lower (Table 1). The polarization curves were very close to straight lines; the values of R_{int} were estimated from the slopes of corresponding regression lines as 146 and 167 Ω for MFC-A and MFC-B were 1 612 and 1 397 Ω, respectively.

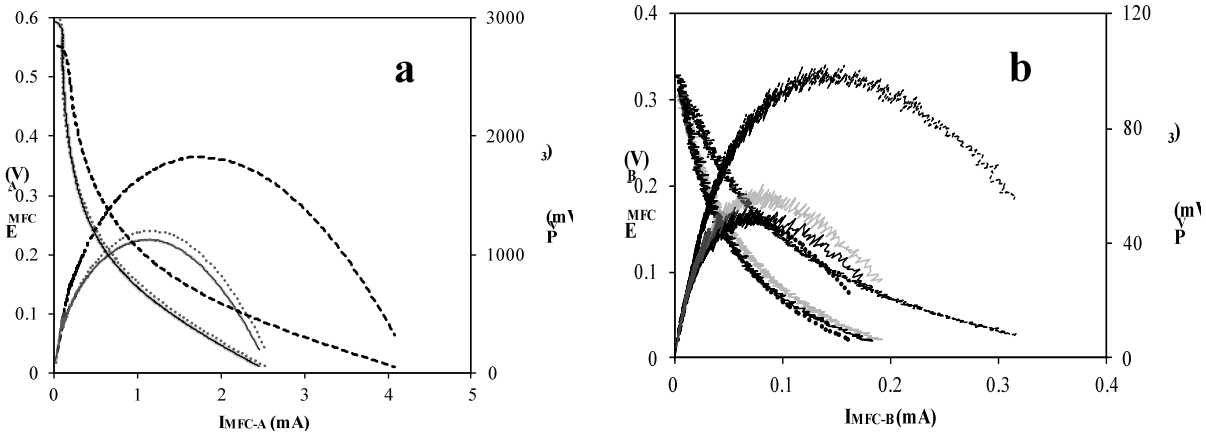

Figure 1. Curves of polarization: (a) MFC-A and (b) MFC-B
(-, face I; -, face II; .., series and --, parallel) and volumetric power (-, face I; -, face II; .., series and --, parallel) of microbial fuel cells using a sulphate-reducing and $Ru_xMo_ySe_z$

The MFC-A with graphite anode made of small triangular pieces showed higher values of $P_{V\text{-}max}$ by a factor of 22.6 and 23.4. The proportion of R_{int} decreased by a factor of 11 and 8 for MFC-A. Parallel connection significantly decreased the internal resistance of the cell and almost doubled volumetric power for FMC-A and MFC-B, respectively. Also, it outstandingly increased the volumetric power efficiently. The $P_{V\text{-}max}$ for MFC-A was comparable with the value reported by Zhong et al. [13]. Thus, our work demonstrated that parallel connection was more appropriate regarding electrochemical characteristics of cells than series connection.

Table 1. Effect of the type of anodic material on cell characteristics MFC-A and MFC-B with different connections of their two faces (electrodes).

Type cell	Type connection	$E_{MFC,OCP}$ (V)	$P_{An\text{-}max}$ (mW/m^2)	$P_{V\text{-}max}$ (mW/m^3)	$I_{MFC\text{-}max}$ (mA)	R_{int} (Ω)
MFC-A Graphite triangular pieces	**Separate faces**	0.591	5.2	1200	2.5	146
		0.593	4.9	1125	2.4	167
	Series[a]	0.628	2.5	1124	2.9	162
	Parallel[b]	0.506	4.1	1829	4.1	69
MFC-B Sandwich electrodes with carbon cloth anode	**Separate faces**	0.332	4.2	53	0.2	1 612
		0.311	4.7	60	0.2	1397
	Series[a]	0.313	1.9	48	0.2	1874
	Parallel[b]	0.308	4.1	102	0.3	820

[a] the two facial electrodes were connected in series; [b] the two facial electrodes were connected in parallel; MFC, new design of single chamber cell; $E_{MFC\text{-}OCP}$, open circuit potential; $P_{An\text{-}max}$, maximum power density; $P_{V\text{-}max}$, maximum volumetric power; $I_{MFC\text{-}max}$, maximum current intensity.

Afterwards, first each face of the MFC-C with the application Pt as a cathodic catalyst for oxygen reduction reaction was characterized by separate (left and right). Second, the MFC-C was characterized with the two faces connected in series and parallel (Figure 2).

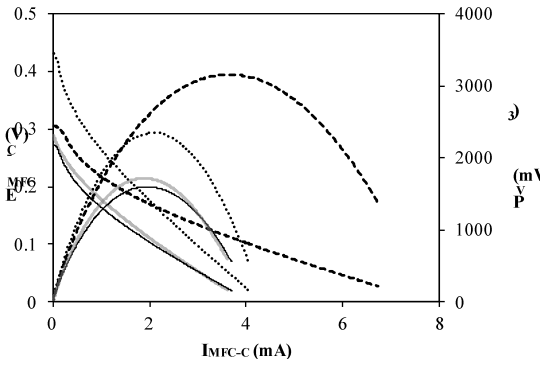

Figure 2. Curves of polarization of MFC-C (-, face I; -, face II; .., series and --, parallel) and volumetric power (-, face I; -, face II; .., series and --, parallel) of microbial fuel cells using a sulphate-reducing and Pt

Values of $E_{MFC,\ OCP}$ obtained from the separate faces were relatively low, 0.276 and 0.325 V for the left and right face, respectively. Series and parallel connection showed potentials 0.432 and 0.309 V, respectively (Table 2). The $P_{V\text{-}max}$ values were 1 600, 1 700, 2 349 and 3 158 mW/m^3 for separate faces, and series and parallel connection, respectively. The corresponding R_{int} were 55, 62, 83 and 33. The $P_{V\text{-}max}$ of separate face electrodes was high and comparable with the value 1010 of mW/m^3 reported by [13]. Parallel connection significantly decreased the internal resistance of the cell (33 Ω) and almost doubled volumetric power (Table 2), likely due to increased current intensity of 4.1 mA. The results for $P_{V\text{-}max}$ for parallel connection can increase the volumetric power significantly. The internal resistance values in this work were in the low side of the range reported in the literature [14].

Table 2. Effect the type catalyst for oxygen reduction reaction in the cathode: MFC-A and MFC-C with different connections of their two faces (electrodes).

Type cell	Type connection	$E_{MFC,OCP}$ (V)	$P_{An\text{-}max}$ (mW/m^2)	$P_{V\text{-}max}$ (mW/m^3)	$I_{MFC\text{-}max}$ (mA)	R_{int} (Ω)
MFC-A						
Calcogenide catalyst	**Separate**	0.591	5.2	1200	2.5	146
	faces	0.593	4.9	1125	2.4	167
	Series[a]	0.628	2.5	1124	2.9	162
	Parallel[b]	0.506	4.1	1829	4.1	69
MFC-C	**Separate**	0.276	7.0	1 600	3.7	55
Pt catalyst	**faces**	0.325	7.5	1 700	3.6	62
	Series[a]	0.432	7.9	2 349	4.0	83
	Parallel[b]	0.309	6.9	3 158	7.0	33

[a] the two facial electrodes were connected in series; [b] the two facial electrodes were connected in parallel; MFC, new design of single chamber cell; $E_{MFC\text{-}OCP}$, open circuit potential; $P_{An\text{-}max}$, maximum power density; $P_{V\text{-}max}$, maximum volumetric power; $I_{MFC\text{-}max}$, maximum current intensity.

The relatively low values of $P_{An\text{-}max}$ obtained in this work could be due lack of acclimation of the inoculum to the new subtrate. The microbial consortium in the sulphate-reducing inoculating bioreactor was acclimated to a substrate that consisted of sucrose and acetic acid, as well as sodium sulfate as electron acceptor. After transferring the inoculum to the MFC, the substrate fed was a model extract that neither contained sucrose nor sulphate (the substrate was a mixture of acetic, propionic and butyric acids as well as acetone and ethanol and mineral salts.) That is, the absence of acclimation to the new substrate could have played a negative effect on MFC performance. Furthermore, the inoculum was not previously enriched for electrochemically-active bacteria (also known as anodophilic or exoelectrogenic bacteria). As it is known, most of these microorganisms are dissimilatory metal reducing microorganisms, and their presence and predominance in the consortia anchored in MFCs are associated to high power outputs [17-20].

4. Conclusion

On the one hand, the MFC-A equipped of anodic triangular graphite pieces showed higher values of $P_{V\text{-}max}$ and significant lower internal resistances than the cell B with sandwich electrodes and anodic carbon cloth.

On the other hand, the power derived by cell A with cathode calcogenide catalyst was 42% inferior to that of a similar cell with Pt (cell C) although the cost of the first catalyst is significantly lower (90%) than that of Pt. The lower power harvested using calcogenide catalyst is easily offset by the savings associated to Pt replacement. Since the cost of Pt is US$ 31.4/g, whereas the cost of Ru is US$ 2.63/g, nearly 80-90% savings in the overall cost of cell construction might be achieved by using the calcognide-based catalyst.

Our results have have demonstrated the promising application of graphite anode made of small triangular pieces on performance of a MFC-A that used $Ru_xMo_ySe_z$ as a cathodic catalyst for oxygen reduction reaction.

5. References

[1] A.L. Vazquez-Larios, O. Solorza-Feria, G. Vazquez-Huerta, F. Esparza-Garcia, N. Rinderknecht-Seijas and H.M. Poggi-Varaldo, International Journal of Hydrogen Energy, 36, 6199 (2011).
[2] M. Mahmound, T. A. Gah-Allah, K.M. El-Khatib and F. El-Gohary, Bioresource Tecnology, 102, 10459 (2011).
[3] K. Suárez-Alcántara, A. Rodríguez-Castellanos, S. Durón-Torres and O. Solorza-Feria. J. Power Sources. 171, 381 (2007).
[4] H.P. Poggi-Varaldo, A.L. Vázquez-Larios, and Solorza-Feria, in Fuel cells, Ed. F.J. Rodríguez-Varela, O. Solorza-Feria, E. Hernández-Pacheco, CreateSpace, USA, p. 123 . Montreal, Canada, (2010).
[5] J. Wei, P. Liang and X. Huang, Bioresource Technology, 102, 9335 (2011).
[6] M.H. Zhou, M.L. Chi and J.M. Luo, H.H. He, ; T. Jin, J. Power Sources, 196, 4427 (2011).
[7] A.L. Vazquez-Larios, O. Solorza-Feria, G. Vazquez-Huerta, F. Esparza-Garcia,E. Rios-Leal,N. Rinderknecht-Seijas and H.M. Poggi-Varaldo, J New Mat Electrochem Systems, 13, 219 (2010).
[8] I. Valdez-Vazquez, E. Ríos-Leal, F. Esparza-García, F. Cecchi, H.M. Poggi-Varaldo, Int. J. Hydrogen Energy, 30, 1383 (2005).
[9]H.M. Poggi-Varaldo, L. Valdés, F. Esparza-García, G. Fer-nandéz-Villagómez, Water Sci. Technol., 35 (2/3), 197 (1997).
[10]R. Sparling, D. Risbey, H. Poggi-Varaldo, Int. J. Hydrogen Energy, 22, 563 (1997).
[11]APHA, "Standard Methods for the Examination of Water and Wastewater", American Public Health Association, Washing-ton DC, USA, 1989.
[12]I. Valdez-Vazquez, E. Ríos-Leal, F. Esparza-García, F. Cecchi, H.M. Poggi-Varaldo, Int. J. Hydrogen Energy, 30, 1383 (2005).
[13] C. Zhong, B. Zhang, L. Kong, A. Xue, J. Ni, J Chem Technol Biotechnol, 86, 406 (2011).
[14] H . Rismani-Yazdi , S.M. Carver, A.D. Christy and I.H. Tuovinen, J Power Sources 180 (2), 683 (2008).
[15] K. Sathish-Kumar, O. Solorza-Feria, R. Hernández-Vera, G. Vazquez-Huerta, H.M. Poggi-Varaldo, J New Mat Electrochem Systems, 15 (3):195 (2012).
[16] K. Sathish-Kumar, O. Solorza-Feria, G. Vázquez-Huerta2, J.P. Luna-Arias, H.M. Poggi-Varaldo, J New Mat Electrochem Systems, 15 (3):181(2012).
[17] A.L. Vazquez-Larios, O. Solorza-Feria, G. Vazquez-Huerta, E. Rios-Leal, N. Rinderknecht-Seijas and H.M. Poggi-Varaldo. J. New Mat. Electrochem. Systems, 14, 099 (2011).
[18] H.J. Kim, H.S. Park, M.S. Huyun, I.S. Chang, M. Kim, B.H. Kim, Enzyme Microb., Technol., 30, 145 (2002).
[19] D.R. Bond, D.R. Lovley, Appl. Environ. Microbiol., 69, 1548 (2003).
[20] G. Reguer, K.D. McCarth, T. Meht, J.S. Nicol, M.T. Tuomine, D.R. Lovle, Nature, 435, 1098 (2005).

6. Acknowledgments

ICYTDF and CINVESTAV-IPN (Mexico) financial support to this research is gratefully acknowledged. The technical assistance of the Environmental Biotechnology and Renewable Energy R&D Group and personnel from the Fuel Cell and Hydrogen Group of CINVESTAV is much appreciated.

7. Appendix

E_{MFC}	voltage output of the cell
MFC	microbial fuel cell
MFC-A	new design of a single chamber microbial fuel cell with triangular pieces of graphite as anode and calcogenide catalyst in the cathode
MFC-B	two-face single chamber microbial fuel cell with two sandwich electrode with calcogenide catalyst in the cathode
MFC-C	single chamber microbial fuel cell with triangular pieces of graphite as anode and Pt catalyst in the cathode
P_{An-max}	maximum power density
PEM	proton exchange membrane
P_{V-max}	maximum volumetric power
R_{int}	internal resistance
SR-In	sulphate-reducing inoculum

Microwave Synthesis of Ru_3Pd_6Pt as Cathode in PEM Fuel Cells

F. Leyva- Noyola*, O. Solorza-Feria.

Departamento de Química, Centro de Investigación y de Estudios Avanzados del IPN.,
Av. IPN 2508, A. Postal 14-740, 07360 México D.F., México.
*fleyva@cinvestav.mx

Abstract

In this work is presented a synthesis and characterization of a nanometric and highly dispersed material. The Ru_3Pd_6Pt was produced by microwaves assisted, using the polyol method. The particle size was approximately 9 nm, obtained by xrd data and estimated by tem micrographics. The kinetic parameters obtained shown that a Ru_3Pd_6Pt is an acceptable candidate by using in PEM fuel cells.

Introduction

Historically, the synthesis methods have involved high temperatures and relative high pressures, a long time for synthesis, was used organic solvents that requires an extraction and purification steps. To date synthesis arises as promising as being able to finalize the process in minutes, achieving an efficient way greatly reduce environmental impact. Because microwave energy can be transferred directly to the reactive species, the reactions can be carried out in shorter times than would normally be by employing other methods.

Experimental

Electrocatalyst preparation

The trimetallic electrocatalyst was produced on a conventional microwave oven by polyol method at 190°C by the reduction of corresponding metallic salts $RuCl_3$ (Aldrich), $PdCl_2$ (Aldrich), and H_2PtCl_6 (Aldrich) in ethylene glycol (EG/Aldrich), as reported in literature.[1-5] The system employed its shown in the *Figure 1*. The reaction product was washed several times with acetone and deionized water. Afterwards, the powders was dried at 50°C for 16h and kept in a closed vessel. The resulted dark-fine powder was used for electrochemical measurements [6].

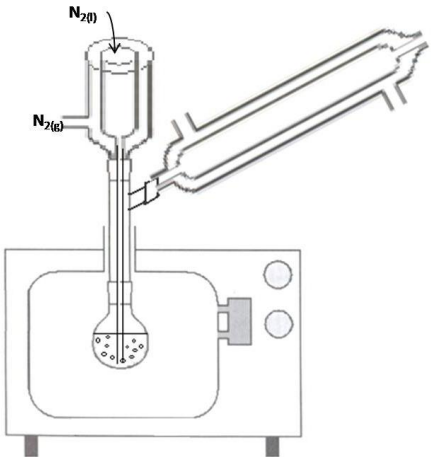

Figure 1. System employed in the synthesis of Ru_3Pd_6Pt

Electrochemical Characterization

Diverse techniques were used to determine the kinetic parameters of the orr on Ru_3Pd_6Pt. Was used the common half cell with three electrodes as working electrode a glassy carbon disc electrode, as counter electrode a platinum mesh and a $Hg_2/Hg_2SO_4/H_2SO_4$ 0.5 M (0.68 V/NHE) as reference electrode. Al measurements are referenced to NHE. The electrochemical surface was determined by the CO_2 stripping technique, at 0.1 V/NHE by the saturation with CO_2 forward by the saturation with N_2. Then rde technique was applied. The hydrodynamic experiments were recorded in the rotation rate range of 100–1600 rpm at 5 mV s^{-1}. All the experiments were performed at room temperature (24°C). Afterward, the corresponding treatment was performed to known the kinetic parameters.

Results and discussion

Physical Characterization

The X-ray diffraction of the Ru_3Pd_6Pt catalyst is shown in *Figure 2.* The powder electrocatalyst showed five diffraction peaks good definite at about 2θ=40°, 47°, 67°, 81° and 87° identified as single hexagonal fcc phase of palladium and in the same range for the single hexagonal fcc platinum. The experimental pattern matches well with the standard crystallographic tables JCPDS cards 01-065-2867 and JCPD 01-065-2868 for Pd and Pt, respectively. The pick on the 43° is attributed to Ru presence. Using Topas Academic Software a particle size was determined around 9 nm.

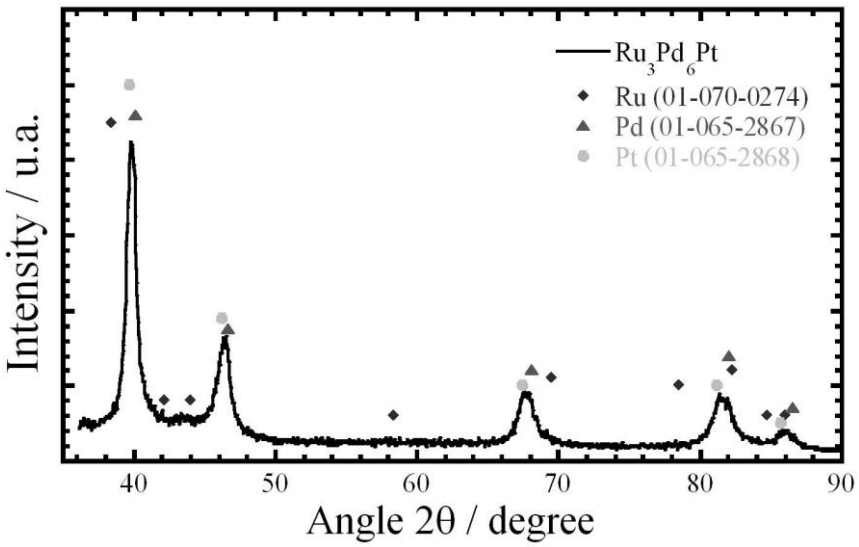

Figure 2. XRD pattern of nanosized particles of Ru_3Pd_6Pt

A transmission electronic micrograph image was shown in a *Figure 3*. A crystalline form immerse in an amorphous part. Analyzing the image in Digital Micrograph 5.0 an estimate of a particle size was determinate around 7 nm with spherical form.

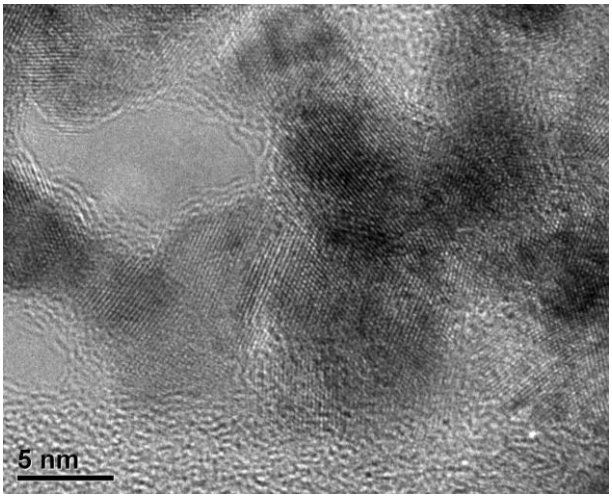

Figure 3. TEM image for Ru_3Pd_6Pt

Electrochemical Characterization

The cyclic voltammetry characterization of the Ru_3Pd_6Pt electrode in the supporting electrolyte was performed in a nitrogen purged H_2SO_4 0.5 M solution, at $100mVs^{-1}$ scan rate. In this experiment the electrode was submitted to 30 cycles in order to obtain a reproducible voltammogram. *Figure 4* presents a corresponding

voltammograms on Ru_3Pd_6Pt oxygen atmosphere that no shows good-definite peaks associated with adsorption/desorption of hydrogen characteristic in polycrystalline noble metals.

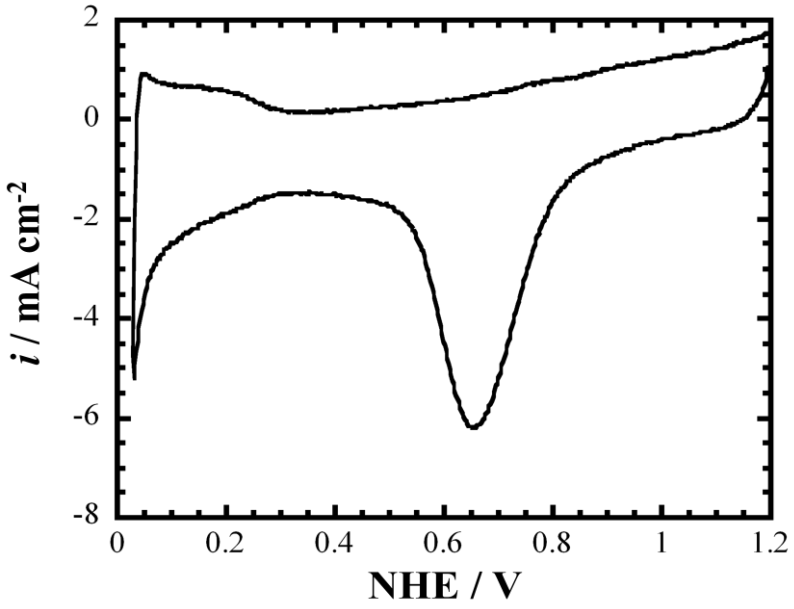

Figure 4. Voltammogram on Ru_3Pd_6Pt in H_2SO_4 0.5 M at room temperature, in oxygenated atmosphere. *v*=100 $mVs^{-1.}$

The CO_2 stripping on Ru_3Pd_6Pt as shown in a *figure 5*. Obtained at 0.78 V/NHE the scan rate was 20 mV s^{-1}. On the *figure 6* is presented a voltammograms obtained after and before de CO_2 stripping technique. Is observed that the characteristic shape no change, that is a good indicator that the material is CO_2 resistant. The area was estimated around a 1.445 cm^2 with a R_f=11.5.

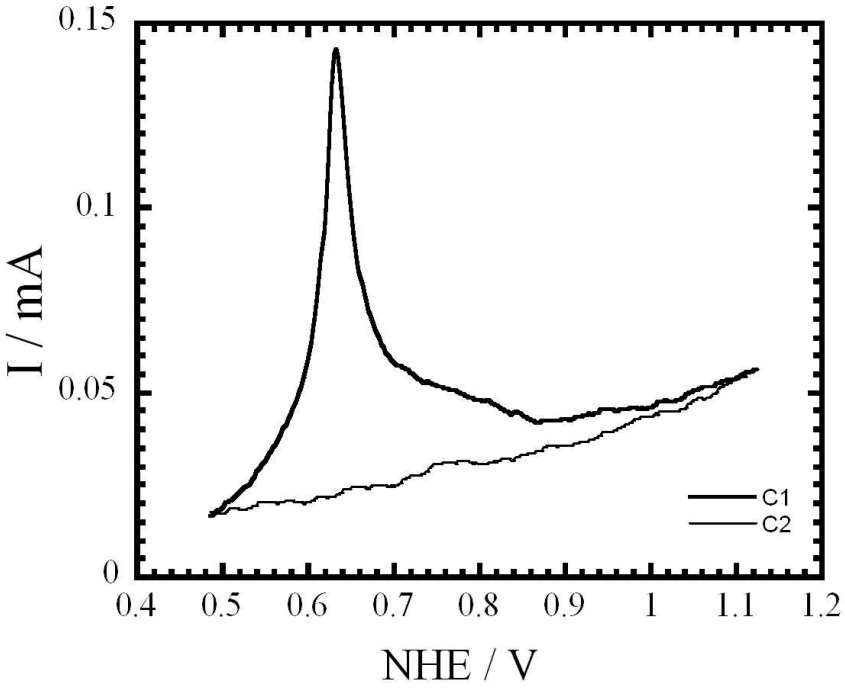

Figure 5. CO_2 stripping on Ru_3Pd_6Pt at room temperature, E=0.78 V. v=20mv s^{-1}.

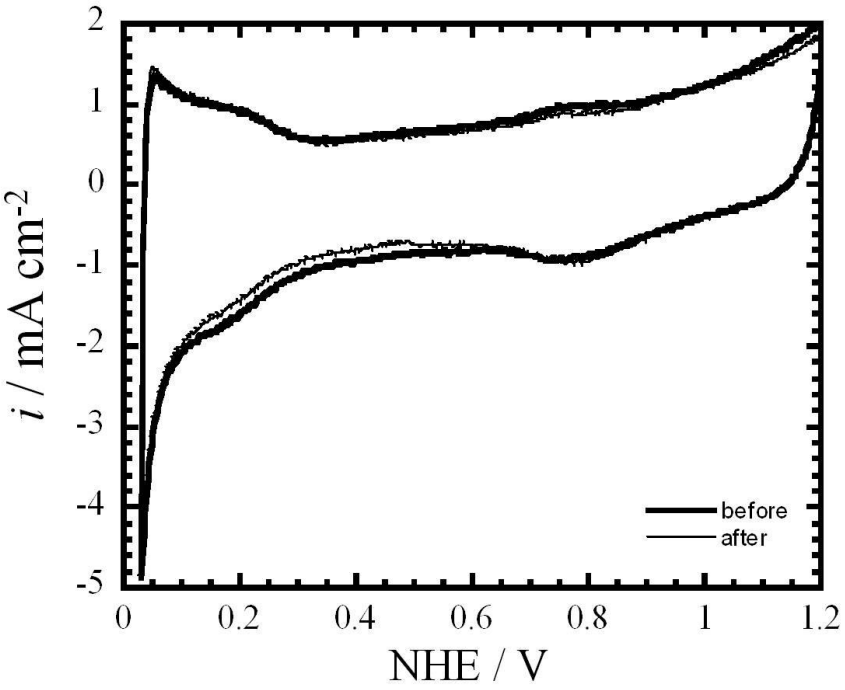

Figure 6. Ciclic Voltammograms on Ru_3Pd_6Pt, in N_2 , before and after the CO_2 stripping. v=100 mv s^{-1}.

Afterwards, the edr was obtained and is shown in the Figure 7. The clasic shape are present in this graphics, the kinetic zone, the difussional and the mixed control was observed. The *figure 8* presents a tafel graph obtained from the analysis of rde. Is observed that the material exhibit a good activity to catalyze the orr on acid media.

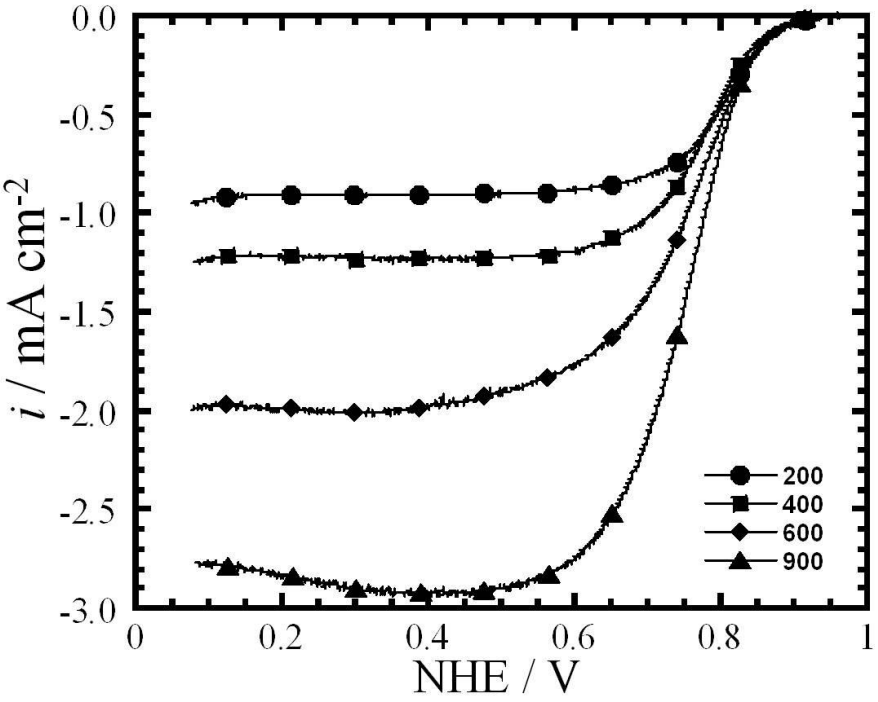

Figure 7. rde graph for orr on Ru_3Pd_6Pt, at room temperature. v =5 mv s^{-1}.

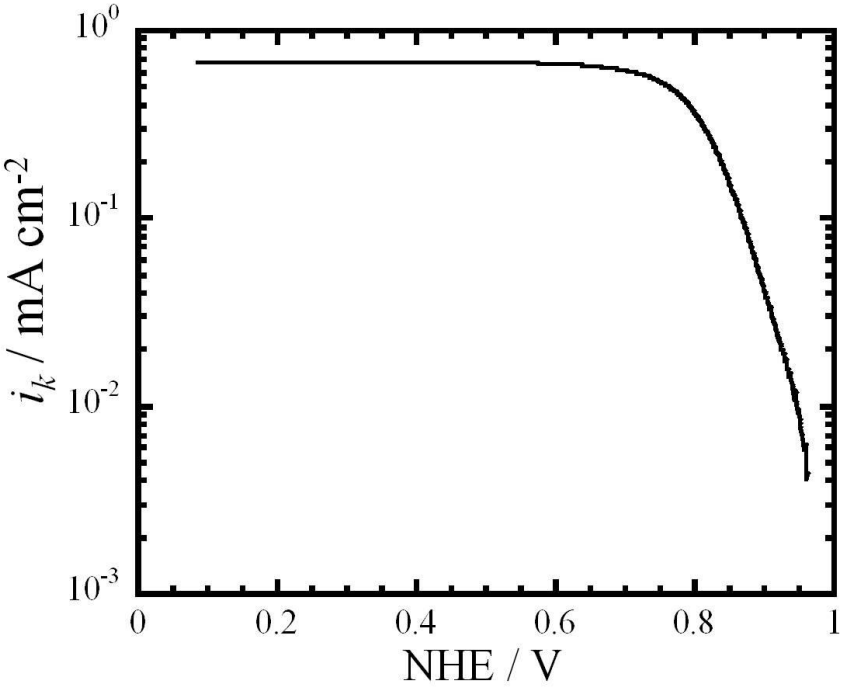

Figure 8. A Tafel plot of Ru_3Pd_6Pt for the orr on H_2SO_4 0.5 M at room temperature.

Conclusions

The kinetic parameters were obtained from the tafel plot. The open circuit potential that exhibit this material was 0.95 ± 0.02. the area calculated from the CO_2 stripping determined from the figure 5 was 1.445 cm^2, tafel slope (-*b*), current density exchange (i_0) and α parameter, was 0.56 ± 0.09 mV dec^{-1}, (9.07 ±1.3) x10^{-5} mA cm-^{2}, respectively. The Ru_3Pd_6Pt material is candidate to be considered as cathodic catalyst for polymer electrolyte membrane fuel cell (pemfc).

Acknowledgements

The autors acknowledgement to CONACyT by the support. FLN acknowledgement to CINVESTAV by the doctorate grand, to Dr. Hector Calderon by the TEM micrographies, to Mr. Tavira by the X-ray diffraction pattern.

References

[1] Y. N. Wu, *J. Power Sources,* **194** (2009) 805–810.

[2]W. Hong, D. Rui, C. Hsin, L. Ching, C. Yui; *Mater. Lett*., **61** (2007) 830.

[3]G. Zhao, J. He, C. Zhang, J. Zhou, X. Chen, T. Wang; *J. Phys. Chem. C,* **112** (2008) 1028.

[4]J. Zhao, P. Wang, W. Chen, R. Liu, X. Li, Q. Nie; *J. Power Sources*, **160** (2006) 563.

[5] P. Ochal, *J. Electroanalytical Chemistry,* **655** (2011) 140.

[6] D.C. Martínez, O. Solorza, *J. Power Sources,* **196** (2011) 4468.

Remediation of a Soil Contaminated with Lindane in an Electrobiochemical Slurry Reactor

B. Camacho-Pérez[1], O. Solorza-Feria[2], E. Ríos-Leal[3], P. A. Vazquez-Landaverde[4], J. Barrera-Cortés[5], M.T. Ponce-Noyola[6], J. Garcia-Mena[7], N. Rinderknecht-Seijas[8], H.M. Poggi-Varaldo[1,*]

[1]Environmental Biotechnology and Renewable Energies R&D Group, Dept. of Biotechnology and Bioengineering, CINVESTAV del IPN, P.O. Box 14-740, 07000 México D.F., México; [2]Dept. of Chemistry, ibídem; [3]Central Analítica, ibídem; [4]CICATA-IPN, Qro., México; [5] Control inteligente de Procesos, ibídem; [6]Microbial Genetics Group, ibídem; [7]Dept. of Genetics and Molecular Biology, CINVESTAV del IPN; [8]ESIQIE del IPN, Mexico D.F., México.
*Author for all correspondence: hectorpoggi2001@gmail.com

ABSTRACT

Lindane is a chlorinated pesticide known for its toxicity and persistence in the environment. Recently, it has been proposed that soil microbial fuel cell technology (SMFC) could be applied to enhance the removal of organic matter, phenol, and petroleum hydrocarbon in contaminated soil with simultaneous electricity output. Yet, there is no information on the application to remediation of soils polluted with pesticides. The purpose of this research was to evaluate the biodegradation of lindane with simultaneous electricity generation in an electrobiochemical slurry reactor (EBCR). The EBCR was inoculated with a sulfate reducing inoculum acclimated to lindane, characterized, and further batch operated for 30 day at room temperature. No external carbon source was supplemented in the experiment 1; the substrate was the soluble natural organic matter (NOM) of the soil. In the experiment 2 the EBCR was supplemented with a stock solution of sucrose: sodium acetate: lactate to give a final concentration of 2g COD/L in the reactor. Results from electrochemical impedance spectroscopy characterization in the EBCR (Experiment 1) showed that the equivalent circuit had an anodic resistance R_1=2064Ω, cathodic resistance R_3 = 192 Ω; and electrolyte/membrane resistance R_2 = 7Ω, totalling a relatively high overall internal resistance R_{int} of 2263Ω. During the batch operation, the EBCR showed a 30% lindane removal efficiency along with a maximum volumetric power volumetric of 165 mWm^{-3}. This value compared favorably with results corresponding to sediments microbial fuel cells that are used to power weather monitoring systems. The organic matter removal was very high (72% as soluble COD, NOM) whereas the coulombic efficiency was low (5.4%). The latter, although, was higher than values reported for microbial fuel cells that degraded leachate-like effluents. In Experiment 2 of the EBCR both cell characteristics and performance significantly improved. The internal resistance as determined by polarization curve was 102Ω when the connection was in parallel. During the batch operation, the EBCR showed a 78% lindane removal and a maximum power volumetric of 634 mWm^{-3}, the organic matter removal was 76% and coulombic efficiency was 15%. Finally, it can be concluded that our EBCR showed a high lindane removal capability.

Keywords: Electrobiochemical slurry reactor, lindane, soil remediation, sulphate reducing

1. Introduction

The widespread use of pesticides has lead to pollution of soil, water bodies and aquifers, and atmosphere [1, 2]. The γ-hexachlorocyclohexane (γ-HCH; also called lindane) is a highly halogenated organic pesticide that has been used

worldwide, particularly in Mexico, in spite of its banning in first world countries [3]. Lindane has been used for crop protection and prevention of vector-borne diseases for many decades [4-7]. Negative impacts of lindane on the environment and human health have been reported worldwide [8]. Due to their hydrophobicity, lindane is tightly bound to the organic matter and clay of soils. This, in turn, decreases their bioavailability. It is commonly recognized that mass transfer of HCH from soil to liquid phase is the limiting process in biodegradation processes used for soil bioremediation [9, 10]. Bioavailability of HCH in polluted soils could be increased by using slurry bioreactors (SB). SB is an ad situ soil bioremediation technology that allows the adjustment and optimization of several process variables such as mixing and water addition, nutrient supplementation, addition of surfactants and solvents to increase pollutant desorption from soil, temperature and pH control, bioaugmentation (seeding the bioreactor with microbial strains or consortia acclimated or specialized in pollutant degradation), etc., with the purpose to increase mass transfer, foster biodegradation and decrease treatment time [11-13]. On the other hand Microbial Fuel Cell (MFC) is a promising technology for the biodegradation of several organic substrates and wastes such as glucose, acetate, xylose, cysteine, cellulose and organic pollutants with simultaneous power generation [14-19]. In this device the microorganisms oxidize different substrates at the anode producing protons and electrons, which flow through an external circuit to the cathode that is in contact with oxygen, in this part the protons are used in the reduction of oxygen producing water [20-22]. Recently, it has been proposed that soil microbial fuel cell (SMFC) technology could be applied to enhance the removal of organic matter, phenol, and petroleum hydrocarbon in contaminated soil and simultaneous electricity output [17-18]. The purpose of this research was to study the biodegradation of lindane and simultaneously electricity generation using an electrobiochemical slurry reactor (EBCR) for the remediation of a polluted, heavy soil.

2. Experimental

2.1 Chemicals

γ- HCH isomer (97 % purity) was purchased from Sigma-Aldrich. Lindane is a moderately lipophilic, organo-chlorinated substance characterized by a high partition coefficient octanol-water Kow ≈ 4*103, with low solubility in water, approx. 7 mg/L at 20ºC, and slightly polar due to the strong electronegative effects of chlorine atoms bound to the aliphatic ring. Chlorobenzene (CB), dichlorobenzene isomers (1,2-DCB, 1,3-DCB) and 1,2,4 trichlorobenzene (99–99.9% purity) , hexane and acetone were of analytical grade.

2.2 Lindane and metabolite analysis

Lindane was analyzed by Headspace-Solid Phase Microextraction-Gas Chromatography- Electron Capture Detector (HS-SPME-GC-ECD). The procedure for the extraction of HCH residues in the soil slurry reactor was performed according by Quintero *et al.* [23]. The intermediate metabolites in the experiment 1 were analysed in an Agilent Technologies GC/MS with an autosampler Gerstel (MPS-2 Twister), the oven temperature were programed as follows: hold time 40°C, 2 min; ramp rate at 3°C/min to 180°C; ramp rate at 8°C/min to 270°C. The injection volume was 1µl via a split-less injection at 280°C. Helium was used as a carrier at a flow rate of 1.0ml/min. The intermediate metabolites in the experiment 2 were analyzed in a Perkin Elmer gas chromatograph equipped with an electron capture detector. Selected samples of EBCR (experiment 2) were analyzed in a Perkin Elmer GC-MS, the oven temperature were programed as follows: hold time 40°C, 6 min; ramp rate at 3°C/min to 180°C; ramp rate at 10°C/min to 300°C. The injection volume was 1µl via a split-less injection at 250°C. Helium was used as a carrier at a flow rate of 1.0ml/min.

The soil pH was determined in a slurry soil/deionized water 1:2 (w/w) [10], soil texture was measured by the hydrometer method, biochemical oxygen demand (BOD) was estimated according to the Standard Methods (Method 507) and organic matter content was estimated by the method of oxidation with $K_2Cr_2O_7$ [24]. In sulphate reducing seed reactor (Table 1) were determined: pH, sulphate, organic matter content such as COD and biomass according to the Standard Methods (methods 423, 426C, 508, and 209E respectively; 25). The alkalinity was analysed according to Poggi-Varaldo and Oleszkiewicz [26].

Table 1. Performance of sulphate reducing seed reactor used for inoculation of electrobiochemical slurry reactor

Parameter	
Lindane (%)	76.36± 15.2
pH (-)	7.55 ± 0.25
COD (%)	52.87 ±18.24
Biomass (mg VSS/L)	1469.11 ± 674.269
Factor α (–)	0.17 ± 0.10
Sulpate(%)	76.81± 20.48

2.3 Soil

An agricultural soil with high contents of organic matter and clay (Table 2), contaminated with a dose of 100 mg lindane/kg dry soil.

Table 2. Main physico-chemical characteristics of mineral agricultural soil used in this work

Parameter	
Source	Huajuapán de León, Oaxaca
Type	Cambisol
pH	7.31 ± 0.06
Organic matter (%)	8 ± 0.09
COD (mg COD/kg dry soil)	5100 ± 436
BOD (mg BOD_5/kg dry soil)	3725 ± 353
Clay (%)	43 ± 0.79
Sand (%)	37 ± 2.70
Silt (%)	21 ± 3.33
Texture	Clayish
Hydraulic conductivity	Low to moderate

2.4 Electrobiochemical slurry reactor

The EBCR consisted of a Plexiglass cylinder approximately 6 cm in diameter and 8 cm in height (308 mL capacity), the anodes used in this experiment were graphite discs (5cm D x 0.5 cm) and the cathodes were of Toray carbon cloth, the cathodes were in contact with atmospheric air (Figure 1). The electrodes were separated by a cation exchange membrane (Nafion 117, coated with 0.5 mg/cm2 platinum catalyst, Pt 10wt%/C-ETEK) and was inoculated with a sulfate reducing inoculum acclimated to lindane [27].

2.5 Experimental design

2.5.1 Experiment 1

The EBCR was batch operated for 30 day at room temperature. The concentration of soil was 66%. No external carbon source was supplemented; the substrate was the soluble natural organic matter of the soil (NOM). Measurements of the power output were performed using a Multimeter ESCORT 3146A.

2.5.2 Experiment 2

The EBCR was batch-operated for 30 day at room temperature. The concentration of soil was 33% w/v. The EBCR was fed a solution stock of sucrose: sodium acetate: lactate to give a final concentration of 2g COD/L in the EBCR at 15 y 25d. The mix was with nitrogen the first 15 days, afterwards mixing was performed in a shaker at 100 rpm. Measurements of the power output were done using a Multimeter ESCORT 3146A. The process controls were EBCR under open-circuit and non-EBCR conditions as the biotic control and abiotic control respectively.

2.6 Determination of internal resistence of the electrobiochemical slurry reactor

2.6.1 Electrochemical impedance spectroscopy in the experiment 1

The internal resistance (R_{int}) of EBCR was calculated as a function of cell voltage using electrochemical impedance spectroscopy (EIS). The electrochemical impedance spectra were recorded over a frequency range of 1 mHz to 100 kHz [28-30], equivalent circuit models were fitted to the data using the program of ZView2.

2.6.2 Polarization curve method in the experiment 2

The internal resistance of was determined using the polarization curve method, by varying the external resistance ($100\text{-}10^5\Omega$) according to procedures suggested by Logan *et al*. [20], Poggi-Varaldo *et al*. [21], Vázquez-Larios *et al*. [22], Sathish-Kumar *et al*. [31], this was carried out 0d y 7d of operation.

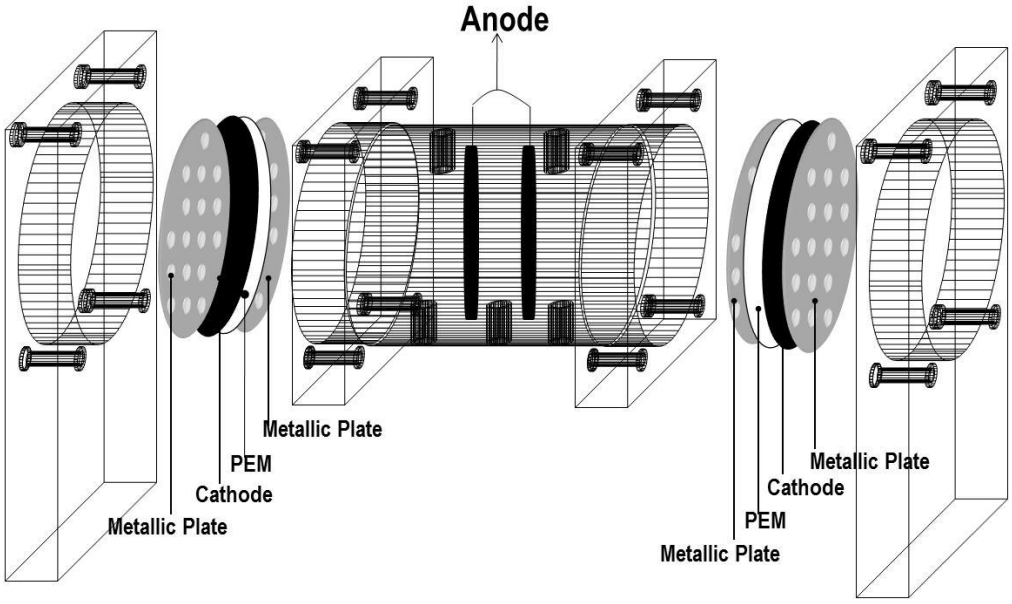

Figure 1. Schematic diagrams of electrobiochemical slurry reactor

3. Results and discussion

3.1 Experiment 1

3.1.1 Determination of internal resistance

Internal resistance is an important factor in the characterization of MFCs, because when an MFC is operated with an external resistance under an external resistance equal to its internal resistance will result a maximum value of power. Results from experiment showed that the equivalent circuit obtained from the Nyquist plot (Fig. 2) had anodic resistance R_1=2064 Ω, cathodic resistance R_3 = 192 Ω; and electrolyte/membrane resistance R_2 = 7 Ω; so the total internal resistance was 2263 Ω. Compared with microbial cell with matrix of soil, this value is lower than 10 kΩ reported by Ringelberg *et al*. [32]. They [32] worked with a cylinder (2.2cm X 10cm, D X h) as the reactor, a non-contaminated soil with texture silt loam with organic content of 11.1%, whereas the anode was carbon cloth with 16 cm^2 of surface area and the cathode was carbon cloth coated on one side with 0.5 mg Pt/cm^2. On the other hand, our internal resistance was higher than that reported by Wang *et al*. [18] and Huang et al. [17]. The former worked with a U-tube air-cathode soil MFC and a soil with texture was silt loam, the anode and cathode (connected in parallel) where carbon mesh, the cathode was coated with 0.1 mg/cm^2Pt. They reported an internal resistance of 1 000 Ω. Their soil had 28.3 3 g total petroleum hydrocarbon/kg of soil. They also observed a pollutant removal of 15% in 25 days of batch operation. On the other hand Huang *et al.* [17] found an internal resistance of 100 Ω in a system used to phenol from waterlogged soil. The paddy soil (phenol, 80mg/L) was covered with 3.0 cm of water, the anode was a layer of carbon felt (15.0cm ×12.5cm × 0.5cm) and cathode was GORE-TEX cloth (15.0cm × 12.5cm), coated with Ni-based paint (7.0g) and Pt/C solution mixed with Nafion (0.094g). Phenol removal was 90.1% in 10 days. This relatively high result could be ascribed to the fact that phenol is not strongly sorbed on to soils and can be degraded by a great variety of microorganisms and its toxicity is quite relative. In contrast, lindane is known to be very recalcitrant, toxic, and hydrophobic [7, 10].

3.1.2 Perfomance of the electrobiochemical slurry reactor

The electricity generation reached a voltage output of approximately 330 mV at 7 days (Fig. 3, table 3), power density normalized with the anode 6.6 mW/m^2 and volumetric power 165 mW/m^3. The voltage remained constant until day 20, it is low at 240mV. The organic matter removal was very high (72% as soluble COD, NOM) whereas the coulombic efficiency was low (5.4%).

3.1.3 Lindane removal and intermediate metabolites

The EBCR showed lindane removal efficiency 30%; after 30 d operation metabolites from lindane degradation/transformation were not detected (Figure 4)

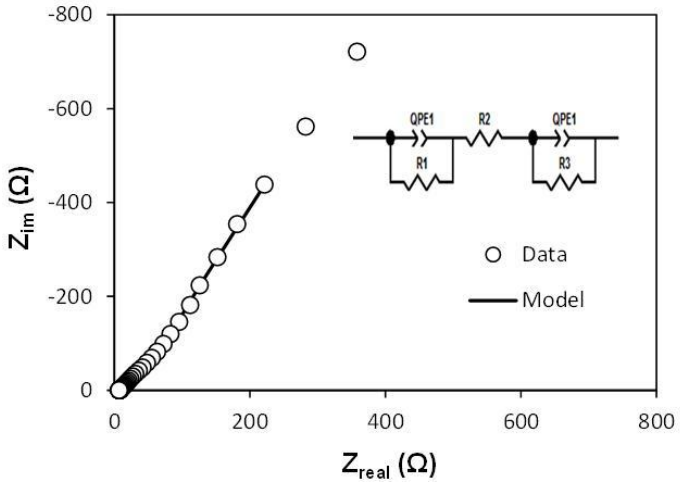

Figure 2. Nyquist plot and equivalent circuit in the Experiment 1

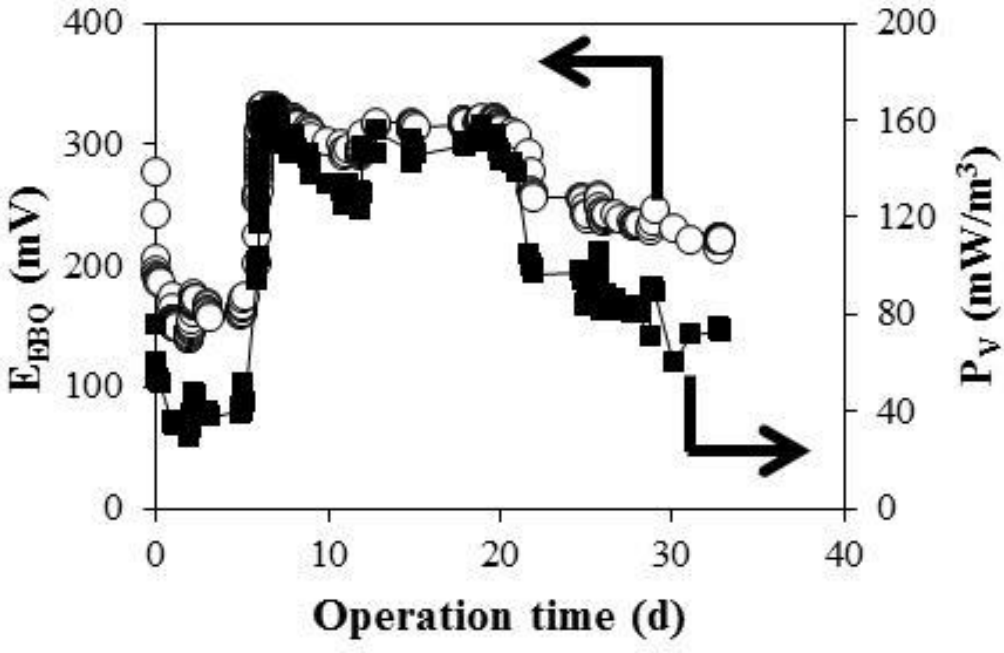

Figure 3. Electricity generation by an electrobiochemical slurry reactor during batch operation for 30 d in the Experiment 1.

Table 3. Average performance of the electrobiochemical slurry reactor in Experiment 1.

Parameter	Value
$\eta_{Lindane}$ (%)	27.60 ± 6.33
$P_{An\text{-}max}$ (mWm^{-2})	6.62
$P_{V\text{-}max}$ (mWm^{-3})	165.31
$E_{EBCR\text{-}max}$ (V)	0.33
$I_{EBCR\text{-}max}$ (mA)	0.15
$P_{EBCR\text{-}max}$ (mW)	0.05
$P_{An\text{-}ave}$ (mWm^{-2})	4.12 ± 1.35
$P_{V\text{-}ave}$ (mWm^{-3})	103± 34
$E_{EBCR\text{-}ave}$ (V)	0.26± 0.07
$I_{EBCR\text{-}ave}$ (mA)	0.12 ± 0.03
$P_{EBCR\text{-}ave}$ (mW)	0.03 ± 0.01
η_{COD} (%)	72.36± 15
η_{SO4} (%)	22.07± 0.01

Notes: $\eta_{Lindane}$, lindane removal efficiency; P_{An}, surface area power density; P_V, volumetric power; E_{EBCR}, voltage; I_{EBQR}, current intensity; P_{EBCR}, power delivered; η_{COD}, organic matter removal efficiency as COD; η_{SO4}, sulphate removal efficiency. Subindices: max, maximum; ave, average.

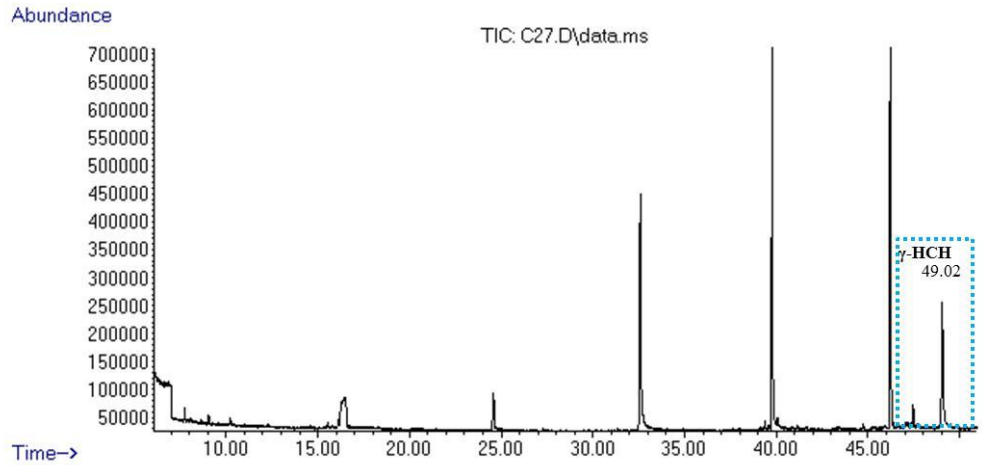

Figure 4. GC-MS detection of intermediate metabolites in electrobiochemical slurry reactor at time 30 days in the Experiment 2.

3.2 Experiment 2

3.2.1 Characterization of the electrobiochemical slurry reactor

The polarization curves and the power variation with current intensity of the EBCR at time 0 days are shown in Figure 5a and 5b respectively. The values obtained from the polarization curves method were 2046, 1288, 897 y 255Ω for face A, face B, connection in series and parallel, respectively (Table 4). The maximum volumetric power was obtained when the connections were in parallel (739 mW/m^3) followed for the face B, connection in series and face A with 421, 340 and 86 mW/m^3 respectively.

After 7 days of operation another reactor characterization was carried out. The internal resistances decreased very much compared to those of the first characterization. Their values were approximately o 140, 339, 442, 102 Ω for face A, face B, connection in series and connection in parallel, respectively. The maximum volumetric power was obtained for parallel connection (1531 mW/m^3, Table 4, Fig. 6); it was twice the volumetric power obtained with characterization at 0 days. The improved characteristics might be a consequence of the increased microbial activity resulting from enrichment of the biofilm on the anode [33]. The internal resistance was smaller than that obtained by Ringelberg *et al*. [32] and Wang *et al*. [18] who reported values of 10kΩ and 1kΩ, respectively. On the other hand the internal resistance obtained when the connection were in parallel was similar to low internal resistances of 100 Ω reported by Huang *et al*. [17] and Yan *et al.* [34].

3.2.2 Performance of the electrobiochemical slurry reactor

Figure 7 shows voltage generation of the device when the anodes and cathodes of the EBCR were connected in parallel. The voltage with the EBCR in open circuit conditions (at the early 20 h) was approximately 530 mV (phase I). The voltage remained stable when the cell was operated with an external resistance of 120 Ω (first hours of phase II); however the voltage decreased to less than 200 mV afterwards. So, open circuit conditions were re-established in phase III) where an expected increase of voltage occurred. Subsequently, in phase IV, the cell was operated with an external resistance of 220 Ω and a drastic voltage decrease was observed. Again, open circuit conditions were re-established in phase V. Phase VI was run with an external resistance of 560 Ω. Approximately at day 8 the cell contents was mixed with nitrogen gas. It was found that cell voltage significantly increase after each mixing episode; however, after mixing the voltage decrease was very important (down to between 100 to 200 mV, Fig. 7, days 8 to 15). Due to pneumatic and hydraulic difficulties of mixing by bubbling N_2 gas, starting at day 15 the cell content was continuously mixed in a shaker at 100rpm. Voltage output recovered and was stabilized around 300 mV. This was accompanied by supplementation with 2g/L substrate (sucrose: sodium acetate: lactate) that was used as the fuel in the EBCR at 15d. Electricity generation began to increase and reached a voltage output of approximately 303 mV (Fig. 7). The power density normalized to anode area was 21.3 mW/m^2 and the average volumetric power was 531 mW/m^3. At approximately 20 days of operation, the cell reached a maximum voltage output of 329mV and volumetric power of 629 mW/m^3 (Table 5); the voltage remained constant until day 24. Afterwards, it decreased

again to a value of 260 mV. On day 25 the EBCR was fed with 2 gCOD/L of substrate and reached a voltage of 321mV, the EBCR voltages decreased below 280 mV at 28 day.

The maximum voltage output of the EBCR (330mV) and maximum power (25mW/m^2) were higher than those reported by Wang *et al.* [18] (155 mV and maximum power 0.85 mW/m^2) for a cell loaded with soil polluted with total petroleum hydrocarbon. Our results also compared very favorably to those observed by Yan *et al.* [34], a voltage as low as 17 mV in the treatment of sediment contaminated with phenanthrene and pyrene.

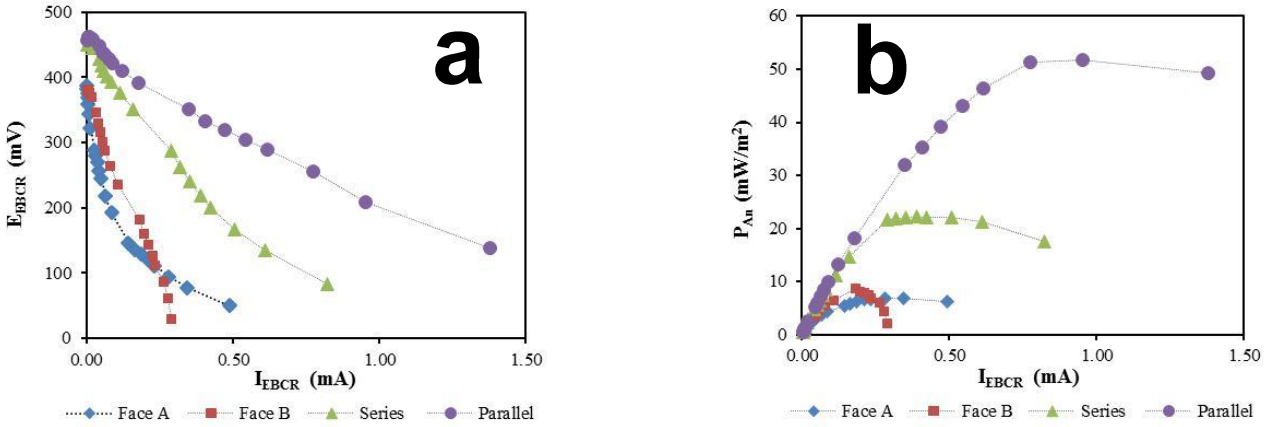

Figure 5. Characterization of the electrobiochemical slurry reactor at t0d (a) Polarization curves, (b) power densities in the Experiment 2

Table 4. Average values of several variables in electrobiochemical slurry reactor characterization after at 0days in the Experiment 2

Parameter	Face A	Face B	Series	Parallel
$R_{int}(\Omega)$	2046	1288	897	255
$P_{An\text{-}max}$ (mWm^{-2})	6.88	33.72	13.60	29.57
$P_{V\text{-}max}$ (mWm^{-3})	86	421	340	739
$I_{EBCR\text{-}max}$ (mA)	0.49	1.14	1.02	1.50
$E_{EBCR\text{-}max}$ (V)	0.39	0.38	0.45	0.46
$P_{EBCR\text{-}max}$ (mW)	0.03	0.13	0.10	0.23
$P_{An\text{-}ave}$ (mWm^{-2})	2.72	6.13	5.08	0.87
$P_{V\text{-}ave}$ (mWm^{-3})	34	76	127	22
$I_{EBCR\text{-}ave}$ (mA)	0.09	0.15	0.20	0.02
$E_{EBCR\text{-}ave}$ (V)	0.22	0.26	0.33	0.37
$P_{EBCR\text{-}ave}$ (mW)	0.01	0.02	0.04	0.07

Notes: P_{An}, surface area power density; P_V, volumetric power; E_{EBCR}, voltage; I_{EBQR}, current intensity; P_{EBCR}, power delivered. Subindices: max, maximum; ave, average.

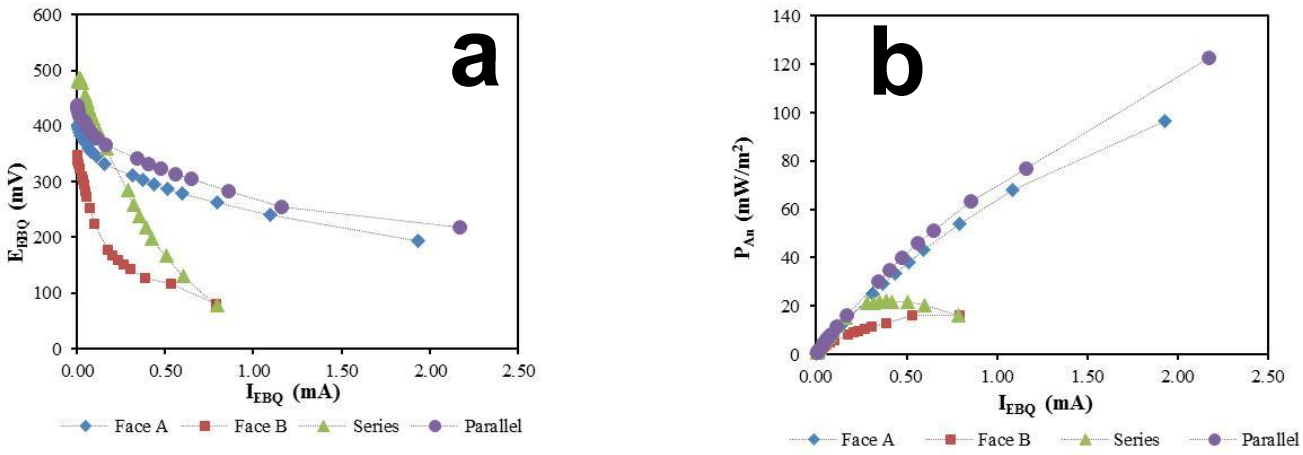

Figure 6. Characterization of the Electrobiochemical slurry reactor at t7d (a) Polarization curves, (b) power densities in the Experiment 2

Table 5. Average values of several variables in electrobiochemical slurry reactor characterization after at 7days in the Experiment 2

Parameter	Face A	Face B	Series	Parallel
$R_{int}(\Omega)$	140	339	442	102
$P_{An\text{-}max}$ (mWm^{-2})	96.60	16.32	13.93	61.27
$P_{V\text{-}max}$ (mWm^{-3})	1207	204	348	1531
$I_{EBCR\text{-}max}$ (mA)	1.93	0.79	1.03	2.17
$E_{EBCR\text{-}max}$ (V)	0.41	0.35	0.49	0.44
$P_{EBCR\text{-}max}$ (mW)	0.37	0.06	0.11	0.47
$P_{An\text{-}ave}$ (mWm^{-2})	19.91	5.88	4.95	12.12
$P_{V\text{-}ave}$(mWm^{-3})	249	73	124	303
$I_{EBQ\text{-}ave}$ (mA)	0.30	0.15	0.19	0.33
$E_{EBQ\text{-}ave}$ (V)	0.34	0.25	0.34	0.38
$P_{EBQ\text{-}ave}$ (mW)	0.08	0.02	0.03	0.09

Notes: P_{An}, surface area power density; P_V, volumetric power; E_{EBCR}, voltage; I_{EBQR}, current intensity; P_{EBCR}, power delivered. Subindices: max, maximum; ave, average.

Table 6. Average performance of electrobiochemical slurry reactor in the Experiment 2

Parameter	Value
□Lindane (%)	78
Rint (Ω)	560
Pan-max (mWm-2)	25
$P_{V\text{-}max}$ (mWm^{-3})	634
$E_{EBCR\text{-}max}$ (V)	0.33
$I_{EBCR\text{-}max}$ (mA)	0.59
$P_{EBCR\text{-}max}$ (mW)	0.20
□Coul (%)	15
□COD (%)	76

Notes: P_{An}, surface area power density; P_V, volumetric power; E_{EBCR}, voltage; I_{EBQR}, current intensity; P_{EBCR}, power delivered, $\square_{COD}$, organic matter removal efficiency as COD. Subindices: max, maximum.

On the other hand, Huang *et al.* [17] registered a power density slightly superior (ca. 30 mW/m^2) and a lower voltage (150 mV) in the treatment of a waterlogged soil polluted with phenol.

3.2.3 Lindane removal and intermediate metabolites

Lindane removal achieved in the EBCR was 78%, whereas the removals of the biotic (live) control and abiotic control slurry reactors were 80 and 3%, respectively. Main metabolites due to lindane degradation were detected by analysis by GC/MS in the EBCR: 1,2,3-trichlorobenzene (1,2,3 TCB), 1,3-dichlorobenzene (1,3-DCB), 1,2-dichlorobenzene (1,2-DCB), and chlorobenzene (CB) (Figure 8).

Lindane removals observed in our EBCR compared very favorable with lindane removals reported for standard slurry bioreactors in the literature. Okeke *et al.* [35] carried out experiments with SB inoculated with *Pandorea* sp., with a presumably anaerobic operation of 9 weeks duration. Initial lindane concentration was 100 mg/kg; they found removals of 59.6% γ-HCH, Quintero *et al.* [5] treated a sandy soil polluted with a mixture of isomers α, β, γ and δ-HCH (100 mg/kg each) in anaerobic SB. Starch was supplemented at 2 g/L every 3 days. High removals of nearly 100% for α and γ isomers of HCH and 65 to 70% for β and δ HCH were found.

On other hand, Robles-Gonzalez *et al.* [10] assessed the bioremediation of a heavy soil polluted with 100 mg lindane/kg in full sulfate reducing slurry bioreactors. Removal was 88% whereas the detected metabolites after 30 d operation were PCCH; 1,2,4-TCB; 1,2,3-TCB; CB, and benzene.

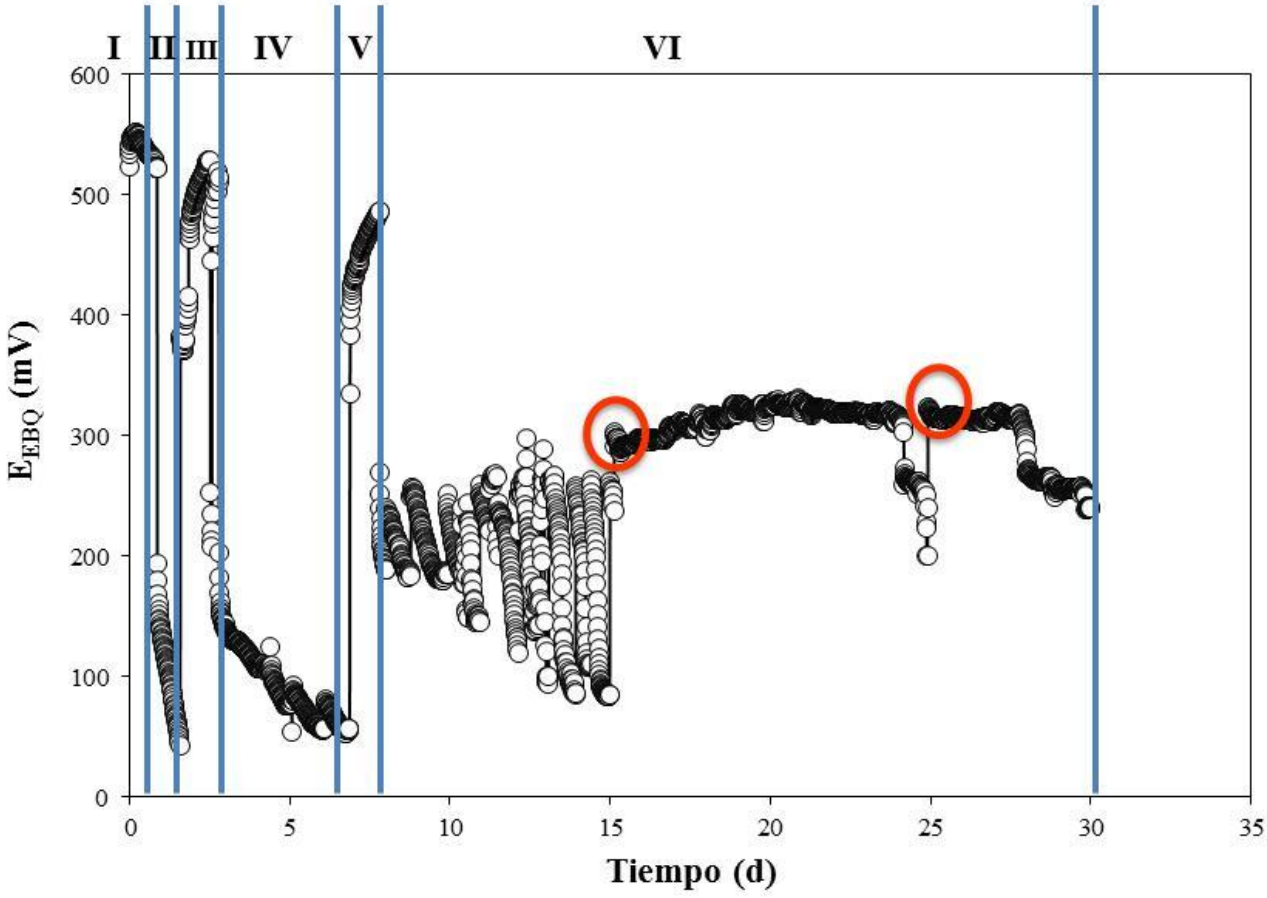

Figure 7. Electricity generation in electrobiochemical slurry reactor during batch operation for 30 d in the Experiment 2. The addition of substrate is indicated by the red circles. Phase I, open circuit; phase II, closed circuit with external resistance 120Ω; phase III, open circuit; phase IV, external resistance 220Ω; phase V, open circuit; phase VI, external resistance 560Ω.

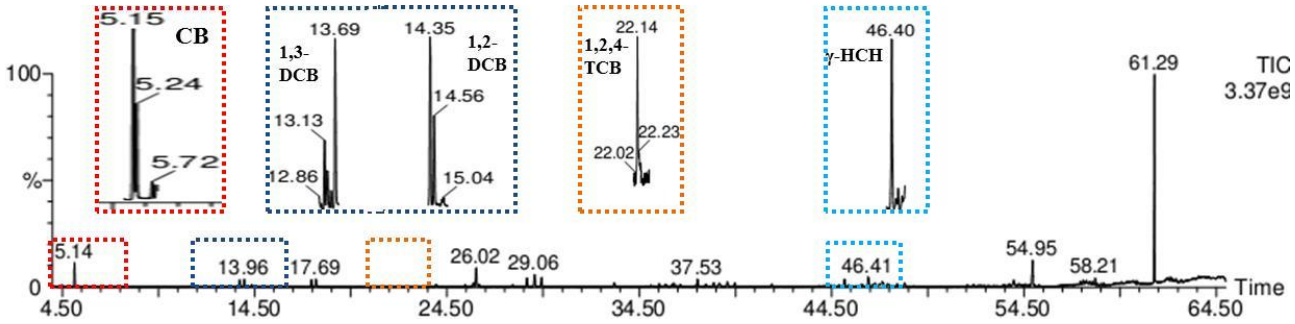

Figure 8. GC-MS detection of intermediate metabolites in electrobiochemical slurry reactor at time 30 days in the Experiment 2.

Quintero *et al.* [23] reported the degradation of HCH isomers in slurry reactors in anaerobic conditions. They found traces of diverse intermediate metabolite, such as pentachlorocyclohexane isomers, tetrachloro-cyclohexene, 1,2,3-trichlorobenzene, 1,3-dichlorobenzene and clorobenzene. The low concentrations of the metabolites indicated that intermediate compounds were not accumulated and they proceed to their further degradation to CB, the end product in the degradation mechanism. In a work by Boyle [36] it was found that lindane could be dechlorinated by anaerobic bacteria (sulfate-reducing bacteria among others) with generation of monochlorobenzene and benzene as main intermediates. Quintero *et al.* [23] observed total depletion of α and γ-HCH in a polluted soil after 3 days anaerobic incubation; they used an initial lindane concentration of 100 mg kg-1 soil, bioaugmentation with a high concentration of methanogenic anaerobic sludge (8 g VSS L^{-1} in the bioreactor), and starch (2 g COD/L) as electron donor. During the degradation, traces of diverse intermediate and end-products compounds were detected, such as pentachlorocyclohexane isomers (PCCH), tetrachlocyclohexane (TCCH), 1,2,3-trichlorobenzene (1,2, 3-TCB), 1,3-dichlorobenzene (1,3-DCB), chlorobenzene CB.

The relatively high lindane removals obtained in our work in only 30 d of EBCR operation are very promising: EBCR emerges as a fast and attractive technology for pesticide degradation and soil remediation. Indeed, it has been reported the recalcitrance (persistence) of organo-chlorinated pesticides in soils, with half lives of the order of 2 to 5 years. In particular, lindane has an average half-life of 2.6 years in soils, depending on the physico-chemical characteristics of soils (texture, organic matter, depth, etc.) as well as environmental conditions [37].

4. Conclusion

-The bioremediation of lindane in soil can be significantly enhanced generation in an ECBR, with the additional bonus of simultaneous electricity generation, compared to conventional slurry bioreactor and other bioremediation technologies.

-Mixing and the supplementation with organic substrate seemed to significantly improve the EBCR performance, both the efficiency of the removal of lindane and the production of electricity significantly increased.

-We detected intermediate metabolites typical of anaerobic degradation pathways of lindane that were similar to those reported in previous research in conventional anaerobic slurry bioreactors.

5. Akcnowledgements

The authors wish to thank CINVESTAV del IPN and ICYTDF for partial support to their research, as well as CONACYT for a graduate scholarship to BC-P. The excellent technical help of Ms Ana L. Vazquez-Larios, M. Sc. (advice on polarization curve in Experiment 2), Mr. Rafael Hernández-Vera, M. Sc. (training on determination of several environmental parameters), Mr. Cirino Rojas Chávez (chromatographic analyisis), Mr. Andrés Rodríguez (membrane preparation and cell assemblage), and Mr. Armando Barbosa-Fernández (Mechanic Workshop, cell construction) is sincerely appreciated.

6. References

[1] J. Vijgen, International HCH & Pesticides Association (2006).

[2] S. Sang, S. Petrovic, V. Cuddeford, Lindane: a review of toxicity and environmental fate (1999).

[3] El lindano en México. Instituto Nacional de Ecología (2004).

[4] Y. Nagata, T. Hatta, R. Imai, K.Kimbara, M. Fukuda, K. Yano, M. Takagi, Biosci Biotechnol Biochem, 57: 1582-1583 (1993a).

[5] Y. Nagata, T. Nariya, R. Ohtomo, M. Fukuda, K. Yano, M. Takagi, J Bacteriol, 175: 6403-6410 (1993b).

[6] J.C. Quintero, M.T. Moreira, G. Feijoo, J.M: Lema, Chemosphere, 61: 528-536 (2005).

[7] B. Camacho-Pérez, E. Ríos-Leal, N. Rinderknecht-Seija, H.M. Poggi-Varaldo, J Environ Manage, 95: S306 S318 (2012).

[8] J.E. Haugen, F. Wania, N. Ritter, M. Schlabach. Environ Sci Technol, 32:217-224 (1998).

[9] J.C. Quintero, T.A. Lú-Chau, M.T. Moreira, G. Feijoo, J. M. Lema, Int Biodeter Biodegr, 60: 319-326 (2007).

[10] I.V. Robles-González, E. Ríos-Leal, I. Sastre-Conde, F. Fava, N. Rinderknecht-Seijas, H.M. Poggi-Varaldo, Process Biochemistry, (2011).

[11] R. Boopathy, Bioresource Technol., 74(1): 63-67 (2000).

[12] S. Venkata-Mohan, K. Sirisha, N. Chandrasekhara-Ra, P.N. Sarma, S. Jayarama-Reddy, J Hazard Mater, B116: 39-48 (2004).

[13] I.V. Robles-González, F. Fava, H.M. Poggi-Varaldo, Microb Cell Fac, 7:5 (2008).

[14] H. Liu, R. Ramnarayanan, B.E. Logan. Environ Sci Technol, 38(7):2281–2285 (2004).

[15] J.M. Morris, S. Jin, J Environ Sci Health, B43(1):18–23 (2008).

[16] F. Rezaei, T. L. Richard, B. E. Logan, J Power Sources, 192:304–309 (2009).

[17] D. Huang, S. Zhou, Q. Chen, B. Zhao, Y. Yuan, L. Zhouang, Chem Eng J, 172: 647– 653 (2011).

[18] X. Wang, Z. Cai, Q. Zhou, Z. Zhang, C. Chen, Biotechnol Bioeng, 109(2):426-433(2011).

[19] A. Ortega-Martínez, K. Juárez-López, O. Solorza-Feria, M.T. Ponce-Noyola, E. Ríos-Leal, N.F. Rinderknecht-Seijas, H. M. Poggi-Varaldo, J New Mat Electrochem Systems, 15 (3):187-194 (2012).

[20] B.E. Logan, B. Hamelers, R. Rozendal, U. Schroder, J. Keller, S. Freguia, P. Aelterman, W. Verstraete, K. Rabaey. Environ Sci Technol, 40(17): (2006).

[21] H. M. Poggi-Varaldo, A. Carmona Martínez, A. L. Vázquez-Larios and O. Solorza-Feria, J. New Mat Electrochem Systems, 12:49-54 (2009).

[22] A .L. Vázquez-Larios, O. Solorza-Feria, G. Vazquez-Huerta, F. Esparza-Garcia, E. Rios-Leal, N. Rinderknecht-Seijas, H.M. Poggi-Varaldo, J. New Mat. Electrochem. Systems, 13: 219-226 (2010).

[23] J.C. Quintero, M.T. Moreira, J.M. Lema, G. Feijoo, Chemosphere 63:1005–1013 (2006).

[24]I.V. Robles-González, E. Ríos-Leal, R. Ferrera-Cerrato, F. Esparza-García, N. Rinderkenecht-Seijas, H.M. Poggi-Varaldo, Process Biochem 41(9):1951–60 (2006).

[25] American Public Health Association. Standard methods for examination of water and wastewater, APHA-AWWA-WEF. 15th ed. Washington, DC: Ameri-can Public Health Association; 1981.

[26] Poggi-Varaldo HM, Oleszkiewicz JA. Environ Technol, 13:409–21(1992).

[27] Camacho-Pérez, B. Biorrestauración de suelos agrícolas contaminados con agroquímicos utilizando reactores de suelos activados convencionales y electrobioquímico de nuevo tipo. Bioremediation of agricultural soils polluted with lindane using slurry bioreactors and a novel bioelectrochemical reactor. Sc D Thesis, Interim Report. CINVESTAV del IPN, México D.F., México (2012).

[28] A.L. Vázquez-Larios, O. Solorza-Feria, G. Vazquez-Huerta, E. Rios-Leal, N. Rinderknecht-Seijas, H.M. Poggi-Varaldo, J New Mat Electrochem Systems, 14, 099-105 (2011a).

[29] K. Sathish-Kumar, O. Solorza-Feria, R. Hernández-Vera, G. Vazquez-Huerta, H.M. Poggi-Varaldo, J New Mat Electrochem Systems, 15 (3):195-201 (2012a).

[30] A. L.Vázquez –Larios, O. Solorza-Feria, G. Vázquez-Huerta, F. Esparza-García, N. Rinderknecht-Seijas, H.M. Poggi-Varaldo, Int J Hydrogen Energ, 36:6199-6209 (2011b).

[31] K. Sathish-Kumar, O. Solorza-Feria, G. Vázquez-Huerta, J.P. Luna-Arias, H.M. Poggi-Varaldo, J New Mat Electrochem Systems, 15 (3):181-186 (2012b).

[32]D. B. Ringelberg, K. L. Foley, C. M. Reynolds. Appl Microbiol Biotechnol, 90:1805–1815 (2011).

[33] N. Lu, S.G. Zhou, L. Zhuang, J.T. Zhang, J.R. Ni, Biochem Eng J 43:246 –251 (2009).

[34] Z. Yan, N. Song, H. Cai, J. H. Tay, H. Jiang, J Hazard Mater 199–200: 217– 225 (2012).

[35] B.C. Okeke, T. Siddique, M.C. Arbestain, W.T. Frankenberger, J. Agric. Food Chem, 50: 2548-2555 (2002).

[36] A.W. Boyle, M.M. Haggblom, L.Y. Young, FEMS Microbiology Ecol. 29:379-387 (1999).

[37] Commission for Environmental Cooperation.The North American Regional Action Plan (NARAP) on Lindane and Other Hexachlorocyclohexane (HCH) Isomers. Draft for public comment dated 5 October 2005. http://www.cec.org/pubs_docs/documents/index.cfm?varlan=english&ID=1821.

Abbreviations and Acronyms

1,2, 3-TCB	1,2,3-trichlorobenzene
1,3-DCB	1,3-dichlorobenzene
1,4-DCB	1,4-dichlorobenzene
Ave	Average
BOD	Biochemical oxygen demand
CB	Chlorobenzene
COD	Chemical oxygen demand
EBCR	Electrobiochemical slurry reactor
E_{EBCR}	Voltage
EIS	Electrochemical impedance spectroscopy
GC-MS	Gas chromatography coupled to mass spectrometry
HCH	Hexachlorocyclohexane
I_{EBQR}	Current intensity
Max	Maximum
MFC	Microbial Fuel Cell
NOM	Native organic matter
P_{An}	Surface area power density
P_{EBCR}	Power delivered
P_V	Volumetric power
R_{int}	Internal resistance
SB	Slurry bioreactors
SMFC	Soil microbial fuel cell technology
SR	Sulphate reducing

Greek characters

□	Removal efficiency

Capacitance Improvement of Carbon Aerogels by the immobilization of Polyoxometalates Nanoparticles

D.A. Baeza-Rostro[1*], A. K. Cuentas-Gallegos[1]

[1] Centro de Investigación en Energía-Universidad Nacional Autónoma de México
Privada Xochicalco S/N Col. Centro, AP 34, CP 62580 Temixco, Morelos, México
e-mail: dabr@cie.unam.mx

ABSTRACT

A Hybrid material was prepared by the immobilization of H3PMo12O40 polyoxometalate nanoparticles (POM) on to the surface of a carbon aerogel (CA) matrix, in order to determine its potential application as electrode material for a supercapacitor cell. Several aerogels matrices with different microstructure properties and activation degree were exposed to a POM solution 1.15mM to determine the key properties for the immobilization of POM nanoparticles. All matrices and hybrid materials were characterized by ATR, nitrogen isotherms. For the electrochemical characterization our materials were grounded with 10% of Teflon and 20% conducting carbon to make a film that was pressed onto a stainless steel grid and cyclic voltammetry was used as the electrochemical technique, using 0.5 M H2SO4 as electrolyte. The highest degree of activation and smaller pore size of the aerogel matrix were the key factors influencing the immobilization and dispersion of POM nanoparticles, which improved the capacitance behavior making this material suitable for its application as supercapacitor electrode material.

1. Introduction

Carbon aerogels are porous materials where their porosity and pore size distribution can be controlled by modifying the synthesis parameters. In these materials the electrolyte can access almost all pores and is for this reason that they are promising electrode materials for their application as supercacitors [1].

As we can find in many reports, some factors influencing the electrochemical performance of carbon aerogels and many others carbonaceous materials used as electrode materials for electrochemical devices have been identified. Some of these factors are surface area, pore size, and surface functional groups concentrations, among others[2]. These factors can be modified by the synthesis parameters and the material activation methodology. The activation of carbon materials can be carried out by a chemical or a thermal route. In the first activation route some surface active groups can be added to the matrix (OH functional group), while the thermal activation increases the surface area, probably due to the mass loss in the material. [3]

Oxygen based functional groups are required to incorporate polyoxometalate particles (POM) on to a carbon matrix. Therefore, an activation process such as the chemical route has to be carried out in order to obtain a POM-based hybrid material with a carbon aerogel matrix. POM particles are of great interest in energy storage applications such as in electrode materials for supercapacitors [4], [5], [6], due to their reversible multielectron redox reactions.

In the present study, a porous carbon material aerogel-type was prepared by using a molar ratio of resorcinol (R)/ formaldehyde (F) of 0.5 and a resorcinol (R)/Na_2CO_3 catalyst (C) of 100, in order to obtain an aerogel matrix with pores in the range of 2-5nm and high surface area. The novelty of this work is the incorporation of molecular oxides polyoxometalate-type (POMs) on to the surface of chemically activated aerogel, in order to improve capacitance.

2. Experimental

2.1 Synthesis of carbon aerogel and incorporation of POMs

Carbon aerogels (CAs) were produced using a R/F molar ratio of 0.5 and a molar ratio of R/C of 100. All reagents were used as purchased: Resorcinol (99% purity) from Reasol, formaldehyde from Fermont (37.4%; methanol stabilized), and sodium carbonate by Fermont (99.7% purity). All solutions were prepared with deionized water. First, all reagents in solution were stirred and placed on a cylindrical crystal jar in an oven at 85 °C for 96 hours to obtain the corresponding precursor gel. Then the solvent exchange was carried out by adding acetone in order to prepare the RF gel for the supercritical drying. This solvent exchange was carried out during three days by multiple replacement of residual water with fresh acetone. Subsequently the CO_2 supercritical drying was carried out by keeping the RF gel at 30 °C and under 7.4 MPa, using a SFT-100 equipment. This process was followed by carbonization during 30 min at 850 °C in order to obtain the carbon aerogels (CA) with high surface area, as previously reported [7], [8], [9].

Activated carbon aerogel was prepared according to the following procedure: the chemical activation [10] of carbon aerogel was performed by the dissolution of KOH in ethanol and mixing with CA using a KOH/CA mass ratio of 0.5/1 and 5/1. The mixture was dried at 110 °C and then carbonized in a tubular furnace at 850°C for 3 hours using a heating rate of 5°C/min. After the mixture cooled down to room temperature, the resultant materials were taken out and washed with 10% HCl and deionized water. Finally, the materials were dried at 110°C for 6h.

The incorporation of POM particles onto this CA matrix to obtain a hybrid material was performed by mixing in an ultrasonic bath for 3h, 0.04 g of CA in a 1.7 mM $H_3PMo_{12}O_{40}$ (Fermont) solution. The obtained suspension was filtered off and washed with a pH=2 solution, and finally the material was dried at 100°C for 1h.

2.3 Structure and physical properties

The materials were degassed at 120 °C under vacuum to remove all the adsorbed species before nitrogen adsorption and desorption isotherms were taken, using an *Nova* 1200*e* (Quantachrome). The BET surface area (S_{BET}) was analyzed by BET (Brunauer-Emmett-Teller) theory, and ATR analyses were performed directly over the sample to detect the vibration frequency changes for each functional groups present in the carbon aerogels, as well for the confirmation of the polyoxometalates presence.

2.4 Electrochemical characterization

To determinate the electrochemical performance of the prepared electro-active materials, cyclic voltammetry (CV) technique was used in an Arbin SuperCap model SCTS8 potentiostat using a 3-electrode cell with 0.5 M H_2SO_4 solutios as the electrolyte. A Pt gauze was used as the counter electrode, sulfate saturated electrode (SSE) as the reference electrode, and our electro-active materials as the working electrode. The working electrodes were prepared by mixing our electro-active materials (CA and Hybrids) (60%) with Teflon (10%) and conducting carbon (30%) in ethanol, this mixture was stirred under heat until alcohol evaporation (≈1.5 h) to obtain a paste that was pressed on to a stainless steel grid (316L, chemically resistant to acidic media) used as the current collector. The CV current was normalized by the electro-active material weight of the composite electrode and all characterizations were made after purging with nitrogen.

3. Results and discussion

The S_{BET} was calculated in a relative pressure range between 0 and 0.3, these results are presented in Table 1. The surface area of the carbon aerogel matrix (ACPQ2-100) decreased when incorporating the polyoxometalate (ACPQ2-100/POM) from 334m^2/g to 274m^2/g, probably due to the pore obstruction by POM particles. This phenomenon has being observed in some others carbon matrices in the presence of POM's [11], [12], [13], [14], [15], [16], [17], [18]

and other functional groups like anthraquinone [19]. The mesoporosity of the materials are confirmed by the hysteresis observed on the isotherms (not shown here).

Table 1. Surface area of samples ACPQ2-100 and ACPQ2-100/POM.

Sample	S_{BET} (m^2/g)
ACPQ2-100	334
ACPQ2-100/POM	274

Carbon aerogel (ACPQ2-100) ATR spectrum is shown in Figure 1, where a peak at 3340 cm^{-1} is detected and is related mainly to OH functional group as expected, and in less degree to absorbed water due to the hydrophilic nature of this matrix. The peaks at 2850 and 2918 cm^{-1} are related to the stretching vibrational mode of -CH_2 group, at 1055 cm^{-1} and 1220 cm^{-1} region is related with CH-O-CH linkage between the two resorcinol molecules as expected in the poly-condensation reaction between resorcinol and formaldehyde. The peak at 1475 cm^{-1} corresponds to the scissors vibration of CH_2 group, and the peak at 1614 cm^{-1} region is realated with the stretching vibrational mode of aromatic rings. [20], [21], [22]. The absorption bands at 800, 876, 955 and 1060 cm^{-1} region can be considered as an evidence of the diluted presence of POM particles [23].

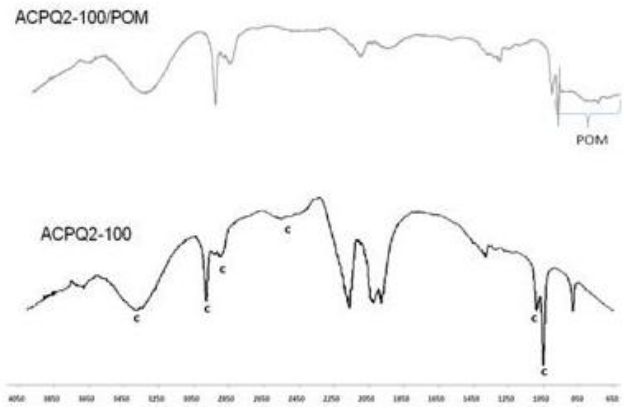

Figure 1. ATR spectra from ACPQ2-100 and ACPQ2-100/POM samples with the vibrational modes correspond to carbon aerogels and polyoxometalate.

Figure 2 shows the cyclic voltammograms of samples ACPQ2-100 (CA matrix) and ACPQ2-100/POM (hybrid material) in 0.5 M H_2SO_4. The most relevant difference between the voltammograms of these samples is their profile change. The CA matrix (ACPQ2-100) voltammogram shows a profile deviated in the negative voltage range from the typical rectangular shape characteristic of a capacitive behavior, which is indicative of the resistive nature of this material. On the other hand, the hybrid material voltammogram shows a more evident rectangular profile, confirming its capacitive behavior and less resistive contribution. In addition, three redox pairs at -0.13V/-0.1V (a), -0.27V/-

0.24V (b) and -0.5V/-0.47V (c) are detected and correspond to the six electron transfer of polyoxometalate particles confirming its presence [23]. In equation 1 we show these multiple reversible redox reactions.

$$PMo_{12}{}^{VI}O_{40}{}^{3-} + ne^- + nH^+ \Leftrightarrow H_nPMo_n{}^{V}Mo_{12-n}{}^{VI}O_{40}{}^{3-}\ ,\quad n= 2, 4 \text{ o } 6. \qquad \textbf{(1)}$$

These results suggest that functional groups (OH) generated during the chemical activation of the matrix ACPQ2-100 are responsible for its resistive nature, since in the hybrid material this phenomena is considerably reduced probably due to the bonding of these OH groups with POM particles.

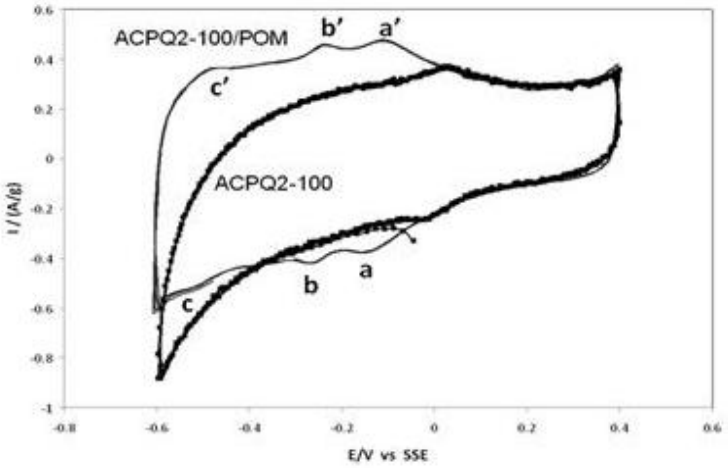

Figure 2. Cyclic voltammetry carried out at a scan rate of 10 mV/s for the hybrid material ACPQ2-100/POM and its corresponding array ACPQ2-100. The sweep potential was started in the negative direction.

From these voltammograms, capacitance values were calculated to eq. (2).

$$C = I\left(\frac{t}{\Delta V}\right) \qquad \textbf{(2)}$$

Where C is the capacitance I is the applied current, t is the discharge time and ΔV is the potential change as a function of discharge process. Capacitance values of 156 F/g for ACPQ2-100 CA matrix and of 188 F/g for ACPQ2-100/POM hybrid material were obtained, confirming the capacitance improvement in the hybrid material due to the incorporation of POM particles through their bonding with OH functional groups of the activated CA matrix.

4. Conclusions

Incorporation of POM particles on to the surface of CA matrix (ACPQ2-100) with a BET surface area of 334 m^2/g was confirmed by a decrease in BET surface area (274 m^2/g) due to pore obstruction, by ATR, and by the presence of three reversible redox processes characteristic of POM ACPQ2-100/POM hybrid material showed an improved electrochemical behavior, with a rectangular shape voltammogram profile indicative of a capacitive behavior with a smaller resistive nature compared to its AC matrix, aside from the faradic contribution of the three redox process of the POM particles. These results are reflected in the improved capacitance value from 156F/g for the CA matrix to 188F/g for the hybrid material.

5. Akcnowledgements

We acknowledge the technical work of Patricia Altuzar-Coello and the financial support granted from CONACYT Basic Science Project 154259 and PAPIIT Project IN105410.

6. References

[1] H. Pröbstle, R. Saliger, J. Fricke, in: K.K. Unger, G. Kreysa, J.P. Baselt, Studies in Surface Science and Catalysis, 128, 371, (2000).

[2] Junbing Wang, X. Y. Journal of Power Sources, 185, 589. (2008).

[3] R. Saliger et al. Journal of Non-Crystalline Solids, 225, 81 (1998).

[4] P. Gómez-Romero, K. Cuentas-Gallegos, M. Lira-Cantú and N. Casañ-Pastor, Journal of Materials Science, 40, 1423, (2005).

[5] A.K. Cuentas-Gallegos, M. Gonzales-Toledo, and M.E. Rincón, Revista Mexicana de Física S **53,** 91, (2007).

[6] Pedro Gómez-Romero, Malgorzata Chojak, Karina Cuentas-Gallegos, Juan A. Asensio, Pawel J. Kulesza, Nieves Casañ-Pastor, Mónica Lira-Cantú, Electrochemistry Communications, 5, 149, (2003).

[7] Mirzaeian, M. H. Journal of Materials Science, 44, 2705. (2009).

[8] Tamon, h. Ishizaka, T. Araki and M. Okazaki. Carbon, 36, 1257. (1998).

[9] R.W. Pekala, J.C. Farmer, C.T. Alviso, T.D. Tran, S.T. Mayer, J. M. Miller, and B. Dunn. Journal of Non-Crystalline Solids, 225, 74. (1998).

[10] Xianhua Zeng, D. R. Electrochimica Acta, 53, 5711. (2008).

[11] Cuentas-Gallegos, A. K. et al. Journal of New Materials for Electrochemical Systems, 13, 369. (2010).

[12] Damico Gall, et al. Chemistry of Materials, 8, 2523. (1996).

[13] J. Alcañiz-Monge, et al. Microporous and Mesoporous Materials, 115, 440. (2008).

[14] Mukai, S. R. Applied Catalysis A: General, 256, 99. (2003).

[15] Ghetti, P., Ricca, L., Luciana, A. Fuel, 75, 565. (1996).

[16] Pastor-Villegas, J.J., Gómez-Serrano, V., Durán-Valle, C.J., Higes-Rolando, F.J. Journal of Analytical and Applied Pyrolysis, 50, 1. (1999).

[17] Cuentas-Gallegos, A. K. et al. Journal of Nano Research, 14, 11. (2011).

[18] Cuentas-Gallegos, A. K. et al. Journal of New Materials for Electrochemical Systems, 13, 369. (2010).

[19] (a)Grégory Pognon, Thierry Brousse, Daniel Bélanger. Carbon 49, 1340. (2011). (b) Grégory Pognon, Thierry Brousse, Laurent Demarconnay, Daniel Bélanger. Journal of Power Sources, 196, 4117. (2011).

[20] Jun Li, e. al. Journal of Power Sources, 158, 784. (2006).

[21] C. Liang, e. al. Journal of Non-Crystalline Solids, 271, 167. (2000).

[22] Conley, R. T. Espectroscopía Infrarroja. Madrid Ed. ALHAMBRA, S.A. (1979)

[23] A.K. Cuentas-Gallegos, M. Lira-Cantu, N. Casañ-Pastor, and P. Gómez-Romero. Advanced Functional Materials, 15, 1125. (2005).

Capacitance Improvement Based on Cell Design

R. López-Chavéz* 1,2, A.K. Cuentas-Gallegos 1

1Centro de Investigación en Energía-Universidad Nacional Autónoma de México Privada Xochicalco S/N Col. Centro, AP 34, CP 62580 Temixco, Morelos, México
2Instituto Tecnológico de Zacatepec. Av Tecnológico S/N col centro , CP 62760 Zacatepec, Moleros, Mexico, mail: rlch@cie.unam.mx, rodolfo_lo_ch@hotmail.com

ABSTRACT

In the present work we show results related with the influence of the type of binder used to elaborate active electrodes made of activated carbon (DLC), for the assembly of supercapacitor cells. A Nafion 5%w solution and/or Kinar Flex (Polyvinylide fluoride, PVDF) were used as binders at different concentrations, using DLC carbon as the active material to make the electrodes by aerography, and carbon paper as support and current collector. Thickness of the electrodes was controlled by the weight of active material (DLC carbon). Cyclic voltammetry technique was used to characterize these electrodes in a 3-electrode cell assembly, using as counter electrode a Pt mesh, a SSE reference electrode, and a 0.5M H2SO4 solution as the electrolyte. The electrodes made with binder were assembled in a symmetric supercapacitor cell and for comparison a similar cell was constructed with binder-free electrodes. These cells were electrochemically characterized by galvanostatic cycling, showing capacitance values of 38F/g for binder-free electrode symmetric cell, and a stable behavior during 7000 charge-discharge cycles.

Key words: Supercapacitor, Design, Binder Free, Electrochemical Capacitor, Electrodes.

1. Introduction

An electrochemical supercapacitor also called supercapacitor or ultracapacitor can be defined as a device that stores electrical energy in the electrical double layer that is formed at the interface between an electrolytic solution and an electronic conductor [1]. Supercapacitors are designed to bridge the gap between batteries and capacitors to form fast charging energy-storage devices of intermediate specific energy [2]. The use of supercapacitors is growing along with demand for specific requirements for different applications, ranging from small sizes with limited energy content, to levels of hundreds of kW in various vehicles (passenger hybrids cars, hybrid buses and trains) and for electric applications. The variety of applications also determines the need to clarify the measurement procedures to determine the properties of supercapacitors (SC) of the properties for supercapacitors, which may vary when they are used in different operating conditions.

An ideal SC can be represented with a first-order electric equivalent circuit, as described in Figure 1. It is comprised of four ideal circuit elements, which include a capacitor *C1*, a series resistor *R*1, a parallel resistor *R*2 and a series inductor *L*1. *R1* represents the equivalent series resistance (ESR) and accounts for the power loss during charge and discharge. *R2* is the parallel resistance responsible for the energy loss due to capacitor self-discharge. This model is the simplest one and also the most adequate for low and medium power applications. In high power applications the non-ideal behavior of electrochemical capacitors cannot be neglected, depending on temperature, current, power, frequency, in case of alternate current systems, and also on SC category [3].

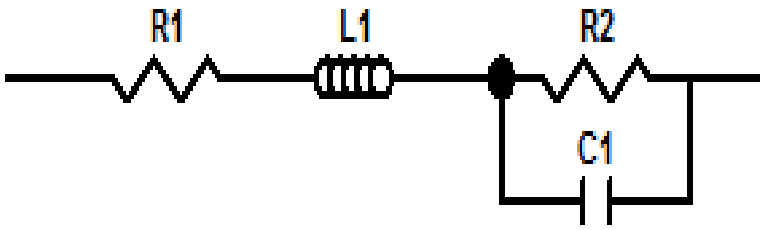

Figure 1. First order electric equivalent circuit of a capacitor

There have been many studies of materials for electrochemical capacitors, and testing for small laboratory devices and prototypes as well for a wide range of commercial products. Many of the materials testing laboratory and small devices have involved the use of cyclic voltammetry, galvanostatic cycling and AC impedance test [4], [5], [6]. In these tests, small currents, limited potentials intervals and/or AC frequencies are used. To test larger prototypes and commercial devices, regularly DC tests similar to those used with batteries are used[7]. In this case we are using cyclic voltammetry, galvanostatic cycling, electrochemical impedance spectroscopy, for our electrodes characterization.

On the other hand, one of the challenges of today is the portability of energy: lighter devices, more compact and more flexible for energy storage are required by a number of devices that can be used on different items from cloth to space applications, in which the cost per weight and volume is very high [8]. A number of recent studies, initiatives and products have been reported and proposed for the development of flexible energy devices based on different chemistries, including supercapacitors [9-14].

Our works shows a systematic study on electrode fabrication in order to reduce resistance (R), with capacitance values (C) as high as possible. Also, an evaluation of different current collectors in a lab-scale assembly was carried out as well as a prototype thin-cell was characterized, where the electrolyte was considerably reduced.

2. Experimental

2.1 Electrode Fabrication

Two series of electrodes were prepared using DLC (activated carbon from NORIT) as active material with Kinar Flex (PVDF polyvinylidene fluoride, Arkema) or Nafion solution (5wt%, Aldrich reagent) as binders in different concentrations. First, a suspension (ink) made of active material and binder was obtained, followed by their deposition on to the surface of the current collector by an aerography process, and finally a drying procedure was followed at room temperature for 24 hours. This impregnation technique produced well distribution of the active material on the surface of carbon paper (2 cm X 2 cm) used as supporting material and current collector, making their performance just a function of the used binder in each electrode. In order to obtain the series of electrodes based on Nafion (N-Elect), the ink was prepared by ultrasonication in an open vessel for 1 hr of a suspension made with the active material (DLC), 2 ml 2-propanol, and varying the concentration of Nafion (1, 2, 3, 4 and 5wt%). In the case of Kinar Flex based electrodes (KF-Electr) , the active material was stirred for 24 hours with different amounts of Kinar Flex (3, 4, 5, 10 wt%) in acetone.

The electrodes were characterized electrochemically by cyclic voltammetry in a three-electrode cell, using as reference electrode a saturated sulfate electrode (SSE), a platinum mesh as the counter electrode, and our fabricated electrodes as the working electrode. Impedance spectroscopy was carried out at open potential circuit (OPC)

2.2 Lab-Supercapacitor Assembly

A lab-scale assembly was used to evaluate different current collectors using an excess of electrolyte. For this assembly two acrylic plates and four Teflon screws were used as mechanical support of the 2-electrode cell. Figure 2 shows the components for this supercapacitor assembly, where two identical electrodes separated by a filter paper to avoid electric contact are pressed with the acrylic plates, immersed in 0.5 M H_2SO_4 electrolyte, and sealed with a plastic bag to avoid electrolyte evaporation.

Figure 2. Lab-assembly supercapacitor.

In this cell assembly a stainless steel mesh as current collector coupled to a carbon paper support, and a carbon cloth current collector and support were evaluated. A binder-free suspension made from 0.1 g DLC and 2 ml of 2-propanol was ultrasonicated for 1 hr and deposited by aerography on the surface of 4 cm^2 electrodes before the assembly.
The electrochemical devices were characterized by galvanostatic cycling at a constant current that was setup to obtain a complete discharge of the supercapacitor cell in 100 s. Cyclability test were carried out by 7000 charge-discharge cycles and the capacitance was calculated according to eq. (1).

— (1)

where C is the capacitance I is the applied constant current, t is the discharge time (≈100s) and ΔV is the potential window.

2.3 Prototype Cell

A portable prototype with a thin and flat configuration cell package is shown in Figure 3. In this case it is possible to assess the electrolyte contribution (ionic source depletion) to the cell performance, since it is restricted by the cell design. The cycling stability through the retained capacitance was investigated in 7000 charge-discharge galvanostatic cycles, using a current that permits a 100s discharge time.

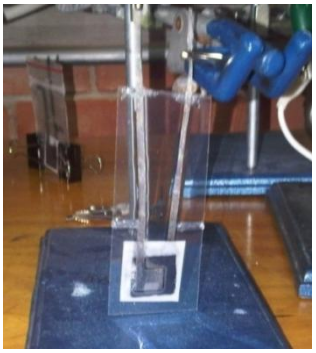

Figure 3. Prototype thin-supercapacitor cell.

3. Results and Discussion

ELECTRODE EVALUATION

The influence of binders on the electrode performance for supercapacitor applications was investigated electrochemically by cycling voltammetry analysis for the two series of electrodes earlier described: N-Elect and KF-Elect, prepared with Nafion and Kinar Flex respectively. All experiments were carried out in 0.5 M H_2SO_4 at 25 °C.

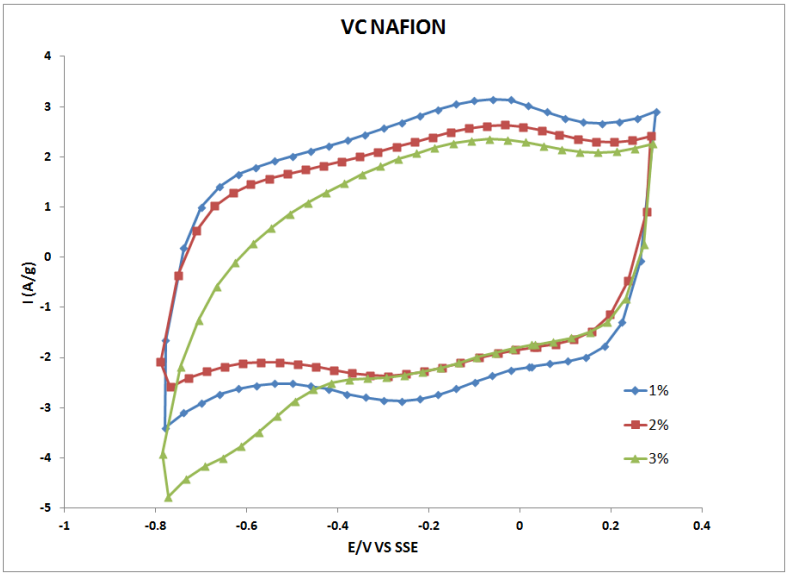

Figure 4.- Electrode Cyclic voltammetry response of N-Elect at different binder concentration, 0.5 M H2SO4 and scan rate 20 mVs-1.

Figure 4 shows the cyclic voltammetry carried out at 20mV/s for all electrodes of N-Elect series with different amounts of Nafion, where a potential range from -0.8 to 0.3 V was used to avoid electrolyte decomposition. For 1 and 2 wt% Nafion concentrations, the voltamperometric profile almost remained a rectangular form, typical response of charge accumulation on the double layer. For binder concentrations higher than 2 wt% (3, 4 and 5 wt%) an inclination of the voltammogram profile is observed on the cathodic limit and is related with the increase of electrode

resistance. The capacitance values calculated from the voltamogram integer as we seen in eq. 1 for low-resistance electrodes are 245 F/g for 1% Nafion electrode and of 202 F/g for 2% Nafion electrode. Therefore, the 1 wt% Nafion electrode resulted in the best performance with higher capacitance value and lower resistance, determined by cyclic voltammetry.

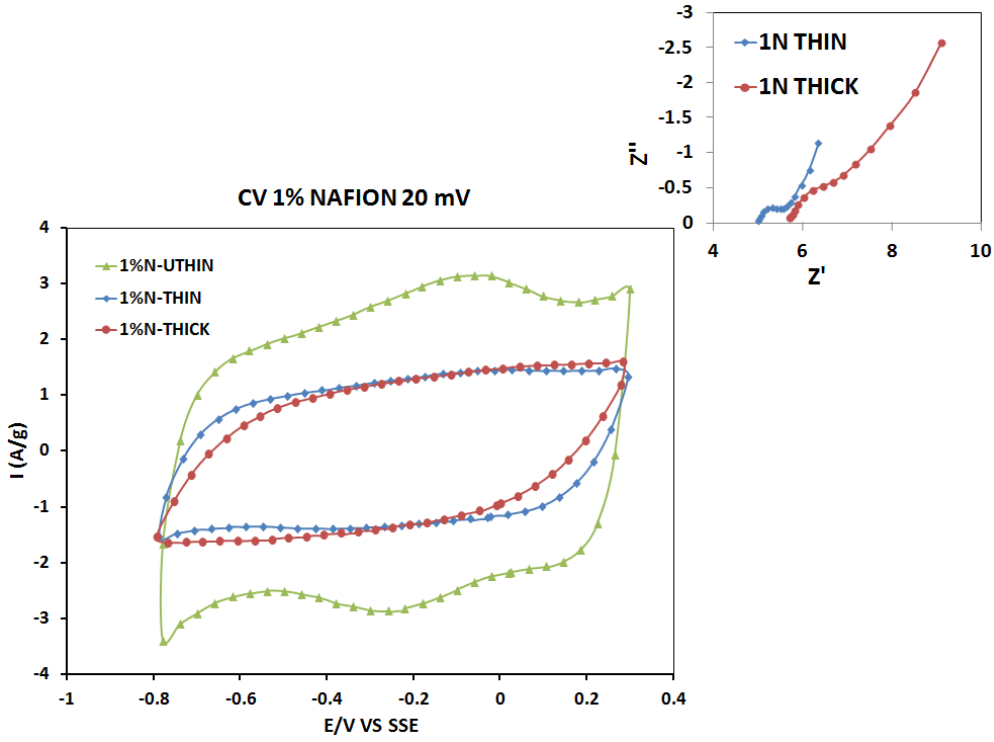

Figure 5. Cyclic Voltammetry of Nafion 1% electrodes with different thickness carried out at 20 mv/s and in the inset electrochemical impedance of these electrodes are shown.

Thickness of electrodes in supercapacitor cells is a parameter that needs to be improved due to variation in resistance, which is an important parameter to take into consideration for these high power devices. Therefore, the electrode thicknesses of 1% Nafion formulation was varied and are labeled as 1%N-Thick, 1%N-Thin, and 1%N-Ultrathin. Figure 5 shows the voltammograms of these electrodes, where the capacitive profile is observed with higher current range for the 1%N-Ultrathin electrode. The inclination or deviation from the rectangular profile is related with resistance in the electrode and these phenomena increases with the thickness increase of the electrode. In the inset of figure 5 the electrical response from Electrochemical Impedance Spectroscopy (EIS) of two prepared electrodes: 1N-thin and 1N-thick electrodes are shown as an example. Series resistance is very similar in both electrodes (about 1.25 Ωcm^{-2} , because the area in the electrode is $4cm^2$), demonstrating the low resistance of the electrodes using this fabrication method. On the axis cut the charge transfer resistance can be detected, showing a

lower value for 1%N-thin electrode than for 1%N-thick electrode. In addition, at very low frequency range it is observed that the species diffusion in 1N-thin electrode is greater than 1N-thick electrode. The behavior observed in these two electrodes can be related with a better porosity distribution in 1%N-thin that makes the surface of the electrode more accessible to the electrolyte. Also, it is observed a combined charge mechanism in 1N-thick electrode due to the appearance of a non-defined Warburg semi-infinity diffusion at low frequencies, which has been observed in electrochemical systems occurring incomplete charge transfer process in non porous medium.

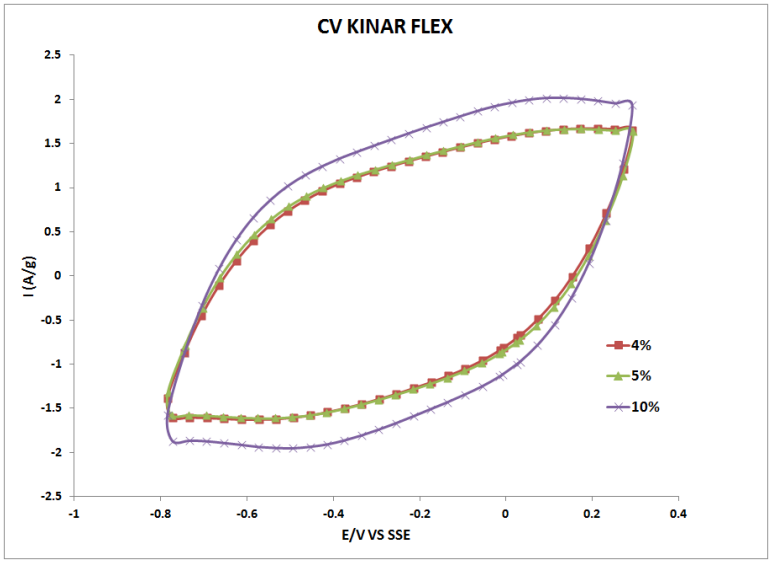

Figure 6.- Cyclic Voltammetry of KF-Electr series in 0.5M H2SO4 electrolyte using a scan rate 20mVs-1

Figure 6 shows the voltammetry response of KF-Electr series as a function of binder concentration. The voltammograms show the typical charge storage mechanism (rectangular profile) of carbonaceous materials controlled by double layer adsorption. Nevertheless, the observed inclination in all electrodes indicates the higher resistance contribution compared to N-Electr series. The use of 10 wt% Kinar Flex showed a moderate current range increase and the electrode resistance is lower than the other concentrations. Capacitance values were obtained from these profiles, resulting in 120F/g for 4%-KF, 121F/g for 5%-KF, and 149F/g for 10%-KF.

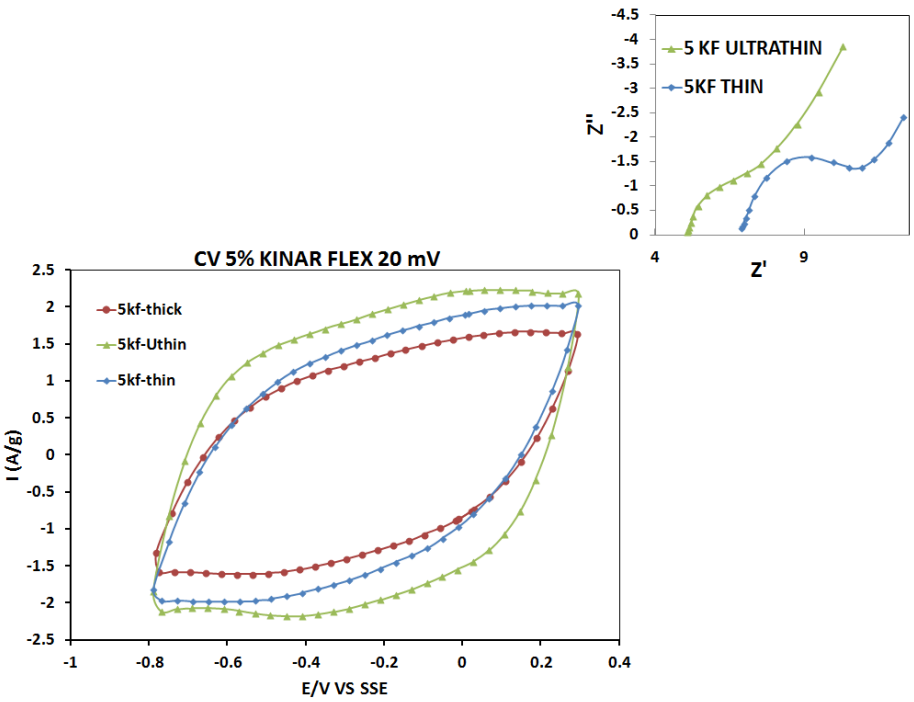

Figure 7. Cyclic Voltammetry of 5%-KF with different thicknesses and electrochemical impedance spectroscopy on the inset.

As for the N-Electr series, variation of the thickness was carried out for 5 and 10%-KF electrodes and the cyclic voltammetry and electrochemical impedance spectroscopy (EIS) results are shown in figures 7 and 8. In general, the voltammograms resistance evidenced by the inclination of the profile varied with the film thickness in both concentrations of Kinar Flex used. The resistance decreased as the electrode went from thick to ultrathin.

The EIS results of 5KF electrodes was carried out for the thin (5KF-Uthin) and thick electrode (5KF-thin). The calculated series resistance values (ESR) detected on EIS were very similar in both electrodes, indicating the similar setup operation conditions where the experiments were carried out. 5KF-Uthin electrode showed a lower charge transfer resistance than 5KF-thin electrode [15]. The lower charge transfer resistance is due to the better ion-electron interaction at the porous interface of the thin electrode. The semiconductor nature of thick electrode controls the transfer mechanism at very low frequency, indicating the presence of a non-diffusion process on the electrode surface.

In figure 8 the electrical response from EIS is shown for the two prepared electrodes: thin and thick electrodes at very high binder concentration (10KF-Uthin and 10KF-thin electrodes respectively). The influence of high binder concentration does not affect significantly the series resistance of the electrochemical systems, but it clearly affects the electron transfer mechanistic processes in both electrodes. Thin electrode (10KF-Uthin) shows a simple electronic transfer formed by a charge transfer resistance and diffusion process due to low-porosity concentration. In the case of thick electrode (10KF-thin), it is shown a more complex mechanism to transfer electrons at intermediate

frequencies. It is probably due to charge transfer resistance coupled to adsorption process as a function of thick semiconductor material (carbon) and low-porosity degree. This combined process produces a change in the response of the electric properties of ion-electron interaction in this kind of material.

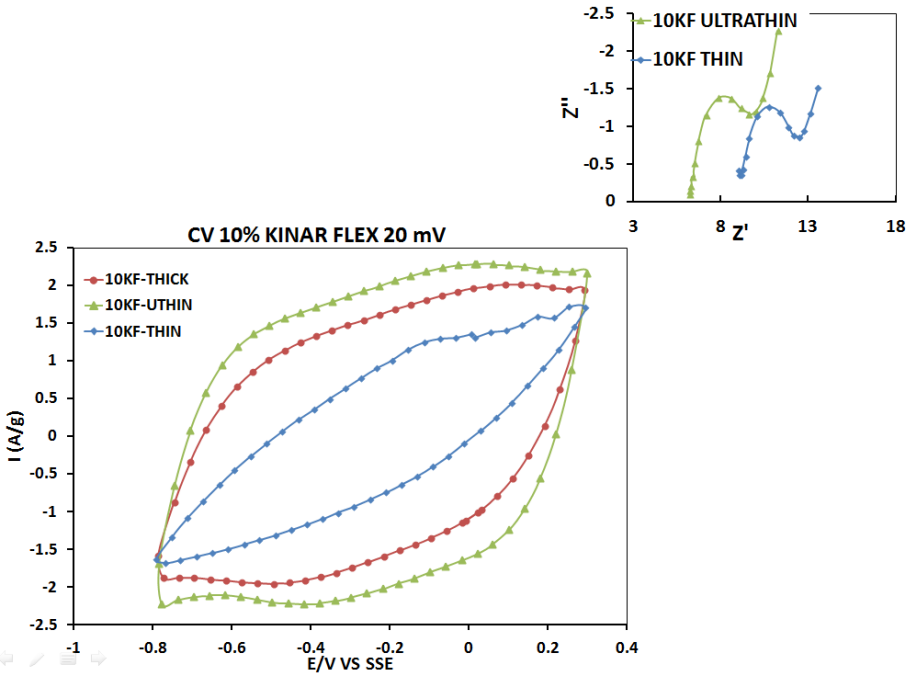

Figure 8. Cyclic Voltammetry of 10%-KF with different thicknesses and electrochemical impedance spectroscopy on the inset.

LAB AND PROTOTYPE SUPERCAPACITOR ASSEMBLY

Binders are normally used in supercapacitors to promote stability performance over 5,000 charge/discharge cycles, but the use of binders also affects the capacitance and resistance of the electrochemical devices, as shown previously. A Lab-assembly has been carried out with bind-less electrodes in order to evaluate different current collectors and a prototype has been developed to evaluate the electrolyte limitations due to design and the results are shown in Figure 9.

Lab assemblies shown in figure 9 using stainless steel mesh as current collector and carbon paper as support (Lab mesh-paper) resulted in 50% less specific capacitance (≈21F/g) than when using carbon cloth as current collector and support (Lab Cloth, 38F/g). This result could be associated to the extra component (stainless steel mesh) resulting in a higher contact resistance with the carbon paper. Carbon paper is so hydrophilic that the electrolyte migrates to the metal connections by capillarity, destroying them when long cycling is carried out. Therefore, since the extra

resistance introduced by the stainless steel mesh to prevent contact oxidation cannot be eliminated, the carbon cloth has shown its excellent properties as a current collector and support for electrode materials assembled in a supercapacitor cell. In addition, the inset on Figure 9 shows the cycling stability of this Lab cell through 7000 charge-discharge cycles.

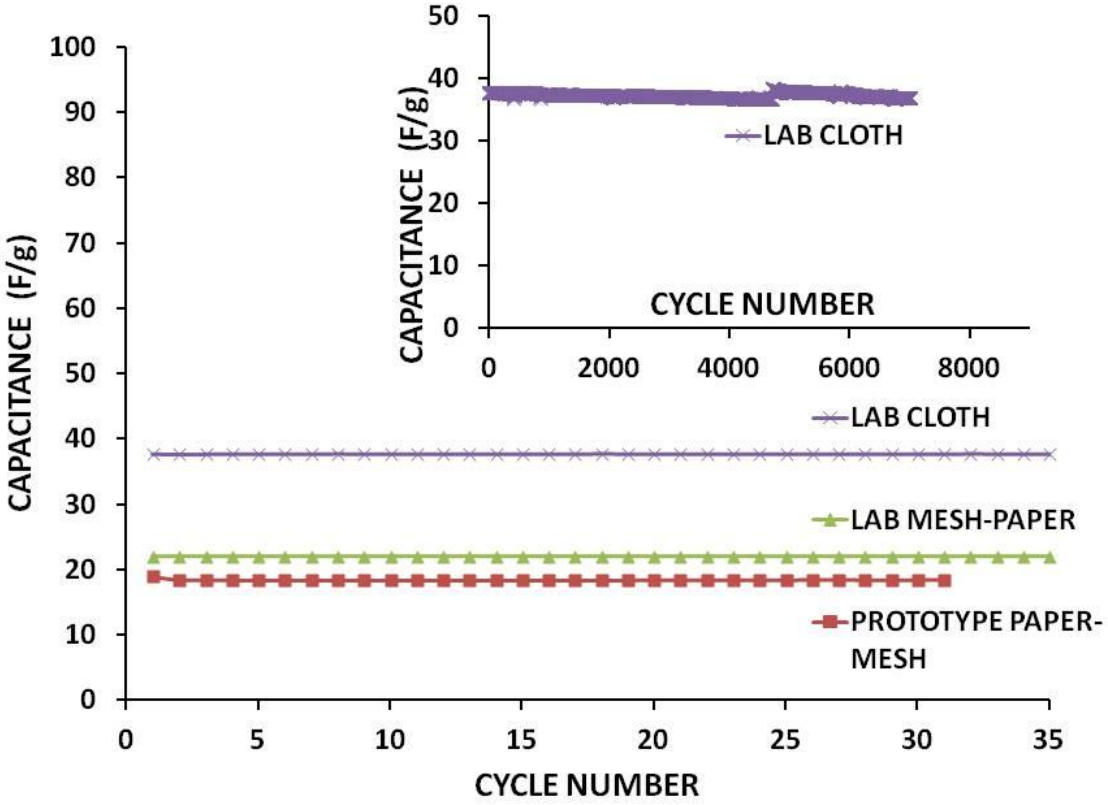

Figure 9. Galvanostatic cycling of Lab and Prototype assemblies using different current collectors using a voltage window of 1.1 V , 0.5M H2SO4 as electrolyte, and 6.5 mA discharge current for cloth based electrode and 3.9 mA discharge current for mesh/paper based electrode.

A thin-prototype has been developed to evaluate the electrolyte limitations due to design. In the thin-prototype and the lab assembly using a mesh-paper as current collector and support, differences can be hardly observed in capacitances values during the first 30 charge-discharge cycles. These results suggest that the electrolyte quantity in the prototype is not a limiting factor and the 2F/g difference in both assemblies could be more related with other parameters as pressure that is not studied here.

4. Conclusions

For conventional electrodes in supercapacitor applications, it is possible to consider the use of 1 wt% Nafion solution as binder for optimum electrode performance, obtaining the maximum specific capacitance and minimum electric resistance contribution, considering the importance of the film thickness in the electrode. The use of carbon cloth as support and current collector for electrode materials resulted in a minimum contact resistance, maximizing the capacitance value up to 38F/g. A prototype design has been proposed and it is also possible to consider the use of carbon cloth in portable devices as current collector, avoiding the ionic source depletion due to reduced amount of electrolyte.

5. Acknowledgements

We acknowledge the technical work of M.I. Francisco Ginez Carbajal, M.I. María Adriana García López, Dr. Sergio Alberto Gamboa Sanchez, and the financial support granted from CONACYT Basic Science Project 154259 and PAPIIT Project IN105410.

6. References

[1] Martin Winter, Ralph J. Brodd, Chem. Rev. 104, 4245 (2004).

[2] Graeme A. Snooka, Pon Kao, Adam S. Best, Journal of Power Sources, 196, 1 (2011).

[3] M. Conte, Fuel Cells, 10, 806, (2010).

[4] B. E. Conway, Electrochemical Capacitors: Scientific Fundamentals and Technological Applications, Kluwer Academic Plenum. New York (1999).

[5] Basics of Electrochemical Impedance Spectroscopy (EIS), Appl. Note AC-1, Princeton Applied Research (2008).

[6] A. Hammar et al., "Electrical Characterization and Modeling of Round Spiral Supercapacitors for High Power Applications (AC Impedance Testing)," paper presented at ESSCAP 2006, Lausanne, Switzerland.

[7] Andrew Burke, Marshall Miller, Electrochimica Acta, 55, 7538, (2010).

[8] Alexis Laforgue, Journal of Power Sources, 196, 559, (2011).

[9] Ying-Ying Horng, Yi-Chen Lu, Yu-Kuei Hsu, Chia-Chun Chen, Li-Chyong Chen, Kuei-Hsien Chen, Journal of Power Sources, 195, 4418, (2010).

[10] Liangbing Hu, Mauro Pasta, Fabio La Mantia, LiFeng Cui, Sangmoo Jeong, Heather Dawn Deshazer, Jang Wook Choi, Seung Min Han and Yi Cui, Nano Letters, 10, 708, (2010).

[11] Martti Kaempgen, Candace K. Chan, J. Ma, Yi Cui and George Gruner, Nano Letters, 9, 1872, (2009).

[12] Chuizhou Meng, Changhong Liu, Shoushan Fan, Electrochemistry Communications, 11, 186, (2009).

[13] Victor L. Pushparaj, Manikoth M. Shaijumon, Ashavani Kumar, Saravanababu Murugesan, Lijie Ci, Robert Vajtai, Robert J. Linhardt, Omkaram Nalamasu and Pulickel M. Ajayan, Proceedings of the National Academy of Sciences, 104, 13574, (2007).

[14] Chuizhou Meng, Changhong Liu, Luzhuo Chen, Chunhua Hu, and Shoushan Fan, Nano Letters 10 (2010) 4025-4031.

[15] A. Lasia, Electrochemical Impedance Spectroscopy and Its Applications, Modern Aspects of Electrochemistry, B. E. Conway, J. Bockris, and R.E. White, Edts., Kluwer Academic/Plenum Publishers, New York, Vol. 32, p. 143. 1999.

Comparison of a Chemical and an Electrochemical Enrichment Methods of a Saline Inoculum for Microbial Fuel Cells

K. Sathish-Kumar[1], O. Solorza-Feria[2,1], J. Tapia-Ramírez[3], , N. Rinderkenecht-Seijas[4], H. M. Poggi-Varaldo[4,1*]

[1]Doctoral Program of Nanoscience and Nanotechnology, Centro de Investigación y de Estudios Avanzados del IPN, Mexico D.F., México
[2]Depto. Química, Hydrogen and Fuel Cells Group, Centro de Investigación y de Estudios Avanzados del IPN, México D.F., México
[3]Dept. of Genetics and Molecular Biology, Centro de Investigación y de Estudios Avanzados del IPN, Mexico D.F., México
[4.] ESIQIE-IPN, Division Basic Science, Campus Zacatenco, Mexico D.F., Mexico
[5]Environmental Biotechnology and Renewable Energies R&D Group, Dept. Biotechnology and Bioengineering, Centro de Investigación y de Estudios Avanzados del Instituto Politécnico Nacional, P.O. Box 14-740, 07000 México D.F., México.
[*]Author for correspondence: Phone: 5255 5747 3800 x 4324, Fax: 5255 5747 3313.
E-mail: hectorpoggi2001@gmail.com

ABSTRACT

In microbial fuel cells (MFCs) efficient extracellular electron transfer microbes, also known as anode-respiring bacteria, play an important role on cell performance. These type of microbes can be developed by application of enrichment procedures. The objective of this study was to compare a chemical (only ***C***, final terminal electron acceptor Fe(III), an electrochemical (only ***E***), and a hybrid method (***E*** followed by ***C***) enrichment methods departing from a saline-sodic soil inoculum. In the electrochemical enrichment procedure in an electrolysis cell, the inoculum was subjected to a continuous electrical stress continually by posing the cell at -150mV/SCE. The only ***C*** enrichment method delivered powers superior to the only ***E*** one (higher values of $P_{An,max}$ = 49 mW/m^2 and $P_{V,max}$ = 558 mW/m^3 of C compared to 33 and 379 of only ***E***). Interestingly, overall resistance as determined by EIS was lower for only E (1240 Ω) than for only ***C*** (1632 Ω). Yet, the hybrid ***E*** method (***E*** followed by ***C*** as given by three serial transfers after the enrichment in the electrolysis cell), showed electrochemical characteristics consistently superior toboth only ***C*** and only ***E*** methods (higher $P_{An,max}$ and $P_{V,max}$, lower internal resistance). Further detailed electrochemical studies of only ***E***-method showed that the anodic resistance decreased with the time of operation of the electrolysis cell that would be consistent with the adaptability/enrichment purpose of the method. Also, Cyclic Voltammetry peaks with values close to those reported for bacterial cytochromes appeared with time of cell operation.

To the best of our knowledge, this is the first time that it is reported that serial transfers with Fe(III) as electron acceptor to an inoculum previously enriched in an electrolysis cell, leads to improved characteristics of microbial fuel cell and increased Fe(III)-reducing capability of the inoculum.

Key words: electrochemical active bacteria, electrolysis, enrichment, exocellular electron transfer, Iron (III), microbial fuel cell

1. Introduction

A microbial fuel cell is an electro-biochemical reactor capable of directly converting organic matter into electricity. In the anodic chamber the microorganisms anoxically oxidize the organic matter and release electrons and protons. Electrons are transported to the anode that acts as an intermediate, external electron acceptor. The electrons flow through an external circuit where there is a resistor or a device to be powered, producing electricity and finally react at the cathode with the protons and oxygen producing water. Microbial fuel cells (MFCs) constitute a promising technology for sustainable production of alternative energy and waste treatment [1].MFCs performance is depends on the internal resistance, cell architecture, type of inocula and some other factors[2,3].

In microbial fuel cells (MFCs) efficient extracellular electron transfer microbes (EETM) also known as anode-respiring bacteria (ARB) can play an important role on cell performance. Selection of the suitable microbes for MFCs by the different redox potentials of electron acceptors, the energetic requirements of a cell vary depending upon the terminal electron acceptor, for example: *(i)* internal electron acceptor (such as fumarate), *(ii)* external electron acceptor such as insoluble Fe (III) and *(iii)* solid electrode with an internal electron acceptor. There is some evidence that the anode potential, rather than the acceptor concentration, regulates the thermodynamic energy available for ARB to grow [4]. It is generally accepted that ARB communities should be capable of switching their respiratory mechanism in order to maximize the energy obtained for ATP production as the anode potential changes. In a mixed ARB community, several respiratory pathways could be available, and the community may be able to maximize energy efficiency by adapting to the anode potential. Torres et al., 2009 used activated sludge as inoculum and found that the two electrodes at the lowest potential showed a faster biofilm growth and produced the highest current densities, reaching a value up to 10.3 A/m^2. Therefore, anodic potential regulation as incisive selective pressure on microbial community can be an important tool for enrichment of efficient ARB community growth.

Cho et al.[5] performed a chemical enrichment by successive cultures of *Shewanella oneidensis* MR-1. Actually the serial cultures implemented with a soluble electron donor (lactate) and acceptors (fumarate) were mainly aimed at preadapting the bacterial metabolism to the anaerobic environment in the MFC. Compared with unadapted bacteria, the anaerobically adapted cells showed improved efficiency in electricity generation of around 30%, even after re-exposure to air. This suggests an adaptation of the microbial population due to metabolic adaptations or genetic mutations [5].

Rabaey et al.[6] have described enrichment by successive transfers of a bacterial consortium from the anodic compartment of an MFC [6]. The biofilm formed on the anode was scratched and used to inoculate a new MFC. During the enrichment period, the power output increased from 0.6 W·m-2 of anode surface to a maximum of 4.31W·m-2. It was concluded that microbial fuel cells enhanced the growth of bacteria that could use the electrode as a final electron acceptor. EETM is likely that combination of multiple enzymes to catalyze the oxidation of carbon

sources such as glucose and transfer electrons to the electrode by: *(i)* direct electron transfer (membrane bound enzymes, bacterial nanowire); *(ii)* indirect electron transfer (self mediator/mediator) [7-10].

It is known that interspecies electron transfer is a key process in methanogenic and sulphate-reducing environments. The objective of this study was to compare three methods of enrichment: chemical (final terminal electron acceptor – Fe(III)), electrochemical (final terminal electron acceptor- solid anode poised with -150 mV vs. Saturated calomel electrode), and a hybrid method (electrochemical followed by chemical) of a saline-sodic soil inoculum from Texcoco lake, Mexico, D.F. The final terminal electron acceptor in the electrochemical method was a solid electrode surface through this more efficient ARB community selected for MFCs applications. An electrochemical tool was used to characterize the ARB community developed at anode surface.

2. Experimental

Sampling for inoculum and enrichment

Samples were collected from the former Texcoco lake in a sterile anaerobic container and preserved aseptically. The sampling site is the dry bottom of a historically desiccated lake in central Mexico; it accumulated the salts in that process and the soils are known to be saline-sodic (Table 1 from [11]) Electrochemically enriched Texcoco soil bacterial community was enriched and preserved in modified Soap Lake basal medium (SLBM) called SL3 medium [12]. This medium was used in enrichment, preservation and electrolysis cell process. The culture was preserved in Refrigerator at -10ºC.

Table 1. Characteristics of Texcoco soil

Site	Salinity	pH	Conductivity of the extract	Texture
Former Texcoco Lake	80-90 g L^{-1}	9.5-11	200 mS cm^{-1}	Sandy clay loam

Electrochemical set-up and electrode preparation

The working (geometrical area- 14.05 cm^2) and counter electrodes (geometrical area- 20.5 cm^2) were Graphite rods. A saturated calomel electrode was used as a reference electrode. The modified SL3 medium with 15mM of sodium acetate was used as carbon source. Potentials were applied with a 273A Potentiostat/Galvanostat from EG&G Princeton Applied Research. Temperature was set at 30ºC. Graphite rods were submerged in 0.5 M KCl solution for 3 h, after that the graphite rods were polished with 1500b sand paper and rinsed with deionized water before use. The graphite rods were submerged in 0.5 M KCl solution overnight in order to activate them. In order to selectively grow the electro active biofilm of ARB, a potential step of -150 mV was applied over 150 day. During this period, the current was monitored. Later on the biofilm was sup cultured using SL3 medium.

Chemical (*C*) and electrochemical (*E*) method of enrichment

Initial inoculum of Texcoco soil was incubated in 1g of soil for Chemically activated Halo alkaliphilic bacteria: 1g of

biofilm scarped from the bioelectrolysis cell for electrochemically active halo alkaliphilic bacteria into 99 ml modified SL3 medium for both chemically and electrochemically activated Halo alkaliphilic bacteria with 15mM of sodium acetate used as carbon source and 20 mM iron (III) citrate as terminal electron acceptor, After the incubation period of 12 days taken the 1 ml of above culture solution was transferred into fresh 99 ml modified SL3 medium (serial transfer I) . Afterwards, similar cultures every 12 days time intervals up to serial transfer III (hybrid ***E***) (Fig 1.). Iron reduction and SCMFC characteristics were evaluated using inoculum of each serial transfer.

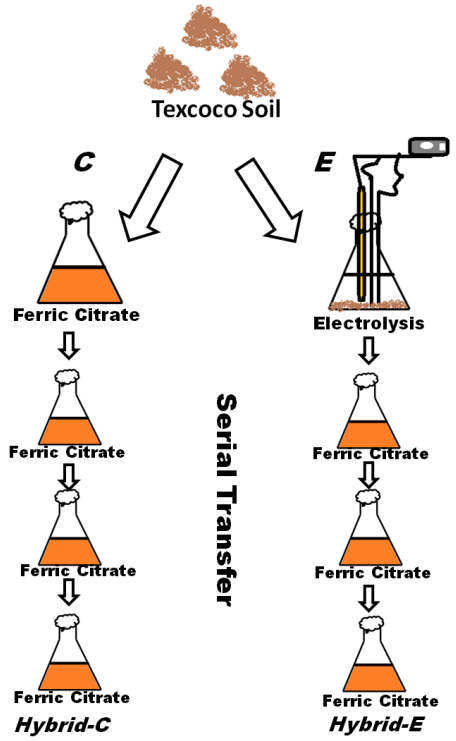

Figure 1. Schematic representation of the ***C*** and ***E*** enrichment serial transfer

Vertical single-chamber microbial fuel cell (SCMFC)

Construction of single chamber microbial fuel cell (SCMFC) details can be found elsewhere [13]

Electrochemical impedance spectroscopy and linear sweep voltammetry studies

Impedance spectra of biofilm were obtained at the open circuit potential (Eocp). The amplitude of the signal perturbation was 10 mV, the frequency range scanned was from 100 kHz to 1 mHz. Impedance experiments were performed in the potentiostat/galvanostat Volta lab model PGZ402. Data fitting was accomplished by appropriate software, such as Z-view. Liner sweep voltammetry (LSV), was run at the recommended scan rate of 1mV s-1 starting from the measured open circuit potential [14] using a 273A Potentiostat/Galvanostat from EG&G Princeton Applied Research.

Cyclic voltammetry

Cyclic voltammetry (CV) studies were performed on the SCMFC with a PARSTAT 2273 Potentiostat/Galvanostat from Princeton Applied Research. The working electrode was the anode. The reference electrode was a standard calomel electrode (SCE) that was in contact with the cell liquor through a saline bridge known as Luggin capillary tube placed closely to the working electrode. The counter electrode was the cathode. The scan rate was 15mV/s.

Most probable number of iron reducing bacteria

Initial inoculum of Texcoco soil was incubated in 1g of soil for Chemically activated Halo alkaliphilic bacteria: 1g of biofilm for electrochemically active halo alkaliphilic bacteria into 99 ml modified SL3 medium for both chemically and electrochemically activated Halo alkaliphilic bacteria with 15mM of sodium acetate used as carbon source and 20 mM iron (III) citrate as terminal electron acceptor, set to be 10^{-1} dilution and 10 ml of above inoculum transferred into 90 ml of SL3 medium set to be 10^{-2} dilution, from that 10 ml of inoculum transferred into 90 ml of SL3 medium as 10^{-3} dilution. Similarly continue the dilution up to 10^{-5} dilution. After the incubation period (~12 days) it was performed the iron reduction test in a plastic well using ferrozine technique [15].

HPLC and UV-Vis spectrophotometer analysis

Secondary metabolism of E-HAB in SCMFC was analysed through HPLC. UV-Vis Spectrophotometery was carried in the wavelength of 200-800nm.

Protein estimation and Sodium Dodecylsulfate Poly(acrylamide) Gel Electrophoresis (SDS-PAGE) Experiments

Protein was precipitated by the trichloroacetic acid (TCA) method [16] from the supernatant solution of the liquor in the SCMFC. Bradford method was used to estimate the protein [17]. SDS-PAGE experiments were run with electrophoresis unit of Bio-Rad [16].

3. Results and discussion

Enrichment of electrochemical active halo alkalophilic bacteria (E-HAB) was performed by variation of current intensity during biofilm formation at -150mV vs SCE as shown in Fig.2a. During the first 5 days, the recorded current was very small. After 5 days, the current started to increase and attained the maximum value of 1.8 mA in the 28th day. Subsequent to 30 days the current decreased down to 0.4mA. Addition of carbon source at 75th day lead to an increase in the current up to 0.8mA in at 135th day (Fig2a). Variation of current intensity during biofilm formation at -150mV vs SCE resembled the bacterial sigmoidal growth curve; the latter is in agreement with previous reported

works [18]. During the first 5 days, the growth of microbial colonies was observed on the graphite rod (anode) in the log phase related to low current. Following 5 days, the biofilm ARB grew and attained the maximum current in the 28th day, probably due to attaining the stationary phase. The depletion of substrate probably lead to the microbial colonies to decline phase of growth, that started in the 30th day. By adding the carbon source at the 75th day the bacterial community started to grow again; this was reflected by the current increment and attained 0.8mA in the stationary phase.

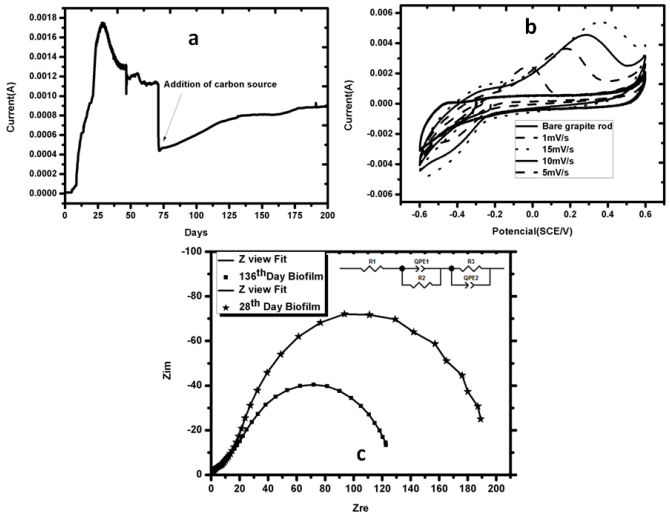

Fig. 2 (a). Variation of Current (A) during biofilm formation at -150mV vs saturated calomel electrode. (b). Cyclic voltammetry of initial GR at 15mV/s. the cyclic voltammetry of biofilm in bicarbonate buffer (0.1M) with 15mM of sodium acetate as carbon source were measured at different scan rates. (c). Electrochemical impedance spectroscopy of biofilm electrode.

Cyclic voltammetry (CV) experiments were performed for further investigate the electrochemical character of the biofilm. In the initial 4 days, the cyclic voltammograms showed no peaks, presumably due to the fact that the biofilm has not been completely formed (results not shown). CV was performed at the 28th day at a different scan rate upto 15 mV/s. Midpoint potential deduced from the cyclic voltammetry, was +108mV vs standard hydrogen electrode (SHE). This value is close to the alkaliphilic cytochromes potential range [19]. Concomitantly, it could be related to the soluble/membrane-bound cytochromes from alkaliphilic bacteria [19]. By increasing the scan rate the anodic peak shifted to more positive values (Fig. 2b). Even though there was an anodic peak, the corresponding cathodic peak did not provide the same area under the anodic curve (anodic charge). This suggests that an irreversible process is occurring. A similar pattern occurred at the 136th day (data not shown). One of the possible reasons for the irreversible process would be fouling of the electrode surface by strong irreversible adsorption of chemicals [20], or to an increased thickness of the biofilm. Membrane bound enzymes (cytochrome) of biofilm is required to be independent of the electroactive ARB`s metabolism [21].

Electrochemical impedance spectroscopy (EIS) at 28th day and 136th day revealed two semicircles (Fig. 2c). The impedance spectra at 28th day and 136th day were fitted to an appropriate equivalent circuit (EC). A simple EC used

for describing the electrochemical properties of the ARB biofilm is shown in Fig. 2(c). The obtained values of the resistance of the film (R2) were 11.1Ω for the 28th day and 5.5 Ω for the 136th day. From the EIS, the high frequency semicircle could be associated to ARB biofilm electrical properties. The low frequency semicircle was probably linked to the processes occurring at the biofilm/solution interface. The tendency of biofilm resistance was decreased with time of operation. This may be due to the adaptability / enrichment of electroactive bacteria on the surface of the graphite rod which may reduce the internal resistance.

Comparison of of the enrichment methods is shown in Tables 2 and 3. When comparing the ***only C*** (results of 3rd transfer in Table 2) and ***only E*** methods (results of 0 transfer in Table 1), ***only C*** was superior with higher values of $P_{An,max}$ = 48.5 and $P_{V,max}$ = 558 of ***C*** compared to 33 and 379 of ***E***. Yet, the overall resistance as determined by EIS was also lower for ***only E*** (1240 Ω) than for ***only C*** (1632 Ω) (Table 3). When considering the ***hybrid E*** method (***E*** followed by ***C*** as given by the three serial transfers), the electrochemical characteristics ot the ***hybrid E*** were consistently superior to ***only C*** (higher $P_{An,max}$ and $P_{V,max}$, lower internal resistance).

Table 2. Serial transfer studies for enrichments of alkaliphilic inocula for a single chamber microbial fuel cell.

Serial transfer	Enrich-ment metod	Concentration of Fe(II) (mM)		Most Probable Number	$P_{An,max}$ (mW/m^2) $P_{V,max}$ (mW/m^3)
		Initial	Final		
0	***E***	6.2±0.1	31.3±0.6	6148±2	33.0±0.6 378.9±1.1
	C	4.7±0.02	22.7±0.3	8500±15	16.0±0.3 183.7±0.7
I-Serial Transfer	***E***	8.5±0.3	46.8±0.7	5144±5	42.5±1.0 488.9±4.7
	C	6.2±0.5	36.9±0.8	5144±5	31.9±0.6 367.3±0.8
II-Serial Transfer	***E***	13.0±0.5	78.2±1.1	3450±1	52.5±1.2 603.5±0.6
	C	10.3±0.5	69.6±0.3	6148±1	37.4±0.4 430.0±1.5
III-Serial Transfer	***E***	16.0±0.8	79.8±0.7	3399±1	81.2±0.6 934.2±1.8
	C	14.3±0.2	70.1±1.0	4012±2	48.5±1.0 557.6±1.1

Iron reducing activity of both ***E*** and ***C***-enriched inocula increased with the transfer number (Table 2). In general, serial transfer studies of iron reduction activity showed improved characteristics of microbial fuel cell, in agreement with findings of Cho and Ellington [5] and Rabaey et al. [6]. Unexpectedly, MPN of Fe(III)-reducing bacteria was reduced by 40 to 50% of the initial amount for the last transfer in both enrichment methods (Table 2).

Table 2. Electrode and membrane/electrolyte resistances of the MFC by EIS with enriched inocula

Serial Transfer	Enrich-ment metod	R_a	R_c	R_m	$R_{int}=R_a+R_c+R_m$
0	*E*	1098±2	534±1	0.86±0.01	1632±2
	C	1292±2	580±1	0.83±0.03	1872±2
I	*E*	981±1	152±1	0.69±0.02	1132±2
	C	1152±3	468±2	0.86±0.05	1620±1
II	*E*	874±2	209±1	0.41±0.04	1083±2
	C	1081±4	471±1	0.79±0.02	1552±4
III	*E*	620±1	227±2	0.53±0.05	837±1
	C	977±2	263±1	0.65±0.03	1240±1

The supernatant solution collected from the SCMFC was qualitatively analyzed through HPLC technique. It revealed the presence of acetic acid, butyric acid, ethanol, and propionic acid. This is may be associated to mixed microbial flora respiration end products. Afterwards, fresh SL3 medium was added to the SCMFC which was already seeded with the biofilm of the sodic-saline inocula. Then, cyclic voltammetry was performed. Fig.3. shows the voltammogram of the bare carbon cloth and biofilm formed on carbon cloth seeded with E-HAB in SCMFC.

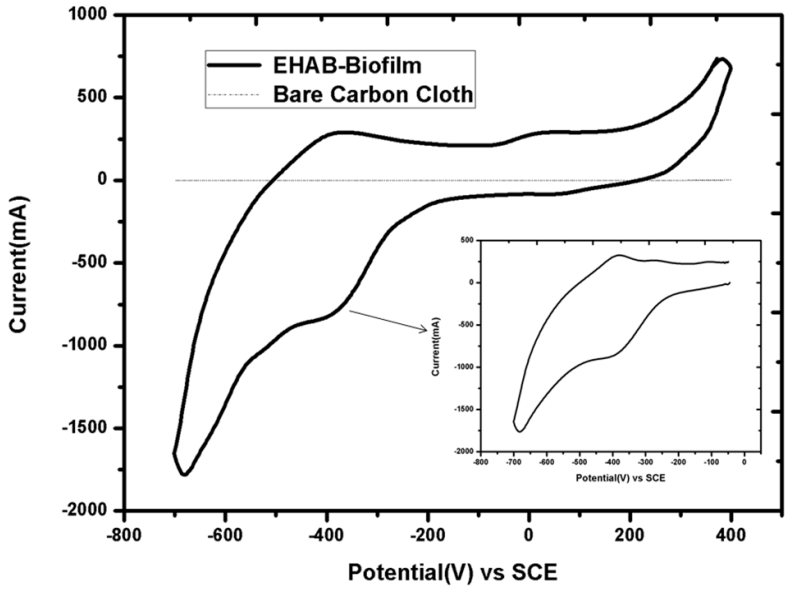

Figure 3.Cyclic voltammetry of the bare and biofilm formed carbon cloth at the scan rate of 15mV/s

The bare carbon cloth did not show any electrochemical response from which we conclude that there is no current generation in the absence of microflora in the SCMFC. Biofilm formed on carbon cloth exhibited two redox

reactions on the surface with midpoint potentials of -385mV and 18mV vs SCE, respectively. The midpoint potential of -385mV might be associated with membrane bound enzymes of the sodic-saline micro-flora, whereas the potential 18mV/SCE could be associated to the soluble cytochrome activity in agreement with results previously reported [22].

The protein content of the liquor in the SCMFC was 363µg/mL. The supernatant solution from E-HAB in the SCMFC contained a protein with a molecular weight ~45kDa as shown by SDS-PAGE (Fig. 4). It may resemble the soluble excreted cytochrome responsible for the midpoint potential of 18mV. The direct electron transfer could be achieved through the cytochrome (membrane bound/soluble excreted), fostering the communication/charge transfer between the electrode and microbes.

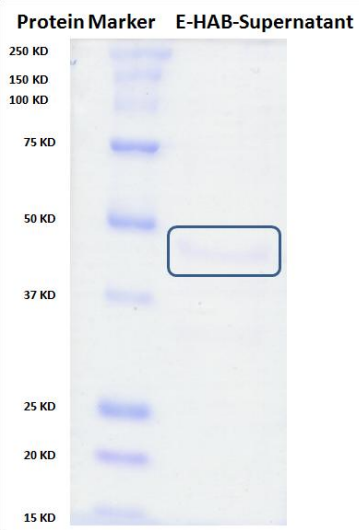

Figure 4. SDS-PAGE analysis of EHAB supernatant solution from SCMFC

Supernatant solution from E-HAB in the SCMFC exhibited a small absorption shoulder at 410 nm (Fig. 5). This was in accordance with the oxidized state of the cytochrome reported by Tomlinson and Ferguson [23].

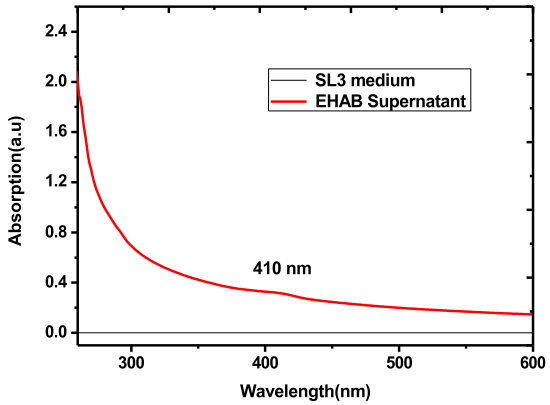

Figure 5. UV-Vis Spectrophotogram of the pure SL3 medium and supernatant solution from SCMFC

4. Conclusion

The ***only C*** enrichment method was superior to the ***only E*** one (higher values of $P_{An,max}$ = 49 and $P_{V,max}$ = 558 of ***C*** compared to 33 and 379 of ***only E***) whereas overall resistance as determined by EIS was lower for ***only E*** (1240 Ω) than for ***only C*** (1632 Ω).

Yet, if we consider the ***hybrid E*** method (***E*** followed by ***C*** as given by the three serial transfers), the electrochemical characteristics of the ***hybrid E*** were consistently superior to ***only C*** (higher $P_{An,max}$ and $P_{V,max}$, lower internal resistance).

Detailed electrochemical studies of ***only E***-method showed that the anodic resistance decreased with the time of operation of the electrolysis cell, that would be consistent with the adaptability/enrichment purpose of the method. Also, CV peaks with values close to those reported for bacterial cytochromes appeared with time of cell operation.

In general, serial transfer studies with Fe(III) as electron acceptor showed improved characteristics of microbial fuel cell and increased Fe(III)-reducing capability of inocula.

Analysis from the Cyclic voltammetry, SDS-PAGE, and UV-Vis Spectrophotometry revealed that the cytochrome (membrane bound/ soluble excreted) might play a vital role in the direct electron transfer in the SCMFC seeded with E-HAB inocula.

5. Acknowledgements

The authors wish to thank SEP and CINVESTAV-IPN for providing a Ph.D. fellowship to one of the authors (KSK). CINVESTAV-IPN and ICYTDF provided partial financial support to this research. The excellent technical assistance of Mr. Rafael Hernández-Vera, M.Sc, GBAER, DBB, CINVESTAV-IPN, is sincerely appreciated.

6. References

[1] A. L. Vázquez-Larios, O. Solorza-Feria, G. Vázquez-Huerta, F. Esparza-García, N. Rinderknecht-Seijas, H. M. Poggi-Varaldo, International Journal of Hydrogen Energy, 36, 6199 (2011).

[2] A.L. Vazquez-Larios, O. Solorza-Feria, G. Vazquez-Huerta, E. Rios-Leal, N. Rinderknecht-Seijas, H.M. Poggi-Varaldo, J. New Mat. Electrochem. Systems, 14(2), 99-105 (2011).

[3] H. M. Poggi-Varaldo, A. Carmona-Martínez, A. L. Vázquez-Larios, O. Solorza-Feria, J. New Mat. Electrochem. Systems, 12, 49-54 (2009)

[4] C. S. I. Torres, R. Krajmalnik-Brown, P. Parameswaran, A.K. Marcus, G. Wanger, Y.A. Gorby, B.E. Rittmann, Environ. Sci. Technol, 43, 9519 (2009).

[5] E. J. Cho and A.D. Ellington, Bioelectrochemistry, *70* (1), 165 (2007).

[6] K. Rabaey, N. Boon, S.D. Siciliano, M. Verhaege, W. Verstraete, Appl. Environ. Microbiol., *70* (9), 5373 (2004).

[7] D. Prasad, S. Arun, M. Murugesan, S. Padmanaban, R. S. Satyanarayanan, S. Berchmans, V. Yegnaraman, Biosensors and Bioelectronics, 22, 2604 (2007).

[8] Y. Qiao, S.-J. Bao, C. M. Li, Energy & Environmental Science, 3, 544 (2010).

[9] G. Reguera, K. D. McCarthy, T. Mehta, J. S. Nicoll, M. T. Tuominen and D. R. Lovley, Nature, 435, 1098 (2005).

[10] A. J. M. Stams and C. M. Plugge, Nat Rev Micro, 7, 568 (2009).

[11] J. Alcocer and W. Williams, International Journal of Salt Lake Research, 5, 45(1996).

[12] M. R. Mormile, M. F. Romine, M. T. Garcia, A. Ventosa, T. J. Bailey, B. M. Peyton, Syst Appl Microbiol, 22, 551 (1999).

[13] K. Sathish-Kumar, O. Solorza-Feria, G. Vázquez-Huerta, J. P. Luna-Arias, H. M. Poggi-Varaldo, J. New Mat. Electrochem. Systems, 15, 181 (2012).

[14] B. E. Logan, B. Hamelers, R. Rozendal, U. Schröder, J. Keller, S. Freguia, P. Aelterman, W. Verstraete, K. Rabaey, Environ. Sci. Technol, 40, 5181 (2006).

[15] D. R. Lovley, E. J. P. Phillips, Appl Environ Microbiol 51, 683 (1986).

[16] K. Sathish Kumar, R.Amutha, P. Arumugam and S. Berchmans, ACS Applied Materials & Interfaces, 3, 1418 (2011).

[17] M. M. Bradford, Anal. Biochem. 72, 248, (1976)

[18] A. Larrosa-Guerrero, Scott K. Katuri, C. Godinez, I. Head, T. Curtis, Applied Microbiology and Biotechnology, 87, 1699 (2010).

[19] D. B. Hicks, T.A. Krulwich, Biochimica et Biophysica Acta (BBA) - Bioenergetics, 1229, 303 (1995).

[20] D. E. Reed, F.M. Hawkridge, Analytical Chemistry, 59(19), 2334 (1987).

[21] C. I. Torres, A. K. Marcus, H-S Lee, P. Parameswaran, R. Krajmalnik-Brown, B. E. Rittmann, FEMS Microbiology Reviews, 34, 3 (2010).

[22] M. Kitada, R. J. Lewis, T. A. Krulwich, J. Bacteriol. 154, 330 (1983).

[23] E. J. Tomlinson and S. J. Ferguson, Proceedings of the National Academy of Sciences, 97, 5156 (2000).

Notation

ARB	anode respiring bacteria
C	chemical enrichment method
CV	cyclic voltammetry
E	electrochemical enrichment method
EIS	electrochemical impedance spectroscopy
HAB	halo alkalophilic bacteria
Hybrid-***E***	serial transfer III of *E*
SCMFC	single chamber microbial fuel cells
SDS-PAGE	sodium dodecylsulfate poly(acrylamide) electrophoresis

Biohydrogen Production in Fluidized Bed Bioreactors: Room Temperature vs 35°C

K. M. Muñoz- Páez [1], J. García-Mena [2], M. T. Ponce-Noyola[3], A. C. Ramos-Valdivia[3], I. V. Robles- González[4], N. Ruiz-Ordáz[5], L. Villa- Tanaca[5], N. Rinderknecht-Seijas[6], H. M. Poggi-Varaldo[1*].

[1]Environmental Biotechnology and Renewable Energies R&D Group, Dept. Biotechnology and Bioengineering. CINVESTAV-IPN. P.O. Box 14-740, México D.F.; [2]. Dept. Genetic and Molecular Biology, ibidem; [3] Dept. Biotechnology and Bioengineering, ibidem; [4] NOVA Universitas. Oax., México; [5] ENCB-IPN. México, D.F.; [6] ESIQIE- IPN, México D.F., Mexico. *Author for all correspondence: hectorpoggi2001@gmail.com

ABSTRACT

Hydrogen is considered a versatile and clean bio-fuel and research on biological production of H_2 has boosted in the last years. Two key issues on biohydrogen production from organic substrates in submerged fermentation are *(i)* type of bioreactor, and *(ii)* temperature of operation. Anaerobic fluidized bed reactors (AFBR) exhibit attractive features for the production of H_2 although their application for this purpose is scarce. On the other hand, use of ambient temperature of operation could help to decrease the use of energy to maintain the temperature at higher levels; yet little is known on dark fermentation in the psychrophilic range. Thus, the aim of this work was to compare the H_2 production in a lab scale AFBRs at two levels of operational temperature: ambient temperature (A) and 35 °C (M) and two organic volumetric loading rates B_v: 5 and 8 g sucrose /(L d), with a constant hydraulic residence time of 1 day.

The increase of B_v from 5 to 8 g sucrose/L day had a positive effect on the performance of our anaerobic fluidized bed reactors; the H_2 productivity increased 2100 and 1684% for AFBR-A and AFBR-M, respectively. With a B_v of 8 g sucrose/L the average performance of AFBR-A was superior to that of AFBR-M: 1.8 times for the H_2 concentration in the biogas (54% and 31% respectively) and 2.1 times for the H_2 productivity (1330 and 580 mLH_2/(Lbed day), respectively). The volatile organic acids (VOA) contributed to most of the soluble microbial products at both temperatures with ratios VOA/SOLV of 18.99 and 1.68 for A and M, respectively (ratio of total volatile organic acid/total solvent products). In conclusion, the H_2 production in an AFBR-A at ambient temperature showed encouraging results for H_2 production in submerged fermentation of moderate concentration of sucrose.

Key words: anaerobic fluidized bed bioreactor, biohydrogen, dark fermentation, sucrose.

1. Introduction

In the last 10 years, interest on biohydrogen has increased exponentially [1]. Hydrogen is one of the most promising fuel candidates: *(i)* it is a versatile, safe, renewable, environmentally compatible and economic fuel [2], *(ii)* it is more secure to manage than domestic natural gas [3], *(iii)* its combustion in automobiles is 50% more efficient than

gasoline, and *(iv)* it possesses an energy content per unit mass of 142 KJ/g o 61,000 Btu/lb [3] that is 2.7 times greater than that contained in certain hydrocarbon [4].

There are several technologies to generate H_2; they can be classified as biological, chemical and electrochemical. Chemical technologies include steam reforming, electrolysis and partial oxidation process [5]. On the other hand the biological production processes can be classified into three categories: bio-photolysis, photo-fermentation and dark fermentation [6-8]. We focus here on biological process because they are environmentally friendly and consume less energy. Particularly, H_2 production by dark fermentation exhibits several advantages: *(i)* many fermentative bacteria are capable of high hydrogen generation rate, *(ii)* H_2 is produced throughout the day and night at a constant rate since it does not depend on energy provided by sunlight, and *(iii)* bioreactors have a relatively small footprint when solid substrate dark fermentation is chosen [9-13].

Sustainability of biohydrogen production depends on the attainability of renewable substrate and the establishment of fermentation conditions that augment both the rate and the yield of hydrogen production [14]. There are factors that determine optimal hydrogen production, such as: *(i)* pH, *(ii)* temperature, *(iii)* concentration of electron donor, *(iv)* type of the reactor, *(v)* alkalinity, *(vi)* nutritional history of the cells, *(vii)* method of inoculum enrichment and method of methanogenesis inhibition used, and *(viii)* type of inocula, among others [15-19]. The thermal regime of operation can affect the growth rate and metabolic activity of microorganisms [20]. This fermentation processes can be conducted at mesophilic (25–40 ◦C), thermophilic (40–65 ◦C), extreme thermophilic (65–80 ◦C), or hyperthermophilic (>80 ◦C) temperatures [21]. Selection of the temperature of incubation should take into account that the heat energy needed to conserve higher fermentation temperatures can diminish the net energy gain of biogas production [22, 23], therefore it is interesting to study the production of hydrogen at ambient temperature (without heating).

Several studies of hydrogen production have been conducted in continuous stirred tank reactors. The continuous stirred tank reactor is one of the most used because of its simple construction, easy operation and effective homogeneous mixing. However, the hydraulic retention time (HRT) controls microbial growth and therefore the HRT must be greater than the maximum rate of growth of microorganisms, higher speeds because the dilution caused loss of microorganisms [24]. To avoid this inconvenient, several mechanisms and devices have been incorporated to bioreactors in order to retain the active microbial biomass, usually by immobilization. In this way, both growth and concentration of microorganisms are essentially independent of the HRT, and high cell concentrations of biomass can be achieved inside the bioreactors [25-27].

Recent studies have found that favorable immobilized-cell anaerobic hydrogen production systems include anaerobic fluidized bed reactors (AFBR; [28]). Tbe AFBR consists of a tall column containing an inert support or granules that

are held in suspension due to the drag force of the upward flow where the microorganisms are retained in the form of biofilm [29,30] and has been widely used as a system for treating wastewater, characterized by high efficiency and the use of low hydraulic retention time [31,32]. In this type of reactor, the accumulation of biogas and deposition of particles take place in different compartments located in the column [33]

Among the advantages of the AFBR we find the following: *(i)* at speeds high mass transfer, *(ii)* it has the ability to control and optimize the thickness of the biofilm by attrition and special devices, *(iii)* the biomass support can be chosen for applications specific, *(iv)* the treated effluent recirculation means it has excellent hydraulic pattern that prevents short circuits and dead zones [34, 35]. Even though AFBR exhibits positive features for the production of biogases such as H_2 it has been used primarily for the treatment of wastewater [27,32,36]. Some materials that have been used for H_2 production are activated carbon [28], zeolite [37] and expanded clay [38].
To the best of our knowledge, there are no studies for H_2 production by AFBR at low temperatures. Therefore, this work was aimed to evaluate the H_2 production in an anaerobic fluidized bed reactor using two incubation temperatures: ambient temperature and 35 °C.

2. Experimental

Bioreactors. The laboratory-scale AFBRs consisted of glass columns of 4.5 cm internal diameter, 185 cm length and 3 L of working volume; loaded with 1 L of granular activated carbon (1-2 mm diameter) colonized by an anaerobic consortium. The hydraulic residence time was 1 day (fluidized bed volume basis).

Experimental design. The experimental design examined the effect of two factors on H_2 production in AFBR, *i.e.* two temperatures of operation: 35ºC (AFBR-M) and ambient temperature (AFBR-A), and two volumetric loading rates (B_v, 5 and 8 g sucrose/(L d).) All AFBRs were operated at 1 d HRT

Inocula. AFBRs were seeded with digestates from methanogenic substrate anaerobic digesters degrading sucrose. Those digesters were operated at mesophilic conditions. Before loading into the reactor the digestates were pre-treated by heat-shock (90ºC, 1h)

Substrate. The organic carbon source was either 5 or 8 (g/L) of sucrose. The reactors were fed with a synthetic wastewater with the following composition (mgL^{-1}; [28, 39]): CH_4N_2O (125); $NiSO_4*6H_2O$ (1); $FeSO_4*7H_20$ (5); $FeCl_3*6H_2O$ (0.5); $CoCl_2*2H_2O$ (0.08); $CaCl_2*6H_2O$ (47); SeO_2 (0.07); KH_2PO_4 (85); K_2HPO_4 (21.7); $Na_2HPO_4*2H_2O$ (33.4); $NaHCO_3$ (1 g/L). Either 5 or 8 g of sucrose per liter were added, depending on the operation B_v.

Analyses. The main monitoring parameters were hydrogen production, pH and soluble metabolites. Hydrogen and methane contents in biogas were determined by gas chromatography [13] in a Gow-Mac chromatograph model 350 fitted with a thermal conductivity detector (TCD) and Molecular Sieve 5A packed column (injector, detector and column temperatures were 25, 100 and 25 ºC, respectively). Argon was the carrier gas. Soluble metabolites (volatile organic acids, lactic acid, and solvents) were determined in the effluent that was filtered through a glass-membrane filter and an aliquot of the filtrate was injected in a gas chromatography Varian Star 3400 equipped with a FID for metabolite concentration determination. The injector and detector temperatures were set at 250ºC. Nitrogen was used as a carrier gas with a 20 mL/min flow rate. The oven temperature was programmed as follows: 60 ºC for 2 min, increasing to 140 ºC at 5ºC/min, and then kept constant at 140ºC for another 6 min. A 50 m 0.32 mm internal diameter fused silica capillary column coated with 0.2 mm CP-Wax 57 CB was used.

3. Results and discussion

3.1 Effect of increase the volumetric loading rate

Overall, there was a significant performance improvement of bioreactors at the highest B_v. In the first period of operation at B_v of 5 g sucrose/(L d) low concentration of H_2 in biogas and H_2 productivity was observed (Figure 1a, d, Table 1). After 20 days the B_v was changed to 8 g sucrose/L day; the H_2 in biogas increased by 5.2 and 6.3 times in AFBR-A and AFBR-M, respectively, whereas the H_2 productivity was enhance by 22 and 33 times in AFBR-A and AFBR-M, respectively.

In the first 8 days of the second period H_2 production was no observed in AFBR-M, on the other hand methane production was registered(Figure 1 a & b). This was consistent with reported hydrogen consumption by methanogenesis [40]. Therefore the presence of CH_4 could indicate that heat treatment was not sufficient to eliminate the methanogenic microorganisms in the inocula, particularly in the AFBR-M [28]. It is known that heat treatment of the inocula is intended to eliminate non-sporulating, hydrogen-consuming microorganisms such as methanogenic archaea [41].

After 8 day in the second period we removed bicarbonate in the synthetic wastewater in order to allow the pH diminish naturally. Once the pH dropped down to 4.5 the concentration of CH_4 in the biogas decreased (Figure 1 b & c). This was in agreement with other studies where it was observed that the combination of heat-treatment of inocula and lower pH value repress the methane-forming microorganisms [16, 40].

Acetic acid (HAc), Butyric acid (HBu), Propionic acid (HPr), Ethanol (EtOH) and Butanol (BuOH) were the soluble microbial products (SMP) detected in this fermentation (Table 1). The volatile organic acids (VOA) contributed to most of the SMP at both temperatures and both Bv with high ratios TVOA/SOLV (TVOA/SOLV: total volatile organic acid/solvents products) in most cases. Values of TVOA/SOLV were of 55 and 19 for the ambient

temperature reactors operated at B_v=5 and 8 g/(Ld), respectively, and 72, and 1.2 in mesophilic reactors run at B_v=5 and 8 g/(Ld) . The TVOA/SOLV ratio in the first period was almost 3 (AFBR-A) and 24 (AFBR-M) times higher than in the second period.

This could be due to pH values below 4.5 (*ca.* 10 days) in the second period which is known to be associated to solventogenesis and decreased H_2 harvesting [42-44].

The presence of HPr in the first period was higher than that in the second period in both reactors and at both temperatures. The may be due to the low pH 4.5 at increased B_v of 8 g sucr /(L d) since it is known that low pH could inhibit propionic production [25,28, 37] (Zhang et al. ,2007, Koskinen et al. 2007, and Barros et al. 2010). In the first period de HPr/SMP was higher in AFBR-M and the propionate fermentation is related with low production of H_2 [37] Koskinen et al., 2007) and it can be associated with the low H_2 productivity observed.

3.1 Effect of temperature of incubation

In general, operation at ambient temperature was associated to better bioreactor performance than in mesophilic regime of operation (Table 1). The average H_2 concentration in the biogas in AFBR-A in the 2 nd period was 1.8 times superior than that of AFBR-M (56 and 32% H_2, respectively; Table 1). Similarly the H_2 productivity in AFBR-A was 2.1 times superior than that of AFBR-M (1232 and 589 $NmLH_2$/(Lbed d), respectively; Table 1). In the second period, the average value of 56% of H_2 concentration in biogas from the AFBR-A was in the range of 40–60% reported in other studies with AFB-A (Table 2).

Our results agree with findings of [45] that operated well mixed batch reactors at 22 °C and 37 ° C. They observed that the H_2 production was 1.3 times superior in a reactor operated at 22ºC. This result could be attributed to the gradual changes in pH induced by slower kinetics at lower temperature; indeed lower temperatures cater more time for hydrogen producing bacteria to adjust to pH dynamics in unbuffered reactors [46]. Methane was observed in the biogas of AFBR-M in both periods of operation (Figure 1 b), in contrast no CH_4 was detected in AFB-A. Since both bioreactors received the same inocula, the fact that methane production was more noticeably in the AFBR-M, could be related to its operation temperature 35 ° C which is reported to be the optimum for methanogenic microorganisms [47].

The $TVOA/SOLV_{AFBR-M}$ was 11.3 lower than $TVOA/SOLV_{AFBR-A,}$ in the second period; the higher contribution of solvents (ethanol and butanol) in the AFBR-M may indicate that the fermentation was being diverted to a solvent production which is consistent with the low production of H_2 obtained. Interestingly, at similar pH values in both

bioreactors the solvent production was not observed in AFBR-A. This could be attributed to the fact that a low temperature allows more time to adapt to changes in pH as we mention above [46].

Furthermore the main solvent generated in AFBR-M was ethanol (36%) and the ethanol-type fermentation is related with low production of H_2 [37, 48, 49].

In the AFBR-A the major byproduct was butyric acid (59 %). this was in agreement with literature reports of butyrate production in the pH range of 4.0-4.5 [50]. The A/B (acetic to butyric acid ratio, on COD basis) has been apply as a surrogate indication of H_2 production in acidogenic systems [37, 51]. In general a higher A/H ratio higher than 0.80 indicates a higher H2 yields, likely with hydrogen production from hexoses with acetogenesis. Values lower than 0.8 are likely associated with hydrogen production from hexoses with butyrogenesis [52]. In our work, A/B ratios were close to 0.8 or lower (Table 1) and this mith indicate that the carbon flow was directed into products another than acetate, HBu for AFBR-A and EtOH for AFBR-M (Table 1; [53]).

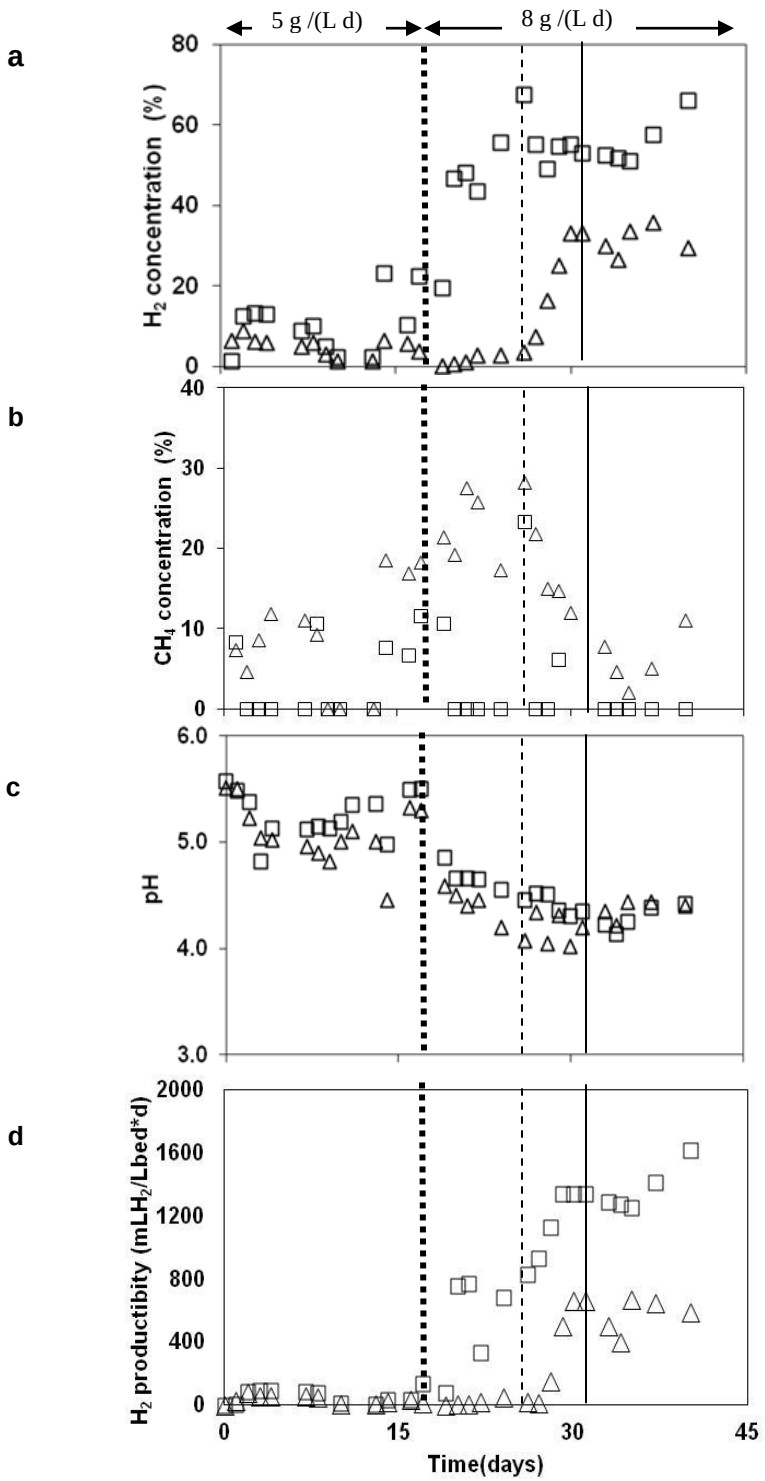

Figure 1. Time courses of: (a) H_2 concentration in biogas; (b) CH_4 concentration in biogas; (c) pH and H_2 productivity □: AFBR-A; Δ: AFBR-M. Note:bold dotted line indicates the change of Bv=5 g sucrose/L to 8 g sucrose/L. Lines in Bv= 8 g sucrose/L indicate the beginning of the steady state: solid line AFBR-A and dotted line AFBR-M

Table 1. Average performance of AFBR-A and AFBR-M.

Reactor / Parameter	Bv = 5 g sucr/(L.d)		Bv = 8 g sucr/(L.d)	
	AFBR-A	**AFBR-M**	**AFBR-A***	**AFBR-M***
pH	5.22 ± 0.26	5.04 ± 4.20	4.35 ± 0.13	4.29 ± 0.16
H_2 concentration (%)	10.6 ± 6.9	5.0 ± 2.2	56.0 ± 6.2	31.6 ± 3.1
Biogas production (mLH_2/ day)	791 ± 410	57 ± 44	2222 ± 449	1900 ± 191
H_2 productivity (mLH_2/L_{bed} day)	56 ± 44	33 ± 26	1232.9 ± 241	589 ± 103
Soluble microbial products (mg COD/L)				
Acetic acid	1101.2 ± 238.8	951. 2 ± 110.3	957.1 ± 236.0	1172.7 ± 196.0
Propionic acid	782.5 ± 180.1	1024.9 ± 325.4	318.1 ± 32.8	341.8 ± 69.0
Butiric acid	838. 1 ± 164.5	1403.8 ± 372.9	2097.1 ± 427.3	1382.5 ± 321.0
Lactic acid	ND	ND	ND	ND
Acetone	ND	ND	ND	ND
Methanol	ND	ND	ND	ND
Ethanol	106. 0 ± 71.6	53.1 ± 27.5	88.3 ± 17.9	1654.7 ± 49.8
Butanol	31. 1 ± 15.3	ND	89.2 ± 10.5	68.3 ± 7.0
EtOH/SMP (%)	0.8 ± 1.3	1.7 ± 0.9	2 ± 0	36 ± 4
BuOH/SMP (%)	1.1 0.3	-------	3 ± 0	1 ± 0
HAc/SMP (%)	39.9 ± 2.7	43.0 ± 14.0	27 ± 3	25 ± 1
HPr/SMP (%)	28.1 ± 2.1	40.2 ± 9.7	9 ± 2	7 ± 0
HBu/SMP (%)	30.1 ± 2.7	45.0 ± 11.0	59 ± 2	30 ± 3
A/B	1.3 ± 0.2	0.8 ± 0.1	0.5 ± 0.1	0.9 ± 0.1
TVOA (mg COD/L)	2721. 7 ± 311.8	2594.9 ± 818.2	3372 ± 650	2897 ± 59
SMP (mg COD/L)	2771.2 ± 277.2	2630. 3 ± 849.0	3550 ± 676	4621 ± 643
TVOA/SOLV	55	72	19	1.2

*The average data was obtained under steady-state conditions: AFBR-R: day 8 to 22 and AFBR-M: day 15 to 22. A/B: acetic to butyric acid ratio. EtOH: ethanol; BuOH: butanol; HAc: acetate; HPr: propionate; HBu: butyrate; TVOA: total volatile organic acids= HAc+HPr+HBu; SMP: soluble microbial products=TVOA+EtOH+BuOH. Based in COD/L

Table 2. Hydrogen production using anaerobic fluidized bed reactor

Inocula	**Conditions**	**Support material**	**Substrate concentration (mg/L)**	**Y' Hydrogen Pseudoyield ($molH_2$/Kg substrate fed) H_2 % in biogas**	**Soluble microbial products**	**Ref.**
Anaerobic sludge hs (105°C, 45 minutes)	HRT:0.5-4 h pH:4.0 T:37° C	Activated carbon	Glucose (1000)	6.44 @ HRT of 0.5–2 h. 57-61%	Acetic acid Butyric acid Propionic acid Ethanol	1
Anaerobic sludge hs (90°C, 10 min)	HRT:8-1 h pH: 3.7-4.1 T:30°C Lote:48 h	Expanded Clay	Glucose (2000)	13.39 @ HRT of 3.7-4.1h 20-30%	Acetic acid Butyric acid Ethanol	2
Sludge hs (90°C 10 min followed by ice cooling to 25°C)	HRT: 8-1 pH: 3.8 30°C Lote:48 h	Expanded Clay	Glucose (2000)	12.72 @ HRT of 2 h 21.8-37.6%	Acetic acid Butyric acid Ethanol	3
Anaerobic sludge hs (90°C 10 min)	HRT:8-1 h pH: 5.5 T:30°C	Expanded clay Polystyrene	Glucose (4000)	14.00@ HRT of 2 h 50% 10.6 @ HRT of 2h 40% 16-47%	Acetic acid Butyric acid Propionic acid Ethanol	4
Anaerobic sludge hs (90°c, 10 min)	HRT: 8-1 h pH: 5.5 T: 30°C	Ground Tire Pet	Glucose (4000)	11.94@ HRT of 1 h 52-96% 10.39@ HRT of 1 h	Acetic acid, Butiric acid Lactic acid Ethanol	5
Methanogenic sludge hs (90ºC, 1 h)	HRT:1 day pH: 4.5-5.0 T: 30 ºC ambient	Activated carbon	Sucrose (8000)	3.59 @ ambient temperature@ HRT of 1 day 55.96% 1.65@ HRT of 1 day @ 35ºC 1.68%	Acetic acid, Butiric acid Propionic acid Ethanol Butanol	6

Notes: hs: heat-shock, HRT: hydraulic retention time; References: 1. [28]; 2.[24] ; 3.[38]; 4.[25], 5. [54] ; 6. This study

4. Conclusion

-The increase of B_v from 5 to 8 g sucrose/L day had a positive effect on the performance of our anaerobic fluidized bed reactors; the H_2 productivity increased 2100 and 1684% for AFBR-A and AFBR-M, respectively.

-The combination of heat-treatment of inocula and lower pH value avoided the methane production in the second period of operation at B_v of 8 g sucr/(L d).

-In the second period of operation at Bv = 8 g sucr/(L d) the performance of the reactor at ambient temperature was outstandingly superior to that at mesophilic regime; the H_2 concentration and the H_2 productivity in the ambient reactor were nearly two- fold of the values in the mesophilic reactors

5. Acknowledgements

The authors wish to thank CINVESTAV del IPN and ICYTDF for partial support to this research, and CONACYT for a graduate scholarship to KMM-P. The excellent technical help of Mr. Cirino Chávez-Rojas (Central Analítica) and Mr. Rafael Hernández-Vera from the GBAER-EBRE Group, CINVESTAV del IPN, is gratefully acknowledged.

6. References

[1] K.L. Kovács, G. Marótia, R. Rákhelya, R. Int. J. Hydrogen Energy, 31, 1468. (2006).
[2] O. Mizuno O., R. Dinsdale, F.R. Hawkes, D.L. Hawkes DL., T. Noike. Bioresource Technol. 73, 65 (2002).
[3] D. Das, & N.T. Veziroglu. Int. J. Hydrogen Energy, 33, 6057. (2008).
[4] R. Ramachandran, & R.K. Menon. Int. J. Hydrogen Energy, 23(7), 598 (1998).
[5] I. Dincer, I. Renewable and Sustainable Energy Reviews, 4, 175 (2000)
[6] P.C. Hallenbeck, & D. Ghosh. Trends in Biotechnology, 27(5), 297(2009).
[7] E. Eroglu, I. Eroglu, U. Gunduz, M. Yucel. Bioresour. Technol, 99, 6808, (2008).
[8] V.S. Mohan. J. Sci. Indust, 67 (11), 961, (2008).
[9] C. Escamilla-Alvarado, E. Ríos-Leal, E., M.T. Ponce-Noyola, H.M. Poggi-Varald. Process Biochemistry doi: 10.1016/j.procbio.2011.12.006 (2012).
[10] P. Kongjan, S. O-Thong, M. Kotay, B, Min, I. Angelidaki. Biotechnol Bioeng, 105(5), 908, (2010).
[11] I. Valdez-Vazquez, H.M. Poggi-Varaldo, H.M. Renewable Sustainable Energy Rev, 13 (5), 1013 (2009b).
[12] I.Valdez-Vazquez, R. Sparling, D. Risbey, N. Rinderknecht-Seijas, H.M. Poggi-Varaldo. Bioresource Technology, 96, 1913, (2005).
[13] H.M. Poggi-Varaldo, L. Valdés, F. Esparza-García, G. Fernández-Villagómez. Water Science and Technology, 35, 2–3, 204 (1997)
[14] M. Ferchichi, E. Crabbe, G.H Gil, W. Hintz, A. Almadidy J. Biotechnol, 120, 409 (2005)
[15] I. Valdez-Vazquez, H.M. Poggi-Varaldo. Int. J. Hydrogen Energy, 34, 3646 (2009).
[16] I. Valdez-Vazquez, H.M. Poggi-Varaldo. Renewable Sustainable Energy Rev, 13(5), 1013(2009).
[17] H. Argun, F. Kargi, K.I. Kapdan, R. Oztekin. Int. J. Hydrogen Energy, 33, 6115 (2008).
[18] J.Z. Li, N.Q. Ren. China Environmental Science (China) 18 (5), 402 (1998).
[19] K. Sasikala, C.V Ramana, P.R. Rao, M. Subrahmanyam, M. Int J Hydrogen Energy, 15 (11):797 (1990).
[20] K. Lee, P. Lin, J Chang. Int. J. Hydrogen Energy, 31(4), 472(2006).
[21] D.B. Levin, L. Pitt, M. Love. Int J Hydrogen Energy, 29(2),185 (2004).
[22] C. Escamilla-Alvarado, M.T. Ponce-Noyola, E. Ríos-Leal, H.M. Poggi-Varaldo, H.M. Environmental Microbiology and Biotechnology in the frame of the Knowledge-Based Bio and Green Economy Bologna. Sub-session 2.2. Organic waste and effluent biorefinery S82 (2012).
[23] K.R.J. Perera, B. Ketheesan, Y. Arudchelvam, N. Nirmalakhandan. Int. J. of Hydrogen Energy, 37(1), 178(2012).

[24] E.L. Cavalcante de Amorim, A.R. Barros, M.H.R.Z. Damianovic, E.L. Silva. Int J Hydrogen Energy, 34,790. (2009).
[25] A.R. Barros, E.L. Cavalcante de Amorim, C.M. Reis, G.M. Shida, E.L. Silva. Int. J. Hydrogen Energy, 35, 3388. (2010).
[26] P.C. Hallenbeck, D. Ghosh. Trends in Biotechnology, 27(5), 297(2009).
[27] C. Garibay-Orijel, C. Hoyo-Vadillo, T. Ponce-Noyola, J. García-Mena, H.M. Poggi-Varaldo. Biotechnol. Bioeng, 94, 960 (2006).
[28] Z.P Zhang, J.H. Tay, K.Y. Show, R. Yan, D.T. Liang, D.J. Lee, W.J. Jiang. Int. J. Hydrogen Energy, 32, 191. (2007).
[29] F.R. Hawkes, I. Hussy, G. Kyazze, R. Dinsdale, D.L. Hawkes. Int. J. Hydrogen Energy, 32,184 (2007).
[30] N. Qureshi, B.A. Annous, T.C. Ezeji, P. Karcher, I.S. Maddox, I.S. Microb Cell Fact, 4, 24 (2005).
[31] C.N. Lin, S.Y. Wu, J.S. Chang, J.S. Int J Hydrogen Energy, 31, 2210 (2006).
[32] C. Garibay-Orijel, E. Ríos-Leal, J. García-Mena, H.M. Poggi-Varaldo. J. Chem Technol Biotechnol, 80, (10), 1187 (2005)
[33] M. Fuentes, N.J. Scenna, P.A. Aguirre, M.C. Mussati. Chem. Eng and Processing, 47,1540 (2008)
[34]J. Iza. Water Sci Technol, 24,132 (1991).
[35] M.S. Switzenbaum. Enzyme Microb Technol, 5, 250 (1983).
[36] H.M. Poggi-Varaldo, J.D. Barcenas-Torres, C.U. Moreno-Medina, J. García-Mena, C. Garibay-Orijel, E. Ríos-Leal, N. Rinderknecht-Seijas. J. Environ Manage. In Press. doi:10.1016/j.jenvman.2012.03.015(2012).
[37] P.E.P. Koskinen, A.H. Kaksonen, L.A. Puhakka. Biotechnol Bioeng, 97(4), 758 (2007)
[38] G.M. Shida, A.R. Barros, C.M dos Reis, E.L. Cavalcante de Amorim, M.H.R.Z. Damianovic, E.L. Silva. Int J Hydrogen Energy, 34, 3688. (2009).
[39] J.A.C. Leite, B.S. Fernandes, E. Pozzia, M. Barboza, M. Zaiata, M. Int. J. Hydrogen Energy, 33, 586(2008).
[40] S.E. Oh, S. Van Ginkel, B.E. Logan. Environ. Sci. Technol, 37, 5190(2003).
[41] B. Baghchehsaraee, G. Nakhla, D. Karamanev, A. Margaritis, G. Reid. Int J Hydrogen Energy, 33,4073 (2008)
[42] B.E. Logan, S.E. Oh, I.S. Kim, S. Van Ginkel, 36 (11), 2535 (2002)
[43] R. Sparling, D. Risbey, H.M. Poggi-Varaldo. Int. J. Hydrogen Energy, 22, 566 (1997)
[44] I. Valdez-Vazquez, R. Sparling, N. Rinderknecht-Seijas, D. Risbey, H.M. Poggi-Varaldo. Bioresour. Technol , 96, 1913 (2005)
[45] V. Gadhamshetty, D.C. Johnson, N. Nirmalakhandan, G.B. Smith, S. Deng, S. Int. J. Hydrogen Energy, 34, 1243 (2009).
[46] F. Y. Chang, C.Y. Lin. Int. J. Hydrogen Energy, 29, 39 (2004).
[47] M.H. Gerardi. Microbiology of Anaerobic Digesters, John Wiley and Sons, NewYork. (2009)
[48] N.Q. Ren, B.Z. Wang, J.C Huang. Biotechnol Bioeng, 54(5), 433 (1997)
[49] P.E.P.Koskinen, S.R. Beck, J. Orlygsson, L.A. Puhakka. Biotechnol. Bioeng, 101, 690 (2008).
[50] H.H.P Fang, H. Liu. Bioresour Technol, 82, 93 (2002)
[51] S.Y. Wu, C.H. Hung, C.N. Lin, H.W. Chen, A.S. Lee, J.S. Chang. Biotechnol Bioeng, 93(5), 946 (2005).
[52] M. T. Madigan, J. M. Martinko, P. V. Dunlap, and D. P. Clark, Brock Biology of microorganisms, Pearson Eductaion, New York, (2009).
[53] S. Van Ginkel, S. Environ Sci Technol, 35,4730 (2001).
[54] A.R. Barros, M.A.T. Adorno, I.K. Sakamoto, S.I. Maintinguer, M.B.A. Varesche, E.L. Silva. Bioresource Technology, 102, 3847 (2011)

Notation

B_v	volumetric loading rate
COD	chemical oxygen demand, (mg/L)
HRT	hydraulic retention time, (day)
HAc	acetic acid concentration, (mgCOD/L)
HBu	butyric acid concentration, (mgCOD/L)
HLac	lactic acid
HPr	propionic acid concentrarion, (mgCOD/L)

EtOH ethanol concentration, (mgCOD/L)
BuOH butanol concentration (mgCOD/L)
SMP soluble microbial products, (mgCOD/L)
TVOA total volatile organic acids, (mgCOD/L)
VOA volatile organic acids
Y' hydrogen pseudo yield, ($molH_2$/mol $substrate_{fed}$ or $molH_2$/Kg substrate fed)

9th International Symposium on New Materials and Nano-Materials for Electrochemical Systems
XII International Congress of the Mexican Hydrogen Society
Merida, Mexico, 2012

Evaluation of Pre-Treatments on the First Stage of an Anaerobic Digester for Enhancing Bio-H_2 Production

K. Peña Muñoz[1*], H. Steinmetz[1]

[1] Institute for Sanitary Engineering, Water Quality and Solid Waste Management (ISWA), University of Stuttgart
Bandtäle 2, 70569 Stuttgart, Germany, phone +49-711-685-65439, e-mail: kristy.pena-munoz@iswa.uni-stuttgart.de

ABSTRACT

Wastewater Treatment (WWT) is an essential public service that simultaneously consumes a large amount of energy and produces a significant amount of by-products (e.g. sludge). There is, however, excellent conservation potential through the production of biogas in Anaerobic Digestion (AD), and the use of it as a renewable source of energy in-situ. It is well know that each cubic meter (m^3) of biogas contains the equivalent of 5-7.5 kWh of calorific value, if the composition of CH_4 lies between 50-75% of the total biogas composition [1]. Nevertheless, to increase the conservation potential in a two-stage digester, a pre-treatment to the feedstock and seed should be applied. This pre-treatment increases the yield of hydrogen (H_2) by 10% in the first stage of the AD [2]. Additionally, the pre-treatment should selectively inhibit methanogenesis and increase the production of acetic acid and acetate, thus achieve the highest possible H_2 yield [3]. Furthermore, several techniques have been appointed as potential pre-treatments due to their simplicity, contribution to hydrolysis of organic material presented in the biomass, and inactivation of methanogenic bacteria [4]. Moreover, H_2 has the highest energy content per unit weight of any known fuel (120.21 MJ/kg) [3]. This is particularly interesting, as there are additional socio-economic benefits for using bio-H_2 as a source of energy. These include the reduction of green-house gas (GHG) emission, by reducing the final amount of CH_4 produced through AD, and the creation of a viable renewable energy source.

This study focused exclusively on 4 pre-treatments: temperature shock, pH control, chemical addition and a combination of the above mentioned. Therefore, the aims of this research were:

1) To study the influence of different pre-treatments on the first stage of a two-stage anaerobic digester, using glucose as substrate.
2) To select the most suitable pre-treatment for enhancing the bio-H_2 production for scaling-up.

Keywords: Anaerobic digestion; Bio-hydrogen production; Climate Change; Pre-treatment;

1. Introduction

One of the biggest challenges to overcome in Wastewater Treatment Plants (WWTPs) in developing countries is the reduction of energy consumption, and optimization of the different processes and services at the facility. From a technical point of view, in these countries, the use of Anaerobic Digestion (AD) of sewage sludge reduces the transportation costs of dry sludge to landfills, and partially eliminates the need for filter presses or any other drying systems. Therefore, one of the first resulting indirect benefits is the reduction of the amount of sludge sent to landfills, reducing the Green House Gas (GHG) emissions (as methane) at the landfill. Some other environmental benefits from AD include odor reduction, pathogen control, minimization of sludge production, and conservation of nutrients [5]. In addition, WWTPs are large energy users with excellent conservation potential because of biogas production, which has become one of the main sources of renewable energy [1]. Literature references report that 0.29 to 0.33 Nm^3 of CH_4 can be produced for each kilogram of Chemical Oxygen Demand (COD) digested at 35°C [6, 7]. Furthermore, hydrogen (H_2) represents one of the most promising steps toward a sustainable energy system, due to its high energy content per unit weight 120.21 MJ/kg (while CH_4 is only 50.2 MJ/kg), and its potential as a renewable energy source [3]. H_2 is a clean green fuel only if it is produced from renewable sources (e.g. wind, biomass) or through AD; making it easy to transport and store [5]. Recent works suggest that the theoretically yield of hydrogen is 4 mol H_2/mol substrate [8, 9, 10]; however, practically 1.5 to 2.5 mol H_2/mol glucose can be produced [3, 9]. Additionally, some challenges to overcome in the following years for the commercialization of bio-H_2 production are: a) the use of efficient microbial strains which can use different organic materials as feedstock, b) the low rate of H_2 production after the complete process, c) the comprehension of the metabolic pathway that drives the production of H_2, d) the cost and mass production of certain pre-treatments, and e) the improvement of the H_2 yields of the processes using cheaper raw material as substrates [5].

In biogas production through a single-stage AD process, the CH_4 formation takes away a significant portion of the reactants, acetate and H_2, which are produced by "H_2-producing bacteria" and simultaneously consumed by "H_2-consuming bacteria". In contrast, a two-stage AD produces H_2 and carbon dioxide (CO_2) in the first stage, whereas the second stage produces CH_4 and CO_2. One of the main characteristics of the pre-treatments is the selective inhibition of methanogenesis, increasing the production of acetic acid and acetate, and thus achieving the highest possible H_2 yield [4]. Several pre-treatments have been appointed for enhancing the production of H_2 in a two-stage digester, such as a low pH control [11], temperature shock of the inoculums for removing hydrogen consuming non-spore forming bacteria [8], and chemical addition by means of specific methanogenic inhibitors [4]. Special attention has been given to pre-treatments with Microwave (MW), due to its uniformity on heating and the precise control of the process temperature that is applied to the sludge. Significant concentration of soluble COD (sCOD), phosphate and ammonia are released; reduction of capillary suction and improvement of the sludge dewaterability and high water content in the sewage sludge can absorb MW energy efficiently [12, 13]. Furthermore, MW irradiation seems

to be a potential method because of its synergetic effect on pathogenic destruction and thermal heating for anaerobic digestion at 35°C. In addition, MW energy has a strong ability to penetrate dielectric material to produce thermal and non-thermal effects on microbes, increasing potential food for methane producing bacteria, and lowering the hydraulic retention time (HRT) [13]. Further, sludge is a multiphase medium that can be effectively absorbed by the MW energy, but the degree of degradation depends on the intensity of the MW irradiation [12].

Based on an extensive literature review, three main pre-treatment have been identified as the most cost-effective and adequate techniques. These includes: (i) heat-shock as microwaves (MW) and water bath and WB; (ii) combination of heat shock with chemical addition (specific methanogen inhibition); and (iii) addition of specific methanogen inhibitors, or chemical additions of bromoethanosulfonate (BES), iron (Fe III) chlorhidric acid (HCl) or chloroform ($CHCL_3$). In addition, the objective of this paper was to identify the specific condition and concentration for applying the pre-treatment to the feedstock and seed in a real-case WWTP in Mexico.

2. Experimental

Two reactors (R1 and R2), made of borosilicate glass, clear, with round bottom, were used for the experiments. The reactors have a total volume of 12 L, with a working volume of 10 L (sludge) and 2 L headspace volume (biogas). Two point nine liters of inoculum (sludge) for the reactors (R1 and R2) were taken from the anaerobic digester of the Wastewater Treatment Plant for Research and Education (LFKW) at the University of Stuttgart (Germany). The anaerobic digested sludge (ADS) or inoculum was diluted to 7.2% Total Solids (TS) concentration and strained through a 10 mm sieve to eliminate coarse material that could interfere with further analysis. The ADS was placed inside R1 and R2 under continuous stirred conditions for the guarantee of well-suspended biomass in the mix liquor, and to represent the composition of a real effluent. In addition, the R1 and R2 were installed in a controlled temperature room (37°C), while the temperature of the sludge was 35ºC. The pH was regulated by means of a pH glass electrode and a pH programmable controller, which controlled 2 solenoid dosing pumps for automatic addition of a sodium hydroxide (NaOH) solution 25% or a hydrochloric acid (HCl) solution 25% to maintain the operation pH level at 5.6. This value has been reported to be the optimum for batch bio-H_2 production [3, 9, 10]. It is important to clarify that the initial pH of the ADS was 7.8 and was gradually reduced until reach the operation pH value of 5.6. Figure 1 shows the setup of experiments that were used for these batch experiments.

According to previous work at our laboratory [2] two important conditions were considered: glucose or substrate was used as feedstock to represent a real effluent from municipal wastewater with an Organic Loading Rate (OLR) of 10 g COD/L and a specific solution of nutrients was added to ensure healthy bacteria growth. The produced biogas quantity was measured with a drum-type gas meter twice per day. This gas was collected for each experiment in gas bags, and then analyzed with a gas analyzer equipped with an infrared detector for CH_4 and CO_2 and a thermal conductivity detector for H_2. The biogas amount was registered into a log book. The analyses of concern were determined according to the German DIN-Norm and performed twice weekly: one for the influent and again for the

effluent. The analyses included: Total Solids (TS), Volatile Solids (VS), Chemical Oxygen Demand (COD), nitrogen (N) and phosphate (PO4); these last three parameters were analyzed as total and soluble form.

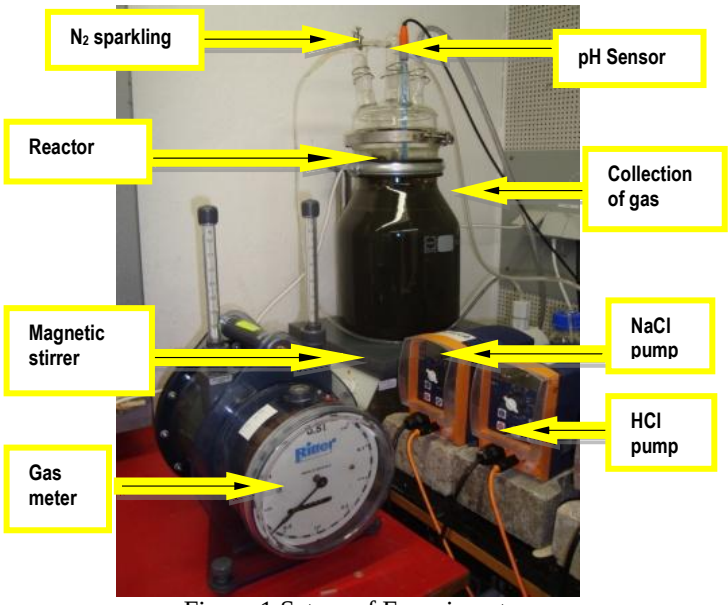

Figure 1 Set up of Experiment

Glucose and sucrose were determined spectrophotometrically after enzymatic digestion by a test kit according to the manufacturer's instructions. Gas Chromatography was also used to analyze organic acids (Volatile Fatty Acids- VFA). VFAs were analyzed in a GC Perkin Elmer equipped with a capillary injector, a FI detector, and a Varian column at a detection / injector temperature of 280°C with a programmable temperature as: 3 min. 70°C, in 6 min. 100°C, 20 min. 240°C. Each set of experiment was operated in batch during 120 h and pH 5.6.

Previous experiences have shown that this operation time gives a better control for short operation time experiment under a batch mode [2]. Table 1 outlines the 21 different pre-treatments under study, including the order in which the mix of nutrients and glucose (feedstock) were added.

Table 1 Pre-treatments

Pre-treatment	Label	Description	Conditions	Label	Pre-treatment	Description	Conditions
i Heat shock	WB 90°C/20 min	WB + G + n	@90°C for 20min	pH3		G + n + HCl	addition of HCL 25% for pH3 during 24hr
	MW 2.5min @900W	MW + G + n	2.5 min under 900W	BES 5mM		G +n + BES	5 mM
	MW 5 min @900W		5 min under 900W	BES 7mM			7 mM
	MW 7 min @900W		7 min under 800W	BES 8 mM			8 mM
	MW 10min @900W		10 min under 800W	BES 10 mM			10 mM
ii Combination: heat shock and chemical addition	WB 90°C + pH4	WB + HCl + G + n	@ 90°C for 20min + pH4 during 17hr	CHCL3 0.05%	iii Chemical addition	G + n + CHCl3	0.05 %V/V
				CHCL3 0.75%			0.075%V/V
	MW 5min @800W + pH4	MW + HCl + G + n	5 min @ 800W + addition of HCL 25% for pH4 during 17hr	CHCL3 0.10%			0.10%V/V
	MW 3min@800W + pH4	MW + HCl + G + n	3 min @ 800W + addition of HCL 25% for pH4 during 17hr	CHCL3 0.15%			0.15%V/V
	CHCL3 0.075 + pH4	G + n + CHCl3	0.075 %V/V + addition of HCL 25% for pH4 during 17hr	Fe III (5mM)		G + n + Fe III	5 mM
	Fe III (7mM) + pH4	G + n + Fe III	7mM +pH4 (17hr)	Blanc glucose	CONTROL SAMPLES	Blanc Glucose	G+n+ no pre-treatment

	Fe III (7mM) + pH6		7mM+pH6 (17hr)	Blanc no glucose		Blanc no Glucose	No G+ no pre-treatment

G: Glucose; n: nutrients; WB: Water Bath; MW: Microwaves; $CHCL_3$: Chloroform; Fe III: Iron 3 Chloride; HCl: Hydrochloric acid; BES: Bromo-ethane-sulfonate;

3. Results and discussion

The biogas measurement for each pre-treatment (Figure 2) included CH_4, H_2 and CO_2, registered in L over 120 h. No CH_4 was detected at any of the pre-treatments. The most representative performances in terms of cumulative biogas production were: *WB 90°C +pH4* by means of 61.7 L of biogas; *MW 7min@800W; BES 8mM* and *MW 5 min @ 800W+pH4* by means of 44.5; 41.6 and 33.10 L of biogas respectively; *$CHCl_3$ 0.10%* and *BES 7mM*, by means of 24.8 and 25 L of biogas, respectively. The production of H_2 and CO_2 was in the following order (H_2; CO_2, in L): *MW 5min @ 800W +pH4 (15; 17) > BES 8mM (13.9; 26.8)> WB 90°C +pH4 (9.7; 4.8) > BES 7mM (8.11; 10) > CHCl30.10% (5.28; 17.6 L) > MW 7min@800W (1; 9).* The rest of the pre-treatments produced, in average, less than 1.5 L of H_2, and less than 9 L of CO_2 .

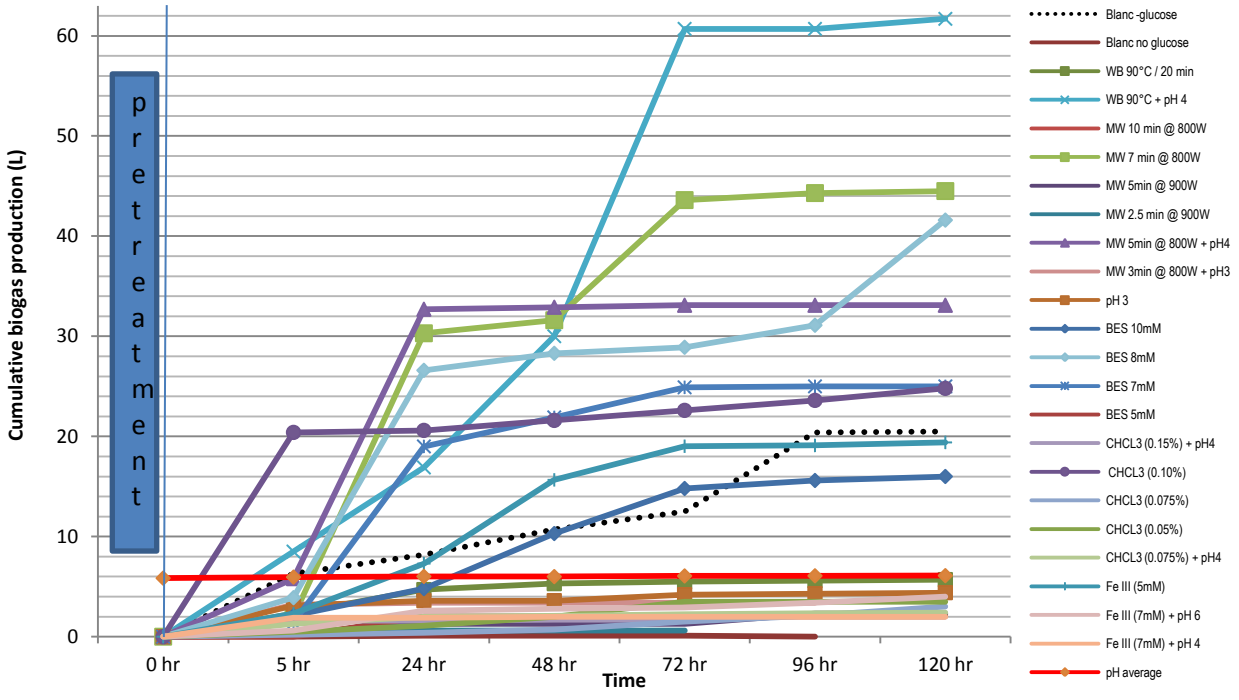

Figure 2 Gas productions after different pre-treatments (under pH 5.6, over 120 hr)

According to previous experiment in our laboratory, the maximum H_2 yield was 0.59 to 0.66 mol H_2 / mol glucose in a 120 h batch process, if applying a heat shock pre-treatment and a specific mix of nutrients [2]. Figure 3 shows the yields of H_2 for each pre-treated sample. The best performances were as follow: *MW5min@ 800W+pH4* and *BES 8mM* by means of 0.96 and 0.88 mol H_2/mol glucose respectively; *WB 90°C +pH4* and *BES 7mM* by means of pH of

0.62 and 0.52 mol H_2/mol glucose respectively; *$CHCl_3$ (0.10%)* be means of 0.34mol H_2/mol glucose. The rest of the pre-treatments showed a low performance, in comparison to *Blanc 1 and Blanc 2*.

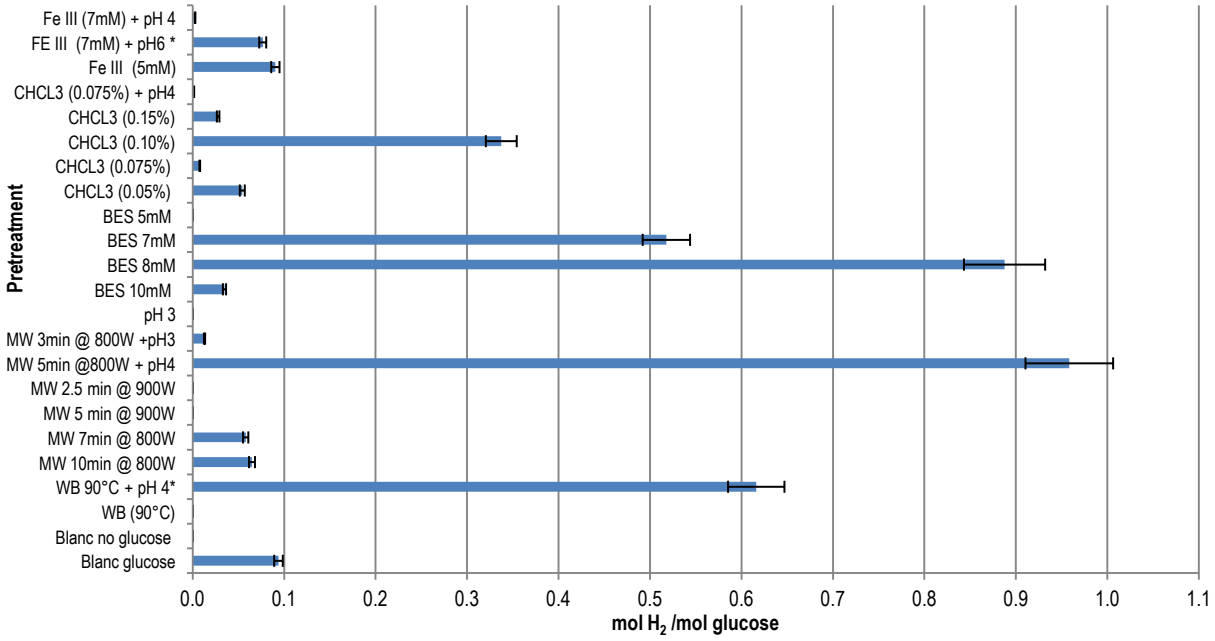

Figure 3 Hydrogen yield production from digested sludge

Conversely, the relationships soluble (s) and total (c) Chemical Oygen Demand (sCOD/cCOD) were calculated to give an idea of the solubilization of organic matter and its indirect relation to volatile fatty acids (VFA) production. Additionally, this relationship will be used as a design parameter for scaling up an anaerobic reactor in a WWTP in Mexico. The experimental results showed that the initial value for sCOD/cCOD for the *Blanc no glucose* (no pre-treatment) was 0.05, reducing to 0.02 after 5 days; while the same relation for the *Blanc glucose* (no pre-treatment) was 0.42, reducing to 0.36 after the same time. This reduction was observed in the 21 experiments, with an initial average sCOD/cCOD relationship of 0.46 and a final average sCOD/tCOD relationship of 0.09. In other words, the average reduction of sCOD was 19.4%. Nonetheless, two pre-treatments pointed out a different behavior, where the sCOD/tCOD ratio doubled. The situation corresponded to the pre-treatments: *BES 10 mM and $CHCL_3$ (0.05%)* by means of 0.83 and 0.89 respectively. Finally, the highest solubilization of organic materia was observed in: *MW 5 min@900W* by means of 33.6%, while the lowest solubilization was observed in *$CHCl_3$ (0.015%)* by means of 7.86%. While the increase of sCOD in comparison to the *Blancs*, was observed mainly in nine pre-treatment (in mg/L): *MW 5 min@900W* (12500) > *FeIII (5mM)* (11500) > *pH 3* (10600) > *MW5min @ 800W+pH4* (10500) > *WB*

90°C +pH4 (10400) > *Fe III (7mM)+pH6* (10100) > *BES (5mM)* (9860) > *BES (8mM)* (9800) > *BES (7mM)* (9490) > *Blanc 1*(9370).

One final parameter to consider is the "food to microorganism" relationship (F/M), which is a controlling parameter suggesting that microorganisms must satisfy their maintenance energy requirements prior to synthesizing new biomass. Decreasing the supply of substrate per unit biomass resulted in gradual decrease in the biomass yields, but at the same time it resulted in gradual increase in the bacteria mediated inert COD as a side effect. According to previous studies in our department [2], for anaerobic digestion, the F:M lowest limit is 1.5, while the upper limit is 3.5. The optimal value for this research was set between and 2-2.5. This condition followed by almost all pre-treated samples. The F:M ratio after pre-treatment for 9 specific parameters is listed as follow: *MW 5min @ 900W + pH 4* as 2.44; *BES 5mM* as 2.24; *WB 90°C+pH 4*as 2.62; *MW 5 min @ 900W* as 2.58; *pH 3* 2.25; *BES 7mM* as 2.18; *Fe III (5mM)* as 2.06; *BES 8mM* as1.71; and *Fe III (7mM)+pH6* as 1.26.

In order to achieve the highest possible H_2 yield, glucose has to be fermented to acetate. In addition, it has been reported [9, 14] that H_2 is not produced in propionate fermentation, rather in butyrate and acetate-ethanol fermentation, especially after a pre-treatment, which enhance the formate production. Therefore, butyrate-acetate fermentation has been appointed by several researchers as the main pathways followed by the bacteria for bio-H_2 production, due to its potential to change to butanol production (where H_2 is directly consumed or it production is inhibited). Additionally, under a pH controlled environment, the most stable pathway is the ethanol-acetate fermentation, because only acetic acid is produced as the main acid in this pathway. One more point that must be considered before analyzing the results is: that the hydrolization and fermentation of carbohydrates, proteins and lipids to VFA are pH dependent, thus the higher the initial pH is, the lower the total H_2 production potential is [11].

This section shows the results of nine selected pre-treatments and the their VFA production. The VFA of interests were: acetic acid (HOAc), propianic acid (HOPr), butyric acid (HOBu), valeric acid (HOVa) iso-valeric acid (iso-HOVa) and caproic acid (HOCa). Especially attention was given to HOAc, due to its relationship with the acetate-ethanol fermentation and a possible high yield of H_2. Additionally, the yield of H_2 can be very low when propionate or any other reduced products such as alcohol or lactic acid are formed [14]. The working pH remained under 5.6. Mainly 3 VFA were produced: HOAc, HOPr and HOBu; while iso-HOVa, HOVa and HOCa were detected in very low concentrations. Figure 4 presents the amount of VFA for the initial (in) and final (out) condition for 9 selected pre-treatments. The HOAc was produced in the following order (mg/L): *MW 5min@800W+pH4* (3828) > *BES 5mM* (3091) > WB *90°C + pH 4* (3308) > *MW 5min@900W* (2240) > *pH 3* (2036) > *BES 7mM* (2128) > *BES 8mM* (1996) > *Fe III (5mM)* (2016) > *Fe III (7mM) +pH6* (1888). While for the same pre-treatment, the HOBu was as follows: (mg/L): *pH 3* (238) < MW *5min@800W+pH4* (681) < *BES 5mM* (693) < *BES 7mM* (990) < *Fe III (5mM)* (1344) < WB *90°C + pH 4* (1360) < *Fe III (7mM) +pH6* (1369) < *BES 8mM* (1852) < *MW 5min@900W* (2690). The results suggest that the metabolic pathway, followed by the majority of pre-treatments during this research, was the acetate

fermentation (acetogenesis), with CO_2, H_2 and acetate as main products from the acetogenesis. These products will be converted to methane in a second-stage through methanogenic bacteria. In addition, the tendency to produce Butyrate or Acetate was described by the relationship HOAc:HOBu (out). Literature reports for 1 mol H_2/mol hexose a ratio HBu:HAc of 0.75-1.25 with butyrate as main product and HOAc:HOBu ratio between 3-4, with acetate as main product, under a pH range 5.5 to 5.7 [11]. For the 9 experiments, the average HOAc:HOBu ratio was 4.6.

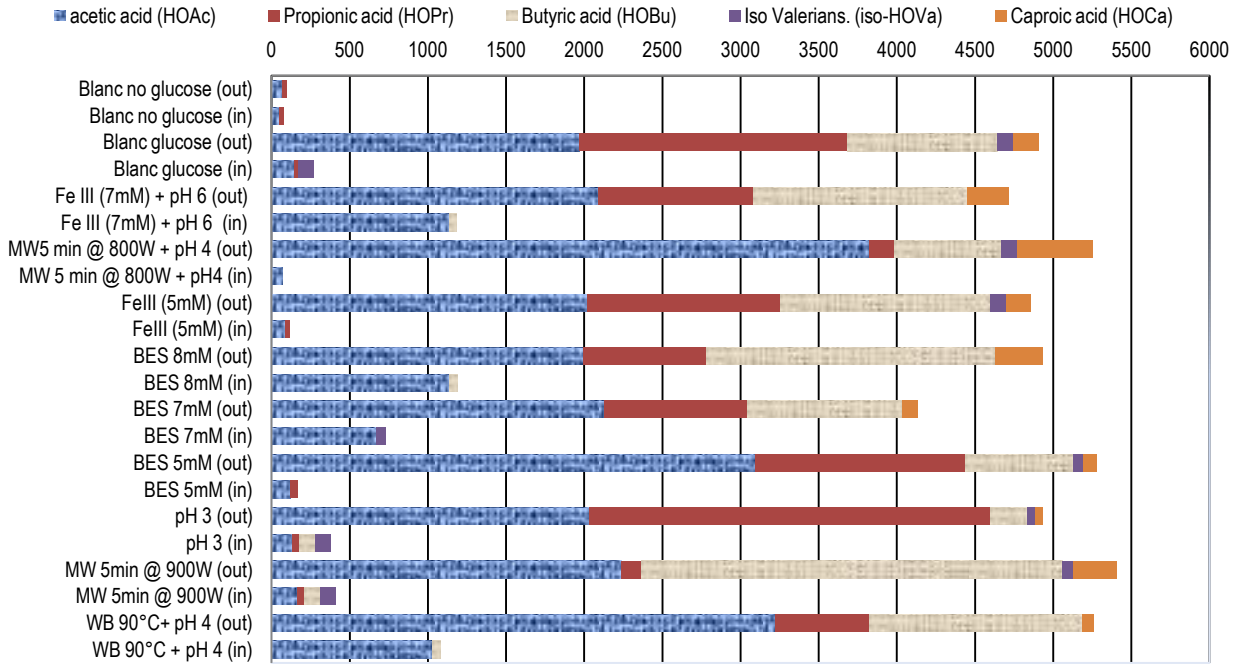

Figure 4 Volatile Fatty Acids production (9 experiments -input and output in mg/L)

4. Conclusions

After a deep literature review, the operation parameters for the first stage of a two-stage anaerobic digester were selected. Additionally, 4 pre-treatments were evaluated in 21 set of experiments. Previous work at our laboratory suggested the use of a specific nutrient of mix for guaranteeing a healthy F:M relationship. These conditions were the key factor for a good performance of the 21 experiment. It was confirmed that the combination of heat shock and chemical treatment with HCl (for working under a controlled pH level) enhance the H_2 production in the first stage of a two-stage anaerobic digester. Especial attention was given to the use of MW as the most suitable heat shock pre-treatment. These set of experiment helped to select design parameters for the scale-up of an anaerobic digester in a WWTP located in Mexico city. At the moment the 3 most representative pre-treatment for the full design are: a) *MW 5min@800W+pH4* with a H_2 yield of 0.96molH2/mol glucose, HOAc and HOBu production by means of 3828mg/L and 681 mg/L respectively; b) *WB 90°C + pH4* with a H_2 yield of 0.62mol H_2/mol glucose, HOAc and HOBu production by means of 3224mg/L and 1360 mg/L respectively; c) *BES 7mM* produced a H_2 yield of 0.52 mol

H_2/mol glucose, HOAc and HOBu production by means of 2128mg/L and 990 mg/L respectively. For the final implementation of a pre-treatment, a cost-benefit analysis and energy balance should be performed. Additionally, it was found that the use of selective inhibitor of methanogenesis (e.g. BES) has to include an environmental impact assessment, since there are not enough studies focused on the environmental effects of its by-products.

5. Acknowledgements

The author acknowledges the financial support provided by the Alexander von Humboldt Foundation (AvH) and the Instituto de Ciencia y Tecnología (ICYT-DF). In addition, the author is thankful to the Wastewater Technology (AWT) Department and AWT-Laboratory Staff at the Institute for Sanitary Engineering, Water Quality and Solid Waste Management (ISWA) for their technical support and scientific discussions to carry out this project.

6. References

[1] Bundesministerium für Ernährung, Landschaft und Verbraucherschutz, Biogas Basisdaten Deutschland (Stand Juni 2010), Germany (2010).

[2] I. Mariakakis, J. Krampe and H. Steinmetz, Effect of pH control and substrate concentration on the hydrogen yield from fermentative hydrogen production, Procedure for 12th IWA Congress on AD-Mexico, (2010).

[3] I. Valdez Vazquez and Hector Poggi Varaldo, Hydrogen production by fermentative consortia, Renewable sustainable Energy Reviews, 13:1000-1013 (2009). [4] J. Wang and W. Wan, Comparison of different pretreatment methods for enrichment hydrogen-producing bacteria from digested sludge, International journal of hydrogen energy, 33: 2934-2941 (2008).

[4] J. Wang and W. Wan, Comparison of different pretreatment methods for enrichment hydrogen-producing bacteria from digested sludge, International journal of hydrogen energy, 33: 2934-2941 (2008).

[5] D. Das, Advances in bio-hydrogen production processes: an approach towards commercialization, International Journal of hydrogen energy, 34: 7349-7357 (2009).

[6] Deutsche Vereinigung für Wasserwirtschaft, Abwasser und Abfall, e.V., Merkblatt DWA-M 363 Herkunft, Aufbereitung und Verwertung von Biogasen, Germany (2010).

[7] H. Kroiss, Anaerobe Abwasserreinigung, Wiener Mit., Wasser-Abwasser-Gewässer, Band 62, Austria (1984).

[8] R. Thauer, Energy conservation in chemotrophic anaerobic bacteria, Bacteriol Review, 41:100-180 (1977)

[9] J. Wang and W. Wan, Factors influencing fermentative hydrogen production: A review, International journal of hydrogen energy, 34: 799-811 (2009).

[10] C. Li and H. Fang, Fermentative Hydrogen Production From Wastewater and Solid Wastes by Mixed Cultures Environmental Science and Technology, 37:1–39 (2007).

[11] S.M. Khanal, W.H Chen, L. Li, S. Sung. Biological hydrogen production: effects of pH and intermediate products. International journal of hydrogen energy, 29:1123-1131 (1994).

[12] S.Beszédes, Z. László, Z.H. Horváth, G. Szabó, C. Hodúr, Comparison of the effects of microwave irradiation with different intensities on the biodegradability of sludge from the dairy- and meat-industry, Bioresource Technology 102: 814–821 (2011).

[13] L.Guo, X.M.Li, X.Bo, Q.Yang, G.M. Zeng, D. Liao, Impacts of sterilization, microwave and ultrasonication pretreatment on hydrogen producing using waste sludge. Bioresour Technol 99:3651e8 (2008).

[14] K. Steinbusch, Liquid biofuel production from volatile fatty acids. Not published Ph D Thesis from Wageningen University, Netherlands (2010).

Electrochemical Activity of Pt/oxide-C Composites on the Oxygen Reduction Reaction

B. Ruiz-Camacho[1,2*], R.G. González-Huerta[1], M.A. Valenzuela[1], N. Alonso-Vante[3], J.R. Vargas García[4].

[1]Laboratorio de Catálisis y Materiales, ESIQIE-Instituto Politécnico Nacional, Zacatenco 07738, México D.F. México.
[2]Ingeniería en Energía, Universidad Politécnica de Guanajuato, Av. Universidad Norte s/n, Juan Alonso Cortazar Guanajuato, C.P. 38438, México.
[3]IC2MP UMR-CNRS 7285, University of Poitiers, 4 rue Michel Brunet, F-86022 Poitiers, France.
[4] Depto. Ing. Metalúrgica, ESIQIE-Instituto Politécnico Nacional, Zacatenco 07738, México D.F. México.

Tel: *52* (461) 4414300. Ext. 4317, mail:beatrizr@upgto.edu.mx

ABSTRACT

Pt-TiO_2-C composites have been synthesized by photo-deposition and vapor-phase impregnation-decomposition methods. These electrocatalysts were characterized by XRD, H_2 chemisorption, TEM and XPS techniques. The main objective of this work was to compare the electrochemical activity of both composite materials on the oxygen reduction reaction taking a Pt/C sample as reference electrocatalyst. X-ray diffraction permitted to identify the crystallographic planes of Pt (*fcc*). TEM images showed Pt particle size less than 10 nm in all synthesized samples. Surface composition results (XPS) revealed a modification of Pt electronic properties depending of the preparation method. The platinum-oxide interaction on the Pt-TiO_2-C samples promoted the electrocatalytic activity for oxygen reduction reaction compared with Pt supported on carbon.

Keywords: Pt/TiO_2-C catalysts, Chemical vapor deposition, Oxygen Reduction Reaction

1. Introduction

The short life time of the electrocatalysts has recently been recognized as one of the most important issues to be addressed before PEMFC becomes commercially viable [1-7].The degradation of Pt/C catalysts over time is mainly attributed to the loss of electrochemical surface due the corrosion and electro-oxidation carbon leading to significant electrochemical activity loss [7-9]. One alternative for increase the stability of the electrocatalysts is the use of more stable support. The emerging candidates as supports are the conducting oxides like TiO_2 [10-15], WO_3 [12, 16], SnO_2 [17-18] and NbO_2 [18] to produce stables oxide-carbon nanocomposites as substrates to Pt. These novel metal-oxide-carbon electrocatalysts have demonstrated an increase on the electrochemical stability and an enhancement on the ORR catalytic activity. For instance, the $Pt/TiO_2/C$ composite present a higher electrocatalytic current per unit area than a conventional Pt/C [19-23]. This behavior was explained in terms of the presence of oxide produced modifications in the electronic properties of Pt surface, a synergetic effect of the interaction metal-oxide increases the electronic density of the Pt orbital, these changes are favorable for the oxygen adsorption and electrochemical activity [24-25], therefore $Pt–TiO_2–C$ could be used as promising stable catalysts in low temperature H_2/O_2 fuel cells cathodes.

Recently, the photo-deposition method has been used for prepared electrocatalysts of Pt-C and Pt-oxide-C [11, 23, 26-29]. In order to improve the advantages obtained in the last researches, in this work we probed a new methodology as alternative method (vapor-phase impregnation-decomposition technique) to prepare actives and stable electrocatalysts for PEMFC. The use of this last technique mentioned produced well dispersed nanoparticles ranging from 1-10 nm depending on their chemical nature [30].

In the present research we have developed an experimental procedure to obtain and characterize 10%Pt-5%TiO_2-C electrocatalysts prepared by photo-deposition and vapor-phase impregnation-decomposition methods. 10%Pt-C electrocatalysts were prepared by the same methods in order to compare each other. The solids physical properties were studied by XRD, H_2 chemisorption, TEM and XPS techniques. The electrochemical activity was evaluated in the ORR at room temperature in acid medium.

2. Experimental

2.1. Pt-TiO_2-C and Pt-C preparation by photo-deposition method

10 wt.% Pt-5 wt.% TiO_2-C (S1) catalyst was produced in two steps: i) first the TiO_2-C nanocomposite was synthesized by sol-gel method and ii) the nanoparticles platinum were photo-deposited onto TiO_2-C sustrate by irradiation. The TiO_2-C substrate was prepared following the L. Timperman et al.[1, 26-27] methodology. The synthesis of 10 wt.% Pt-C (S2) electrocatalysts was carried out following the same methodology described above using an alcoholic solution of H_2PtCl_6 dispersed over Vulcan carbon as substrate. Under this condition the suspension was continuously stirred and irradiated by 3 h in N_2 atmosphere. Then, the resultant suspension was heated at 100 ºC overnight to remove the solvent by evaporation [27].

2.2. Pt-TiO_2-C and Pt-C preparation by vapor-phase impregnation-decomposition

A thermal horizontal tube quartz reactor were used for the vapor phase impregnation decomposition (V) method. Platinum acetylacetonate ($C_{10}H_{14}O_4Pt$, Aldrich), titania nanoparticles (rutile fase, Aldrich) and carbon Vulcan were mixed in the tube quartz at 10:5:85 weight ratio at room temperature to synthesized the 10 wt.% Pt-5 wt.% TiO_2-C-V (S3). The vapor-phase impregnation-decomposition was carried out following the lietrature reports [30]. The sample 10 wt.% Pt-C-V (S4) were synthesized using the same conditions above mentioned using the 10:90 (Pt:C) weight ratio.

2.3. Physical characterization

X-ray diffraction (XRD) patterns were collected on a Bruker D8 AXS equipment using a Cu anode (K_α, λ=1.5406 Å) and a Bragg-Brentano configuration. The angle 2θ was varied from 30 to 90º with 0.2° min^{-1} and 35 kV. Particle size distribution was obtained with a high resolution transmission electron microscopy using a JEOL-JEM-2200 field emission operated at 200 kV. XPS measurements were carried out using a JEOL JPS9010MC spectrometer with a MgKα radiation source of 1253.6 eV. The Pt (4f) and TiO_2 (2p) signals were collected by XPS technique. The position of the C (1s) peak (284.5 eV for the JEOL JPS-9010MC spectrometer) was used to correct the binding energies of Pt-C and Pt-TiO_2 electrocatatalyst. XP spectra were fitted using XPS Peak v4.1 software.

2.4. Electrochemical measurements

All electrochemical measurements were carried out at 25 °C in a single, conventional, three-electrode test electrochemical cell in a 0.5M H_2SO_4 aqueous solution. A platinum mesh was used as the counter electrode, and Hg/Hg_2SO_4/0.5M H_2SO_4 (MSE = 0.680 V/NHE) as the reference electrode. The potentials in this paper were related to normal hydrogen electrode (NHE). The electrochemical measurements were performed in a Potentiostat (EG&G PAR 263A) and a Pine MSRX rotation speed controller. Glassy carbon disk with a cross-sectional area of 0.19 cm^2 was used as a support for the thin films and used as an ink-type working electrode. The catalytic ink was prepared with 1mg of catalyst, 6 µl of 5 wt% solution Nafion® (Du Pont, 1100 EW) and 60 µl of ethyl alcohol. For RDE experiments, 8 µl of this sonicated mixture were deposited on glassy carbon electrode.

Before the ORR measurements, cyclic voltammetry (CV), in a nitrogen-saturated electrolyte, was performed to clean the electrode surface from 0.0 to 1.2 V at 50 mV s^{-1}. Hydrodynamic experiments were recorded at oxygen atmosphere in the rotation range of 100, 400, 900, 1600 and 2500 rpm at 5 mV s^{-1}.The current density was calculated using the geometric surface area.

The experimental techniques selected to determinate the Electrochemical Active Surface Area (EAS) were cyclic voltammetry in argon saturated 0.5 M H_2SO_4 at 50 mV s^{-1} by integrating the hydrogen-adsorption/desorption region (EAS H_{upd}) and the oxidation of the carbon monoxide (CO stripping) (EAS_{CO}) [31]. In CO stripping technique, the electrode potential was held at 0.1 V/NHE and CO bubbled by 5 min. Thereafter, the electrolyte was satured with argon in order to remove the CO from solution. Two cycles were done from 0.05 V to 1.2 V/NHE at 5 mV s^{-1}.

3. Results and discussion

3.1 X-ray difraction

Fig. 1 shows the XRD diffraction patterns of Pt-TiO_2-C-P (S1), Pt-C-P (S2), Pt-5TiO_2-C-V (S3) and Pt-C-V (S4) electrocatalysts. The S1 and S2 powder electrocatalysts synthesized by photo-deposition method showed five diffraction peaks at 2θ values of 39.8º, 46.2º, 67.4º, 81.2º and 85.7º characteristics of the (111), (200), (220), (311) and (222) planes of face-centered cubic structure of platinum. For S1 electrocatalyst not sharp peaks correponding to titanium oxide were observed, indicating that TiO_2 deposited are very small nanocrystals or have an amorphous structure.. The samples S3 and S4 prepared by vapor-phase impregnation-decomposition method showed a breadth XRD peaks of the fcc platinum structure. S3 catalyst showed other peaks at 2θ vales of 36.1°, 41.2°,44.0°, 54.3°, 56.6°, 69° (indicated by asterisks in Fig. 1) that can be ascribed to the (101), (111) (210), (211), (220), (301) planes of TiO_2 (rutile phase commercial).

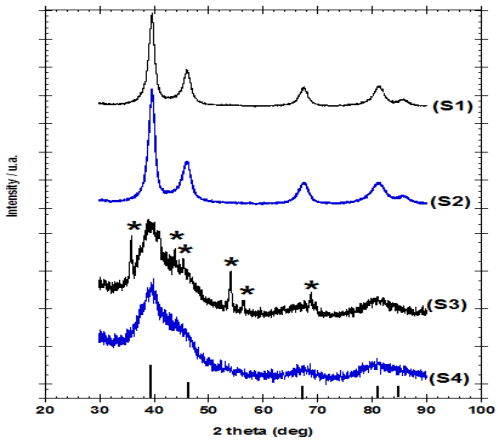

Figure 1. X ray difraccion patterns of 10 wt.% Pt-5 wt.% TiO_2-C-P (S1), 10 wt.% Pt-C-P (S2), 10 wt.% Pt-5 wt.% TiO_2-C-V(S3) and 10 wt.% Pt-C-V(S4) electrocatalysts synthesized by photo-deposition (upper) and by vapor-phase impregnation-decomposition (bottom). The (*) corresponding to crystalographic position of TiO_2 rutile phase.

3.2 TEM images

Fig. 2 presents a TEM images of Pt/TiO_2/C (S1 and S3) and Pt/C (S2 and S4) electrcatalysts synthesized by both methods. The micrograph of S1 catalyst prepared by photo-deposition method reveals a selective deposition of Pt nanoparticles onto TiO_2 surface (platinum nanoparticles on the carbon Vulcan is not observed). The dispersion of TiO_2 prepared by sol-gel method onto the carbon was non-homogeneous. Sample S2 shows a good dispersion of Pt nanoparticles onto the carbon substrate with a particle size about 5-10 nm was observed on the sample S2 prepared by same methodology. The catalysts S3 and S4 prepared by vapor-phase impregantion-decomposition showed boht

similar morphology and distribution of metallic particles. They had a small average platinum particle size between 3-4 nm with a homogeneos distribution onto the carbon..

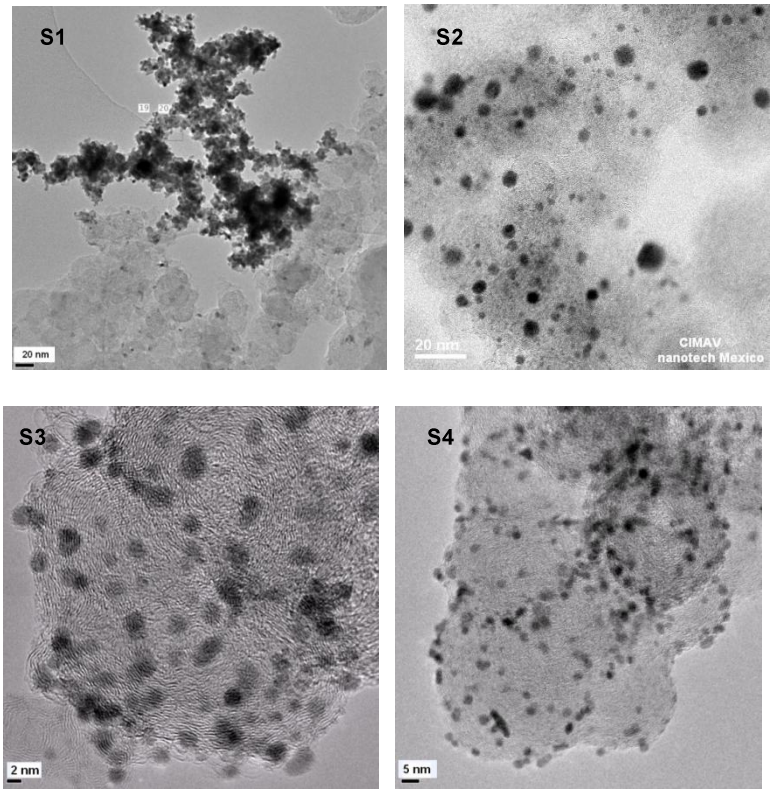

Figure 2. TEM images of 10 wt.% Pt-5 wt.% TiO_2-C-P (S1), 10 wt.% Pt-C-P (S2), 10 wt.% Pt-5 wt.% TiO_2-C-V(S3) and 10 wt.% Pt-C-V(S4) electrocatalysts.

3.3 XPS analysis

Fig. 3 shows XPS details of the Pt 4f signal of (a) Pt-TiO_2-P and (b) Pt-C-P catalysts prepared by photo-deposition compared with (c) Pt-TiO_2-V and (d) Pt-C-V materials synthesized by vapor-phase impregnation-decomposition method. The aim of this technique is analyze the metal-oxide interaction (Pt-TiO_2) using both synthesis methods, the results were compared with XP spectrum of Pt-C. The BE value reported for $Pt^0$4f7/2 is about 71.2 eV [33].

In the fig. 3(a) Pt-TiO_2-P XP spectra, the binding energy (BE) of values of 71 eV and 74.2 eV were associated to the 4f 7/2 and 4f 5/2 signals of metallic Pt (Pt^0), whereas the fig 3 (b) Pt-C-P XP spectra of the material prepared with the same methodology by (photo-deposition) show a shift up in this values at 71.3 eV and 74.6 eV. This becomes evidence that Pt deposited on TiO_2 has different electronic properties, as compared to Pt deposited on carbon substrate. Also is observed that two doublets were necessary to fit the fig. 3(b) XP spectra the 4f signal. The doublets were assigned to different oxidation states of Pt according to literature data [30, 34-35]. Signals 4f 7/2 at 72.4 eV and

4f 5/2 at 75.8 eV were associated to oxidized Pt^{4+}andPt^{2+} in PtO particles. It is rather related to incorporation of Pt into TiO_2 structure, which cause lattice strain and observed BE shifts [23]. The presence of the oxide in the photo-deposition method helps to reduce the Pt precursor to metallic platinum, according to Eq. 1-3. This is not observable in the Pt-C sample prepared using the same methodology, Pt^0 and PtO are deposited on carbon substrate.

XP spectras of fig 3(c) Pt-TiO_2-V and fig. 3(d) Pt-C-V show similar results, the presence of TiO_2 modifies the electronic properties of Pt. A shift down in the values of BE of metallic platinum (Pt^0) of 4f 7/2 at 71.3 eV and 4f 5/2 at 74.3 eV was observed in Pt-TiO_2-V sample. The 3(d) Pt/C-V catalyst present a BE of $Pt^0$4f 7/2 at 71.5 eV and $Pt^0$4f 5/2 at 74.8 eV, also this material show one doublet of oxide platinum (Pt^{2+}) at 76.0 eV.

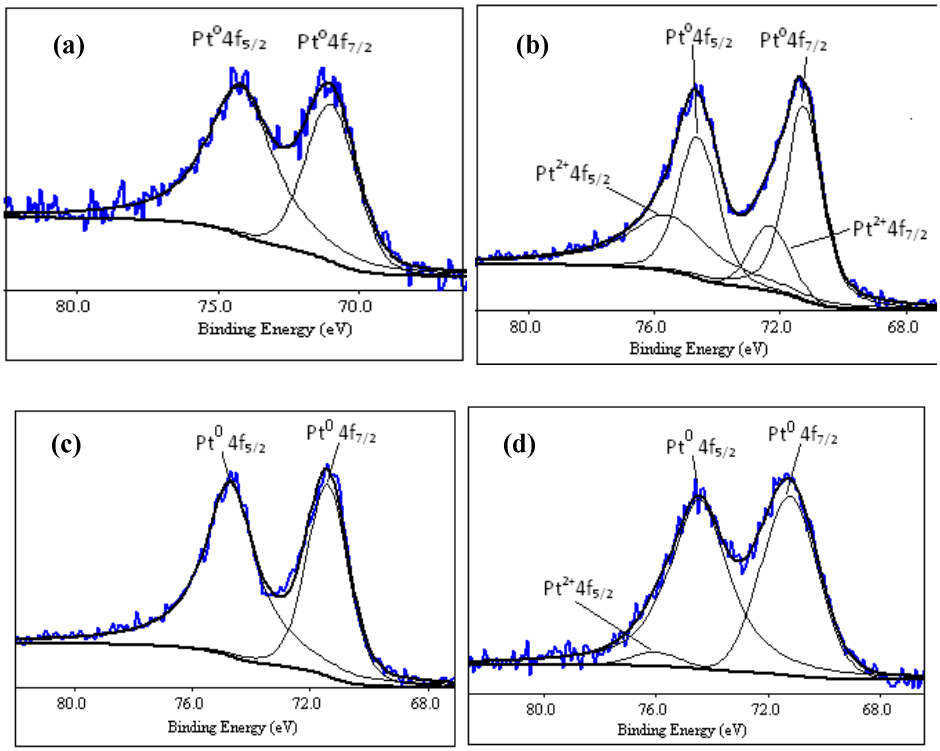

Figure 3. Pt 4f signals of XPS spectra of (a)10%Pt-TiO_2-P, (b) 10%Pt-C-P, (c) 10%Pt-TiO_2-V and (d) 10%Pt-C-V electrocatalysts.

3.4 ORR electrochemistry

Fig. 5 displays the ORR activity of Pt-TiO_2-C compared with Pt-C prepared by photo-deposition and vapor-phase impregnation-decomposition in oxygen saturated 0.5 M H_2SO_4 at a rotating speed of 900 rpm at 25°C. As observed, the Pt-TiO_2-C electrocatalysts show a shift of the EDR curves toward more positive electrode potentials versus the Pt/C, prepared using both methodologies. Table 1, summarize the kinetic parameters deduced for the ORR on the Pt-

TiO_2-C and Pt-C electrocatalysts in 0.5 M H_2SO_4 at 25°C. The interaction of Pt-oxide substrate shows an ORR kinetic current of 86.62 μA cm^{-2}_{Pt} for Pt-TiO_2-C-P while Pt-C-P reaches only 68.48 μA cm^{-2}_{Pt}. Similars results were found in catalysts prepared by vapor-phase impregnation-decomposition, Pt-TiO_2-C-V shows higher kinetic current (56.74 μA cm^{-2}_{Pt}) than Pt-C-V (46.72 μA cm^{-2}_{Pt}).

Table 1. Electrochemical parameters and active surface of Pt-C and Pt-TiO_2-C electrocatalysts sythesizedby photo-deposition and vapor phase impregnation-decomposition methods.

	EAS_{CO} (cm^2)	EAS (H_{upd}) (cm^2)	E_{oc}, V (NHE)	-b, (mV dec^{-1})	Koutecky-Levich slope (mA^{-1} $rpm^{1/2}$)	*j_k a 0.9 V /NHE (μA/cm^2_{Pt})
(S1)	0.83	0.86	0.99	105	107.6	86.62
(S2)	0.75	0.76	0.96	70	101.7	68.48
(S3)	4.1	3.9	0.98	69	112.0	56.74
(S4)	0.87	0.71	0.95	66	98.2	46.72

*EAS from CO stripping

3.5 ORR electrochemistry

Fig. 5 displays the ORR activity of Pt-TiO_2-C compared with Pt-C prepared by photo-deposition and vapor-phase impregnation-decomposition in oxygen saturated 0.5 M H_2SO_4 at a rotating speed of 900 rpm at 25°C. As observed, the Pt-TiO_2-C electrocatalysts show a shift of the EDR curves toward more positive electrode potentials versus the Pt/C, prepared using both methodologies.

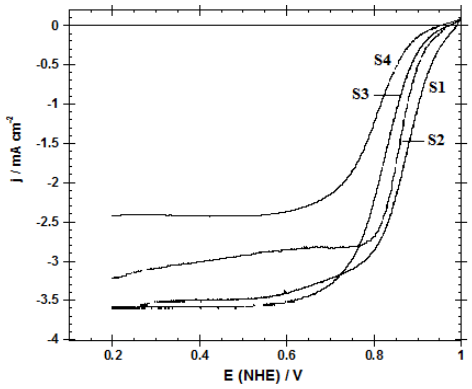

Figure 5. ORR curves of (S1) 10%Pt-5%TiO_2-C-P, (b) 10%Pt-C-P, (c) 10%Pt-5%TiO_2-C-Vand (d)10%Pt-C-Vin oxygen saturated 0.5 M H_2SO_4 at 25ºC, scan rate of 5 mV s^{-1} and 900 rpm as rotating speed.

The influence of the oxide is observed in the open circuit potential (E_{oc}) wich is obtained for the different samples (Table 1). Pt-C materials showed E_{oc}=0.95-0.96 V (NHE) range. A value of E_{oc}=0.96 V (NHE) is typical of Pt electrodes. Pt-TiO_2-C samples had higher open circuit potential (0.98-0.99 V (NHE) range) than Pt-C materials, this means that Pt-TiO_2-C samples possesses better oxygen adsorption capacity than Pt-C. Pt-TiO_2-C-P sample present a value of the Tafel slope around -0.120 V(NHE) dec^{-1}, while the Pt-C-P, Pt-TiO_2-C-V and Pt-C-V show a Tafel slope

aroud -0.60V(NHE) dec^{-1}, as the theorical values for the first order reaction kinetics. These differents values depends of the energy of the oxygen adsorption and means that the transfer of the first electron to the O_2(ads) molecule is the determined step of the kinetic reaction. All prepared samples had a similar Koutechky-Levich (K-L) slope like theoretical value (100.7 mA^{-1} $rpm^{1/2}$). Pt-TiO_2-C-P and Pt-TiO_2-V show higher K-L slopes (107.6 and 112 mA^{-1} $rpm^{1/2}$, respectively) than Pt-C-P (101.7 mA^{-1} $rpm^{1/2}$) and Pt-C-V (98.2 mA^{-1} $rpm^{1/2}$). From the RDE experiments a multielectron charge transfer process (n=4e^-) for the oxygen reaction was determined

Table 1, summarize the kinetic parameters deduced for the ORR on the Pt-TiO_2-C and Pt-C electrocatalysts in 0.5 M H_2SO_4 at 25°C. The interaction of Pt-oxide substrate shows an ORR kinetic current of 86.62 μA cm^{-2}_{Pt} for Pt-TiO_2-C-P while Pt-C-P reaches only 68.48 μA cm^{-2}_{Pt}. Similars results were found in catalysts prepared by vapor-phase impregnation-decomposition, Pt-TiO_2-C-V shows higher kinetic current (56.74 μA cm^{-2}_{Pt}) than Pt-C-V (46.72 μA cm^{-2}_{Pt}).

4. Conclusions

The smallest size nanoparticles of Pt (2-3 nm) with a homogeneous dispersion onto TiO_2-C nanocomposite were obtained by vapor-phase impregnation-decomposition method. XPS results gives an evidence that Pt deposited on TiO_2-C substrate has different electronic properties than Pt deposited on carbon substrate. The electronic changes are related to incorporation and interaction between Pt and TiO_2 structure, which produced a synergetic effect. It generate that Pt-TiO_2-C had better electrocatalytic activity for ORR than to Pt/C.

References

[1] J.Stumper, C.Stone, J. Power Sources 176(2008) 468.

[2] R.K. Ahluwalia, X. Wang, J. Power Sources 177 (2008) 167.

[3] J. Larminie, A. Dicks, Fuel Cell Systems Explained, second ed., John Wiley & Sons Inc., West Sussex, England, 2003.

[4] P. Costamagna, S. Srinivasan, J.Power Sources 102 (2002) 242.

[5] J. Chen, B. Lim, E. P. Lee, Y. Xia, Nano Today 4 (2009) 81.

[6] B. Lim, X. Lu, M. Jiang, P.H.C. Camargo, E Chul Cho, E.P.Lee, Y. Xia, Nano Lett., 8 (2008) 4043-4047.

[7] E. Antolini, Appl. Cat. B 88 (2009) 1.

[8] H. Kangasniemi, D.A. Condit, T.D. Jarvi, J. Electrochem. Soc. 151 (2004) 125.

[9] M. Roen, C.H. Paik, T.D. Jarvi, J. Electrochem. Solid-State Lett. 7 (2004) 19.

[10] W.Vogel, L.Timperman, N. Alonso-Vante, Appli. Catal. A 377 (2010) 167.

[11] L. Timperman, Y.J. Feng, W. Vogel, N. Alonso-Vante, Electrochim. Acta 55 (2010).7558.

[12] J, Shim, C.-R. Lee, H.-K. Lee, J.-S. Lee, E.J. Cairns, J. Power Sources 102(2001) 172.

[13] L. Xiong, A. Manthiram, Electrochim. Acta 49 (2004) 4163.

[14] N. Rajalakshmi, N. Lakshmi, K.S. Dhathathreyan, Int. J. Hydrogen. Energy 33 (2008) 7521.

[15] S.v. Kraemer, K. Wikander, G. Lindbergh, A. Lundblad, J. Power Sources180 (2008) 185.

[16] M. Gustavsson, P. Ekström Hanarp., L. Eurenius, G. Lindbergh, E. Olsson, J. Power Sources 163 (2007) 671.

[17] K. Sasaki, L. Zhang, R. R. Adzic, PCCP 10 (2008) 159.

[18] K.-W. Park, K.-S. Seol, Electrochem. Commun. 9 (2007) 2256.

[19] N.R. Elezovic, B.M. Babic, V.R. Radmilovic, L.M. Vracar, N.V. Electrochim. Acta 54 (2009) 2404.

[20] X.-Y.Xie, Z.-F. Ma, X. Wu, Q.-Z. Ren, X. Yuan, Q.-Z. Jiang, Electrochim. Acta 52 (2007) 2091.

[21] V. Mentus Slavko, Electrochim. Acta 50 (2005) 3609.

[22] N.R.Tacconi, C.R. Chenthamarakshan, K. Rajeshwar, W.Y. Lin, T.F. Carlson,L. Nikiel, W.A. Wampler, S. Sambandam, V. Ramani, J. Electrochem. Soc. 155 (2008) 1102.

[23] L. Timperman, A. Lewera, W. Vogel, N. Alonso-Vante, Electrohem. Comm. 12 (2010) 1772.

[24] L.G.R.A. Santos, K. Freitas, E. A. Ticianelli, J. Solid State Electrochem. (2007) 1541.

[25] K.-S. Lee, I.-S. Park, Y.-H. Cho, D.-S. Jung, N. Jung, H.-Y. Park, Y.E. Sung, J. Catal. 258 (2008) 143.

[26] B. Ruiz-Camacho, M. A. Valenzuela, J. A. Pérez-Galindo, F. Pola, M. Miki-Yoshida, N. Alonso-Vante, R. G. González-Huerta, J. New Mat. Electrochem. Syst., 13 (2010) 183.

[27] B. Ruiz Camacho, R.G. González Huerta, M. A. Valenzuela, N. Alonso-Vante, Top Catal. 54 (2011) 512.

[28] L. Timperman, A.S. Gago, N. Alonso-Vante, J. Power Sources 196 (2011) 4290.

[29] M. Harada and H. Einaga, Formation Mechanism of Pt Particles by Photoreduction of Pt Ions in Polymer Solutions, Langmuir 22(2006) 2371.

[30] R.G. González Huerta, M. A. Valenzuela, R. Vargas García, N. Alonso-Vante, M. Tufiño Velázquez, B. Ruiz Camacho, J. New Mat. Electrochem. Syst., 15 (2012) 123.

[31] K.J.J. Mayrhofer, D. Strmcnik, B.B. Blizanac, V. Stamenkovic, M. Arenz, N.M.Markovic, Electrochim. Acta 53 (2008) 3181.

[32] B.C. Beard, P.N. Ross, J. Electrochem. Soc. 133 (1986) 1839.

[33] J. F. Moulder, W. F. Stickle, P. E. Sobol, K. D. Bonden, Handbook of X-ray Photoelectron Spectroscopy. A Reference Book of Standard Spectra for Identification and Interpretation of XPS Spectra, Physical Electronics, Inc. , Minnesota, USA, 1995, pp. 1-31.

[34] C.J. Corcoran, H.Tavasool, M.A. Rigsby, P.S. Bagus, A- Wieckowsky, J. Power Sources 195 (2010) 7856.

[35] X. Chen and C. Burda, J. Phys. Chem. B 108 (2004) 15446.

[36] J.M. Doña Rodríguez, J.A. Herrera Melián, J. Perez Peña, J. Chem. Ed. 77 (2000) 1195.

[37] K.J.J. Mayrhofer, B.B. Bliznac, M. Arenz, V.R. Stamenkovic, P.N. Ross, N.M. Markovic, J. Phys. Chem. B 109 (2005) 14433.

Performance Improve of a PEM Electrolyzer, Decreasing the Ohmic Resistance because of Manufacturing and Assembly Processes

J. L. Corona-Guinto[1*], R. G. González-Huerta[2], J. M. Sandoval-Pined[1], P. A. Tamayo-Meza[1], R. Silva-Casarin[3]

[1]Instituto Politécnico Nacional – ESIME – UA – Edificio de Posgrado y Campus Virtual, México, D.F. 02250, Tel. 5729 6000, Ext. 64525
[2]Instituto Politécnico Nacional – ESIQIE – Laboratorio de Electrocatálisis.
[3] Universidad Nacional Autónoma de México – Instituto de Ingeniería – Ciudad Universitaria.
[*]Cel: 5538831965, mail : cogui_f1@hotmail.com

ABSTRACT

Proton Exchange Membrane Electrolyzer (PEME) can be coupled to Renewable Energy Sources (photovoltaic panel, wave energy conversion device, wind turbine, etc) to obtain the necessary electricity for splitting the water. The ideal thermodynamic voltage for hydrogen production by water electrolysis is 1.23V; however the difference between actual electrolyzer voltage and the reversible electrolyzer voltage for the reactions is called overvoltage. One of the sources of overvoltage in an electrolyzer is ohmic overpotential, which arising due to the resistive losses from wrong manufacturing and assembly processes. The study goal was manufacture a high efficiency and performance PEME to produce hydrogen as an energy carrier, minimizing the ohmic overpotential. More suitable processes for the manufacture of a PEME were analyzed and proposed. Prototype methodology was used to design the electrolyzer and specify assembly processes. This methodology validates the final prototype when it was built. The PEME performance was obtained by Chrono-potentiometric technique. The experiments were carried out by applying the current pulse and determining the potential as a function of time. It is connected to a galvanostat in order to obtain its response Voltage vs. time. Experiments were recorded in the current range of 1 to 300mA at 300s. The PEME constructed had a current efficiency of 74% and an energy efficiency of 61% with overpotential of 1.8V, generating 1.456$mlH2.min^{-1}$ at 200mA. The current efficiency of the previous prototype with the same features was 11% and an energy efficiency of 3% with overpotential of 4.7V generating 0.21 ml_{H2} min^{-1} at 200mA. The energy efficiency improved from 3 to 61% and production of hydrogen in ml_{H2} min^{-1} increased by 593% in performance.

Keywords: PEM electrolyzer; Performance improve; Manufacturing and assembly processes; Design methodology of prototypes.

1. Introduction

Mexico generates around 74% of its energy from fossil fuels [1], this situation involve about 2% of global emissions of greenhouse gases into the atmosphere, which puts Mexico at 15th place of the nations polluters, the main reason is because annually about 130 million tons of CO_2 are emitted to the environment [2]. One of the alternatives that have been proposed to minimize the pollutions effects is to incorporate new sources of renewable energy. There are energy sources that can be obtained from natural fuel to be used in several applications, with less environmental impact than fossil fuels, gas and coal use.

Although renewable energy sources represent a great benefit to the depletion of fossil fuels and the impact of environmental pollution, there is a downside in terms of constant use because they are intermittent, i.e. renewable energy are not available all the time when they are required, and its storage and distribution are not fully developed. That is the main reason to propose the use of hydrogen as a carrier energy, which is a fuel that does not produces pollutants to the environment [3] and can be stored and transported anywhere to be use when it is required.

Hydrogen can be used in fuel cells to transform chemical energy into electric energy by means of a continuous process by reduction and oxidation reactions in the presence of a catalyst and removes the reaction products. There are a large number of applications of fuel cells; one of the most important of these applications is in transportation vehicles such as automobiles, airplanes, and even space shuttles.

Although the hydrogen is an excellent source of clean energy, it is not in nature state and must be extracted from some minerals or water [4-5]; in order to obtain hydrogen, a device called electrolyzer could be used. The way to generate hydrogen from water is trough electrolysis.

The design of a PEM electrolyzer will be able to be integrated to a source of renewable energy, which will generate electric energy to produce pure hydrogen as an energy carrier.

2. Experimental

This section gives a brief explanation of a GAMP methodology, which is a platform for DPEV methodology development, this was used to design and manufacture an electrolyzed prototype. Each of the specifications, auxiliary methods and validations stages to establish the design strategy are explained on this experimental section.

2.1. GAMP methodology

Good Automated Manufacturing Practice methodology – GAMP, which is shown in Diagram 1, was developed for the International Society for Pharmaceutical Engineering – ISPE. The ISPE is an affiliation society for professionals who are involved in the manufacture of pharmaceutical products. The ISPE, which now has 22,000 members in 90 countries around the world, works to keep professionals informed about pharmaceutical industry on the latest technological and regulatory trends that are occurring in the market. Core members of ISPE are pharmaceutical professionals using expert knowledge to create high quality, cost effective solutions and Good Manufacture Practices – GMP [6]. The GAMP methodology is based in the GMP which is defined by the World Health Organization – WHO as "The part of quality assurance which ensures that products are consistently produced and controlled with appropriate quality standards for the intended use and as required by the marketing authorization" [1,6].

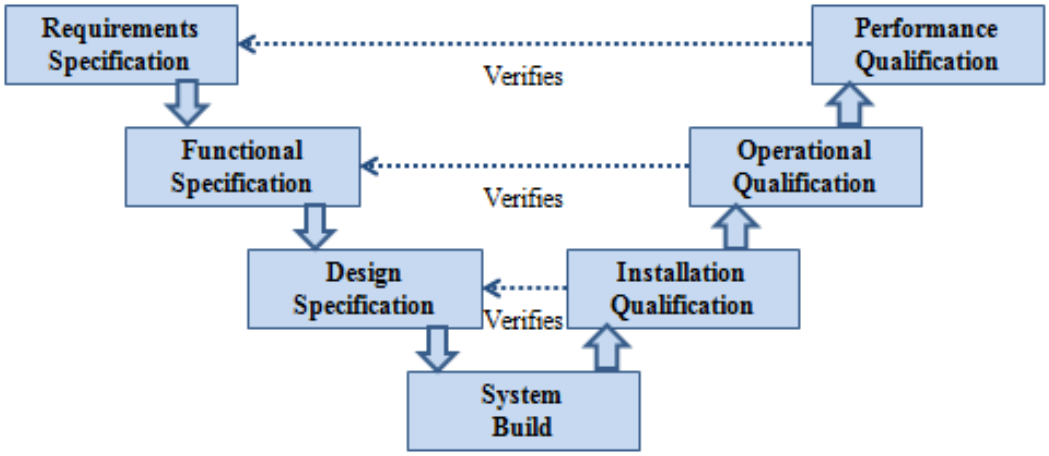

Diagram 1. GAMP-5 Methodology developed for the ISPE.

2.2. DPtSQ Methodology

Design methodology for Prototypes through specifications and qualifications – DPtSQ, sets all specifications for all different stages of prototype development, from idea conception until prototype building; in order to do it is necessary to use some support methods to determine the requirements for each stage. After the prototype building, the DPtSQ methodology provides a qualification process for each specification stage to validate and approve the design and manufacture of each parameter specified. Tests and inspection methods are designed and used to support the qualification processes to approve the prototype operation, installation in a system, and manufacture and assembly processes. Diagram 2 shows the DPtSQ methodology.

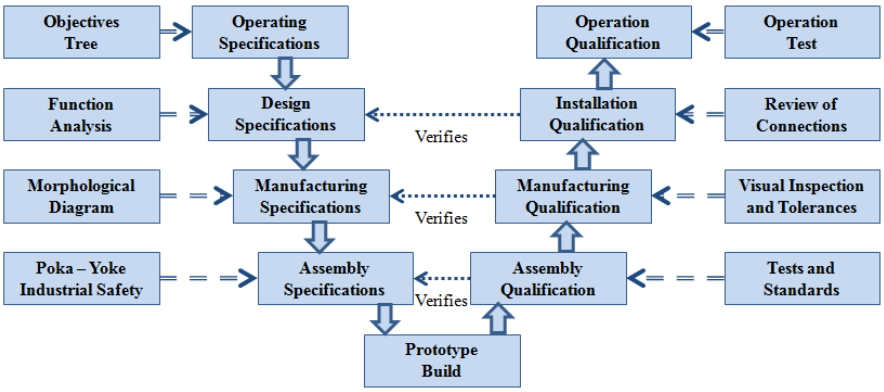

Diagram 2. DPtSQ Methodology supported on GAMP Methodology.

2.3. Operating Specifications

To determine the "Operating Specifications" is necessary to identify and clarify the prototype goals, then satisfy the main targets and link between them. Using the Objectives Tree method, it is be able to determine all the objectives of the prototype which sets 3 fundamental steps: 1) to make a list of objectives; 2) to sort the list in sets of objectives from higher to lower level; 3) to draw a diagram with data obtained. Diagram 3 shows hierarchy of each objective and interrelationships.

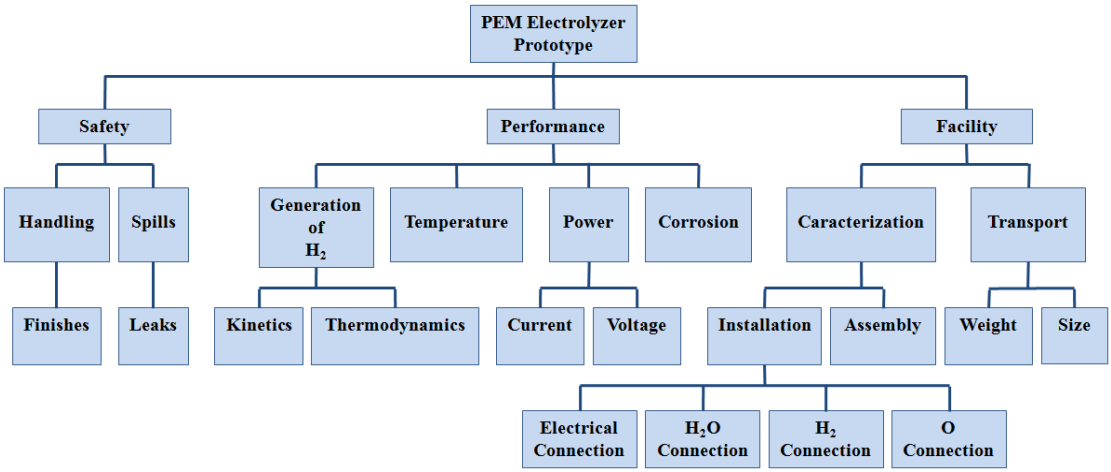

Diagram 3. Objectives Tree for a PEM Electrolyzer Prototype.

2.4. Design Specifications

Function analysis method is used to determine the "Design Specifications" which sets the required functions and system limits for a new design. There are 5 steps to complete this process [7]; 1) Expressing the overall roll of design in terms of converting inputs into outputs (black box); 2) Splitting overall function into a set of secondary functions;

3) Drawing a block diagram to show the interactions between the secondary functions, (clear box); 4) Drawing the system boundaries which define the functional limits for the prototype design; 5) Defining the appropriate components for secondary functions and their interactions. The diagram 4 shows the black box used for this prototype design; then overall function was divided into secondary functions and was drawn the line of the system boundaries as shown in Diagram 5. H_2O represent the distilled water entering the system; E_{CEL} is the electrical potential needed to carry out the oxidation reaction; H_2 is the hydrogen obtained from the system; O the oxygen; and finally L represents the heating lost.

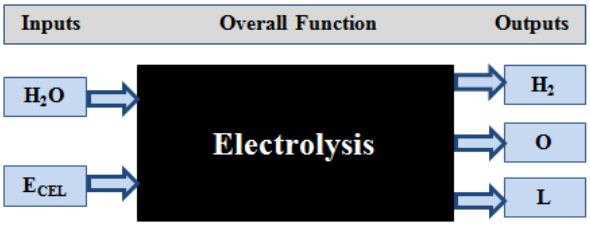

Diagram 4. Black box model for a PEM electrolyzer.

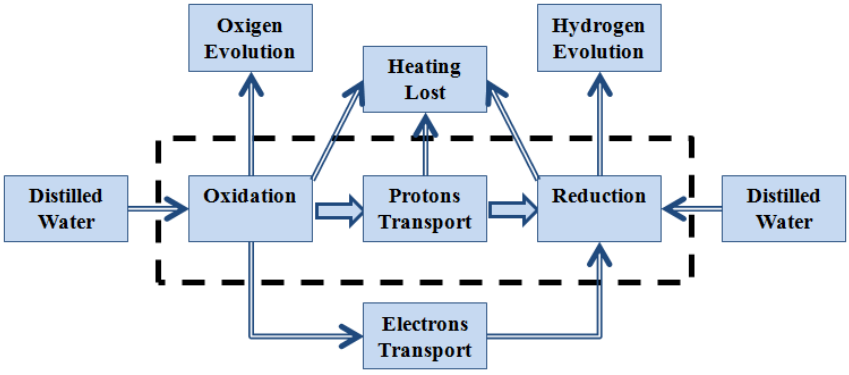

Diagram 5. Clear box model for a PEM electrolyzer.

2.5. Manufacturing Specifications

Morphological diagram is used to determine the "Manufacturing Specifications", which has the target to generate an alternatives range for product manufacture and extend the search for new potential solutions. This method involves 3 steps [7]; 1) Each one of the prototype components can be manufactured with different manufacturing processes, so it is necessary to make a list of processes; 2) Drawing a diagram that contain alternatives for each of the components; 3) Selecting the correct processes making an analysis of their characteristics, properties, benefits and costs. Table 1 shows the processes selected supported by this method.

Table 1. Morphological diagram for manufacturing processes of a PEM electrolyzer.

Products	Manufacturing Processes						
Current Distributor	(cutting) Shears	(cutting) Laser	(cutting) Flame	(cutting) Milling	(cutting) CNC	(cutting) Waterjet	(cutting) Plasma
Gas Diffuser	(cutting) Scissors	(cutting) Cutter	(cutting) Trimmer				
Catalytic Ink	(mixture) Manual	(mixture) Ultrasound	(mixture) Automatic	(mixture) Vibration			
Membrane (PEM)	(cutting) Scissors	(cutting) Cutter	(cutting) Trimmer				
Catalytic Layer	(print) Manual	(print) Airbrushing	(print) Serigraphy	(print) Spraying	(print) Tape-cast		
Housing	(cutting) Milling	(cutting) CNC	(drilling) Drill	(drilling) Drill press	(thread) Tap	(thread) Lathe	
Seals	(cutting) Scissors	(cutting) Cutter	(cutting) Trimmer	(cutting) Punching			

Alternative Manufacturing Processes Manufacturing Processes Selected

2.6. Assembly Specifications

Devices named Poka-Yokes are used to determine the "Assembly Specifications" to avoid mistakes; safety standards are used during the assembly processes in order to prevent accidents. Poka-Yokes technique is use to eliminate human and operation mistakes, simple and effective techniques to eliminate or reduce defects; it is a tool to achieve quality "Zero Defects". These devices aim to prevent omissions, lack of understanding, identification mistakes, inexperience, volunteer mistakes, inadvertent mistakes, slowness mistakes, lack of standards, mistakes by surprise and intentional mistakes. 3 levels of hierarchy must be taken into Poka-Yokes design: 1) level 3 – Making obviously that a mistake has occurred; 2) level 2 – Making obviously that a mistake will occur; 3) level 1 – Eliminating the possibility of mistakes. Table 2 shows the Poka-Yokes devises designed for this prototype.

Table 2. Poka-Yokes designed to development of PEM electrolyzer prototype.

Level of Poka-Yoke	Type of Poka-Yoke	Purpose of Poka-Yoke	Location of Poka-Yoke
Level 2	Marks of positive and negatives poles	To identify the polarities	Housing
Level 2	Identification marks of hydrogen and oxygen	To identify the gas being generated	Housing
Level 1	Notches – Interference fit	To put the power distributors	Housing
Level 1	Guide pin assembly	To assemble the housings	Housing
Level 2	Notches – Clearance fit	To put the teflon seals	Housing
Level 2	Mark for recognition of polarity MEA	To put properly the MEA	MEA
Level 2	Membrane covering fixture	To impregnate electrocatalytic ink	External device
Level 1	Fixture for mounting of diffusers and membrane	To assemble MEA	External device

The standards used for operator safety were as follows.

- NOM-005-STPS-1998. Health and safety conditions in the workplace for the handling, transport and storage of hazardous chemicals.
- ISO-14062. Integration of environmental considerations in the design and product development.
- NOM-017-STPS-1994. Relating to personal protective equipment for workers in the workplace.
- NMX-S039-SCFI-2000. Safety products, protective gloves against chemicals, specifications and test methods.

2.7. Prototype Build

4 specifications stages were defined, it proceeds with PEM electrolyzer prototype construction using the results found in each of the stages previously evaluated.

a) Membrane activation

Nafion® membrane must pass through activation process for its correct functionality; the aim of this process is to release the sodium content in this polymeric material. The membrane was introduced into a container with hydrogen peroxide at temperature range of 80°C and 100°C for one hour; then the membrane was placed in other container with 2.46 ml cm^{-2} hydrogen peroxide solution and sulfuric acid at 2.19 ml cm^{-2} due to the active area at range temperature of 80°C and 100°C for one hour. After that the membrane was deposited in a container with distilled at the same temperature and time; finally it was placed in a container with distilled water at room temperature and was left for 24 hours. The reason of the temperatures is because it is the optimal range of Nafion® operating temperature and over 150°C the membrane begins crystallization process and the molecular structures of the material are broken. The Photographs 1 and 2 show part of the activation process.

Photograph 1. Activation at 80° for 1 hr.

Photograph 2. Hydrated with distilled water

b) Preparation of the electrocatalytic solutions

To electrodes construction was necessary to prepare an anodic solution for the oxidation process and a cathodic solution for the reduction process. The cathodic solution was a mixture of 1.2 mg cm^{-2} of 10% platinum etek, 40 µl cm^{-2} of liquid Nafion® and 700 µl cm^{-2} of chromatic grade ethanol; this last one as diluent. The anodic solution was a mixture of 1.44 mg cm^{-2} of ruthenium oxide, 1.65 mg cm^{-2} of iridium oxide, 54 µl cm^{-2} of liquid Nafion® and 667 µl cm^{-2} of ethanol; both solutions was exposed in an ultrasonic process to dilute the particles homogeneously in the solution. The Photograph 3 shows the ultrasonic process mentioned.

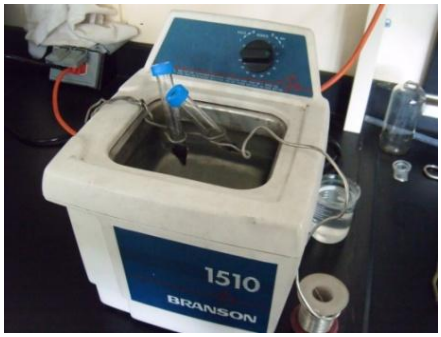

Photograph 3. Solution mixture using ultrasound

c) Construction of the electrodes

The next step was defined to electrodes construct, the electrocatalytic solutions prepared were impregnated in the membrane by airbrushing process; one membrane side was impregnated with anodic solution while the other was impregnated with cathodic solution; the airbrushing process was manual because there are not an automated process in the laboratory; it is necessary to identify properly the cathodic and anodic side of the membrane. The airbrushing process is completed when both solutions are entirety deposited on both faces of the membrane. The airbrushing process is shown in Photograph 4.

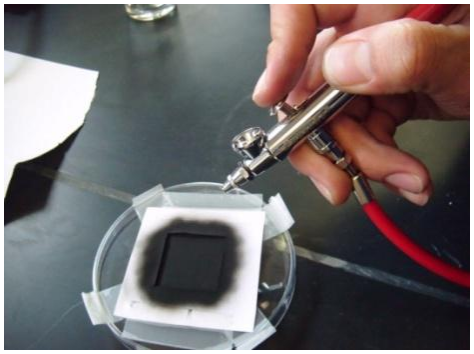

Photograph 4. Anodic solution impregnated in the membrane by airbrushing process

d) MEA Assembly

For MEA assembly, it is required to join gas carbon diffusers fiber with the membrane in order to provide a permanent contact; the process involves to introduce them into a membrane press placing between both diffusers and to protect this set with a pair of micas and a pair of aluminum plates; the hot pressing is affected at 120°C temperature with only 2 tons pressure for 5 seconds, then the pressure is released and adjusted to 0.4 tons; pressure is applied again, in this time for 2 minutes period with the plates of the press at the same temperature. 120°C is the temperature of a vitreous composition of the Nafion® membrane, above this temperature is produced a good microstructural joint between both materials, however the atomic links are broken at 150°C and a decomposition process can be initiated. Photograph 5 shows the press used in this process and MEA assembly is shown in Photograph 6.

Photograph 5. Hot press process

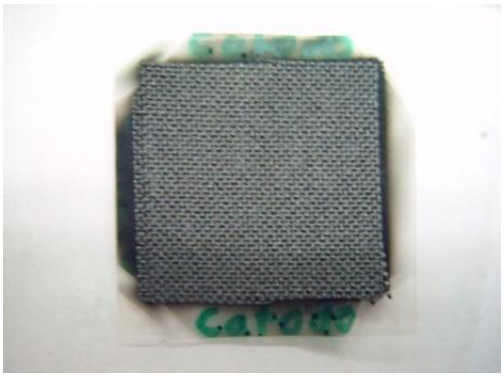

Photograph 6. MEA assembly

e) Prototype assembly

Last step was defined to assembly all the components previously manufactured of the PEM electrolyzer prototype, housings, Teflon seals, current distributors and MEA. Housings was manufactured with acrylic due to the properties of this material, such as impermeability to gases produced, resistance to the operating temperature of the PEM

electrolyzer prototype, and low cost. Current distributors was manufactured with stainless steel mesh to conduct electrical current and allow flow of gasses through themselves; screws, nuts, washers, quick connectors and silicon were used to complete the final assembly. The use of the designed Poka-Yokes helped the placement and orientation of each of the components. All the components were correctly placed in housings and the silicon was applied between current distributors, Teflon seals, and housings, in order to avoid leakages. Photograph 7 a housing with its components correctly placed, and the complete assembly is shown in Photograph 8.

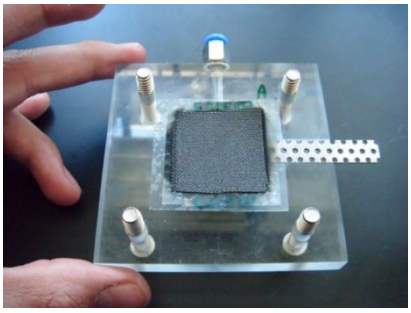

Photograph 7. Housing with MEA, current distributor, and seal

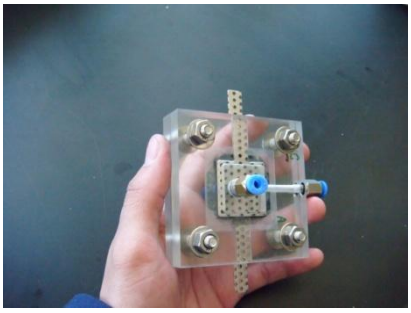

Photograph 8. PEM electrolyzer assembled

2.8. Assembly Qualification

To validate the assemblies made, first, it was used a visual inspection of the prototype reviewing the perfect seal of both housings, position of the washers, adjustment of the screws and the quick connectors, the correct state of the current distributors. In the MEA assembly process was verified adherence between gas diffuser and membrane. Placement of current distributors and seals was also inspected before assembling the entire prototype. To verify the absence of internal leakage was designed a test in which certain ports were blocked and water was introduced into the system using a water low pressure pump. The test is verified as successful when there are no leaks in free ports; the test was carried out according to the configuration of Table 3.

Table 3. Internal leakage test

Interconnected ports	Pressurized port	Blocked port	Free port	
Anode-Oxygen	Anode	Oxygen	Cathode	Hydrogen
Cathode-Hydrogen	Cathode	Hydrogen	Anode	Oxygen

Second test was defined to block the ports on the evolution of oxygen and hydrogen to supply water with the same pump, verifying that internal leakage are not observed at the juncture of the prototype housings; and finally one last test was performed to validate the assembly, this test consist of filling the water tanks of the prototype to a low pressure and keeping them for 24 hours to subsequently see if there is any type of leak.

2.9. Manufacturing Qualification

To validate that manufacture of each component, visual inspections was performed to verify gas diffusers, seals and membrane did not display defective edges; "go – no go" Poka-Yokes were designed to verify the specified dimensions of the elements of PEM electrolyzer prototype. The "go – no go" Poka-Yokes designed for this stage of qualification are shown in Table 4.

Table 4. "go – no go" Poka-Yokes designed to verify the specific dimensions of elements of PEM electrolyzer prototype.

Level of Poka-Yoke	Type of Poka-Yoke	Purpose of Poka-Yoke	Location of Poka-Yoke
Level 2	"go – no go" fixture to specific size of water tanks	To validate size of the water tanks	External device
Level 2	Calibrated screws	To validate size of the connection thread	External device
Level 1	"go – no go" fixture to specific size of current distributors	To validate size of the current distributors	External device

2.10. Installation Qualification

To validate the installation, the prototype was placed in a test table where it was electric and hydraulic connected to verify that there were no liquid or gas leaks and electrical connectors were right with power distributors when the prototype is integrated into a system. The photograph 9 shows the prototype mounted in the table test with its connections.

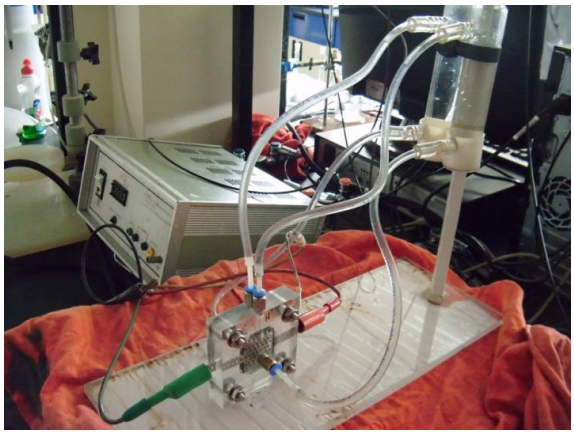

Photograph 9. PEM electrolyzer prototype connected in the table test.

2.11. Operation Qualification

In order to validate the operation of the prototype, characterization test were performed using the technique of potentiometry, for which it was necessary to have a table test consisting of a galvanostat potentiometer, a mounting

base, two graduated cylinders storage gases, a container of deionized water, two water low pressure pumps and a stopwatch. The characterization test consisted of running operation of the prototype, which water was introduced into PEM electrolyzer through the anodic and cathodic ports, circulating an electric current to different levels of intensity in each test taking care to not exceed 5 volt, since this voltage is initiated a degradation process in the membrane. Galvanostat potentiometer is able to determine the voltage required to circulate the current intensity that has been setting. First phase consisted of visually checking the gases generation, then the voltage vs. current curves were obtained, the same to determine the efficiency of a PEM electrolyzer. The second phase consisted of measuring the amount of hydrogen that was extracted using a stopwatch and measuring the volume generated per unit time. The evolution of hydrogen and measuring of the hydrogen generated are shown in the photographs 10 and 11 respectively.

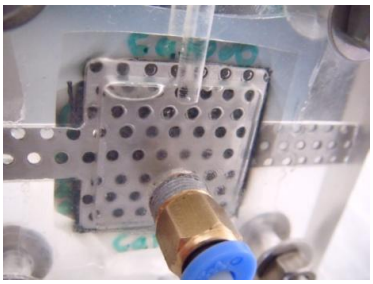

Photograph 10. Evolution of hydrogen

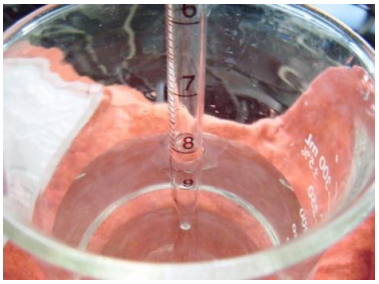

Photograph 11. Hydrogen measurement

3. Results and discussion

Methodology raising specifications at each stage was established to design and fabricate this PEM electrolyzer prototype; prototype qualities were evaluated by tests that guarantee the optimal itself operation. PEM electrolyzer built with this methodology shows favorable results compared with other prototypes built without a methodology that involves aspects of manufacturing and assembly processes that finally contribute positively to the PEM electrolyzer prototype achievement. The results obtained by characterization of PEM electrolyzer prototype by potentiometry tests showed a good efficiency of it exhibit a low resistance ohmic getting a current of 300mA with only 1.92V and obtained a productivity of hydrogen in the range of 2.137$mlH_2.min^{-1}$. The amount of hydrogen produced per unit time resulted higher that other prototypes characterized by the same tests. Graphic 1 shows performance curve obtained by potentiometry in which there is a current of 300mA below 2V.

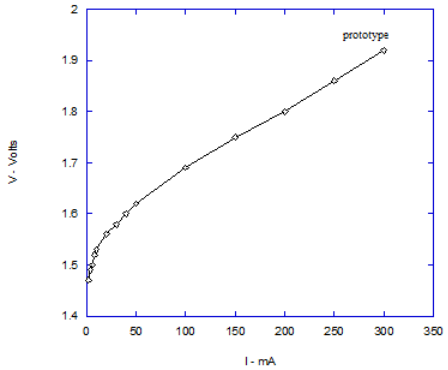

Graphic 1. Performance curve of PEM electrolyzer prototype

Graphic 2 shows a comparative of the results obtained between the PEM electrolyzer prototype and other preliminary prototype built without application of the methodology presented in this work. The results of the characterization tests show differences between both performance curves; the best performance curve is marked as "prototype", with 300mA below 2V while the other curve shows the performance of the preliminary prototype with about half in current with the same voltage 150mA below 2V reaching the 300mA above 2V. The data presented are important because the amount of hydrogen produced per unit time is proportional to the current flowing through the active area of the PEM electrolyzer prototype; it is convenient to work with the most current but without reaching the 5V because the membrane suffers severe irreversible degradation with this voltage.

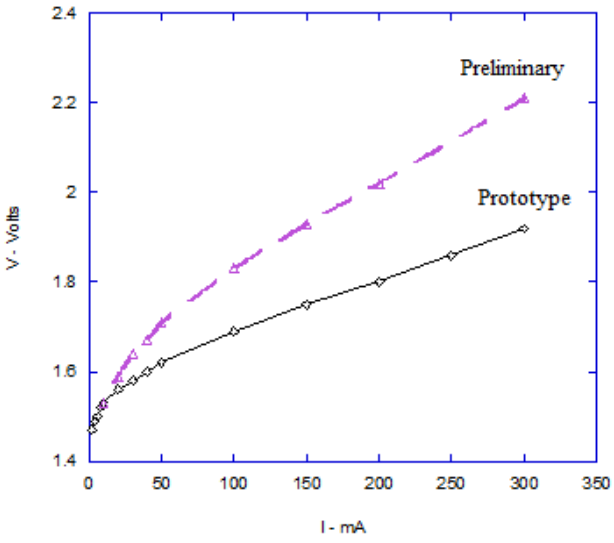

Graphic 2. Comparison of performance between PEM electrolyzer prototype and a preliminary prototype

4. Conclusions

To achieve greater current flowing through the active area of the PEM electrolyzer prototype with the same voltage results in a reduction of the ohmic resistance due to proper selection and treatment of manufacturing and assembly processes. Increase the amount of hydrogen generated per unit time using the same amount of energy result in costs reduction of hydrogen generation and becomes a major contribution to development of hydrogen economy. The results presented in this work show the effectiveness of the methodology developed for this research since it involves factors that were not previously covered in development of this kind of prototypes; other design methodologies do not involves stages with processes and tests to validate each of the stages developed during the conception of the prototype.

5. Akcnowledgements

This work has been supported by CONACyT project 130254 and IPN under multidisciplinary project SIP-1338. JLCG thanks the PIFI and CONACyT programs for the financial support (scholarship).

6. References

[1] M en I. Hilda Hernández Muñoz, Dr. Jorge Marcial Islas Samperio, Dr. Fabio Luigi Manzini Poli, M en I. Paloma Macías Guzmán, Nuevas Energías Renovables: Una Alternativa Energética Sustentable para México (Análisis y Propuesta) – Instituto de Investigaciones Legislativas del Senado de la República – 2004.

[2] CITE AS: Boden, T.A., G. Marland, and R.J. Andres. 2011. Global Regional, and National Fossil-Fuel CO2 Emissions. Carbon Dioxide Information Analysis Center, Oak Ridge National Laboratory, U.S. Department of Energy, Oak Ridge, Tenn., U.S.A. doi 10.3334/CDIAC/00001_V2011 http://cdiac.ornl.gov/trends/emis/tre_mex.html .

[3] J. L. G. Fierro, L. Gómez y M. A. Peña, El Hidrógeno: Un Vector energético no Contaminante para Automoción – Instituto de Catálisis y Petroleoquímica. CSIC

[4] Omar Solorza-Feria, Elvira Ríos-Leal, y Héctor M. Poggi-Varaldo, Energías Renovables Biológicas-Hidrógeno-Pilas de Combustible-Primera Edición – Libros de Ciencia y Tecnología N° 1 ISBN 978-968-5441-11-7 – 2008.

[5] Rosa de Guadalupe González Huerta, Ernesto López Chávez, Blanca Velázquez Morales, Hidrógeno: Introducción a la Energía Limpia – Universidad Autónoma de la Ciudad de México – 2009.

[6] International Society for Pharmaceutical Engineering – http://www.ispe.org/about-ispe

[7] Nigel Cross, Métodos de Diseño: Estrategias para el Diseño de Productos – Limusa Wiley - 2010

Oxygen Reduction Reaction on Pt/C Electrocatalysts Obtained by a Photo-Chemical Route

R. G. González Huerta[1], M. A. Valenzuela[1], O. Martínez-Álvarez [2], H. H. Rodríguez[2], B. Ruiz-Camacho[1,2*,]

[1]ESIQIE-IPN, Laboratorio de Catálisis, UPALM, CP 07738, México D.F
[2]Ingeniería en Energía, Universidad Politécnica de Guanajuato, Av. Universidad Norte s/n, Juan Alonso Cortazar Guanajuato, C.P. 38438, México.

ABSTRACT

Platinum nanoparticles with homogeneous dispersion on carbon Vulcan was obtained at room temperature by irradiation of an alcoholic solution of $C_{10}H_{14}O_4Pt$ with UV-light. The electrocatalyst were characterized by X-ray diffraction and transmission electronic microscopy techniques. TEM micrographs and XRD results confirmed the formation of platinum nanoparticles (4 nm) with a high dispersion onto the carbon. The electrochemical active surface area was determinate by CO stripping and hydrogen-adsorption/desorption reactions. The electrochemical activity and stability of Pt/C for the oxygen reduction reaction (ORR) were determined by rotating disk electrode (RDE) at different temperatures. An apparent enthalpy of activation $\Delta H\# = 58.7$ kJ mol-1 was calculated from the electrochemical results from 25 to 50°C. The main reaction pathway was quantifying by rotating ring-disk electrode (RRDE). The maximum amount of hydrogen peroxide produced in the ORR reaches a value of 3.8% at 0.36V/NHE following preferentially the four-electron transfer mechanisms to water formation. The current densities results revels that Pt catalysts with high activity and selective for the ORR can be obtained by the photo-deposition method.

Key words: Platinum electrocatalyst, photo-chemical, oxygen reduction, rotating disk electrode

1. Introduction

Proton exchange membrane fuel cells (PEMFC) has been receiving much attention as power sources for vehicles, portable devices and stationary applications due to their high energy conversion efficiencies and low pollutant emissions. The performance of a membrane electrode assembly for PEMFC greatly depends on the activity and loading amount of the electrocatalysts [1]. Platinum supported on high surface area carbon is still the catalyst most widely used in the fuel cell, this is for both electrodes: anode and cathode [2-3]. One of the major challenges in this field is the development of high-performance cathode catalysts in order to reduce the high overpotential present during the oxygen reduction reaction (ORR) [4-6]. The kinetics of oxygen reduction reaction is determined by various factors, which involve the geometric and electronic parameters of the material that catalyzes the reaction. One of the most important aspect in the ORR is the interaction of oxygen molecule with active sites of the catalyst, this is related with the catalytic activity, that is, with the size of its particles, its geometry and composition, its

dispersion and interaction with the support, it is important to control these factors during the synthesis process of the catalyst by means of an appropriate selection of the synthesis method [7-8].

Pt supported electrocatalysts for PEMFC normally are synthesized in the presence of a capping agent via reduction of a Pt precursor, decomposition of an organometallic complex, or a combination of these two routes [9-10]. However, in order to improve the metal dispersion, reduced the nanometer sizes and improve the interaction between the catalyst and the support, in the present work we prepared Pt nanoparticles with a homogeneous dispersion on carbon Vulcan using a photochemical route as synthesis method [11-16]. One of the advantages of this technique is the facile and low cost to synthesize nanometer platinum particles without thermal treatments with the possibility of employ both inorganic and organic precursors [17]. In this work, we report results concerning to the synthesis, physical characterization and electrochemical activity of the Pt/C catalyst for the ORR. Also, the mechanism of the catalyst activity toward water formation and the effect of temperature on the ORR kinetics for the Pt catalyst were investigated.

2. Experimental

2.1 Electrocatalysts preparation

10 wt.% Pt/C catalyst was synthesized by a photo-chemical method [16-17]. The platinum nanoparticles deposition onto the carbon Vulcan was carried out using a commercial photo-reactor (Luzchem Model LZV-4V) with 14 UV black light lamp of 20 W with the main wavelength at 365 nm. A platinum aqueous solution ($C_{10}H_{14}O_4Pt$ (Aldrich)) (5×10^{-4} M), prepared with an excess of ethanol (1:3), was bubbled with Nitrogen to remove the dissolved oxygen. Under this condition, the alcoholic solution was continuously stirred and irradiated for 3h. After this time irradiation, the quantity of Vulcan carbon necessary was added to obtain the 10 wt.% Pt/C catalyst. The resultant suspension was heated in an oven at 100 ºC overnight to remove the solvent by evaporation. The product obtained was a powder of the metallic platinum nanoparticles supported on carbon, labeled Pt/C-photo.

2.2 Physical characterization

The particle size distribution and the surface morphology of Pt/C-photo sample was obtained with Transmission Electron Microscopy technique (TEM) using a JEOL-JEM-2200 field emission operated at 200 kV. The dry samples obtained after the irradiation were prepared by dispersion in ethanol by ultrasound and the resulting suspension was deposited onto a copper mesh and dried at ambient conditions before TEM analysis.

X-ray diffraction (XRD) patterns of platinum catalyst were collected on a Bruker D8 AXS equipment using a Cu anode (K_α, λ=1.5406 Å) and a Bragg-Brentano configuration. The angle 2θ was varied between 20 to 100º with a stepwidth of 0.2° min^{-1} and 35 kV.

The H_2 chemisorption (pulse method) analysis was performed to determine the average active particle size and metal dispersion (it is defined like the relation between the number of Pt surface atoms and the number of Pt total

atoms).This analysis was carried out applying pulses of H_2 to the sample using an Autochem II 2920 equipment (Micromeritics) with a thermal conductivity detector (TCD) [16].

2.3. Electrochemical Characterization

Rotating disk electrode (RDE) and rotating ring-disk electrode (RRDE) techniques were employed to determine the activation energy and main reaction pathway, quantifying the amount of hydrogen peroxide produced during the oxygen reduction reaction. For RDE experiments, 8 µl of a sonicated mixture of 1mg of Pt catalyst, 60 µl of ethyl alcohol (spectrum grade) and 8µl of 5wt% Nafion® solution (Du Pont, 1000EW) were deposited on a glassy carbon electrode (GC) with a cross-sectional area of 0.19 cm^2.

For RRDE experiments, a commercial RRDE-PAR glassy carbon disk (diam=4.57 mm) and platinum ring with N=0.21 of nominal collection efficiency was used. The catalytic ink was prepared with 1mg of catalyst, 8 µl of 5 wt% Nafion® solution (Du Pont, 1100 EW), 100 µl of water and 100 µl of ethyl alcohol (spectrum grade). 8 µl of this suspension were deposited on the disk of working electrode surface. The current density was calculated using the geometric surface area.

The electrochemical measurements to RRDE were carried out at room temperature in a single, conventional, three-electrode test electrochemical cell. A platinum mesh was used as the counter electrode, and $Hg/Hg_2SO_4/0.5M\ H_2SO_4$ (MSE=0.680 V/NHE) as the reference electrode. RDE experiments were carried out in a water thermostated three-compartment cell for temperature control.The reference electrode was placed outside the cell, kept at room temperature and connected by a porcelain Luggin capillary. The temperature of the cell was controlled by a thermostat (Haake F3) from 293 to 323 K.

All experiments were performed in a Potentiostat AutoLab PGSTAT12 and a Pine MSRX rotation speed controller. A 0.5 M H_2SO_4 (Merck) aqueous solution was used as electrolyte, prepared from distilled water.The potentials in this paper are related to normal hydrogen electrode (NHE). Before the ORR measurements, cyclic voltammetry (CV) was performed from 0 to 1.2 V at 50 mV s^{-1} in an argon-saturated electrolyte, to clean the electrode surface. Ten cycles were necessary to stabilize the current–potential signal. Thereafter, the acid electrolyte was saturated with pure oxygen and maintained on the electrolyte surface during the RDE and RRDE tests. Hydrodynamic experiments were recorded in the rotation rate range of 100 to 1600 rpm at 5 mV s^{-1}. Between each measurement, the acid electrolyte was saturated with pure oxygen for 5 minutes to obtain the stable open circuit potential.

The experimental techniques selected for determination of Electrochemical Active Surface Area (EAS) were the cyclic voltammetry in in argon saturated 0.5 M H_2SO_4, at 50 mV s^{-1} by integrating the hydrogen-adsorption/desorption reaction (H_{upd}), Eq. (1), and the oxidation of adsorbed carbon monoxide or CO stripping technique. The electrode potential was held at 0.1 V/NHE and CO bubbled by 5 min. Thereafter, the CO was removed by purging the electrolyte with argon by 15 min and the test electrode swept from 0.05 V to 1.2 V/NHE until the post-CO oxidation was completed. Eq. (2):

$$EAS_{H\,upd} = \frac{Q_H}{0.210\,mC\,cm^{-2}} \quad (1)$$

$$EAS_{CO} = \frac{Q_{CO}}{0.420\,mC\,cm^{-2}} \quad (2)$$

where, Q_H and Q_{CO} are the measured charges for H_{upd}, and CO oxidation (mC), respectively. 0.21 mC cm^{-2} and 0.42 mC cm^{-2} corresponds to the charge required to oxidize a monolayer of adsorbed hydrogen and carbon monoxide species on Pt, respectively [18].

3. Results and discussion

3.1. Physical characterization results

Figure 1 shows the XRD diffraction patterns of Pt/C-photo sample. The powder electrocatalyst showed five diffraction peaks at 2θ values of 39.8º, 46.2º, 67.4º, 81.2º and 85.7º characteristics of the (111), (200), (220), (311) and (222) planes of face-centered cubic structure of platinum.

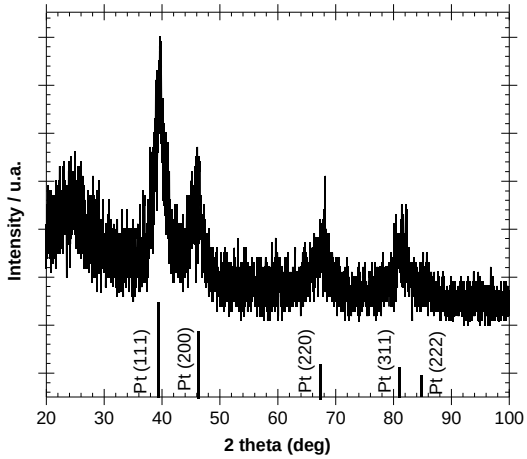

Figure 1. X ray diffraction patterns of Pt/C-photo catalyst synthesized by photo-deposition method.

TEM micrograph of platinum supported on carbon prepared by photo-deposition method is shown in figure 2. According to the figure 2, a homogenous distribution of Pt nanoparticles less than 5 nm onto de carbon was obtained. The average particle size and platinum dispersion on carbon support were investigated by H_2 chemisorption as complementary study.

Table 1. Physical and electrochemical parameters of Pt/C-photo sample.

Catalyst	***Average particle size (mn)**	***Platinum dispersion (%)**	**EAS $_{CO}$(cm^2_{Pt})**	**EAS (H_{upd}) (cm^2_{Pt})**
Pt/C-photo	5.2	21.5	5.5	5.01

*Estimated by H_2 chemisorption technique.

The results are reported in Table 1. Assuming spherical Pt particles, Pt/C-photo catalyst shows a small nanometer size (5.2 nm) with a platinum dispersion of 21.5 %. These results mean that the photo-chemical route allows preparing right Pt nanoparticles dispersed onto the carbon, by irradiation of the platinum acetil-acetonate precursor at room temperature.

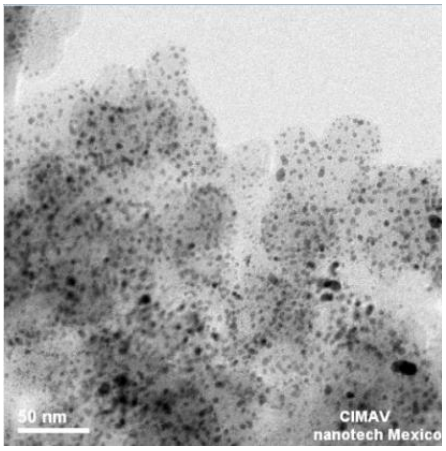

Figure 2. TEM graph for Pt/C-photo electrocatalysts synthesized by photo-deposition method.

3.2. Electrochemical characterization

Figure 3(a) shows a representative set of polarization curves for the ORR on the Pt/C-photo electrocatalyst in 0.5M H_2SO_4 at 318 K. Well defined kinetic currents (j_k) (0.93-0.83 V/NHE), mixed-diffusion limiting currents (0.83-0.60 V/NHE) and diffusion limiting currents (j_d) (0.2-0.6 NHE) are observed in polarization curves. It is considered that the increase in limiting currents on high performance electrocatalysts is associated with the increase of molecular oxygen diffusion in the boundary layer through the electrode surface. The reduction reaction is fast enough at high cathodic overpotentials, associated in almost all the cases to a flat limiting plateau. An explanation of the well defined catalytic current plateau of figure 3(a) could be associated to the existence of a uniform distribution of electrocatalytic sites on the electrode surfaces. When distribution of active sites is less uniform and the electrocatalytic reaction is slower, the current plateau is more tilted.

Table 2. Electro-kinetic parameters of Pt/C-photo electrocatalysts at different temperature.

Temperature K	**Slop Tafel mV dec^{-1}**	**Transfer coefficient α**	**Exchanger Current Density J_o mA cm^{-2}**
298	-82.10	0.72	1.30 x 10^{-6}
303	-82.48	0.73	1.55 x 10^{-6}
308	-81.78	0.74	1.81 x 10^{-6}
313	-81.17	0.76	3.03 x 10^{-6}
318	-80.78	0.79	5.60 x 10^{-6}
323	-79.28	0.80	7.17 x 10^{-6}

Figure 3(b) shows the mass transport corrected Tafel plots obtained for the Pt/C photo-electrocatalyst ink-type electrode on which oxygen reduction kinetics studies were conducted at different temperatures, from 293 to 323 K. The Tafel plots were obtained after the measured currents were corrected for diffusion to give the kinetic currents in the mixed activation–diffusion region, calculated from Eq. (3):

$$j_k = j\frac{j_d}{j_d - j} \tag{3}$$

Where $j_d/(j_d–j)$ is the mass transfer correction. The Tafel plots at all temperatures show a linear behavior in the mixed activation–diffusion region and a deviation of the kinetic current occurs with higher slope at high current density.

The kinetic parameters deduced for the oxygen reduction on Pt/C-Photo catalyst ink-type electrodes at different temperatures are presented in Table 2. The temperature analysis on the kinetic parameters is important in the cathodic reaction of a fuel cell. Effects such as the increase of the current and shift of the curves to more positive potentials were observed with the temperature rise. This behavior indicates an enhancement of the kinetic reduction of the adsorbed oxygen with the temperature. The dependence of the reversible oxygen electrode potential, E_r, on temperature [19] was evaluated using the value of ΔG° (H_2–O_2 cell) at each temperature using equations (4) and (5):

$$\Delta G^0 = \left[-70650 - 8T\ln T + 92.84T\right] \quad \text{cal mol}^{-1}, \tag{4}$$

$$E_r = -\Delta G^0 / nF \tag{5}$$

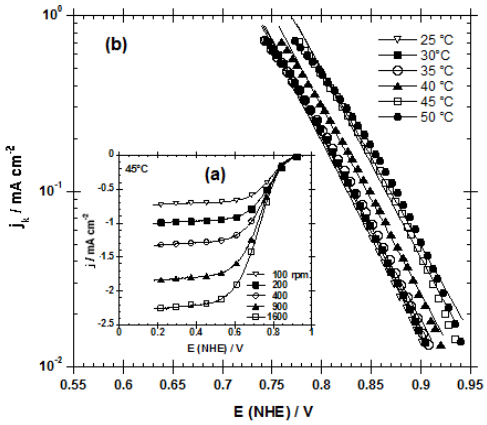

Figure 3. (a) Steady-state current-potential curves for ORR at different rotating speed, in oxygen saturated 0.5 M H_2SO_4 electrolyte at 5 mV s^{-1} and 45°C, (b) Mass-transfer corrected Tafel plots at different temperatures on Pt/C-photo electrocatalyst.

The temperature dependence of the exchange current density in Table 2 was analyzed via conventional Arrhenius analysis. Figure 4(a) shows an Arrhenius plot constructed for the Pt/C-Photo electrocatalyst in 0.5M H_2SO_4. The apparent enthalpy of activation, $\Delta H^{\#}$, was calculated from the linear regression analysis of the slope of the Arrhenius equation represented by the equation (6),

$$\frac{d\log j_o}{d(1/T)} = -\frac{\Delta H^{\#}}{2.303R} \tag{6}$$

An apparent enthalpy of activation $\Delta H^{\#}$ = 58.7 kJ mol^{-1} was calculated from the slope of this plots. This value is in agreement with apparent activation energies reported for platinum-base electrocatalysts for the ORR in acid media [20]. The apparent activation energy of 58.7 kJ mol^{-1} determined in 0.5M H_2SO_4 lies in the range of 25–60 kJ mol^{-1} reported for other materials for the oxygen reduction in acid media [19, 21]. One should keep in mind that the assessment of the activation energy at the reversible oxygen potential is only an estimate of the activation energy, i.e. $\Delta H^{\#}$ is the apparent activation energy.

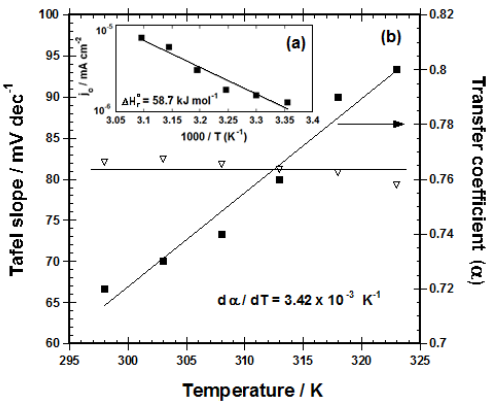

Figure 4. (a) Electrochemical Arrhenius plot of the exchange current density at the reversible potential for the ORR. (b) Variation of Tafel slope and transfer coefficient with temperature

The Tafel slope, *b*, is dependent on temperature according to the relation given by equation (7) [20]:

$$b = \frac{dE}{d\log i} = \frac{-2.303RT}{\alpha nF} \tag{7}$$

where: *n* and α are the number of electrons transferred and the transfer coefficient, respectively. Theoretically, *b* is temperature dependent if α is assumed to be invariant with temperature. Temperature dependence of the Tafel slope and transfer coefficient are shown in figure 4 (b). Here it can be observed that an experimental average Tafel slope of

-80 mV dec^{-1} is practically invariant with temperature for all the samples, leading to a dependence of the transfer coefficient with temperature. An increased linear variation of the charge transfer coefficient with respect to the absolute temperature ($d\alpha/dT$= 3.42 x10^{-3} K^{-1}) is also shown in figure 4. This behavior represents a significant feature and has been considered as an exception in the ORR rather than a rule in this electrochemical process [20-22]. In general the transfer coefficient α varies with the absolute temperature by the linear relationship, equation (8):

$$\alpha = \alpha_H + T\alpha_S \tag{8}$$

Where α_H is the enthalpic and α_S the entropic component to α.The term α_H is related to the change of electrochemical enthalpy of activation with electrode potential; mean while α_S is related to the change of electrochemical entropy of activation with electrode potential [23]. α_H and α_S were evaluated from the slope and interceptof a nominated Conway plot of the reciprocal of the Tafel slope against 1/T (plot not included) give the equation (8)

$$\alpha_{M1} = \alpha_H + T\alpha_S = -0.326 + 0.0035K^{-1}T \tag{9}$$

α_H is found to be -0.326 and α_S=3.5×10^{-3} K^{-1}. The value of α_H, suggests a less enthalpic contribution of the electrocatalyst to the ORR than entropy transfer coefficient (α_S). Thus, entropy transfer-coefficient is the determining factor for the catalytic activity of this reaction, indicating that the activation entropy turn over plays one of the most important roles in this cathodic electrochemical process.

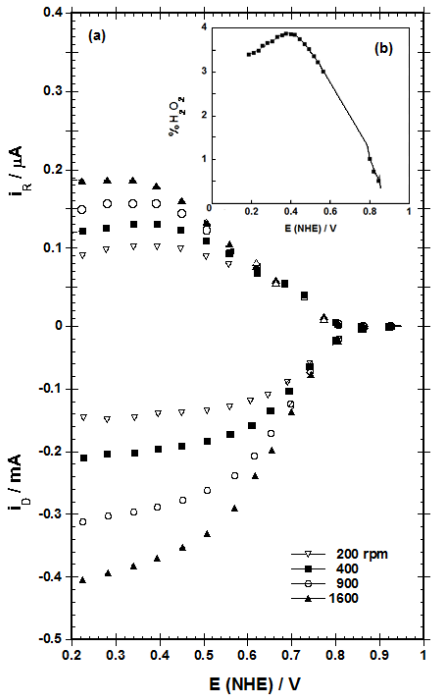

Figure 5. (a) Steady state polarization curves at different rotation speed as a function of disk potential for ORR in 0.5 M H_2SO_4 at 25 °C. (b) Percentage of hydrogen peroxide produced for the ORR.

The ORR is a complex reaction that proceeds via several consecutive and parallel elementary steps. It has been accepted that this occurs along two principal pathways: the first is the direct reduction to water with the transference of $4e^-$; the second is the so-called "peroxide pathway", which involves the transfer of $2e^-$ to the formation of H_2O_2 as intermediate. In this study, the RRDE technique was used in order to determine the amount of hydrogen peroxide produced [24]. The collection efficiency (N) was obtained experimentally from the slope of an i_R versus i_D plot at different rotation speeds, using as an electrolyte a $5x10^{-3}$ M $K_3Fe(CN)_6$ solution in 0.1 M K_2SO_4. A value of N = 0.16 for this arrangement was calculated on the thin film formed on the glassy carbon electrode. The ring potential was kept at +1.48V (NHE) during all of the electrochemical experiments, where oxidation of the H_2O_2 formed by O_2 reduction on the disk electrode is limited by diffusion.

Steady-state polarization curves obtained for the ORR in the disk and the currents for the hydrogen peroxide oxidation in the ring to Pt/C-Photo electrode are shown in Figure 5. In the oxygen saturated solution, the diffusion currents in the disk and ring are observed as a function of rotation speed. The peroxide percentage was evaluated from the following equation [25]:

$$\%H_2O_2 = \frac{200\ I_R/N}{I_D + I_R/N} \tag{10}$$

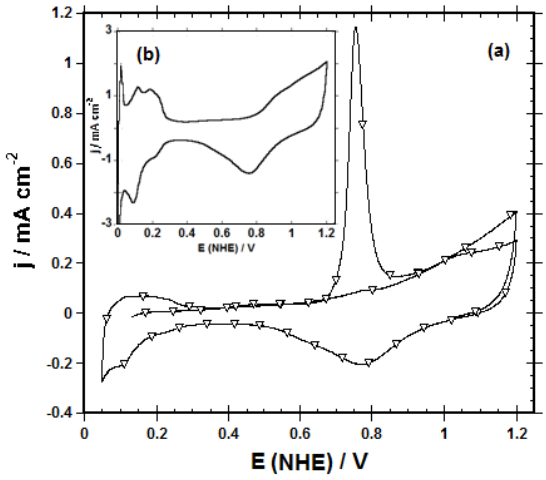

Figure 6. (a) Steady state polarization curves at different rotation speed as a function of disk potential for ORR in 0.5 M H_2SO_4 at 25 °C. (b) Percentage of hydrogen peroxide produced for the ORR.

Figure 5(b) shows that the quantity of hydrogen peroxide formation depends on the potential. The maximum amount of H_2O_2 produced in the electrochemical process of the ORR reaches a value of 3.8 % at 0.36 V/NHE on Pt/C-Photo electrode. The maximum amount of peroxide is preferable at more cathodic potentials because the fuel cell operates between 0.8 V (NHE) and 0.6 V (NHE).These results indicate that the Pt/C-Photo has a yield near 96.2 % for the

ORR (i.e., $\%H_2O = 100- \%H_2O_2$), following preferentially the four-electron transfer mechanisms to water formation. Figure 6 (a) shows the CO-stripping curves corresponding to electrocatalyst Pt/C-photo. Table 1 summarizes the electrochemical active area EAS (CO) obtained under the oxidation CO curve. In order to complement the results, the electrochemical active surface area (EAS) was calculated in hydrogen adsorption-desorption region (H_{upd}), figure 6 (b). The H_{upd} charge is estimated for hydrogen adsorption/desorption in the CV profile after the conventional correction for the pseudocapacity in the double layer region. Similar EAS were found by both techniques, CO stripping and Hupd. The EAS depends of the particle size, distribution and quantity of surface particles. In this case, the real surface area differs highly from the geometric one, indicating high catalytic activity. The electrocatalysis mechanism is based on the electrode–electroactive species charge transfer through the electrode surface. So the reaction rate, and consequently the electric current, is proportional to the electrode real surface area [26].

4. Conclusions

Pt nanoparticles can be prepared at room temperature by the photo-deposition method. The physical characterization of the synthesized platinum showed a homogeneous distribution of platinum nanoparticles onto the carbon with an average particle size of 5 nm. Pt/C electrocatalyst showed activity and selectivity towards the ORR process in acid medium. The ORR followed preferentially the four-electron transfer mechanism to water formation. The effect of temperature on electrochemical parameters showed that the Tafel slope is directly proportional to the temperature with the transfer coefficient a temperature-independent factor.

Acknowledgements

This work has been supported by the IPN under project SIP-20113593 and CONACYT project 130254. BRC thanks PIFI and CONACyT programs for the financial support (scolarship).

References

[1] B. Zhang, L.J. Chen, K.Y. GE, Y.C. Gou, B.X. Peng, Chinese Chemical Letters, 16, 1531-1534 (2005).

[2] E. Antolini, Appl. Catal. B, 88, 1-24 (2009).

[3] L.G.R.A. Santos, K.S. Freitas, E. A. Ticianelli, J. Solid Stated Electrochem 11, 1541-1548 (2007).

[4] J.J. Salvador-Pascual, S. Citalán-Cigarroa, O. Solorza-Feria, J. PowerSources, 172. 229-234 (2007).

[5]S. Chen, P.J. Ferreira, W. Sheng, N. Yabuuchi, L.F. Allard, Y. Shao-Horn, J. Am. Chem. Soc. 130, 12818-13819 (2008).

[6] L. Zhang, J. Zhang, D.P. Wilkinson, H. Wang, J. Power Sources 156, 171-182 (2006).

[7] B. Ruiz Camacho, M. Torres Rodríguez, O. Solorza Feria, J. New Mat. Electrochem.Syst. 12, 043-047 (2009).

[8] S. Zhang, X.-Z. Yuan, J.Z. Cheng Hin, H. Wang, K. A. Friedrich, M. Shulze. J. Power Sources 194, 588-600 (2009).

[9]John Regalbuto, "Catalyst Preparation Science and Engineering", CRC Press, Taylor and Francis Group, New York, 2007.

[10] J. Chen, B. Lim, E.P. Lee, Y. Xia, Nano Today 4, 81-95 (2009).

[11] H. Einaga, M. Harada, Langmuir 21, 2578-2584 (2005).

[12] L. Timperman, Y.J. Feng, W. Vogel, N. Alonso-Vante, Electrochim. Acta 55 7558-7563 (2010)

[13] K. Rajeshwar, N. R. de Tacconi, C. R. Chenthamarakshan, W. A. Wampler, T. Carlson, and W.-Y. Lin, U.S. Patent, pending.

[14] N. R. Tacconi, C.R. Chenthamarakshan, K. Rajeshwar, W.-Y. Lin, T.f. Carlson, L. Nikiel, W.A. Wampler, S. Sambandam, W. Ramani, J. Electrochem. Soc. 155 B1102-B1109 (2008).

[15] C. Crisafulli, S. Scire, S. Giuffrida, G Ventimiglia, R. Nigro, Appl. Catal. A, 306, 51-57 (2006).

[16] B. Ruiz Camacho, M.A. Valenzuela, J.A. Perez Galindo, F. Pola, M. Miki-Yoshida, N. Alonso-Vante, R. G. González Huerta, J. New Mat. Electrochem. Syst. 13, 183-189 (2010).

[17] Ruiz Camacho, R. G. González Huerta, M. A. Valenzuela, N. Alonso-Vante, Top. Catal. 54, 512-518 (2011).

[18] T. Vidakovic, M. Christov, K. Sundmacher, Electrochim. Acta 52, 5606-5613 (2007).

[19] K. Suárez-Alcántara, A. Rodríguez-Castellanos, R. Dante, O. Solorza-Feria, J. Power Sources 157, 114–120 (2006).

[20] R. G. Gonzalez-Huerta, A. R. Pierna and O. Solorza-Feria, J. New Mat. Electrochem. Syst. 11, 63-67 (2008).

[21] J.J. Salvador-Pascual, V. Collins-Martínez, A. López-Ortíz, O. Solorza-Feria, J. Power Sources 195, 3374–3379 (2010).

[22] V. S. Murthi, R. C. Urian, and S. Mukerjee, J. Phys. Chem. B 108, 11011-11023 (2004).

[23] A. Damjanovic, J. Electroanal. Chem. 355, 57-77 (1993).

[24] G. Ramos-Sánchez, A.R. Pierna, O. Solorza-Feria, Journal of Non-Crystalline Solids 354, 5165–5168 (2008).

[25] U.A. Paulus, T.J. Schmidt, H.A. Gasteiger, R.J. Behm, J. Electroanal. Chem. 495, 134-145 (2001).

[26] José M. Doña Rodríguez,* José Alberto Herrera Melián, Jesus Pérez Peña, J. Chem. Edu., Vol. 77 No. 9, 1195-1197 (2000).

Biohydrogen Production through Solid Substrate Fermentation of Organic Municipal Wastes: a Multivariable Evaluation

C. Escamilla-Alvarado [1], M.T. Ponce-Noyola [2], E. Ríos-Leal [3], N. Rinderknecht-Seijas [4], H.M. Poggi-Varaldo [1,*]

[1]Environmental Biotechnology and Renewable Energies R&D Group, Dept. of Biotechnology and Bioengineering, Centro de Investigación y de Estudios Avanzados del IPN, P.O. Box 14-740, 07000 México D.F., México; [2]Microbial Genetic Group, ibidem; [3]Central Analítica, ibídem; [4]Escuela Superior de Ingeniería Química e Industrias Extractivas del IPN, Mexico D.F., México.
*Author for all correspondence: hectorpoggi2001@gmail.com

Keywords: *biohydrogen; high total solids; intermittent venting; municipal organic solid wastes; nitrogen supplementation*

ABSTRACT

Municipal solid waste (MSW) generation is a constant problem on growing cities. The organic fraction (OFMSW), ca. 60% of MSW, is being literally 'wasted' despite its applicability on energy production. Therefore, this work was focused on hydrogen production from the OFMSW with a double purpose: *(i)* to evaluate the effect of the total solids content (20.9 and 35% TS), temperature (35 and 55 ºC) and mass retention time (MRT, 21 and 14 d) on semi-continuous fermentation, and *(ii)* to test the supplementation with nutrient nitrogen in the form of waste activated sludge in batch mini-reactors.

Firstly, in the semi-continuous fermentation, it was found that factors had significant influence on hydrogen productivity in the order: total solids > MRT > temperature. Significant interactions amidst factors were only observed between TS and temperature or MRT. Indeed, best hydrogen productivity averaged up to 123 NmL H_2/(kg_{wmr} d) at 20.9 %TS, 55 ºC and 21 d MRT. Secondly, in the batch fermentation, supplementation with nitrogen in the form of activated sludge did not show a significant effect. Highest results were P_{H2} = 1 983 μmol_{H2}/gVS and R_{H2} = 68.3 μmol_{H2}/(gVS h) in the mini-reactors without addition of alkalinity or sludge. No significant lag phase was observed in none of the experimental units. Microorganisms introduced through supplemented sludge might have affected fermentation, particularly boosting hydrogen consumption.

In general, variations and inhibition of hydrogen production were related to low pH and lactic acid and solvent deviation of the fermentation. This was in agreement with reports of a strong correlation between high lactic acid concentrations and inhibition of hydrogenogenesis.

1. Introduction

The incoming oil age decline has promoted over 15 years of intensive research for developing alternative energy technologies; hydrogen production is among them [1]. One of the promising technologies for hydrogen production is through the dark fermentation of biomass [2]. For the sake of process economic feasibility, it has been suggested that the substrate ought to be inexpensive and inexhaustible [1, 3]. Indeed, municipal solid wastes are a major source of biomass as organic wastes (OFMSW): in Mexico, 102 000 ton/day are produced and its the organic fraction (paper and food wastes) represents up to 60% of the total [4].

OFMSW are biosolids with 50-70% water contents, yet its application to biofuel production has been mainly studied at low solids (<10% TS) fermentation [5]. It is noteworthy that submerged culture under such conditions employs large dilution water volumes, thus generating polluted wastewaters. Although less studied, solid substrate fermentation (SSF) has advantages such as reactor volume reduction, no leachate generation and high H_2 productivities [6, 7].

Although important investigations have determined the factors influencing the process performance (such as solid contents, temperature and mass retention time), there is a lack of comprehensive experiments in the open literature embracing all these factors in such a way to find interactions and the optimal operating conditions. For instance, high solids content means more OFMSW being treated but also a possibility of osmotic stress to microorganisms. Due to the complexity of the temperature strong influence on biochemical processes and microbiological interactions, a consensus on which thermal regime is better has not yet been determined. Furthermore there is a wide variability amidst processes, inocculum and substrates employed. Moreover, comparisons of mesophilic and thermophilic regimes are still scarce in high solids semi-continuous hydrogenogenesis process, as most studies have operated bioreactors mainly in the mesophilic range of temperature [7-11].

On the other hand, the organic load or mass retention time (MRT) can significantly affect the organic matter available to microorganisms and metabolic deviations from hydrogenogenic conditions [7, 8, 12]. Despite its importance, the information on the effect of MRT on solid substrate dark fermentation is still scarce, except for recent reports from our group [5, 13].

Moreover, it has been supposed that OFMSW by itself provides all the nutrients required for dark fermentation. However, carbon to nitrogen (C/N) ratio of municipal organic wastes is usually high, up to 76 [14], yet for anaerobic fermentation the suggested C/N ratio is 25-35 [15]. This may suggest that nitrogen may be supplemented as ammonia or in the form of organic nitrogen, such as manure, waste sludges, or food wastes [16, 17].

Therefore, this work was focused on the hydrogen production from the OFMSW in SSF with a double purpose: *(i)* to evaluate the effect of the total solids content (20.9 and 35% TS), temperature (35 and 55 ºC) and mass retention time (MRT, 21 and 14 d) on semi-continuous fermentation, and *(ii)* to evaluate the supplementation with nutrient nitrogen in the form of waste activated sludge.

2. Materials and methods

2.1. Effect of total solids, temperature and mass retention time on SSF

First hydrogenogenic set of experiments was carried out in glass bioreactors containing 500 g biosolids [5]. The OFMSW consisted of dried food wastes from cafeteria (60% w/w) and waste office paper (40% w/w). It was implemented a 2^3 experimental design for evaluating the effect of the total solids content (TS, 20.9 or 35 %), temperature (35 or 55 ºC) and mass retention time (MRT, 21 and 14 d) on semi-continuous hydrogen production.

2.2. Nitrogen and alkalinity supplementation at thermophilic and mesophilic regimes

The organic nitrogen and alkalinity supplementation studies were performed on batch, solid substrate anaerobic hydrogenogenic fermentation in intermittently vented mini-reactors (SSAHF-IV) containing 80 g biosolids, according to set-up described by Muñoz-Paez *et al.* [13]. Experimental design basis was 2^3. Factors were temperature (35, 55 ºC), C/N ratio (basal 50, 30 adjusted with activated sludge), and alkalinity (none, 0.06 g $CaCO_3$/g dry substrate with phosphate salts).

2.3. Analyses

Analyses were performed to solid samples taken from OFMSW and bioreactors. Volatiles solids (VS) and total solids (TS), pH, volatile organic acids (VOA), lactic acid and solvents were analyzed as reported elsewhere [18]. Biogas production was measured by acid brine displacement [5]; gas volumes were normalized to 273 K and 101.15 kPa (reported as NmL or NL). H_2 and CH_4 contents were determined in a GOW-MAC gas chromatograph model 350 fitted with TCD and a Molecular Sieve 5A packed column. Water availability of these mixtures was determined with a thermohigrometer Thermoconstanter Humidat RTD-33/TH-2 (Novasina, Zurich, Switzerland), according to specifications in manual. Analyses were performed by triplicate.

2.4 Response variables

Acetate to butyrate ratios A/B (on COD basis) is an indirect indicator of hydrogenogenesis. Theoretically, acetic fermentation from hexose would yield four mol of hydrogen whereas butyric yields only two. If we assume that 50% of hexose is fermented to H_2 plus acetic acid whereas the other 50% is fermented to H_2 plus butyric acid, then A/B relationship would be 0.802 (on COD basis). Consequently, a value greater than 0.802 would mean that hydrogen generation coupled to acetic acid production was favored [9].

The ρ ratio indicates whether metabolism was leaned to acidogenesis or solventogenesis. This parameter is the product of the sum of the organic acids, divided by the sum of the solvents. Low rho values would be associated to solventogenesis, and consequently, related to poor hydrogen generation [19, 20]. Lactic acid is considered also an important parameter in dark hydrogen fermentation. Lactic acid fermentation is known to act as a hydrogen sink similarly to solvents [5].

3. Results and discussion

3.1 Effect of total solids, temperature and mass retention time on SSF

It was observed that hydrogen productivities (I_{H2}) were positively influenced by 20.9% TS, 21 d MRT and thermophilic regime. Indeed, I_{H2} averaged up to 123 NmL H_2/(kg_{wmr} d) with factor 20.9% TS (Table 1). The I_{H2} in thermophilic regime was higher to that in mesophilic operation (Table 1). In general, the highest I_{H2} were related to the highest organic acids to solvent ratios (ρ) and the lowest production of lactic acid. According to Table 2, the factors were significant to I_{H2} in the order TS > MRT > temperature. Significant interactions ($p < 0.0554$) amidst factors only occurred between TS and temperature or MRT (Table 2). Acetate to butyrate ratios A/B (on COD basis) were 0.62 to 0.68, meaning that hydrogen fermentation with butyric acid generation was the prevailing one in all the reactors.

Effect of total solids

Total solids (TS) influence on response variables (Table 1) was very pronounced. During operation, hydrogen contents reached up to 40 - 50% in selected bioreactors working at 20.9% TS. Reactors at 35% TS were below 25% H_2. Furthermore, difference in I_{H2} amidst 21 and 35% TS was over 15 fold. Although the A/B ratios were similar, the production of VOA and solvents for each TS content was markedly different: the ΣVOA was 0.7 fold higher whereas the ΣSolvents was 3.4 fold lower. Consequently, the ρ for 20.9% TS was over 5 fold superior to that of 35% TS. The higher ρ in the 20.9% TS fermentation indicated acidogenic fermentation prevalence over solventogenic fermentation. Oppositely, the 35% TS fermentation showed a performance leaned to solventogenesis. Furthermore, the [HLac] was almost 4 fold superior for 35% TS. This was in agreement with reports of a strong correlation between high lactic acid concentrations and inhibition of hydrogenogenesis [5]. All these results clearly show the superiority of using 20.9% TS OFMSW.

Moreover, the water availability might be affecting the performance of the anaerobic fermentation, by the simple equation that the higher the TS, the lesser of water availability. The water activity (a_w) and water potential (Ψ) of the OFMSW in this work were 0.9300 (Ψ = -9.2 MPa) and 0.9550 (Ψ = -5.8 MPa) for 35 and 20.9 %TS respectively. The water available to microorganisms can decrease by the osmotic effect (interaction with solute molecules, ionic or not) and by the matric effect (*i.e.*, adsorption of water to the surfaces of solids) in SSF. Likely, both mechanisms could have contributed to low a_w and high Ψ in our OFMSW [21, 22]. Indeed, in soils an a_w of 0.90 is related to the inability of plants to withdraw water from soil (*i.e.*, permanent wilting point). Extra effort is required for a microbe to grow in a medium with low a_w because it must spend energy to maintain a high internal solute concentration in order to retain water [15]. Therefore it is likely that metabolism of most fermentative bacteria in our H-bioreactors was adversely affected by the low availability of water [23].

Table 1. Main effects of temperature, total solids and mass retention time on response variables

Factors	Levels	I_{H2}[a] (21)[b]	ΣVOA[c] (1195)[b]	ΣSolvents[d] (223)[b]	A/B[e] (0.1)[b]	ρ[f] (2.5)[b]	[HLac][g] (1734)[b]
Thermal	35 ºC	55.3	11 285	1 415	0.68	8.5	12 639
regime	55 ºC	75.7	8 070	2 508	0.62	11.3	13 672
Mass retention time	14 d	48.1	10 154	1 957	0.62	10.5	14 470
	21 d	82.8	9 200	1 967	0.68	9.3	11 841
Total solids	20.9 %	122.9	12 186	888	0.65	16.3	5 432
	35 %	8.1	7 168	3 035	0.65	3.4	20 879

Notes: [a] Hydrogen productivity (NmL H_2/(kg_{wmr} d)); [b] standard error of the experimental design (EED = $(MSS_{error}/r)^{0.5}$); [c] Volatile organic acids accumulation (mg COD_{VOA}/kg_{wmr}); [d] Solvent accumulation (mg $COD_{solvent}$/kg_{wmr}); [e] Acetic acid to butyric acid ratio (mg $COD_{acetic\ acid}$/mg $COD_{butyric\ acid}$); [f] ΣVOA/ΣSolvents factor; [g] Lactic acid accumulation (mg $COD_{lactic\ acid}$/kg_{wmr}).

Table 2. Significance probability of the effects for the response variables in the H-stage

	I_{H2}[a]	ΣVOA[b]	ΣSolvents[c]	A/B[d]	ρ[e]	[Hlac][f]
Model	**0.0009**	**0.0013**	**< 0.0001**	0.4348	**0.0022**	**< 0.0001**
Temperature	0.1864	**0.0052**	**0.0001**	0.7423	0.1578	0.4239
MRT	**0.0396**	0.2919	0.9508	0.6387	0.5247	**0.0643**
TS	**< 0.0001**	**0.0003**	**< 0.0001**	**0.0623**	**< 0.0001**	**< 0.0001**
Temp x MRT	0.1361	0.6849	0.0630	0.7210	0.6227	0.6882
Temp x TS	0.1161	**0.0007**	**< 0.0001**	0.1871	**0.0079**	**0.0192**
MRT x TS	**0.0554**	0.4984	0.9452	0.8667	0.6397	0.7892
Temp x MRT x TS	0.1224	0.4595	0.1385	0.4849	0.5728	0.4327

Notes: Same keys as in Table 1.

Effect of Temperature of operation

The thermophilic temperature (55 ºC) had a positive but not significantly noticeable effect on I_{H2} (Table 2). Indeed, thermophilic regime had an increase of 36% in I_{H2} when compared to mesophilic regime (Table 1). Analysis of operation variables does not show a clear explanation for the difference on I_{H2}. For instance, the only significant differences amidst these thermal regimes only occurred for ΣVOA and ΣSolvents. Lactic acid concentrations in meso and thermo regimes were not significantly different. The ρ had higher but no significant different value in the thermophilic regime. A partial explanation was given by Youn and Shin [24], who compared H_2 production at thermophilic (55 ºC) and mesophilic (35 ºC) regimes in submerged dark fermentation of food waste (6.7 %). In that work they found that thermophilic operation had higher hydrogen production, and they ascribed this to the higher

temperature in thermophilic reactors that helps reducing the dissolved hydrogen concentration, thus being more effective in releasing hydrogen than mesophilic reactors. Another plausible explanation might be the microbiological profiles fostered by temperature and substrate [25]. Thermophilic and mesophilic regimes exhibit different microbial communities. Two of the principal genera related to hydrogen production in thermophilic regimes are *Thermoanaerobacterium sp.* (more specifically *T. thermosaccharolyticus*) and *Clostridium thermocellum* [6, 26-29]. On the other hand mesophilic regime is more likely to show diverse hydrogen producing communities [30], which may include *Clostridium pasteurianum*, *C. acidisoli*, *C. butyricum*, *C. acetobutylicum*, [31-33].

Some authors claim the superiority of thermophilic processes over the mesophilic ones [27, 34, 35]. However, some other authors allege the mesophilic regimes to be more economically feasible process [3, 9, 36], or at least to have a larger infrastructure distribution [37, 38]. For instance, the net energy gain at both thermal regimes was negative in most hydrogenogenesis cases analyzed by Perera *et al.* [36]. As a measure to overcome negative energy balances, they proposed coupling either methanogenic process or direct electricity production via microbial fuel cells. Indeed, according to Escamilla-Alvarado *et al.* [5] the use of thermophilic regime is fully justified in coupled processes producing hydrogen and methane (H-M process) despite its higher power consumption for heating. With productivities of 202 mL $H_2/(kg_{wmr}$ d) at 21 d TRM and 55 ºC in hydrogenogenic reactor, and 2 023 NmL $CH_4/(kg_{wmr}$ d) at 55 ºC when feeding a methanogenic bioreactor with fermented solids from 14 d MRT hydrogenogenic reactor, the energetic balance proved that the net power was positive. Indeed, the net energy was twice (even higher) the energy invested in the H-M process. Moreover, the highest contribution to the energy balance corresponded to the methanogenic stage, which accounted for 95-98% of the total power potential.

Effect of Mass Retention Time

The MRT also had significant influence on I_{H2} (Table 2). The I_{H2} at 21 d MRT was 2 fold higher than hydrogen productivity at 14 d MRT (Table 1). It is known that hydrogen is produced during the exponential growth of hydrogenogenic microorganisms [39]. Although 14 d MRT regime provided a higher organic load to microorganisms, this was not reflected on a higher I_{H2}. This could have been a consequence of excessive substrate addition. For instance, [HLac] was higher in bioreactors operated at 14 d MRT, indicating a lactic deviation.

Furthermore, the high amount of metabolites produced could be used as substrate in, for example, methane production through dark fermentation (submerged or solid substrate), photoheterotrophic hydrogen production, etc. Solids remaining after metabolites extraction could also be further used. In this regard, Muñoz-Páez *et al.* [13] washed fermented solids from a first batch dark fermentation of OFMSW and subjected them to a second fermentation round (re-fermentation), thus obtaining 15% increase on total cumulative biohydrogen production (*ca.* 2.4 mmole H_2/mini-reactor). They ascribed this phenomenon to the elimination of inhibiting organic metabolites present at the end of the first batch.

Concentration of lactic acid in our bioreactors was very high compared to that reported in works in submerged fermentation [29, 31, 34, 40]. This pointed out that our SSF process showed a significant lactic deviation that probably could have impaired biohydrogen generation. At present, it is not clear if hydrogenogenesis failure was due to the lactic deviation or due to the secretion of bacteriocins by lactic acid bacteria (LAB), or both. Microorganisms such as *Lactobacillus* sp., *Enterococcus* sp. and *Bifidobacterium* spp. are identified as the main responsible for lactic acid production. LABs also produce bacteriocins, which are proteins with bactericidal activity directed against many Gram-positive bacteria including most renowned hydrogen producing microorganisms, those belonging to the *Clostridium* genus [41]. Neverthelesss, lactic acid could be extracted from the solid matrix and be used in other applications such as food, pharmaceutical, leather and cosmetic industries, and as precursor for biodegradable plastic [42].

3.2. Nitrogen and alkalinity supplementation at thermophilic and mesophilic regimes

Highest results of hydrogenogenesis performance in batch experiments in terms of cumulative hydrogen production (P_{H2}) and hydrogenogenesis rate (R_{H2}) were respectively 1 983 μmol_{H2}/g VS and 68.3 μmol_{H2}/(g VS h), which belonged to the thermophilic mini-reactor with no addition of alkalinity nor sludge (TOO treatment in Table 3). Operation of batch process was carried out for 250-450 h. Controls did not show significant hydrogen production.

One and two cycles of hydrogen production were obtained. Exponential hydrogen production from OFMSW fermentation was evident up to first 50 h (Fig. 1 and 2). This result was similar to that of Watanabe and Yoshino [40], who had its maximum production of hydrogen near the 50 h of batch glucose fermentation. Indeed, in our work 75% of the P_{H2} was reached during a similar period. It is known that the microorganisms of genera *Clostridia* produce hydrogen during its exponential growth phase. When stationary phase is reached, the metabolism is shifted towards solvent generation [25]. Once the stationary production of hydrogen was reached, the mini-reactors were sparged with N_2 gas in order to overcome the partial pressure inhibition of hydrogen, and thus initiate a new cycle production. This technique generated a new cycle of hydrogenogenesis for the thermophilic regime but did not for the mesophilic one. Other works have used this strategy, thus obtaining from 2 [13, 43] to 5 hydrogen-producing cycles [44]. Despite the lesser hydrogenogenesis cycles, our cumulative P_{H2} was comparable and higher to those with higher number of cycles (Table 4). Another strategy to increase hydrogen production is through the already mentioned re-fermentation of the fermented solids from a hydrogenogenic batch [13].

During the first cycle of operation, P_{H2} and maximum R_{H2} were higher in thermophilic regime than mesophilic one (Fig. 1 and 2). No lag phase was observed: at 14 h most mini-reactors had hydrogen contents superior to 30%. In contrast, other works presented lag times up to 350 h for heat-shock treated hydrogenogenic inocula, and 180 h for


Sociedad Mexicana del Hidrógeno A.C.
Mexican Hydrogen Society
CICY
Yucatan Center for
Scientific Research

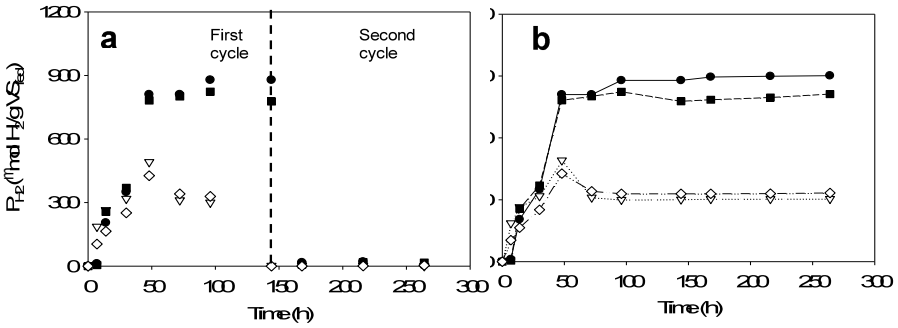

Figure. 1. Mesophilic hydrogen production: (a) cumulated per cycle, (b) cumulated sum. Keys: ●, no sludge or alkalinity addition; ▽, only sludge addition; ■, only alkalinity addition; ◇, sludge and alkalinity addition

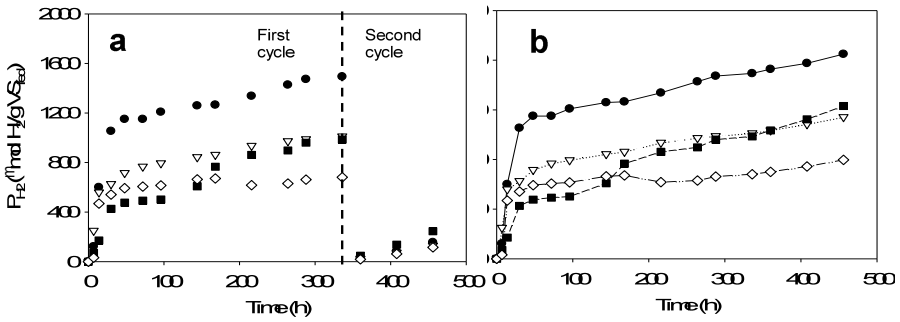

Figure. 2. Thermophilic hydrogen production: a) per cycle, b) cumulated. Keys: ●, no sludge or alkalinity addition; ▽, only sludge addition; ■, only alkalinity addition; ◇, sludge and alkalinity addition

Table 3. SSAHF-IV results

Reactors[a]	P_{H2}[b] cum (µmol H_2/g VS)	P_{H2}[b] cum (µmol H_2/reactor)	R_{H2}[c] max (µmol H_2/(g VS h))	pH_f	ΔpH	C/N
1 (MOO)	912 ± 83	14 311 ± 791	27.6 ± 3.8	5.66	2.50	44.5 ± 2.7
2 (MNO)	304 ± 35	5 253 ± 365	26.6 ± 2.4	5.87	2.02	29.3 ± 2.0
3 (MOA)	812 ± 179	12 742 ± 1 698	36.0 ± 9.2	6.07	1.34	44.8 ± 3.2
4 (MNA)	333 ± 74	5 752 ± 773	14.9 ± 2.0	6.25	1.11	31.4 ± 2.7
5 (TOO)	1 983 ± 17	30 931 ± 274	68.3 ± 10.4	6.20	1.62	47.2 ±5.0
6 (TNO)	1 488 ± 369	25 554 ± 6 337	44.2 ± 4.2	6.41	1.32	36.8 ± 6.0
7 (TOA)	1 785 ± 124	27 840 ± 1 948	16.0 ± 2.0	6.39	1.02	53.2 ±3.6
8 (TNA)	1 238 ± 130	21 265 ± 656	62.4 ± 5.9	6.86	0.39	38.9 ± 2.9
Control C	0.0 ± 0.0	0.0 ± 0.0	ND	5.71		25.7 ± 2.0
Control F	3.2 ± 0.2	50.4 ± 4.6	ND	5.38		34.6 ± 2.2

Notes: [a], M stands for mesophilic regime, T for thermophilic regime, N for sludge addition, A for alkalinity supplementation, O is no addition of sludge or alkalinity; [b] cumulated hydrogen production; [c], hydrogenogenesis rate.

Table 4. Batch hydrogenogenesis using organic waste

Operating conditions	P_{H2} cumulated (µmol H_2/g VS)	R_{H2} max (µmol H_2/(g VS h))	C/N	$pH_{initial}$	pH_{final}	Ref
OFMSW 25% TS, 55 ºC (4 cycles)	1 363	2.69	18.3	9.0	NR	[3]
OFMSW 24.5 % TS, 55 ºC	1 346	7.19	18.3	7.34[a]	NR	[3]
OFMSW 24.5 % TS, 35 ºC (2 cycles)	186	1.55	-	6.3[a]	NR	[43]
ASW 18.0 %TS, 35 ºC (5 cycles)	3 220	NR	19.0	6.65[a]	NR	[44]
OFMSW 20.9% TS, 55 ºC (2 cycles)	1 983	68.3	55.3	7.82	6.20	This work

Notes: [a] pH adjusted, NR, not reported

acetylene inhibition of methanogenic archaeas [3]. The P_{H2} in the second hydrogen producing cycle for our mini-reactors at thermophilic regime was in average, 10% of that obtained in their first cycles.

Effect of N nutrient supplementation

Apparently, the sludge supplementation affected negatively the cumulative P_{H2} ($p < 0.0008$), whereas it did not have any significant effect on R_{H2} ($p = 0.8$). The sludge addition was expected to favor the fermentative process by

adjusting C/N ratio to 30 (according to literature). Negative results of sludge addition might be due to two reasons: *(i)* alkalinization of pH beyond the optimum for dark fermentation due to the release of ammonium cations, and *(ii)* contamination of culture by hydrogenotrophic microorganisms from activated sludge.

In the respect to the alkalinization explanation, it is known that excess nitrogen addition might be counterproductive since it may favor the production of ammonium in anaerobic environments [45]. Its generation does not only have the capability to increase the pH in the medium, but also to capture H^+ which could have been used for H_2 generation. For instance, glutamic amino acid hydrolysis may produce hydrogen and ammonium (Ec. 1). Lay *et al.* [46] reported hydrogen production from soluble condensed molasses (CMS), a by-product from molasses microbial fermentation, which contains high amounts of carbohydrates and amino acids as monosodium glutamate. Indeed, they ascribed their higher hydrogen production from CMS than from molasses either because CMS contained glutamate as a good substrate for hydrogen-producing bacteria, or because CMS contained other microorganisms that could convert glutamate into hydrogen. On the other hand, according to Strohm *et al*. (2007) reduction of nitrate to N_2 (denitrification) or to ammonia (nitrate ammonification) is the highest-energy-yielding process, and therefore a more favorable reaction (Eq. 2).

$$H_2NC(C_3H_5O_2)COO^- + 2H_2O \rightarrow 2CH_3COO^- + NH_4^+ + CO_2 + H_2 \quad (1)$$

$$C_6H_{12}O_6 + 3NO_3^- + 6H^+ \rightarrow 6CO_2 + 3NH_4^+ + 3H_2O \quad (\Delta G^{0'}=-1870 \text{ KJ/mol glucose}) \quad (2)$$

Regarding the second explanation, hydrogenotrophic bacteria could have been present in the sludge supplemented and thus have been introduced into our batch mini-reactors. Hydrogenogenesis, as many biological processes, is susceptible of microbial contamination and consequently to hydrogenogenic failure. For instance, Escamilla-Alvarado *et al*. [5] ascribed hydrogenogenesis unstability to lactic and solvent deviations. Moreover, at 72 h a drop on I_{H2} and presence of methane in the biogas in concentrations up to 9% v/v at 144 h, were observed on mesophilic mini-reactors supplemented with sludges (MNO and MNA treatments, Table 3). This could be due to the presence of hydrogenotrophic microorganisms in the sludge such as acetogenic and solventogenic bacteria, or even methanogenic archaea [5, 31, 32]. To overcome such problem, all the mesophilic min-reactors were subjected to a new thermal shock 93 ºC for one hour. From this pretreatment on, the hydrogen production was not re-started, yet methane production was utterly inhibited. The thermophilic mini-reactors received also the heat-shock pretreatment at 144 h just as a preventive measure. Methane production was not evident throughout their operation.

It is noteworthy that methane production at low pH is not usual. Yet, anaerobic digesters have also been reported to work at pH 4.0 - 5.3 when using acetic acid for methane production. Taconi *et al*. [47] ascribed this phenomenon to the simplicity of their feed, consisting only of acetic acid. However they did not discard the possibility of

microenvironments at neutral pH, as previously proposed by de Beer *et al*. [48]. Indeed, in our case niches of high pH were likely to occur due to the physiology of the granules formed in our 20.9% TS solid substrate. Moreover, mixing in our bioreactors was poor. So according to mass transfer in biofilms and biological solids, diffusion of nutrients, salts, gas and heat diminish exponentially throughout the particles. These niches could be a protective against pH variations and excessive heat to microorganisms inside the particles [48].

Effect of thermal regime

The P_{H2} and R_{H2} were positively affected by thermophilic regime ($p < 0.0004$ and $p < 0.0025$, respectively). Mini-reactors in thermophilic regime averaged almost two-fold the I_{H2} and the R_{H2} of the mesophilic mini-reactors. In thermophilic regime after the exponential hydrogen production observed in the first cycle, a constant production rate occurred in all the mini-reactors (Fig. 2). This constant hydrogen production was kept even after gas sparging. Indeed, the exponential hydrogen production was not repeated in the second cycle. Final pH on mesophilic reactors was in the range 5.5 – 6.3. In mesophilic regime, run MOO showed the highest P_{H2} and R_{H2}, and also presented the lowest pH in mesophilic runs. Indeed, there was a correlation between pH and P_{H2}.

Regarding the methanogenic deviation already discussed, only the mesophilic mini-reactors supplemented with sludges exhibited methane production. Probably, thermophilic temperature could have served as a selective barrier that avoided hydrogenotrophic microorganisms progression as previously proposed by Youn and Shin [24].

Effect of alkalinity supplementation

Alkalinity in form of phosphate salts supplementation did not have a positive effect on P_{H2} and the R_{H2} ($p < 0.05$ and $p = 0.1$, respectively). Previous experiments from our workgroup reported that alkalinity 0.11 g CaCO3/g dry substrate on 20.9 %TS semi-continuous SSF of OFMSW had a positive influence on higher hydrogen productivity [49]. The supplementation of alkalinity performed in our study was 0.06 g $CaCO_3$/g dry substrate in order to control the pH variations. The negative effect in our work of alkalinity supplementation was probably due to an alkalinity that may have promoted an increase in osmotic pressure on the one hand, or a deviation from the optimal initial pH in the mini-reactors on the other hand, or even both [6]. It is noteworthy that pH in our mini-reactors was not adjusted previously to the beginning of fermentation. For instance, mesophilic mini-reactors had their initial pH in the range 7.36 – 8.16, whereas thermophilic ones were 7.25 – 7.82 (data not shown). This work demonstrated that heat-shocked inocula had the capacity to acidify the solid substrate thus favoring hydrogenogenesis. It was evident that mini-reactors supplemented with phosphate salts had a lower ΔpH, which was a result of buffer capacity provided by the salts. Therefore we ascribe the higher P_{H2} to a final pH closer to the optimal, *i.e.* a higher ΔpH. Nonetheless it was also likely that each thermal regime could have a different optimal pH.

4. Conclusion

In semi-continuous hydrogenogenic fermentation of OFMSW, high total solids content in the feedstock affected negatively the hydrogen productivity. The 21 d MRT promoted 2 fold higher hydrogen productivities compared to that at 14 d MRT. Thermophilic regime had higher but no significantly different productivities than mesophilic regime. It was observed that variations and inhibition of hydrogen production were mainly related to low pH, high lactic acid and solvents production.

Regarding the studies on N nutrient supplementation on batch hydrogenogenic fermentation of OFMSW, both the sludge and alkalinity supplementation did not have a positive effect on P_{H2} in any of the thermal regimes. It seems that the intrinsic C/N of OFMSW was sufficient to produce high amounts of hydrogen (P_{H2} = 1 983 μmol H_2/g VS, R_{H2} = 68.3 μmol H_2/(g VS h)). On the other hand, it could be inferred that microorganisms introduced through supplemented sludge may have affected fermentation, particularly boosting hydrogen consumption. Side exploration of the effect of temperature indicated that this factor had considerable influence on hydrogen production. Finally, despite the few or inexistent multiple cycles, the hydrogen productions in our work were comparable to those in literature of SSAHF-IV. It is very likely that there would be a maximum of hydrogen that might be harvested, independently of the cycles.

Several observations were identified from results in this research. Further hydrogen experiments should focus on increasing productivities and stability. Major efforts should be made towards:

i) Reducing/avoiding lactic deviation
ii) Increasing mixing in the bioreactors
iii) Bioaugmentation with hydrogenogenic fermentative bacteria from *Clostridium* genus

These technology improvements should be implemented in such a way that they do not compromise the economic feasibility of the process.

5. Acknowledgements

Partial financial support to biofuel research of our Group by CINVESTAV-IPN and ICYTDF (Grant PICCO 10-27) is gratefully acknowledged. The authors wish to thank Dr. Juan A. Salazar-Montoya and Mr. Miguel Marquez, Technician, for assistance in water activity determinations. CE-A kindly appreciates a graduate scholarship from CONACYT. HMP-V warmly acknowledges the company Stat-Ease Inc. Co. for a free license of the software Design-Expert v8.0.

6. References

[1] J. Benemann, Nature Biotechnol, 14, 1101 (1996).

[2] D. Das, Int J Hydrogen Energy, 34, 7349 (2009).
[3] I. Valdez-Vazquez, E. Rios-Leal, A. Carmona-Martinez, K. M. Munoz-Paez, and H. M. Poggi-Varaldo, Environ Sci Technol, 40, 3409 (2006).
[4] INEGI, Instituto Nacional de Geografía, Mexico, (2009).
[5] C. Escamilla-Alvarado, E. Ríos-Leal, M. T. Ponce-Noyola, and H. M. Poggi-Varaldo, Process Biochem, http://dx.doi.org/10.1016/j.procbio.2011.12.006, (2012).
[6] I. Valdez-Vazquez and H. M. Poggi-Varaldo, Ren Sust Energy Rev, 13, 1000 (2009).
[7] X. Wang and Y. Zhao, Int J Hydrogen Energy, 34, 245 (2009).
[8] S. K. Han and H. S. Shin, J Air Waste Manage Assoc 54, 242 (2004).
[9] D. Liu, D. Liu, R. J. Zeng, and I. Angelidaki, Water Res, 40, 2230 (2006).
[10] P. Robledo-Narváez, C. Escamilla-Alvarado, T. Ponce-Noyola, and H. M. Poggi-Varaldo, in The Third International Meeting in Environmental Biotechnology Engineerging (I. Sastre-Conde, ed.), Palma de Mallorca, Spain, (2008), p. 130.
[11] S. Venkata-Mohan, G. Mohanakrishna, and P. N. Sarma, Int J Hydrogen Energy, 33, 2156 (2008).
[12] H. M. Poggi-Varaldo, C. Escamilla-Alvarado, F. J. Esparza-Garcia, E. Rios-Leal, M. T. Ponce-Noyola, and N. F. Rinderknecht-Seijas, New Biotechnology, 25, S253 (2009).
[13] K. Muñoz-Páez, E. Ríos-Leal, I. Valdez-Vazquez, N. Rinderknecht-Seijas, and H. Poggi-Varaldo, J Environ Management, 95, S355 (2012).
[14] R. E. Speece, in Anaerobic digestion of Biomass (D. P. Chynoweth and R. Isaacson, eds.), Elsevier Applied Science Publishers LTD, New York, (1987).
[15] D. J. Hills and D. W. Roberts, Agric Wastes, 3, 179 (1981).
[16] C. Y. Lin and C. H. Lay, Int J Hydrogen Energy, 29, 41 (2004).
[17] H. M. Poggi-Varaldo, R. Rodriguez-Vazquez, G. Fernandez-Villagomez, and F. Esparza-Garcia, Appl Microbiol Biotechnol, 47, 284 (1997).
[18] H. M. Poggi-Varaldo, J. Trejo-Espino, G. Fernandez-Villagomez, F. Esparza-Garcia, S. Caffarel-Mendez, and N. Rinderknecht-Seijas, Water Science and Technology, 40, 179 (1999).
[19] I. K. Kapdan and F. Kargi, Enzyme and Microbiol Technol 38, 569 (2006).
[20] D. Y. Lee, Y. Ebie, K. Q. Xu, Y. Y. Li, and Y. Inamori, Bioresource Technology, 101, S42 (2010).
[21] A. Brown, Bacteriol Rev, 40, 803 (1976).
[22] D. S. Reid, in Contemporary microbial ecology (D. C. Elwood, Latham, M.J., J. N. Hedger, and J. M. Lynch, eds.), Academic Press, London, (1980), p. 15.
[23] L. N. Csonka, Microbiol Rev, 53, 121 (1988).
[24] J. H. Youn and H. S. Shin, Waste Manage Res, 23, 32 (2005).
[25] H. H. P. Fang, T. Zhang, and H. Liu, Appl Microbiol Biotechnol, 58, 112 (2002).
[26] H. Liu, T. Zhang, and H. H. P. Fang, Biotechnol Lett, 25, 365 (2003).
[27] H. S. Shin, J. H. Youn, and S. H. Kima, Int J Hydrogen Energy, 29, 1355 (2004).
[28] Y. Ueno, H. Fukui, and M. Goto, Environ Sci Technol, 41, 1413 (2007).
[29] D. Karadag, A. E. Mäkinen, E. Efimova, and J. A. Puhakka, Bioresour Technol, 100, 5790 (2009).
[30] T. M. LaPara, C. Nakatsu, L. Pantea, and J. Alleman, Appl Environ Microbiol, 66, 3951 (2000).
[31] S. H. Kim, S. K. Han, and H. S. Shin, Process Biochem, 41, 199 (2006).
[32] P. E. P. Koskinen, A. H. Kaksonen, and J. A. Puhakka, Biotechnol Bioeng, 97, 742 (2007).
[33] S. Y. Wu, C. H. Hung, C. N. Lin, H. W. Chen, A. S. Lee, and J. S. Chang, Biotechnol Bioeng, 39, 934 (2006).
[34] C. F. Chu, Y. Y. Li, K. Q. Xu, Y. Ebie, Y. Inamori, and H. N. Kong, Int J Hydrogen Energy, 33, 4739 (2008).
[35] H. Hartmann and B. K. Ahring, Water Sci Technol, 53, 7 (2006).
[36] K. R. J. Perera, B. Ketheesan, V. Gadhamshetty, and N. Nirmalakhandan, Int J Hydrogen Energy, 35, 12224 (2010).
[37] L. de Baere, Water Sci Technol, 41, 283 (2000).
[38] B. Demirel, P. Scherer, O. Yenigun, and T. T. Onay, Critical Reviews in Environmental Science and Technology, 40, 116 (2010).
[39] P. C. Hallenbeck, Water Sci Technol, 52, 21 (2005).
[40] H. Watanabe and H. Yoshino, J Mater Cycles Waste Manag, 13, 113 (2011).
[41] T. Noike, H. Takabatake, O. Mizuno, and M. Ohba, Int J Hydrogen Energy, 27, 1367 (2002).

[42] R. Datta, S. P. Tsai, P. Bonsignore, S. H. Moon, and J. R. Frank, FEMS Microbiol Rev, 16, 221 (1995).
[43] K. M. Muñoz-Páez, J. Pareja-Camacho, R.-L. E., M. T. Ponce-Noyola, F. J. Esparza-García, J. García-Mena, and H. M. Poggi-Varaldo, in Proceedings of the 5th IWA International Symposium on Anaerobic Digestion of Solid Waste and Energy Crops (M. Hamdi, F. Cecchi, and J. Mata-Alvarez, eds.), Hammamet, Tunisia, (2008).
[44] P. N. Robledo-Narváez, G. Calva-Calva, M. T. Ponce-Noyola, E. Ríos-Leal, J. Galíndez-Mayer, R. Olvera-Ramírez, C. Estrada-Vázquez, L. A. Ortega-Clemente, and H. M. Poggi-Varaldo, in 12th World Congress on Anaerobic Digestion, Guadalajara, Mexico, (2010).
[45] M. T. Madigan, J. M. Martinko, P. V. Dunlap, and D. P. Clark, Brock Biology of microorganisms, Pearson Eductaion, New York, (2009).
[46] C. H. Lay, J. H. Wu, C. L. Hsiao, J. J. Chang, C. C. Chen, and C. Y. Lin, Int J Hydrogen Energy, 35, 13445 (2010).
[47] K. A. Taconi, M. E. Zappi, W. T. French, and L. R. Brown, Bioresour Technol, 99, 8075 (2008).
[48] D. de Beer, J. W. Huisman, J. C. Van den Heuvel, and S. P. P. Ottengraf, Water Res, 26, 1329 (1992).
[49] I. Valdez-Vazquez, T. Ponce-Noyola, and H. M. Poggi-Varaldo, Int J Hydrogen Energy, 34, 4291 (2009).

Notation

ASW	agricultural solid waste
a_w	water activity
COD	chemical oxygen demand
LAB	lactic acid bacteria
MRT	mass retention time
OFMSW	organic fraction of municipal solid waste
SSAHF-IV	solid substrate anaerobic hydrogenogenic fermentetation in intermittently vented mini-reactors
SSF	solid substrate fermentation
TS	total solids
VOA	volatile organic acids
VS	volatile solids

Greek characters

ρ	VOA to solvents ratio
Ψ	water potential

Analysis of Microbial Diversity of Inocula used with a Five-Face Parallelepiped and Standard Microbial Fuel Cells

***Ortega Martínez, A.C.*[1], *Solorza-Feria, O.*[2], *Juárez-López, K.*[3], *Poggi-Varaldo H. M.*[1,*]**

[1]Environmental Biotechnology and Renewable Energies R&D Group, Dept. Biotechnology and Bioengineering, CINVESTAV del IPN, P.O. Box 14-740, 07000 México D.F., México
[2]Dept. of Chemistry, ibídem
[3] IBT-UNAM, Cuernavaca, México
*Tel: 57473800 ext. 4306, hectorpoggi2001@gmail.com

ABSTRACT

This work had a double purpose: *(i)* to study the effect of inoculum (sulfate-reducing (SR) and enriched (E) inocula on the characteristics of one-chamber standard microbial fuel cell (MFC-S) and parallelepiped cell and *(ii)* to analyze the bacterial communities in cells operated with either SR or E.

The MFC-P consisted of a parallelepiped built in plexiglass with a liquid volume of 270 mL. Five faces of this cell were fitted with 'sandwich' cathode-membrane-anode assemblages (CMA). The internal resistances were 400 and 84, and 230 and 292 Ω; and volumetric powers were 655 and 1800 mW/m^3, and 5804 and 1772 mW/m^3 for the faces connected in series and parallel and the MFC-P loaded with SR and E, respectively. Anode density powers were 18.4 and 50 mW/m^2, and 209 and 64 mW/m^2 for the faces connected in series and parallel and the MFC loaded with SR and E, respectively. The MFC-S of 150 mL consisted of one-chamber plexiglass cell with electrodes separated 7.8 cm. The values of R_{int} were 4602 and 1593 Ω, and volumetric powers were 52 and 76 mW/m^3, for the MFC-S loaded with SR and E, respectively.

Regarding the enrichment of the microbial inoculum, we could achieve a 419 mM Fe^{+2} concentration at the end of the 3rd and last transfer; this was an evidence of the increase of either the Fe(III) reducing microflora, or Fe(III)-reducing activity, or both. Furthermore, 100 mM Fe^{+2} concentration was achieved on day 4 of the first transfer, while this concentration in last transfers was achieved in just the first day of incubation. There was a significant difference in community composition between both inocula. *Clostridia* predominated in the community of the biofilm derived from the SR inoculum; this class is believed to be responsible for the direct electron transfer to the anode according to other literature reports. Predominant microbes in the biofilm derived from the E belonged to *Deferribacteres* class; this class is known to contain c-type cytochromes. Current evidence suggests that a series of c-type cytochromes associated with the inner membrane, the periplasm, and the outer membrane might interact to transfer electrons to the outer membrane surface. Shannon indices were 1.27 and 1.38 for the community derived from SR and E inoculum, respectively.

As conclusion, parallel connection of cell faces significantly improved the electrochemical characteristics of the cell. E inoculum was better than SR on the performance of the MFCs as well as, performance of MFC-P was better than MFC-S performance, feed with both inoculua. Also, the SR-derived community was sligthtly diverse than the E-

derived one. Both communities harbored microbes that are electrochemically active.

Key words: enriched inoculum, internal resistance, microbial fuel cell.

1. Introduction

A microbial fuel cell (MFC) is a promising technology for generating electricity directly from biodegradable compounds using bacteria under anaerobic conditions [1,2]. The power generation in a MFC is still insufficient for the practical applications. In order to improve theMFC performance, efforts have been made to improve reactor configuration and to enrich more electrochemically active bacteria [3-10].

The actual voltage output of an MFC is less than the predicted thermodynamic ideal voltage due to irreversible losses; this limits MFC performance. The three major irreversibilities that affect MFC performance are: activation losses, ohmic losses, and mass transport losses. These losses are defined as the voltage required to compensate for the current lost due to electrochemical reactions, charge transport, and mass transfer processes that take place in both the anode and cathode compartments. The electrochemical limitations on the performance of MFC are due to the internal resistance (R_{int}) [11,12]. The primary component of R_{int} is ohmic resistance, which can be further divided into the electrolytic resistance and ohmic resistance of electrodes, and the transfer resistance electrodes. The R_{ohmic} is dominated by the R_{ion} associated to the electrolyte(s) resistance [12.13]. The low voltage has been a large obstacle in energy recovery from MFCs as this voltage is too low to be used directly for many practical applications. For example, a single light emitting diode (LED) requires a minimum voltage of 2 V [14], a single MFC can produce a maximum working potential of only 0.3–0.7 V because of thermodynamic constraints. Thus, effective methods of boosting MFC voltages are needed. Several approaches have been used to increase MFC voltages [15]. One approach is to produce voltage (and/or current) high enough for practical application, therefore, the connection of multiple MFC units in series and/or parallel is necessary [16]. In series linking of six MFCs, Aelterman *et al.* (2006) [17] produced a usable output (2.2 V at 228 W/m3), but this system used a hexacyanoferrate cathode that is not suitable for large scale wastewater treatment. Shimoyama *et al.* (2008) [18] reported a more implementable system, consisting of a series of cassette electrodes with air cathodes.

On the other hand, optimizing the growth conditions for the electrochemically active bacteria in the anode is also an important consideration for improving the performance of MFCs [3]. A fuel cell type electrochemical device can be used to enrich a microbial consortium using wastewater as the electron donor [19]. Molecular techniques are now widely applied to assess the diversity of microbial communities by analyzing the 16S rDNA sequence [20]. MFC systems can be a tool for selecting key electrochemically active bacteria (EAB) for cell inoculum, although recent research has been focussed on ex-cell enrichment procedures, that is, inoculum enrichment in flasks by serial transfers and other methods before loading to the MFC. The differences in bacterial populations between the enriched cultures may also be due to the types of fuel cells used for the enrichment studies.

The aims of this work were to to characterize an design and characterize a novel, multiface parallelepiped MFC (MFC-P) in the perspective of decreasing the internal resistance (R_{int}) and increasing volumetric power (P_v) output,

and to characterize one-chamber standard microbial fuel cell (MFC-S), both loaded with either sulphate-reducing inoculum (SR) and enriched inoculum (E) in order to compare the performance with different inocula and different cells, and to analyse with molecular ecological techniques the bacterial community in MFCs and differences in the bacterial population between MFC fed with sulphate-reducing inoculum and enriched inoculum.

2. Experimental

2.1 Characterization of MFC-S and MFC-P loaded with SR and E inocula

2.1.1. Physical models of the cells

MFC-P consisted of a parallelepiped built in plexiglass with a liquid volumen of 1 000 mL (Figure 1A). Five faces of this cell were fitted with 'sandwich' cathode-membrane-anode assemblages (CMA). Each CMA (from inside to outside) consisted of an anode made of Toray carbon cloth, the proton exchange membrane (Nafion 117), and the cathode made of flexible carbon-cloth containing 0.5mg/cm^2 Pt catalyst (Pt 10 wt%/C-ETEK, and a perforated plate of stainless steel 1 mm thickness.

On the other hand, a standard cell of 150 mL MFC-S was fitted with a circular anode made of stainless steel plate 1 mm thickness with a Toray flexible carbon-cloth sheet placed in one circular face and a cathode in the opposing face made of (from inside to outside): proton exchange membrane (Nafion 117), a Toray flexible carbon-cloth painted with Pt catalyst, and a perforated plate of stainless steel 1 mm thickness. Separation between electrodes was 7.8 cm (Figure 1B).

The MFC-P had a ratio ξ = 19.1 (1/m) whereas the corresponding value of the standard MFC-S was 12.9 (1/m).

*2.1.2.Model Extract and Biocataly*st

The cells, MFC-S and MFC-P, were loaded with 7 and 15 mL, respectively, from a model extract [21-23]. The model extract was concocted with a mixture of the following substances (in g/L): acetic, propionic and butyric acids (4 each) as well as acetone and ethanol (4 each) and mineral salts such as $NaHCO_3$ and Na_2CO_3 (3 each) and K_2HPO_4 and NH_4Cl (0.6 each). Organic matter concentration of model extract was ca. 25 g COD/L. The cells, MFC-S and MFC-P, were loaded with 143 and 255 mL, respectively, of biocatalyst (SR and E inocula). SR inoculum was obtain from a sulphate-reducing, mesophilic, complete mixed, continuous bioreactor. The bioreactor had an operation volume of 3 L and was operated at 35°C in a constant temperature room. The bioreactor was fed at a flow rate of 150 mL/d with an influent whose composition was (in g/L): sucrose (5.0), Acetic acid (1.5), $NaHCO_3$ (3.0), K_2HPO_4 (0.6), Na_2CO_3 (3.0), NH_4Cl (0.6), plus sodium sulphate (7.0). The initial COD and biomass concentration in the MFC-S liquor were ca. 1 450 mg O_2/L and 1100 mg VSS/L, the concentration and biomass in the MFC-P liquor were ca. 1600 mg O_2/L and 1400 mg VSS/L.

The enriched inoculum was obtained with serial transfers. Sediment sample was suspended in nitrogen filled pressure tubes containing media with ferric citrate (55 mM) as electrons acceptor and sodium acetate (2 M) as electrons donor. The tubes were incubated at 30°C for 7 days in the dark conditions. The enrichment procedure was

repeated 3 times [24].

The bioreactor with enriched inoculum had an operation volumen of 1.5 L was operated at 35°C in a constant temperature room. The bioreactor was fed at a flow rate of 75 mL/d an influent whose composition was (in g/L): Sodium acetate (2.0), $NaHCO_3$ (1.8), Na_2CO_3 (0.5), Na_2SeO_4 (0.1). The initial COD and biomass concentration in the MFC-S liquor were ca. 950 mg O_2/L and 800 mg VSS/L, the concentration and biomass in the MFC-P liquor were ca. 1000 mg O_2/L and 900 mg VSS/L.

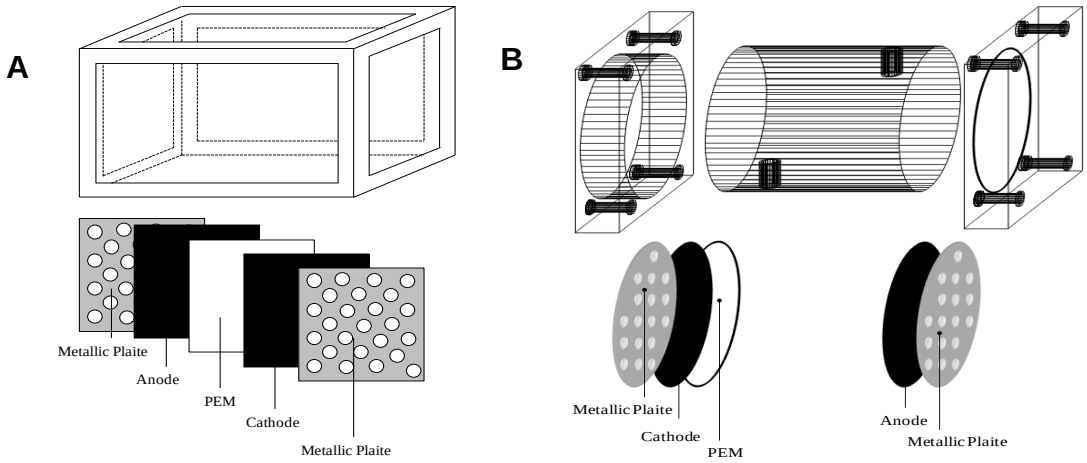

Figure 1. Schematic diagrams of microbial fuel cells: (A) type P (parallelepiped cell), and (B) type S (standard design).

2.1.3 Determination of internal resistence of the cells

The internal resistance of cells was determined using the polarization curve method, by varying the external resistance (R_{ext}) and monitoring both the voltage and the current intensity, according to procedures suggested by Clauwaert *et al.* (2007) [25] and Logan *et al.* (2006) [1]. For the MFC-P, characterization was first carried out with the five faces connected in series and second with faces connected in parallel. In brief, MFCs were loaded with substrate and inocula as described above. MFCs were batch-operated for 8 h at room temperature. The circuit of the MFCs were fitted with an external variable resistance. In this regard, we carried out the polarization curve of the MFCs, relating mathematically the cell voltage (E_{MFC}) and current intensity (I_{MFC}) against the external resistance value, forwards and backwards regarding the external resistance (R_{ext}) values. *Ab initio*, the MFCs were operated at open circuit for 1 h. Afterwards, the R_{ext} was varied from 100 Ω to 100 KΩ and viceversa. After this, the cell was set to open circuit conditions for 1 h in order to check the adequacy of the procedure (values of initial and final open circuit voltages should be close). The voltage was measured and recorded with a multimeter. The current was calculated by the Ohm's Law as indicated below.

2.1.4 Analytical methods and calculations

The COD and VSS of the liquor of sulphate-reducing seed bioreactor and cell were determined according to the Standard Methods [26]. The current intensity I_{MFC}, the power P_{MFC} and the power density P_{An} were determined according to [2].

The power per unit volume or volumetric power P_V was calculated as follows:

$$P_V = \frac{E^2_{MFC}}{V_{MFC} \cdot R_{ext}} \quad (1)$$

where R_{ext} is the external resistance, E_{MFC} is the voltage, and V_{MFC} is the cell volume.

2.1.5 Dermination of Fe(III) reduction

Fe(III) reduction activity was determined using a previous method [27]. A half mL of culture was aseptically sampled with a syringe and mixed with 1 mL HCl solution (0.5 N). This mixture was reacted for 15 min. at room temperature, and then centrifuged for 5 min. The micture of supernatant (0.1 mL) and ferrozine solution (1mL, 1 g/L in 50 mM HEPES buffer) was reacted for 15 min before measurement of optical density at 562 nm using a spectrophotometer. The fresh medium was used as a control sample instead of culture. Ferrous ethylenediammonium sulfate tetrahydrate ($C_2H_{10}N_2O_4SFeSO_4 4H_2O$) was used to make a standard Fe(II) solution [24].

2.2 Analysis of bacterial community

The biofilm formed on the carbon cloth electrodes from the anodes was used for DNA extraction using a PowerSoil DNA Isolation Kit (Mo Bio Laboratories, Inc. Carlsbad, CA) according to the manufacturer's instruction. Total genomic DNA was used as template for PCR amplification of approximately 1500 pb of 16S rDNA with a forward primer (27f, 5´-AGAGTTTGATCCTGGCTCAG-3´) and a reverse primer (1492r, 5´-GGTTACCTTGTTAACGACTT-3´) [28]. The PCR products were purified and cloned into TOPO TA cloning vector pCR2.1 according to the manufacturer´s instructions (Invitrogen, Carlsbad, CA). Then they were transformed into competent cells of *E. coli* XL1-Blue by electroporation. White transformants were transferred to plates containing LB broth (25ug/mL kanamycin and 200ug/mL ampicillin), grown overnight at 37°C. Plasmids were isolated using High Pure Plasmid kit (ROCHE, Indianapolis, IN) subsequently clones were digested (2 h, 37°C) with *EcoR1* (BioLabs, New England) for the presence of inserts.

2.2.1 Sequencing and phylogenetic analysis

Inserts were sequenced on the sense and antisense stands at the Instituto de Biotecnologia de la Universidad Nacional Autonoma de Mexico using a Taq FS Dye Terminator cycle fluorescence-based sequencing with an automated capillary sequencer (Perkin Elmer, model 3130xl, Applied Biosystems). The sequencing reaction was performed using M13F-pUC (5´-GTTTTCCCAGTCACGTTGTA-3´) and M13R-pUC (5´-TTGTGAGCGGATAACAATTTC-

3´). 16s RNA gene sequences of aproximately 1500 nucleotides retrieved from each clone were assembled and edited using Bioedit. All sequences were further analyzed with Bellerephon chimera check program and with BLAST program (National Center for Biotechnology Information) [29] to determine the closest available database sequences. Multiple sequence aligments were performed using ClustalW and MEGA 5.0 software. Phylogenetic analyses were performed aligned sequences by the Neighbor-Joining algorithm with Kimura 2 parameter distance and bootstrapping of 1000 replicates in the Phylip program.

2.2.2 Calculations of ecological indices

Shannon-Weaver diversity index has been a popular index in the ecological literature [30]. Shannon-Weaver index is defined as:

$$H' = -\sum_{i=1}^{S} (p_i \log p_i) \qquad (2)$$

where:

p_i = is the proportion of characters belonging to the *i* type of letter in the string of interest. In ecology, p_i is often the proportion of individuals belonging to the *i* species in the dataset of interest.

Pielous evenness index is a measure of a biodiversity which quantifies how equal the community is numerically [31]. This index [32] is defined as:

$$J' = \frac{H'}{\ln S} \qquad (3)$$

where:

H´= is the number derived from the Shannon-Weaver index

S´= is the total Lumber of species

J´= is contrained between 0 and 1

Poggi´s divergence index is defined as.

$$\Delta p = \frac{(n'_A + n'_B)}{(n_A + n_B)} \qquad (4)$$

where:

n_{AB}= number of bands that are present both in lane A and lane B

n'_A= number of bands of lane *A* absent in lane *B*

n'_B = number of bands of lane *B* absent in lane *A*

n_A= total number of bands in lane A

n_B= total number of bands in lane B

3. Results and discussion

3.1 Characterization of MFC-S loaded with SR and E

The polarization curves and the power variation with current intensity of the MFC-S loaded with SR and E are shown in Figure 2A and Figure 2B, respectively.

The internal resistences were calculated as the slopes of the sets of aligned points of the corresponding polarization curves; the values were 4602 and 35 Ω for the MFC loaded with SR and E, respectively (Table 2).

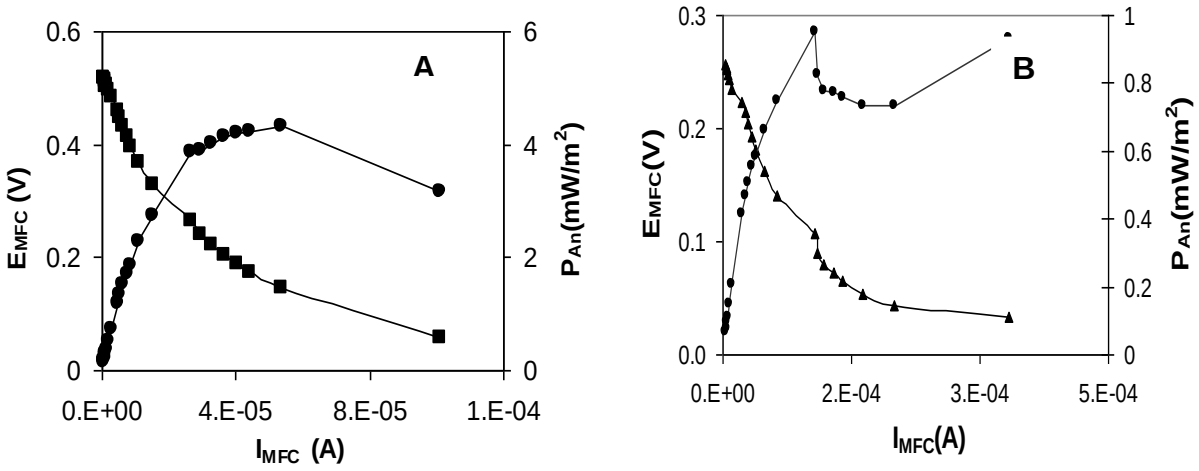

Figure 2. Polarization curves of MFC-S: (A) loaded with SR and (B) loaded with E.

Maximum volumetric powers P_V in MFC loaded with SR and E were 52 and 76 mW/m^3, respectively, and anode density powers P_{An} of the MFC loaded with SR and E were 4.3 and 6.4 mW/m^2, respectively. When MFC was loaded with E, the voltage was 0.65 V; this voltage is higher than MFC load with SR (0.52 V). All the other response variables in MFC-S loaded with E were higher than MFC-S loaded with SR (Table 1).

Table 1. Effect of inocula SR and E on characteristics of a standard microbial fuel cell

Parameter	MFC-S SR	MFC-S E
R_{int} (Ω)	4602 ± 40	1593 ± 5
$P_{An\text{-}max}$ (mW m^{-2})	4.3 ± 0.7	6.4 ± 1.2
$P_{V\text{-}max}$ (mW m^{-3})	52 ± 14	76 ± 21
$I_{MFC\text{-}max}$ (mA)	0.10 ± 0.1	0.33 ± 0.1
$E_{MFC\text{-}max}$ (V)	0.52 ± 0.05	0.65 ± 0.04
$P_{MFC\text{-}max}$ (mW)	0.008 ± 0.002	0.015 ± 0.03

E inoculum was better than SR inoculum on the performance of MFC-S, this could be due that the electrochemically

active bacteria in MFCs are thought to be iron-reducing such as *Shewanella* and *Geobacter* species [33-34]. A number of bacteria have been isolated with the ability to use Fe(III) as a terminal electron acceptor [35-36]. Although there is evidence that a soluble electron carrier is involved in the electron transfer to the water-insoluble electron acceptor [37-38], direct contact between the bacterial cells and the electron acceptor is required for the dissimilatory Fe(III) reduction [35,39]. Among the Fe(III)-reducers, *Shewanella putrefaciens* [40] and *Geobacter sulfurreducens* [41] are known to localize the majority of their membrane-bound cytochromes on the outer memebrane; and the former is electrochemically active [42-43].

On the other hand, performance of MFC-S loaded with E inoculum was superior to performance of MFC-S loaded with SR inoculum (46% higher $P_{V/max}$, 65% lower Rint), these results are similar to those reported by Wang *et al*. (2010) [44] who developed a rapid selection method to enrich for a stable and efficient anodophilic consortium for MFCs. They compared the characteristics of their MFC inoculated with the enriched consortium with those of cell inoculated with original biofilm or activated sludge. They found that power density achieved with the enriched consortium (226 mW/m^2) was higher (by 10%) then those of the original biofilm (209 mW/m^2) and activated sludge (192 mW/m^2).

In general, in our work performance of MFC-S with both inocula was relatively modest. This could be due to the architecture of cell wich has a spacing inter-electrode of 7.8 cm, therefore the internal resistance values are high and power densities are low. The significant decrease of R_{int} with decrease of inter-electrode distance is consistent with previous experiments on the effect of electrode spacing on internal resistance of MFC [45-48].

3.2 Characterization of MFC-P loaded with SR and E inocula

The polarization curves and the power variation with current intensity of the MFC-P loaded with SR inoculum and connected in series and parallel, are shown in Figure 3A and Figure 3B, respectively. The figures 4A and 4B show the variation with current intensity of the MFC-P loaded with E inoculum and connected in series and parallel, respectively.

The values of R_{int} were 400 and 84 Ω for the MFC-P loaded with SR inoculum and connected in series and parallel, respectively, and 292 and 130 Ω for the MFC-P loaded with E, connected in series and parallel, respectively In particular, the proportion of R_{int} decrease in our work was similar to that reported elsewhere [11, 29]. Also, the effect of using enriched inoculum was significantly beneficial.

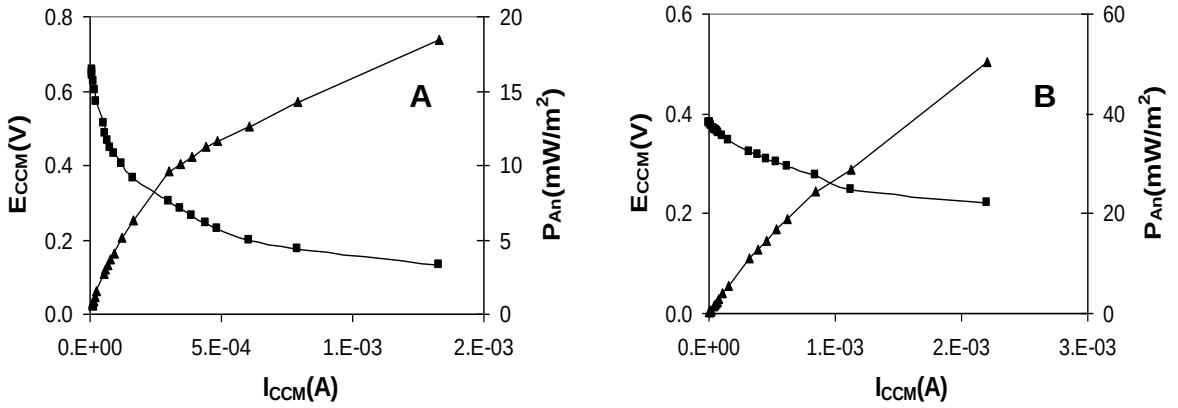

Figure 3. Polarization curves of MFC-P: (A) connection in series and (B) connection in Parallel.

Maximum volumetric powers P_V in MFC-P loaded with SR inoculum and connected in series and parallel were 655 and 1800 mW/m^3, respectively, and anode density powers P_{An} of the MFC-P connected in series and parallel were 18.4 and 50 mW/m^2, respectively. During the connection in series, the voltage was 0.66 V; this voltage was almost double of that obtained when the MFC-P was connected in parallel (0.34 V). All the other response variables in MFC-P connected in parallel were higher than MFC connected in series (Table 2).

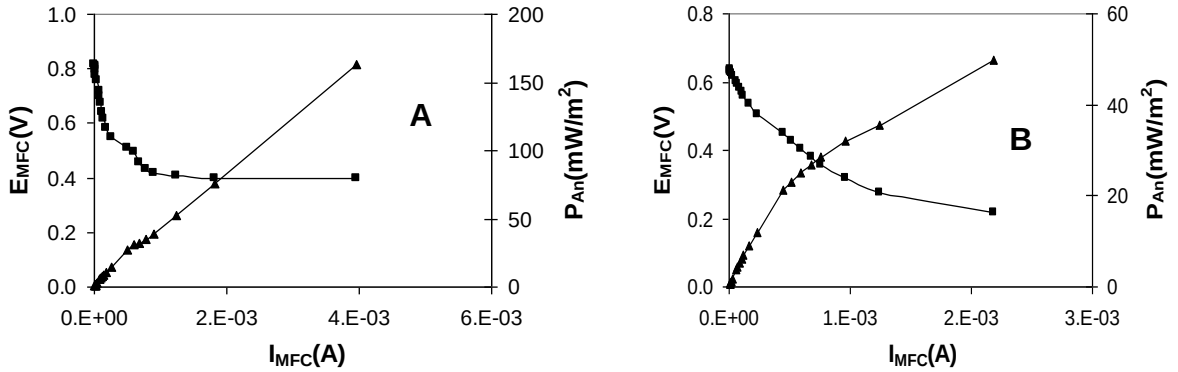

Figure 3. Polarization curves of MFC-P loaded with E: (A) connection in series and (B) connection in parallel.

On the other hand, the values of maximum volumetric powers in MFC-P loaded with E inoculum and connected in series and parallel, respectively, maximum volumetric powers were 1772 and 5 804 mW/m^3, and anode density powers P_{An} were 64 and 209 mW/m^2. When MFC-P loaded with E was conected in series, the voltage was 0.82 V; this voltage is higher than MFC-P connected in parallel (0.64 V). All the other response variables in MFC-P loaded with E connected in series were higher than MFC-P connected in parallel (Table 2).

Table 2. Characterization of a MFC-P using SR and E inocula and connected in series and parallel

Parameter	MFC-P Series SR	MFC-P Parallel SR	MFC-P Series E	MFC-P Parallel E
R_{int} (Ω)	400 ± 40	84 ± 5	292 ± 40	130 ± 5
$P_{An\text{-}max}$ (mW m^{-2})	18 ± 0.7	50 ± 1.2	64 ± 0.7	209 ± 1.2
$P_{V\text{-}max}$ (mW m^{-3})	655 ± 14	1800 ± 21	1772 ± 14	5804 ± 21
$I_{MFC\text{-}max}$ (mA)	1.3 ± 0.1	2.2 ± 0.1	2.2 ± 0.1	3.4 ± 0.1
$E_{MFC\text{-}max}$ (V)	0.66 ± 0.05	0.34 ± 0.04	0.82 ± 0.05	0.64 ± 0.04
$P_{MFC\text{-}max}$ (mW)	0.19 ± 0.02	0.49 ± 0.03	0.49 ± 0.002	1.5 ± 0.03

Parallel connection decreased the R_{int} by presumably increasing the cross sectional area for ion flow.

Energy loss in the series connection is known to be caused by lateral ion cross-conduction between electrodes; this phenomenon is common when fuel cell arrays sharing the same electrolyte are connected in series to increase voltage output [16]. Parallel conection of multiple electrodes of MFC-P signficantly increased $P_{V\text{-}max}$ compared to that of the MFC connected in series. Also, multiple MFC-P can be connected in series, forming a stacked system in order to increase the voltage. However, when this is done the stack usually undergoes voltage reversal, resulting in a dramatic decrease of stack voltage [15].

Parallel connection decresed not only the internal resistence by increasing the cross sectional area for ion flow, but also possibly diminished the electrode overpotential by increasing the total electrode suface area.

On the other hand, series connection showed an inverse trend to those in the parallel connection, with one order of magnitude higher resistence. Energy loss in the series connection is known to be caused by lateral ion cross-conduction between electrodes [16].

The relatively low values of P_{An} obtained in this work could be due to the be the surface area electrode material, the effect of the larger anode surface area on power was show with several material such as plain graphite, carbon cloth, graphite foam; this effect was relatively insignificant by adding graphite granules or using graphite fiber brushes in the MFC. Those material increased the surface area [4,8].

Parallel conection of multiple electrodes of MFC-P signficantly increased $P_{V\text{-}max}$ compared to P_V of MFC-P connected in series (Table 2).

On the other hand, E inoculum was better than SR inoculum on the MFC-P performance, this could be due to the the presence of iron-reducing bacteria are, probably electrochemically active bacteria. Chang *et al*. (2006) [49] defined EAB as bacteria that possess the ability to transfer electrons from oxidized fuel (substrate) to a working electrode without mediators. Dissimilatory metal-reducing bacteria (DMRB), wich are capable of the reduction of soil metal oxides, are known EAB species, including *Geobacter* and *Shewanella* spp. It was shown that the anode electrode in MFCs served as the electron acceptor for growth and metabolism of EAB, which are capable of current production in the absence of a mediator.

3.3 Analysis of bacterial community

3.3.1 Enrichment procedure

The figure 4 show the results of serial transfers procedure. A concentration of 100 mM Fe^{+2} was achieved on day 4 at the stage inoculation, while this concentration in the other stages is achieved on the first day.

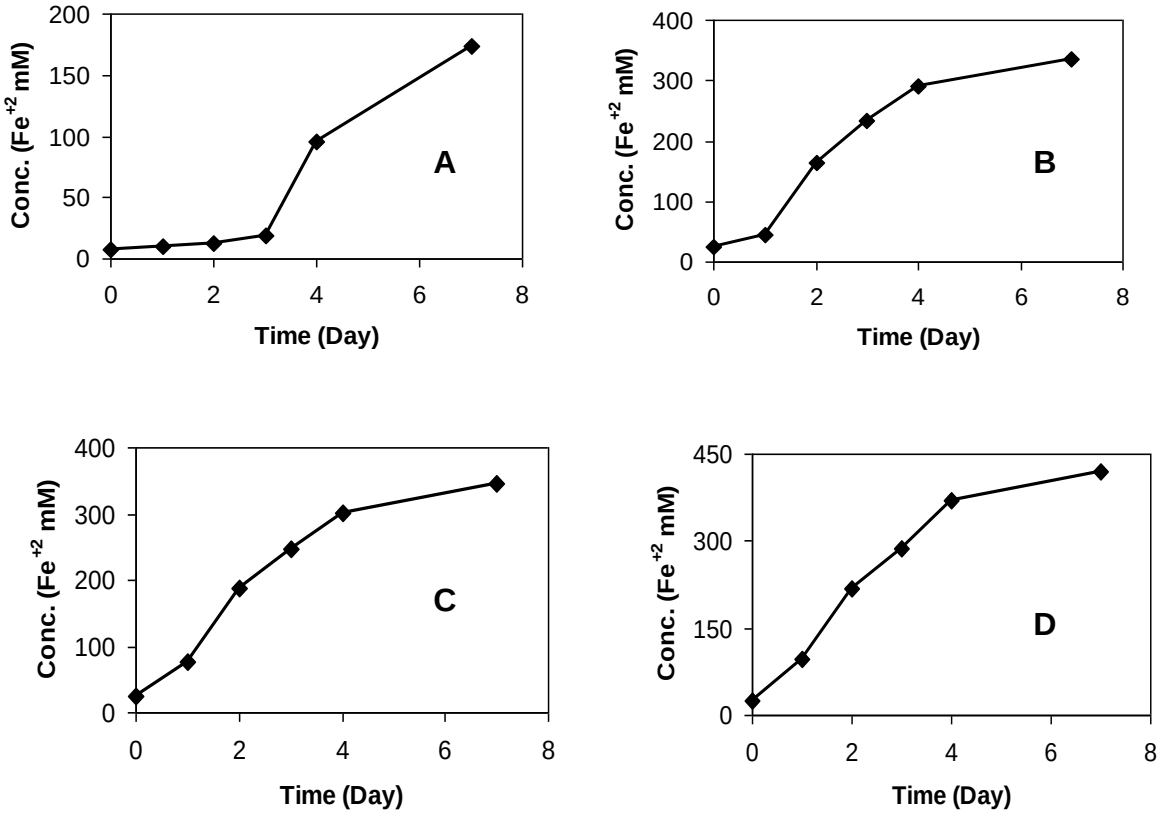

Figure 2. Serial transfers procedure. (A) Inoculation, (B) First Transfer, (C) Second Transfer, (D) Third Transfer.

Table 3 show Fe^{+2} initial and final concentration in serial transfers procedure. We could achieve a 419 mM Fe^{+2} final concentration in the last transfer, this value is more than twice what was obtained in the final inoculation stage. All this is an evidence that the enrichment procedure was successful.

Tabla 3. Concentrarion of Fe^{+2} mM during serial transfer procedure

Stage	Initial Fe^{+2} mM	Final Fe^{+2} mM
Inoculation	7.3	173
First Transfer	25.5	336.5
Second Transfer	25.5	345.7
Third Transfer	25.9	419.9

Our results are similar to those reported by Hyun *et al*. (1999) [24] who isolated a Fe(III)-reducer from the natural enviroment. Soil samples were collected from various paddy fields and enriched with ferric citrate as a source of Fe(III) under anaerobic conditions. The final enriched culture showed the highest Fe(III)-reduction activity. Bacterial growth was coupled with oxidation of lactate and pyruvate to Fe(III)-reduction, final concentration Fe^{+2} was 192.3 mM and 231.9, respectively, this results were obtained after 4 days

Table 4 shows the bacterial population obtained from biofilm of the MFC-S loaded with sulphate-reducing inoculum and enriched inoculum. *Clostridiales bacterium* was present in both inocula.

The major clones amplified from biofilm of the MFC-S loaded with sulphate-reducing inoculum were: *Clostridia* (42%), 98% identity with *Clostridiales bacterium*; *δ-Proteobacteria* (16%), 99% identity with *Desulfovibrio desulfuricans*; *Firmicutes* (16%), 96% identity with *Alkaliphilus oremlandii*, and an *Uncultured bacterium* (26%) 93% identity with *uncultured bacterium*.

The major clones amplified from biofilm of the MFC-S loaded with sulphate-reducing inoculum were: *Deferribacteres* (25%), 97% identity with *Geovibrio ferrireducens*; *Deferribacteres* (25%), 97% identity with *Geovibrio Thiophilus*; *Deferribacteres* (25%), 97% identity with *Denitrovibrio acetiphilus*, and a *Clostridia* (25%) 98% identity with *Clostridiales bacterium*.

There was a significant difference in community composition between both inocula. *Clostridia* predominated in the community of the biofilm of the MFC fed with sulphate reducing inoculum, whereas in the the biofilm of the cell loaded with enriched inocula the predominant microbes belonged to *Deferribacteres* class.

Table 3. The bacterial diversity on biofilm of MFC loaded with different inocula.

Inocula	Similar relatives (clones)	Identity (%)	Abundance (%)	Phylum (class)
Sulphate-reducing	*Desulfovibrio desulfuricans (1)*	100	16	*δ-Proteobacteria*
	Clostriales Bacterium (3)	99	42	*Clostridia*
	Alkaliphilus oremlandii (1)	96	16	*Firmicutes*
	Uncultured Bacterium (2)	93	26	*Uncultured bacterium*
	Geovibrio ferrireducens (1)	97	25	*Deferribacteres*

Enriched	*Geovibrio Thiophilus (1)*	97	25	*Deferribacteres*
	Denitrovibrio acetiphilus (1)	97	25	*Deferribacteres*
	Clostridiales Bacterium (1)	98	25	*Clostridia*

Our results were similar to those observed by Fung *et al*. (2006) [50], who enriched electrochemically active bacteria in a MFC using glucose and glutamate (copiotrophic conditions); their enriched population consisted of *γ-Proteobacteria* (36.5%), followed by *Firmicutes* (27%) and *δ- Proteobacteria* (15%). Logan and Regan (2006) [51], observed that the bacterial communities that develop in MFC show great diversity, ranging from primarily *δ-Proteobacteria*, that predominate in sediments MFCs to communities composed of α- , β-, *γ*- or *δ-Proteobacteria*, Firmicutes and uncharacterized clones in other types of MFCs. On the other hand *Geovibrio ferrireducens, Geovibrio thiophilus* and *Denitrovibrio acetiphilus* are known to contain c-type cytochromes [52]. Current evidence suggests that a series of c-type cytochromes associated with the inner membrane, the periplasm, and the outer membrane might interact to transfer electrons to the outer membrane surface.

The bacterial population in the anodic biofilms of our cell was not as rich as found in other types of inocula. For instance, diversity given by Shanon-Weaver index [30] was 1.27 and 1.38 and the species evenness given by Pielou´s evenness index [31] was 0.66 and 0.71, for the sulphate reducing and enriched inoculum, respectively (Tabla 4). These values mean that diverstiy of inocula was relatively low and the evenness was low-to-moderate, respectively.

Tabla 4. Ecological indices of the biocatalysts

Inoculum	**Shanon-Weaver**	**Pielou´s evenness**	**Divergence index of Poggi**
SR	1.27	0.66	0.75
E	1.38	0.71	

4. Conclusion

MFC-P whose main features were the assemblages or ‘sandwich’ arrangement of the cathode-memebrane-anode and the extended surface area of electrodes (higher ξ) exhibited a performance significantly superior to that of a similar cell (standard cell) where the electrodes were separated. The characterization experiments showed that the MFC-P lead to significant reduction of cell internal resistances compared to the standard cell. The improvement in P_V was ascribed to the combined effects of increased ξ and decrease of R_{int}.

The R_{int} of the MFC-P loaded with both inocula was significantly lower than that of the standard cell; this result was ascribed to both the changes in cell architecture and decrease of the inter-electrode distance.

Our results confirm the advantages of the ‘sandwich’ assemblage of CMA over separated electrodes, and demonstrate the convenience of parallel connection of faces in multi-face MFC-P in order to further abate the

internal resistance of the new design cell and increse volumetric power P_V.

The enrichment procedure was successful and indicates the presence of iron-reducing bacteria. Enriched inoculum improved the characteristics of both types of cells used in this work.

On the other hand, we demostrated the successful application of molecular ecological techniques to analyze bacterial diversity, direct 16S rDNA analysis showed low species richness and low-to-moderate evenness. Microbial community anchored in the MFC consisted primarily of *Clostrdiiales bacterium* and *Desulfovibrio desulfuricans*, the last one is a member of *δ*-subdivision of Proteobacteria. These bacteria are recognized to be capable of exocellular electron transfer collectivelly defined as a community of "exoelectrogens". Geovibrio ferrireducens, Geovibrio thiophilus and Denitrovibrio acetiphilus are known to contain c-type cytochromes, current evidence suggests that a series of c-type cytochromes associated with the inner membrane, the periplasm, and the outer membrane might interact to transfer electrons to the outer membrane surface.

Acknowledgements

The authors wish to thank CINVESTAV-IPN and ICYTDF, Mexico, for financial support to this reserch. Areli del C. Ortega-Martinez received a graduate scholarship from CONACYT, Mexico. The excellent technical help with molecular biology analysis of Ms Ana Lilia Tirado-Chamú (BSBiochemEng) from IBT-UNAM, and personnel of Environmental of Biotechnology and Renewable Energy R&D Group CINVESTAV-IPN is appreciated.

References

[1] B. E. Logan, B. Hamelers, R. Rozendal, U. Schröder, J. Keller, S. Freguia, P. Aelterman, W. Verstraete, K. Rabaey, Environ. Sci. Technol., 40, 5181 (2006).
[2] H. M. Poggi-Varaldo, A. Carmona-Martínez, A. L. Vázquez-Larios, O. Solorza-Feria, J. New Mat. Electrochem. Systems, 12, 49 (2009).
[3] L. Zhang, X. J. Zhu, Q. Li, D. Liao, D. Ye, J. of Power Source, 196, 15 (2011)
[4] Q. Deng, X. Li, J. Zuo, A. Ling, B.E. Logan, J. Power Sources, 195, 4 (2010).
[5] Y. Feng, Q. Yang, X. Wang, B. E. Logan, J. Power Sources 175 (2010).
[6] P. Aelterman, S. Freguia, J. Keller, W. Verstraete, K. Rabaey, Appl. Microbiol. Biotechnol. 78 (2008).
[7] X. Cao, X. Huang, N. Boon, P. Liang, M. Fan, Electrochem. Commun. 10 (2008).
[8] H. Liu, S. Cheng, L. Huang, B. E. Logan, J. Power Sources 179 (2008).
[9] S. You, Q. Zhao, J. Zhang, J. Jiang, C. Wan, M. Du, S. Zhao, J. Power Sources 173 (2007).
[10] H. Liu, R. Ramnarayanan, B. E. Logan, Environ. Sci. Technol. 38 (2004).
[11] A. L. Vazquez-Larios, G. Vazquez Huerta, F. Esparza-Garcia, E. Rios-Leal, O. Solorza-Feria, H.M. Poggi-Varaldo, J. New Mat. Electrochem. Systems, 13, 219 (2010).
[12] H. Rismani-Yazdi, S. M. Carver, A. D. Christy, O. H. Tuovinen, J. Power Sources, 180, 683 (2008).
[13] R. O'Hayre, S. W. Cha, W. Colella, F. B. Prinz, "Fuel cells fundamentals", John Wiley & Sons. New York, USA, 2005 p. 409.
[14] W. Hill, The art of electronics, Cambridge University Press, 1989.
[15] Y. Kim, M. C. Hatzell, A. J. Hutchinson and B. E. Logan. Energy Environ. Sci. 2011
[16] B. Wang, J. I. Han, Biotechnol. Lett. 312, 387 (2009).
[17] P. Aelterman, K. Rabaey, H. T. Pham, N. Boon, W. Verstraete, Environ. Sci. Technol., 40, 3388 (2006)
[18] T. Shimoyama, S. Komukai, A. Yamazawa, Y. Ueno, B. E. Logan, K. Watanabe, Appl Microbiol Biotechnol., 80, 325 (2008)

[19] B. H. Kim, H. S. Park, H. J. Kim, G. T. Kim, I. S. Chang, J. Lee and N.T. Phung, Appl. Microbiol. Biotechnol. 63 (2004) 672.
[20] N. T. Phung, J. Lee, K.H. Kang, I. S. Chang, G.M. Gadd, B. H. Kim, Microbiol. Lett., 233, 77 (2004).
[21] I. Valdez-Vazquez, E. Ríos-Leal, F. Esparza-García, F. Cecchi, H. M. Poggi-Varaldo, Int. J. Hydrogen Energy, 30, 1383 (2005).
[22] H. M. Poggi-Varaldo, L. Valdés, F. Esparza-García, G. Fernandéz-Villagómez, Water Sci. Technol., 35, 197 (1997).
[23] R. Sparling, D. Risbey, H. M. Poggi-Varaldo, Int. J. Hydrogen Energy, 22, 563 (1997).
[24] M. S. Hyun, B. H. Kim, I. S. Chang, H. S. Park, H. J. Kim, G. T. Kim, M. Kim, D. H. Park, J. Microbiol., 37, 4 (1999)
[25] P. Clauwaert, K. Rabaey, P. Aelterman, L. De Schamphelaire, T. H. Pham, P. Boeckx, N. Boon, W. Verstraete, Environ. Sci. Technol., 41, 3354 (2007).
[26] APHA, "Standard Methods for the Examination of Water and Wastewater", 17th edn., American Public Association, Washington DC, USA, 1989.
[27] D. R. Lovely, E. J. P. Phillips, Appl. Environ. Microbiol., 51 (1986)
[28] W. G. Weisburg, S. M. Barns, D. A. Pelletier, D. J. Lane, J. Bacteriol., 173, 697 (1991).
[29] A. Ortega-Martínez, K. Juarez-López, O. Solorza-Feria, M. T. Ponce-Noyola, E. Ríos-Leal, N. Rinderknecht Seijas, H. M. Poggi-Varaldo, J. New Mat. Electrochem. Systems, IN PRESS (2012).
[30] C.E. Shanon, Bell System Technical J., 27, 379 (1948)
[31] C.P.H. Mulder, E. Bazeley-White, P.G. Dimitrakopoulos, A. H., M. Scherer-Lorenzen, B. Schmid, "Species evenness and productivity in experimental plant communities", Oikos, 104, 50 (2004).
[32] H. M. Poggi-Varaldo, J. D. Barcenas-Torres, C. U. Moreno-Medina, J. Garcia-Mena, C. Garibay-Orijel, E. Rios-Leal, N. Rinderknecht-Seijas, J. Environ. Manag., In press, doi: 2012.03.15 (2012).
[33] B. H. Kim, D. H. Park, P. K. Shin, I. S. Chang, H. J. Kim, United States Patent, (1999)
[34] D. R. Bond, D. E. Holmes, L. M. Tender, D.R. Lovley, Science, 295 (2002)
[35] D. R. Lovley, Microbiol. Rev., 55 (1991)
[36] K. H. Nealson, D. A. Safarini, Annu Rev. Microbiol., 48 (1994)
[37] D. K. Newman, R. Kolter, Nature, 405 (2000)
[38] C. E. Turik, I. S. Tisa, F. Jr Caccavo, Appl. Environ. Microbiol., 68 (2002)
[39] K. P. Nevin, D. R. Lovley, Appl. Environ. Microbiol., 66 (2000)
[40] C. R. Myers, J. M. Myers, J. Bacteriol., 174 (1992)
[41] J. R. Lloyd, V. A. Sole, C. V. G. Van Praagh, D. R. Lovley, Appl. Environ. Microbiol. 66 (2000)
[42] B. H. Kim, T. Ikeda, H. S. Park, H. J. Kim, M. S. Hyun, K. Kano, K. Takagi, H. Tatsumi, Biotechnol. Tech. 13 (1999b)
[43] B. H. Kim, H. J. Kim, M. S. Hyun, D. H. Park, J. Microbiol. Biotechnol., 9 (1999c)
[44] A. Wang, D. Sun, N. Ren, C. Liu, W. Liu, B. E. Logan, W. M. Wu, Biores. Technol., 101 (2010).
[45] Y. Z. Fan, H.Q. Hu, H. Liu, J. Power Sourc., 171, 2 (2007).
[46] J. K. Jang, T.H. Pham, I.S. Chang, K.H. Kang, H. Moon, K.S. Cho, and B.H. Kim, Process Biochem., 39, 8 (2004).
[47] T. Song, Y. Xu, Y. Ye, Y. Chen, S. Shen, and J. Chem, J. Chem. Technol. Biotechnol., 84, 3 (2008)
[48] H. Liu, S.A. Cheng, and B.E. Logan, Environ. Sci.Technol., 39, 14 (2005).
[49] I. S. Chang, H. Moon, O. Bretschger, J. K. Jang, G. I. Park, K. H. Nealson, B. H. Kim, J. Microbiol. Biotechnol., 16 (2006)
[50] C. Y. Fung, J. Lee, I. S. Chang, B. H. Kim, J. Microbiol. Biotechnol., 16, 1481 (2006).
[51] B. E. Logan, J. M. Regan, Trends in Microbiol., 14, 512 (2006).
[52] P. H. Janssen, W. Liesack, B. Schink, Int. J. Syst. Evol. Microbiol., 52, 1341 (2002).

Abbreviations

CMA	'sandwich' arrangement cathode-membrane-anode
COD	chemical oxygen demand

E	enriched inoculum
E_{MFC}	MFC voltage
EAB	electrochemically active bacteria
I_{MFC}	current intensity
$I_{MFC-max}$	maximum current intensity
LED	light emiting diode
MFC	microbial fuel cell
P_{An}	power density
P_{An-max}	maximum power density
P_{MFC}	MFC power
P_V	volumetric power
P_{V-max}	maximum volumetric power
PCR	Polymerase chain reaction
PEM	proton exchange membrane
R_{ext}	external resistance
R_{int}	internal resistance
R_{ohmic}	ohmic resistance
R_{ion}	Ionic resistence
SR	Sulphate-reducing inoculum
V_{MFC}	MFC operation volume
VSS	volatile suspended solids

Methanol Electrooxidation on Au-Pd/C in Alkaline Media: The Dissolution of Palladium in the Bimetallic Alloy - A Case Scenario

V-H Ramos-Sánchez[1], Diana Brito-Picciotto[2], Ramón Gómez-Vargas[3], and Edgar Valenzuela[4,*]

[1]Facultad de Ciencias Químicas, Universidad Autónoma de Chihuahua, Nuevo Campus Universitario, Circuito Universitario, Chihuahua, Chih., México. C.P. 31125
[2]Unidad de Energía Renovable, Centro de Investigación Científica de Yucatán, A.C., Calle 43 #130, Col. Chuburná de Hidalgo, Mérida Yuc., México. C.P. 97200
[3]Energías Renovables y Protección del Medio Ambiente, Centro de Investigación en Materiales Avanzados, S.C., Miguel de Cervantes #120, Complejo Industrial Chihuahua, Chihuahua, Chih., México. C.P. 31109
[4]Cuerpo Académico de Energía y Sustentabilidad, Universidad Politécnica de Chiapas, Calle Eduardo J. Selvas S/N, Col. Magisterial, Tuxtla Gutiérrez, Chis., México. C.P. 29010
[*]Tel: (961)6120484, fax 6120499, mail: edgarvm@gmail.com

ABSTRACT

Among the familiar types of fuel cells, a new technology is emerging. Alkaline direct alcohol fuel cells (ADAFC) have attracted much attention, since they overcome many of the major issues of its predecessors, such as carbonation and alcohol crossover. Historically, either in acid or alkaline media, Pt has shown the best catalytic activity for methanol electrooxidation. Unfortunately, the high price and limited supply of Pt make it prohibitive for large scale production. In ADAFC, the weaker specific adsorption of spectator ions in basic media; and higher coverage of adsorbed OH at low potential permit superior catalytic performance of other noble catalysts for methanol electrooxidation.

In this context, the present work is concerned with two different carbon supported alloys, AuPd and Au_2Pd. These alloy compositions were chosen for comparison, but also, in the case of the latter, to set a scenario where Pd is depleted due to its unavoidable dissolution during continuous operation of an alkaline direct methanol fuel cell (ADMFC). Thus, the bimetallic catalysts were synthesized by chemical reduction with $NaBH_4$; supported in commercial carbon black; and later fully characterized to obtain parameters such as chemical composition, alloying degree, particle size, and electrocatalytic activity. Exclusively, the AuPd/C demonstrated capability to promote the electrooxidation of methanol. This proved that, within these bimetallic alloys, in conditions of dissolution of Pd and ensuing enrichment of Au, a null catalytic activity is attained.

1. Introduction

Among the familiar types of fuel cells, a new technology is emerging, which is not quite an alkaline fuel cell (AFC) nor a direct alcohol fuel cell (DAFC), but a hybrid. These alkaline direct alcohol fuel cells, ADAFC hereinafter, have recently attracted much attention, since they overcome many of the major issues encountered in the two abovementioned parent technological approaches. As a matter of fact, the exploitation of alkaline anion exchange membranes (AAEM) as electrolyte in ADAFC brings with it inherent benefits, such as carbonation prevention and reduced alcohol crossover. Besides, a basic medium, on the other hand, eases both alcohol oxidation and oxygen reduction.[1,2]

Either in acid or alkaline media, platinum (Pt) has shown the best catalytic activity for methanol electrooxidation. Therefore, Pt and Pt-based catalysts have been traditionally used in direct methanol fuel cells (DMFC).[3] However, the high price and limited supply of Pt make it prohibitive for large scale production. Here, alkaline direct methanol fuel cells (ADMFC) become the obvious choice due to their weaker specific adsorption of spectator ions in basic media; and higher coverage of adsorbed OH at low potential, necessary for methanol electrooxidation. These two characteristics even permit superior catalytic performance of other noble catalysts in alkaline media, according to the following reactions:

$$CH_3OH+6OH^- \rightarrow CO_2+5H_2O+6\bar{e} \quad \left[E_a^o = 0.81V\right] \tag{1}$$

$$\tfrac{3}{2}O_2+3H_2O+6\bar{e} \rightarrow 6OH^- \quad \left[E_c^o = 0.40V\right] \tag{2}$$

Despite its slightly larger particle size, when compared to Pt, palladium (Pd) can be a suitable catalyst for ADMFC. Actually, it has been shown that Pd exhibits an outstanding synergistic effect in combination with gold (Au) in bimetallic alloys, [4] which make acceptable the use of Au, a precious metal twice more expensive than Pd.[5,6] This improvement in catalytic activity and chemical stability is almost certainly due to the suppression of Pd dissolution in a highly oxidizing medium [7] that in turn results of the capacity of Au to withdraw electrons within the bimetallic alloy, as the most electronegative metal in the periodic chart. Thus, it is not surprising that since 1960s Au-Pd had been investigated mainly as an alternative catalyst for hydrocarbon refining. [8]

Overall, among the key factors that affect the activity of a bimetallic catalyst during the electrooxidation process in an ADAFC are the components arrangement, surface structure, particle size, and alloying degree. For instance, it has been demonstrated that Pd particles in the range between 5 and 7 nm show an enhanced catalytic performance. [9] Added to this, and even more important are the particular geometric effects exhibited by Au-Pd at various alloy homogeneities.[10] At this last point, the catalyst synthesis route plays an important role in controlling metal deposition and ultimately the alloying degree in bimetallic particles.

Indeed, incomplete alloying of Au-Pd can be originated due to a faster reduction of Au, when employing sodium borohydride ($NaBH_4$), particularly if both catalyst precursors are dissolved in tandem.[8] Thus, if the aforesaid occurs, it is expected to encounter both Au and Au-Pd particles, rather than isolated Pd particles; such chemical behaviour, it is understood in terms of the redox potentials of Au (1.00 V) and Pd (0.62 V), which do not allow a galvanic reaction to occur for the electrodeposition of Pd, through the reduction of the $PdCl_4^{=}$ ion, on the surface of Au.

In this context, the present paper is concerned with the synthesis and characterization of a low metal loading catalyst: Au-Pd/C. Data from two different carbon supported alloys, AuPd and Au_2Pd, is discussed. These alloy compositions were chosen for comparison, but also, in the case of the latter, to set a scenario where palladium is depleted due to its unavoidable dissolution during continuous operation of an ADMFC. To our knowledge, the electrocatalytic performance of such bimetallic alloy for methanol oxidation has not yet been investigated.

2. Experimental

Preparation of Au-Pd/C electrocatalysts

Carbon-supported AuPd nanoparticles with two different compositions [3:1] and [1:1], Au_2Pd and AuPd hereinafter, were synthesized by simultaneous chemical reduction of $HAuCl_4$ and Na_2PdCl_4 in presence of $NaBH_4$ as a reducing agent.

The Au_2Pd and AuPd nanoalloys were prepared by dissolving appropriate amounts of $HAuCl_4$ and Na_2PdCl_4 in 50 mL of deionized water, as summarized in **Table 1**. The two resulting aqueous solutions were then heated at 50°C under air atmosphere. In tandem, a protective agent was obtained by dissolving 300 mg of Polyvinylpyrrolidone (PVP40) in 100 mL of methanol. Afterwards, each of the two aqueous solutions containing the precursors were mixed, separately, with 50 mL of the solution containing PVP40 and kept under stirring under air atmosphere. These metallic admixtures were then chemically reduced by the drop-wise incorporation of 6 mL of a 66 mM $NaBH_4$ solution. All reagents were high purity, 99.99% or better, from Sigma Aldrich, except for $NaBH_4$ which was obtained from Fluka.

Table 1. The amounts of precursors weighed and expected compositions of Au-Pd particles synthesized in this study.

Sample	System	mmol Au	mmol Pd	mg $HAuCl_4$	mg Na_2PdCl_4
Au_2Pd	[3:1]	0.99	0.33	33.63	9.70
AuPd	[1:1]	0.66	0.66	22.42	19.41

The aforesaid procedure yielded two colloidal dispersions, AuPd and Au_2Pd. In order to obtain either of the supported bimetallic catalysts, AuPd/C or Au_2Pd/C, 1 g of carbon black (Vulcan XC72) were oxidized with 500 mL

of H_2O_2 (30wt%) at 40°C, and just before the carbon paste got dry, 1 mL of the corresponding colloidal dispersion was added, and then treated at 330°C under nitrogen atmosphere for 20 minutes.

Characterization Methods

X-ray diffraction (XRD) was carried out directly on the supported electrocatalysts using a Siemens D5000 diffractometer with a step of 0.1° from 5° to 90° 2θ, 5s/step; and employing a Cu Kα radiation´s wavelength of 1.541877 Å. Thermogravimetric analysis (TGA) was performed within a TGA Q500 from TA Instruments. The sample (*ca.* 20 mg) was heated in a platinum pan from room temperature up to 950°C at a temperature slope of 10°C/min and with a constant flow of 50 mL/min of N_2. X-ray fluorescence (XRF) measurements were made in a Horiba XGT-1000WR spectrometer equipped with a Rh X-ray source and a high purity Si detector. A Jeol 100 CX was used for transmission electron microscopy (TEM) analysis of the bimetallic particles. For this purpose, a drop of each of the nanoparticle colloidal dispersions was placed separately on a copper grid and later dried for its observation under the microscope.

Electrochemical Measurements

Electrochemical characterization of the supported catalysts was conducted at room temperature (20 ± 0.5°C) in a three-electrode glass cell consisting of a platinum rod as counter electrode; a saturated calomel electrode (SCE) serving as reference; and carbon paper with an area of 1 cm^2 acting as working electrode. The reference electrode was fixed close to the working electrode through a Luggin capillary. The working electrode was produced by dropping a suitable amount of alcoholic sol containing the catalyst onto the carbon paper; such sol was prepared dispersing ultrasonically 20 mg of the carbon supported electrocatalyst in 0.5 mL of isopropanol to which 25 µL of 5wt% Nafion solution were added, during 20 minutes.

Cyclic voltammetry (CV) and electrochemical impedance (EIS) measurements were performed in 0.5 M NaOH in absence and presence of 1.0 M methanol, using a Voltalab Potentiostat/Galvanostat model PGZ 301. In both experimental scenarios, the electrolyte (0.5 M NaOH) was bubbled with high purity nitrogen gas for deaeration during one hour before initiating any electrochemical analysis. Whereas voltammogram curves were acquired at 50, 25 and 10 mV/s; impedance spectra were recorded at open circuit potential within the frequency range between 100 kHz to 10 mHz and the amplitude of the AC signal at 10 mV.

3. Results and discussion

Catalyst Characterization

Figure 1 shows the micrographs of the Au_2Pd and AuPd colloidal dispersions. A qualitative interpretation of TEM analysis through the micrographs (insets in **Fig. 1A** and **1B**) obtained from high angle annular dark field scanning transmission electron microscopy (Z-contrast) revealed that there was not just one single phase occurring in the colloidal dispersions, as would be expected; which is likely to result of an incomplete alloying process between Au and Pd during simultaneous chemical reduction. All of the above derived from the fact that under Z-contrast conditions, the micrographs exhibited several dots within the specimens in which the brightness was not similar.

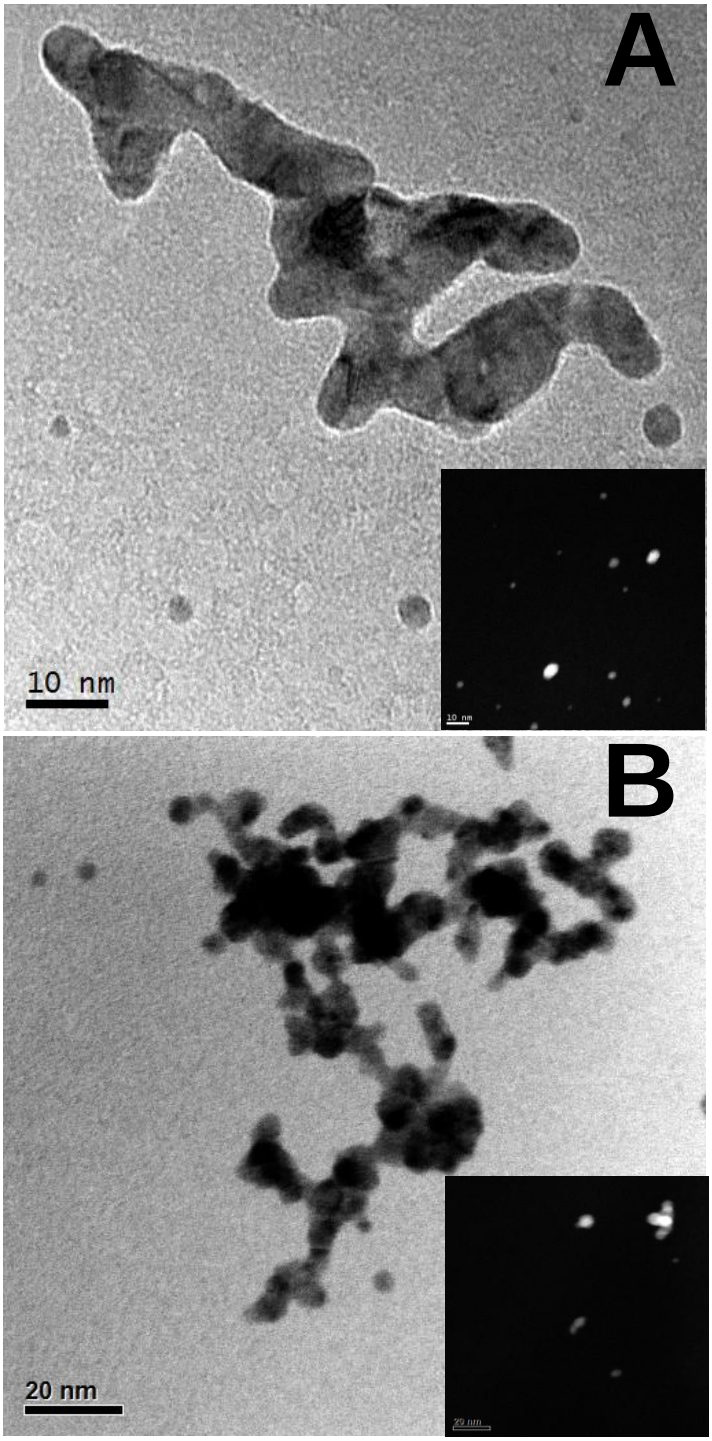

Figure 1. TEM images of the colloidal dispersions of: A) Au_2Pd; and B) AuPd. Inset in each figure displays a HAADF-STEM micrograph of its corresponding system.

Since it was, therefore, important to verify the alloying degree in both bimetallic systems, XRD and XRF were exploited. **Figure 2** displays the XRD patterns of Au_2Pd/C and AuPd/C. In both cases, the diffractograms revealed peaks that relate to the (111), (200), (220) and (311) planes indexed for Au (JCPDS 04-0784) and Pd (JCPDS 05-0681) in their face centered cubic structures. Although all of these XRD features observed in the diffractograms result of the sum of two single diffraction peaks, it was remarkable to notice an isolated reflection for tetragonal PdO, evolving from the convolution of its facets (002) and (101); such observation made clear that the asymmetric peak *ca.* 45° should also include a significant contribution from the (110) plane of PdO (JCPDS 75-0584). The unexpected occurrence of PdO is evidence of an inadequate catalyst supporting process, which did not avoid oxidation of the free metallic Pd, produced due to an incomplete alloying process. With respect to the carbonaceous catalyst support, the diffractograms allowed to identify unequivocally a broad band *ca.* 25°, attributed to the (002) plane of turbostratic carbon, which is clearly evident in both XRD patterns. Isolated reflections for Au-Pd (alloy) and PdO, *ca.* 39° and 32° respectively, were chosen to estimate the mean crystallite size according to the Debye-Scherrer equation. Peak fitting analysis correspondingly indicated crystallite sizes of about 5 nm and 19 nm for Au-Pd and PdO. Also using the results of the peak fitting analysis of the XRD patterns, the alloying degree in both catalysts was calculated using Vegard's law, based particularly on the position of the (111) peak for Au-Pd; since that is one of the two Au-Pd reflections free of contribution from PdO. According to the above, the atomic percent of alloying Au in Au_2Pd/C was 77% and 64% in AuPd/C. These values were, however, in discrepancy with the XRF atomic compositions, as shown in **Table 2**. This provides further support to the abovementioned argument that sustains that oxidation of free metallic Pd gives rise to PdO; as a matter of fact, such difference among atomic compositions yields that 33% and 50% of the Pd within Au_2Pd/C and AuPd/C, respectively, is in the form of PdO.

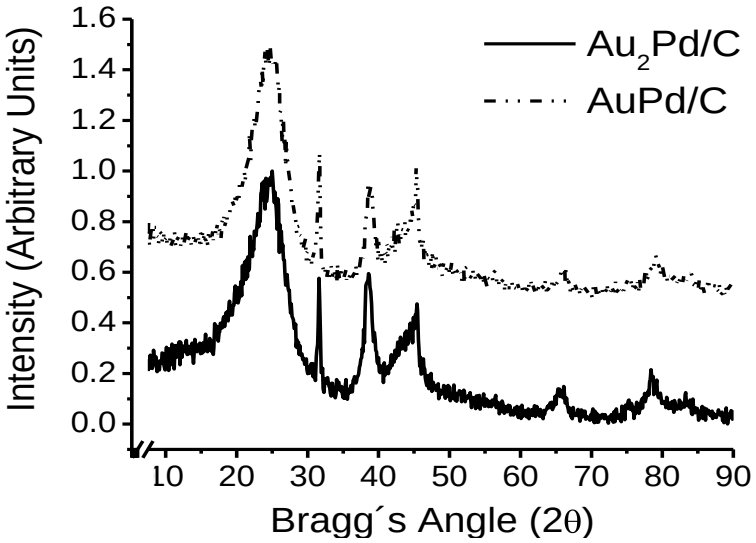

Figure 2. X-ray diffractograms of the bimetallic supported catalysts.

In order to determine the metal loadings of the two supported catalysts TGA was exploited. **Figure 3** presents the analytical thermograms of Au_2Pd/C and AuPd/C. Several insights were inferred through simple observation. In the case of Au_2Pd/C, it is evident an early weight loss that stabilizes around 100°C that, accordingly, it has been associated with water evaporation. Another drop, *ca.* 300°C, solely observed in Au_2Pd/C was attributed to a palladium hydride (PdH_x) that decomposes at such temperature, releasing hydrogen. Despite not being apparent in **Figure 2**, PdH_x was considered, since its corresponding XRD reflections could easily be obscured by the (111) and (200) peaks of Au-Pd. Besides, PdH_x could be feasibly produced *via* dissociation of BH_4^- ions and later absorption of chemisorbed hydrogen atoms into its lattice.[11] Then, a uniform behavior was observed for both catalysts, where full thermal decomposition of the carbonaceous support was achieved at 550°C; followed by the melting and ultimate conversion of PdO to Pd starting at 750°C.[12] Thus, based on the analytical thermograms, the actual metal loadings in Au_2Pd/C and AuPd/C were 4.56% and 5.56%, respectively. Note that, in virtue of the above, metal loadings were determined in the flat region situated between 550°C to 750°C with the aim of incorporating the mass contribution of PdO within the metal loadings of both catalysts.

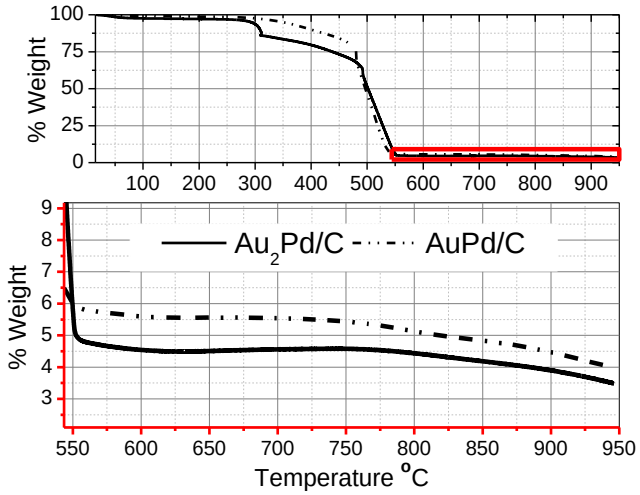

Figure 3. *Top*: Thermograms of Au_2Pd/C and AuPd/C. *Bottom*: Zoom in on the PdO decomposition region.

Table 2. Summary of relevant characterization results of the supported catalysts prepared in this study.

Sample	Composition		Components	Crystallite sizes (nm)		Metal loading
	Alloy	Atomic		Au-Pd	PdO	
Au_2Pd/C	$Au_{0.77}Pd_{0.23}$	$Au_{0.67}Pd_{0.33}$	Au-Pd, PdO; PdH_x; H_2O; C	4.8	16.9	4.56%
AuPd/C	$Au_{0.64}Pd_{0.36}$	$Au_{0.48}Pd_{0.52}$	Au-Pd; PdO; C	5.6	21.6	5.56%

Electrochemical Performance

The cyclic voltammograms for the Au_2Pd/C and AuPd/C in alkaline media are shown in **Figure 4**. Whereas the main plot in **Figure 4** is intended to observe methanol electrooxidation; the inset within should display the characteristic hydroxyl (OH^-) adsorption/desorption process.

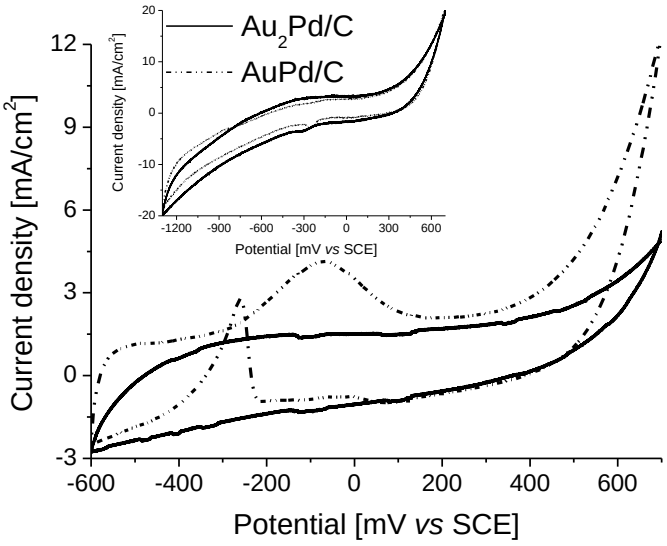

Figure 4. Cyclic voltammograms of methanol electrooxidation on the Au-Pd electrodes in 0.5 M NaOH solution containing 1.0 M methanol with a scan rate of 10 mV/s. *Inset*: Cyclic voltammetry of hydroxyl (OH^-) adsorption/desorption in 0.5 M NaOH solution at 10 mV/s.

Although similar, both voltammograms presented in the inset in **Figure 4** revealed two distinct cathodic peaks *ca.* -300 mV, which were attributed to the reduction of PdO (**Reaction 3**), already present in both catalysts, as demonstrated by the XRD patterns. It is noteworthy that no clear evidence of sorption processes was found. Even though, the electrochemically active surface area (ECSA) was calculated for AuPd/C (434.9 cm^2/mg) based on the PdO reduction peak; subsequently the electrocatalytic activity was only qualitatively assessed due to the significant uncertainty derived of the occurrence of PdO in the original composition of both catalysts and therefore the abovementioned value for ECSA of AuPd/C should be taken with caution.

$$PdO + H_2O + \bar{e} \rightarrow Pd + 2OH^- \qquad (3)$$

At this point, and despite the lack of adsorption and desorption peaks; it was outstanding to observe in **Figure 4**, only for AuPd/C, the capability of promoting electrooxidation of methanol in alkaline media, even if it is at a higher onset potential (-437 mV) with respect to Pd/C (-590 mV).[13] Methanol oxidation in alkaline media has been characterized by two anodic peaks obtained during the forward and reverse scan. The former is usually related to the oxidation of freshly chemisorbed species from methanol adsorption; whereas the latter is fundamentally associated to removal of the carbonaceous species originated during the aforesaid chemisorption process.[13] It should be noted

that during cyclic voltammetries the forward sweep was restrained in order to avoid water oxidation that could lead to oxygen production, which ultimately would interfere. Therefore it was suffice to observe just one of the anodic peaks to verify the electrocatalytic activity of AuPd/C. Finishing with a detailed description of the cyclic voltammogram of methanol oxidation on the surface of AuPd/C, there is a broad anodic peak centred at -75 mV caused by the formation of an oxide of the alloy. The complementary cathodic peak corresponding to the reduction of the oxide of the alloy is diffuse, and roughly centred at 70 mV.

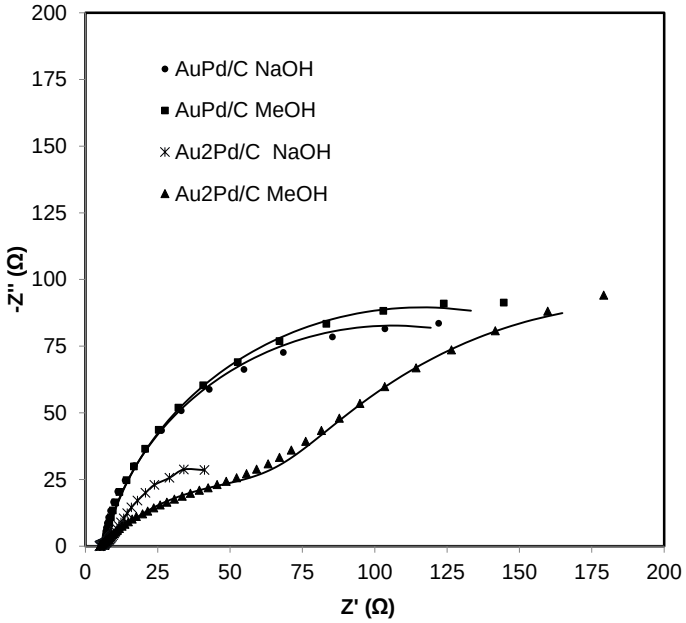

Figure 5. Nyquist plots of the EIS results obtained for Au_2Pd/C and AuPd/C in alkaline media, whether in presence or absence of methanol. Whereas experimental data is represented by dots; simulations are presented as solid lines.

Impedance results are shown in **Figures 5**. The EIS experimental data was simulated using ZPLOT software. The values obtained for the Charge Transfer Resistances (R_{CT}) and Constant Phase Elements (CPE) are summarized in **Table 3**, and the electric equivalent circuits used for the simulation are presented in **Figure 6**.

Table 3. Electrical elements and their values employed during simulations of the electrochemical data.

Sample	MeOH	R_{CT1} (Ω)	CPE_1 (F)	n	R_{CT2} (Ω)	CPE_2 (F)	n
Au_2Pd/C	(-)	109.60	0.0074	0.52	245	0.039	0.80
Au_2Pd/C	(+)	6	0.04	0.70	80	0.15	0.87
AuPd/C	(-)	200	0.057	0.87			
AuPd/C	(+)	220	0.042	0.87			

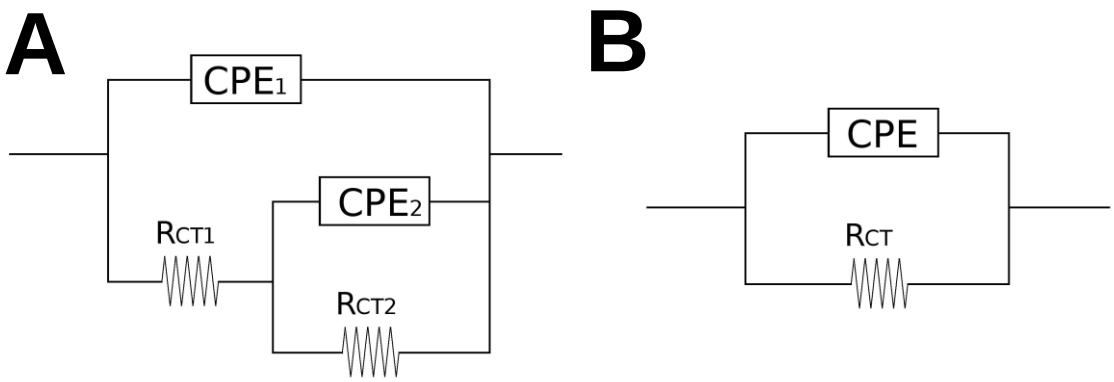

Figure 6. Electrical equivalent circuits used during simulations of the EIS results. A) Au_2Pd/C; and B) AuPd/C.

In both materials, a response controlled by a Faradaic process was observed. For the AuPd/C sample, the Nyquist diagrams in presence and absence of methanol were represented with a single semicircle slightly depressed. This response is typical for an electrode/electrolyte interface, where the charge transference between the catalyst and the chemical species in the electrolyte is accomplished in one single step. [14]. This behaviour is highly desirable in a catalyst, since as the number of steps involved in the oxidation/reduction of species diminishes, the overall kinetics of the process is increased.

A complete different scenario was observed in the Au_2Pd/C sample where two overlapped semicircles were obtained. This response is attributed to two different processes associated to an additional interface comparable to the AuPd/C system. According to the TGA and XRD results of Au_2Pd/C, PdH_x is also occurring within the catalyst. As a matter of fact, PdH_x contributes to the EIS analysis, and is represented by the second semicircle present solely in Au_2Pd/C impedances. This additional interface provides an additional opposition to the charge transference between the chemical species and the catalyst. This observation is in agreement with the voltamperometric analysis that shows a higher catalytic activity of AuPd/C with respect to Au_2Pd/C.

4. Conclusions

A complete characterization of Au_2Pd/C and AuPd/C, prepared by co-reduction in aqueous solution, revealed that an inadequate thermal treatment during catalyst supporting process coupled to an incomplete alloying process yielded a significant amount of PdO in both systems. Nevertheless, and contrary to what it would be expected, AuPd/C demonstrated electrocatalytic activity to promote methanol oxidation in alkaline media, although at higher potentials than Pd/C on its own. In fact, cyclic voltammetry put forward nanostructured PdO, as the active phase in AuPd/C, rather than the bimetallic nanoalloy.

On the other hand, there was an implicit suggestion that the deficiency of palladium in Au_2Pd/C could be associated to a preferential reaction pathway, in which the occurrence of PdH_x is benefited over the reduction reaction, and ultimately the alloying process.

5. Akcnowledgements

The authors would like to thank Jorge Ivan Carrillo Flores, Daniel Lardizábal Gutiérrez and Enrique Torres Moye from CIMAV, S.C. for the technical assistance provided throughout the present study.

This research was funded by the Public Education Ministry (SEP, México) through the PROMEP program under grant PROMEP/103.5/09/0424.

6. References

[1] Bidault, F., et al., Review of gas diffusion cathodes for alkaline fuel cells. Journal of Power Sources, 2009. 187(1): p. 39-48.

[2] Tripković, A.V., et al., Methanol electrooxidation on supported Pt and PtRu catalysts in acid and alkaline solutions. Electrochimica Acta, 2002. 47(22–23): p. 3707-3714.

[3] Antolini, E. and E.R. Gonzalez, Alkaline direct alcohol fuel cells. Journal of Power Sources, 2010. 195(11): p. 3431-3450.

[4] Nutt, M.O. et al., Improved Pd-on-Au bimetallic nanoparticle catalysts for aqueous-phase trichloroethene hydrodechlorination. Applied Catalysis B: Environmental, 2006. 69(1–2): p. 115-125.

[5] Palladiumprice. 06/02/2012]; Available from: http://palladiumprice.org/.

[6] Goldprice. 06/02/2012]; Available from: http://goldprice.org.

[7] Zhang, J. et al., Stabilization of platinum oxygen-reduction electrocatalysts using gold clusters. Science, 2007. 315: p. 220-222.

[8] Park, S.Y. et al., The effective bimetallic component of Pd–Au/C for electrochemical oxidation of borohydrides. Current Applied Physics, 2010. 10(2): p. S40-S43

[9] Zhou, W. and J.Y. Lee, Particle Size Effects in Pd-Catalyzed Electrooxidation of Formic Acid. The Journal of Physical Chemistry C, 2008. 112(10): p. 3789-3793.

[10] Venezia, A.M. et al., Activity of SiO2 supported gold-palladium catalysts in CO oxidation. Applied Catalysis A: General, 2003. 251(2): p. 359-368.

[11] Phan, T-H and R.E. Schaak, Polyol synthesis of palladium hydride: bulk powders vs. nanocrystals. Chemical Communications, 2009. 45(21): p.3026-3028

[12] Greenwood, N.N. and A. Earnshaw, Chemistry of the Elements, 1997. Butterworth-Heinemann, Oxford, UK.

[13] S. S. Mahapatra and J. Datta, Characterization of Pt-Pd/C Electrocatalyst for Methanol Oxidation in Alkaline Medium, International Journal of Electrochemistry, 2011, Article ID 563495, 16 pages.

[14] Zhang, J. et al., EIS-assisted performance analysis of non-noble metal electrocatalyst (Fe–N/C)-based PEM fuel cells in the temperature range of 23–80°C. Electrochimica Acta, 2009. 54(6): p. 1737-1743.

Electrocatalytic Properties of NiMo Nanoparticles for the Hydrogen Evolution Reaction

Savidra Lucatero, Gabriel Tamayo, Diego Crespo, Ernesto Mariño and Marcelo Videa*

Tecnológico de Monterrey, Monterrey, N.L., Mexico cp 64849.
Corresponding author: (52) 81 83284489, mvidea@itesm.mx

ABSTRACT

Previous work recently presented by our group focused on the electrocatalytic activity of NiMo alloys for the hydrogen evolution reaction (HER). The performance of electrodeposits fabricated by means of current pulses from a binary Ni-Mo electrolyte was characterized by cyclic voltammetry. The deposition time was kept constant at 2 seconds in all cases, whereas the pulse current density was varied in the range of 7 to 107 mA/cm^2. As a follow-up work, this investigation gathers information on compositional analysis and morphological features of electrodeposits. Electron microscopy imaging indicated that at the electrodeposition conditions utilized, the formation of nanoparticles (NPs) was favored; NP size ranged between 30 to 50 nm and was not significantly affected by variations in the intensity of the current pulse. Compositional analysis of the deposits suggested that Ni content in the electrodeposits was sensitive to changes in the applied current density, whereas Mo content was unaffected. The presence of oxygen within the materials suggested that oxide formation is highly probable. The electrosynthesis of two different catalytic materials was indicated by electrochemical characterization of the deposits; each showing different electrocatalytic activity, oxidation potential and electrochemical stability. The material with the greatest catalytic activity has also the disadvantage of being highly unstable, since its elimination reduces almost completely the activity for the HER. Ongoing work on compositional analysis and electron microscopy imaging is being helpful to further confirm the presence and distribution of such different catalytic materials within the electrodeposits, as well as their composition.

1. INTRODUCTION

One of the biggest challenges that we face today is the need to shift our energy consumption which currently is heavily dependent on fossil fuels to a more environmentally friendly and sustainable source of energy. The world energy demand is a natural consequence of our search for economic wealth and technological development but it is also tied to an unbalanced increase in the concentration of CO_2 in the atmosphere, responsible for the greenhouse effect, with the direct consequence of an steady increase in the average temperature of the earth [1, 2]. Nevertheless, the cost of fossil fuels will only increase as these reserves significantly decline, bounding most of the current development of alternative energy sources to a cost-effective target. Among the proposed alternatives, hydrogen is a fuel with zero emissions of greenhouse gases (GHG), which has generated great interest in its use. To make its use feasible it is necessary to develop a method of obtaining it environmentally clean and economically viable. The use of solar energy in the electrolysis of water represents a process that is completely sustainable and environmentally friendly [3].

The hydrogen evolution reaction (HER) is essential in this process. The cost efficiency of the production of hydrogen using this method is limited by the efficiency of the energy conversion and the cost of the materials used in the hydrogen evolution reaction, in particular the electrocatalysts for which precious metals are commonly used [4]. As alternatives to platinum, some of the most important and studied metal catalysts are nickel and binary or ternary alloys are Ni-V, Ni-Ti and Ni-Mo [5, 6, 7]. Many studies report the particular catalytic activity of the nickel molybdenum (NiMo) system for the HER. This system has demonstrated superior performance [7] and long term stability [8] compared to bare nickel and other nickel alloys, requiring lower overpotentials [7]. In addition, Crespo *et al* [9] showed that NiMo nanoparticles deposited on a glassy carbon electrode presented a current exchange density of 3.09×10^{-4} A/cm^2 compared to 2.6×10^{-6} A/cm^2 for nickel.

2. EXPERIMENTAL METHODOLOGIES

The composition of the electrolytic bath used for NiMo alloy deposition contained the following, 0.2M $NiSO_4 \cdot 6H_2O$ (Sigma Aldrich), 0.06M $Na_2MoO_4 \cdot 2H_2O$ (Mallinckroft Chemical Works), 0.136M $Na_3C_6H_5O_7 \cdot 2H_2O$ (Baker Analyzed Reagent) and deionized water; the pH was adjusted to 9.0 adding NH_4OH.

Electrodeposition experiments were performed using a three-electrode arrangement connected to an EG&G PAR potentiostat/galvanostat, model 273A. The working electrode was made from a glassy carbon rod. The rod was encapsulated in a resin and only its cross section was exposed (7×10^{-2} cm^2) and polished with alumina powder with particle diameters of 1, 0.1 and 0.02 μm. The electrode was polished for 30 seconds on each particle size. After each polishing process, the electrode was rinsed with deionized water and cleaned by immersion in an ultrasonic bath for 30 seconds. The reference electrode was a Hg/Hg_2SO_4 electrode (−0.641V vs SHE) and the auxiliary electrode was constructed with a platinum

mesh. All three electrodes were fitted into a Teflon cap to hold them in position and placed in a glass cell with 50 mL of the solution. Current pulses of varying intensity were applied in order to deposit the nickel and molybdenum ions from the electrolytic bath; the pulse time was kept constant at 2 seconds in all cases. The current density range used for the electrodeposition experiments was between 7 and 107 mA/cm^2. Each deposition experiment was performed in triplicate to verify reproducibility of the results.

Electrodeposited NiMo alloys were visualized under a FEI scanning electron microscope (Nova Nano SEM 200) and images captured at an accelerating voltage of 15 kV. Quantitative compositional analysis of the deposits was conducted by means of energy dispersive spectrometry (EDAX) integrated to the electron microscope.

Nanoparticle size was quantitatively measured by image analysis (Image J, NIH, Baltimore, MD). Processing of original SEM files consisted of binary image reconstruction at a predetermined grayscale threshold. Approximately 300 in-focus objects were measured to obtain representative determinations of particle size.

The cyclic voltammetry (CV) technique was used to characterize the electrocatalytic activity of NiMo deposits, each electrode was transferred to a 0.78M H_2SO_4 solution, and a potential sweep from the open circuit potential of the system (usually −0.4V vs Hg/Hg_2SO_4) to −0.9V and back to the starting potential was performed. The activity of the deposit was a direct measure of the current generated at a fixed overpotential of 100 mV.

3. RESULTS AND DISCUSSION

The polarization potential behavior, the electrochemical characterization, as well as the electrocatalytic activity of fabricated deposits have been previously discussed elsewhere [10], and will be briefly summarized next. Additional work presented here included results on compositional analysis and morphological features of electrodeposits.

Previous results regarding the effect of the applied current density on the polarization potential behavior (Figure 1) suggested that at current densities above 35 mA/cm^2 a fast polarization leading to a minimum and a recovery towards a steady state are obtained, but at this and higher current densities the potential drops again and a second minimum is observed at longer times. This is best shown in Figure 1 b), where the time is plotted in logarithmic scale. This observation suggests that two different materials were deposited at current densities above 35 mA/cm^2. The electrochemical characterization of deposits consistently suggested the synthesis of two completely different materials, with distinct electrocatalytic activities for hydrogen evolution. The most active material, whose oxidation potential occurred at −241mV vs Hg/ Hg_2SO_4, was named Ia, whereas a second material, showing lower catalytic activity, but higher electrochemical stability than Ia, was referred as IIa. This was found to oxidize at 128mV vs Hg/ Hg_2SO_4.

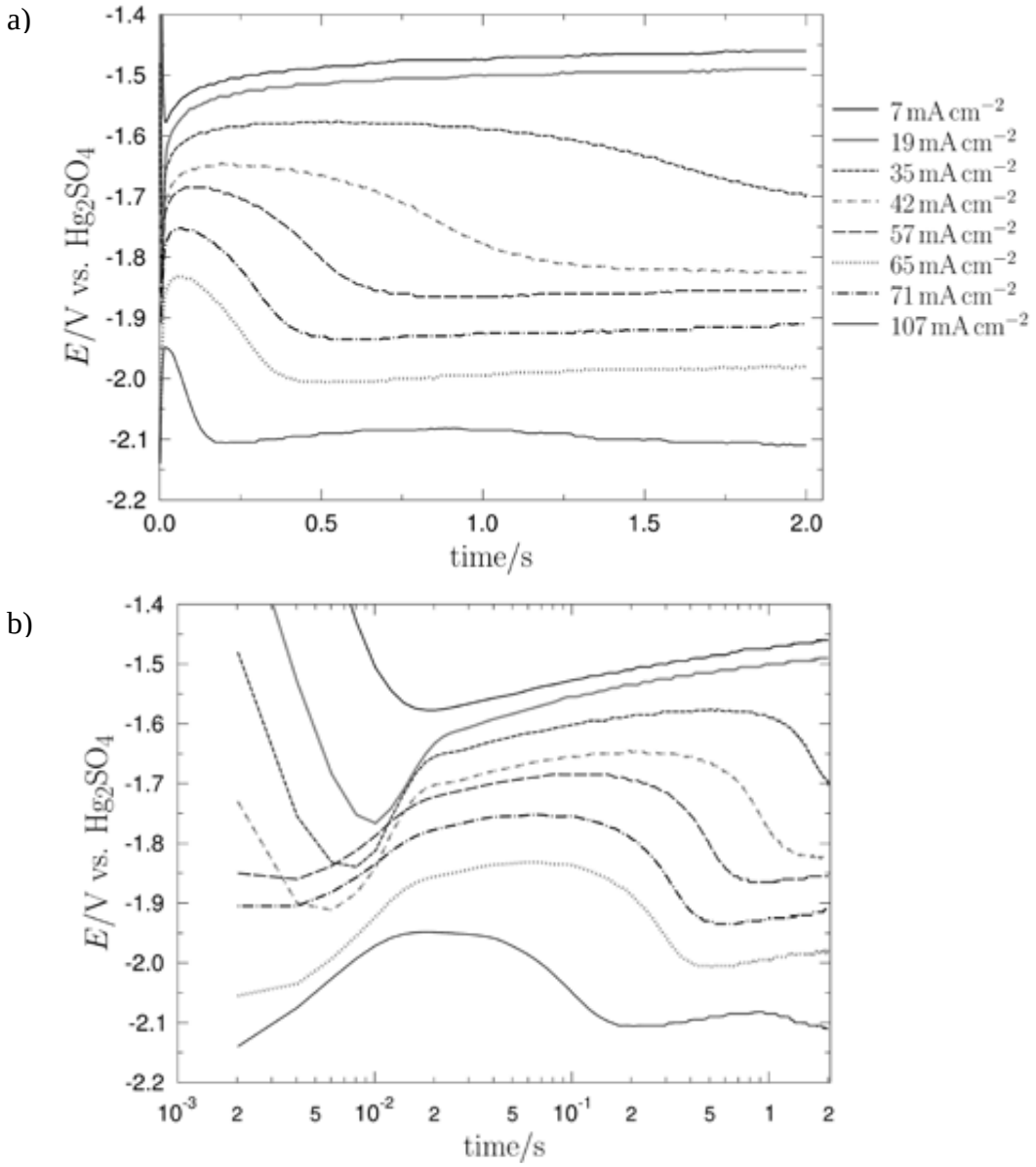

Figure 1. Polarization curves generated upon applying current pulses at different intensities in the range of 7 to 107 mA/cm^2. The time-axis is in a rectangular (a) and logarithmic (b) scale.

The catalytic activity of electrodeposits for hydrogen evolution was characterized by means of cyclic voltammetry. Figure 2 a) shows voltammograms generated by materials obtained at different current pulsing conditions. The current measured a given potential is a relative measure of the speed at which hydrogen is being formed on the electrode surface where the NiMo catalyst sits, and therefore of its electrocatalytic activity. Figure 2 b) shows a correlation between the current density used in the preparation of electrodeposits and the current generated at a potential of -0.9V vs Hg/Hg_2SO_4. It was observed that the activity of the deposits rapidly increases as the current density of the pulse used increases and reaches its largest activity for the electrodeposits prepared with current densities between 70 to 100 mA/cm^2. The activity of the deposits obtained at currents greater than 100 mA/cm^2 remained practically constant.

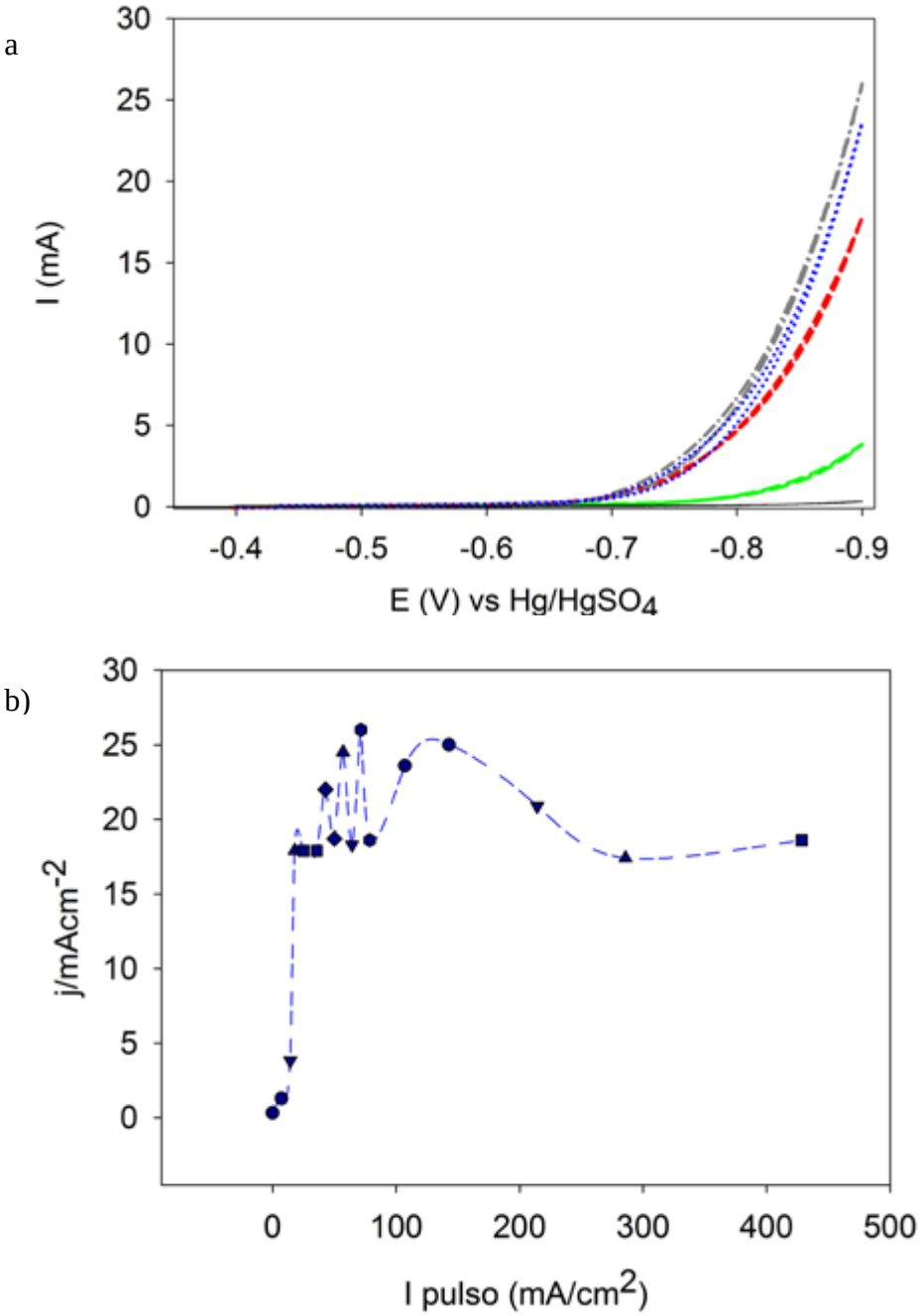

Figure 2. a) Electrocatalytic performance of deposits obtained using current pulses of 25, 35 and 71 mA/cm^2. b) Current generated -0.9V as function of pulsing current fabrication conditions.

3.1. Compositional and morphological characterization of deposits

Figure 3 shows scanning electron microscopy (SEM) images of electrodeposits obtained at an applied current density of 15 mA/cm^2 (a) and b)) and 70 mA/cm^2 (c) and d)). Figures 3 a) and 3 c) were captured at a magnification of 60000X, whereas in Figures 3 b) and 3 d), this parameter was set-up at 120000X. Nanoparticles (NPs) were observed in both cases, *i.e.* at 15 and 70 mA/cm^2. However higher density (number of nanoparticles per unit area) was found when the applied current pulse was 70 mA/cm^2 in

comparison to that observed at 15 mA/cm^2. These results were consistent with an expected higher nuclei formation upon increasing the intensity of the current pulse. NP size distributions were obtained by means of quantitative image analysis following the procedure detailed in the Experimental Section. A mean size of 39 and 45 nm was determined when the current pulse was, respectively, 15 and 70 mA/cm^2. These results indicate that the influence of the applied current density on the size of nanoparticles was not very significant.

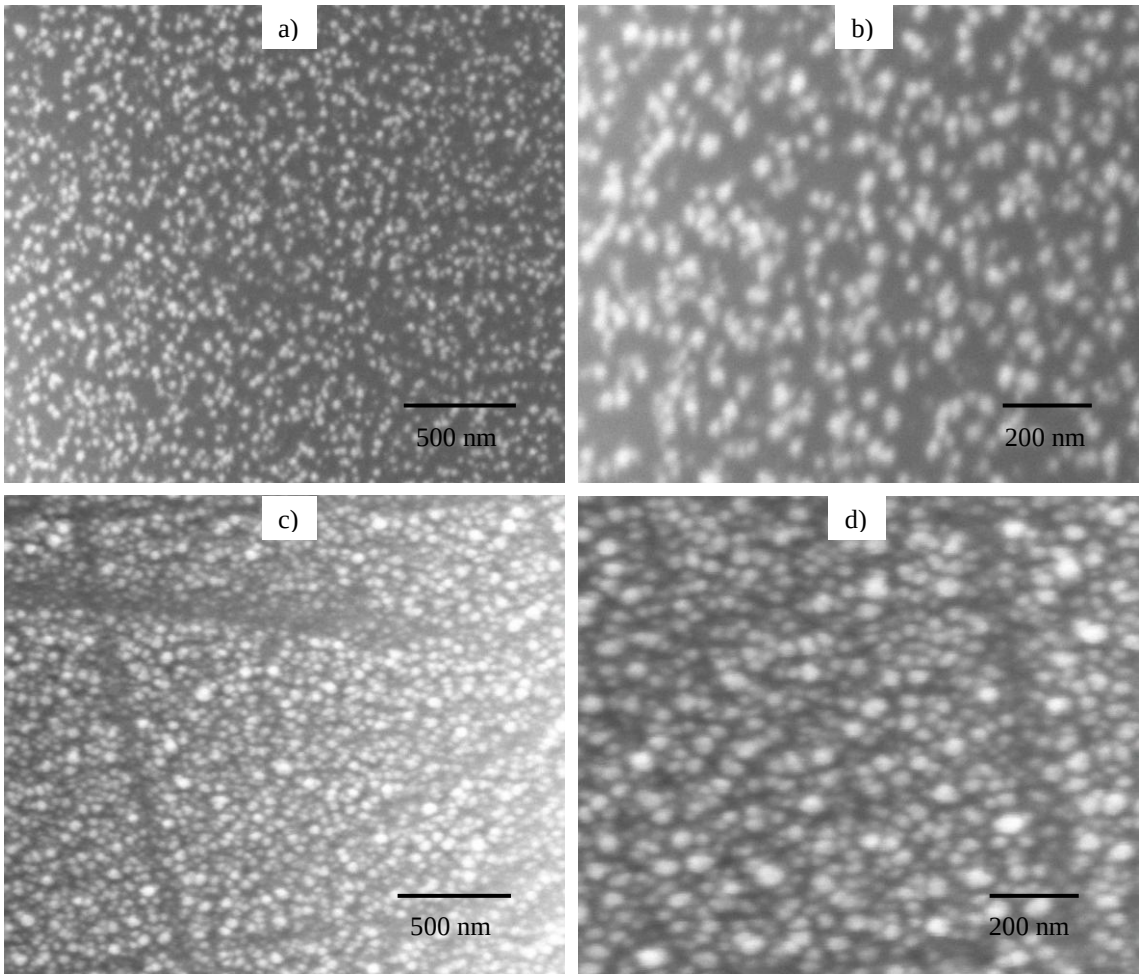

Figure 3. Scanning electron images of electrodeposits fabricated at 15 mA/cm^2, a) and b) and 70 mA/cm^2, c) and d). The magnification is 60000X in a) and c), and 120000X in b) and d).

In Figure 4, energy dispersive spectrometry (EDXS) results show the compositional analysis of fabricated electrodeposits. The applied current density in Figure 4 a) was 15 mA/cm^2, whereas that in Figure 4 b) was 70 mA/cm^2. Electrodeposit composition was affected by applied current density; a higher Ni content (~4 wt %) observed when the current pulse was 70 mA/cm^2 contrasted with that determined at 15 mA/cm^2 (~2 wt %). A Mo content of approximately 0.75 wt % was practically unaffected by upon changing the current pulse from 15 to 70 mA/cm^2.

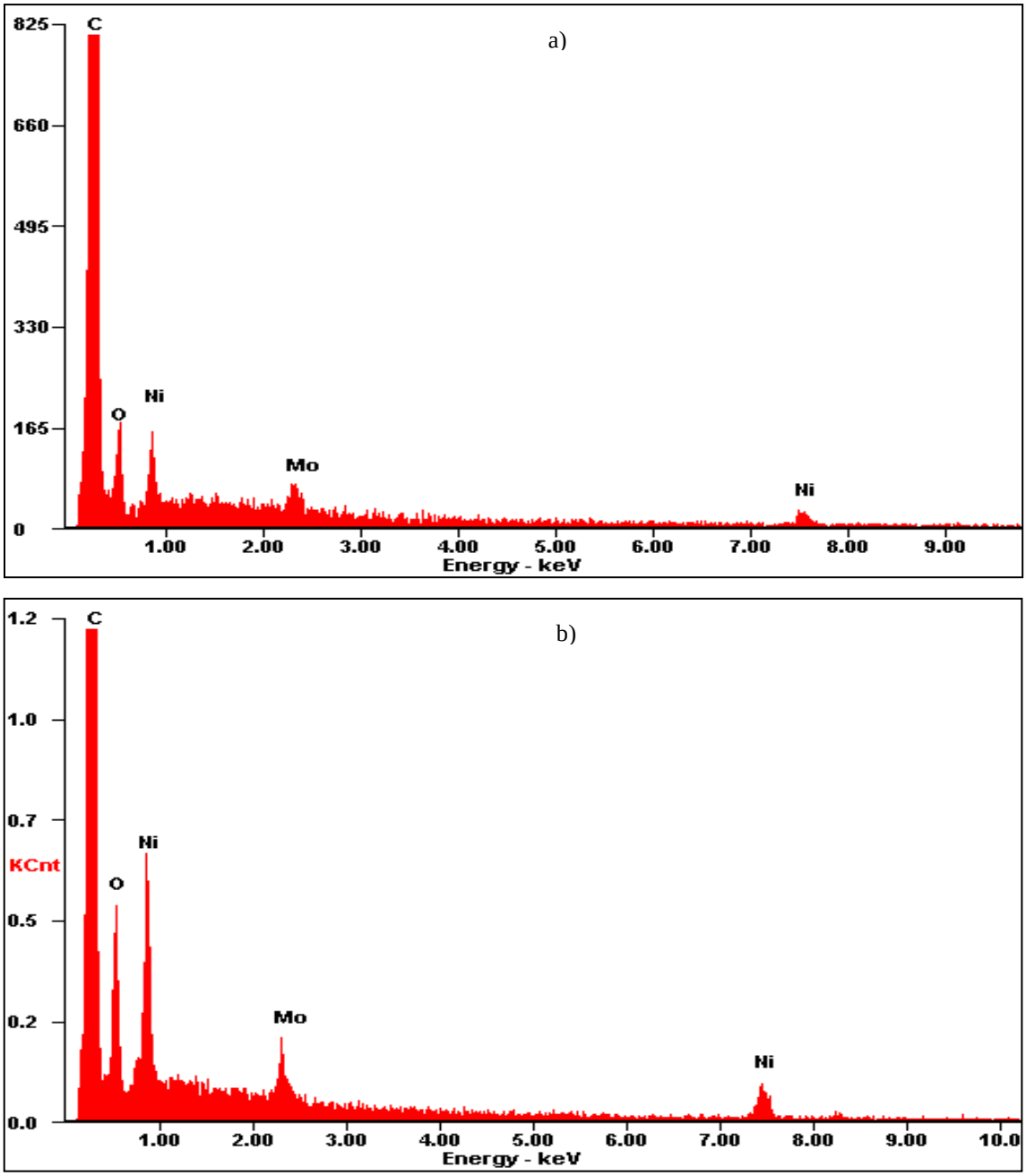

Figure 4. EDXS analysis of electrodeposits fabricated at 15 and 70 mA/cm^2, a) and b), respectively.

EDXS mapping of deposits shown in Figures 3 a) and 3 c), *i. e.* fabricated at 15 and 70 mA/cm^2, respectively, are presented in Figure 5. In Figures 5 a), 5 c) and 5 e) the respective detection of Mo, Ni and O within the deposit obtained at 15 mA/cm^2 is presented; Figures 5 b), 5 d) and 5 f) show the distribution of Mo, Ni and O in the deposit fabricated at 70 m/cm^2. These results suggested a rather uniform composition of the material throughout the sample, in other words, an approximately identical composition is expected at any point. Additional EDXS analyses of deposits fabricated at different current densities are needed to detect compositional heterogeneities throughout the samples and confirm the possible presence and distribution of two different catalytic materials mentioned above. This work, to be

conducted, will be helpful in understanding the role of each material type in the catalytic performance of deposits, as well as the pulsed current conditions at which the deposition of each type is promoted.

The presence of oxygen was evident from EDXS results presented in Figures 4 and 5, and suggested that oxide formation is highly probable. Further EDXS analysis will provide information on the way this oxygen gets incorporated within the electrodeposits, as well as on its role on the catalytic activity of NiMo alloys.

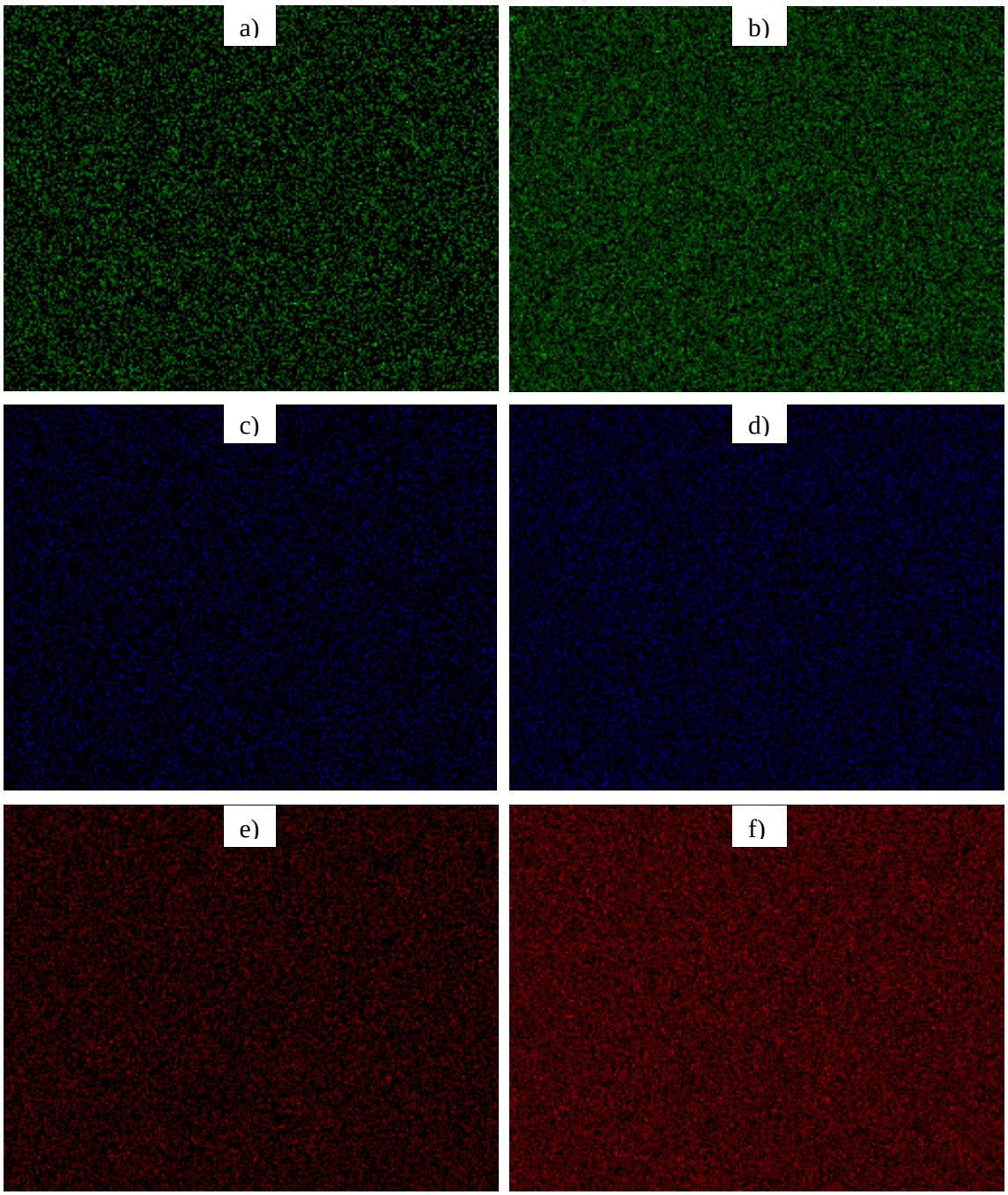

Figure 5. EDXS mapping of electrodeposits fabricated at 15 (a), c) and e) and 70 mA/cm^2 (b), d) and f)). Images a) and b) present Mo distribution within the samples, whereas images c) and d) show Ni detection. O distribution is given by images e) and f).

4. CONCLUSIONS

Electrodeposition of NiMo alloys using a binary electrolyte and current pulses showed the formation of nanoparticles ranging in the size of 30 to 50 nm in diameter. The applied current density did not significantly affect nanoparticle size, when changed from 15 to 70 mA/cm^2. Compositional analysis od deposits indicated a higher Ni content as the intensity of the current pulse was increased; being ~2 wt % at 15 mA/cm^2 and approximately twice as much at 70 mA/cm^2. Mo content was unaffected upon changing the applied current density from 15 to 70 mA/cm^2. Electrodeposits showed compositional uniformity at any point within the sample and further studies are needed to confirm the synthesis of distinct types of catalytic materials suggested by the electrochemical characterization of deposits.

5. ACKNOWLEDGEMENTS

The authors acknowledge the financial support provided by CONACyT through the program Colaboración Interamericana de Materiales (No 101939). The research funding from the Tecnológico de Monterrey, Campus Monterrey through the Research Chair in Nanomaterials (CAT120) is also greatly acknowledged.

6. REFERENCES

[1] N.S. Lewis and D.G. Nocera, PNAS, 103, 15729 (2006).

[2] F. Hernández, C. Rodríguez, J.L. Hernández, Renewable and sustainable Energy Reviews, 14, 772-780 (2010)

[3] D. Gust, T.A. Moore, A.L. Moore, Acc. Chem. Res., 42, 1890-1898 (2009).

[4] W. Hu, Int. J. Hydrogen Energy, 25, 111-118 (2000).

[5] A. Damian, S. Omanovic, J. Power Sources, 158, 464-476 (2006)

[6] S. M. Fernández-Valverde, E. Ordoñez-Regil, G. Cabañas-Moreno, O. Solorza-Feria, J. Mex. Chem. Soc., 54(1), 2-6 (2010).

[7] J. Panek, A. Budnio, Surf. Coat. Tech., 201, 6478-6483 (2006)

[8] P. Kedzierzawski, D. Oleszak, M. Czachor-Janik, Mat. Sci. Eng. A-Struct., 300, 105-112, (2001).

[9] M. Videa, D. Crespo, G. Casillas, G. Zavala, J. New Mat. Elec. Syst., 13(3), 239-244, (2010)

[10] G.Tamayo, Thesis, Chemistry Department, ITESM, Monterrey, Mexico, (2010).

[11] G.Tamayo, D. Crespo, M. Videa, in Proceedings of the XI International Hydrogen Congress, Cuernavaca, Mexico, September 20-23, (2011).

Roadmap for Hydrogen Technology in Urban Public Transport in the Metropolitan Area Of Merida, Yucatan

A.B. Contreras-Terán[1*], J. Fortuna-Espinosa[2], D.V. Ponce-Marbán[1], E. Escobedo-Hernández[1], M.A. Smit[1]

[1.] *Renewable Energy Unit, Yucatan Center for Scientific Research (CICY), Calle 43 No. 130, Col. Chuburná de Hidalgo, 97200 Mérida, Yucatan, Mexico.*
[2.] *Total Energy - Hydrogen Consulting Services, Guillermo Ortega Vargas, Mzna. 3, 25-4, Fracc. los Heroes, Sección II, 50246, Toluca, Mexico.*

Abstract

This work is a first step towards a road map for hydrogen technology in the transport sector in the city of Merida, Yucatan, Mexico. In the case of the Metropolitan Area of Merida (MAM) approximately 34.3 % of the mobility is by public transport, with approximately 750,000 trips and moving 352,262 habitants every day. For this reason, it is important to improve the efficiency of the local transport system, in order to supply the demand with a high quality service. In addition, the public transport system consists of an obsolete fleet of approximately 1,700 units. As a consequence it is generating high operation costs due to maintenance and serious environmental pollution. The local public transport system indeed is one of the major causes of carbon emissions.

In this study it is proposed to replace part of the existing transport system by hydrogen-based technology, in order to achieve a more sustainable public transport infrastructure. This road map includes the selection of a specific route and estimation of the required hydrogen production, from clean renewable energy sources connected to the grid according to the potential of natural resources. Also, the challenges that need to be overcome along the implementation of the hydrogen technology are analyzed. Based on an interpretation of environmental, economical and social benefits, the most adequate chain for production, distribution, storage and conversion of hydrogen, according to the requirements of the MAM and available hydrogen technologies, is being determined. Finally, the economical feasibility for this proposal is determined.

Keywords: Hydrogen technology, Metropolitan Area of Merida, Urban Public Transport.

1. Introduction

Nowadays, sustainable development is one of the global biggest challenges, being at the same time an opportunity to develop new projects. According to the last population census of INEGI (National Institute of Statistic and Geography) the Yucatan state had around of 1,955,577 inhabitants in 2010 and it is expected to reach 2,180,690 inhabitants in 2020 [1, 2].Therefore, it is important to mention that approximately 52.5 % of the population of the Yucatan state is concentrated in the Metropolitan Area of Merida (MAM). The MAM is composed by six municipalities: Progreso, Ucú, Umán, Kanasín, Conkal and Merida [3].In the case of MAM, the transport system is one of the major local pollutants that is currently expanding throughout the city. According to a mobility study approximately 34.3 % of the mobility within the MAM is by public transport [4].

Likewise, according to the department of transport of the Yucatan state, approximately 750,000 trips are made daily by 362,752 habitants every day [5]. In addition, the public transport system consist of 247 routes and approximately 1,700 units that use approximately 51 million gallons of fuel per year and produce 135 kton/day of CO_2 emissions, being a sign of high operating costs and serious environmental pollution [5].

In order to implement a more sustainable public transportation infrastructure that includes hydrogen fuel cell buses, we must produce the energy carrier, hydrogen, from clean renewable energy sources. In this project we analyze the options that the MAM has to put us onto the clean hydrogen pathway, and the challenges that need to be overcome along the implementation of hydrogen technology. Therefore, it is expecting to get the best chains of production, distribution, storage and conversion of hydrogen, according to the potential of the MAM and the available hydrogen technologies options. Likewise, it is expected to determinate the possible environmental and social benefits, as well as the dimension of energy charge for produce hydrogen from renewable sources, in this case specifically from wind and photovoltaic because of the detection of potential areas in the zone of Yucatan, with moderate wind resources of an average 4-6 m/s range [6, 7] and with daily high solar radiation of > 5 kWh/m^2 [8, 9]. Also the region has 4 central powered electricity plants with the capacity of annual electricity production of 7,721,000 MWh [10].

In order to produce clean hydrogen by the separated from water via electrolysis, electricity can be taken from the grid (from a variety of sources) and generated by wind turbines or photovoltaics that feed the hydrogen production facility directly [11].

2. Experimental

The development of this work is based on the information available in data base of several Mexican institutions like SENER, INEGI, SCT, SEDUMA, PEMEX, CFE. The next paragraph describes the methodology followed for this work.

First it has been necessary to describe the characteristics of mobility within the MAM and the structures of the Urban Public Transport (UPT). One specific route was selected for gradual hydrogen bus implementation. Next, available H_2 technologies (H_2 buses and electrolyzers) were analyzed according their technical specifications and local requirements and an estimation of required hydrogen production and electrical energy could be calculated. In order

to determine the implementation strategy an analysis of regional electrical energy resources was performed; and based on the previous information, the emission reduction potential could be determined according to emissions factors of IUPT (International Urban Public Transport): 70 gr/passenger/km for CO_2, 1 gr/passenger/km for CO, 0.5 gr/passenger/km for HC and 0.9 gr/passenger/km for NO_x [12] and the average emission factor of electricity that is 0.4698 tonCO_2eq/MWh [13]. Finally, a cost analysis was realized, based on theoretical costs for different energy sources for the chains of production, distribution and supply of H_2 and others costs taken for direct price quotes. The internal rate of return (IRR) and the net present value (NPV) were determined in order to evaluate the economical feasibility of this work; besides, a sensibility and risk analysis has been made with a variation in 10 % of the cost of economic variables of income and expenditures obtained in this work. Based on the information obtained in the different parts of this project, conclusions are drawn on the technical- economic viability for the implementation of H_2 technology in the UPT in the MAM. The next diagram demonstrates the methodology.

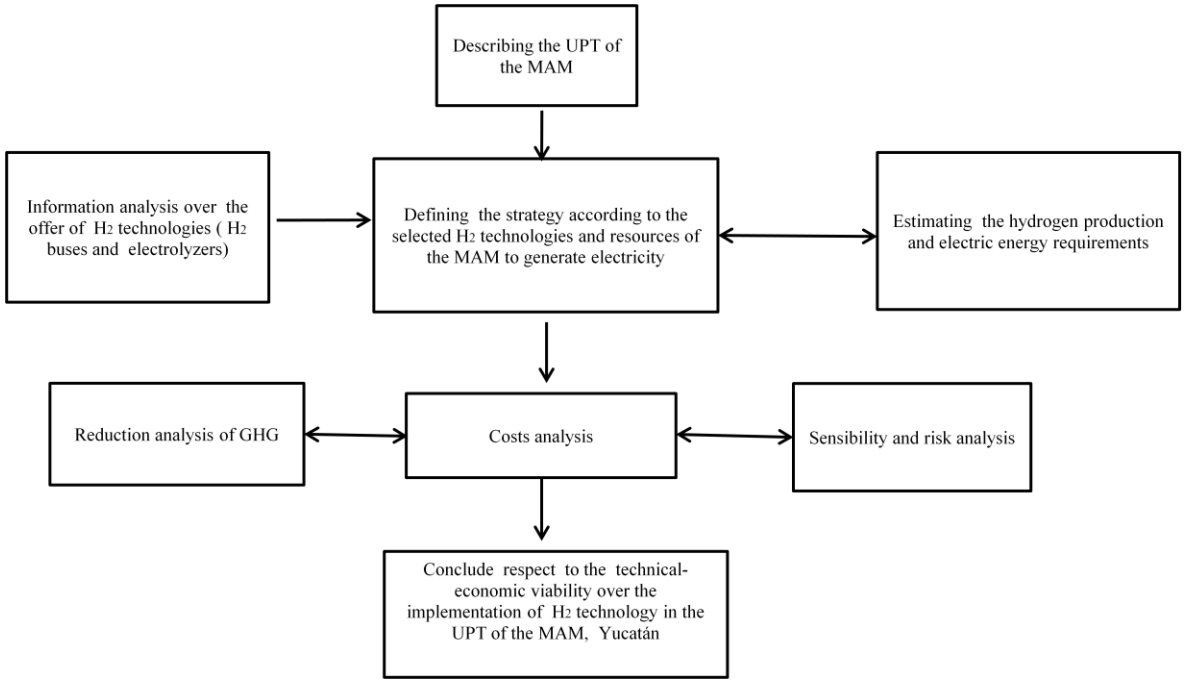

Figure 1. Methodology diagram for the technical-economic evaluation H_2 technology in the UPT in the MAM.

3. Results and discussion

First, it was necessary to define the principal stakeholders that potentially play a role in the implementation of this pilot project, main stakeholders include federal government secretaries like SENER (secretary of energy) and SCT (secretary of communications and transport), state government secretaries such as SEDUMA (secretary of urban development and environment) and DTEY (transport department of the Yucatan state), local transport business

organizations of the MAM, research and educational institutes such as CINVESTAV (Center for Research and Advanced Studies of the National Polytechnic Institute), CICY (Yucatan Center for Scientific Research),UADY (Autonomous University of Yucatan) and ITM (Merida Institute of Technology) and finally national energy companies such as CFE (The Federal Electricity Commission), PEMEX (Mexican Petroleum) , and a number of private companies. Besides it is necessary to obtain financial support of international organizations such as World Bank, NadBank, ONU and governmental organizations; for example, the European Union.

A gradual implementation of H_2 buses is proposed for one specific route for in the UPT based on analysis of the characteristics of the MAM and the available renewable hydrogen technology. The strategy consist in a short time period (2014-2020), for metropolitan circuit route, which circumscribes the city of Merida, is 63 Km long, has a fleet of 40 buses, buses operating 18 hours each day [14]. For H_2 production, electrolysis using renewable energy sources is considered. The estimation of hydrogen production and electrical demand has been estimated according to the characteristics and needs of the electrolyzers system Hystat 60 (Hydrogenics) with a flow rate of 5.5 kg/hr and conversion efficiency of 53.4 kWh/kg [15] and transport model based on the Citaro autobus (Mercedes-Benz), which has an autonomy of 200 km for 35 kg of H_2 [16]. Based on this information, it has been estimated that each H_2 bus will perform 6 full trips per day and needs running 378 km per day requiring 66.15 kg of H_2.

It is considered to introduce 4 H_2 buses in 2014, and increase up to a total of 20 H_2 buses in 2016, 28 H_2 buses in 2018 and 40 H_2 buses in 2020. In order to supply the total H_2 demand for these buses a yearly hydrogen production of 110 H_2 ton/year for 2014 is required 516 H_2 ton/year for 2016, 700 H_2 ton/year for 2018 and 994 H_2 ton/year for 2020. The required yearly renewable energy production is of 7 GWh/year for 2014, 34 GWh/year for 2016, 46 GWh/year for 2018, 65 GWh/year for 2020.The amount of water needed is of 1,752 m^3 for 2014, 8,176 m^3 for 2016, 11,096 m^3 for 2018 and 15,768 m^3 for 2020. Also, it has been determinate the emission reduction from clean fuel is in order of 16 kton/year of CO_2eq , 0.2 kton/year of CO, 0.1 kton/year of HC, 0.2 kton/year of NO_x. The emission reduction from using renewable energy instead of fosil energy for H_2 production is around 31 kton of CO_2eq/year. Therefore, a total yearly GHG (Green House Gases) reduction of 47 kton of CO_2eq can be achieved, as is shown in the figure 2.

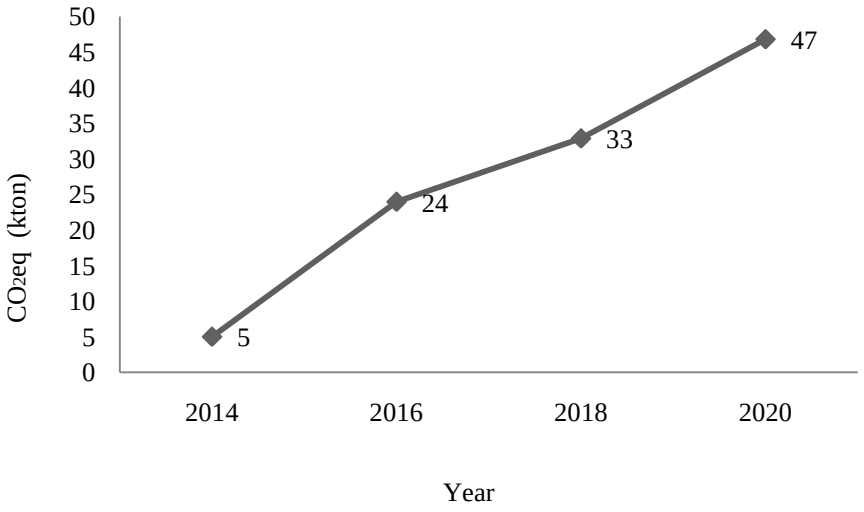

Figure 2. Total CO_2eq avoided emissions for H_2 technology implementation for UPT in the MAM.

Once that the requirements of H_2 production, electrical demand, GHG and pollutants reductions have been estimated; an economical analysis was performed in order to determine which are the most sensitive variables and the economical needs for this technology application. The basic cost calculations are based on theoretical cost of hydrogen production in midsize electrolysis plants, including the initial investment, as well as the variable and fixed costs for the chain of production, distribution and supply of H_2. Different schemes of energy production are compared [11, 17] and the calculated hydrogen cost is of 5.33 USD/kg H_2 for an onsite electrolysis grid power system, 4.26 USD/kg H_2 for an onsite electrolysis wind turbine power system, 4.78 USD/kg H_2 for an onsite electrolysis hybrid wind turbine/grid power system, 7.66 USD/kg H_2 for an onsite electrolysis photovoltaic power system and 5.69 USD/kg H_2 for an onsite electrolysis hybrid solar photovoltaic/grid power system. Besides, apart from direct income from transport users, an additional income from carbon bonds is estimated to be 5 USD for each ton of CO_2 [18]. The cost of water is considered to be 1.01 USD/m^3 in 2014 [19]. The project has been evaluated with a real rate of 7.69 %, considering a minimum acceptable rate of return of 12 % (the rate at which public projects in the Yucatan state are evaluated) and also considering an inflation of 4 %. The amount that the government sector has to provide trough financial mechanisms in order to support the project is indicated in the figure 2. An average amount of 20 million USD a year is needed (actual subsidies for local transport amount to 7,757,952 USD/year).The table 1 indicates in ascendant order the variables that are financially more sensitive and represent a high risk in case of variation and show that the amount of government support is the most sensitive variable, followed by the cost of the fuel cell bus, the cost of H_2 production chain, the price of transport service, carbon bonds and the water cost is the less risk variable. It was noted that in Mexico there is a lack of financial and legal support as well as of norms and standards that stimulate the implementation of clean energy technologies.

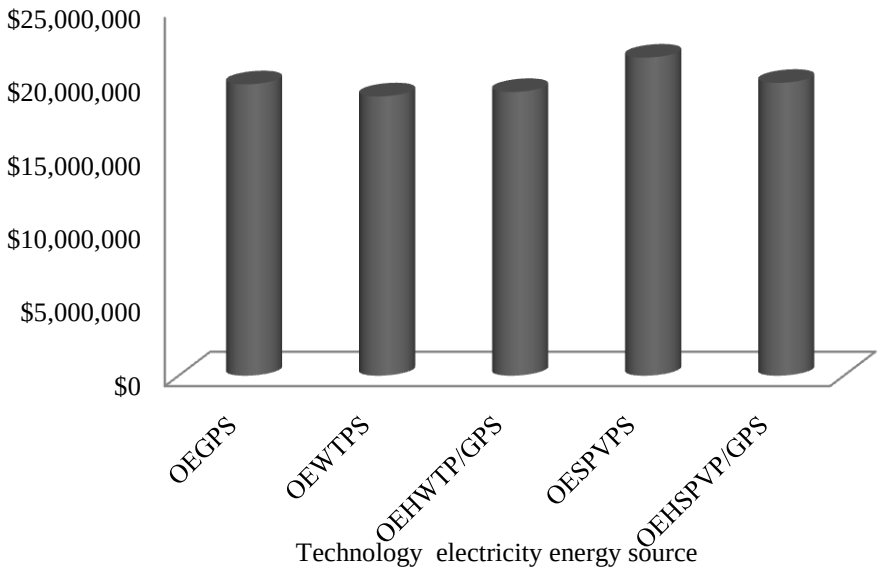

Figure 3. The amount of necessary money by government in order to support the H_2 technology implementation for UPT in the MAM.

Table 1. Results of sensitive analysis for different energy sources technologies.

.

	OEGPS		OEWTPS		OEHWTP/GPS		OESPVPS		OEHSPVP/GPS	
Variable	IRR (%)	NPV(USD)	IRR (%)	NPV(USD)	IRR (%)	NPV(USD)	IRR (%)	NPV(USD)	IRR (%)	NPV(USD)
Governmental economic support	33.51	10,413,009	30.12	9,981,094	31.77	10,138,546	37.21	11,368,312	33.79	10,464,491
Cost of Citaro Fuel Cell Bus	26.25	7,178,907	24.05	7,178,907	25.17	7,178,907	28.21	7,178,907	26.41	7,178,907
Cost of H_2 Chain	15.02	1,994,943	12.60	1,559,040	13.76	1,778,955	18.77	2,835,332	8.42	127,569
Price of Transport service	12.37	1,106,568	11.37	1,106,568	11.84	1,106,568	13.71	1,106,568	12.46	1,106,568
Carbon Bonds	7.87	31,445	8.05	92,074	8.11	92,074	8.50	92,074	8.21	92,074
Water costs	7.66	-5,820	7.67	-5,820	7.66	-5,820	7.63	-5,820	7.66	-5,820

4. Conclusions

A gradual implementation of hydrogen technology in public transport was proposed for one specific route in Merida, and energetic, environmental and economic requirements were determined.

It can be concluded that H_2 bus implementation in Merida is technically and sustainably viable. However, according to the sensitivity and risk analysis, it is necessary to obtain financial support, from governmental funds and international collaborations.

5. Akcnowledgements

The authors thank financial support from CONACyT, project 116157.

6. References

[1] Proyección poblacional del Estado de Yucatán. www.conapo.gob.mx. (mayo 2011).

[2] INEGI. Censo de Población y Vivienda 2010. www.inegi.com.mx. (mayo 2011).

[3] Zona Metropolitana de Mérida (PDF). Delimitación de las zonas metropolitanas de México 2005. Instituto Nacional de Estadística y Geografía. www.inegi.com.mx. (mayo 2011).

[4] Estudio integral de vialidad y transporte urbano para la ciudad de Mérida, Yucatán, informe ejecutivo, Hueltron, S.A. de C.V; año 2002. (SEDESOL, Gobierno del Estado de Yucatán y Ayuntamiento de Mérida 2001-2004). http://www.mda.cinvestav.mx/oumid/HTML/Indicadores/4_MANEJO%20AMBIENTAL_HTML/IE11_RESUMEN.html.(mayo 2011).

[5] Dirección de Transporte, Secretaria General de Gobierno, Gobierno del Estado de Yucatán. Programa de modernización del transporte público de la ciudad de Mérida transporte responsable. 2009.

[6] National Renewable Energy Laboratory, International Wind Resource Maps. U.S. Department of Energy. http://www.nrel.gov/wind/images/mexico-yucatan-windmap.gif, (septiembre 2011).

[7] Soler-Bientz Rolando, Preliminary results from a network of stations for wind resource assessment at North of Yucatan Peninsula. Energy 36, 1 (2011), pp. 538-548.

[8] Proyecto Tech4CDM en México, La Energía Solar Térmica en México, Unión Europea. http://www.tech4cdm.com/uploads/documentos/documentos_La_Solar_Termica_en_Mexico_6e00ee9f.pdf. 2009.

[9] Aguilar - Fraga Alain, Caracterización de la energía eléctrica fotovoltaica en las condiciones ambientales del norte de la ciudad Mérida Yucatán. Tesis de maestría, Centro de Investigación Científica de Yucatán, Posgrado en Energía Renovable, 2011.

[10] Dirección General de Planeación Energética, SENER; Prospectiva del Sector Eléctrico 2009-2024; México, http://www.energia.gob.mx/res/PE_y_DT/pub/Prospectiva_electricidad%20_2009-2024.pdf, (2009).(octubre 2011)

[11] National Research Council. "Front Matter". The Hydrogen Economy: Opportunities, Costs, Barriers, and R&D Needs, The National Academies Press, Washington, DC. ISBN 0-309-09163-2 (Book), ISBN 0-309-53068-7 (PDF), (2004).

[12] Racero Moreno Jesus. Planes de movilidad urbana ll jornada de movilidad sostenible, Mérida, 9 febrero 2010. http://www.meridasostenible.org/jornadas/Jornadas_Movilidad/II%20jornada/Racero_Merida.pdf.(mayo 2011)

[13] Programa GEI México, Asociación de Técnicos y Profesionistas en Aplicación Energética (ATPAE). Estimación del factor de emisión eléctrico para inventarios de emisiones corporativas de GEI, Factor de emisión eléctrico, (2008).

[14] Mapa de la ruta del Circuito Metropolitano. http://www.merida.gob.mx/transporte/descargas/circuito_metro.zip, (octubre 2011)

[15] Hydrogenics, Advanced Hydrogen Solutions, Catalogo en Español de estaciones de servicio HySTAT, http://www.hydrogenics.com/hydro/brochure/IndustrialBrochure_SP/files/assets/downloads/publication.pdf (septiembre 2011).

[16] Technical Data Citaro Fuel CELL Hybrid http://www2.mercedesbenz.co.uk/content/unitedkingdom/mpc/mpc_unitedkingdom_website/en/home_mpc/bus/home/new_buses/models/regular_service_busses/citaro/FuelCELL_Hybrid.html.(junio 2011).

[17] Busby Rebecca L. Hydrogen and Fuel Cells a comprehensive guide, PennWell, USA. Appendix E. 445 p. ISBN 1-59370-043-1, (2005).

[18] Instituto Nacional de Ecología. El sector privado y el cambio climático, http://cambio_climatico.ine.gob.mx/sectprivcc/mercadobonoscarbono.html. (marzo 2012).

[19] Junta de agua potable y alcantarillado de Yucatán, Tarifas de agua año 2012 en Mérida. http://www.japay.yucatan.gob.mx/tarifas/index_tarifas.php. (abril 2012)

Effect of Sb- Doped SnO_2 Supports Heat Treatment on the Oxygen Evolution Reaction

V. Ávila-Vázquez[1], J.C. Cruz[2], M. Galván-Valencia[1], J. Ledesma-García[3], L.G. Arriaga[2], S. M. Durón-Torres[1,*]

[1]UACQ, Universidad Autónoma de Zacatecas, Campus Siglo XXI-Edificio 6, Zacatecas, 98160, México
[2]Centro de Investigación y Desarrollo Tecnológico en Electroquímica, Parque Tecnológico Querétaro, Sanfandila, Pedro Escobedo, 76703, México.
[3]División de Investigación y Posgrado, Facultad de Ingeniería, Universidad Autónoma de Querétaro, Cerro de las Campanas, Querétaro, 76010, México.
[*]Tel: 4929256690 ext 6130, mail: duronsm@prodigy.net.mx

ABSTRACT

It has been recognized the role of supports in electrocatalysis as a way to increase both specific activity and lifetime of electrocatalysts. Due its stability, some doped SnO_2 supports could be used as an alternative to carbon black in PEM water electrolysis. In this work, IrO_2 catalyst was mixed in a colloidal mini-mill with SnO_2 supports doped with antimonium (ATO) in a fixed proportion (50:50 wt %) and the mixtures were used as anode material for Oxygen Evolution Reaction (OER). ATO supports were obtained by reaction between Sn and Sb chloride precursors in alcoholic medium at moderate temperature, followed by an annealing procedure at 500 °C and different times of treatment (between 3 h and 15 h). The electrodes were evaluated in terms of OER by Linear Scan Voltammetry (LSV) and Electrochemical Impedance Spectroscopy (EIS) techniques. Electrokinetic parameters as Tafel Slope and Exchange Current Density for OER were obtained as a function of the different annealing times material support. Furthermore, the Charge Transfer Resistance (Rct) for oxygen evolution obtained from the Nyquist impedance spectra was compared. Although the LSV results showed a similar behavior for the OER of the several electrodes studied, the EIS analysis presented some distinctive Rct values for the electrodes assayed. The electrodes that showed minimum Rct values corresponded to those prepared with supports of 3 and 12 h of annealing time. These results could suggest that the ATO conductive properties depend strongly on the time of thermal treatment of the oxide in the synthesis procedure.

1. INTRODUCTION

In recent years, new technologies are being developed for energy generation in a clean, efficient and sustainable way. The fuel cells (FC), water electrolyzers (WE) and the unified regenerative fuel cells (URFC) that combines FC and WE in a single unit, represent viable options for electrochemical hydrogen production and power generation in an environmental friendly way. Although some of these devices are now commercially available, problems about the cost, availability and performance of catalysts and supports remain as the principal drawbacks of the hydrogen electrochemical energy conversion systems. The electrochemical reactions of oxygen: oxygen reduction reaction (ORR) and the oxygen evolution reaction (OER) usually are the slowest reactions in FC, WE and

URFC, representing thus limiting factors for these devices developing. In this sense, an important number of studies are currently dedicated to promote the electrochemical reactions of fuel cells and electrolyzers mainly based on the research and developing of new effective electrode and support materials for oxygen reactions [1-9].

Although it is commonly acknowledged the use of noble metals as catalysts in FC and WE, it has been found that Pt and other electrocatalytic metals show a better performance in the ORR than in the OER, presenting a high overpotential for the oxygen evolution. It has been noted that the oxides of Ir and Ru, and their combination with other metals; produce materials that are more convenient for OER catalysts. By the other side, despite of that the Vulcan coal and others carbonaceous materials show a well behavior as catalytic supports in FC, the high electrical potential used in an electrolyzer corrodes them, producing degradation of carbon material and a loss of electrical contact. Consequently, the research studies in electrochemical devices besides of finding catalysts with an activity enough for both oxygen reactions are focused in obtain support materials with the sufficient stability and electronic conductivity required in the anodic conditions of a WE [10, 11].

In the FC a potential near of 1 V vs. ENH is reached at the operation conditions, while in the WE is necessary to apply a potential proximate to 1.6 V vs. ENH for splitting the water into H_2 and O_2. An oxygen electrode in a URFC operates alternatively at these two potential values, so that it is not advisable to use Vulcan carbon as support for the preparation of electrodes. The main disadvantage is that the operation with high potentials promotes the degradation of coal, limiting the electron transfer when a URFC operates mainly in the fuel cell mode. For this reason it is necessary to find an alternative support, which must be stable to a high potential of operation and it provides a higher electrical conductivity for the reactions of the oxygen electrode [12, 13].

Tin oxides have been used as transparent conductive films in liquid crystal displays, photodetectors, solar cells, gas sensors and protective films [14-17]. Recent studies have shown that the doped ceramic materials with a conductive material, as is the case of ATO, means a new field in the study of the electrode supports science [18-20]. The ATO has characteristics of high resistance to corrosion in acid media and when it is doped with conductive species as Sb^{5+}, its electrical conductivity increases to 10^2 or 10^3 Ω^{-1} cm^{-1}. Studies indicate that the ATO could be used as catalyst support for OER in WE, being reported an improvement in the stability of the support as compared with an undoped oxide, in the conditions of oxygen evolution [18, 21]. Recent researches indicate that the characteristics of micro-structural and the nano-metric size of the ATO both depend strongly on the heat treatment of oxide in the stages of synthesis and the relative amount of doping agent [19].

This paper shows the preliminary results of the study of the OER kinetics of an IrO_2 catalyst supported on ATO. The catalytic materials composed of IrO_2 with ATO obtained at different times of heat treatment (between 3 h

and 15 h) were used to evaluate the dispersibility of catalyst and kinetic parameters as Tafel slope and transfer charge resistance respect to OER in acid medium. The study was based in the electrochemical techniques of cyclic voltammetry (CV), linear voltammetry (LV) and electrochemical impedance spectroscopy (EIS).

2. EXPERIMENTAL SECTION

2.1 Synthesis of antimony doped tin oxide (ATO)

ATO supports were obtained by reaction between Sn and Sb chloride precursors in alcoholic medium at moderate temperature, followed by an annealing procedure at 500 °C and heat treatment times of 3 h, 6 h, 9 h, 12 h and 15 h. The supports prepared by this procedure are denoted as ATO (nh) where n means the number of hours of thermal treatment.

2.2 Electrochemical characterization

2.2.1 Electrodes preparation

The electrodes were prepared from a catalytic ink comprising 90 µL of Nafion ® (5 wt. %, Aldrich), 540 µL of ethanol spectroscopic grade, 6 mg of IrO_2 and 6 mg of ATO. The ink was obtained using a FRITSCH/PULVERISETTE 23 mini-mill for a period of 0.5 h in order to homogenize the mixture and promote dispersion of the ink. Later, the resulting suspensions were hold in an ultrasonic bath for 0.5 h in aim to gain additional dispersion of mixture. Subsequently, a volume of each ink was deposited on a clean polished glassy carbon disk electrode (GCE) (A = 0.07068 cm^2). The coated GCEs were dried in a furnace at 80°C for 10 min. In order to comparison a Pt supported on ATO (3h) electrode and IrO_2 supported on Vulcan carbon electrode were used Finally, IrO_2 and Pt films supported on ATOs were used as working electrodes for the OER kinetic studies. All the current values reported in this paper are normalized to the electrode geometric area.

2.2.2 Electrochemical characterization of electrodes

All the experiments were performed in a double-compartment electrochemical glass cell. An Hg/Hg_2SO_4/0.5 M H_2SO_4 (ESM = 0.69V vs. NHE) electrode was used as reference which was positioned as close to the working electrode as possible by means of a Luggin capillary. A Pt-mesh was used as counter-electrode and the aqueous electrolytic medium was 0.5 M H_2SO_4 at room temperature. The electrochemical measurements were performed using an EG&G PAR VersaSTAT 3 Potentiostat/Galvanostat. In this study, all measured values of potential are reported respect to the normal hydrogen electrode (NHE).

Cyclic voltammetry (CV) was carried out to evaluate the effect of different ATO in the IrO_2 or Pt electrodes by scanning the potential at a rate of 50 mV s^{-1} between -0.16 V and 1.54 V under a N_2 atmosphere electrolyte solution. Oxygen evolution experiments were performed by linear scan voltammetry (LSV) at a scan rate of 5 mV s^{-1} in the anodic direction from 0.59 V to 1.69 V in O_2-free electrolyte solution at a constant electrode rotation frequency of 1000 rpm. The rotation rate was controlled by a PINE MSRX precision rotating system.

In addition, electrochemical impedance spectroscopy (EIS) experiments were carried out in the potentiostatic mode in the 100 kHz to 10 mHz frequency range. The impedance spectra were registered with a logarithmic data collection scheme at 10 steps per decade at 1.57 V of potential with alternate signal amplitude of 10 mV.

3. RESULTS AND DISCUSSIÓN

3.1 Evaluation of the supports by cyclic voltammetry

Figure 1 shows cyclic voltammograms obtained for IrO_2 supported on ATOs in N_2 saturated 0.5 M H_2SO_4 solution. The CV diagrams reveal that the electrochemical response for IrO_2 is practically unchanged with the use of different ATO as support. Also is showed that the current density (j) attributed to IrO_2 supported on ATO (3h) and ATO (9h) are greater than the rest of the ATOs, this enhancement may be considered evidence that the dispersion of IrO_2 is improved with the use of this supports. The off-peak potential for oxygen evolution on all the IrO_2/ATO electrodes appears near to 1.45 V, although on the ATO(3h) and ATO(9h) supported electrodes the onset was about 50 mV more negative than the rest of ATOs as showed in Figure 1.

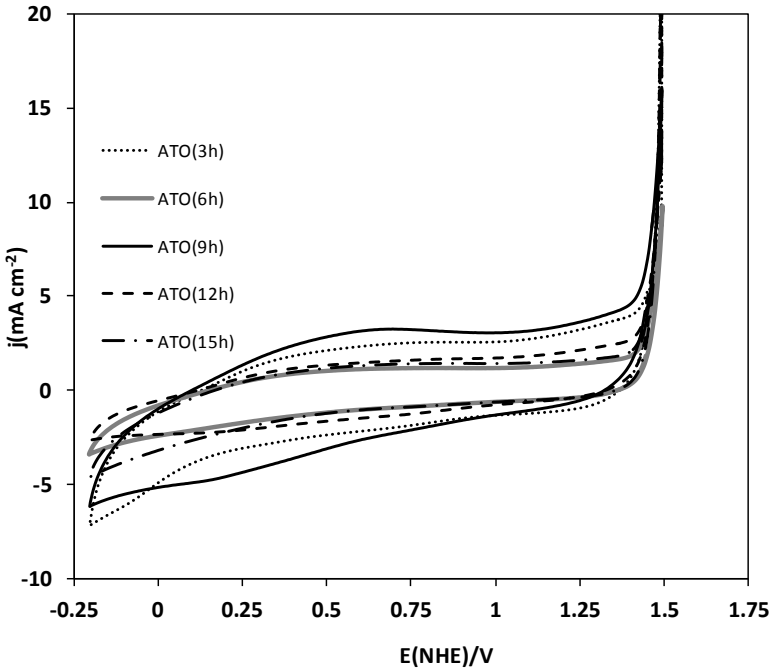

Figure 1. Cyclic voltammograms of GCEs coated with IrO_2/ATOs (with different heat treatment times: 3h, 6h, 9h,12 h, 15h) in 0.5 M H_2SO_4 at 50 mV s-1. 50 wt % IrO_2/ATOs, with atmosphere: N_2 and room temperature.

The Figure 2 compares the cyclic voltammograms obtained for IrO_2 and Pt supported on ATO (3h) and IrO_2 supported on Vulcan carbon in N_2 saturated 0.5 M H_2SO_4 solution. The CV of Pt supported on ATO (3h) shows that the reactions associated with the surface of Pt in an acid medium are limited by the support, avoiding identify the characteristic peaks of Pt on a clearly way [22], nevertheless the general electrochemical behavior in acid medium of platinum is still outlined in the voltammogram. The voltammograms corresponding to IrO_2 catalyst show broad waves corresponding to the redox reactions over the Ir surface, these waves are more evident when Vulcan is used as support. In the voltammograms of Figure 2 also can be observed that the potential onset for oxygen evolution in the Pt/ATO electrode appears near to 1.7 V, while the corresponding oxygen evolution peaks of IrO_2/ATO and IrO_2/C electrodes appear at potential values about 300 mV more negative.

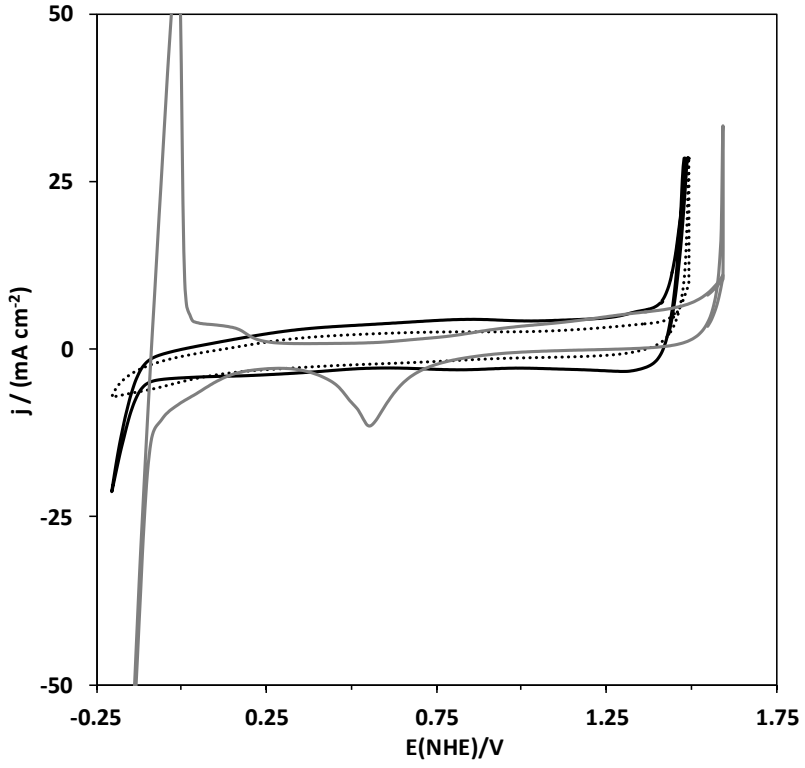

Figure2. Cyclic voltammograms of IrO_2/ATO (3h) (….), Pt/ ATO (3h) (dashed line) and IrO_2/C (solid line) electrodes in N_2 satured 0.5 M H_2SO_4 at 50 mV s^{-1}.

3.2 Oxygen evolution activity of the IrO_2 supported on ATO

The Figure 3 shows linear scan voltammograms for OER with IrO_2 support on ATO (with different heat treatment times: 3h, 6h, 9h,12 h, 15h) in 0.5 M H_2SO_4 at a scan rate of 5 mVs^{-1}. Since the IrO_2 catalyst used in the electrode preparation was the same in the different mixtures, and the proportion catalyst-support was maintained fixed in a 50:50 weight percent ratio, the voltammograms displacement observed in Figure 3 indicate that the OER depend on the ATO annealing times used in the electrodes. It is observed that the OER begins in a potential near to 1.45 V when the IrO_2 is supported on ATO (3h) and ATO (12h), while that for the IrO_2 supported on other ATO the EOR onset occurs near to 1.5 V. It is means that EOR is facilitated when ATO 3h or 12h annealed is used as support for IrO2. As a consequence, the higher current densities are obtained when the ATO (3h) and ATO (12h) are used as supports for EOR. In Table 1, the values of current density obtained at a potential of 1.57 V corresponding to the different IrO_2/ATO electrodes studied, are showed.

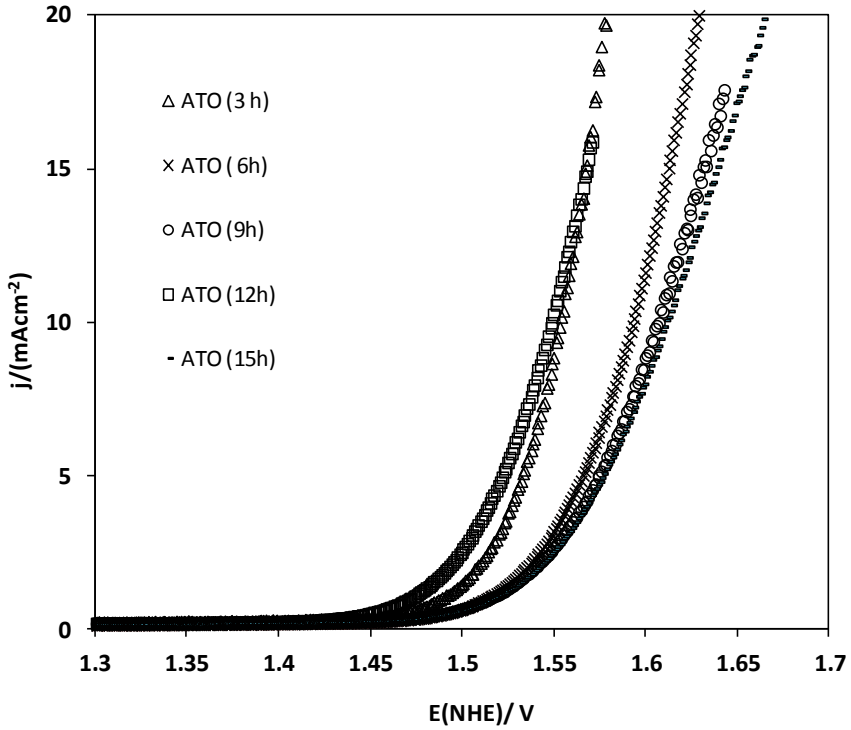

Figure 3. Linear scan voltammograms for OER of IrO_2/ATO (with different heat treatment times) electrodes in N_2 satured 0.5 M H_2SO_4 at ν=5 mVs^{-1}.

In Figure 4 the linear scan voltammograms for OER with IrO2 supported on ATO (3h) and IrO_2 supported on carbon are shown [23]. In order to comparison the voltammogram corresponding to EOR on Pt/ATO (3h) is included. It can be observed that the oxygen evolution occurs in a potential about 100 mV more negative when the IrO_2 is supported on carbon respect to the onset OER potential obtained with the IrO_2/ATO (3h) electrode. This little difference in overpotential could be put sideways in considering the disadvantage of carbon supports that suffer an easy corrosion at the high potentials used in the electrolysis process. Then the IrO_2 supported on ATO (3h) and finally Pt supported on ATO (3h). In Figure 4 also can be seen the poor catalytic activity of Pt for OER.

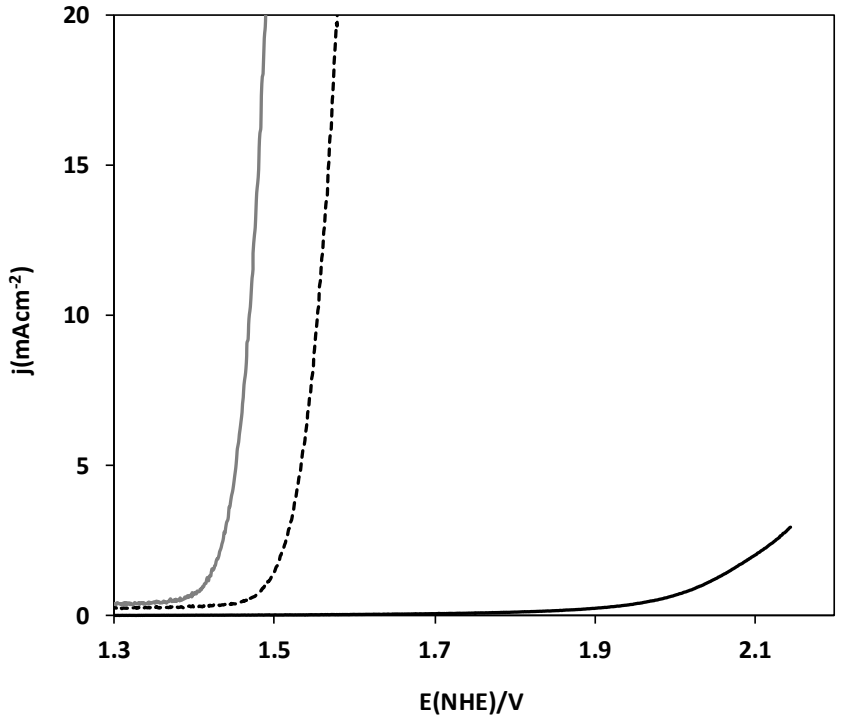

Figure 4. Linear voltammograms for OER on IrO_2/ATO (3h) (-----), Pt/ ATO (3h) (solid line) and IrO_2/C (dashed line) electrodes in N_2 satured 0.5 M H_2SO_4, at ν=5 mVs^{-1}.

Tafel plots were obtained from LSV curves for OER after ohmic drop (IRs) correction due to the electrolyte resistance (Rs). This correction was done by subtracting the IR to the applied potential [24]. The R_s-values were obtained by electrochemical impedance spectroscopy (EIS) for each electrode. R_s values were in the 3 Ω – 7.5 Ω interval which are mainly attributed to a combined resistance between the solution resistance and the electrode film resistance. Figure 5 shows the Tafel curve for OER on IrO_2 supported on ATO (3h) electrode after IR correction, a Tafel slope (*b*) value of 62 mV dec^{-1} was obtained. A value close to 60 mV dec^{-1} has been observed for OER on some metal oxides in the low overpotential region (η_{low}) [25, 26], for this slope value has been proposed the following mechanism [27]:

$$OH_{ads} \rightarrow O^{-}_{ads} + H^{+} \quad (1)$$

$$O^{-}_{ads} \rightarrow O_{ads} + e \quad (2)$$

$$O_{ads} + O_{ads} \rightarrow O_2 \quad (3)$$

Being the reaction limiting step (rls) for the oxygen evolution process, the reorganization of the oxygen-species over the surface Ec. (1) before transfer of the first electron. Similarly to the graph shown in Figure 5, Tafel were plots obtained for each of the support under study, showing similar Tafel slope values. These results are presented in Table 1.

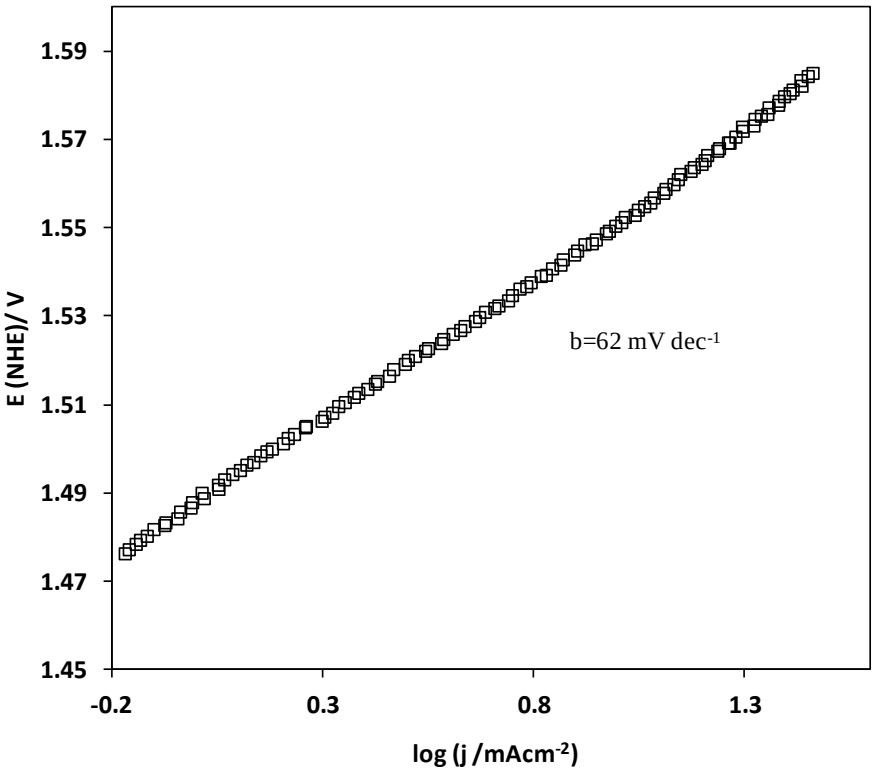

Figure 5. Tafel Plot for OER for IrO_2/ATO (3h) after IR correction.

Figure 6 shows a comparison of Tafel curves for OER on IrO_2/ATO (3h), IrO_2/ATO (15h) and IrO_2/C electrodes after IR correction. In the potential interval shown, some Tafel curves exhibit two linear slopes related with changes in the EOR kinetic mechanism, in this case the Tafel slope data at high overpotential (η_{high}) show values close to 120 mV dec^{-1}. These results indicate a change in mechanism where the rls is the first transfer electron in the electrolysis of the water molecule. In Figure 5 this behavior is clearly observed for IrO_2/ATO (15h) and IrO_2/C electrodes. The two Tafel slope behavior in OER has been observed in other metal oxide electrodes. The similar values of *b* observed in the IrO_2/ATO and IrO_2/C electrodes, could mean that the OER mechanism is the same in both supports and that the oxygen evolution is developed mainly on the Ir surface.

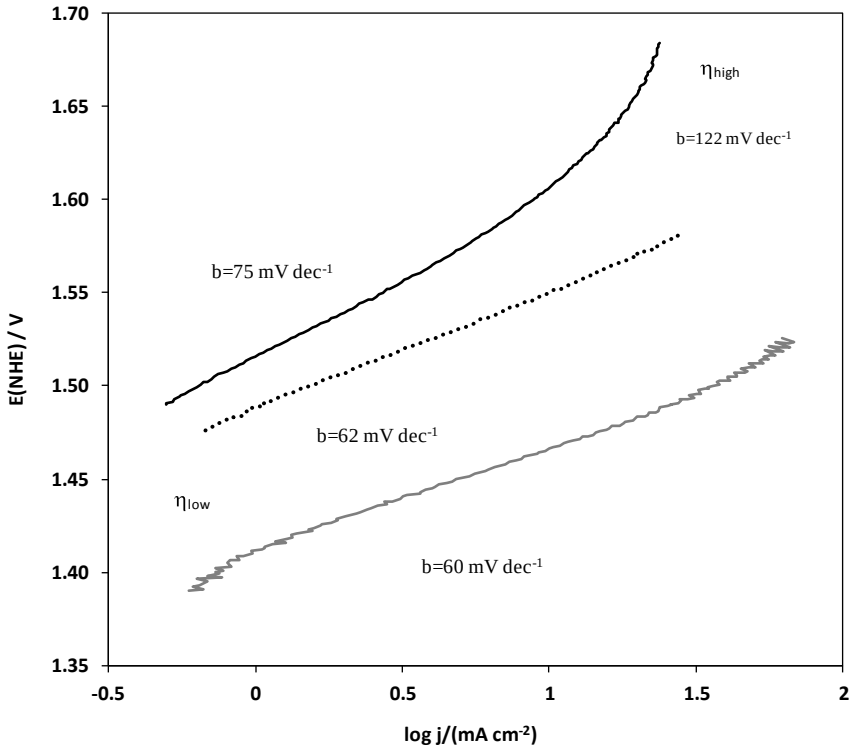

Figure 6. Tafel Plots comparison for OER on IrO_2/ATO (3h) (…..), IrO_2/ATO (15h) (solid line) and IrO_2/C (dashed line) after IR correction.

3.3 Electrochemical impedance spectroscopy performance for OER

EIS measurements for oxygen evolution was carried out on IrO_2/ATO electrodes in O_2-free 0.5 M H_2SO_4 solution, in the potensiostatic mode at an anodic potential of 1.57 V. Figure 7 shows the Nyquist plots for OER on IrO_2 supported on ATO. The depressed semicircles presented in Figure 7 were adjusted by a CNLS fitting to the following equivalent circuit [28]:

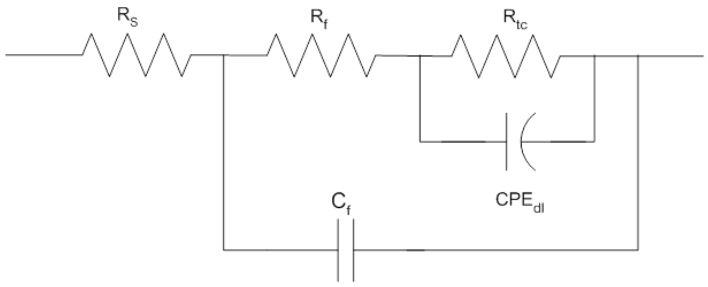

Where R_S is the electrolytic solution resistance, R_f and C_f the resistance and capacitance of the film of catalyst/support/Nafion system, and R_{tc} the resistance of charge transfer associated with the OER in parallel with CPE_{dl} the constant phase element corresponding to the impedance of a double layer over an heterogeneous material electrode surface [28]. The values of R_S and R_{tc} calculated for the IrO_2/ATO electrodes are resumed in Table 1 along with other OER kinetic parameter values.

In consistency with the LSV results, the Nyquist plots of Figure 7 show that OER is faster when the IrO_2 is supported on ATO (3h), followed by supporting on ATO (12h) as can be seen by their smaller semicircles in the complex impedance plane. In contrast, the ATO (15h) support shows the bigger Rtc value (c.a. 577 Ω) that means the slowest reaction rate for oxygen evolution on the support materials studied in this work. The rest of ATO supports obtained at other heat treatment times showed intermediate Rtc values.

With the results of this study it was not possible to explain the non-linear behavior obtained for the annealing times of ATO preparation effect on the OER catalytic activity obtained over the IrO_2/ATO electrodes.

Table 1. Onset potential and kinetics parameters for OER on IrO_2/ATO electrodes in O_2 free 0.5 M H_2SO_4.

	E_{OER} (NHE)/V	*j* /(mA cm^{-2}) @ 1.57 V	Rs / Ω	Rct / Ω @ 1.57 V	b / (mV dec^{-1})	
					η_{low}	η_{high}
IrO_2/ATO(3h)	1.5	16.2	4	42	62	-
IrO_2/ATO(6h)	1.55	5.7	3	230	68	-
IrO_2/ATO(9h)	1.55	4.5	3.5	321	78	120
IrO_2/ATO(12h)	1.5	15.8	7.5	184	65	-
IrO_2/ATO(15h)	1.55	4.5	4.5	577	75	122
IrO_2/C	1.41	-	4.1	284 @ (1.49V)	60	-
Pt/ATO(3h)	2	-	6.8	1050 @ (2V)	-	-

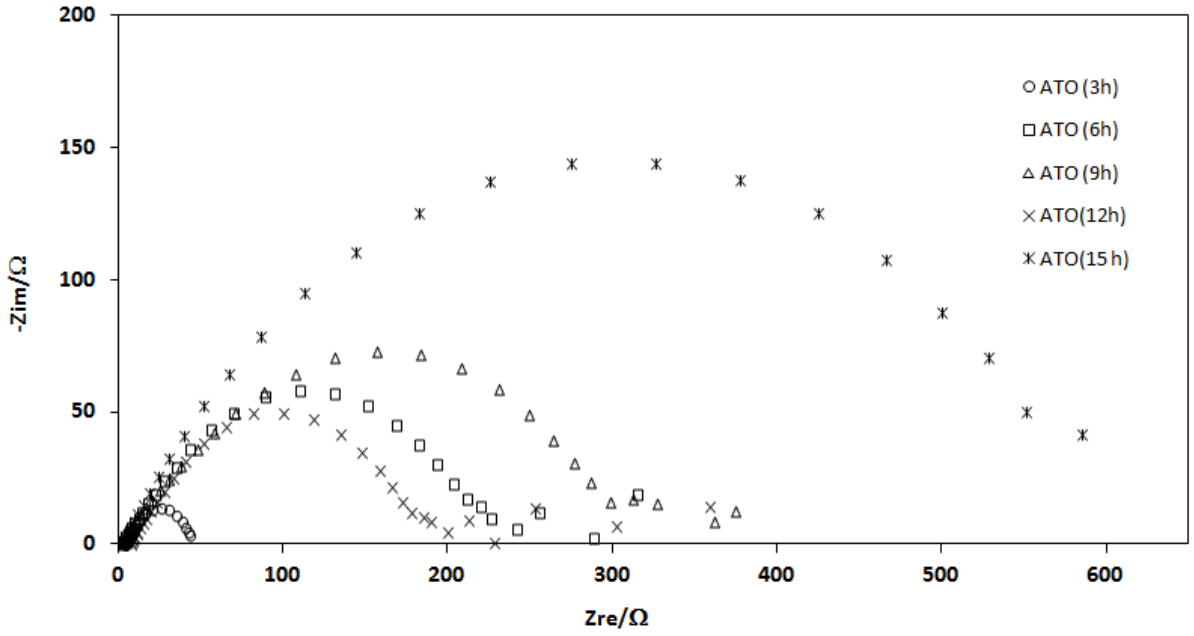

Figure 7. Nyquist plots for OER on IrO_2 /ATO electrodes at anodic potential value of 1.57 V, in O_2-free 0.5 M H_2SO_4 solutions

4. CONCLUSIONS

Electrochemical studies were performed for the OER on IrO_2/ATO electrodes. The OER was assessed using the ATO with different heat treatment time as support. The results show that the catalytic activity of the electrocatalyst depend on the annealing time of ATO supports, the best behavior corresponding to ATO (3h) followed by the ATO(12h) one. Further characterization of ATO is necessary to explain the non-linear behavior of thermal times respect to its performance as a support for the OER.

The study has showed that the Sb-dopped SnO_2 (ATO) is a promising supports for WE and URFC. The OER onset potential of IrO_2 on ATO is near to observed on the Vulcan carbon, this could mean that the electronic conductivity and catalyzer dispersion properties are similar in both support materials.

5. ACKNOWLEDGMENTS

The authors wish to thank the mexican CONACyT (Project 167012) for financial support of this work.

6. REFERENCES

[1] M. Momirlan, T. N. Veziroglu, Int. J. Hydrogen Energy, 30, 795 (2005).

[2] F. Barbir, Solar Energy 78, 661 (2005).

[3] A. Marshall, B. Borresen, G. Hagen, M. Tsypkin, R. Tunold, Energy, 32, 431 (2007).

[4] G. Chen, S. R. Bare, T.E. Mallouk, J. Electrochem. Soc. 149, A1092 (2002).

[5] S.D. Yim, W.Y. Lee, Y.G. Yoon, Y.J. Sohn, G.G. Park, T.H. Yang, Ch. S. Kim, Electrochim. Acta, 50, 713 (2004).

[6] S.Song, H.Zhang, X.Ma, Z.Shao, Int. J. Hydrogen Energy, 33, 4955 (2008).

[7] Y. Zhang, Ch. Wang, N. Wan, Z. Mao, Int. J. Hydrogen Energy 32, 400 (2007).

[8]L. H. Franzen, J. E. Vilt, and D. C. Johnson, J. Electrochem. Soc., 4, 141, (1994).

[9]E.Gileadi, Electrode Kinetics for Chemists, Chemical Engineers, and Materials Scientist, VCH Publishers, Ed John Wiley & Sons 51 - 52, (1993).

[10]J. Ma, S. Sui, Y. Zhai, J. Power Sources , 177, 470, (2008).

[11]V. Rashkova, S. Kitova , T. Vitanov, Electrochim Acta, 52 ,3794 (2007)

[12]B. L.García, R.Fuentes, J. W.Weidner, J.Electrochem. Soc., 10, B108 (2007)

[13] J. P. Meyers, R. M. Darling, J. Electrochem. Soc., 153, A1432, (2006)

[14]M.I.B. Bernardi, C.M. Barrado, L.E.B. Soledade, E.R. Leite, E. Longo, J.A. Varela, J. Mat. Science, 13, 403 (2002)

[15] J. Santos-Peña, T. Brousse, L. Sánchez, J. Morales, D.M. Schleich, J. of Power Sources, 97, 232 (2001).

[16] V. K. Yatsimirskii, N. P. Maksimovich, A. G. Telegeeva, N. V. Nikitina, and N. A. Boldyreva, Theoretical and Experimental Chemistry, 41:3, 187 (2005).

[17] R. Subasri , T. Shinohara, Electrochem. Comm. 5, 897 (2003).

[18]A. T. Marshall, R. G. Haverkamp, Electrochim. Acta, 55, 1978 (2010).

[19] X. Wu, K. Scott, Int. J. of Hydrogen Energy, 36, 5806 (2011).

[20] M. Manesse, R. Sanjines, V. Stambouli, R. Boukherrou, S. Szunerits, Electrochem. Comm. 10, 1041 (2008)

[21]F. Vicent, E. Morallón, C. Quijada, J. L. Vázquez, A. Aldaz, F. Cases, J. App. Electrochem., 28, 607 (1998).

[22]S. Gilman and D. Chu in Handbook of fuel cells: Fundamentals, technology and application. Ed. W. Vielstich, A. Lamm and H. A. Gasteiger, Vol. 2, p. 652. Ed. John Wiley & Sons, New York (2003).

[23]I.L. Escalante-García, S.M. Durón-Torres, J.C. Cruz y Arriaga- Hurtado L.G., Proceedings of the XXIV meeting of the Mexican Society of Electrochemistry, Paper 105, Puerto Vallarta, Jal, México, May 31 – June 5, 2009.

[24]J.M. Hu J.Q. Zhang, Ch.N. Cao, Int. J. Hydrogen Energy, 29, 791 (2004).

[25] J. C. Cruz , V. Baglio, S. Siracusano, V. Antonucci , A. S. Aricò, R. Ornelas, G. Osorio-Monreal, L. Ortiz-Frade, S. M. Durón-Torres, L. G. Arriaga, International Journal of Electrochemical Science, **6**, 6607 6619 (2011).

[26] I.L. Escalante García, S.M. Durón Torres1, J.C. Cruz, L.G. Arriaga Hurtado, J. New Mat. Electrochem. Systems, 13, 227 (2010).

[27]E. Guerrini and S. Trasatti. Electrocatalysis in Water Electrolysis in Catalysis for Sustainable Energy Production (eds. P. Barbaro and C. Bianchini), Wiley-VCH, Weinheim, pp.235 (2009).

[28] I. D. Raistrick, D. R. Franceschetti, J. R. Macdonald. The Electrical Analogs of Physical and Chemical Processes in Impedance Spectroscopy Theory, Experimentand Aplications (Eds. E. Barsoukov, J.R. Macdonald), JohnWiley & Sons, New Jersey, (2005).

Fuel Cell Stack Prototype Used to Power a LED's System

R. González Huerta[1*], A. Martínez Reyes[2], O. Solorza Feria[3], C. Cortés Escobedo[4], G. Contreras Puente[5], M. Tufiño Velázquez[5], A. Avila Trejo[6], C. Varela Colmenares[6]

[1]ESIQIE-IPN, Laboratorio de Electrocatálisis, UPALM, CP 07738 México, D.F.
[2]ESIME-IPN, Av. de las Granjas 682 Col. Sta. Catarina Del. Azcapotzalco-México, D.F.
[3]CINVESTAV-IPN, Depto. de Química, C.P. 07360 México, D.F.
[4]CIITEC-IPN, Cda. Cecati s/n, CP 02250 México, D.F.
[5]ESFM-IPN, Departamento de Física, UPALM, CP 07738 México, D.F.
[6]SOLERGIA S.A de C.V, Escuadrón 201-50, CP 07330 México, D.F.

[**]email: rosgonzalez_h@yahoo.com.mx

ABSTRACT

Petroleum supply will be in increasingly higher demand as heavily populated developing countries expand their economies and become more energy intensive. Air quality and global climate impact are other major concerns with this continuing dependence on fossil energy sources. Widespread use of hydrogen as an energy source in Mexico could help address concerns about energy security, global climate change, and air quality. Fuel cells is an important enabling technology for the hydrogen future and it has the potential to revolutionize the way we power our nation, offering cleaner and more efficient alternatives to supply energy than fossil fuels. In this work, a fuel cell stack prototype was designed and manufactured with three single assemblies to power a LED's system. The combination of anode/membrane/cathode is referred to as the membrane/electrode assembly, MEA. The three MEA's were prepared by placing the gas diffusion electrode (GDE, standard carbon cloth with 0.5 $mg_{Pt}\cdot cm^{-2}$), at both sides of the Nafion 115 membrane, followed by hot-pressing of 10 $kg\cdot cm^{-2}$ at 120 °C for 2 min. The effective area for each single MEA was 28 cm^2 being 84 cm^2 the total anodic and cathodic geometric area. The MEA's were tested with a commercial fuel cell system (Compucell GT, Electrochem) at 25 °C and atmospheric pressure. The performance achieved was a 2.7 V open circuit voltage, achieving a 7.4 W peak power, the optimum performance is at 2 V–2 A. The lamp was integrated by 16 LED's connected in parallel.

Keywords: Prototype, fuel cell stack, LED's system.

1. Introduction

The world now faces tremendous challenges associated with pollution, greenhouse gas emission, climate change and the need for a sustainable development. Providing reliable, environmentally friendly, and affordable energy has been a goal for many countries throughout the world. The rising consumption of energy and falling accessibility of natural resources are increasing the cost of electricity. Therefore, renewable energy has received more attention recently. Solar radiation is considered the most preferred renewable energy source for its availability and inexhaustibility [1]. However, due to the sporadic characteristics of natural resources, it has been a challenge to generate a highly reliable power with photovoltaic (PV) modules [2]. To overcome this limitation, previous studies were conducted using a fuel cell as another energy source and simulated results showed that a PV/fuel cell hybrid power system may be a feasible solution for standalone applications [3-5]. Since a multi-source hybrid power system increases energy availability in a significant way [6-7]. Fuel cells is an important enabling technology for the hydrogen future and it has the potential to revolutionize the way we power our nation, offering cleaner and more efficient energy supply alternatives than fossil fuels.

Production of hydrogen from renewable energy resources has the potential to bring a local energy solution. Water electrolysis is an attractive option to generate renewable hydrogen and oxygen with solar energy without any purification process and is one of the most important energy related electrochemical processes, because water is an inexhaustible natural resource and hydrogen a renewable non-polluted energy source [1-5]. Water electrolysis is a proven method for continuous production of hydrogen by converting electrical into chemical energy. Conversely, a fuel cell is an electrochemical cell which can continuously convert the chemical energy stored in a fuel into electrical energy. The launching of hydrogen and fuel cell technology in the market is now the starting block of renewable energy technology. There are no barriers to the introduction of hydrogen and fuel cells either from a technological perspective or from a safety point. Hydrogen has been produced and utilized in industry for over a hundred years [2], and can be produced by a number of different sources using a variety of techniques. When hydrogen is produced from coal, oil or natural gas, the by-products will be harmful to the environment if they are not handled in an environmentally reliable way. In this work, a stack fuel cell prototype was designed and manufactured with three single assemblies to power a LED's system. The three membrane-electrodes assemblies MEA's were prepared by placing the gas diffusion electrode (GDE, standard carbon cloth with 0.5 mg_{Pt} cm^{-2}), at both sides of the Nafion 115 membrane.

2. Experimental

The objective of the fuel cell stack design was to be simple, self-contained, and to achieve optimal performance with respect to size. The complete system includes the fuel cell stack and the LED's system. However, it is not included in the system design the hydrogen storage device, neither the hydrogen fuel pressure regulator nor the electronics system. A fuel cell consists of several components; these must be machined according to established design. Each

part of the fuel cell is very important and can help to optimize the operating conditions, providing a better performance.

2.1 Bipolar plates

The fuel cell used at the present study was designed and in-home built by our research group. Bipolar plates, BPs, being one of the most important components in PEMFC stacks, must perform a number of functions in order to achieve good stack performance and lifetime. BP supply the reactant gases through the flow channels to the electrodes and serve the purpose of electronically connecting one cell to another in the electrochemical cell stack. These plates also provide structural support for the thin and mechanically weak MEAs and means to facilitate water management within the cell. Plate topologies and materials facilitate these functions. Topologies can include straight, serpentine, or interdigitated flow fields, internal manifolding, internal humidification, and integrated cooling. Therefore, optimal design must be sought for the BPs because the above functions have conflicting requirements on the BP design. The essential requirements for BPs, in respect to physicochemical characteristics, are: a uniform distribution of the reactant gases over the respective active electrode surface to minimize the overpotential concentration; high values of electronic conductivity for current collection; high mechanical strength for stack integrity; impermeability to reactant gases for safe operation; resistance to corrosion in severe cell environment for long lifetime; cheap materials, easy and automated fabrication for low cost. One of the main obstacles to large-scale commercialization of fuel cells is the gas flow fields and BPs, including the development of low-cost lightweight construction materials, optimal design and fabrication methods and their impact on PEMFC performance (i.e., energy efficiency and power density). As much as 50% increase in the output power density has been reported [7] just by appropriate distribution of gas flow fields alone. In spite of all the group efforts, the time-effective design and optimization of the gas flow fields and BPs remain one of the important issues for the cost reduction and performance improvement of PEM fuel cells. As to the geometrical configurations of the gas flow fields, a variety of different designs are known and the conventional designs typically comprise either pin, straight or serpentine designs of flow-field channels [1,7].

In this work, two flow field designs in AUTOCAD were done, horizontally, straight and parallel flow field and transverse, straight and parallel flow field. The flow fields design influences the fuel cell performance and can help to optimize the operating conditions on the reagent area, providing a better distribution of gas over the diffuser and exits the water in a more efficient way. It should be noted that the design of the flow fields is limited to the machinery that is type of specialized tools to work with sufficient accuracy. The current collector plate material was low porosity graphite, in order to avoid mixing of the gases and it is resistant to corrosion, high pressures and moderate temperatures. The machined current collector plates with flow fields was performed on a CNC milling machine CNC EMCO Concept MILL 55 mark, especially for graphite. At this stage monopolar and bipolar plates were fabricated.

2.2. Membrane electrode assemblies

The MEAs have an active area of 28 cm^2 providing a total active area of 84 cm^2 for the entire fuel cell stack. The MEAs were selected based on both the characteristics of performance and simplification of the system design. The electrolyte used was Nafion® N-115 type ionomer membrane. The catalyst loadings on the anode and cathode side were 0.2 mg Pt/cm^2. A carbon cloth type gas diffusion layer was used for both the anode and cathode sides of the MEAs. The MEAs were tested with a commercial fuel cell system (Compucell GT, Electrochem 890B) in a single cell rig with 5 cm^2 active geometrical area. The gas pressures (gp) at the anode and cathode sides were kept at 30 psi for H_2 and 34 psi for O_2, respectively. The fuel cell test station was operated with high purity H_2 and O_2 at 100 cm^3 min^{-1}. The temperature of the humidified reactant gases was kept 5 ºC above the temperature of the cell. The performance was measured under steady-state conditions at 25 ºC and atmospheric pressure.

2.3. Current collectors

The current collectors used are constructed out of 0.36 mm thick plates of high conductivity brass alloy machined with a guillotine. Also included with the current collectors are two tabs per collector, which are used for attaching power leads and voltage sensing leads for testing.

2.4. End plates

The endplates of the fuel cell stack consist of two 1 cm thick aluminum sheets with a 12-hole bolt pattern designed to accept M3 type fasteners. The end plate located on the anode side, or the fuel inlet side, of the stack contains two ports for hose fittings to supply each of the cells with hydrogen. Two ports were included instead of one because it allows the cell to be purged of water and air.

2.5. Gaskets/sealing

Due to the effusion characteristics of hydrogen, a significant amount of study and focus was required for the design of sealing the fuel cell stack. In order to prevent hydrogen from leaking from the gas inlet fittings to the mani-folding in the bipolar plates an “x-ring” was placed between the fittings, through the current collector, and to the first flow channel plate. An x-ring type seal was used as it provides more points of contact than an o-ring giving a better probability of a good seal. In order to prevent hydrogen from leaking from the perimeter of the flow channel plates, two separate gaskets were used. A 0.04 mm was placed around the perimeter of the flow channel plate on the anode side of each cell. A 0.02 mm Teflon gasket was used to provide sealing on the cathode side of the flow plates to prevent hydrogen crossover and to protect the Nafion of the MEAs from damage.

3. Results and discussion

Figure 1 shows the two flow field designs; horizontal, straight and parallel flow field, figure 1(a) is better than transverse, straight and parallel flow field, figure 1(b). Because of the fabricating horizontally channels is easier than transverse and efficiency is nearly the same.

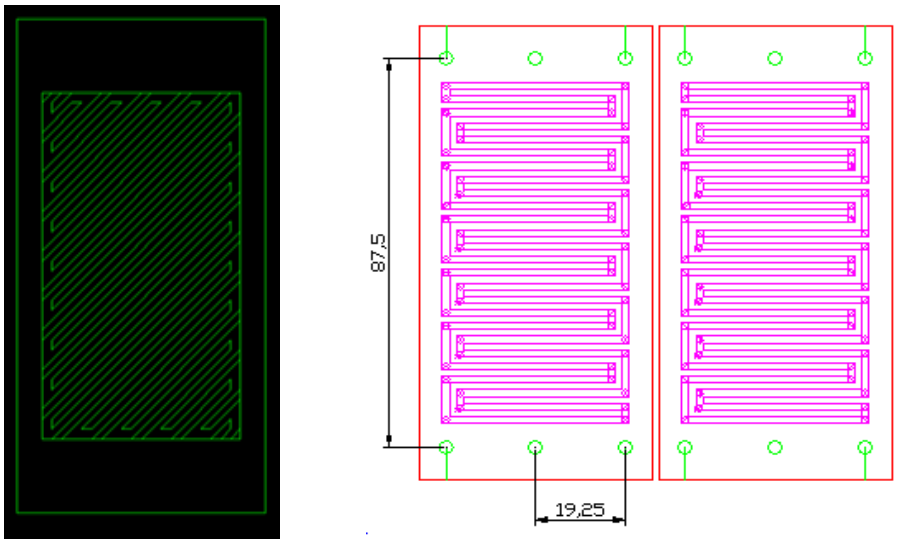

Figure 1 Variation of configuration in straight or parallel flow field design

When the reactant flow channels are formed on the anode and cathode plates, the plates are normally referred to as fluid flow-field mono-polar plates. When the flow channels are formed on both side of the same plate, one side serves as the anode plate and the other side as the cathode plate to the adjacent cell, and the plate is called bipolar (separator) plate.

The primary compartments of the PEM fuel cell have are shown in figure 2. Advantages of fuel cells in comparison with other type of equipments which produce energy are: higher efficiency, no existence of mobile parts and as a result lack of sonic pollution, no emissions of environmental polluting gases such as SOx, NOx, CO2, CO, among others. On the opposite side, the main disadvantage of fuel cells is their high cost, but it is expected that this problem will be solved by applying the new technologies and mass production of these fuel cells.

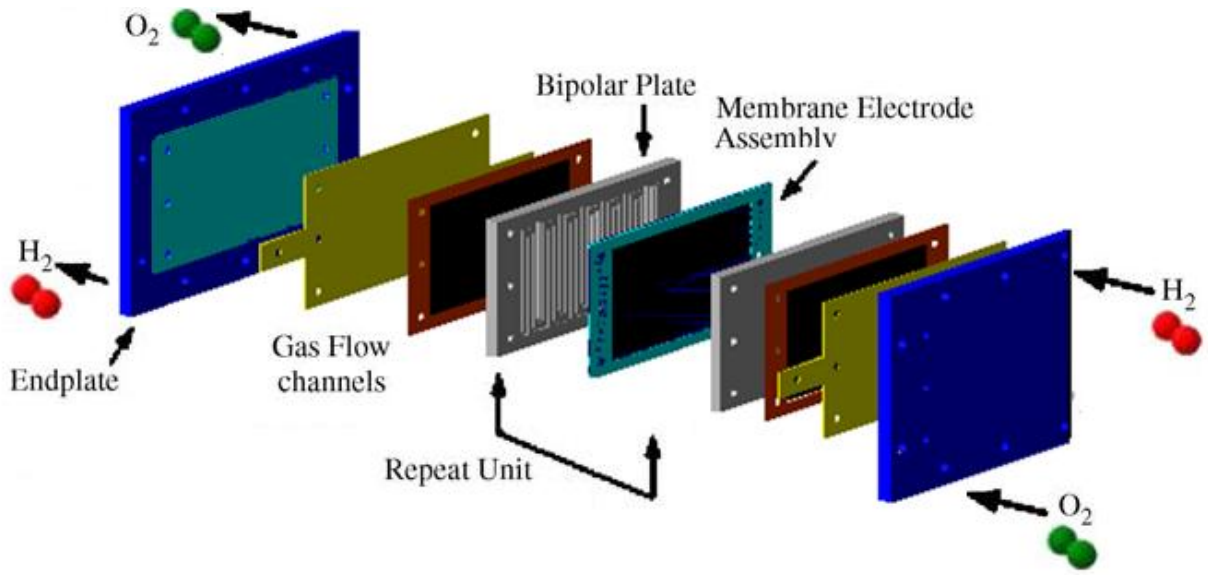

Figure 2. Stack components of fuel cell

The hydrogen feeded fuel cell stack designed in this project contains three individual cells, each having a 28 cm^2 active area. The three cells are stacked in a series configuration with current collectors placed on the anode and cathode sides. An image of the CAD model used for fuel cell stack design is show in figure 3. The components considered in the volume size restriction are the endplates, current collectors, bipolar plates, all sealing materials, and the membrane electrode assemblies (MEA). The components not included in this volume are the fasteners, hose fittings, and the current collector tabs. The dimensions of these components are 114.5 mm x 63 mm x 45 mm when the stack is fully assembled and compressed. Images of the fuel cell stack are shown in figure 4.

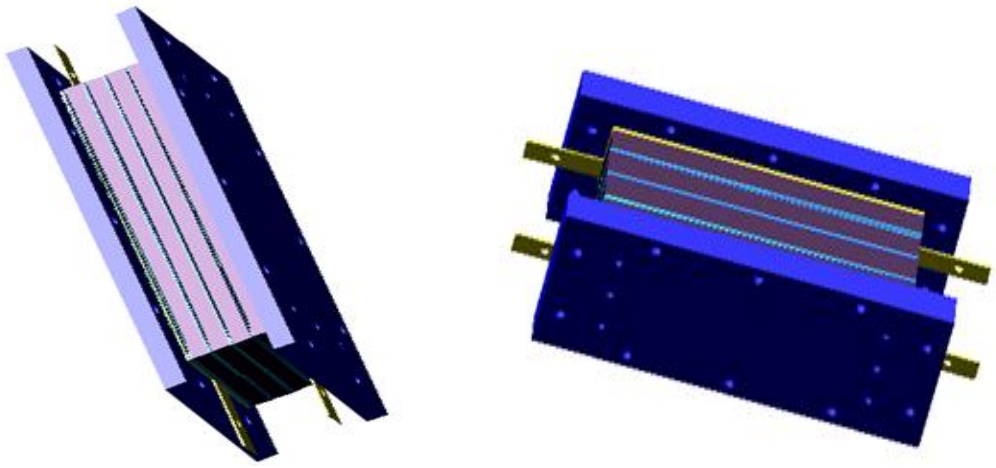

Figure 3. CAD model used for fuel cell stack design.

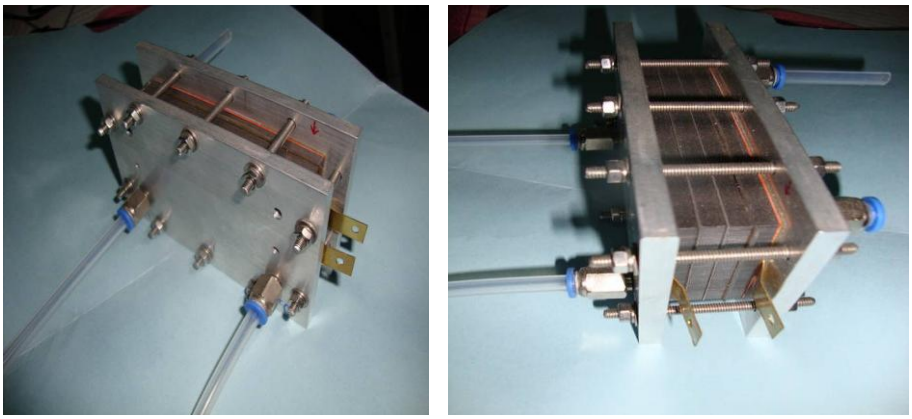

Figure 4. Images of PEM Fuel Cell Stack.

In the fuel cell the chemical energy of the stored in hydrogen is converted to electrical energy. Figure 5 shows the performance (cell voltage-current-power) of the stack containing MEAs with 0.2 mg Pt/cm^2 on anode and cathode catalyst. The fuel cell was tested with a commercial fuel cell system (Compucell GT, Electrochem), without pressure and flow rate of 100 cm^3 min^{-1} of both gases at cell temperature of 25 °C.

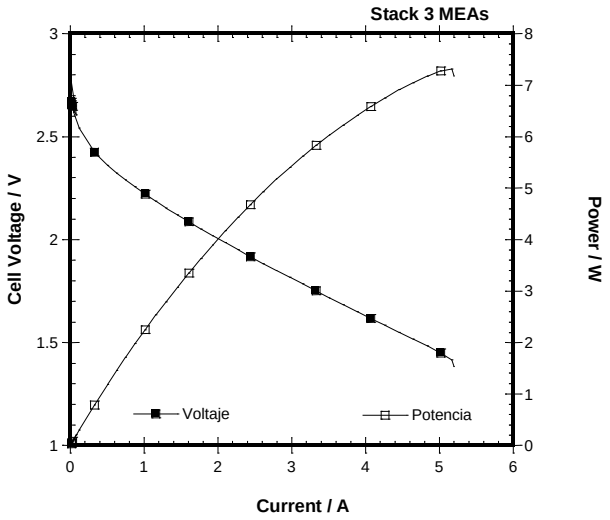

Figure 5. H_2/O_2 fuel cell stack performance curves at 25 °C.

The open-circuit potential is 2.8 V lower than the reversible potential of 3.69 V. This behavior is attributed to the crossover of hydrogen from the anode to the cathode sides and also to a mixed potential that results from the galvanic currents in the oxygen electrode, which is caused by platinum oxidation. At low overvoltage low current arises due to the slow kinetic rate of the oxygen reduction. In the intermediate current the transfer of the conductive

protons from the anode to the cathode is predominant. The global power output under hydrogen and oxygen saturation conditions from figure 6 is 2 A and 4 W evaluated at 2.0 V. Figure 6 shows the picture of the integrated fuel cell connected to the LED's system.

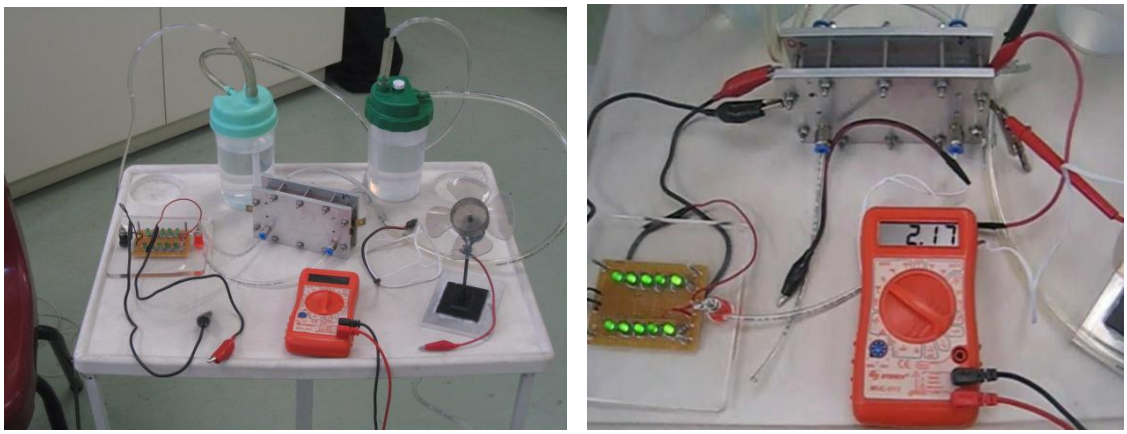

Figure 6. Images of the fuel cell system in operation.

4. Conclusions

A PEM fuel cell system was designed, constructed, and experimentally tested, which has a continuous power output of 4 W and a peak power output of 7 W. This fuel cell was coupled to a LED's systems.

The next stage of this project is to scale up the fuel cell to power a 50 W LED's system. The results of testing and analysis reveal that significant improvements can be made to future designs to greatly improve performance and efficiency. The polarization curve of the fuel cell indicates significant concentration losses at higher power densities which also reduce the efficiency of the fuel cell. The fuel cell is also the greatest contributor to power loss in the entire system. Therefore, the most significant improvements can be made from a more efficient design of the cathode flow channel geometry and the use of a more efficient and a more properly sized cell stack?. Further, a controller power could be used to increase the efficiency of the power electronics. This would reduce the amount of fuel consumed when the fuel cell system is at idle and when operating at low power output.

5. Akcnowledgements

This work was partially supported by the Instituto de Ciencia y Tecnología del Distrito Federal-México (ICYTDF) in the Project "Desarrollo de celdas de combustible tipo PEM para la iluminación de bajo consumo energético" under grant number PIEMP 11-31 and in the Multidisciplinary Project IPN-SIP 1338.

6. References

[1] Frano Barbir, *PEM Fuel Cells: Theory and Practice*, 1-429, Ed. ELSEVIER (2005).

[2] W. Vielstich et al, *Handbook of Fuel Cells, Fundamental Technology and Aplications*. Vol 2-3, John Wiley, England, (2003).

[3] K. Suárez Alcántara, O. Solorza Feria, *Fuel Cells*, 10, 84. (2010)

[4] A. Rodríguez Castellanos, E. López Torres, O. Solorza Feria, *J. Mex. Chem. Soc.*, 51, 55 (2007).

[5] K. Suárez Alcántara, A. Rodríguez Castellanos, O. Solorza Feria, Rev. Int. Contam. Ambient., 24, 183 (2008).

[6] Kristopher Inman, Zakaria Ahmad, Zhongying Shi, Xia Wang, Int. J. Hydrogen Energy 36 13868 (2011).

[7] Xianguo Li, Imran Sabir, Int. J. Hydrogen Energy 30 359 (2005).

9th International Symposium on New Materials and Nano-Materials for Electrochemical Systems
XII International Congress of the Mexican Hydrogen Society
Merida, Mexico, 2012

Evaluation and Comparative Analysis of Pt-Mo/C Catalysts Synthesized by Different Methods for Application as Anodes in Direct Methanol Fuel Cells

O. Ugalde Reyes [1], P. Roquero [1*], R. Hernández Maya [1],
A. L. Ocampo Flores[1], E. Sosa Hernández [2], C. Ángeles Chávez[2].
[1] Facultad de Química. Universidad Nacional Autónoma de México. Avenida Universidad 3000. México D.F. CP 04510
[2] Instituto Mexicano del Petróleo. Eje Central Lázaro Cárdenas 152. México D.F. CP 07730
[*]Phone: (5255) 5622 5363, e-mail contact: roquero@unam.mx

ABSTRACT

It has been found that Pt-Mo catalysts can play an important role in direct methanol fuel cell systems. This activity is explained by some authors in terms of different mechanisms such as the bifunctional mechanism, the ligand effect, the hydrogen spillover effect and it has also been proposed a physical blocking effect of some Pt sites by Mo species. In this work, constant composition materials $(Pt_{0.8}Mo_{0.2})_{0.25}/C_{0.75}$ were synthesized in two different ways, in order to have different surface structures and to compare their activities towards methanol oxidation. The first catalyst consists of two active phases (Pt and Mo) simultaneously deposited on the carbon support. The second catalyst is obtained by the synthesis of monometallic materials (Pt/C and Mo/C) that are mixed and vigorously stirred in suspension, in diethyl ether.

Monometallic and bimetallic materials were synthesized by a carbonyl thermolysis method using, as precursors, molybdenum hexacarbonil ($Mo(CO)_6$) and hexachloroplatinic acid (H_2PtCl_6) and using Vulcan XC-72 carbon as support. The synthesized materials were studied by cyclic voltammetry and current-sampled voltammetry tests to evaluate their activities. X-ray diffraction and transmission electron microscopy were carried out in order to determine the relationships between the active phases.

1. Introduction .

Platinum is recognized as the most active catalyst for the oxidation reaction of methanol and, so far, it has been indispensable in the formulation of such materials. However, the formation of different organic intermediates during the methanol oxidation reaction, which are adsorbed on the surface of Pt, cause metal poisoning, reducing its efficiency as a catalyst. Previous studies indicate that the modification of the Pt catalyst with other transition metal lead to interesting results in the methanol oxidation at low potential (lower than in pure Pt) [1]. Some studies suggest that the presence of metal oxides at the catalyst surface can supply oxygen-containing species, promoting the removal of CO (which is the major contaminant) and other organic species adsorbed at Pt sites [2.3].

It is well known that bimetallic materials showed increased activity in the electro-oxidation reaction of CO, yielding CO_2. This activity is explained by some authors in terms of the so-called bifunctional mechanism whereby the formation of reactive species containing oxygen takes place at lower potential than in pure Pt, promoting the complete oxidation of CO [2.3]. However, other researchers propose that it is an electronic effect (or binder) [4], responsible for the increased activity. In this case, the presence of a second metal modifies and weakens the bond Pt-organic species so that the adsorption energy of CO on these materials is different [4]. Other theories suggest the existence of a hydrogen spillover effect. In this phenomenon, a proton (H^+) migrates from a Pt site to form metallic bronzes in the promoting phase and leaving Pt active sites available for adsorption of a methanol molecule [5]. Moreover, it has been suggested that, by modifying the surface of a Pt catalyst with metallic molybdenum and MoO_3 species the chemisorption of CO on the surface of Pt (110) can be suppressed due to a physical partial blocking effect of Pt sites by molybdenum, allowing the presence of free active sites for the oxidation reaction and preventing the adsorption of CO at the crystaline platinum plane in which it most strongly adsorbs [6].

Currently the most widely used catalysts to direct methanol fuel cells (DMFC) are formulated with Pt and Ru. Recent works have demonstrated the influence of the structure of particles formed by different oxidation states of Ruthenium in this kind of catalysts to improve the performance of devices using these materials [7, 8]. It is commonly accepted that the Pt-Ru electrocatalyst provides superior activity for the electro-oxidation of methanol in DMFC´s. However it has been reported that Ruthenium from several commercial catalysts dissolves into and migrates through the proton exchange membrane (PEM). This process results in loss of activity from oxidation of fuel in the anode and the Pt catalyst activity for oxygen reduction at the cathode decreases [9].

Some research groups and industry laboratories are working on proton exchange membrane fuel cell (PEMFC) with the objetive of achieving power densities useful in technological applications and reduce costs to facilitate market entry. Different synthesis methods and characterization techniques for these catalysts and devices have been proposed [10]. Among the commonly used methods to synthesize these materials are: the thermolysis of metal carbonyls [11]; the chemical reduction to obtain small particles at low temperatures (below 100 ° C), and the support treatment to achieve optimal performance [12-18].

Studies on the catalytic effects that take place on bimetallic surfaces, product of pure metals and modified by the deposition of a second metal, are related to the technological development of low temperature fuel cells. One of the main objectives in this research field is the understanding of the CO oxidation. Some researchers have emphasized the use of CO as a test molecule to show the electronic effect associated with this reaction. The CO desorption energy is apparently related to strong intermetallic bonds and mixed orbitals of the active phases.
Methanol is probably the most studied one–carbon atom molecule, because it is a fuel with high energy density, that can power fuel cells at low temperature. Hence, a catalyst with high activity for the oxidation reaction of methanol must also have high activity for CO oxidation [19]. In this work, we prepared and studied catalysts

formulated with constant Pt and Mo loadings. One series of these materials was prepared with both active phases simultaneously supported on carbon. The second series consisted of monometallic, carbon-supported Pt and Mo solids, that were mixed in suspension. From the comparison of results from the characterization tests carried out for both series, it is expected to establish if long distance effects between active phases can take place in the methanol electrochemical oxidation.

2. Experimental

2.1 Catalysts synthesis.

As a first step, Pt hexacarbonyl complex was synthesized by bubbling CO, at 25 cm^3 min^{-1}, during 24 h, through an aqueous H_2PtCl_6 dissolution. This complex is used as the precursor for the Pt phase in the catalysts and this synthesis procedure allows to have control on the Pt particle size [12,20,21]. The Pt-Mo/C catalyst preparation was carried out by the thermolysis of Pt and Mo carbonyl complexes. Comercial Mo hexacarbonyl (Aldrich) was employed. The adequate amounts of the metallic carbonyl species to obtain solids with a formulation $(Pt_{0.8}$-$Mo_{0.2})_{0.25}/C_{0.75}$ in weigth percent, are disolved in 1,2-dichlorobenzene and Vulcan XC-72R is added as a suspended phase simultaneously. The temperature of the system is increased up to 110 °C and maintained during 4 h, with vigorous stirring. After this stage, the solvent is distilled. The solid is washed twice with diethyl ether and placed in N_2 atmosphere, at 400 °C during 2 h. The bimetallic material designed **(Pt-Mo/C)** is thus obtained.

In a second step, starting with the Pt hexacarbonyl and Mo carbonyl complexes, monometallic materials were separately synthezised. Afterwards, the Pt/C and Mo/C solids, were mixed by mechanical stirring in diethyl ether suspension during 5 hr at room temperature, to yield the same overall composition as the bimetallic catalyst. The solid is placed in N_2 atmosphere, at 400 °C during 2 h. The obtained product from this suspension mixture shall be designated **(Pt+Mo/C).**

2.2 Electrode preparation and electrochemical measurements.

An ink containing 1 mg of each catalyst dispersed in a 10 µL 2-propanol, 10 µL Nafion™ resin liquid mixture, was prepared. The dispersion was placed in an ultrasound bath during 15 min and 5 µL of the ink were placed on the tip of a commercial vitreous carbon disk electrode with the aid of a micropipette. The solvent is evaporated at ambient temperature and a catalytic solid layer is obtained. The catalyst content in this electrode is 2.54 mg cm^{-2}, referred to the geometrical surface area of the disk. (0.5 cm diameter). Cyclic voltammetry experiments were carried out in a three electrode cell at 25 °C.

The catalyst layer was used as working electrode, a saturated calomel electrode (SCE) was used as reference and a graphite rod as counter electrode. An aqueous 0.5 M H_2SO_4 solution was employed as supporting electrolyte in all experiments. The working solution is a 1.0 M methanol, 0.5 M H_2SO_4 electrolyte. Working media were degassed by bubbling nitrogen during 15 min previous to each experiment. Voltammetry results presented here were obtained at a potential scan rate of 30 mV s^{-1}, with a Voltalab 50 potentiostat. Potentials are referred to the

Normal Hydrogen Electrode (NHE). Before each experiment, electrodes were activated by applying 50 potential cycles, between 300 and 1000 mV vs. NHE in a sulfuric acid solution.

2.3 Characterization by physical techniques

The materials were analyzed by means of High Resolution Transmission Electron Microscopy in a JEOL 2010 microscope working at 200 kV and by Scanning Electron Microscopy. The catalysts were dispersed in isopropanol, in an ultrasound bath for 1 h and the microscope copper grids were impregnated with the liquid.

3. Results and discussion.

(Pt-Mo) catalysts displayed better performances than the (Pt+Mo) material. This performance is observed as a decrease in the oxidation potential of organic species. In figure 1, the voltammetry results of the last potential cycle from the Pt+Mo/C and Pt-Mo are presented. A higher current is observed with (Pt-Mo), suggesting that this material provides an increase in the oxidation catalytic activity. The methanol adsorption – oxidation peak appears at a lower potential than with (Pt+Mo). The same behavior is observed in the reverse sweep, where the organic intermediates oxidation – desorption peak is observed. Furthermore, an analysis of the cyclic voltammetry curves showed that the active phases simultaneously deposited display methanol oxidation current peaks higher than the material obtained from suspension mixing. Much higher electrical charges transferred per VC cycle are obtained in the bimetallic catalyst.

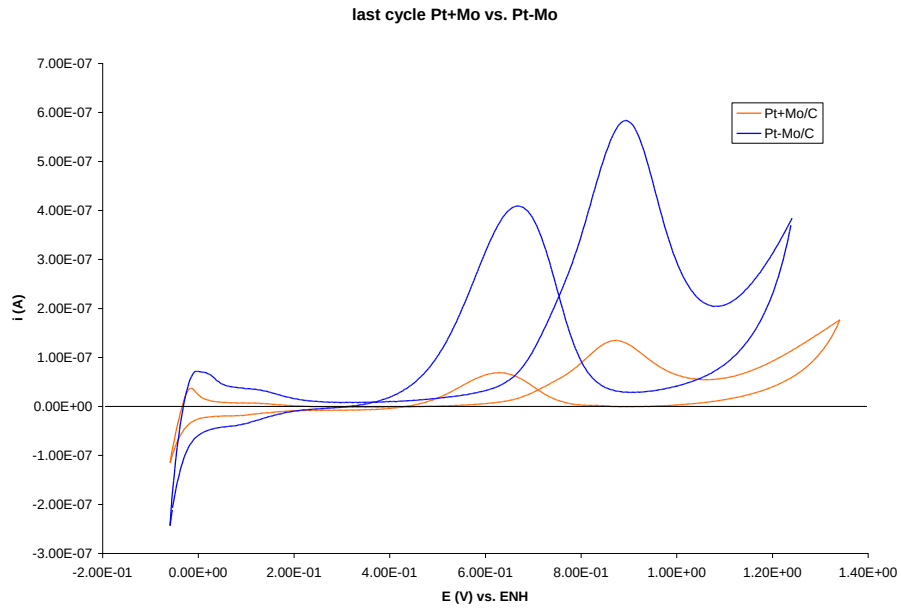

Figure 1. Cyclic voltammetry results from the Pt-Mo/C and Pt+Mo/C materials, in 1.0 M methanol, 0.5 M $H_2 O_4$, at 30 mV s^{-1}.

SEM and TEM images of the (Pt-Mo/C) material, presented in figure 2, reveal that particle sizes of all active phases are not homogeneus, as there are particle sizes from 5 nm to clusters between 50 and 100 nm. In the case

of this materials, a uniform dispersion of the metals on the carbon support is observed although the metallic phases reveal agglomeration in some regions. This can be related to the high activity obtained with this material: if water dissociation is expected to occur on Mo surfaces, and organics adsorption – oxidation takes place on Pt, then the fact of having molybdenum adjacent to platinum can play a role in the catalytic performance improvement.

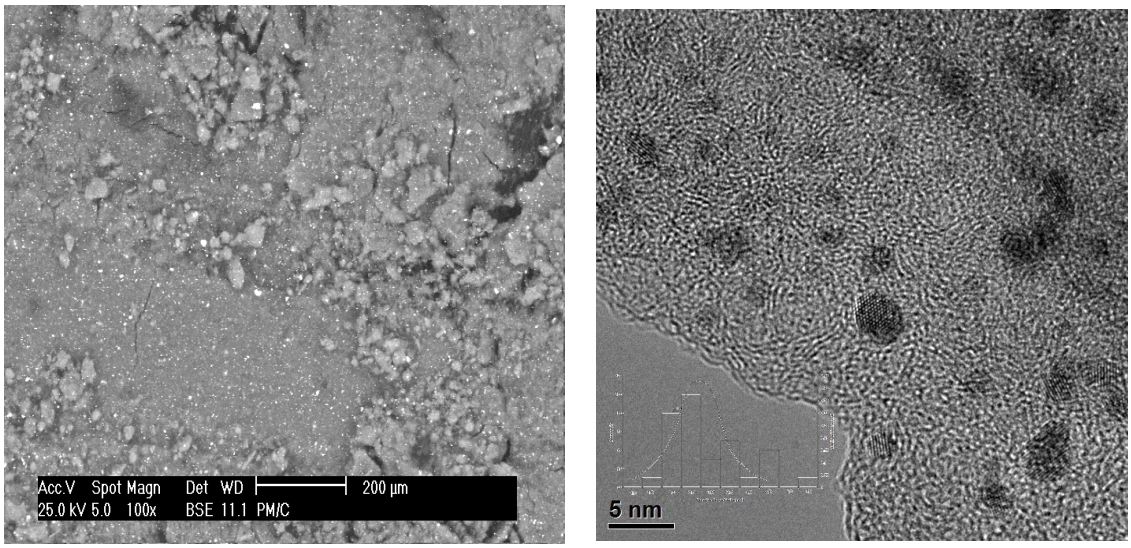

Figure 2. SEM and TEM Micrographs of the Pt-Mo/C material.

In figure 3 is shown an analysis of the charge transferred per cycle in the VC, the difference is large because the transferred charge into the (Pt-Mo) material is higher than the material that was mechanically mixed. This could support theories on the different propsed mechanisms, such as the bifunctional mechanism, the ligand effect, and even the physical blocking effect of Pt sites by Mo species.

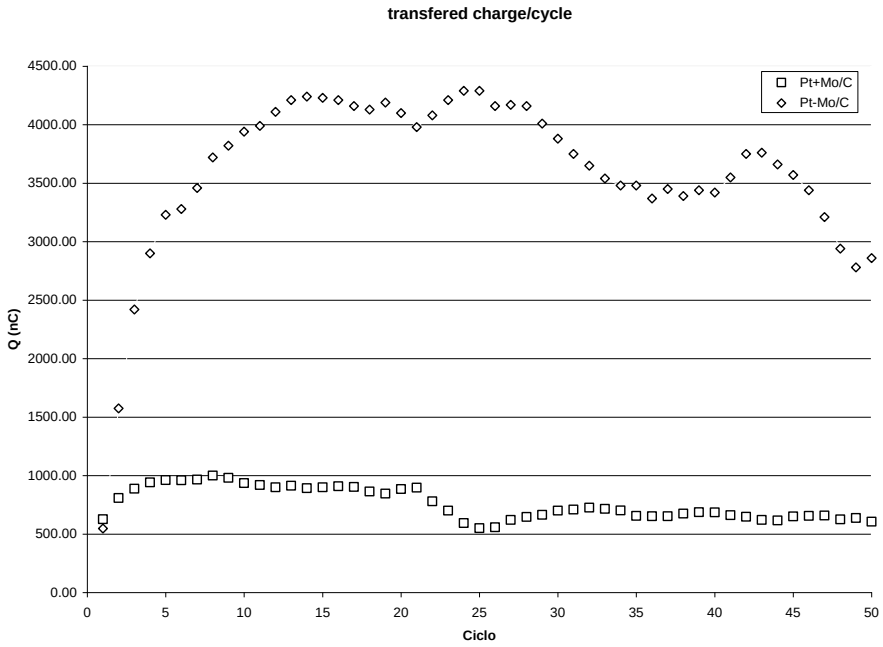

Figure 3. Transferred charge vs. cycle of materials Pt+Mo and Pt-Mo.

4. Conclusions.

The synthesis method allowed to retain the original proportions, although the particle size is not homogeneous, with particles sizes ranging from 5 nm to 100 nm.

The presence of molybdenum allowed the decrease of reaction potentials, which results in a higher catalytic activity. The transferred charge is greater in the material obtained by simultaneous synthesis. This suggests that the promoting role of Mo is due to a short distance effect.

As in previous studies, in this work we demonstrate that Pt – Mo materials can be employed in this kind of device with similar performances and lower production costs than Pt-Ru. The obtained results show that the catalysts synthesized by this method present all the requirements to be efficiently used in direct methanol fuel cells or can be employed in this kind of device with similar performance and lower production costs.

5. Akcnowledgements

OUR and RHM acknowledge the grants provided by Conacyt Mexico.

6. References.

1. Ermete Antolini, Flavio Colmati, Ernesto R. Gonzalez, *Electrochem. Comm*., 9 (2007), 398-404.
2. M. Watanabe and S. Motoo, *Journal of Electrolytical Chemistry*, 60, (1975), 267-273.
3. M. Watanabe and S. Motoo, *Electroanalytical Chemistry and Interfacial Electrochemistry*, (1975), 275-283.

4. J.L. Gómez de la Fuente, M.V. Martínez-huerta, *Catalisys*, 88 (2009), 505-514.
5. J. G. Kim, J. Z. Zhyu, J. R. Regalbuto, *Journal of Catalysis*, 139 (1993), 153-174.
6. Z. Jiang, W. Huang, H. Zhao, Z. Zhang, *Journal of Molecular Catalysis A: Chemical* 268 (2007) 213–220.
7. Kazuki Hirakawa, Mitsuhiro Inoue, *Electrochimica Acta* 55 (2010) 5874-5880.
8. Naoko Fujiwara, Kazuaki Yasuda, *Electrochimica Acta*, 47 (2002) 4079-4084.
9. E.H. Jung, T.H. Yang, *International Journal of Hydrogen Energy*, 32 (2007) 903-907.
10. L. Liu, L. Zhang, *ECS* 19 (23) 43-51 (2009).
11. William Hernando Lizcano-Balbuena, Ernesto Rafael Gonzalez, *Electrochimica Acta* 49 (2004) 1289-1295.
12. A.J. Dickinson, L.P.L. Carrette, J.A. Collins, K.A. Friedrich, U. Stimming, *Electrochimica Acta*, 47, (2002), 3733-3739.
13. Ermete Antolini, Ernesto Gonzalez, *Materials Chemistry and Physics*, 101 (2007) 395-403.
14. Beena K. Balan, Alexei L.N. Pinheiro, *J. Phys. Chem.* C 2009, 113, 17572-17578.
15. Kleber Bergamaski, Alexei L.N. Pinheiro, *J. Phys. Chem*. 2006 B, 110, 19271-19279.
16. Dao-Jun Guo, *Journal of Power Sources* 195 (2010) 7234-7237.
17. M. Sakthivel, *Journal of Power Sources* 195 (2010) 7083-7089.
18. Flavio Colmati, Ermete Antolini, Ernesto R. Gonzalez, *Applied Catalysis B: Environmental* 73 (2007) 106-115.
19. Rodrigues da Silva Marcelo, Springer Science+Business Media, LLC (2010)
20. L. C. Ordóñez, P. Roquero, P. J. Sebastian, J. Ramírez, *Int. J. Hydrogen Energy* 32 (2007) 3147 – 3153.
21. O. Ugalde Reyes, P. Roquero, R. Hernández Maya, A.L. Ocampo Flores, and E. Sosa Hernández, *ECS Transactions*, 36 (1) 21-28 (2011)

Appendix.

Figure 1. Cyclic voltammetry results from the Pt-Mo/C and Pt+Mo/C material, in 1.0 M methanol, 0.5 M H_2 O_4, at 30 mV s^{-1}.

Figure 2. SEM and TEM Micrographs of the Pt-Mo/C material.

Figure 3. Transferred charge vs. VC cycle of Pt+Mo and Pt-Mo materials.

Sustainable Hydrogen Production in Yucatan

Rodrigo Patiño*

Departamento de Física Aplicada, Cinvestav – Unida Mérida
Apartado Postal 73, Cordemex, 97310 Mérida, Yucatán, Mexico
*Tel: +52(999)9429438, e-mail: rtarkus@mda.cinvestav.mx

ABSTRACT

More than 90 % of the hydrogen production in the world depends on carbon compounds, principally fossil fuels, and its use as energetic vector is only justified in some applications as fuel for spaceships or demonstrative buses or cars. The goal of this proposal is to compare different approaches for sustainable hydrogen production as a commercial activity in rural communities in Yucatan. The Yucatan peninsula is a particular region at the Southeast of Mexico, where a fragile environment is present in combination with poor rural Mayan communities. Moreover, energy supply in this region depends mainly on fossil fuels provided from other regions. However, in Yucatan, solar radiation and winds have an important potential application that has not been exploited yet. An application of these renewable energy sources could be hydrogen production as an economic activity promoting rural development of the region.

According with meteorological analysis, as well as with the consideration of energy requirements and efficiency of commercial electrolysis systems, an estimation of the hydrogen production is evaluated, considering both investment and maintenance costs. This estimation may be a reference in order to propose small industries for the production of hydrogen in specific rural communities in Yucatan. A transportation network organized by the regional government could be a solution to consume this hydrogen as fuel, although a number of other applications may be proposed depending on the regional energy requirements. Finally, the bioproduction of hydrogen is explored in order to compare it with the simple hydrolysis systems. Until the moment, as far as we can research, there are not commercial methods to produce biohydrogen and it is necessary to evaluate the capacity of bioprocesses to produce hydrogen.

1. Introduction

In Mexico, the Yucatan Peninsula includes three federal states: Campeche, Quintana Roo and Yucatán, which involve 7.1% of the national territory but only 3.7% of the total population (Table 1). In the national context, the three States represent in surface the 6.5% of the urban areas, the 5.2% of the agriculture regions and the 13.5% of the natural protected areas.

Table 1. Key information for the three Mexican states in the Yucatan Peninsula.[a]

State	Campeche	Quintana Roo	Yucatán	Peninsula
Surface (thousands km^2)	57.9	42.4	39.6	139.9
Population (million)	0.82	1.33	1.96	4.11
% Rural Population	25	12	16	17
% Indigenous Speaking Population	12	16	30	22
% National Gross Domestic Product	1.2	1.6	1.4	4.2
Urban areas surface (km^2)[b]	184.66	217.01	421.05	822.72
Agricultural surface (km^2)	2,341.65	1,238.15	7,844.78	11,424.58
Natural protected areas surface (km^2)[c]	17,544.12	12,500.97	4,451.30	34,496.39

[a] Values from the National Census 2010 [1], unless any other reference is given.

[b] Values for the year 2005 [1].

[c] Values for the year 2010 [2].

Being an important oil and natural gas producer in the last decades, Mexico has been energetically independent, with both the oil and the electrical sectors as Federal industries: Petróleos Mexicanos (PEMEX) and Comisión Federal de Electricidad (CFE), respectively. In the last years, the annual energy supply has reached more than 8 EJ in the country (around 75 GJ per capita). More than 90% of this energy is produced from fossil fuels and almost the half is used in transportation [3]. Table 2 includes a comparison of the general energy data in the Peninsula, in which electricity is produced exclusively from fossil fuels in 16 different plants, representing around 4 % of the total production and consumption in Mexico. Not only fragile ecosystems are detected in the region, there are also important touristic services, which generate important economic incomes. For these reasons, it is important to develop a systematic analysis to detect potential energy production from renewable sources in the zone. A special interest is in proposing sustainable processes, where not only economic but also environmental and social issues should be considered.

Table 2. Electrical services in the three states, compared with the national supply.

	Campeche	Quintana Roo	Yucatán	Peninsula	Mexico
Installed capacity (MW)[a]	449	285	1,532	2,266	51,172
Brut generation (TWh)[b]	2.0	Not available	8.7	-	241.5
Annual sells (TWh)[b]	1.1	3.6	2.8	7.5	186.6
% Population with electrical services[c]	95.8	94.5	96.6	95.7	96.2
Electrical supply (kWh per capita)[d]	1,331	2,734	1,454	1,843	1,661

[a] Values for March 2011 [4].

[b] Values for the year 2010 [3].

[c] Values form the 2010 National Census [1].

[d] Estimated values with the 2010 sells and the National Census population.

The general aim of this project is to develop an analysis of sustainable processes to use renewable sources of energy in the States of Campeche, Quintana Roo and Yucatan, Mexico. The natural resources to be considered are solar, wind and biomass, with interest to produce clean electricity and gaseous fuels (methane and hydrogen).

2. Methodology

Databases from both satellite and meteorological sources were used to analyze the solar and wind resources of the region. The National Renewable Energy Laboratory (NREL) has published an analysis of the solar potential in the region as a renewable source of energy [5]. The solar resource potential is shown in three different modes for Mexico, Central America and the Caribbean Islands: (i) for use with horizontal flat-plate collectors, (ii) for use with flat-plate collectors tilted at latitude, and (iii) for use with 2-axis tracking concentrating collectors. The data were developed from NREL's Climatological Solar Radiation Model, but the resolution is reduced to a geographical grid with cells of approximately 40 km by 40 km in size; the modeled values are accurate to approximately 10% of a true measured value within the grid cell. The NREL has published also an analysis of the wind potential in this specific region as a renewable source of energy and a database (provided by Anthony Lopez in the GIS group) is available for the offshore wind potential in Mexico.

The Cinvestav-Merida manages at the moment four meteorological stations in the state of Yucatan. The oldest is installed in the Merida campus, and three more are installed in the North cost: from east to west, they are in Telchac Puerto, Chelem and Sisal. The stations are installed on towers at 10 m height and automated records are periodically performed every 10 minutes; the corresponding databases were provided by David Valdés in the Department of Recursos del Mar.

The System Advisor Model (SAM), developed by the NREL [6] was used here to analyze two hypothetical medium-scale electrical plants: a wind farm in Sisal, where the best wind potential is found in the region, and a PV plant in Merida, where the maximal energy requirements are found. For every plant, a 500 kW installation was considered, which is the maximal capacity allowed by CFE-Mexico for commercial electricity production. Although most of the default values were used, different variations were tested for every plant, representing a number of scenarios.

3. Results and discussion

Table 3 resumes the solar potential for the Yucatan Peninsula from the NREL database with a satellite model; it is possible to see that tilted collectors represent the best way to use the solar radiation in the region. However, considering photovoltaic (PV) systems, there is only a small fraction of these solar resources that can be transformed to electricity. Following the methodology proposed by Denholm and Margolis [7], under Standard Test Conditions (1000 $W \cdot m^{-2}$ of solar irradiance at 25°C), a 13.5 % efficiency is considered for the PV modules (commercial systems range from 6 to 26 %). Moreover, when a minimal spacing is considered between arrays to allow maintenance, the total system power density (per unit of array area) is reduced from 135 to 65 $W \cdot m^{-2}$. Finally, the efficiency of the inverter to convert direct current (DC) generated by the PV modules to alternating current (AC) depends on many variables, a value of 70 % was considered in this work. An annual estimation of (92 ± 3) $GWh \cdot km^{-2}$ is obtained as a rough average in the region with tilted PV systems.

Table 3. Annual Solar Radiation in the Yucatan Peninsula.

	Radiation ($kWh \cdot m^{-2} \cdot day^{-1}$)		
Collectors	**General Range**	**More Frequent Range**	**Average[a]**
Horizontal	4.5-6.0	5.0-5.5	5.2 ± 0.2
Tilted	5.0-6.0	5.0-5.5	5.5 ± 0.2
2-Axes	3.5-6.0	4.5-5.0	5.0 ± 0.4

[a] Uncertainty is the standard deviation of the mean value.

If it is considered the electricity consumed in the region during 2009: 7,617.31 GWh, and using the estimated solar-to-electricity potential for the region, a surface of only (83 ± 3) km^2 is required to supply the electrical needs of the Yucatan Peninsula. If considering that the electrical consumption is about 10 % of the total primary energy supply, less than 900 km^2 of land surface would be needed to satisfy the energetic needs of the whole region with PV technologies. To compare, this surface represents roughly about the half of the urban area of Merida or the 0.6 % of the total surface in the Yucatan Peninsula.

The solar resources in the region could also be analyzed as a footprint, defined by Denholm and Margolis [7]. When the annual electrical demand of the region, 1,843 kWh per capita, is divided by the corresponding PV energy density, (92 ± 3) $kWhm^{-2}$, the solar electric footprint is only (20 ± 1) m^2 per capita. This means that if every inhabitant installs 20 m^2 of a PV system, the electrical demand should be satisfied for the region. This footprint can be diminished to around the half if the PV systems are installed in small arrays. The USA average is 181 m^2 per capita, ranging from 354 in the state of Wyoming to 89 in the state of California. At this point, it is natural to question why so a "small" system is not already installed. The answer is easy: there are a number of restrictions, including relatively high costs, intermittent output and land use. In the Unites States, by instance, scarcely 1% of the electricity supply is provided by PV systems.

Analyzing the wind resources in the Yucatan Peninsula, only a stretch line in the Caribbean coast (Riviera Maya) and a small tip at the Northwest of the Peninsula (Sisal), beside other smaller areas, show moderate to good potential use (Class 4). Nevertheless, the Riviera Maya beaches in Quintana Roo are reserved as environmental protected areas or touristic zones and a wind farm in this surface would be not appropriate. Considering the Sisal region in the state of Yucatan, an assessment of the annual wind energy density could be envisaged through a number of scenarios using a three-factor analysis, with minimal and maximal values for every factor: the capacity factor, the height of the wind turbines and the capacity density. Table 4 describes the eight proposed scenarios for 1.5 MW wind turbines with 77-m rotor diameter; note that for this turbine, the recommended capacity density is 5 $MWkm^{-2}$ [8]. In the USA, the most popular wind turbines in the last 5 years are in the size range from 1.01 to 1.5 MW, although the market for capacities larger than 1.5 MW has been increasing [9].

Table 4. Scenarios to determine the annual wind energy density in the Sisal region.

Scenario (Wind Class 4)	Capacity factor (%)	Height (m)	Capacity density ($MW \cdot km^{-2}$)	Energy density[a] ($GW \cdot km^{-2} \cdot year^{-1}$)
1	30	50	2	7 – 8
2	30	50	10	33 – 41
3	30	100	2	9 – 11
4	30	100	10	45 – 55
5	50	50	2	11 – 14
6	50	50	10	54 – 68
7	50	100	2	15 – 18
8	50	100	10	75 – 92

[a] Ranges correspond to minimal and maximal power densities for wind Class 4.

Assuming the capacity factor of 33.8% suggested by Aabakken [10], the capacity density of 5 $MWkm^{-2}$ calculated by [8], and a height of 80 m that is the average installation in for wind turbines in the USA [9], the annual energy density for the Sisal region is (25.3 ± 2.3) $GW \cdot km^{-2} \cdot year^{-1}$, where the mean and the uncertainty values correspond to the Class 4 wind power densities range. The annual electrical needs of the state of Yucatan, 2,939.55 GWh, would require a wind farm of (116 ± 12) km^2. If compared with PV systems, wind turbines require more land; however, wind plants could combine uses with other activities as agriculture [8].

Since Denmark's first project in 1991, Europe has held the lead in offshore wind, but the installed capacity and the technologies are still limited [11]. However, interest is being spread to the international community and the market is continuing to expand. Analyzing the potential of wind resources at 90 m over the sea level, maximal wind speeds (8 to 9 $m \cdot s^{-1}$) are observed in the Caribbean Sea, but an enormous shipment density can be detected also in this marine region. However, most of the national Gulf of Mexico presents an attractive wind potential (7 to 8 $m \cdot s^{-1}$) without high density of shipment routes. Moreover, around the Yucatan Peninsula, the oceanic waters are shallow, characterized by short bathymetric distances, diminishing technical barriers to install offshore wind farms. Nevertheless, any offshore wind development have to be evaluated in the context of hurricanes that frequent the region, and an risk factor must be considered in the structural design of any turbines that are put in place.

Table 5 condensates the average values for the meteorological data in four stations in the Yucatan state. In general, the average values are in good agreement with those from the NREL database. These average values are also consistent with those reported by the NASA-USA [12] from satellite measurements and correlation models in a low-resolution grid, but with 22-year averages for temperature and solar radiation values, and a 10-year average for wind speed values. The NASA information complements those from the meteorological stations to estimate monthly mean values for diffuse horizontal and direct normal radiations, as well as atmospheric pressure and albedo values. Annual files with 8,760 hourly variations of the solar and wind resources can be constructed for every meteorological station in order to analyze with more detail their potential for electricity production. These files are used to analyze the performance and economics of renewable energy technologies.

Table 5. Average values from four meteorological stations owned by Cinvestav-Merida in the state of Yucatan.

	Mérida	**Telchac**	**Chelem**	**Sisal**
Temperature (^oC)	26.4	25.4	25.2	24.2
Global horizontal radiation ($kW \cdot h^{-1} \cdot day^{-1}$)	5.30	5.64	5.82	5.31
Wind speed ($m \cdot s^{-1}$)	2.64	4.98	4.59	5.06

Tables 6 and 7 show the main results for two hypothetical 500-kW plants with a 30-year lifetime, using the System Advisor Model (SAM). The economic analysis has to be improved for the conditions in Mexico, but give an idea of the cost differences among proposed scenarios. Table 6 represents different scenarios for the hypothetical wind plant in Sisal. Scenarios 3 to 6 consider four different turbine models and sizes: Endurance Wind E-3120 (E), with 50 kW of capacity and 19.2 m of rotor diameter; Northern Power Northwind 100 (N), with 100 kW of capacity and 21 m of rotor diameter; AOC 15-50 Wind Turbine (A), with 63 kW of capacity and 15 m of rotor diameter; and WTIC Jacobs 31-20 (W), with 20 kW of capacity and 9.4 m of rotor diameter. All of these turbines are supposed to be installed at 80-m height. The most attractive model is that of scenario 3 and it is used to compare with a 30 m hub-height installation (scenario 1), a plant with just 100 kW of installed capacity (scenario 2), and the same plant in scenario 3 but installed in Mérida (scenario 7).

Table 6. Wind farm at Sisal considering different scenarios.

Scenario	**1**	**2**	**3**	**4**	**5**	**6**	**7**
Turbine model	E	E	E	N	A	W	E
Hub height (m)	30	80	80	80	80	80	80
Total surface (m^2)[a]	9,600	1,920	9,600	5,250	6,000	11,750	9,600
Total installation cost (M$US)[b]	2.540	0.556	2.540	1.996	2.334	4.173	2.540
Produced energy (GWh·$year^{-1}$)	1.530	0.388	1.940	1.298	1.244	1.205	0.548
Pay back period (years)	12.3	11.2	9.0	11.4	14.8	> 30	> 30
LCOE nominal (¢US/kWh)[c]	8.69	6.87	6.85	8.21	9.88	17.65	24.24
LCOE real (¢US/kWh)[c]	6.67	5.23	5.26	6.30	7.58	13.54	18.60

[a] Estimated from the recommendation 10D x 5D by Denholm [8].

[b] Land costs are not included; differences in hub-height installation costs are not considered.

[c] Levelized costs of electrical energy, accounting the effect of inflation (real) or excluding it (nominal).

From these results, it is possible to see that the type of installed turbines is determinant for the performance of the wind plant, and not just the costs but also the technical characteristics are important. The hub height is also important for the amount of transformed energy, but the installation costs should be different and the model must be adjusted in this case. It is interesting, however, that no big economic differences can be found when the plant is reduced five times in installed capacity; this could motivate different size projects, depending on financial and land availabilities. Nevertheless, the local wind resources are extremely important and it is shown here that Mérida is not a good place to install a wind plant.

Table 7 resumes a series of scenarios for the hypothetical PV plant installed in Merida. A big variety of commercial systems are available in the SAM database; but the PVWatts System Model was used instead to simplify the comparisons. Scenario 1 is for a plant with an installation of just 100 kW, while the other scenarios are for a 500-kW plant. Scenarios 2 to 4 give the differences when the type of installed array is changed from tilted to tilted with one tracking axis and to 2-axis tracking. Scenario 5 considers a lower DC-AC conversion than the other systems. Finally, scenario 6 is for the same system in scenario 3 but installed in Sisal.

Table 7. PV plant in Mérida considering different scenarios.

Scenario	**1**	**2**	**3**	**4**	**5**	**6**
AC-DC conversion (%)	77	77	77	77	70	77
Array	1-axis	Tilted	1-axis	2-axis	1-axis	1-axis
Total surface (m^2)[a]	2,083	7,692	10,417	25,000	10,417	10,417
Total installation cost (M$US)[b]	0.450	2.249	2.249	2.249	2.235	2.249
Produced energy (GWh $year^{-1}$)	0.172	0.705	0.860	0.901	0.781	1.011
Pay back period (years)	24.5	> 30	24.5	22.7	28.4	19.0
LCOE nominal (¢US/kWh)[c]	13.80	14.70	13.80	13.17	15.12	11.74
LCOE real (¢US/kWh)[c]	10.59	11.28	10.59	10.11	11.60	9.01

[a] Estimations from PV array power density values given by Denholm and Margolis (2008).

[b] Land costs are not included; differences in array-installation costs are not considered.

[c] Levelized costs of electrical energy, accounting the effect of inflation (real) or excluding it (nominal).

The results let see again that the performance and costs of a system are not important when a 100 kW or a 500 kW plants are installed. However, the pay back period and the LCOE values should be reviewed to verify if there is not an error in the calculations. The performance of the systems is improved if one or two tracking axis arrays are installed, reducing the cost of the produced electricity, but again the model should be reviewed in the installation costs. Moreover, the land-use in the 2-axis arrays diminishes its interest if the footprint is considered. Finally, when comparing the results for a PV plant in Merida and in Sisal, it is important to remark the importance of the location of the plant, accordingly with the available regional resources but also with the needs of energy. Not only the electricity production costs should be considered but also the lost of transmission when the energy is not consumed at the place of production. In addition, the retail prices should be considered when connected to the electricity grid in commercial systems.

When comparing the scenario 3 in table 6 for a wind farm, with the scenario 6 in the table 7 for a PV plant, both installations in Sisal, the land requirements and installation costs are similar. However, the wind system gives an economical advantage over the PV system in the levelized costs of electrical energy. Nevertheless, the use of the land should be reviewed with more detail: the wind plant allows another open-air activities among the installed turbines, including agronomical production. On the other hand, the PV installations are also attractive because of the potential shadow they can offer: when direct radiation is avoided in some systems, an important amount of energy consumption is saved from refrigeration systems. More scenarios can be reviewed considering specific interests of the Yucatan state government, investors and municipalities. A review of the local costs should be also done to consider them in the economical analysis, including retail prices for the regional grid pricing structure. In addition, some social and environmental implications must be added to the balance in order to have a full view of the advantages of investing in renewable energies.

The potential for hydrogen production from renewable resources in the United States have been already studied [12-13]. The typical energy requirements for electrolyzers range from 53 to 70 kWh per kilogram of hydrogen, with an average of 58.8 kWh kg^{-1}. Saur and Ramsden [14] have used an efficiency value of 50 $kWh \cdot kg^{-1}$ and an operating capacity factor of 98% for wind electrolysis plants. In addition to the energy requirements for water electrolysis, some more energy is required if hydrogen is used for refueling stations in transportation systems. Around 72 kWh per kilogram of produced hydrogen is considered for a small filling station, with approximately more 3 $kWh \cdot kg^{-1}$ needed for compression, storage and dispensing [13]. These values were considered to estimate the hydrogen production capacity of the electrical plants proposed just before. Table 8 presents an estimation of hydrogen produced with electrical energy from wind farms and PV plants in Mérida, Telchac, Chelem and Sisal. If a 12-passenger hydrogen-powered shuttle bus is used, with an efficiency of about 9.3 km per kilogram of hydrogen, it is possible to calculate the distance that could be driven every day from the hydrogen fuel station.

Table 8. Estimation of hydrogen production from PV or wind plants in Yucatan.

Plant		Transformed energy ($GWh\ year^{-1}$)	H_2 production ($kg\ year^{-1}$)	H_2 production ($kg\ day^{-1}$)	Driven distance ($km\ day^{-1}$)
Wind	Sisal	1.940	25,867	70.9	659.1
Wind	Telchac	1.882	25,093	68.7	639.4
Wind	Chelem	1.574	20,987	57.5	534.7
PV	Chelem	1.016	13,547	37.1	345.2
PV	Sisal	1.011	13,480	36.9	343.5
PV	Telchac	0.988	13,173	36.1	335.6
PV	Merida	0.860	11,467	31.4	292.2

As can be observed, the hydrogen plants using wind technologies have better yields than using PV systems. In addition, the communities along the coast of Yucatan show better results than Mérida. A more detailed analysis must be done in order to consider the costs involved in these systems, the requirements of water for electrolysis, and the social and environmental implications to establish a network of public transportation fueled by hydrogen in the region.

Finally, table 9 gives an estimation of a microalgae (*Chlamydomonas reinhardtii*) plants for hydrogen production in Mérida, with an average of the hydrogen production in the PV and wind plants analyzed before. It is interesting to see the potential of hydrogen production considering the land required in every plant. Although wind farms require more extensions of land, the net production of hydrogen is twice that of the PV plant and 2.5 times that of the microalgae plant. It has been remarked before that PV plants are more expensive than wind farms. Therefore, wind farms are more convenient to install than PV systems. For the microalgae plant, it is necessary to evaluate the required costs of installation and operation, since the hydrogen production is not so far away from that of wind systems. Therefore, additional research and technological development is expected for the algae production in order to have an alternative renewable system to the wind and PV systems in the region.

Table 9. Hydrogen production plants in Mérida.

Plant	Annual hydrogen production ($kg \cdot m^{-2} \cdot year^{-1}$)
Wind-Hydrogen	2.50
PV-Hydrogen	1.24
Microalgae-PV-Hydrogen	0.96

4. Conclusions

According with satellite databases, solar resources are an interesting possibility for the Yucatan Peninsula to produce energy. However, from meteorological measurements, wind resources are also important and even more attractive than PV systems to produce hydrogen as an energy vector. A system of wind-hydrogen plants along the Yucatan coast is proposed here as an alternative economical activity to fuel a public transportation system.

5. Acknowledgements

This work was mainly hosted by the Hydrogen Technologies and Systems Center at the National Renewable Energy Laboratory (NREL) and financed through the Fulbright NEXUS Program, in which RP participated as Scholar. Personal thanks are given for technical support to Ali Jalalzadeh, Genevieve Saur, Robert Remick, Maria Ghirardi, Anthony Lopez and David Valdés.

6. References

[1] INEGI-Mexico (2011). Several databases can be consulted in the web page: http://www.inegi.org.mx/

[2] SEMARNAT-Mexico (2011). Several databases can be consulted in the web page: http://www.semarnat.gob.mx/

[3] SENER-Mexico (2011). Several databases can be consulted in the web page: http://www.sener.gob.mx/

[4] CFE-Mexico (2011). Data can be consulted in the web page: http://www.cfe.gob.mx/

[5] NREL-USA. A database can be consulted in the web page: http://www.nrel.gov/gis/mapsearch/

[6] SAM-NREL. https://www.nrel.gov/analysis/sam/

[7] P. Denholm and R. M. Margolis. Energy Policy, 36, 3531 (2008).

[8] P. Denholm. Renewable Energy, 31, 1355 (2006).

[9] DOE-USA. 2010 Wind Technologies Market Report". U.S. Department of Energy, United States (2011).

[10] J. Aabakken. Power Technologies Energy Data Book". 4 ed. Technical Report NREL/TP-620-39728, United States (2006).

[11] W. Musial and B. Ram. Large-scale Offshore Wind Power in the United States: Assessment of Ppportunities and Barriers". Technical Report NREL/TP-500-40745, United States (2010).

[12] A. Milbrandt and M. Mann. Potential for Hydrogen Production from Key Renewable Resources in the United States. Technical Report NREL/TP-640-41134, United States (2007).

[13] J. I. Levene, M. K. Mann, R.M. Margolis and A. Milbrandt. Solar Energy, 81, 773 (2007).

[14] G. Saur and T. Ramsden. Wind Electrolysis: Hydrogen Cost Optimization". Technical Report NREL/TP-5600-50408, United States (2011).

Use of a Try-functional Crosslinking Agent in Styrene/Acrylic Acid Copolymers to Enhance Mechanical Properties for their use as Membranes in Fuel Cells

R. Benavides[1*], L.W. Oenning[1], M.M.S. Paula[2], L. Da Silva[2], C. Kotzian[3]

[1]Centro de Investigación en Química Aplicada, Blvd. Enrique Reyna H. 140, Saltillo, Coahuila, 25294 México.
[2]Laboratorio de Sintesis de Complexos Multifuncionais, Universidade do Extremo Sul Catarinense, Criciuma, SC, Brasil
[3]Hospital Universitario-UAdeC, Av. Madero 1291, Saltillo, Coah.,25000, México
[*]Tel: +52(844)438 9830 xt. 1322, fax (844)438 9839, mail: robertob@ciqa.mx

ABSTRACT

Polymer electrolyte membranes used in hydrogen fuel cells need some mechanical resistance in order to stand for the humid environment observed into a cell in operation. Alternative copolymers to the well-known Nafion membranes are the styrene/acrylic acid copolymers; with advantages in cost and availability of raw materials to prepare them. Previous attempts to improve mechanical properties of such materials involved crosslinking with divinyl benzene, but in this work we are reporting the use of the tryfunctional monomer TMPTMA (trimethylol propane trimethacrylate) for such purpose. Copolymers with a PS/AA ratio of 94/6 were prepared by radical polymerization reaction, including TMPTMA at 0.1, 0.01 and 0.001 %mol concentrations. Reactions were followed by percentage yield (gravimetry), FTIR and crosslinking level by gel percentage evaluation (soxhlet extraction) with three different solvents (water, THF and dicloromethane). Thermal transitions were followed by DSC, stability by TGA and mechanical properties by DMA. FTIR spectra show typical bands from the copolymer while the corresponding bands to crosslinking are overlapped; however, gel percentage evaluations show higher level of crosslinking for the 0.1% TMPTMA copolymer and lack of solubility in water. DSC thermograms indicate increment of Tg and TGA a small increment in thermal stability for crosslinked copolymers. Elastic modulii suggests a rubbery material for TMPTMA crosslinked copolymers while loss modulus confirm Tg enhancement as observed by DSC. 0.1 % TMPTMA copolymer does not even form a membrane due to insolubility and infusibility.

1. Introduction

Recent restrictions in environmental pollution from mankind activities have initiated the search for modern alternatives to energy generation. Although, fuel cells technology is not considered a new option for such purpose, optimization of their cost is quite recent. The most important item into a polymeric fuel cell is the polyelectrolyte membrane (PEM) and the well-known Nafion has been used for decades for mobile applications [12], although sulphonated polystyrene membranes were the first low temperature commercial options offered from General Electric Company since 1960 [8].

Alternative materials to improve Nafion´s membranes include 3 groups: modified perfluorosulphonic acid polymers, complex acid-base membranes and sulphonated hydrocarbon alternated polymers. The latter include diverse materials, have low cost, absorbe water in a wide temperature interval and can be recycled [15]. Sulphonation is the most common method to cleave ionic groups into the backbone consisting of an aromatic electrophilic substitution reaction in the case of styrenic polymers, where a hydrogen from the aromatic ring is changed by a sulphonic group [15, 16].

Liu el al [16] studied ion conductivity and mechanical-dimensional behaviour of sulphonated poly(arilethercetone) bifenilate prepared at different sulphonation grades. They found enhanced mechanical performance and high dimensional stability and ion conductivity, comparing with Nafion. Deb and Mathew [19] studied the synthesis of sulphonated styrene-acrilic acid copolymers with a styrene molar rate of 47-55 %; they also reported their ion exchange properties and suggested their use as pH sensors. Sherazi et al [17] crosslinked ultra high molecular weight polyethylene with styrene and obtained membranes by hot press molding to finally sulphonate with chlorosulphonic acid, obtaining membranes with superior proton conductivity and low permeability to methanol when comparing with Nafion.

A practical way to obtain membranes is the preparation of the crosslinked styrene-divinyl benzene copolymers in one step and their further sulphonation with concentrated sulphuric acid [18]. Recently Paula et al [20] reported the preparation of styrene-acrylic acid copolymers with further sulphonation with sulphuric acid as well, with possibilities of pH and humidity sensors applications. In this report we are showing results when styrene-acrylic acid copolymers are crosslinked with an agent (trimethylol propane trimethacrylate-TMPTMA) to enhance mechanical properties to be able to use them as membranes in fuel cells.

2. Experimental

Synthesis of crosslinked copolymers

A 100 ml glass reactor was loaded with styrene and acrylic acid in a 94:6 molar ratio, TMPTMA crosslinking agent (trimethylol propane trimethacrylate) was also added at three different concentrations: 0.001, 0.01 and 0.1 % mol. Radical copolymerization was carried out using benzoyl peroxide (0.05 % mol) as initiator and keeping reactor temperature at 100 ºC, under nitrogen atmosphere and mechanical stirring (250 rpm) during 2 hours. The copolymer was dissolved with acetone and the solution precipitated with methanol; the latter procedure was repeated twice in order to eliminate low molecular weight material and the solid dried overnight and then into a vacuum oven. The percent of copolymerization yield was calculated by gravimetric measurements.

Characterization of copolymes

An aliquot of each copolymer (0.02 g) was dissolved with THF (1 ml) and the solution deposited in a flat confined glass plate in order to have films of approximately 0.03 mm thickness after solvent evaporation (casting). FTIR spectra of the films were recorded in a Nicolet Avatar 330 instrument. 64 scans and a resolution of 4 cm^{-1} were used.

Gel formation was also evaluated in order to obtain the crosslinking level for each copolymer; as it is an indirect evaluation, three solvents were used: water, dicloromethane and THF. Aliquots of 0.5 g were placed into cellulose thimbles and then into soxhlet extraction systems. The copolymers were extracted with the different solvents during various extraction times: 4, 8 and 12 h. Gel percentage was calculated gravimetrically.

DSC thermograms were obtained from a TA Instruments 2920 MDSC apparatus, a first thermal scan was carried out to eliminate thermal history and the second scan recorded to observe transitions in the -30 to 150 ºC temperature interval at 10 ºC/min thermal ramp. A nitrogen atmosphere was always kept during evaluations.

TGA thermograms were carried out in a Q500 TA Instruments apparatus. Approximately 20 mg of sample was placed into the thermobalance and evaluated from ambient up to 700 ºC, with a 10 ºC/min thermal ramp under nitrogen atmosphere. Mass loss was recorded along temperature and the first derivative calculated for each run.

Dynamic mechanical properties were evaluated by means of a DMA TA Instruments Q800. A tension accessory was used for deformation, with an amplitude of 20 microns and a frequency of 1 Hz in the temperature range of ambient to 130 ºC with a ramp of 5 ºC/min.

3. Results and discussion

Copolimerization reactions were carried out and the yield percentages obtained gravimetrically are relatively low, as shown in the Table 1, particularly for the homopolymer (polystyrene). The highest value was obtained for the copolymer including 0.1% of crosslinking agent, suggesting is due to the reactive media involving the tryfunctional monomer. The latter was an insoluble material due to the high level of crosslinking, unable to use it for making films (membranes) by casting.

Table 1. Yield percentages obtained for reactions

Polymer	Yield (%)
PS	30.5
PS/AA	40.5
PS/AA + 0.001 TMPTMA	37.1
PS/AA + 0.01 TMPTMA	37.6
PS/AA + 0.1 TMPTMA	56

The films obtained from the casting of copolymers synthesized were evaluated by FTIR; except the one prepared with 0.1 % TMPTMA, as mentioned before. FTIR show expected differences, as can be seen in Figure 1.

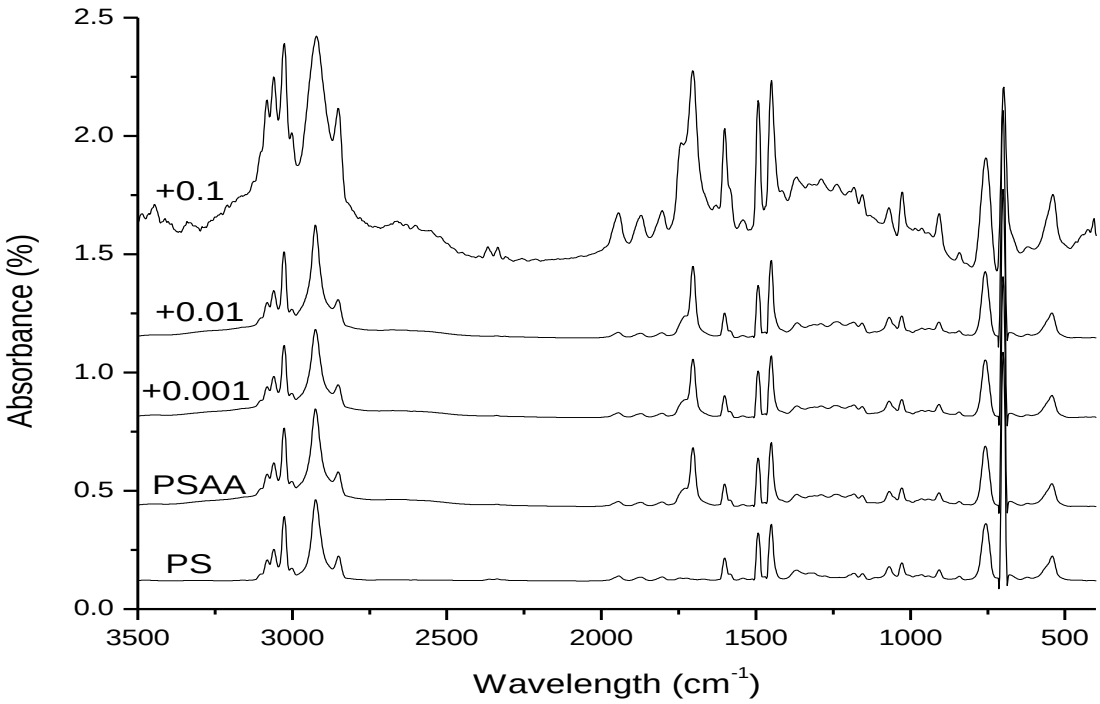

Figure 1.- FTIR spectra of polystyrene (PS), the copolymer with acrylic acid (PSAA) and the copolymer prepared including different levels of TMPTMA.

Polystyrene shows the C-H stretching bands over and below 3000 cm^{-1}, aromatic ring overtones below 2000 cm , and the corresponding ring vibrations at 1600, 1492 and 1450 cm^{-1}, and finally the C-H bendings from backbone at 758 and 700 cm^{-1}, as well as the one from the ring at 541 cm^{-1}. Once the copolymer was prepared (PSAA), the FTIR spectra show a slight broadening for the C-H aromatic and aliphatic bands around 3000 cm^{-1}, as a consequence of the OH group from the acrylic acid. It is also clear the formation of the C=O carbonile stretching band at 1704 cm^{-1} and the C-O stretching band at 1240 cm^{-1}, both coming from the presence of acrylic acid in the copolymer. The C-O-H bending vibration is overlapped with the bands from the aromatic ring at 1430 cm^{-1}.

Indication of TMPTMA into the copolymer is seen as the 1732 cm^{-1} shoulder coming from an esther functionality. The latter is higher for the 0.1 % mol TMPTMA addition to the reaction mixture, as seen in the sequence (Table 2) obtained when correlating such band with an unchanged band from the backbone (758 cm^{-1})

Table 2. Esther formation in copolymers with addition of TMPTMA

Polymer	Band ratio (1732/758 cm^{-1})
PS/AA	0.3704
PS/AA + 0.001 TMPTMA	0.3929
PS/AA + 0.01 TMPTMA	0.4091
PS/AA + 0.1 TMPTMA	1.1262

The extraction properties of materials in water are very important, considering they do have to support humid environments during operation. Extraction in organic solvents are useful to understand the real level of crosslinking during addition of TMPTMA and needed to prepare the membranes. Figure 2 show the results of extraction at different time intervals for the crosslinked materials when using 3 solvents.

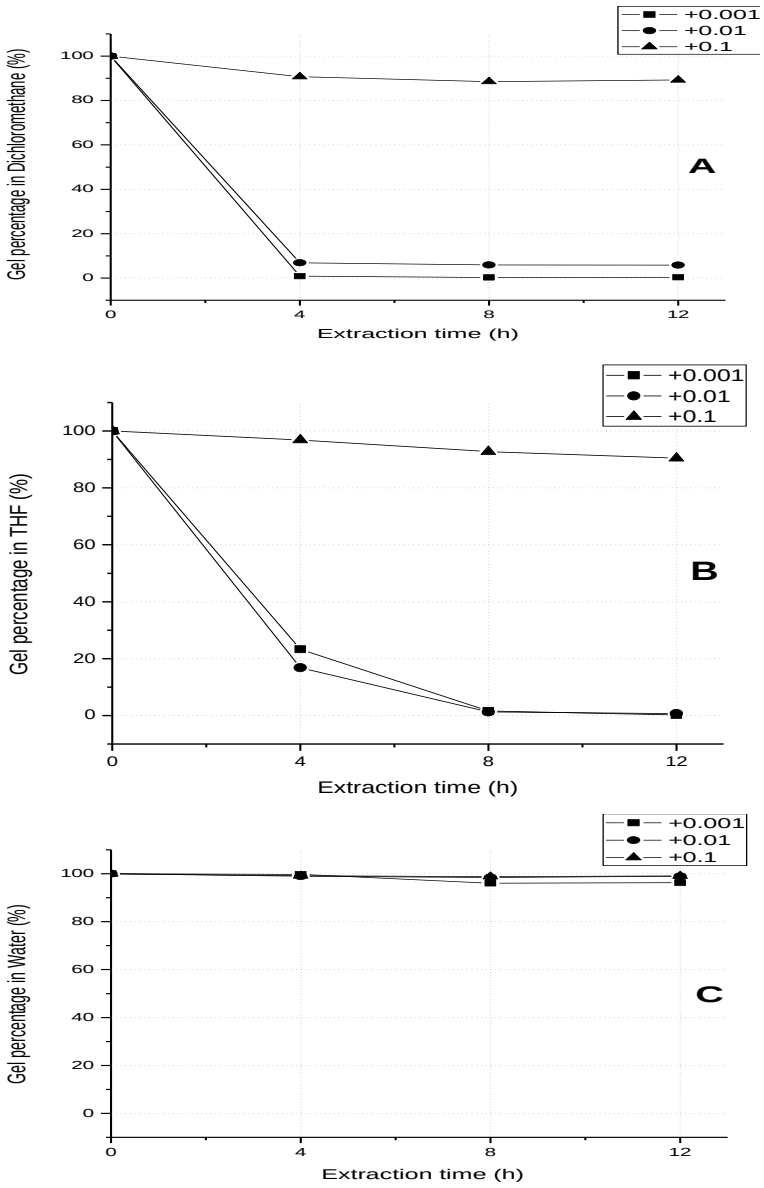

Figure 2.- Percentage of gel obtained for the materials at different times using. Dichloromethane (A), Tetrahydrofuran (B) and Water (C).

It is clear to observe that water does not dissolve any of the crosslinked materials (0.1, 0.01 and 0.001 %TMPTMA) and needs 8 hours to dissolve just the 4% for the 0.001 % material. Dichloromethane is the most effective solvent,

since only 4 hours are needed to dissolve almost all of the low crosslinked materials while THF need 8 hours to do so. None of the solvents dissolve the most crosslinked material with 0.1% TMPTMA.

Thermal transitions were evaluated by DSC in order to identify possible changes in Tg as a consequence of copolymerization and crosslinking reactions. Figure 3 shows DSC thermograms for the materials prepared.

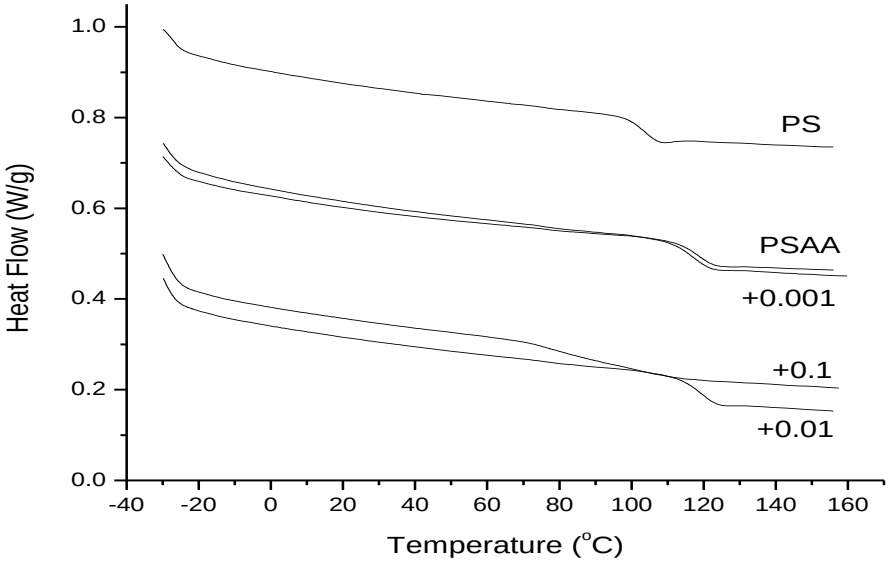

Figure 3.- DSC thermograms for PS, PS+AA and the copolymer added with different levels of TMPTMA

Polystyrene shows its Tg transition at 102ºC as it is well known, but the copolymer with 6 % mol of acrylic acid enhances the transition up to117ºC due to interaccions between acrylic acid functionality. The crosslinked materials with low amount of crosslinking agent (0.001 and 0.01 % of TMPTMA) does not produce any changes to the copolymer transition, however the 0.1 % TMPTMA material reduce the transition considerably as well as extends the thermal interval for it. Such effect has been mentioned to be the consequence of the rubbery status acquired for the higher amount of agent [9].

In order to evaluate changes in thermal stability for the materials prepared, TGA thermograms were obtained and the loss weight is happening at higher temperature as known for styrenic materials (350ºC), and an increment for the crosslinked materials. Figure 4 show their traces and Table 3 the temperature values for the curve maxima from the DTG traces. The most crosslinked material (0.1 % TMPTMA) has the higher thermal stability and the copolymer is more sensible to degradation comparing with the polystyrene homopolymer.

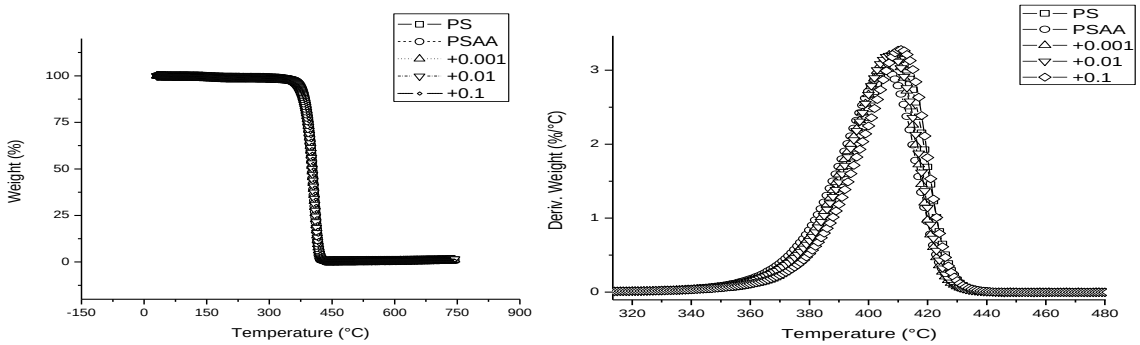

Figure 4.- TGA and DTG thermograms for PS, PS+AA and the copolymer added with different levels of TMPTMA

Table 3. Degradation temperatures obtained by derivative TGA

Polymer	Maxima at DTG curves (°C)
PS	**409**
PS/AA	**405.5**
PS/AA + 0.001 TMPTMA	**407.5**
PS/AA + 0.01 TMPTMA	**407.5**
PS/AA + 0.1 TMPTMA	**411**
TMPTMA	**344, 463, 613**

Mechanical properties were evaluated by means of DMA and the results of elastic and viscous modulii for the materials are shown in Figure 5. The 0,1 % TMPTMA crosslinked material is not included since it was imposible to obtain films for the evaluations.

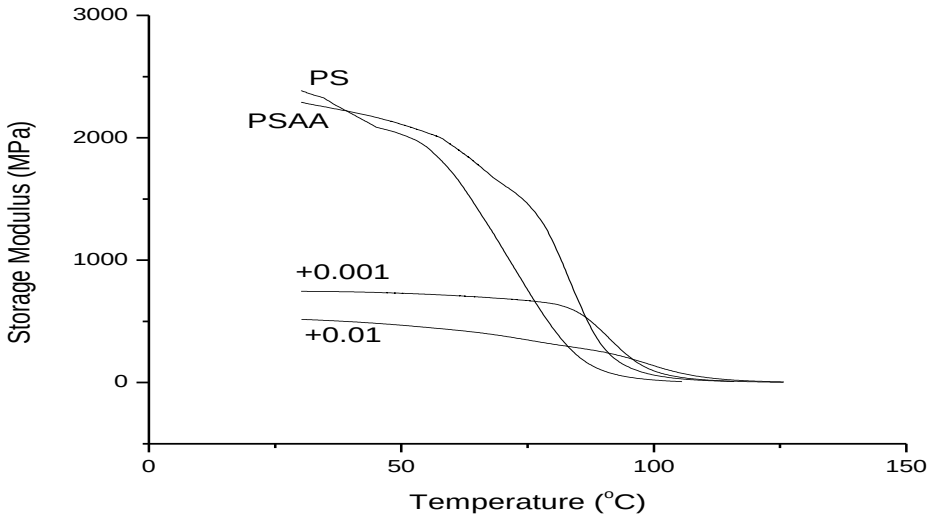

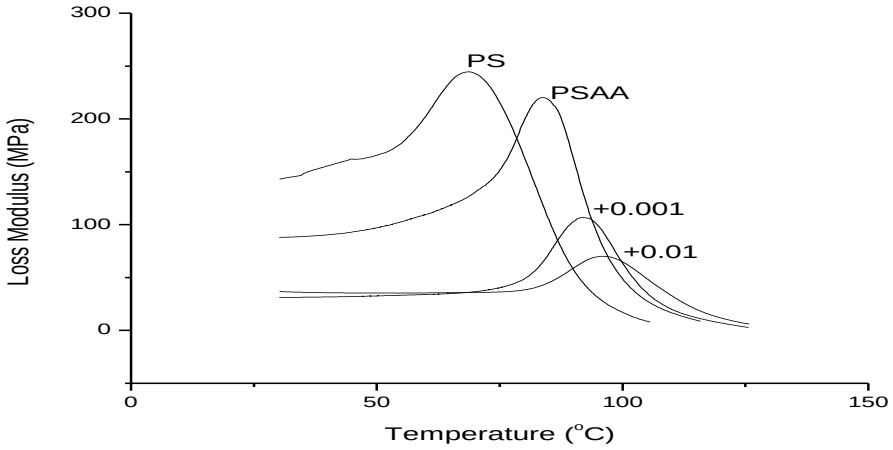

Figure 5.- DMA traces (storage and loss modulus) for materials added with different levels of TMPTMA

The elastic modulus is considerably high for the homopolymer and the copolymer but once the crosslinking agent is added the reduction of E´ values confirm the rubbery behavior of the materials. The viscous or loss modulus traces also confirm the effect observed by DSC, where glass transition temperature is enhanced for the crosslinked materials, with temperature differences in the order of 30ºC.

4. Conclusions

The polystyrene-acrylic acid copolymer was prepared as it is confirmed by FTIR and the addition of TMPTMA effectively worked as crosslinking agent. Water does not extract polymeric material during gel % evaluations but organic solvents evaluated (THF and DCM) are convenient to dissolve and prepare membranes. Glass transition is effectively enhanced when TMPTMA is added as observed by DSC and confirmed by DMA while a rubbery status is obtained specially for 0.01 % TMPTMA addition. Thermal stability is slightly enhanced for crosslinked copolymers.

5. Akcnowledgements

CONACYT is greatly acknowledged by the MSc. grant given to L.W.O. and the economical support through the project 134289.

6. References

[1] B. Gou, W. Ki Na and B. Diong. Fuel cells: modeling, control, and applications. CRC Press, United States of America, (2010).

[2] J. Zhang, PEM Fuel Cell Electrocatalysts and Catalyst Layers: Fundamentals and Applications. Springer, England, (2008).

[3] S. M. J. Zaidi, T. Matsuura, Polymer Membranes for Fuel Cells, Springer: United States of America, (2009).

[4] B. Liu, W. Hu, G.P. Robertson, Y.S. Kim, Z. Jiang and M. Guiver, Sulphonated biphenylated poly(aryl ether ketone)s for fuel cell applications, Fuel Cells, 10, 45 (2010).

[5] P.C. Deb and A. Mathew, A new polyelectrolyte with acid-base indicating properties, Macromolecular Chemistry and Physics, 199, 2527 (1998).

[6] T.A. Sherazi, M.D. Guiver, D. Kingston, S. Ahmad, M.A. Kashmiri, Xue, Xinzhong, Radiation-grafted membranes based on polyethylene for direct metanol fuel cells, Journal of Power Sources, 195, 21, (2010).

[7] E. Drioli, L. Giorno, Membrane Operations: Innovative Separations and Transformations, Wiley-VCH, Germany, (2009).

[8] M.M. Paula, L. da Silva, F.E. da Silva, C.V. Franco, R.B. Nuernberg, T. Gomes and R. Miranda, Humidity and pH sensor based on sulfonated poly-{styrene–acrylic acid} polymer. Synthesis and characterization, Materials Science and Engineering C, 29, 599, (2009).

[9] J.D- Menczel and R.B. Prime, Thermal analysis of polymers: Fundamentals and Applications, John Wiley and Sons, USA, (2009).

Photocatalytic Hydrogen Evolution from Pure Water Using a New Sm_2GaTaO_7 Advanced Compound

Miguel A. Ruiz-Gómez[1,2], Leticia M. Torres-Martínez[1,*], M. Z. Figueroa-Torres[1], Edgar Moctezuma[2], Isaías Juárez-Ramírez[1]
[1]Universidad Autónoma de Nuevo León, UANL, Facultad de Ingeniería Civil, Departamento de Ecomateriales y Energía, Av. Universidad S/N Ciudad Universitaria San Nicolás de los Garza Nuevo León, C.P. 66451 México
[2]Facultad de Ciencias Químicas, Universidad Autónoma de San Luis Potosí, Av. Manuel Nava #6, 78290 San Luis Potosí, S.L.P., México
*Tel: 81 83521983 ext. 222, fax 81 83760477, mail: lettorresg@yahoo.com

ABSTRACT

Overall water splitting to produce hydrogen over a semiconductor photocatalyst is a promising process for clean and sustainable hydrogen production. In this work, a new compound Sm_2GaTaO_7 was successfully synthesized by a conventional solid state reaction. RuO_2 nanoparticles were loaded as cocatalyst onto Sm_2GaTaO_7 surface. X-ray powder diffraction and Rietveld refinement characterization results revealed that Sm_2GaTaO_7 crystallized in the monoclinic system with space group C2/c. The energy band gap (*Eg*) was calculated by Kubelka-Munk formula, obtaining a value in the order of 4.1 eV. By scanning electron microscopy and nitrogen physisorption analysis, it was observed that material presents particle size around 2-3 μm and a specific surface area of 0.5 $m^2 g^{-1}$. The photocatalytic water splitting reaction results revealed that Sm_2GaTaO_7 was able to produce hydrogen from pure water. The hydrogen production activity was enhanced by using the optimal RuO_2 amount, which exceeded 2.4 times the production of pure Sm_2GaTaO_7.

1. Introduction

Actually, hydrogen (H_2) has received special attention as a next-generation energy carrier. H_2 is widely considered to be the future clean energy in many applications, such as environmentally friendly vehicles, domestic heating, and stationary power generation. Photocatalytic water splitting using semiconductor oxide is one of the most promising technologies for sustainable and clean hydrogen production; this is because H_2 could be obtained directly from abundant and renewable sources such as water and solar light [1-5].

Photocatalysts materials that include in their structure cations with d^0 electronic configuration like Ti^{4+}, Zr^{4+}, Nb^{5+} and Ta^5 have been widely studied and showed potential activity for water splitting into H_2 and O_2 [1,4,6-8]. On the other hand, it has been reported that some metal oxides consisting of cations with d^{10} electronic configuration such as Ga^{3+}, In^{3+}, Ge^{4+}, Sn^{4+} and Sb^{5+} are also attractive materials for this reaction [9-11]. Density functional theory results (DFT) revealed that the conduction band of d^{10} metal oxides present a large dispersion which allows higher mobility of the photoexcited electrons than d^0 transition metals [11]. However, pyrochlore-type mixed oxides Sm_2InTaO_7 and Sm_2InNbO_7 that combine cations with 4f-d^{10}-d^0 configuration showed much higher activity for H_2 evolution when compared to $Sm_2Zr_2O_7$ and $InNbO_4$ with 4f-d^0 and d^{10}-d^0 electronic configuration respectively [12,13]. Moreover, some investigations have found that crystalline structure arrangement, particularly, the formation of distorted octahedral units is an important factor to improve the H_2 evolution using 4f, d^{10} and d^0 mixed metal oxides [12-15].

Other way to improve the photocatalytic water splitting reaction is through a surface modification loading Pt, NiO and RuO_2 nanoparticles as cocatalysts. Principally, the cocatalyst materials suppress the electron-hole recombination and generate active sites for gas evolution [1,4].

Among metal oxides with d^{10} configuration, Ga_2O_3 is photocatalytically active for the water splitting reaction, even without loading a cocatalyst [4]. Based on above consideration, this paper is focused on the synthesis by solid state reaction of a new compound, Sm_2GaTaO_7. Their photocatalytic activity for water splitting reaction to produce hydrogen was studied. The hydrogen evolution results were explained in terms of the crystalline structure and the effect of loading RuO_2 nanoparticles.

2. Experimental

2.1 Synthesis by solid state reaction

Sm_2GaTaO_7 was synthesized by solid state reaction using Sm_2O_3, Ga_2O_3 and Ta_2O_5 (Aldrich purity > 99.9 %) as starting materials. The powders were dried before the synthesis at 200ºC for 4 hours. Then, stoichiometric amounts of each reactant were perfectly mixed with acetone in an agate mortar. The mixture was grinding until complete evaporation of acetone. Then, the mixture was placed into a platinum crucible and thermally treated at 1400ºC under an air atmosphere using a heating rate of 1ºC/min with intermediate regrinding to complete the reaction.

2.2 Wet impregnation method

Sm_2GaTaO_7 was impregnated with different content of RuO_2 (0.2, 1.0 and 1.5 weight %) using the stoichiometric amount of ruthenium carbonyl complex, $Ru_3(CO)_{12}$, in tetrahydrofuran. During impregnation, Sm_2GaTaO_7 powders were immersed into solution, the slurry was stirred at 80 ºC until complete evaporation of the solvent. Then, in order to convert the Ru surface species to RuO_2 nanoparticles, each material was thermally treated at 400 ºC by 1 hour under an air atmosphere using a heating rate of 10 °C/min. These materials were labeled as $xRuO_2/Sm_2GaTaO_7$, where "x" denote the weight % impregnated.

2.3 Characterization

Sm_2GaTaO_7 was characterized by X-ray powder diffraction method (XRD) using a Bruker D8 Advance diffractometer and CuKα radiation (λ = 1.5406 Å) as the incident X-ray source. XRD data were collected at room temperature from 10 to 100º with a step interval of 0.01º and a counting time of 1s $step^{-1}$. A detailed analysis of the crystal structure was performed by Rietveld refinement method using TOPAS R3 software [16].

The optical properties were analyzed in the range of 200 – 700 nm at room temperature with a UV–Vis spectrophotometer (Lambda 35 Perkin Elmer Corporation) equipped with an integrating sphere attachment. The energy band gap was determined by Kubelka-Munk function. The morphology and particle size of materials were observed using a JEOL 6490 LV Scanning Electron Microscope (SEM). All samples were stuck to graphite tape and then placed on an aluminum sample holder and located in the SEM chamber. The content of impregnated RuO_2 was determined by energy dispersive X-ray spectroscopy (EDS) analyzing five random zones. The specific surface area (S_{BET}) was determined by physical adsorption of nitrogen at -196 ºC using an analyzer Quantachrome NOVA 2000e. Prior to analysis the samples were degassed at 300 ºC for 1 h.

2.4 Photocatalytic Evaluation

The photocatalytic water splitting reaction was carried out in a reactor with inner quartz cell and a 400 W high pressure mercury lamp as the irradiation source. 0.3 g of photocatalyst was dispersed into 300 mL of pure water under vigorous stirred. Prior to the reaction, argon was bubbled to deaerate the solution. Pressure was set at 100 Torr and temperature was kept at 20 ºC. The amount of hydrogen was analyzed using a chromatograph Varian CP 3380 equipped with a TCD detector and column Hayesep D 100/120 using argon as carrier gas. Reaction evolution was analyzed each 30 minutes during 5 hours.

3. Results and discussion

3.1 Characterization of Sm_2GaTaO_7

According with XRD analysis, Sm_2GaTaO_7 was obtained as a single phase at 1400 ºC and 24 hours. As shown in Figure 1, the diffraction peaks were intensive and narrow, suggesting a good crystallization and large particle size. Sm_2GaTaO_7 was synthesized for the first time, hence there is not standard diffraction pattern for it in the ICDD-PDF (International Centre for Diffraction Data, Powder Diffraction File) database. However, the XRD

pattern obtained for Sm_2GaTaO_7 was quite similar to monoclinic Sm_2FeTaO_7 compound recently reported by our research group [17].

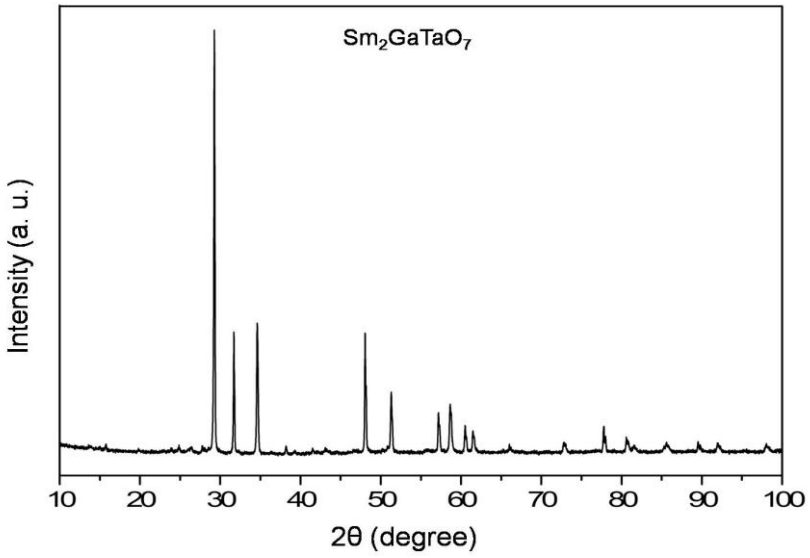

Figure 1. XRD pattern of Sm_2GaTaO_7 synthesized by solid state reaction method at 1400ºC.

To determinate the crystal structure of Sm_2GaTaO_7, a Rietveld refinement was carried out using a theoretical monoclinic unit cell with space group C2/c (No. 15) as a model, recently reported for Sm_2FeTaO_7 [17]. In the model, Ga and Ta ions were assumed to occupy equivalent atomic sites in equal proportion to one another. According to the Rietveld refinement results, experimental and calculated data XRD patterns agreed well with each other, see Figure 2. This means that all X-ray reflections of Sm_2GaTaO_7 can be entirely indexed for a monoclinic crystal structure with the space group C2/c. This results revealed that Sm_2GaTaO_7 and Sm_2FeTaO_7 are isostructural compounds, this is due to their very close ionic radii, Fe^{3+} = 0.64 Å and Ga^{3+} = 0.62 Å [18]. Therefore, Sm_2GaTaO_7 monoclinic structure consists of irregular Ga/Ta octahedra linked at their corners and interconnected into a hexagonal tungsten bronze (HTB)-type network forming 2D HTB blocks, as previously reported for Sm_2FeTaO_7 [17]. The structural arrangement of Sm_2GaTaO_7 differs from $SmTaO_4$ with a fergusonite-type structure that can be regarded as arrays of TaO_4 tetrahedrons that are not linked together [15].

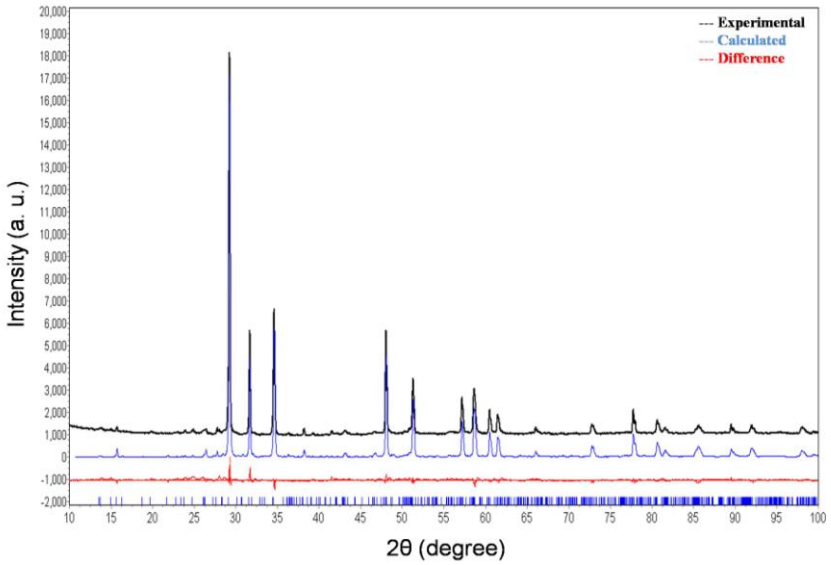

Figure 2. XRD patterns from Rietveld refinement of Sm_2GaTaO_7.

Table 1 shows the crystal data and the reliability factors obtained for Sm_2GaTaO_7, while the refined atomic positions are listed in Table 2. The lattice cell parameters of Sm_2GaTaO_7 are in close agreement to previously reported literature values for similar oxide compounds with monoclinic structure [17,19,20].

Table 1. Crystallographic data obtained from Rietveld refinement results.

Parameter	
a (Å)	13.1386(3)
b (Å)	7.5911(2)
c (Å)	11.5495(3)
β (°)	101.087(2)
Crystal structure	Monoclinic
Space group	C2/c
Z	8
R_{wp}, (%)	6.69
χ^2	1.25

Table 2. Atomic positions of Sm_2GaTaO_7 obtained from Rietveld refinement results.

Atom	Site	Occupancy	x	y	z
Sm1	8(f)	1	0.363(1)	0.129(2)	0.500(1)
Sm2	8(f)	1	0.118(1)	0.135(2)	- 0.009(2)
Ga/Ta1	8(f)	0.5/0.5	0.247(3)	0.111(3)	0.7525(2)
Ga/Ta2	8(f)	0.25/0.25	0.512(4)	0.139(5)	0.292(4)
Ga/Ta3	4(e)	0.5/0.5	0	0.135(3)	0.25
O1	8(f)	1	0.334(3)	0.112(6)	0.306(3)
O2	8(f)	1	0.471(4)	0.128(7)	0.096(3)
O3	8(f)	1	0.218(4)	0.137(6)	0.611(3)
O4	8(f)	1	0.461(3)	0.098(5)	0.726(4)
O5	8(f)	1	0.732(4)	0.142(6)	0.545(3)
O6	8(f)	1	0.031(3)	0.147(6)	0.451(3)
O7	8(f)	1	0.172(2)	0.117(7)	0.762(3)

Figure 3 shows SEM images and EDS spectrum of Sm_2GaTaO_7 and $0.2RuO_2/Sm_2GaTaO_7$ materials. It can be observed that materials exhibit semi-spherical particles with size larger than 1 μm. It could be also observed the presence of particles with neck growths due to sintering process caused by high temperature and long reaction time. The EDS analysis results of RuO_2/Sm_2GaTaO_7 materials revealed that RuO_2 content was 0.2, 0.9 and 1.5 weight percent.

The adsorption analysis results showed that Sm_2GaTaO_7 and RuO_2/Sm_2GaTaO_7 materials had similar specific surface area of around of 0.5 m^2 g^{-1}. This indicates that surface area variation after impregnation was not significant due to the low content of RuO_2 loaded.

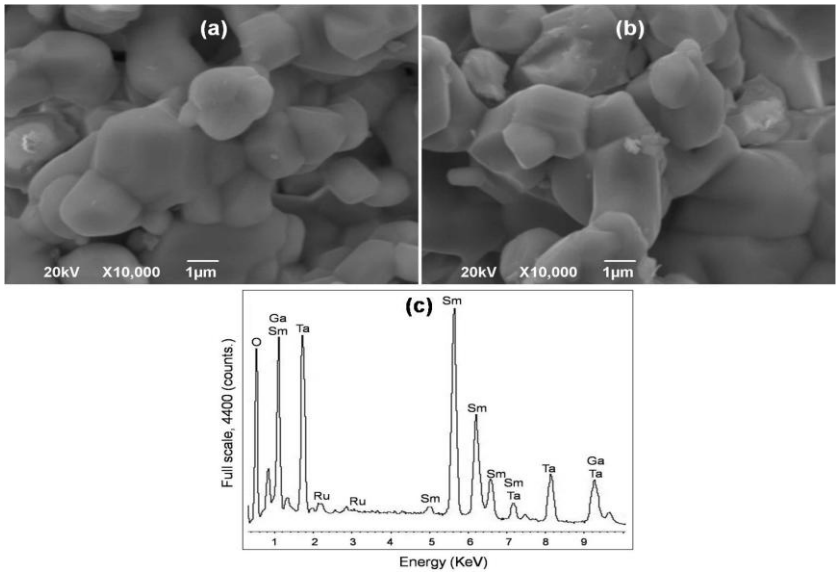

Figure 3. SEM images of Sm_2GaTaO_7 (a), $0.2RuO_2/Sm_2GaTaO_7$ (b) and EDS spectrum of $0.2RuO_2/Sm_2GaTaO_7$.

The UV-Vis diffuse reflectance spectrum of Sm_2GaTaO_7 is showed in Figure 4. The spectrum exhibits the major peak at $\lambda < 320$ nm and also can be noted several peaks at $\lambda > 350$ nm attributed to internal transitions of the partly filled samarium *4f* shell [13,15,21]. According with the Kubelka-Munk analysis results, Sm_2GaTaO_7 possesses an energy band gap (*Eg*) in the order of 4.1 eV. This *Eg* value is comparable to previously reported for similar compounds [15,21].

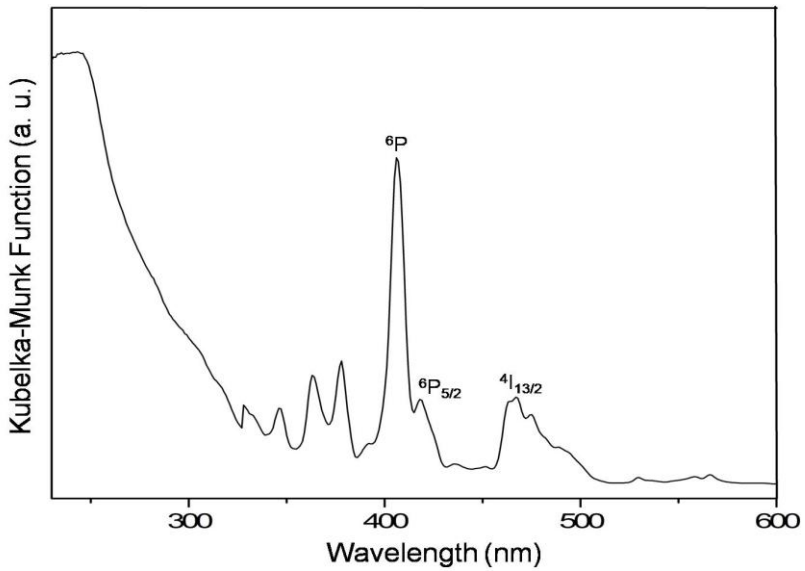

Figure 4. Plot of Kubelka-Munk function of Sm_2GaTaO_7.

Figure 5 shows the UV-Vis diffuse reflectance spectra of Sm_2GaTaO_7 materials. It is evident that the reflectance values gradually decreased (the absorption in opposition increased), as the wt. % RuO_2 amount was increased. After impregnation the samples had a much darker color when RuO_2 content increased, these colored materials necessarily absorbs visible light; which is confirmed by the decreased in reflectance values. These results also confirm the presence of RuO_2 nanoparticles on the Sm_2GaTaO_7 surface.

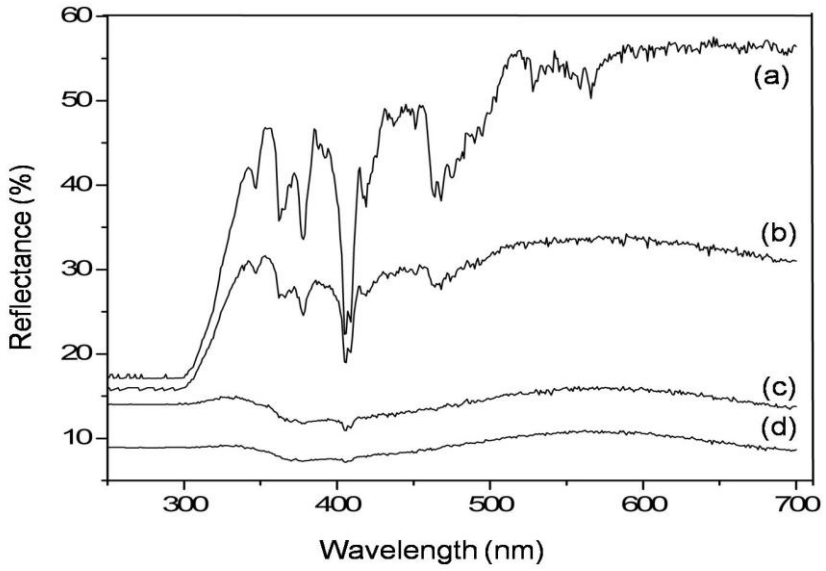

Figure 5. UV-Vis diffuse reflectance spectra of Sm_2GaTaO_7 samples: (a) without RuO_2, (b) 0.2% RuO_2, (c) 0.9% RuO_2 and (d) 1.5% RuO_2.

3.2 Water splitting reaction

Prior the photocatalytic reaction test, blank controls were performed with the same reaction system in dark or in the absence of catalyst. No hydrogen was generated in these conditions. Figure 6 shows the photocatalytic H_2 evolution as a function of irradiation time from pure water. The photocatalytic H_2 evolution are listed in Table 3. Figure 6 shows hydrogen production as function of reaction time. It can be observed that during the first 120 minutes all materials exhibited a similar behavior. After that time, differences can be found in the hydrogen production as function of the RuO_2 wt.% content. The material $0.2RuO_2/Sm_2GaTaO_7$ presents the higher hydrogen production but when the RuO_2 amount increase to 0.9 and 1.5 wt.%, hydrogen production decreases considerably and it is even less than Sm_2GaTaO_7. These results revealed that RuO_2 as cocatalyst provide efficient active sites for H_2 evolution, however an excess in the RuO_2 wt. % amount may cause agglomeration of the RuO_2 nanoparticles reducing the number of active sites for H_2 evolution. Moreover, excessively loaded of RuO_2 hinder light absorption by the base photocatalysts reducing the generation of the electron-hole pair and in some cases could act as recombination centers [1].

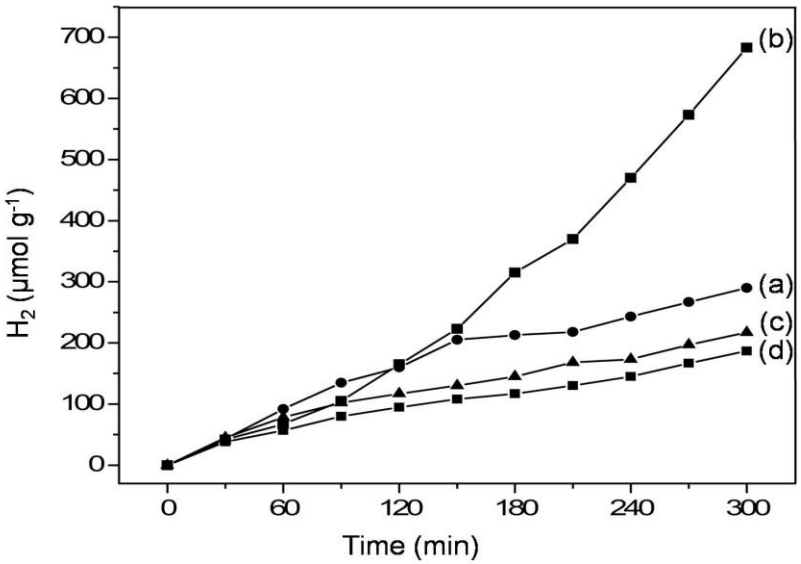

Figure 6. Photocatalytic hydrogen production of Sm_2GaTaO_7 materials: (a) without RuO_2, (b) 0.2% RuO_2, (c) 0.9% RuO_2 and (d) 1.5% RuO_2.

Table 3. Photocatalytic activity of Sm_2GaTaO_7 for hydrogen production

Photocatalyst	**H_2 evolution (μmol h^{-1} g^{-1})**
Sm_2GaTaO_7	58
$0.2RuO_2/Sm_2GaTaO_7$	137
$0.9RuO_2/Sm_2GaTaO_7$	43
$1.5RuO_2/Sm_2GaTaO_7$	37

Although it has been reported that RuO_2 cocatalyst can act as both reduction and oxidation site during water splitting reaction [5]. However, in the present work, it was observed that RuO_2 only acts as reduction site for H_2 evolution because O_2 evolution was not presented. It could be associated with the possible adsorption of O_2 molecules onto the Sm_2GaTaO_7 surface. These was previously reported by some authors [13,22].

Table 4 resumes some H_2 production reported results. In most of the cases, the H_2 production obtained in this work is superior than many of these studies under similar reaction conditions even some of the reported works used sacrificial agents such as methanol and ethanol that under certain condition, they can also undergo photocatalytic reforming to produce hydrogen. This implies that, using an alcohol solution, the origin of the produced H_2 is uncertain and may not be issued exclusively from photocatalytic water splitting [23-25]. The H_2 production rate of Sm_2GaTaO_7 was 39 times higher than $SmTaO_4$ under similar reaction conditions. This higher hydrogen production can be understood from the following aspects. Firstly, the presence of Ga^{3+} makes possible the formation of a 4f-d^{10}-d^0 electronic configuration compound which favors the mobility of the electron-hole pairs [13]. The second one is related with the crystal structure arrangement of Ga/Ta octahedral. The presence of two metals ions with different electronic configuration at the same crystalline site of the Sm_2GaTaO_7 structure

arrangement generate the formation of highly distorted octahedral units facilitating the generation and mobility to the surface of the photogenerated electron-hole pairs. And finally, the use of RuO_2 as cocatalyst decreases considerably the recombination of the electron-hole pairs and provides extra reaction sites for the H_2 evolution. Therefore, Sm_2GaTaO_7 in combination with an optimal amount of RuO_2 as cocatalyst can be considered an attractive material for pure water splitting. This information might be useful for designing new photocatalyst materials for water splitting.

Table 4. Comparative results of specific H_2 evolution from photocatalytic water splitting using different complex oxides

Photocatalyst	Sacrificial agent	Reaction conditions	Light source	Specific H_2 evolution ($\mu mol\ h^{-1}\ g^{-1}$)	Ref.
Sm_2GaTaO_7 0.2 RuO_2/Sm_2GaTaO_7	none	0.3 g of catalyst and 300 mL of pure water	400 W High Pressure Hg lamp	58 137	This work
$SmTaO_4$ 0.7 $Ni/SmTaO_4$	none	0.2 g of catalyst and 200 mL of pure water	400 W High Pressure Hg lamp	1.5 46	15
$RbSmTa_2O_7$	none	0.2 g of catalyst and 200 of mL pure water	400 W High Pressure Hg lamp	53	21
0.2 Pt/Bi_2GaTaO_7 0.2 Pt/Bi_2InTaO_7 0.2 Pt/Bi_2FeTaO_7	methanol	2 g of catalyst, 50 mL of methanol and 320 mL of water	400 W High Pressure Hg lamp	31 497 56	26
Bi_2LaTaO_7 Bi_2YTaO_7	none	1 g of catalyst and 300 mL of pure water	400 W High Pressure Hg lamp	42 34	27
Bi_2AlNbO_7 NiO_x/Bi_2AlNbO_7 $Bi_{1.8}La_{0.2}AlNbO_7$ $NiO_x/Bi_{1.8}La_{0.2}AlNbO_7$	methanol	0.1 g of catalyst, 20 mL of methanol and 400 mL of water	350 W High Pressure Hg lamp	45 74 105 141	28
$La:Cd_2TaGaO_6$ $0.5Pt/La:Cd_2TaGaO_6$ $0.5NiO/La:Cd_2TaGaO_6$	ethanol	0.3 g of catalyst, 45 mL of ethanol and 405 mL of water	300 W High Pressure Hg lamp	300 5700 2833	7

4. Conclusions

The Sm_2GaTaO_7 was synthesized for the first time through solid state reaction. The XRD results indicate that the compound crystallized in the monoclinic system with a space group C2/c. The Sm_2GaTaO_7 was able to produce H_2 from pure water, this result reveals that crystal structure and the constitute elements play an important role in the photocatalytic activity. The RuO_2 acts as an effective cocatalyst to enhance photocatalytic H_2 production activity of Sm_2GaTaO_7. The optimal RuO_2 loading amount was found to be 0.2 wt.%. At this content, H_2 production was 137 $\mu mol\ h^{-1}\ g^{-1}$, which exceeded 2.4 times the production of pure Sm_2GaTaO_7.

5. Acknowledgements

Authors want to thank for the financial support of this research to CONACYT through project CB 98740-2008 as well as PAICYT-UANL-2010 projects and PIFI-2011. Miguel A. Ruiz-Gómez would like to thank CONACYT for his scholarship no. 239336.

6. References

[1] K. Maeda, J. Photochem. Photobiol., C, 12, 237 (2011).

[2] D. Jing, L. Guo, L. Zhao, X. Zhang, H. Liu, et al., Int. J. Hydrogen Energy, 35, 7087 (2010).

[3] J. Zhu and M. Zach, Curr. Opin. Colloid Interface Sci., 14, 260 (2009).

[4] A. Kudo and Y. Miseki, Chem. Soc. Rev., 38, 253 (2009).

[5] K. Maeda, R. Abe and K. Domen, J. Phys. Chem. C, 115, 3057 (2011).

[6] L.M. Torres-Martínez, R. Gómez, O. Vázquez-Cuchillo, I. Juárez-Ramírez, A. Cruz-López and F.J. Alejandre-Sandoval, Catal. Commun., 12, 268 (2010).

[7] Y. Chen, H. Yang, X. Liu and L. Guo, Int. J. Hydrogen Energy, 35, 7029 (2010).

[8] I.S. Cho, S.T. Bae, D.H. Kim and K.S. Hong, Int. J. Hydrogen Energy, 35, 12954 (2010).

[9] J. Sato, N. Saito, H. Nishiyama and Y. Inoue, J. Phys. Chem. B, 105, 6061 (2001).

[10] J. Sato, H. Kobayashi, K. Ikarashi, N. Saito, H. Nishiyama and Y. Inoue, J. Phys. Chem. B, 108, 4369 (2004).

[11] N. Arai, N. Saito, H. Nishiyama, Y. Shimodaira, H. Kobayashi, Y. Inoue and K. Sato, J. Phys. Chem. C, 112, 5000 (2008).

[12] X.D. Tang, H.Q. Ye, H. Liu, C.X. Ma and Z. Zhao, Chem. Phys. Lett., 484, 48 (2009).

[13] X. Tang, H. Ye, H. Liu, C.X. Ma and Z. Zhao, J. Solid State Chem., 183, 192 (2010).

[14] R. Abe, M. Higashi, Z. Zou, K. Sayama, Y. Abe and H. Arakawa, J. Phys. Chem. B, 108, 811 (2004).

[15] M. Machida, S. Murakami, T. Kijima, S. Matsushima and M. Arai, J. Phys. Chem. B, 105, 3289 (2001).

[16] Software Topas R, version 3, Bruker AXS, West Germany, (2005).

[17] L.M. Torres-Martínez, M.A. Ruiz-Gómez, M.Z. Figueroa-Torres, I. Juárez-Ramírez, E. Moctezuma and E. López-Cuellar, Mater. Chem. Phys., 133, 839 (2012).

[18] R.D. Shannon, Acta Cryst., 32, 751 (1976).

[19] G.M. Veith, M.V. Lobanov, T.J. Emge, M. Greenblatt, F. Stowasser, et al., J. Mater. Chem., 14, 1623 (2004).

[20] I. Levin, T.G. Amos, J.C. Nino, T.A. Vanderah, I.M. Reaney, C.A. Randall and M.T. Lanagan, J. Mater. Res., 17, 1406 (2002).

[21] M. Machida, J. Yabunaka and T. Kijima, Chem. Mater., 12, 812 (2000).

[22] J. Yin, Z. Zou and J. Ye, J. Phys. Chem. B, 107, 4936 (2003).

[23] O. Rosseler, M.V. Shanker, M. K. Du, L. Schmidlin, N. Keller and V. Keller, J. Catal., 269, 179 (2010).

[24] T. Puangpetch, T. Sreethawong, S. Yoshikawa and S. Chavadej, J. Mol. Catal. A: Chem., 312, 97 (2009).

[25] J. Wang, C.S. Lee and M.C. Lin, J. Phys. Chem. C, 113, 6681 (2009).

[26] J. Wang, Z. Zou and J. Ye, J. Phys. Chem. Solids, 66, 349 (2005).

[27] J. Luan, X. Hao, S. Zheng, G. Luan and X. Wu, J. Mater. Sci., 41, 8001 (2006).

[28] Y. Li, G. Chen, H. Zhang and Z. Li, Mater. Res. Bull., 44, 741 (2009).

Graphene Oxides for Application in Non-Faradaic Supercapacitors

J M Baas López[1], J. A. Azamar[2], M. Smit[1] and D.E. Pacheco-Catalán[1]*

1. Centro de Investigación Científica de Yucatán (CICY), Calle 43 No. 130, col. Chuburná de Hidalgo, C.P. 97200, Mérida, Yucatán, México.
2. Centro de Investigación y de Estudios Avanzados del IPN, Unidad Mérida, A.P. 73, Cordemex, C.P. 97310, Mérida, Yucatán, México

* contact email: dpacheco@cicy.mx

ABSTRACT

Graphene oxide (GO) was the precursor of graphene, which is the material with unique properties how electrical conductivity, thermal conductivity, mechanical etc. Graphene presents the high specific surface of 2,965 $m^2 \bullet g^{-1}$, and your electric conductivity has been increased by thermo treatments with elevated temperature, and a consequence has been obtained increase the specific surface and low resistance intern, which is favorable for energy storage. Nevertheless, graphene oxide (GO) has attractive properties by energy storage due to your compatibility with different electrolytes due to functional groups present on the surface of carbon structure.

In the literature, have been reported different methods for the obtained of graphene oxide. However in this work, the synthesis of graphene oxide (GO) was realized by Hummer's modified method, because is a method of obtaining at great scale. The process of synthesis consist of four steps: 1.-Pre-thermal oxidation with oxygen flow, 2.- Chemical oxidation of precursors, 3.- Chemical oxidation for the obtainment of graphite oxide and 4.- Exfoliation of graphite oxide by ultrasonic to obtaining the sheets of graphene oxide (GO).

GO obtained was characterized physically and chemically by SEM, EDAX and RAMAN. Also, the GO was evaluated electrochemically by voltammetry cyclic as different scanning rates at 5, 10, 20, 30 and 50 mV/s and limit potential of 0 to 1 V. For realize to the electrochemical characterization of material, this was deposited on carbon cloth electrode of 1 cm^2.

Keywords: Supercapacitors, (GO) Graphene Oxide.

1. INTRODUCTION

Electrochemical capacitors (EC) are often called supercapacitors or ultracapacitors as a result of having a high capacitance in a small amount of area. These devices have been used as energy storage and are classified by mechanism of energy storage, devices; there are two kinds of supercapacitors: the electric double layer capacitors and redox pseudocapacitors [1].

The Electric Double Layer Capacitors (EDLC's) works by accumulation of the electrostatic charges on the surface of electrode-electrolyte, by separation or deposition of electrons in anodes and cathodes, which in turn induced by an applied potential across the device [1]. The positive or negative charge on the surface is balanced by an accumulation of counter ions (ions of opposite charge) of the solution, forming a double-layer of positive or negative charges (or vice versa), these devices employ carbon to generate a load double Layer [2], development of these devices emphasizes the importance of designing new materials to improve the power delivered and the energy storage EDLCs, which include nanostructured materials of carbon aerogels, carbon nanotubes and graphene, etc.

The mechanism by storage energy in the case of pseudocapacitors, is due to both processes EDL and faradic or redox, in conditions thermodynamics defined potentials and the electrode surface and are responsible for accumulation and release a capacitive charge which depends on the repulsive forces between electrolyte absorbed or intercalated ions which performance an important role in extending the operating potential for the development of capacitive charges, on the contrary a force weak repulsive or attractive between ions severely limits the useful operating window [3]. Pseudocapacitive materials generated a significant attraction due to the number of electrons transferred in the redox process which can be compared with the capacitive charge of the EDL; between these materials may be mentioned intrinsically electro-conductive polymers, and metal oxides[1].

The performance of a supercapacitor too dependent on the materials you choose to build their anode and cathode electrodes, between the characteristics of the materials must meet to satisfy the conditions of the electrodes can be found graphene. The graphene is sheet monatomic carbon atoms attached through bonds covalent sp2 (monolayer of graphite) [4], until 2004 did not believe it is possible existence as an isolated sheet, as it is supposed to strictly two-dimensional crystals are thermodynamically unstable. Graphene is a special case of semimetal and has a zero gap metal, having the peculiarity that the density of states at the level of Fermin is zero. Graphene tends to adsorb molecules on its surface, this coupled with its high specific surface area ($2600 m^2 g^{-1}$) , mechanical strength and high conductivity postulated as a possible successor as electrodes of supercapacitors EDLC[5]

Nevertheless, the graphene in reduced state presents weak interaction with electrolyte. The graphene oxide (GO) is one of the most crucial derivatives of graphene, and it exhibits a layered structure with oxygen functional groups bearing the basal planes and edges. The existing functional groups such as carboxyl and hydroxyl groups tend to improve the hydrophobicity of basal planes. The ECs fabricated with the graphene-based electrodes display an exciting potential with high rate capability and reversibility[6].

2. EXPERIMENTAL

To synthesize graphite oxide proceeded to weight 20 g of graphite flakes by Sigma Aldrich with a percentage purity of 70%, the sample was heated to 250 ° C in oxygen saturated atmosphere, this temperature was maintained for 4 hours to remove impurities[4]. Posterior, was applied the method of. Hummer's to synthesize graphite oxide[7] and then graphene oxide (GO).This method employs two stages, first to remove ions and acids with a pre-oxidation thermal of graphite using 2 L of hydrochloric acid solution ratio at 1:10 and the second step is to wash the sample with 2 L of deionized water to remove residual acid for a week in an ultrafiltration cell by Millipore Amicon, after the sample is dried at 60 ° C for 48 hours.

Following, 20 mg of graphite oxide obtained is carried out by chemical reduction by adding 20 ml of a 0.1M solution of sodium boron hydrate; the reduction is realized when the graphite oxide changes your coloration from brown to black, then is begins the hydrogen secondary reaction [8, 9]. The mixture was stirring by ultrasonic bath during one hour for reduced graphene sheets (CRG), and posterior were washed with deionized water and filtered with Millipore Amicon ultrafiltration cell. The sample was dried of vacuum oven at 60 ° C for 24 hours to remove residual water. Finally, 2 mg of reduced graphene was placed in 20 ml of ethylene glycol and was stirred inside an ultrasonic bath for one hour.

The samples were characterized by Raman spectroscopy is a technique which can be inferred in several material properties such as chemical and structural, the depth of analysis extends only a few nanometers in the sample by which is considered a non-destructive technique surface [10, 11]. 2 samples were prepared for spectroscopy Raman, depositing on a microscope slide 100µL of a solution graphene oxide concentration of 5mg in 20ml of ethylene glycol and 100µL of graphene reduced, which were heated to 190 ° C to evaporate all the ethylene glycol.

For the evaluation of the performance electrochemical of these materials, there materials were characterized by cyclic voltammetry was used a cell of three electrodes, the work electrode (WE) was the carbon cloth electrode of 1cm^2 of area and this was deposited 400 µL of reduced graphene solution as the concentration of 2mg/20mL in ethylene glycol. The counter electrode (CE) was a graphite rod with 0.5mm of diameter and as the reference electrode (RE) was used a saturated calomel electrode (SCE). For the tests, was used a solution 0.05 M of H_2SO_4, as the electrolyte, and the window potential of 0 to 0.9 V vs. SCE x 5 cycles at different sweep rates.

3. RESULTS AND DISCUSSION

Morphology changes of graphite oxide by oxidation process, was realized by SEM analysis and by EDAX was determined by elemental analysis. In the figure 1a shows the morphology of graphite flakes by Sigma Aldrich at 70% of purity. Figure 1b shows the morphology of graphite oxide. In this case, the graphite oxide shows mayor irregularity and mayor roughness with respect to graphite (figure 1 a) due to the process of oxidation; this is confirmed with the percent of oxygen present in the sample (Table 1). By means of EDAX analysis was obtained an

average percentage of elements for the two samples, the average was obtained taken six different areas and the values are presented in the Table 1.

There values show differences between graphite and graphite oxide, correspondent to contain of carbon and oxygen, principally. For the case of graphene oxide is observed an increase of contained of oxygen and diminished of carbon, this is possible of the formation of oxygen functional groups.

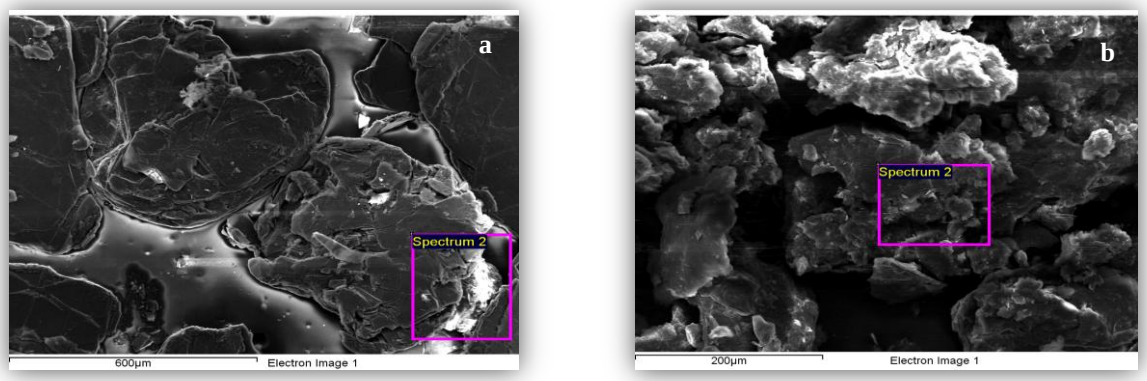

Figure1: SEM images obtained for two different samples: a) graphite flakes at 70% of purity and b) graphite oxide obtained.

Table 1: EDAX analysis for elements present in the samples.

Flake graphite		Graphite oxide	
Element	**%**	**Element**	**%**
C	88.97	C	59.77
O	9.78	O	37.75
Mg	0.05	Si	0.986
Si	0.55	S	0.416
Ca	0.10	Cl	1.022
Fe	0.22	Al	0.054

By mean of Raman spectroscopy can be confirm the obtained of graphene reduced and graphene oxide. However, the equipment used to perform the analysis in this occasion is limited, therefore only be observed the first-order spectrum. For the case of perfect graphite, the first-order of spectrum Raman includes a very narrow and intense peak around of 1580cm^{-1}, this band is called G and its relationship with the graphitic order. This band is shown at 1580 cm^{-1} of Raman shift for highly ordered pyrolytic graphite (HOP) [10], (see Figure 2) which was used as background to compare with the obtained graphene.

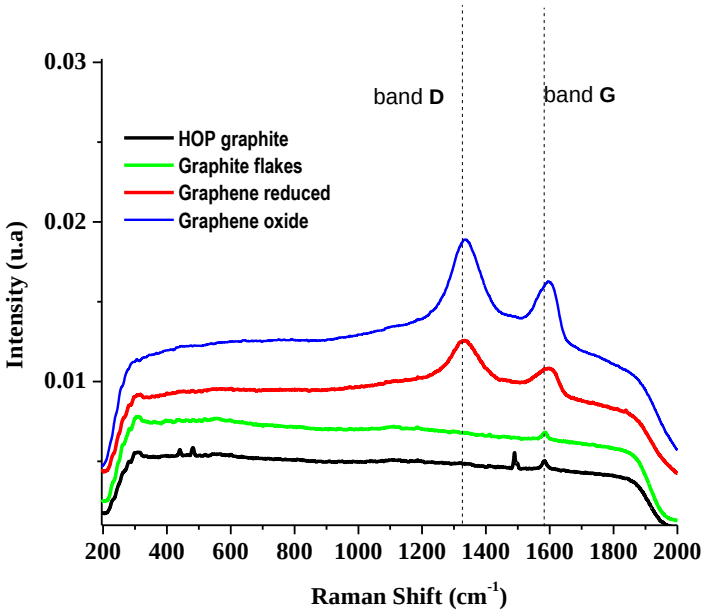

Figure 2: Spectra Raman of graphite flakes (green), HOP graphite (black), graphene oxide (blue) and graphene reduced (red)

Conform the graphite loses its structural order by the introduction of defects caused by oxidation processes, shows the apparition of a band located around 1360cm^{-1} called D [11]. In the figure 2 is showed the appears in the curve of graphene oxide this band at 1339cm^{-1}; in graphene reduced this band appears at 1333cm^{-1}. One of the parameters employed by determined the graphitic order is the ratio of the intensity of the band D with respect to the band G (ID / IG). However there comes a point at which the ratio *I*D/*I*G decreases with increasing the disorder, due to the disappearance of the aromatic rings, which leads to decreasing the intensity of the band D. Table 2 shows the relationship between the intensity of these two bands characteristics obtained from Raman spectra by different samples prepared.

Table 2: Ratio between the intensities of bands D and G

Sample	Intensity D	Intensity G	(*I*D/*I*G)
Graphene oxide	0.018	0.016	1.1
Graphene reduced	0.012	0.010	1.2

Figure 3 shows the cyclic voltammetry obtained from a sweep rate of 80 mV s^{-1} for the carbon cloth electrodes modified and without modified. The curves correspond to the electrodes with graphene oxides and graphene reduced. The Figure 3 b shows low values of current density for carbon cloth electrodes with and without ethylene glycol.

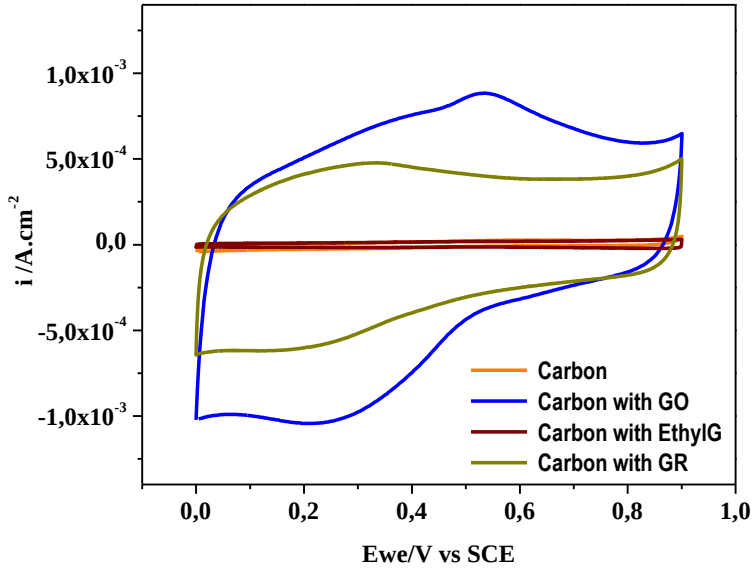

Figure 3: Cyclic voltammetry for electrodes of carbon electrodes with and without ethylene glycol, with graphene oxide and with graphene reduced at 80mV s^{-1} vs SCE.

In the curve of the electrode graphene oxide shows an increase of values of current density with respect to the other materials, additionally presents a peak at 0.52V which is derived from oxidized graphene, this phenomenon is similar to the processes denominate as pseudocapacitance which is attributed to functional groups of oxidants [11]. With respect to the curve of the graphene reduced is observed decreased values of current density and decreases of the peak around the 0.52V as consequence of the reduction processes of the sample. The curve corresponds to graphene reduced present most rectangular shape and ideally forms by material of supercapacitores. Also was observed what the increase of the current densities depositing the active material (around of 4 x 10^{-6} g) by electrode. Comparing the curves correspond to graphene reduced and graphene oxide with respect a cloth carbon and cloth carbon with ethylene glycol can be observed what in the two first cases is observed values mayors of current density comparing with the last two cases.

Capacitance values of the electrodes with graphene reduced and graphene oxide was calculated according to

the following equation, from the curves of cyclic voltammetry [2, 12].

(1)

where C is the specific capacitance based on the mass of material electroactive ($F.g^{-1}$), I it is the current density response ($A\ cm^{-1}$), is the sweep rate ($mV\ s^{-1}$), m is the mass of electroactive materials in the electrodes (g) y V is the potential applied the device (V). The values of specific capacitance of graphene oxide and reduced graphene are shown in Table 3.

Table 3: Values of capacitance and specific capacitance obtained by graphene reduced and graphene oxide.

Sample	Capacitance (F)	Specific capacitance ($F\ g^{-1}$)
Graphene oxide	0.0154	3854.5
Graphene reducid	0.0096	2408.7

4. CONCLUSIONS

It can be concluded that the graphite flakes tend to increase the percentage of oxygen after applying oxidation, indicating the effectiveness of the process. Raman spectroscopy confirmed the modified in the structure of graphene reduced and the graphene oxide with respect at the graphite. The curves obtained by cyclic voltammetry of the graphene oxide and the reduced graphene showed specific capacitance around to 2408.7 $F\ g^{-1}$ with only 4×10^{-6} g active material, therefore become attractive materials for use as electrodes for supercapacitors.

5. ACKNOWLEDGEMENTS

This work was supported by Fordecyt-116157, Conacyt -145411 and the Dr. Ricardo Mis by the conditions of Raman spectroscopy.

6. REFERENCES

[1] A. Davies,A. Yu, *The Canadian Journal of Chemical Engineering*, n/a (2011).
[2] A. Clemente; S. Panero; E. Spila,B. Scrosati, *Solid State Ionics*, **85**, 273 (1996).
[3] M. Winter,R. J. Brodd, *Chemical Reviews*, **104**, 4245 (2004).
[4] J. Horng; C.-F. Chen; B. Geng; C. Girit; Y. Zhang; Z. Hao; H. A. Bechtel; M. Martin; A. Zettl; M. F. Crommie; Y. R. Shen,F. Wang, *Physical Review B*, **83**, 165113 (2011).
[5] D. R. Dreyer; S. Park; C. W. Bielawski,R. S. Ruoff, *Chemical Society Reviews*, **39**, 228 (2010).
[6] C.-T. Hsieh; S.-M. Hsu; J.-Y. Lin,H. Teng, *The Journal of Physical Chemistry C*, **115**, 12367 (2011).
[7] W. S. Hummers,R. E. Offeman, *Journal of the American Chemical Society*, **80**, 1339 (1958).
[8] D. Luo; G. Zhang; J. Liu,X. Sun, *The Journal of Physical Chemistry C*, **115**, 11327 (2011).
[9] S. K. Manepalli; P. Srimathi; R. J. Davis,S. Kumar, *ECS Transactions*, **35**, 57 (2011).

[10] H. T. Kagi, Kazuya; Masuda, Akimasa, Raman frequencies of graphitic carbon in Antarctic ureilites, In *Eighteenth Symposium on Antarctic Meteorites. Proceedings of the NIPR Symposium*, Keizo Yanai, w. H. F., Hideyasu Kojima, Masamichi Miyamoto, Nobuo Takaoka, and Yoshio Yoshida Ed. National Institute of Polar Research: Tokio, Vol. 7, pp 252(1994)
[11] L. Buglione; E. L. K. Chng; A. Ambrosi; Z. Sofer,M. Pumera, *Electroc hemistry Communications*, **14**, 5 (2012).
[12] H. L. Wang; Q. L. Hao; X. J. Yang; L. D. Lu,X. Wang, *Nanoscale*, **2**, 2164 (2010).

Development of Polymeric Enzymatic Electrodes for Ethanol Oxidation

Gutiérrez-Domínguez D. E[1], Pacheco-Catalán D. E.[1], Patiño R.[3], Canto-Canché B.[2], Smit M. A.[1*]

[1]Unidad de Energía Renovable, Centro de Investigación Científica de Yucatán A.C, Mérida Yucatán, México.
[2]Unidad de Biotecnología, Centro de Investigación Científica de Yucatán A.C, Mérida Yucatán, México.
[3]Departamento de Física Aplicada, Cinvestav, Unidad Mérida, Mérida Yucatán, México.
[*]Tel: xxxxxxx, mail: mascha@cicy.mx

ABSTRACT

Enzymatic fuel cells are devices in which enzymes are located in the electrode in order to catalyze fuel oxidation. These biological catalysts, unlike inorganic ones, have the advantage of being selective, renewable and clean. The enzymes are supported onto an electronically conducting material, compatible with the enzymes, for example conductive polymers such as polypyrrole. In this project, polymeric anodes are prepared by immobilizing the enzyme alcohol dehydrogenase from S. cerevisae in polypyrrole, potentiostatically electrodeposited onto carbon paper. The applied enzymatic immobilization procedures are both direct adsorption and crosslinking with glutaraldehyde. The characterization of electrodes is made by cyclic voltammetry using a phosphate buffer solution with ethanol and β-NAD^+ as supporting electrolyte. Tests show that reversible ethanol oxidation and reduction occurs at around $0V_{SCE}$ for the polypyrrole electrodes, recorded current values due to polymer oxidation and reduction are higher by two orders of magnitude than those recorded for ethanol oxidation in carbon enzyme electrodes. Furthermore, the polymeric enzymatic electrodes crosslinked with glutaraldehyde show higher current values than those with adsorbed enzyme, which reflects a better retention of the protein in the electrode. Also, electrodes with crosslinked enzyme preserve catalytic activity for longer times than those with adsorbed enzyme. Spectrophotometric and fluorescence measurements are performed in order to determinate enzymatic activity and quantify protein, respectively. Fuel cell performance will be presented for an enzymatic direct ethanol fuel cell.

1. Introduction

Hydrogen is considered as a clean and safe energy source. The oxidation reaction of this element is object of study as part of the hydrogen technology, which uses the direct electrochemical conversion of hydrogen to generate electricity and heat in fuel cells.

In a fuel cell, hydrogen is oxidized at the anode releasing electrons and protons. While the electrons pass through an external circuit, the protons cross an electrolyte to reach the cathode where they react with oxygen to produce water. However, some limitations in performances coupled with the fact that these devices use catalysts based on precious metals and their alloys, have led to the development of biofuel cells [1].

Biofuel cells operate in the same way as conventional cells with the difference that the inorganic catalyst is replaced by a biological catalyst that could be an organism producing enzymes or the enzymes themselves [2]. The enzyme-based cells are attractive due to the advances reported recently. In this type of cell, the enzyme is located at the electrode to catalyze the fuel oxidation, being involved directly in the reaction that generates electricity, with the advantage of being a renewable and clean catalyst, selective, flexible in the types of fuel used and able to work at low to medium temperatures [3].

Even though in their own environment the enzymes have a very short lifetime, this life time can be increased by immobilization [4]. The electroconductive polymers are materials compatible with.

Polypirrole can be used as support for enzyme immobilization due to its low oxidation potential, environmental stability, sensitivity and good quality matrix [5]. When both elements are linked, they forme and enzymatic electrode and the performance is related to the level of contact between enzyme and polypirrole.

2. Experimental

Enzymatic activity was determinate by continuous spectrophotometry, following the Sigma quality control test for alcohol dehydrogenase (EC 1.1.1.1), and electrochemically by cyclic voltammetry using a carbon paper electrode as working electrode, in a buffer solution with NAD^+, ethanol and 751units/ml of alcohol dehydrogenase as supporting electrolyte.

For electrode preparation, polypyrrole was electrodeposited onto $1cm^2$ carbon paper by a potentiostatic method, applying 0.7V vs $_{SCE}$ for 420s in a solution of 0.1M monobasic sodium phosphate/0.1M pyrrole. The enzymatic immobilization was made by direct adsorption, adding alcohol dehydrogenase (6mg/ml) onto the polymer, and by crosslinking, adding alcohol dehydrogenase (6mg/ml) onto the polymer followed of the addition of 0.1% glutaraldehyde solution. For drying, in both cases, the electrode was kept in a desiccator at room temperature for approximately 5 hours.

The electrode characterization was performed by cyclic voltammetry in a range of -0.3V to 0.3V vs $_{SCE}$ at 100mV/s in a three electrode cell with phosphate buffer solution at pH8.8, NAD^+ and 5mM ethanol as supporting electrolyte.

In order to quantify the amount of protein immobilized onto the electrode, the NanoOrange Proteín Quantitation assay was perfomed. The NanoOrange reagent produces fluorescence in presence of the protein, so it was added to

enzymatic electrodes and incubated to 95°C for 10 min protected from the light. After that, the electrode was cooled to room temperature and the fluorescence intensity was measured in a spectrofluorometer at 580 nm with an excitation wavelength of 470 nm.

3. Results and discussion

The enzymatic activity in solution measured by spectrophotometry was of 365.45 units/ml enzyme. Results for cyclic voltammetry are shown in figure 1. An oxidation peak corresponding to ethanol oxidation can be observed around 0V vs $_{SCE}$, this peak was better defined at a sweep rate of 100mV/s, with values in the order of μA.

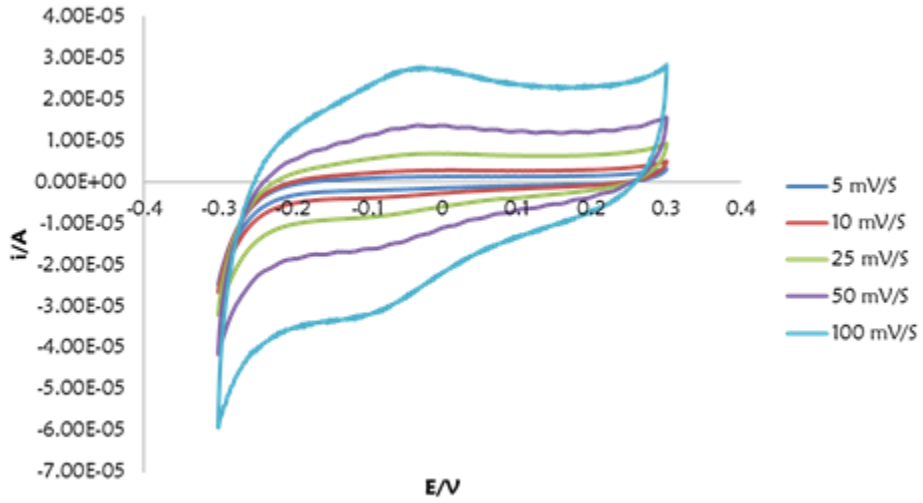

Figure 1 Voltammetry of carbon electrode to different swept potential in phosphate buffer solution 0.1M, pH 8.2, alcohol dehydrogenase 751units/ml, ethanol 2mm and NAD^+ 1.5mM, last cycle.

The amount of polypyrrole deposited was calculated to be 559μg, based on the deposition curve, and its characterization with phosphate buffer solution shows that polymer oxidation and reduction occurs around 0.6V and -1V vs $_{SCE}$, respectively. This process therefore does not interfere in the potential range for enzyme activity.

The polymeric electrode with adsorbed enzyme does not show a defined oxidation peak for ethanol due to the overlap by the polymer oxidation in the same electrolyte conditions generating higher current values than those for the carbon electrode. However, there was an evident change in the performance of polymeric electrodes with and without enzymes in ethanol containing electrolyte, reaching current values in the order of mA for enzyme containing electrodes, related to ethanol oxidation. Moreover, the electrode with crosslinked enzyme generates higher currents than those corresponding to the electrode with adsorbed enzyme, which was related the improved retention of the protein.

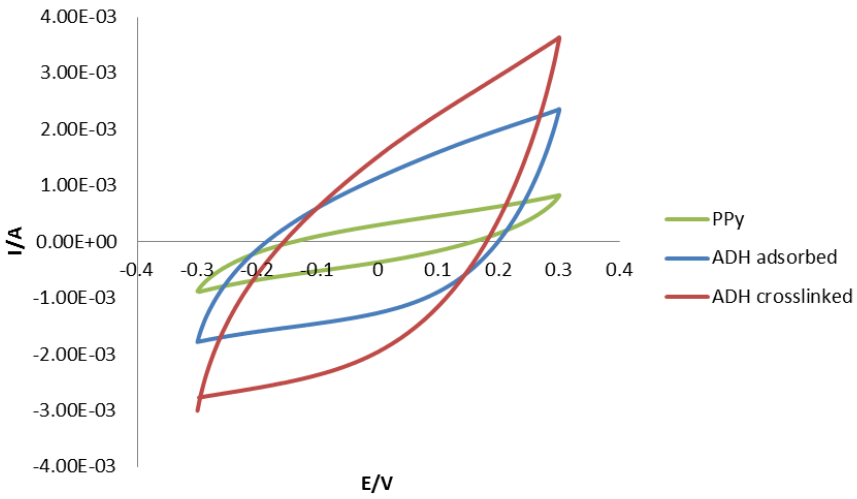

Figure 2 Voltammetry of polypyrrole, enzyme adsorbed electrode and enzyme crosslinked electrode, second cycle.

Cyclic voltammetry was realized over a three day period to determine enzyme degradation. For absorbed enzymatic polymeric electrodes, the current is virtually constant. Small variations probably are result of small temperature change. The current recorded for crosslinked enzyme was more stable.

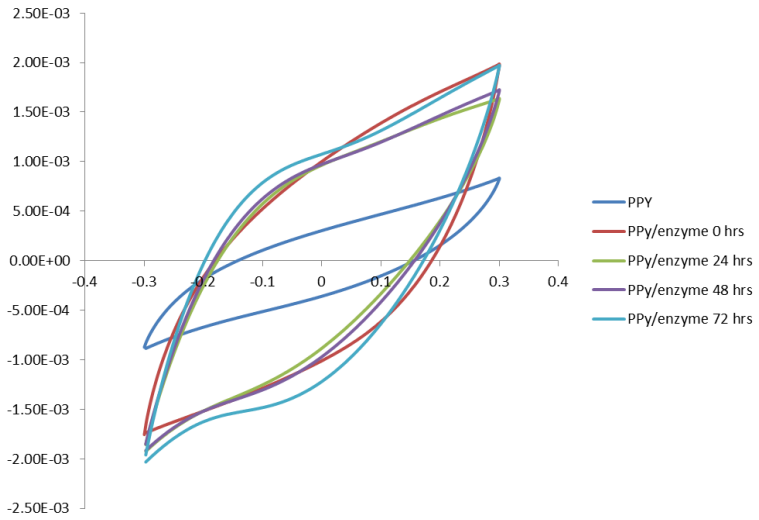

Figure 3 Cyclic voltammetry in different time of adsorbed enzyme electrode, second cycle.

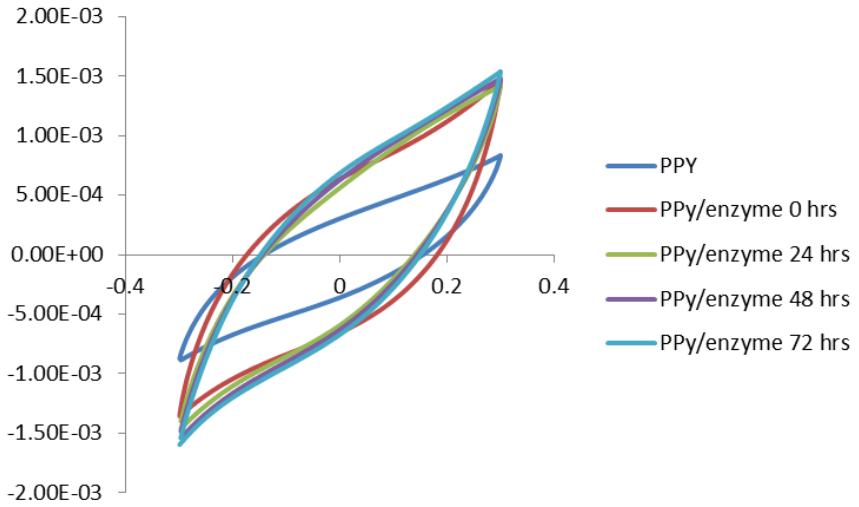

Figure 4 Cyclic Voltammetry in different time of crosslinked enzyme electrode, second cycle.

Finally, it was not possible to quantify the protein by the NanoOrange assay, because of the interaction between the NanoOrange reagent and the polypyrrole, producing higher fluorescence than those emitted by the protein.

4. Conclusions

It was found possible to inmobilize the alcohol dehydrogenase enzyme by direct adsorption and by crosslinking with glutaraldehyde onto polypyrrole electrodes and to maintain biocatalytic activity for ethanol oxidation for several days.

Immobilization of alcohol dehydrogenase onto polymeric electrode results in a better performance than immobilization onto carbon electrode.

The crosslinked immobilization method results in higher stability in enzymatic activity than the direct adsorbed immobilization method.

5. Akcnowledgements

The authors acknowledge financial support by CONACYT projects CIAM 58636 and Fordecyt 116157.

6. References

[1] Anne K. Jones, Emma Sillery, Simon P. J. Albracht and Fraser A. Armstrong, ChemComm, (2002), 866-867.

[2] Sabina Topcagic, Shelley D. Minteer, Electrochem. Acta, 51 (2006) 2168–2172.

[3] Neto, S. Aquino, Electrocatal, 1 (2010) 87-94.

[4] M.H. Osman, A.A. Shah, F.C. Walsh, Biosen and Bioelectron. 26 (2011) 3087-3102.

[5] Shirsat, M. D., Int. J. Electrochem. Sci., 2 (2006) 62-70.

9th International Symposium on New Materials and Nano-Materials for Electrochemical Systems
XII International Congress of the Mexican Hydrogen Society
Merida, Mexico, 2012

Design and Construction of a Demonstrative Hybrid System Consisting of a Solar Panel, a Stack of Regenerative PEM Fuel Cells and Supercapacitors

E. Escobedo[1], A. Morales[2], D. Zavala[2], G. Ortega[1], M. G. Reveles[1], D. Pacheco[1], M.A. Smit[1]

[1]Centro de Investigación Científica de Yucatán (CICY), Calle 43 No. 130,
Col. Chuburná de Hidalgo, C.P. 97200, Mérida, Yucatán, México.

[2]Universidad Autónoma Chapingo, Km. 38.5 Carretera México-Texcoco, C.P. 56230 Chapingo, México.

Email: mascha@cicy.mx

ABSTRACT

The continuous search for improvements in clean energy systems and processes has led to the development of techniques with improved production efficiency and electrical energy storage. Some examples are represented by regenerative fuel cells and supercapacitors.

In this work, we report on a small-scale hybrid renewable hydrogen prototype, which uses a photovoltaic panel to provide electricity (2.8 V) to a regenerative fuel cell stack and also to a supercapacitor module. With the regenerative cell in electrolysis mode, the process of water electrolysis occurs, generating the reactive gases (H_2 and O_2) which are being stored in small water tanks. In fuel cell mode, these gases are fed to the regenerative cell in order to produce electrical energy. The supercapacitors release additional energy when needed.

The electrical energy is sent to a DC engine which allows for the movement of a small toy car. The supercapacitors supply power to the engine at the moment of start when the fuel cell is not able to provide sufficient energy for initial movement. The supercapacitors are rapidly discharged by the engine, and operating depends on the fuel cells until completion of the stored hydrogen.

The fuel cells and supercapacitors were prepared in our laboratory. The fuel cell stack was integrated by two membrane-electrode assemblies (MEA) of 4 cm^2 active area. Ink loading was performed by the drop method using Pt/Ru catalyst for the cathode and Pt catalyst for the anode (fuel cell mode). The supercapacitor electrodes were prepared from mesoporous carbon, polyvinylidene fluoride, and a liquid electrolyte of sulphuric acid is used.

An electrical circuit was designed to control current flow. The toy car with a total weight of 1.2 kg was shown to move at a speed of 2.0 m/s.

1. Introduction

Global fossil energy consumption has increased in recent years due to population growth, increased development and industrialization, causing environmental pollution, climate change, etc. For this reason, the optimization of alternative technologies for clean energy generation, based on low-cost, low-noise, highly efficient and high quality systems, has become a matter of great interest. In this context, hydrogen as a fuel has received considerable attention for its energetic properties, being the fuel with highest energy density [1]. A device to channel this energy vector into electrical energy is represented by the fuel cells of proton exchange membrane (PEMFC).

The present work implements a regenerative PEM-type fuel cell (RFC), which has the particularity of being able to generate hydrogen and oxygen gases by water electrolysis, using electrical energy from a photovoltaic panel in order to perform the process, as well as to generate electrical current as a conventional PEMFC. In this project, the electrical current is provided to a DC engine in order to move a small toy car. An auxiliary boot-up system was incorporated through a bank of supercapacitors, initially charged by the photovoltaic panel.

2. Experimental

The activities were divided in four parts to accomplish the objective:

1. System design.
2. Manufacturing the RFC components and stack.
3. Electrode manufacturing and assembly of supercapacitor
4. System assembly

2.1. System design

Power requirements for the toy car and engine that were used to calculate the parameters of the RFC, were based on experimental work already performed [2]. Was calculated the gas storage system, the supercapacitor module and electrical circuit. the main goal was to produce the electricity needed to drive a 2V engine, 600 mA and a torque of 2kgF * cm. to move the small car of 1200g. (see figure 1).

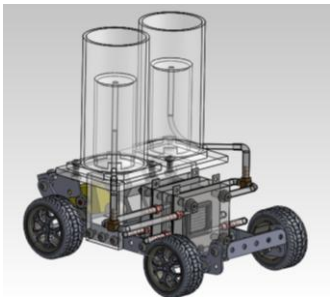

Figure 1. System design

2.2 Manufacturing the components stack URFC

2.2.1 Water storage tanks and gas reactants

Storage tanks were manufactured using acrylic tube of 27.74 mm and 50.80 mm of diameter and with volumetric capacity of 64,16 mm^3 for the water container and 26,70 cm^3 for the reactant gases. Holes for gas transport were of 2.5 mm diameter, as shown in Figure 2.

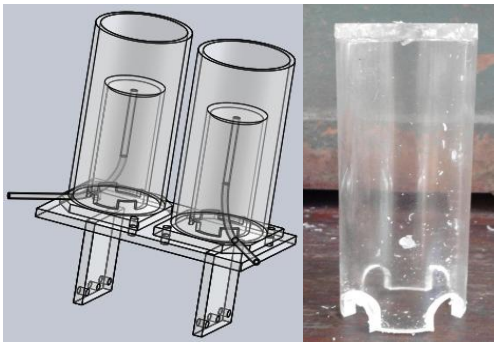

Figure 2. Design and construction of water containers and reactant gases

2.2.2 End plates

The end plates were made of acrylic plate of 1 cm thick using a CNC machine. A channel of 1.5 mm width and perimeter of 80 mm was included for commercial packing in order to prevent leakage of gases and water, as well as holes of 3.18 mm and 0.16 mm for the inlet/outlet of reactant gases and water. Finally, in order to allow compression on the RFC, four holes of 5 mm of diameter were included in the extreme corners of the plates (see figure 3).

.

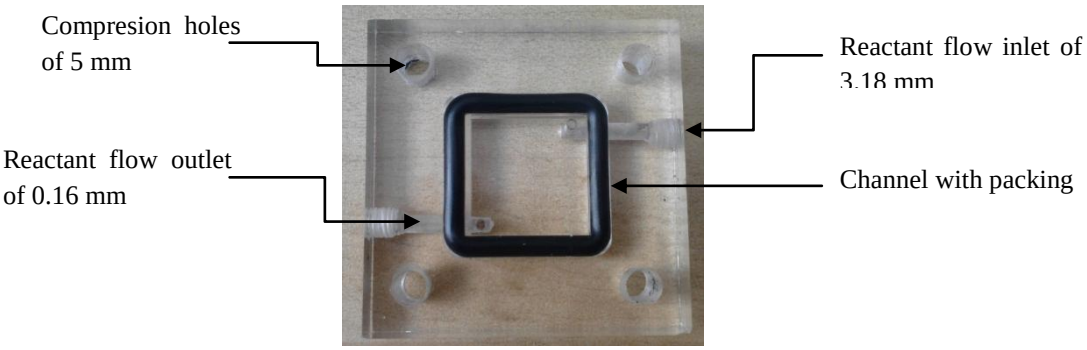

Figure 3. RFC acrylic end plates

2.2.3 Current collector

The current collectors used in the RFC, were machined from a stainless steel (SS316) plate, as shown in figure 4a. The steel provides electrical conductivity in addition to withstand the effects of corrosion from the acid environment. Several holes of 1.98 mm were distributed in the central area of the collector of 4 cm^2. Also, four holes of 5 mm were incorporated to allow the passage of compression screws. A terminal was machine at the top of the collector for connection to an external load. A silicone gasket (FuelCell) of 0.43 mm thick was used between the surfaces of the collectors in order to electrically insulate and support the commercial packing in the leakage of gases, see Figure 4b.

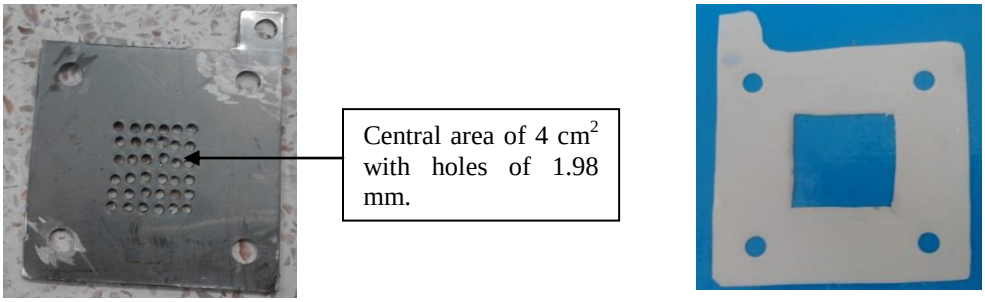

a) b)

Figure 4a). Current collector y **4b)** Silicone gasket for electrically insulate.

2.2.4 Membrane-Electrodes Assembly

The catalytic layer was applied to an area of 4cm^2 of the gas diffusion layers (trademark fuelcell) by the drop method. An ink was prepared from carbon supported platinum (Pt) and platinum/rutenium (Pt/Ru - 20% on Vulcan trademark fuelcell), liquid nafion (5%, trademark Electrochem) and isopropyl alcohol. The electrocatalytic ink was deposited with a catalyst load of 0.5 mg/cm^2. Nafion 115 was used as electrolyte, after activation in H_2SO_4 and H_2O_2. The membrane-electrodes assembly (MEA) was prepared by hot pressing at 120°C with 4000 lb for 4 min [2]. See figure 5.

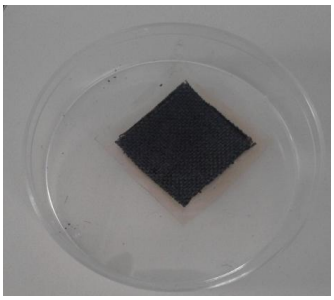

Figure 5. Membrane Electrode Assembly.

MEA's were characterized as conventional fuel cells, injecting a flow of hydrogen and oxygen gas of 0.05 l/min, at a temperature of 25°C in fuel cell test system 850C (Scribner Associates) and using a BioLogic potentiostat/galvanostat.

2.3 Electrode manufacturing and assembly of supercapacitor

Supercapacitor electrodes were prepared as cylindrical pellets of 50 mg each, 13 mm diameter and 1 mm thickness, from a homogeneous mixture of 200 mg of electrode power, with the following proportions [3]:

- 75 wt % of mesoporous carbon type Cummings by Asbury Carbon
- 20 wt% of PVDF polyvinylidene fluoride by Aldrich
- 5 wt % of a high electrical conductivity carbon Super P by 3M

by cold compression of 500 kgf for 15 minutes.

Two electrodes of the same material are mounted in a cell made out of teflon (see Figure 6a), separated by paper microfiber discs (Whatman BS45) and with 1.5 ml of 1M H_2SO_4 as electrolyte, as shown in figure 6b. Current collectors were made of stainless steel A20 to resist acid corrosion. Two supercapacitores (SC1 and SC2) were prepared.

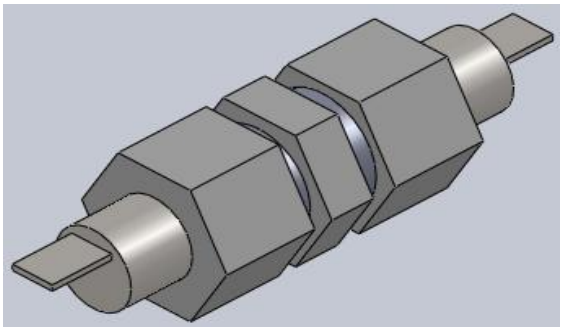

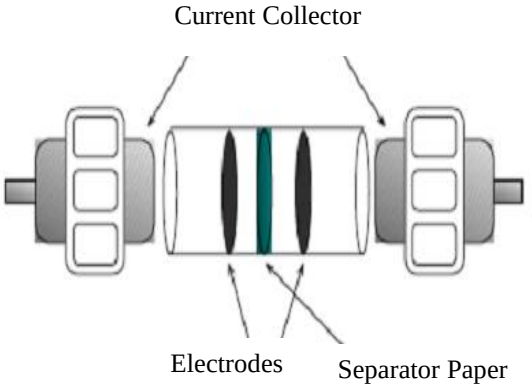

a) b)

Figure 6. Schematic drawing of supercapacitor

Previous to electrochemical characterization, each supercapacitors underwent a pretreatment by cyclic voltammetry (10 cycles, scan rate at 10 mV s^{-1} and potential range of 0 to 1 V), to improve the interaction of electrolyte ions in the porous structure of the material. The electrochemical analysis of the supercapacitors was performed on the Biologic® potentiostat. Cyclic voltammetry was applied at different scan rates, in a potential range of 0 to 1 V. In

order to obtain the values of specific capacitance for each device, galvanostatic cylces were realized at constant current density. The specific capacitance (C_{esp}) of the material was determined from the following equation 1:

$$C_{esp} = \frac{2\left(\frac{td * i}{\Delta V_2}\right)}{X * 0.75} \quad (1)$$

Where: i is the current density, t_d is the discharge time, ΔV_2 is the value of the potential, during the discharge process after the collapse due to internal resistance *(ESR)* of the capacitor, X is the average mass of the two electrodes and 0.75 corresponds to the fraction of active material in the electrode.

2.4 System assembly

For the correct operation of the prototype, it was necessary implement an electrical circuit shown in figure 7, which allows for the different components of the system to be activated and deactivated using four switches. With switches S3 and S4 opened and S1 and S2 closed it is possible to perform electrolysis and to load the supercapacitors bank through the photovoltaic panel. Once completed the tasks, the switches S1 and S2 are opened and S3 and S4 closed, so the RFC begins to release electrons to the engine while at the same time the supercapacitors are discharged in about 10 sec. Thus, the small car receives the necessary energy impulse and time for the RFC to stabilize the power supply in order to satisfy engine demand.

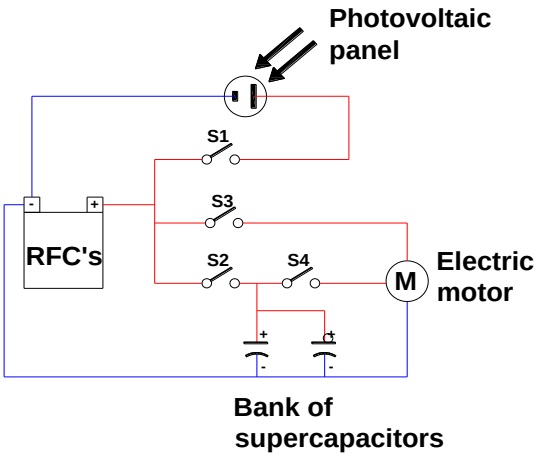

Figure 7 Electric circuit.

All parts of the prototype were assembled (RFC stack with two unit cells, supercapacitor module and the electric engine), as shown in figure 8. The total dry system weight was 940 g and after loading the tanks it was 1200 g. The car speed was 2m/min. Final results are shown in Table 1.

Table 1. Hybrid system performance

Electrolyzer	
Input voltage of photovoltaic panel	2.8 V
Gas production time	15 min
Volume of hydrogen produced	26 cm^3
Volume of oxygen produced	10 cm^3
Cell PEM	
Stack output voltage	1.3 V
Maximum output current	0.85 A
Output power	2.4 W
Supercapacitors	
Operating voltage	1 V
Capacitancia values	≈ 22 F
System	
Speed	2 m/min
Weight	1200 g

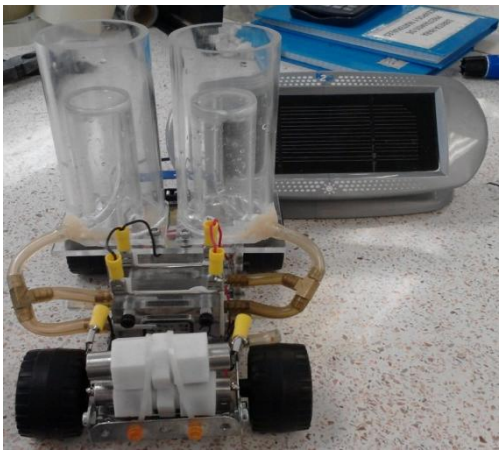

Figure 8. Hybrid renewable hydrogen toy car.

3. Results and discussion

3.1 Characterization of RFC

The results for MEA's characterization (polarization curve and AC impedance spectroscopy) are shown in figure 9.a and b show results the RFC no.1, which has a power of 0.15 W at 0.30 V and 0.50 A with a resistance of 0.75 Ohms. Figure 9 c and d show results for RFC no. 2, which has a power peak of 0.16 W at 0.40 V and 0.4 A. with a ohmic resistance of 0.35 Ohms.

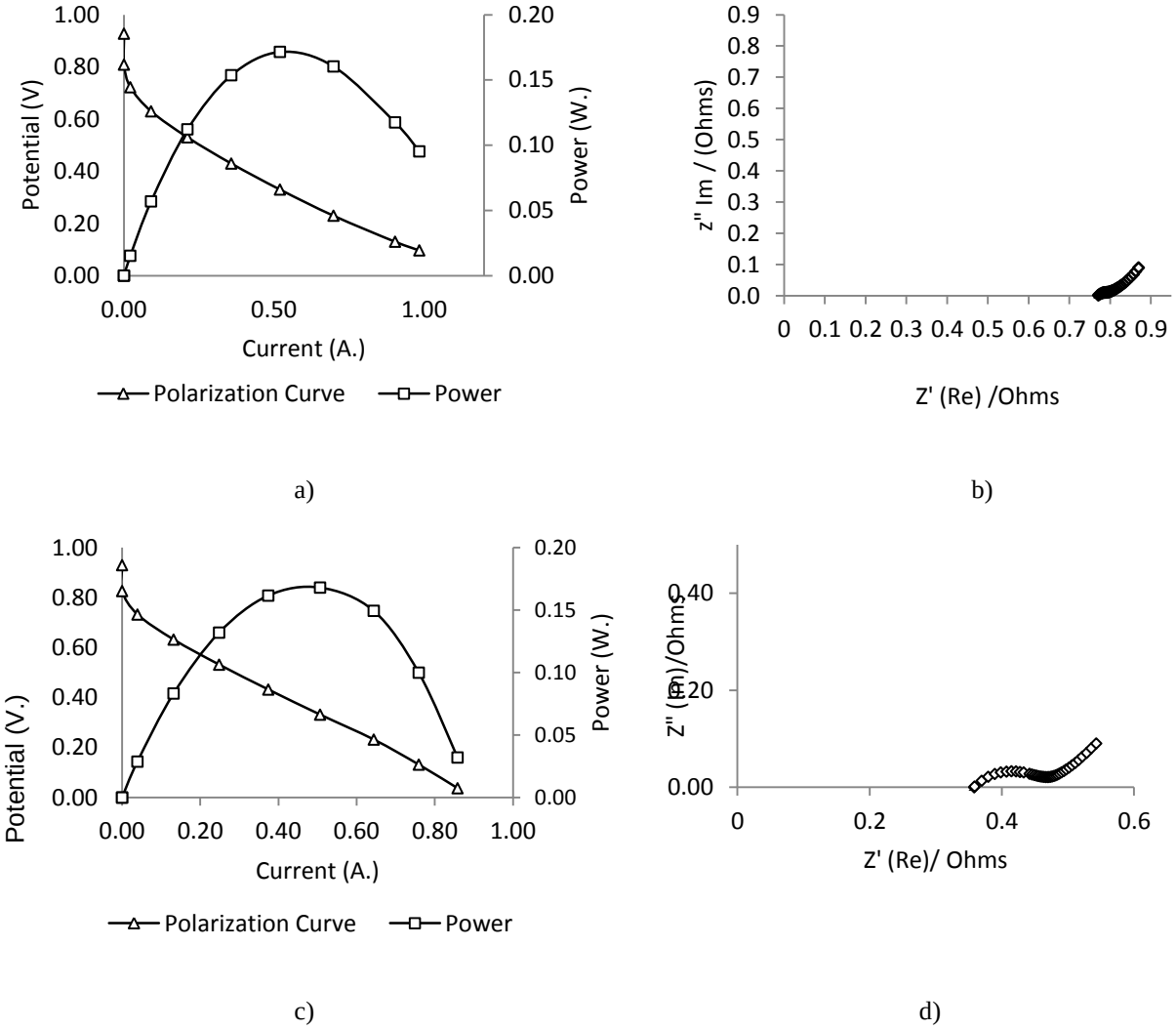

Figure 9. a) Polarization curves and power for RFC 1; b) AC impedance spectrum for RFC 1; c) polarization curves and power for RFC 2; and d) AC impedance spectrum for RFC 2.

3.3 Characterization of supercapacitors

The charge/discharge cycles performed at a constant current density at 10 mA/cm^2 with a potential limit of 1.0 V are shown in figure 10.

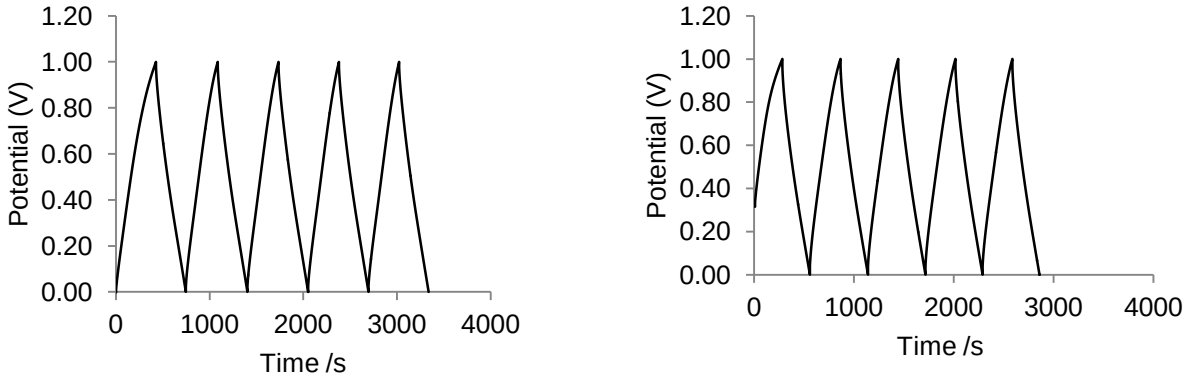

Figure 10. Galvanostatic Charge/discharge cycles for supercapacitors SC1 (left) and SC2 (right).

The SC1 presents a cycle time of 725 s and SC2 of 560 s. The specific capacitance for each capacitor was calculated to be X and Y for SC1 and SC2, respectively.

4. Conclusions

The developed prototype was able to produce, store and consume the gases (hydrogen and oxygen) through the process of electrolysis using electricity from a renewable resource. The implementation of the supercapacitor module allowed increased performance.

The supercapacitors provided the power necessary to the engine at the moment of start, allowing time for the RFC provides the energy sufficient for initial movement.

5. Akcnowledgements

This work was supported by Conacyt project 116157.

6. References

[1] F.J. Rodriguez Varela, O. Solorza Feria, E. Hernández Pacheco, Celdas de Combustible, Sociedad Mexicana del Hidrogeno, (2010). pp.1-3, ISBN 978-0-9809915-2-9

[2] I. J. Novelo Cervera, 'Desarrollo de un prototipo demostrativo de una celda de combustible', B.Sc. thesis, UADY, Mérida, Yucatán, (2010).

[3] J Pompeyo Duarte, , E. Morales, M. A. Smit and D.Pacheco-Catalán; Electrochemical Performance of Supercapacitors Based On Poly(Pyrrole)-Cobalt Supported on Carbon Nanotubes, Proceedings of the XI International Hydrogen Congress (2011), pp.1-7, ISBN978-607-8182-01-5.

[4] Sebastian Altmanna, Till Kazb, Kaspar Andreas Friedrich, Bifunctional electrodes for unitised regenerative fuel cells, Electrochimica Acta 56 (2011) pp. 4287-4293.

[5] Hari P. Dhar, A unitized approach to regenerative solid polymer electrolyte fuel cells, Journal of applied electrochemistry 23 (1993) pp.32-37.

9th International Symposium on New Materials and Nano-Materials for Electrochemical Systems
XII International Congress of the Mexican Hydrogen Society
Merida, Mexico, 2012

Experimental and Theoretical Studies of Nu/Ni-based Catalysts for H_2 Generation

P. López[1], G. Mondragón-Galicia[1], M.E. Espinosa-Pesqueira[1], D. Mendoza-Anaya[1], Ma. E. Fernández[1], A. Gómez-Cortés[2] and R. Pérez-Hernández[1]*

[1]Instituto Nacional de Investigaciones Nucleares, Carr. México-Toluca S/N La Marquesa, Ocoyoacac, Edo. de México C. P. 52750, México
[2]Instituto de Física-UNAM, Apdo. Postal 20-364, México 01000 D.F., México.
*Tel: 55-53297239, mail: raul.perez@inin.gob.mx

ABSTRACT

Cu and Ni were supported on ZrO_2 by the impregnation method, and tested in the oxidative steam reforming of methanol (OSRM) reaction for H_2 production as a function of temperature. Surface area of the catalysts showed differences as a function of the order in which the metals were added to zirconia. Among them, the Cu/ZrO_2 catalyst had the lowest surface area. XRD patterns of the bimetallic catalysts did not show diffraction peaks of the Cu, Ni or bimetallic Cu-Ni alloys, because the metallic active phase was highly dispersed. In addition, TPR profiles of the bimetallic catalysts had the lowest reduction temperature compared with the monometallic samples. The reactivity of the catalysts in the range of 250-375 °C showed that the bimetallic samples prepared by successive impregnation had highest catalytic activity among all the catalysts studied. These results were also confirmed by theoretical calculations. The reactivity of the monometallic and bimetallic structures obtained by molecular simulation followed the next order: $Ni_{shell}Cu_{core}/ZrO2 \approx Cu_{shell}Ni_{core}/ZrO_2 > Ni/Cu/ZrO_2 > Cu/Ni/ZrO_2 > Cu\text{-}Ni/ZrO_2 > Cu/ZrO_2 > Ni/ZrO_2$. These findings agree with the experimental results, indicating that the bimetallic catalysts prepared by successive impregnation show a higher reactivity than the Cu-Ni system obtained by co-impregnation. In addition, the selectivity for H_2 production was higher on these catalysts. This result could be associated also to the presence of the bimetallic Cu-Ni and core-shell Ni/Cu nanoparticles on the catalysts, as was evidenced by TEM–EDX analysis, suggesting that the OSRM reaction may be a structure-sensitive reaction.

1. Introduction

The use of fossil fuels for energy supply in the world has caused various global environmental problems. For this reason it is becoming progressively more important to find ways of providing environmentally friendly energy. One promising alternative to fossil fuels is hydrogen, due to the importance as a clean source of energy, as well as, the increased demand in chemical industry. Hydrogen is a promising fuel for fuel cells and can be produced by steam reforming of natural gas, methanol and gasoline. At present, most of the world's hydrogen is produced from natural gas (~97 % CH_4) by a process called steam reforming. However, steam reforming of methane does not reduce the use of fossil fuels and it still releases carbon to the environment in the form of CO_2. Thus, to achieve the benefits of the hydrogen economy, it is necessary produce hydrogen from non−fossil resources, such as water, methanol or ethanol using a renewable energy source. Among the different feedstocks available, alcohols are very promising candidates because these are easily decomposed in the presence of water and generate hydrogen-rich mixture at a relatively lower temperature. Steam Reforming (SR) and Oxidative Steam Reforming (OSR) of methanol has been extensively studied in recent years by our group [1-7]. However, comparing results between studies is challenging since the reaction evidently is very sensitive to the catalysts used .

2. Experimental

ZrO_2 was prepared by the sol-gel method and calcined a 400 ºC. The prepared support were impregnated with an aqueous solution of $Cu(CH_3CO_2)_2{\bullet}H_2O$ or $NiNO_3{\bullet}6H_2O$ at an appropriate concentration to yield 3 wt % of copper and nickel respectively in the monometallic catalysts. Three bimetallic samples were prepared at 80%Cu and 20%Ni respectively to obtain 3 wt. % of total metallic phase. For the first sample, ZrO_2 was successively impregnated with an aqueous solution of $Cu(CH_3COO)_2$. Then, the excess of water was removed at 80 ºC under constant stirring and the catalysts were dried at 110 ºC and calcined at 400 ºC for 2 h followed by cooling down to r.t. Then, an aqueous solution of $NiNO_3{\bullet}6H_2O$ was added and the resulting solid was calcined at the same temperature and time. The as prepared catalysts will be referred as $Ni/Cu/ZrO_2$. For the second catalyst, the synthesis procedure was changed to the above sample mentioned. The labeling of this catalyst will be referred as $Cu/Ni/ZrO_2$. The third sample ($Cu-Ni/ZrO_2$) was prepared by using a simultaneous impregnation (also called co-impregnation): an aqueous solution of $Cu(CH_3COO)_2$ and NiNO3•$6H_2O$ were added to ZrO_2 and calcined at 400 ºC for 2 h. All the samples were reduced at 450 ºC using a mixture of H_2 (5%)/Ar (50 mL/min) stream for 1.5 h before characterization.

3. Results and discussion

ZrO_2 Xerogel was studied by means of TGA in order to select an appropriate calcination temperature leading to total decomposition of carbonaceous products from the synthesis towards the corresponding oxide. The obtained TGA-DSC curves for the xerogel (Figure not included) showed 22 % of the weight loss and it was attributed to the elimination of the physically adsorbed water, physical and chemical adsorbed alcohol and residual organic material

coming from the synthesis. The observed exothermic peak at 433 ºC on the zirconia xerogel can be ascribed to a change of phase from an amorphous material to crystalline tetragonal zirconia [6]. The specific surface area of bare ZrO2 was 42 m^2/g. After metallic phase impregnation and thermal treatments (calcination and reduction), the surface area of the catalysts diminished and was lower than bare support. Among them, the Cu/ZrO_2 and $Cu\text{-}Ni/ZrO_2$ catalysts had the lowest surface area, as well as, the total pore volume (Table 1).

Table 1. TPR peaks positions, ºC and concentrations (%) of the reducible species in the Cu/Ni-base catalysts

Catalyst	Surface area	Total pore volume	Reduction temperature (ºC)		H_2/MO	
	m^2/g	cm^3/g	Before	after	before	After
ZrO_2	42	0.0736	-	-	-	-
Cu/ZrO_2	12	0.0271	217, 248, 290, 340	174	0.77	0.11
$Cu/Ni/ZrO_2$	28	0.0512	192, 222	171	0.93	0.26
$Cu\text{-}Ni/ZrO_2$	11	0.0262	203, 259	183	0.76	0.09
$Ni/Cu/ZrO_2$	37	0.0582	185, 220	174	0.83	0.21
Ni/ZrO_2	21	0.0333	349, 443	326, 447	0.76	0.63

Figure 1a showed a representative zone of the SEM image of the $Ni/Cu/ZrO_2$ catalyst. It is important to mention that the bare ZrO_2 and the other catalysts had the same morphology, so, particles with spherical tendency. This is understandable because we used the ZrO_2 previously stabilized at 450 °C to obtain the catalysts. Fig. 1b shows the XRD patterns of the catalysts before and after catalytic reaction in the range of 20 to 90 degrees 2θ. An expanded scale was used in order to illustrate the peaks of pure Cu and Ni phases or Cu/Ni alloys present on the ZrO_2. XRD patterns of the samples before the catalytic test evidenced diffraction peaks of the tetragonal and monoclinic phases of the ZrO_2. In addition, diffraction peaks of the metallic Cu and Ni phases were identified on the Cu/ZrO_2 and Ni/ZrO_2 catalysts respectively. The bimetallic catalysts did not exhibit diffraction peaks related to metallic Cu, Ni or bimetallic Cu-Ni alloys. This suggests that all metal particles were highly dispersed. After catalytic test, some changes were observed in the XRD patterns of the Ni/ZrO_2 and the bimetallic $Cu\text{-}Ni/ZrO_2$ catalysts (the later prepared by simultaneous impregnation). On the former catalyst, NiO phase was identified and on the bimetallic sample, a peak of the metallic copper appears. This finding evidences that the active phase is not stable on these catalysts and it was modified by the stream of the reaction.

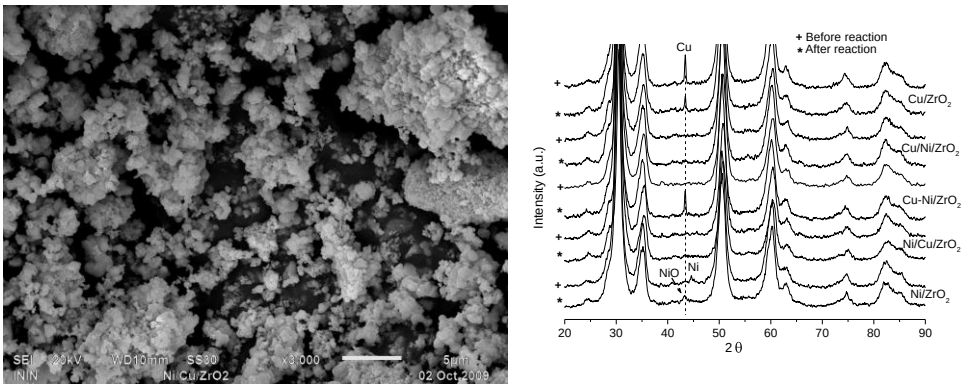

Figure 1. a) Typical SEM images of the fresh $Ni/Cu/ZrO_2$ catalyst. b) XRD patterns of the Cu-Ni base catalysts supported on ZrO_2 (before and after catalytic reaction).

Fig. 2 shows the theoretical calculations of the monometallic and bimetallic models over ZrO_2. After the geometry optimization of the theoretical models, the total energy and the energy of the gap had the next values: $Ni_{(shell)}/Cu_{(core)}/ZrO_2$ (-3193.49, 0.0027) eV, $Cu_{(shell)}/Ni_{(core)}/ZrO_2$ (-3429.43, 0.0159) eV, $Ni/Cu/ZrO_2$ (-3419.37, 0.0185) eV, $Cu/Ni/ZrO_2$ (- 3488.39, 0.021) eV, $Cu\text{-}Ni/ZrO_2$ (-3655.28, 0.108) eV, Cu/ZrO_2 (-3810.23, 0.385) eV and Ni/ZrO_2 (-3832.18, 0.565) eV respectively. It is shown that the bimetallic models simulating the successive impregnation were less stable, because, the energy of the system is high, while, the energy of the bimetallic model prepared by simultaneous impregnation was low, as well as, on the monometallic models. An opposite behavior is observed in the energy of the gab. So, in the former models the energy of the gab is low, while in the later models the energy is high. The gap between HOMO and LUMO of the systems along with the total energy calculated, allows to evaluate the reactivity behavior of the system. So, a large gap of the system combined with a low total energy on the systems, low reactivity is expected. While, if the gap of the system is low and the total energy is large, high reactivity is expected [8]. The results of the theoretical calculations showed that reactivity of these systems followed the next order: $Ni_{(shell)}/Cu(core)/ZrO_2 \approx Cu_{shell}Ni_{core}/ZrO_2 > Ni/Cu/ZrO_2 > Cu/Ni/ZrO_2 > Cu\text{-}Ni/ZrO_2, > Cu/ZrO_2 > Ni/ZrO_2$. These theoretical results obtained after the simulation of the successive impregnation process and based on core-shell structures, show higher reactivity than in the simultaneous co-impregnation ($Cu\text{-}Ni/ZrO_2$) simulated process. Mainly in the literature, the theoretical studies reported are on unsupported core–shell particles and their alloys like Cu-Au particles, on this systems the studies have concentrated on the structural behavior of the clusters [9, 10], but no correlation with the catalytic activity was associated.

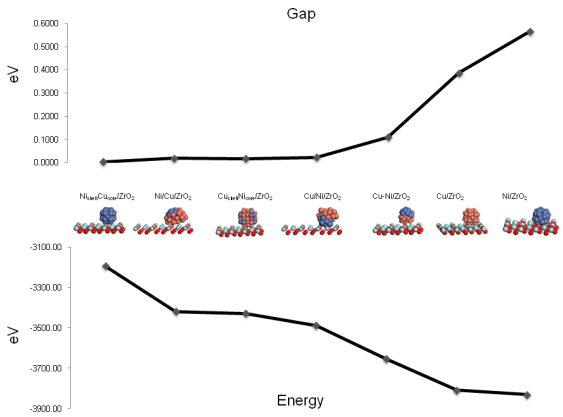

Figure 2. Molecular models of the bimetallic clusters: Top graph corresponds to gap-energy, in bottom graph showed the total energy of the systems. It showed that as the energy gap increases, the total energy of the system decreases, this indicates that the $Ni_{(shell)}Cu_{(core)}/ZrO2$ and $Cu_{(shell)}Ni_{(core)}/ZrO_2$ are the most reactive, while the Cu-Ni/ZrO_2 is less reactive on the bimetallic models.

Oxidative steam reforming (OSR) of methanol reaction was carried out in order to investigate the effect of the active phase addition to the support. Fig. 3a shows the catalytic activity of the copper-nickel-base catalysts supported on ZrO_2 as a function of the reaction temperature. It was possible to observe that the Cu/ZrO_2 catalyst was better than Ni/ZrO_2 sample in the temperatures range studied in this work. This indicates that methanol conversion occurs preferentially on copper than on nickel. It is important to mention that the H_2 chemisorption process did not occur in these samples, for this reason the metal dispersion was not estimated and as a consequence the TOF could not be determined for each catalyst obtain/having a real comparison in the methanol conversion. When Ni was supported on ZrO_2-monoclinic [1], the catalytic activity was similar to the obtained in this work up to 300 ºC. On the other hand, it is clear that the preparation method of the catalyst has a significant influence on the OSRM reaction. The addition of 0.2 wt % of Ni to Cu/ZrO_2 catalyst leads to a considerable improvement in the methanol conversion, compared with the Ni/ZrO_2 sample. Among bimetallic samples, those prepared by the successive impregnation method showed high reactivity than the sample synthesized by simultaneous co-impregnation. The molecular properties HOMO and LUMO calculated by DFT of the bimetallic system prepared by successive impregnation, in special with core-shell particles, evidence that, these kinds of systems had more reactivity than bimetallic structure model obtained by simultaneous co-impregnation. Although experimentally the catalyst surface is different in the samples prepared by successive impregnation method, the theoretical reactivity predictions determined from the energy gap is similar in both bimetallic models, as seen in the in Figure 2. This may explain the catalytic behavior between the two catalytic species. In recently paper Strasser et al. [11] concluded that the platinum-rich shell on Pt-Cu nanoparticles, exhibits compressive strain, which results in a shift of the electronic band structure of platinum and weakening chemisorption

of oxygenated species. These activity–strain relationships were consistent with computational predictions that compressive strain enhances oxygen-reduction reaction. In our case we observed that the catalytic activity is strongly related with the crystallinity and morphology of the active phase, the above mention was corroborated by means of XRD and TEM. The TEM analysis of the bimetallic particle with core-shell morphology; showed that there is no crystalline arrangement point to point or even line to line, which can be observable in the shell of the particle (Figure 3b). The crystalline anisotropy plays an important role in the methanol conversion in this research, because in the case of the core-shell Cu/Ni and Ni/Cu structures, the catalytic property increases in both cases, so the activity is not restricted by any preferred crystallographic direction. In the case of the Cu/ZrO_2 system having a crystalline arrangement in the (111) crystal direction, as seen in the XRD pattern of Figure 2, indicates that there are more particles with this type of crystalline plane which favors the catalytic activity but not as in the case of bimetallic core-shell particles; while in the case of Ni-base catalyst was observed that it has a poor crystallinity as observed in the XRD pattern (Fig. 2) with the (111) crystalline direction. This showed that there are few planes in the (111) crystalline direction influencing the catalytic anisotropic response. This means that even if there is a poorly crystalline monometallic active phase, the response in the catalytic activity does not resemble bimetallic systems with core-shell morphology, as well as when the active phase is a metallic alloy (Cu-Ni). This finding suggests that the OSRM reaction may be structure-sensitive. Yu-Hua et al. [12] studied the methanol decomposition on Ni(1 1 1) and Ni(1 0 0) surfaces using DFT-GGA (density functional theory-generalized gradient approximation). According to their results, the observed different behavior in the methanol interaction with Ni(1 1 1) or Ni(1 0 0), suggests that the methanol decomposition might be a structure-sensitive reaction, as it has been observed in our samples. The $Cu-Ni/ZrO_2$ sample had a similar behavior to the Cu/ZrO_2 catalyst until 300 °C. After this temperature the $Cu-Ni/ZrO_2$ sample exhibited the same catalytic activity than the other bimetallic samples. In addition, was observed that the active phase of the $Cu-Ni/ZrO_2$ catalyst was not stable, because, it was sinterized after catalytic reaction (Fig. 2). This effect could be explained the lower catalytic activity observed on this sample than on the other bimetallic samples prepared by successive impregnation. Mariño et al. [13, 14] found that the conversion of ethanol on the SRE reaction was improved when nickel content increased on the bimetallic Cu-Ni system. This behavior was attributed to the addition of Ni, which favors the segregation of Cu^{2+} ions in the catalytic surface that causes an increase in the catalytic activity. Thus the enhancement on the catalytic activity could be attributed to the bimetallic Cu-Ni species as was previously reported [1,5] and core-shell nanoparticles identified with TEM technique on the $Ni/Cu/ZrO_2$ catalyst. It is worth notice, that the BET surface area of the Cu/ZrO_2 sample is two times lower than $Cu/Ni/ZrO_2$ and $Ni/Cu/ZrO_2$ samples. Thus, the catalytic activity observed on the Cu/ZrO_2 could be attributed to the presence of highly dispersed Cu species rather than Cu bulk as reported for Cu/CeO_2 catalysts [2].

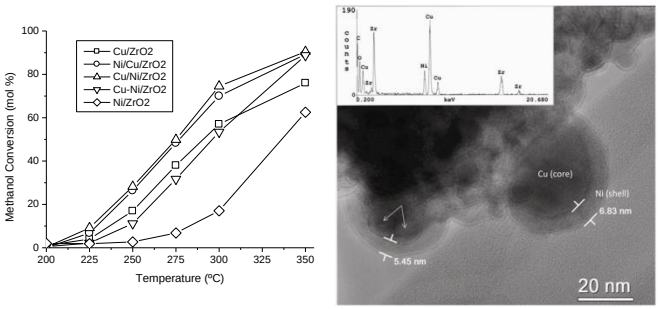

Figure 3. a) Steam reforming of methanol over copper-nickel-base catalysts supported on ZrO_2 (GHVS = 24,000 h^{-1}). b) TEM image of Ni/Cu/ZrO_2 catalyst, core-shell nanoparticles were identified, the left side area shown two particles building the core. Inset image, EDX of the Ni/Cu core-shell nanoparticle. EDX analyses were performed in-situ with a spot of 10 nm and the electron beam was located at the Ni shell area.

During the OSRM reaction with copper-nickel base catalysts supported on ZrO_2, the main products observed were H_2, CO, CO_2 and H_2O. However, a small quantity of methyl formate was also present at temperatures below 275 °C in almost all samples. Above this temperature, the methyl formate was unstable and was not detected. On copper-ZrO_2 systems [1], the production of $(CH_3)_2O$ and CH_2O during the OSRM was observed and it was suggested that they were produced on the support. Fig. 4a shows the hydrogen yield as a function of reaction temperature during the catalytic tests of the copper-nickel-base catalysts on the OSRM reaction. Hydrogen production was negligible up to 225 °C and increase when the temperature was raised. Cu/Ni/ZrO_2 and Ni/Cu/ZrO_2 catalysts prepared by successive impregnation had the same H_2 yield after 250 °C and it was higher than all samples. At the maximum reaction temperature, the H_2 yield is about 2.0 µmol for the Cu/Ni/ZrO_2 and Ni/Cu/ZrO_2 catalysts, this is close to the theoretical value (2.5) if a total reagents conversion is assumed. At this temperature the methanol conversion was nearly 100 %. On the other three samples the H_2 production was close to 1.5 µmol. The CO_2 selectivity (Fig. 4b) is important at the beginning of the reaction and diminished as temperature was increased. This drop in the CO_2 selectivity was pronounced on the samples where the catalytic activity was nearly 100 %. In the case of the CO selectivity, this was produce after 275 °C. The CO production at 350 °C was 10 % for the monometallic samples and close to 40 % for the bimetallic catalysts. The decrease in the CO_2 selectivity and the formation of CO is probably due to the reverse water-gas shift (WGS) reaction that occurred on the bimetallic samples. Taking in account the results from methanol conversion and selectivity, it is considered that CH_3OH form CH_3OCHO and H_2 on the surface of the catalysts as the first step of the OSRM reaction. Then, CH_3OH is oxygenated to CH_3OCHO, and then decomposed to H_2 and CO. CH_3OH was hydrated in order to form CO_2, H_2O and H_2 respectively as reported previously [1].

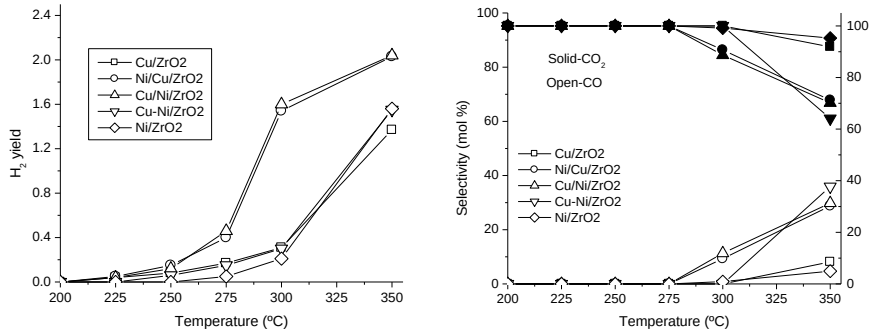

Fig. 4. a) H_2 yield as a function of the metal addition and temperature. (GHVS = 24,000 h^{-1}). b) Evolution on the selectivity of CO_2 and CO as a function of the metal addition and temperature. (GHVS = 24,000 h^{-1}).

4. Conclusions

In the present study, Cu/ZrO_2, Ni/ZrO_2 and three bimetallic copper-nickel catalysts supported on ZrO2 were prepared by the impregnation method. The bimetallic $Cu/Ni/ZrO_2$ and $Ni/Cu/ZrO_2$ catalysts showed higher catalytic activity than bimetallic sample prepared by simultaneous impregnation and the monometallic catalysts on the OSRM reaction. Molecular simulation HOMO and LUMO properties of the bimetallic system prepared by successive impregnation with core-shell particles, confirm that these systems had more reactivity than bimetallic system obtained by simultaneous impregnation. In addition, the H_2 selectivity was higher on these bimetallic $Cu/Ni/ZrO_2$ and $Ni/Cu/ZrO_2$ catalysts. The former catalyst exhibited excellent stability in OSRM reaction and has great potential in fuel cell applications. These results could be associated to the presence of the bimetallic Cu-Ni and core-shell Ni/Cu nanoparticles present on the catalysts, as was evidenced by HREM-TEM–EDX and to the crystalline anisotropy of the active phase that plays an important role in the methanol conversion and selectivity. This finding suggests that the OSRM reaction may be a structure-sensitive reaction

5. Akcnowledgements

Thanks to I.Q. Albina Gutiérrez Martínez, Carlos Salinas Molina and Jorge Pérez for technical support and to the project ININ-CA-711, ININ-CA-009, CONACYT CB-2008-01-104540 and CONACYT J-48924 for financial support. Authors would like to acknowledge Dra. Reyna Natividad Rangel and Dr. Carlos Ángeles for its valuable comments and suggestions on the manuscript.

6. References

[1] Pérez-Hernández R, Mondragón-Galicia G, Mendoza-Anaya D, Palacios J, Angeles-Chavez C, Arenas-Alatorre J. Synthesis and characterization of bimetallic Cu–Ni/ZrO2 nanocatalysts: H2 production by oxidative steam reforming of methanol. Int J Hydrogen Energy. 2008;33:4569-76

[2] Pérez-Hernández R, Gutiérrez-Martínez A, Gutiérrez-Wing C. Effect of Cu loading on CeO2 for hydrogen production by oxidative steam reforming of methanol. Int J Hydrogen Energy. 2007;32:2888-94.

[3] R. Pérez-Hernández, A. Gutiérrez-Martínez, J. Palacios, M. Vega-Hernández, V. Rodríguez-Lugo. Hydrogen production by oxidative steam reforming of methanol over Ni/CeO2eZrO2 catalysts. Int J Hydrogen Energy 36 (2011) 6601-6608

[4] R. Pérez-Hernández, A. Gutiérrez-Martínez, A. Mayoral, F. Leonard Deepak, Ma. E. Fernández-García, G. Mondragón-Galicia, M. Miki, M. Jose-Yacaman. Hydrogen Production by Steam Reforming of Methanol over a Ag/ZnO One Dimensional Catalyst. Advanced Materials Research Vol. 132 (2010) pp 205-219.

[5] P. López, G. Mondragón-Galicia, M.E. Espinosa-Pesqueira, D. Mendoza-Anaya, Ma.E. Fernández, A. Gómez-Cortés, J. Bonifacio, G. Martínez-Barrera, R. Pérez-Hernández. Int J Hydrogen Energy 37(2012) 9018-9027

[6] R. Pérez-Hernández, A. D. Avendaño, E. Rubio, V. Rodríguez-Lugo. Hydrogen Production by Methanol Steam Reforming Over Pd/ZrO2–TiO2 Catalysts. Top Catal (2011) 54:572–578

[7] R. Pérez-Hernández, L. C. Longoria, J. Palacios, Ma. M. Aguila and V. Rodríguez. Oxidative steam reforming of methanol for hydrogen production over Cu/CeO2-ZrO2 catalysts. Energ Mater Mater Sci Eng Energ Syst 2008;3(3):152-157

[8] Yang W, Parr. RG. Hardness, softness, and the fukui function in the electronic theory of metals and catalysis Proc Nati Acad Sci USA. 1985 82:6723-6

[9] Bracey CL, Ellis PR, Hutchings GJ. Application of copper–gold alloys in catalysis: current status and future perspectives. Chem Soc Rev. 2009;38:2231-43.

[10] Rodríguez-López JL, Montejano-Carrizales JM, José-Yacamán M. Molecular dynamics study of bimetallic nanoparticles: the case of AuxCuy alloy clusters. Appl Surf Sci. 2003;219 56-63

[11] Strasser P, Koh S, Anniyev T, Greeley J, More K, Yu C, Liu Z, Kaya S, Nordlund D, Ogasawara H, Toney MF, Nilsson A. Lattice-strain control of the activity in dealloyed core-shell fuel cell catalysts. Nature Chemistry. 2010;2:454-60

[12] Zhou Y-H, Lv P-H, Wang G-C. DFT studies of methanol decomposition on Ni(1 0 0) surface: Compared with Ni(1 1 1) surface. J Mol Catal A: Chemical. 2006;258:203-15

[13] Mariño FJ, Cerrella EG, Duhalde S, Jobbagy M, Lombarde M. Hydrogen from steam reforming of ethanol. Characterization and performance of copper–nickel supported catalysts. Int J Hydrogen Energy 1998;23 1095-101.

[14] Mariño FJ, Boveri M, Baronetti G, Lombarde M. Hydrogen production from steam reforming of bioethanol using Cu/Ni/K/g-Al2O3 catalysts. Effect of Ni. Int J Hydrogen Energy 2001;26 665-8

Synthesis of NaTaO3 by a New Solvo-Combustion Method and its Hydrogen Production Photoactivity

C. Gómez-Solís[1,2],*, I. Juárez-Ramírez[1] , L. M. Torres-Martínez[1], M. Z. Figueroa-Torres[1], M. A. Ruiz-Gómez[1], D. Sánchez-Martínez[1], E. Zarazúa-Morín[1]

[1]Universidad Autónoma de Nuevo León, UANL, Facultad de Ingeniería Civil, Departamento de Ecomateriales y Energía, Av. Universidad S/N Ciudad Universitaria San Nicolás de los Garza Nuevo León, C.P. 66451 México
[2]Facultad de Ciencias Químicas, Universidad Autónoma de San Luis Potosí, Av. Manuel Nava #6, San Luis Potosí, S.L.P. 78290, México
*Tel: (81)83521984 ext. 222, fax (81)83760477, mail: lienquidremo@hotmail.com

ABSTRACT

Significant attention has been paid on the photocatalytic production of hydrogen from water by using semiconductors. The $NaTaO_3$ has been regarded as one of the most promising material for water splitting, since it has shown remarkable water splitting activity due to its high potential to generate charge carriers by absorbing the photons energy. This work reports for the first time the $NaTaO_3$ synthesized trough a new solvo-combustion method, in this case the acetylacetone was used as template and fuel for the combustion reaction. The DRX analysis results showed that $NaTaO_3$ phase could be obtained from the as-grown material. The SEM micrographs revealed that $NaTaO_3$ has hierarchical cubic morphology in the nanometer level. The materials possess a high specific surface area around 50-90 $m^2.g^{-1}$, which is one of the highest reached when compared to other synthesis methods. The UV-visible analysis show a band gap value (*Eg*) close to 3.9 eV. The material exhibited attractive photocatalytic activity for water splitting reaction to produce hydrogen. An enhanced of the hydrogen production was obtained by annealing the material at 600 ºC from 418 to 644 µmol, because of the higher crystallinity degree.

1. Introduction

Several researches have been conducted in order to produce alternative clean energy sources. In this way, hydrogen production is one of the most important technologies studied hardly during the last decade. Particularly hydrogen produced from water splitting reaction by photocatalysis has been attracted considerable attention because of the possibility to develop new or better catalyst materials using metal transition oxides, which are active under UV and visible light irradiation [1,2,4,5]. Some oxides like tantalates, titanates, niobates and tungstanates have been showed important activity for water splitting in comparison with TiO_2, commonly used as photocatalyst [3-9]. Additionally the modifications of electronic structure, crystal structure or physicochemical properties could be enhancing the activity of catalytic materials for water splitting reaction [4-10]. Therefore, it is important to produce catalyst materials with strict control of the composition, homogeneity, size and particle shape, as well as at low temperature. In recent years, several chemical methods such as hydrothermal, solution combustion, sol-gel and co-precipitation have been employed to synthesize new and better materials. Perowskite-type sodium tantalite NaTaO3 has attracted

much attention from researchers due to its highly efficient photocatalytic activity for overall water splitting under ultraviolet (UV) irradiation [15].

This works focus in the synthesis of $NaTaO_3$ material by a new solvo-combustion method with high surface area. $NaTaO_3$ will be tested as catalyst material for water splitting reaction in order to produce hydrogen under UV-light irradiation.

2. Experimental

2.1 Synthesis of $NaTaO_3$ by solvo-combustion method

$NaTaO_3$ powder was prepared by a new solvo-combustion method. Acetylacetone (Aldrich 99.5 %), was mixed with ethanol (DEQ 95 %) in a 1:1 Vol. ratio, the solution was keeping in a reflux system by 10 minutes at 75ºC. Then, etoxide (V) tantalum (99.98% Aldrich) and sodium acetate (DEQ) was added in 1:1 molar ratio (Na:Ta) and kept the system with vigorous stirring during 5 minutes. After that, it was added 1 mL of nitric acid as oxidant agent. Finally, the solution was heated at 180ºC to provoke the solvo-combustion reaction where a polycondensation reaction occurs between acetylcetone and nitric acid. The fresh powder was thermal heated by 2 hours at 400°C and 600ºC.

2.2 Characterization

The crystal structure and phase transformation of the obtained powder were Characterized by X-ray powder diffraction (XRD) using a Bruker D8 Advance diffractometer with CuKα radiation (λ = 1.5406 Å). The morphology and particle size of the synthesized $NaTaO_3$ were determined by Scanning Electron Microscope (SEM) in a JEOL 6490 LV. The energy band gap (*Eg*) was determined by the Kubelka-Munk function using a UV–vis spectrophotometer (Lambda 35 Perkin Elmer Corporation) coupled with an integrating sphere. Specific surface area (S_{BET}) was measured by N_2 physisorption through the BET method using Quantachrome NOVA 2000e equipment.

2.3 water splitting test

The water splitting was carried out at low pressure in a batch-type reactor using an inner irradiation cell and argon as carrier. Firstly, 300 mL of distilled water were bubbled with argon for 15 min. Then, 300 mg of material was dispersed into water under vigorous stirring. The system was kept at 100 Torr and the water temperature was maintained at 25ºC during the test using a cooling system. Afterwards, the batch-reactor was irradiated with a UV source, Hg lamp with intensity of 400 W, and heterochromatic irradiation (λ= 200 to 800 nm). The evolved hydrogen was analyzed using a gas chromatograph with a TCD detector and a packed column Hayesep D 100/120. The analysis was carried out in intervals of 30 minutes for 4 h.

3. Results and discussion

Figure 1 shows the XRD patterns of $NaTaO_3$, fresh and thermal treated samples at 400°C and 600°C. It is evident the presence of $NaTaO_3$ phase from the fresh sample and it becomes more crystalline as the temperature increases. Accordingly to the JCPDS file, $NaTaO_3$ phase detected in the fresh sample and the thermal treated at 400°C correspond to a monoclinic structure. While sample thermal treated at 600°C corresponds to an orthorhombic symmetry. In addition, this sample shows the presence of some peaks corresponding to the secondary phase, $Na_2Ta_4O_{11}$; however its intensity is very low. The presence of the monoclinic symmetry is due to the low temperature of synthesis where the crystal structure is mainly formed by TaO_6 octahedral slightly distorted; however when temperature increases TaO_6 octahedral tends to be highly disordered provoking an orthorhombic arrangement.

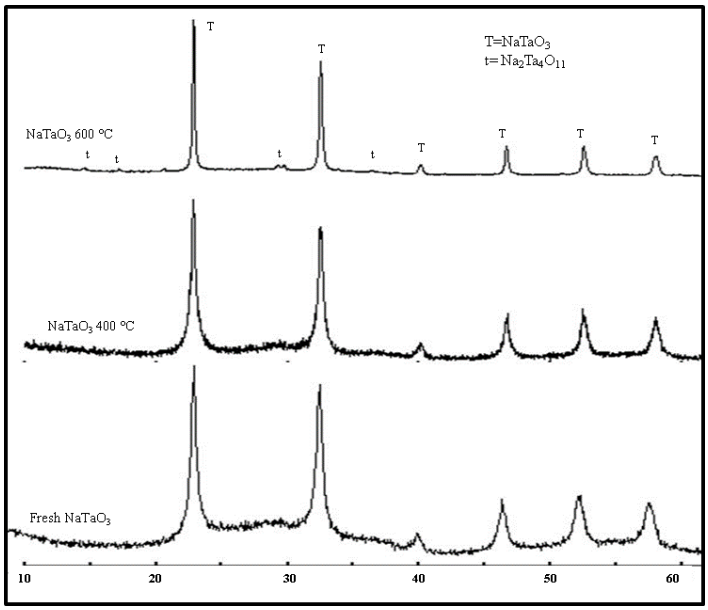

Figure 1. XRD patters of $NaTaO_3$ powders prepared by solvo-combustion method.

Through SEM micrographs it was possible to determine that $NaTaO_3$ particles presented micro-cavities formed by the union of $NaTaO_3$ particles with size lower than 1 micron; it is assumed that $NaTaO_3$ has hierarchical cubic morphology in the nanometer level. The morphology observed is due to the synthesis method; $NaTaO_3$ particles are formed from the fresh sample and its particle size increases as the temperature increase. As it is observed, cavities still remains present after thermal treatment indicating an interesting morphology of $NaTaO_3$ for certain applications.

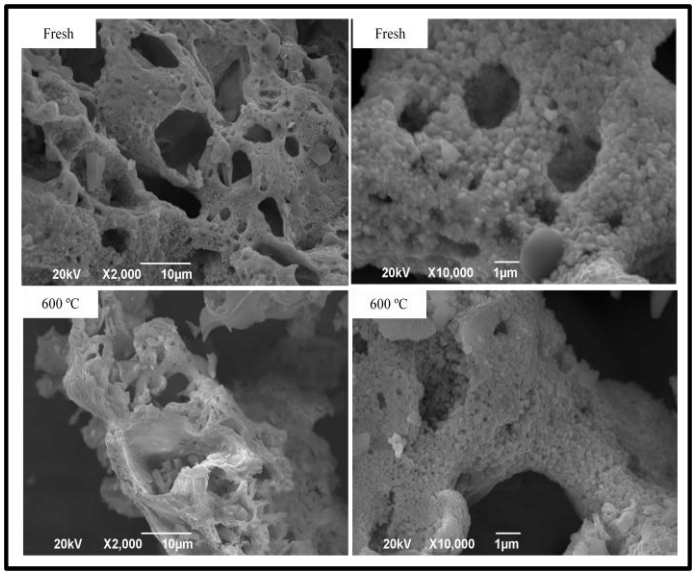

Figure 2. SEM micrographs of $NaTaO_3$ powders prepared by solvo-combustion method.

On the other hand, results about energy band gap (*Eg*) and specific surface area (S_{BET}) indicate that $NaTaO_3$ synthesized in this work shows similar *Eg* values that expected for $NaTaO_3$ material, see table 1. It means $NaTaO_3$ could be absorbing energy efficiently below 400 nm in order to be activated for photocatalytic processes which could be enhanced also due to the S_{BET} values obtained for this material.

Table 1. Energy band gap (*Eg*) and specific surface area values (S_{BET}) for $NaTaO_3$ samples.

Sample	*Eg* /eV	S_{BET} / $m^2.g^{-1}$
Fresh-$NaTaO_3$	3.94	118
$NaTaO_3$-400	3.98	75
$NaTaO_3$-600	4.01	41

The S_{BET} values here obtained are higher than those reported commonly for $NaTaO_3$ prepared by other synthesis methods, see table 2. Therefore $NaTaO_3$ synthesized in this work could be used in several applications where surface area is important such as absorbents, catalysts, substrate, and so on.

Table 2. Comparison of specific surface area values (S_{BET}) for $NaTaO_3$ samples synthesized by several methods.

Synthesis Method	*Temperature/°C*	S_{BET} / $m^2.g^{-1}$	*Ref.*
Solid State	1200	0.6	[11]2006
Sol-Gel	600	23	[12]2007
Sol-Gel	600	14	[13]2010
Electrolysis and Hydrothermal	180	58	[14]2010
Confined Space synthesis route	500	46	[15]2011
Solvo-combustion	fresh	118	This work
	400	75	
	600	41	

Figure 3 shows the hydrogen evolution during the water splitting reaction. The material exhibited attractive photocatalytic activity for water splitting reaction to produce hydrogen under UV-light irradiation. Results here obtained are very similar to the commonly reported for $NaTaO_3$ synthesized by other methods, mainly sample thermal treated at 600°C.

According to these results, it seems that crystal structure is more important than specific surface area. In this case, the fresh-$NaTaO_3$ and $NaTaO_3$-400 produce hydrogen in similar amount, and both samples are monoclinic while $NaTaO_3$-600 is orthorhombic. Recombination process is favored in the monoclinic structure due to the slight distorted TaO_6 octahedral because distance is shorter than distance presented in the orthorhombic structure where TaO_6 octahedral are more distorted.

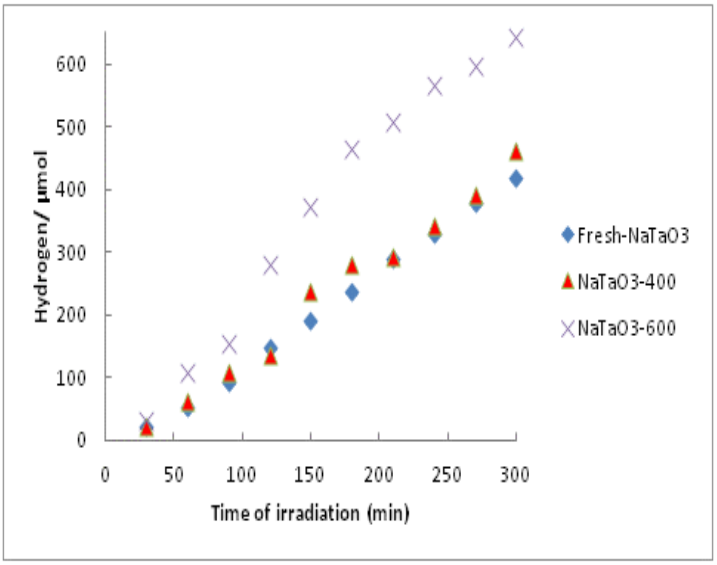

Figure 3. Hydrogen production from water splitting using NaTaO3 semiconductor synthesized by solvo-combustion

Finally, another important aspect of this work in comparison with other reports is that due to the new solvo-combustion method used in this work, $NaTaO_3$ can be obtained in a few minutes at low temperature of synthesis. $NaTaO_3$ synthesized in this work showed high specific surface area and the phase appears from the fresh sample.

4. Conclusions

$NaTaO_3$ was obtained by the first time from the as-grown material using a new solvo-combustion method. $NaTaO_3$ particles have hierarchical cubic morphology in the nanometer level and possess high specific surface area, which is one of the highest values reached when compared to other synthesis methods. This material exhibited attractive photocatalytic activity for water splitting reaction where the crystal structure plays an important role because the fresh-$NaTaO_3$ and $NaTaO_3$-400 produce hydrogen in similar amount, and both samples are monoclinic while $NaTaO_3$-600 is orthorhombic and therefore enhances the hydrogen production.

5. Acknowledgements

Thanks to CONACYT for the financial support through the projects CB-98740, CB-84809 and INFR-2011-3-173625 and PAICYT-UANL2009 through the project IT171-09. Dr Isaias Juarez Ramirez wants to thank to the Nanoscience and Nanotechnology Network to support this project. Also authors want to thank CONACYT for the scholarship for PhD. Student Christian Gomez Solis, No. 201958, Miguel A. Ruiz Gomez, No. 239336 and Elvira Zarazua Morin, No. 87101.

6. References

[1] K. Maeda and K. Domen, J. Phys Chem Lett, 1, 2655 (2010).

[2] X. Hu, G. Li and J.C. Yu, langmuir, 26, 3031 (2010).

[3] M.N. Chong, B. Jin, W.K. Chow, c. Sain , Water Research, 44, 2997 (2010).

[4] J. Kim, D.W. Hwang, H. G. Kim, S. W Bae, J. S. Lee, W. Lib and S. H. Oh, Topics in Catalysis, 35. 295 (2005)

[5] A.L. Stroyuk, A. I. Kryukov, S. Y. Kuchmii, V. D. Pokhodenko, Theorical and Experimental Chemistry, 45 209 (2009).

[6] D.W. Hwang, H.G. Kim, J. Kim, K.Y. Cha, Y.G. Kim and J.S. Lee, Journal of catalysis, 193, 40 (2000).

[7] J. Kim, D.W. Hwang, H. Kim, S. W. Bae, S. M. Ji and J. S. Lee, Chemical Communications, 21, 2488 (2002)

[8] Y. Inoue, Energy & environmental Science, 2, 364 (2009).

[9] A. Iwase, H. Kato and A. Kudo, Catalysis Letters,108, 7 (2006).

[10] M. Tabata, K. Maeda, T. Ishihara, T. Minegishi, T. Takata, K. Domen, The journal of physical Chemistry C, 114, 11215 (2010).

[11] W. Lin, C. Cheng, C. Hu and H. Teng, Applied Physics Letters, 89, 211904 (2006).

[12]C. Hu, H. Teng, Applied Catalysis A: General, 331, 44 (2007).

[13] L.M. Torres-Martinez, R. Gomez, O. Vazquez-Cuchillo, I. Juarez-Ramirez, A. Cruz-Lopez, F.J. Alejandre-Sandoval, Catalysis Communications, 12, 268 (2010).

[14] Y. Cui, L. Liu, Y. Chen, D. Yu, X. Zhou, N. Xu, W. Ding, Solid State Science, 12, 232 (2010)

[15] T. Yokoi, J. Sakuma, K. Maeda, K. Domen, T. Tatsumi and J. N. Kondo, Phys. Chem. Chem. Phys, 13, 2563 (2001).

Feasibility Study to Use Hydrogen as Alternative Source of Energy in Mexico

Oscar Pérez Meza[1*], A. Solís Tenorio[1], R. González Huerta[2]

[1]Universidad Autónoma de Guadalajara UAG, Centro de Energía Renovable, 45129, Zapopan Jal. México.
[2]IPN-ESIQIE, Laboratorio de Electrocatálisis, UPALM, 07738 D.F. México, D.F.
Tel. (01) 333 199 4812, newneon34@hotmail.com

ABSTRACT

Mexican hydrogen industry currently produces 500,000 tons of hydrogen per year. Hydrogen is primarily used as a feedstock, intermediate chemical, or specialty chemical in: chemical production, petroleum refining, metal treating, electronic applications, and food and soap/detergent industries. Main hydrogen production method is steam methane reforming (SMR). Other methods includes: gasification of fossil fuels, partial oxidation and water electrolysis. Some of the produced hydrogen could be used like alternative energy source. United States, Spain and Germany already use it like fuel, this hydrogen is mainly produced by SMR, however there are also projects focuses to produce hydrogen from electrolysis method coupling renewable energies sources (solar energy, wind power, wave energy, etc). In Mexico, SMR is also the main process to obtain hydrogen, 98%, nevertheless Mexichem Plant and Quimikao Plant (where hydrogen is a by-product of Sodium Hypochlorite Process and feedstock to fats hydrogenations respectively) are planning use the hydrogen as fuel, they have several projects where the hydrogen is a potential energetic to reduce energy spending of grid from CFE through fuel cells use, decreasing the energy from the second consumer of electricity in Jalisco. Exist production potential of hydrogen in the country; the SMH (Mexican Hydrogen Society) is working to incorporate into Mexican Legislation the hydrogen as alternative source of energy in Mexico.

Keywords: Hydrogen legislation, electrolysis, renewable energies sources.

1. Introduction

The hydrogen production capacity in mexican refineries in 2011 was 183 MMSCFD (million standard cubic feet per day), used for hydrodesulfurization process in refineries, this process and the largest hydrogen consumer not only in Mexico but the word. Same year, United States generated in refineries 4,114.3 MMSCFD, placing it in the first place worldwide alone followed by Japan and South Korea 1,472.8 MMSCFD and 995. 5 MMSCFD respectively, México is in the global site 16 in the production of hydrogen. In 2010 word production of hydrogen was 13 TSCFD (trillion standard cubic feet per year) [1].

The highest percentage of hydrogen is not used as energy, but as raw material in the hydrodesulfurization process oil and other industrial uses are among the production of hydrochloric acid, production of ammonia, hydrogen peroxide and as feedstock in the hydrogenation of fats and oils. Hydrogen production in refineries where has the highest consumption in the word is through the process of reforming of natural gas SMR, only in the United States 2010 were used 154.503 million cubic feet of natural gas to produce hydrogen, this process in 2009 were consumed 143.004 million cubic feet of gas natural one year before, in 2008 were consumed 188.075 million cubic feet of natural gas to produce hydrogen [2].

2. Analysis of hydrogen production technology

The total cost of investment (TCI) of the following hydrogen production technologies specified in US $/GJ. The TCI is a measure of capital cost of plant per unit of hydrogen produced, processed or stored [7].

2.1. Hydrogen from Steam Methane Reforming SMR

The SMR process is cheaper process with respect to others such as gas gasification and pyrolysis also more environmentally friendly, natural gas, methane at a higher rate (94.9% methane, 2.5% ethane and other gases in concentrations less than 0.2%) is effective to produce hydrogen as it is widely available easy to used and has an extensive hydrogen to carbon ratio which minimizes the formation of CO_2 as a by-product and thus emissions of greenhouse gases are minor compared to the pyrolysis process that needs to heavier hydrocarbons. Over 80% of the hydrogen production is achieved by the reforming process of natural gas. There are four basic steps: pretreatment, where the gas is treated catalytically with hydrogen to remove sulfur compounds, the desulfurized gas is reformed with steam mixing and then pass through a nickel-alumina catalyst to produce a hydrogen-rich gas and as a final step hydrogen purification. In the process using a furnace to raise the temperature of the gas in the first step-pretreatment,

heat also functions to produce steam which is used in the reformation and gas conversion, the use of gas natural furnace fuel and the process gas which is a residue of the last process of purification of hydrogen [3-4].

The scheme presented in figure 1, shows the basic steps of the SMR process. For hydrogen production may be possible one of the criteria to consider in the production of hydrogen is emissions of greenhouse gases (specially CO_2), the SMR process emits 68.2 kg CO_2/GJ and will issue that amount produced 588.24 MW of hydrogen per km^2 at a cost of US $982/Ton H_2. In a process which includes the capture of CO_2 by the same technology SMR only 22.8 kg CO_2/GJ be issued, however, the cost of production increases to US $1,575/Ton H_2 [5]. It should be noted that the construction of plants natural gas reforming at low scale such as 0.27 millions Nm^3/day where hydrogen cost is around US $6.0-7.5/GJ [7].

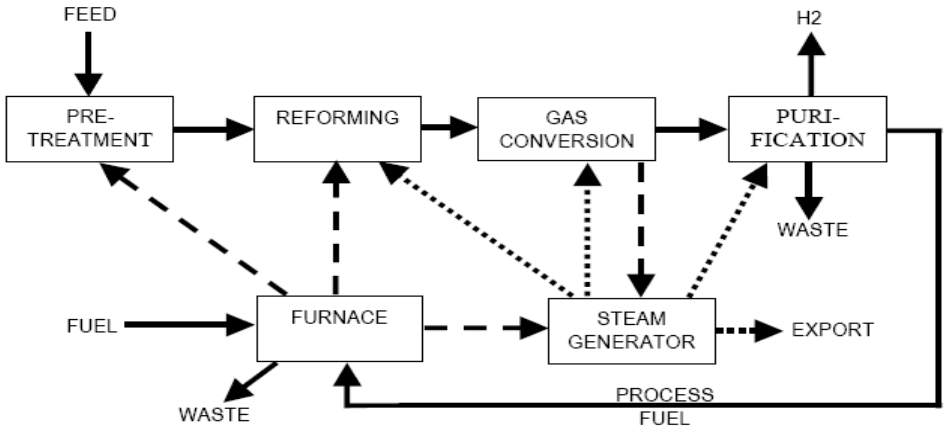

Figure 1. Schematic of SMR Process Showing Heat and Materials Integration

Mexico is one of the largest consumers and producers of natural gas, some of this gas used to produce hydrogen is fed into the hydrodesulfurization plants at refineries in the country, and according to the specific requirements of each refinery infrastructure is developed the safe and efficient hydrodesulfuration unit to provide larger volumes of hydrogen to plants diesel HDS [8]. SMR in plants, CO_2 captured can be categorized before, during and after combustion; eliminating CO_2 before it, when combustion is performed using oxygen instead of air, generating a concentrated stream of CO_2 is compressed for transport and subsequent kidnapping [6].

$$CH_4+H_2O \rightarrow CO+3H2 \quad \text{.....(1)}$$

$$CO+H2O \rightarrow CO2+H2 \quad \text{.....(2)}$$

$$\text{Overall: } CH4+2H2O \rightarrow CO2+4H2 \quad \text{.....(3)}$$

During the compression process of 1 kg hydrogen caused by the SMR process is consumed between 5.0-5.5 m^3 of natural; 4.0-4.5 kg of water, 0.7 to 0.9 kWh of energy and emissions are 9.5 kg of CO_2/kg of hydrogen. In the case of liquefied hydrogen energy consumption in the liquefactions becomes 11-13 kWh per kilogram of hydrogen, this high consumption is reflected in an increased amount of CO_2 emissions of 35-38 kg of CO_2/kg of hydrogen. Although the ideal goal is to reduce total emissions of greenhouse gases for the production of hydrogen, this will be possible only until the renewable energy technologies like PV or wind are developed more efficiently. Currently the process of reforming of natural gas is the best opinion for hydrogen production in Mexico by having the infrastructure and sufficiently effective [9].

2.2. Hydrogen gasification of coal

This technology is competitive in places where oil and natural gas are expensive. It is used to produce synthesis gas from waste oil and coal, although they can feed the refinery waste, biomass and municipal solid waste.

The cost of raw material feed for the gasification process accounts for 25% of the final cost of hydrogen, despite the abundance of coal reserves in the word, it has a significant environmental impact as 132.6 kg CO_2/GJ generating 588 MW per km^2 at a cost of US $1,621/Ton of hydrogen. If this method is performed with CO_2 capture would emit into the atmosphere only 37.5 kg CO_2/GJ generating 588 MW of hydrogen per km^2 but the cost would rise too much as US $3,114/Ton of hydrogen [5].

Compression of 1 kilogram of hydrogen obtained from this process consumes fuel 6.0-7.0 kg coal/ kg H_2, 9 kg of waste and 0.7 to 0.8 kWh of energy issuing 22 kg CO_2 and 13-14 kWh for emitting liquefaction 46 kg CO_2 [9].

2.3. Hydrogen electrolysis

Decomposition of water into hydrogen and oxygen. The electrolyte is a solution of KOH in water; hydrogen is produced at the cathode with nearly 100% purity at low pressures. Considering power consumption efficiency 100% is 40 kWh/kg hydrogen, but in practice is higher energy consumption. The main disadvantage of electrolysis is the cost of electricity. For renewable energy that dominates is the cost of investments in photovoltaic systems or wind to generate electricity that is used in the electrolysis process, in the case of photovoltaic system can be 85% the price of hydrogen [7].

The total capital investments for the installation of hydrogen production by electrolysis with electricity supply network related to its size, for a plant with a capacity of 2.8 million Nm^3/day, the total investments cost TCI is US $2.95/GJ and large plants at 6.75 million Nm^3/day the TCI is US $30.97/GJ. Resource consumption per 1 kg of hydrogen of 55-60 kWh electricity and generates emissions of 41 kg of CO_2 [7].

3. Results and Discussion

Table 1 shows a summary of the estimated costs of hydrogen production in each technology listed above, showing the cost of production and cost to the consumer the estimate is made for a centralized and each of the technologies has transportation distance of 100 km from the hydrogen production plant to the point of delivery [9]. Each of these three scenarios it is observed that the difference in cost between hydrogen production and hydrogen compressed liquid is more than double its generating greenhouse gases, consequently greater, itself one of the objectives is to reduce greenhouse gases, we noted that production of liquid hydrogen is not a good economic or environmental option.

Table 1. Estimated cost of centralized hydrogen production and delivery to user as a liquefied compressed gas [9].

Production technology	Cost of production, $/kg H_2			Cost to consumer, $/kg H_2			CO_2 emission, kg CO_2/kg H_2
	I	II	III	I	II	III	
Compressed H_2							
SMR (natural gas)	1.2	1.9	2.6	1.6	2.4	3.1	9.5
Coal Gasification	1.8	2.0	2.2	2.3	2.5	2.7	21.8
Electrolysis (energy grid)	4.3	6.7	9.2	4.8	7.2	9.7	41.1
Liquefied H_2							
SMR (natural gas)	2.9	3.7	4.4	3.1	3.8	4.5	17.4
Coal Gasification	3.8	3.9	4.1	3.9	4.1	4.2	30.0
Electrolysis (energy grid)	5.7	8.6	11.6	5.9	8.8	11.7	48.6

I. Optimistic estímate, II. Moderate y III. Pessimistic.

The process of electrolysis using energy from the power supply that has a high cost in either scenario and the emissions of greenhouse gases into the atmosphere is much higher even in liquid hydrogen as compressed gas because the electricity used and this process is generated from fossil fuels. Then, gasification is a technology known but cheap and emissions of greenhouse gases are high for the case of compressed hydrogen gas for liquefied hydrogen.

The variation in costs to consumers are more accessible when the production of hydrogen through the process of performing of natural gas, since the variation between production costs and consumers costs is US $0.4, and has lower emissions of greenhouse gases than the process of gasification and electrolysis.

According to table 1, the SMR process is the best option for hydrogen production because de production costs in any of the three scenarios are lower and emissions of greenhouse gases (CO_2) are minimal and technology is completely known. The development of this technology in every region of the planet is determined by policies to reduce emissions of greenhouse gases and objectives of the Kyoto Protocol compliance. The availability of the raw material of SMR process is a fact that will determine the feasibility of the process, natural gas is considered the least polluting fossil fuel opposed to oil and coal so that their abundance is a important factor, for example United Arab Emirates produce about 3 billion cubic feet per day of natural gas and Mexico 5,394.6 cubic feet per day, which only 98% is used and the rest is sent into the atmosphere [14-15]. Despite of the increased production of natural gas in the UAE, according to the International Energy Agency, Mexico has three times the hydrogen production capacity of refineries in the UAE [16]. The hydrogen production plants operate at factor of 90% can produce 36,000 GJ of H_2 per day, enough to power 500,000 PEMFCV or small scale able to produce 108 GJ of H_2 per day, enough to feed 2,200 PEMFCV. However, the large scale hydrogen production is better to transportation demand and power generation [17]. The SMR process efficiency is between 65-75% which is measured in terms of fuel and electricity that they feed. Since the process is highly exothermic SMR produces more steam than it consumes, if the steam generated by the process used in other plant services, this would be at least 10% more efficient, competing with electrolysis renewable sources. The cost of production by SMR varies according to the price of natural gas if consumed at the site where it is produced would cost US $0.65/kg H_2 [17].

According to governments regulations in each country to shift to cleaner energy production based on the use of natural gas as fuel of hydrogen production, there are three scenarios in percentage (%) of the use of natural gas to produce hydrogen through the process SMR. These scenarios range from 10%, 50% and 100% use of NG to produce hydrogen. Figure 1, shows the cost that would generate hydrogen using different percentages of NG, the analysis was made for an annual production of $1.1X10^9$ GJ/ year in the UAE, at present the annual production in Mexico is $2.1X10^9$ GJ/year. Watching the scene using 100% natural gas for hydrogen production, the capital cost is about 50% lower than he scenario using 10% natural gas, operating cost and maintenance (O&M) and the cost of compression and storage are lower, US $0.45/GJ and US $0.265/GJ respectively, only the cost of natural gas is the same. Therefore the total cost of hydrogen production at 100% using of natural gas is US $6.15/GJ, which, compared with

the literature is in the range of US $6.0-7.5/GJ for large scale plants that produce from 1.34 to 25.4 million Nm^3/day of hydrogen [17].

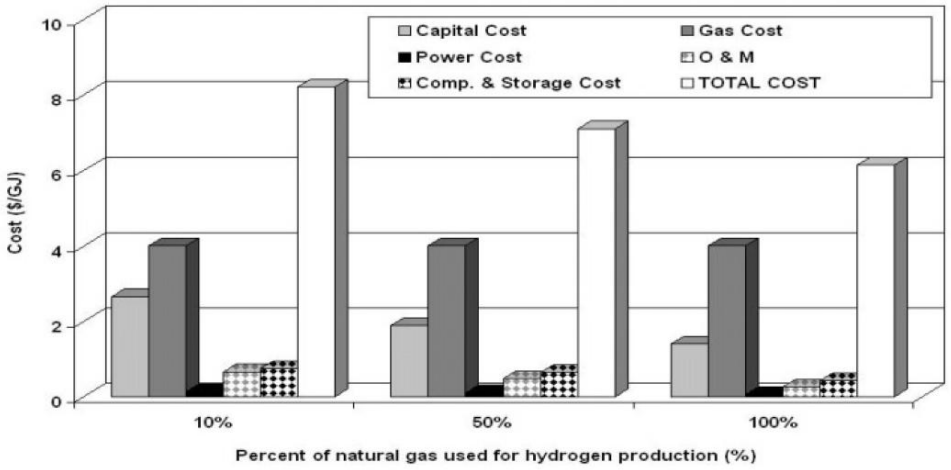

Figure 2. Breakdown of production costs of hydrogen with various percentages of current natural gas production.

Although the price of electricity for hydrogen production by electrolysis is high and emissions of greenhouse gases are higher among these three technologies, there are plants where the production of hydrogen is not the final product basics. An example is the production of hydrochloric acid, which is carried out by electrolysis where common salt or sodium chloride NaCl mixed with demineralised water to form an aqueous mixture with salt (salt magma) and form sodium chloride brine. To this solution should remove impurities and filtered to pass the area of electrolytic cells. Plants producing hydrogen by electrolysis operating with a solution of potassium hydroxide and hydrochloric acid productions woks with a solution of sodium chloride (NaCl), both are brine which uses as electrolyte. Of sodium chloride brine passing through the electrolysis process are obtained the following chemicals: chlorine wet cell liquor and hydrogen damp and water that contain dissolved sodium hydroxide. The main product, chlorine, is cooled, filtered, washed and dried. Chlorinated water which resulted in the washings is used in the production of sodium hypochlorite and chlorite passed once dry blending the area [10]. The technology currently used in the cells is known as “DeNora” corresponding to the Italian company owns the patent, but other technologies such as Stuart IMET Electrolyser (Canada), Norks Hydro (Norway) and Uralkhimmash (Russia) all with efficiencies above 500 m^3/hr of hydrogen and 0.1 to 5 MPa [11].

3.1. Case Study

The hydrogen produced by electrolysis is still an expensive process for the cost of grid electricity for the plant is estimated in 2650 kW/Ton Cl_2, placing it as the second largest consumer of electricity in the state of Jalisco, however, the greater benefit is the sale of hydrochloric acid 30%, liquid chlorine, sodium hypochlorite and soda caustic. The composition of the hydrogen obtained 1i 99.999% pure, suitable for use in devices such as fuel cells and auto supply power. Among the benefits of the current hydrogen is supply to boilers for generating steam to heat and supply to plant where hydrogen is 30% of the mixture and 70% natural gas mixture as feedstock supply companies for through tubing to 0.4 psi pressure for the process of hydrogenation of fats and oils. The hydrogenation process consumes about 2 million cubic meters of hydrogen per year, between 150,000 and 250,000 m^3 each month, according to demand, the cost of hydrogen in a year is about $ 4 billones (US $ 300,000), US $350-500 thousand per month [12]. The price of 1 me of hydrogen produced by electrolysis using the basic process of generation in this business is $ 1.80 significantly lower for the consumer compared to the one shown in table 1 in any of the three scenarios, since the cost are borne y sales of hydrochloric acid, chlorine, sodium hypochlorite and caustic soda [10].

According to data from 2008 to 2011, each month will produce about 84 ton of hydrogen, approximately 83% of the hydrogen is used to generate heat, hydrogenation of fats and oils and the production of hydrochloric acid from the same plant. The remainder of production has no use a raw material or as energy, but must be vented to atmosphere for process safety. The potential of the remaining 17% hydrogen to generate energy could be used in fuel cells to supply power to the plant. A common fuel cell of 5kW in Mexico cost US $15,000 ($200,000 pesos) and needs a supply of maximum flow output of 64 lt/min. Evaluating the hydrogen production conditions of the plant this would generate 57 times per day flow required by the fuel cell.

“The ability to offset peak electricity usage with an emission-free fuel cell system will create significant savings, while reducing our environmental footprint”. Mark Yamauchi, TMS Facilities Operations Manager.

The background to the application of this technology is shown by the company Ballard Power Systems, which developed a system of hydrogen, a by-product of the production process of hydrochloric acid HCl, could be supplied in fuel cells feed with hydrogen and power generation electrical, which has been shown is a prohibitively expensive fuel for these companies that produce Cl_2 through electrolysis. According to the proposal CLEARgen^{TM} Ballard, electricity accounts for 70% the cost of production of chlorine [13].
According to Mexichem S. A. de C. V. company, the cost of electricity is very high, making this company the second largest energy consumer in the state. If the hydrogen vented to the atmosphere could be recovered and used to generate electricity, then the hydrogen would get more value than it now has a raw material or fuel.

4. Conclusions

Therefore, the total cost of hydrogen production at 100% using of natural gas is US $6.15/GJ, which, compared with the literature is in the range of US $6.0-7.5/GJ for large scale plants that produce from 1.34 to 25.4 million Nm^3/day of hydrogen [17]. The operating conditions of gas natural in Mexico for the production of hydrogen compared to the United Arab Emirates, 1.1X109 GJ/year, and show that it is feasible to use the oil for hydrogen production in Mexico with 2.1X109 GJ/year. The most likely is a transition with the highest percentage of use of gas natural for hydrogen production via SMR process is the cheapest compared to other processes, besides being friendlier to the environment. The SMR process can also be more efficient if the current of steam generated is used in other plan services, giving use the product as in the case of the company Mexichem, where the potential for generation of electricity through the use of hydrogen they get as by-product in the process serve as feed for fuel cells; mitigate electric power consumption of the network, allocating the percentage that supply boilers to fuel cells that would deliver clear energy.

5. Acknowledgments

Authors wish to thanks to SMH –CONACYT for their support to attend this event.

6. References

[1] Hydrogen Analysis Resource Center: Worldwide Hydrogen Production Capacity at Refineries

[2] Petroleum and Other Liquids http://www.eia.gov/dnav/pet/pet_pnp_feedng_k_a.htm

[3] Hydrogen Production; Stanko Hoˇcevar and William Summers. Pag. 25-29

[4] John C. Molburg (molburg@anl.gov; 630-252-3264), Richard D. Doctor (rdoctor@anl.gov; 630-252-5913), Hydrogen from Steam-Methane Reforming with CO2 Capture. 20th Annual International Pittsburgh Coal Conference September 15-19, 2003 Pittsburgh, PA2003. Pag. 2-4

[5] Enrique Ortega Valencia*, Juan Luis François Lacouture. Producción de hidrógeno mediante energía nuclear, un escenario sostenible en México. Simposio LAS/ANS 2007, XVIII Congreso Anual de la SNM, XXV Reunión Anual de la SMSR. 2007. Pag. 566.

[6] Liang-Shih Fan, University Distinguished Professor. Chemical Looping Systems for Fossil Energy Conversions. Wiley. 2010. Pag. 147, 148

[7] Ignacio León Meléndez, Producción de Hidrógeno. http://www.google.com.mx/#hl=es-419&output=search&sclient=psy-ab&q=Ignacio+Le%C3%B3n+Mel%C3%A9ndez&oq=Ignacio+Le%C3%B3n+Mel%C3%A9ndez&aq=f&aqi=&aql=&gs_l=hp.3...1124.1124.0.2231.1.1.0.0.0.0.93.93.1.1.0...0.0.2Ld9hjwjBas&pbx=1&bav=on.2,or.r_gc.r_pw.r_qf.,cf.osb&fp=26d659cb607b9ed0&biw=1366&bih=667. Pag. 129-147

[8] Bases de Diseño. Elaboración de Ingeniería Complementaria, Procura y Construcción del Hidrogenoducto de 10" d. N. X 25.4 km para suministro de hidrógeno al Proyecto de Reconfiguración de la Refinería "General Lázaro Cárdenas", Minatitlán, Veracruz. Pag. 2

[9] Yu. V. Sinyak and V. Yu. Petrov. Cost Prospects for Hydrogen Centralized Production. Industries and Interindustry Complexes.2008. Pag. 240-245

[10] Descripción del Proceso. Mexichem Derivados S. A. de C. V. Planta el Salto. Marzo 2011. Pag. 2-3

[11] B. P. Tarasov[a] and M. V. Lototskii[b]. Hydrogen Energetics: Past, Present, Prospects. Russian Journal of General Chemistry, 2007. Pag. 663

[12] Quimikao S. A. de C. V. Planta El Salto.2011

[13] Ballard Power System. Distributed Generation. CLEARgen™ Fuel Cell. http://www.ballard.com/fuel-cell-applications/distributed-generation.aspx.

[14] Climate Analysis Indicators Tool CAIT. http://cait.wri.org. Pag. 3

[15] SENER. Estadísticas Destacadas de Energía. Estadísticas Destacadas del Sector Energético. Marzo 2012. http://www.sener.gob.mx/portal/estadisticas_destacadas_del_sector_energetico.html

[16] Hydrogen Analysis Resource Center: Worldwide Hydrogen Production Capacity at Refineries. http://hydrogen.pnl.gov/cocoon/morf/hydrogen

[17] A. KAZIM. United Arab Emirates University. Department of Mechanical Engineering. Feasibility of Hydrogen Energy Production through Natural Gas Steam Reformation Process in the UAE. 2004

Towards the understanding and control of the photo-deposition of metal nanoparticles on oxides

J. Ma, A. S. Gago, A. Habrioux, N. Alonso-Vante*

IC2MP-UMR CNRS 7285, University of Poitiers, 4 rue Michel Brunet, B27-BP633, 86022, Poitiers, France
*Tel: +33 54945-3625, Fax: +33 54945-3580, mail: nicolas.alonso.vante@univ-poitiers.fr

ABSTRACT

The photo-deposition technique under UV and UV-Vis domain for metal nanoparticles, e.g. platinum, was explored. According to the procedure employed, one can devise various complex mechanisms. This work evidences such complexities by a judicious choice of parameters, such as alcohol chain length, and media. The presence of nanoparticulated oxide anatase-phase enhances the photo-deposition process of metal nanoparticles via the so-called heterogeneous photocatalysis. A description and the effect of mixing of various chemical components in the reactor are given. The control of the nanoparticle size with water as hole-scavenger looks promising.

1. Introduction

The tailoring of stable highly dispersed and efficient electrocatalysts is currently a great challenge. A promising way to achieve this consists in using oxide and/or oxide-carbon composites as supports. Moreover, the technique devised to perform the metal (e.g. platinum) deposits on the support seems also to influence the nature of the interaction between the catalyst and the support. Particularly, the photo-deposition technique [1] is well adapted to induce nanoalloy formation with the metal of the support giving rise to the so-called strong metal substrate interaction (SMSI) [2, 3], thus improving the rate, e.g., the oxygen reduction reaction. The method consists in photo-irradiating an aqueous solution containing the metallic precursor, the oxide, and organic molecules serving as a hole-scavenger. The process is based on the reducing/oxidizing capability of photo-irradiated oxide nanoparticles to achieve the reduction of metallic ions into metal islands and the oxidation of adsorbed water or organic molecule. It is essential to control the synthesis of noble metal based nanoparticles, since the electrocatalytic activity depends on the chemical nature, morphology, crystallographic properties and the position of the d-band center with respect to the Fermi level. Parameters affecting the properties of photo-deposited nanoparticles are still not-well identified and understood. This study aims at understanding of the mechanism of photodeposition of Pt onto TiO_2 substrate, as well as the control of the nanoparticle size.

2. Experimental

2.1 In-situ absorbance monitoring during photodeposition process

The photo-deposition procedure was carried out as follows: 52.6 mg of TiO_2 (anatase), synthesized by sol-gel technique, was mixed in argon-saturated 28 mL water in a photo-reactor provided with two optical quartz windows. Additionally, 6 mL of isopropanol solution containing 34.7 mg of Pt salt ($H_2PtCl_6.6H_2O$) was added into the photo-reactor. The suspension was saturated with Ar and kept under constant stirring for 3 h. The source of ultraviolet (UV) and visible (Vis) radiation used for the experiments was a Xe-lamp (159 W, ITS PS 150-9). In order to prevent the heating of the samples, the infrared (IR) photons were avoided using a hot mirror UV (Edmund Optics, F46507), and a water filter. To follow up in-situ the reaction kinetics, a light detector (Rad Probe, LP 471) was fixed on top of the photo-reactor. The detector was connected to a photo/radiometer (Delta OHM HD 2102.2). Fig. 1 shows a scheme of the photo-reactor. A UV filter (Edmund Optics, F45311) was used to cut $\lambda < 400$ nm. The suspension containing the TiO_2 and H_2O was used to record the irradiance at the beginning of the experiment, A_0. The light detector monitored the evolution of the irradiance, A_1, with time. The ratio A_1/A_0 was calculated to determine the absorbance.

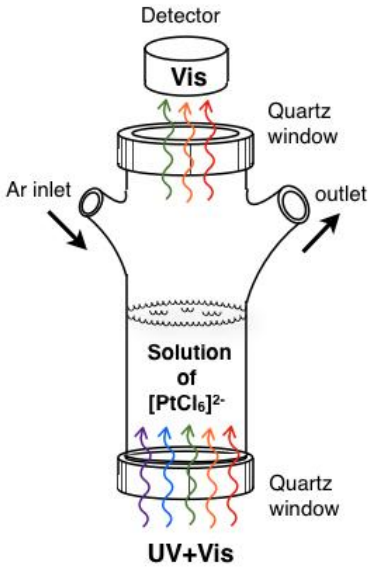

Fig. 1. Photo-reactor used to measure of absorbance changes during photo-deposition process.

2.2 TEM characterization

The morphology of particles was examined with a TEM on a JEOL JEM-2001 equipped with a LaB_6 filament. The samples were characterized under an accelerating voltage of 200 kV and a resolution of *ca.* 0.19 nm.

3. Results and discussion

To investigate the direct reduction of platinum precursor in the presence of isopropanol, the following experiments were performed. In short, an aqueous solution containing both $[PtCl_6]^{2-}$ and isopropanol were successively photo-irradiated by a Xe –lamp equipped either with or without a UV filter. The variation of absorbance of the solution was monitored in-situ. Results are displayed in Fig. 2.

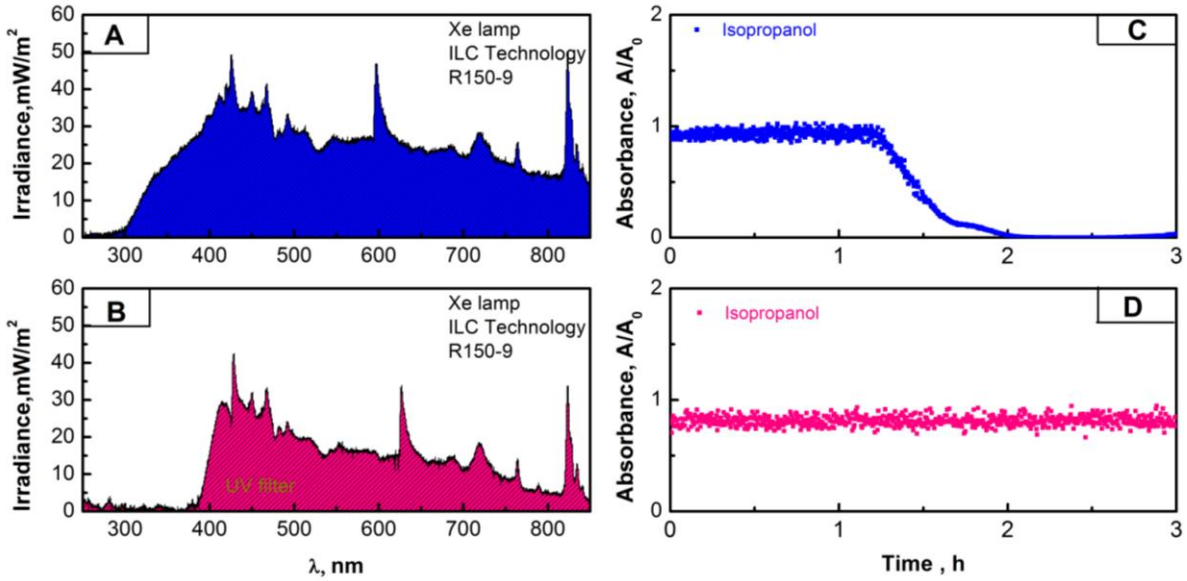

Fig. 2. (A) Output spectrum of the Xe lamp, (B) output XE lamp spectrum with an UV filter, (C) Absorbance evolution of $[PtCl_6]^{2-}$ + isopropanol under irradiation using spectrum (A), and (D) Absorbance evolution under irradiation using spectrum (B).

By comparing the results obtained in Figs. 2C and 2D, one can infer that only the UV spectral region is responsible to modify the absorbance of the solution. Indeed, the energy, hυ, of this spectral region affects the platinum precursor $[PtCl_6]^{2-}$ electronic structure by the electronic *d-d* transition with a maximum peak at 300 nm [4, 5]. The photochemical reaction scheme follows [6-8]:

$$[PtCl_6]^{2-} + h\upsilon \rightarrow [PtCl_6]^{2-*} \quad (1)$$

The excited complex is then able to react with the alcohol molecule to form a radical complex ($[PtCl_6]^{3-}\cdots{}^{\bullet}R$) as represented by equations. (2) – (4):

$$[PtCl_6]^{2-*} + R\text{-}CH_2\text{-}OH \rightarrow [PtCl_6]^{3-} \text{ --- } {}^{\bullet}R\text{-}CH_2O + H^+ \quad (2)$$

$$[PtCl_6]^{3-}\cdots{}^{\bullet}R\text{-}CH_2O \rightarrow [PtCl_6]^{3-}\cdots{}^{\bullet}R + CH_2O \quad (3)$$

$$[PtCl_6]^{3-}\cdots{}^{\bullet}R \rightarrow [PtCl_4]^{2-} + {}^{\bullet}R + 2Cl^- \quad (4)$$

Thereafter, the dissociation of $[PtCl_4]^{2-}$ to form Pt^{2+} species is done [5], equation (5). This latter is then reduced to form platinum clusters, equation (6).

$$[PtCl_4]^{2-} + h\upsilon \rightarrow Pt^{2+} + 4Cl^- \quad (5)$$

$$Pt^{2+} \xrightarrow{RCH_2OH,\, H_2O,\, h\nu} Pt^0 \quad (6)$$

Recently, we have shown that Pt nanoparticles can be selectively deposited onto oxide sites of oxide-carbon composites [3, 9, 10]. However the photo-deposition process is not yet well controlled and optimized. By designing

different experiments in which the components of the reaction medium are systematically varied, we seek to understand the photo-deposition process to control the particle size and distribution on TiO_2. As a result, the changes in the absorbance of different solutions were monitored in-situ. The results are contrasted in Fig. 3. In each panel, a scheme illustrates a possible mechanism.

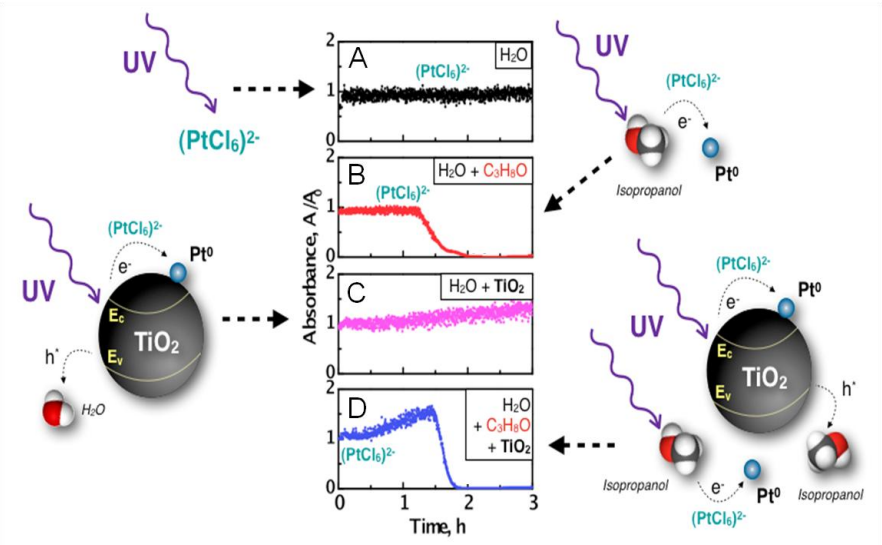

Fig. 3. Absorbance evolution of an aqueous mixture containing $[PtCl_6]^{2-}$, TiO_2, and isopropanol.

From Fig. 3A it looks clear that no variation in the absorbance occurs under UV irradiation when the mixture contained water and $[PtCl_6]^{2-}$. We can assume that no formation of a radical complex, equation (2) takes place in water, and platinum nanoparticles are not generated. However, the presence of isopropanol enhances the deposition of metal clusters. This is confirmed by the change of the absorbance at $t \geq 1h$, and confirmed by the TEM analysis, Fig. 4A. Figs. 3C and 3D depict the phenomenon of heterogeneous photocatalysis induced by TiO_2 (anatase). In both cases the formation of platinum clusters takes place cf. Figs. 4B and 4C. In the absence of a powerful hole-scavenger, e.g., alcohol (Fig. 3C) the formation of platinum clusters occurs as follows: Firstly, one consists in the hole (h^+) – electron (e^-) pair generation at the oxide semiconductor under UV illumination:

$$TiO_2 + h\upsilon \rightarrow h^+ + e^- \qquad (7)$$

The absence of any applied electrical field at the particle favors the hole-electron recombination. Under this condition, the formation of $OH^\bullet$ radicals from adsorbed water via holes is therefore limited, as a result the reaction process channel via the conduction band (cb) is also limited, but stochastic events are possible that leads to the photogenerated electrons to reduce the platinum complex. The process can be summarized in equations (8) and (9):

$$(H_2O)_{ads} + h^+ \rightarrow HO^\bullet + H^+ \qquad (8)$$

$$[Pt^{IV}Cl_6] + 2e^-_{cb} \rightarrow [Pt^{II}Cl_4] + 2e^-_{cb} \rightarrow Pt^0 \qquad (9)$$

This photo-reduction process becomes more complex in presence of isopropanol, cf. Fig. 3D. Indeed, one can imagine several parallel pathways to explain the formation of platinum nanoparticles. The usual mechanism to explain the phenomenon consists in considering that electron-hole pair generation at the TiO_2 under UV illumination, equation (7), the recombination process is somehow inhibited to a certain extent due to the interaction of alcohol and metal complex species at the semiconducting oxide surface which favors the photo-oxidation of the alcohol via holes and photo-reduction of metal ions of the complex via electrons. Other competing mechanisms previously described may also be involved. The first one results from the excitation of $[PtCl_6]^{2-}$ under UV irradiation, equations (1) to (6). The second consists in using water as hole scavenger, equation (8). In the first stage of the reduction process a continuous increase of the solution absorbance of the solution can be clearly seen in Figs. 3C and 3D. The rate of increase is probably related to electron-hole pair recombination and/or to the (cb) electron yield to be transferred to $[PtCl_6]^{2-}$ complex species.

After 3 h of irradiation, the samples tested in process in Figs. 3B, 3C and 3D were analyzed by TEM, Fig. 4. These figures clearly show that the morphology and the size of the nanoclusters greatly depend on the experimental conditions.

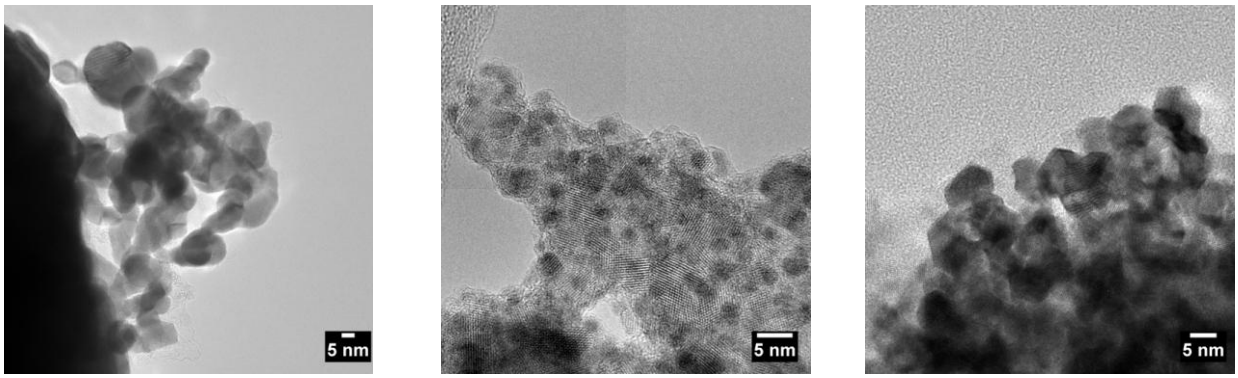

(A) (B) (C)

Fig. 4. Low magnification TEM images showing the size and morphology of Pt photosynthesized in (A) water/isopropanol, (B) water solution and TiO_2, (C) water/isopropanol and TiO_2, after 3 hours of irradiation.

The mean size of platinum nanoparticles has been determined for samples obtained by processes shown in Figs. 3B, 3C, and 3D. They were 10.0, 1.9 and 7.5 nm, respectively. Summing up, small and highly dispersed nanoparticles can be obtained by using only water, TiO_2 and H_2PtCl_6 as reactants, whereas bigger and agglomerated particles are obtained in the other cases. The photolysis process and the absence of a support lead to the agglomeration of Pt nanoparticles (Fig. 4A). Additionally the morphology of particles is highly affected by the procedure used. It seems that particles photo-deposited in presence of water and isopropanol are highly faceted.

4. Conclusions

In this work, the concomitant occurrence of different mechanisms during the photo-deposition process of Pt nanoparticles onto TiO_2 in the presence of water and alcohol, are evidenced. By measuring the irradiance light transmitted through the photo-reactor, it was possible to monitor, in real time, the photo-deposition process. Additionally, encouraging perspectives concerning the control of the nanoparticle size by just using water as hole-scavenger to realize the photo-deposition are given. Interesting information is obtained to optimize the process in order to decrease the amount of precious metals used as cathode materials for fuel cells.

5. Acknowledgements

J. Ma thanks the Region Poitou-Charentes for financial support. The authors thank Mrs. Julie Rousseau for her technical assistance in the TEM images.

6. References

[1] Sugimura, H.; Uchida, T.; Kitamura, N.; Masuhara, H., Chemistry Letters, 2, 379, (1993)

[2] Vogel, W.; Timperman, L.; Alonso-Vante, N., Applied Catalysis A, General, 377, 167, (2010)

[3] Timperman, L.; Feng, Y. J.; Vogel, W.; Alonso-Vante, N., Electrochimica Acta, 55, 7558, (2010)

[4] Einaga, H.; Harada, M., Langmuir, 21, 2578, (2005)

[5] Harada, M.; Einaga, H., Langmuir, 22, 2371, (2006)

[6] Grivin, V. P.; Khmelinski, I. V.; Plyusnin, V. F., Journal of Photochemistry and Photobiology A: Chemistry, 59, 153, (1991)

[7] Grivin, V. P.; Khmelinski, I. V.; Plyusnin, V. F., Journal of Photochemistry and Photobiology A: Chemistry, 51, 379, (1990)

[8] Grivin, V. P.; Khmelinski, I. V.; Plyusnin, V. F.; Blinov, I. I.; Balashev, K. P., Journal of Photochemistry and Photobiology A: Chemistry, 51, 167, (1990)

[9] Timperman, L.; Alonso-Vante, N., Electrocatalysis, 2, 181, (2011)

[10] Ruiz Camacho, R. C.; González Huerta, R.; Valenzuela, M.; Alonso-Vante, N., Topics in Catalysis, 54, 512, (2011)

Fast Synthesis of M@Pt (M=Ru, Pd, Fe_3O_4) Core-shell Nanostructures and their Evaluation as Anodes for the Oxidation of Ethanol

N.M. Sánchez-Padilla[1], S.M. Montemayor[1], F.J. Rodríguez Varela[2,*]

[1]Depto. Materiales Cerámicos, Facultad de Ciencias Químicas de la Universidad Autónoma de Coahuila, V. Carranza s/n, Saltillo, Coahuila, México, CP 25280
[2]Grupo de Recursos Naturales y Energéticos, CINVESTAV Unidad Saltillo, Carr. Saltillo-Monterrey km. 13.5, Ramos Arizpe, Coahuila, CP 25900
*E-mail: javier.varela@cinvestav.edu.mx

ABSTRACT

We report the fast synthesis and electrochemical evaluation of M@Pt core-shell nanostructures (where M=Ru, Pd, Fe_3O_4) for the ethanol oxidation reaction (EOR). Separately, the chemical precursor of each core material was synthesized in $NaBH_4$ in a reduction time of 60 s. The Pt shell was deposited afterwards on the cores also in 60 s using the same reducing agent. Pt-alone nanoparticles were synthesized in one minute as well for comparison purposes. The XRD results indicate that crystalline materials can be obtained with this rapid process. The average particle sizes of the core-shell nanostructures, determined with the Scherrer equation, were in the 6-8 nm range for the nanomaterials. The electrochemical evaluation revealed that the catalytic activity of the novel Fe_3O_4@Pt anode for the EOR is as high as that of the Ru@Pt material. The Pt-alone and Pd@Pt anodes showed a lower activity for such reaction. Durability tests performed on the Fe_3O_4@Pt and Ru@Pt anodes indicated a high stability of these catalysts in acid medium.

1. Introduction

In a society where oil is the major energy source, higher demand and lower supply makes its price fluctuate. Moreover, its use contributes to the global warming. For these reasons, everyday there are more research groups dedicated to find new energy sources or innovating already existing. Hydrogen is one of the fuels that are a promising alternative and it can be used in fuel cells. However, some of the problems related to the use of H_2 are its handling, transportation, storage, and in general, the logistic of its use [1-3]. The use of liquid fuels in fuel cells without reforming (Direct Liquid Fuel cells) is a good energetic option [4-6]. Ethanol is a renewable fuel commonly mentioned as a potential candidate for this application in Direct Ethanol Fuel Cells (DEFC). It offers several advantages over other liquids fuels, including facile transportation, non-toxicity, high energy density and it can be obtained from simple industrial processes [7-10].

One of the biggest challenges for the use of ethanol in fuel cells with proton exchange membranes is the catalyst performance to execute the oxidation at the anode. Pt is widely used on these cells, however, the presence of CO as intermediate from alcohol oxidation decrease significantly its performance. Therefore, there is a growing interest to develop catalyst that can oxidize organic molecules at low potentials and are not affected by the reaction intermediates. Pt-based alloys and nanostructures have proved to be the best option to oxidize alcohols, specifically methanol and ethanol. These nanomaterials have been synthesized by various methods. Although nanocatalysts with good physicochemical and electrochemical properties have been obtained, most processes require long time of synthesis under stirring and/or reflux [2, 6, 11-14].

In this work, we report the fast (one minute reaction times) and efficient synthesis of Pt-alone nanoparticles and M@Pt core-shell nanostructures (where M = Fe_3O_4, Pd and Ru), using the mechanical agitation method (UT) and $NaBH_4$ as the reducing agent. We evaluate the catalytic activity of such nanocatalysts for the EOR in acid medium.

2. Experimental

For this study $Fe(NO_3)_3 \cdot 9H_2O$, $PdCl_2$, $RuCl_3$ and $H_2PtCl_6 \cdot 6H_2O$ as metallic precursors, and $NaBH_4$ as reducing agent were used. All chemicals were purchased from Aldrich and used without further purification. To obtain the *cores*, solutions of $NaBH_4$ (0.001 M) and the metallic sources (0.002 M) were prepared. The metallic salt solution was added dropwise into the solution containing the reducing agent at room temperature and mechanically stirred (UT method). The obtained products were washed and separated by centrifugation at 3000 rpm. The powders were characterized by XRD to determinate the crystallite size and the structural parameters.

To obtain the core-shell nanostructures, the *cores* were suspended on a fresh reducing solution (0.001 M $NaBH_4$) and a $H_2PtCl_6 \cdot 6H_2O$ solution (0.002 M) was slowly added at room temperature under UT stirring. M@Pt materials in a

1:1 (w/o) Me:Pt ratio were obtained. The powders were washed and centrifuged at 3000 rpm. The catalysts were characterized by XRD.

The catalytic activity of the nanocatalysts for the EOR was evaluated with a potentiostat (Voltalab). CVs were obtained in N_2-satured solution. Studies of ethanol oxidation were carried out immediately after the activation with the addition of 10 mL of 0.5 M ethanol into the N_2-satured solution. The electrolyte was 0.5 M H_2SO_4. All electrochemical measurements were taken at 20 mV/s and room temperature.

3. Results and discussion

Figure 1 shows the XRD patterns of the cores. The diffractogram of Fe_3O_4 shows the formation of ferric-ferrous oxide with a spinel-type phase ($FeO{\bullet}Fe_2O_3$ PDF 89-0691). Meanwhile, the Pd pattern shows the formation of a polycrystalline material (PDF 46-1043). On the other hand, the diffractogram of Ru indicates the formation of a quasi-amorphous core.

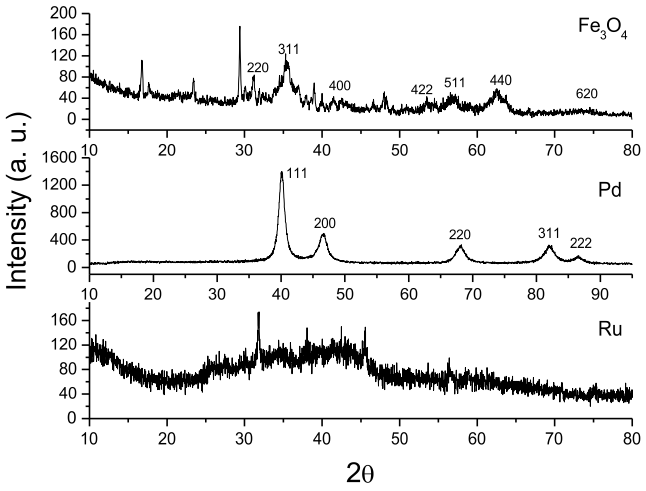

Figure 1. XRD patterns of the cores: Fe_3O_4, Pd and Ru.

Figure 2 shows the XRD patterns of Pt-alone and the nanostructures (after deposition of Pt on the *cores*). In all cases the main peaks related to Pt (PDF 4-0802), with cubic structure and cell parameter a = 3.9120 Å, can be observed. The Fe_3O_4@Pt material also shows the peaks related to magnetite. Because the sets of Pt and Pd are almost the same (both Pd and Pt have cubic structures and cell parameters likely 3.8930 vs 3.9120 Å respectively), the diffractogram of the Pd@Pt nanostructure indicates the planes related to Pt. Since the Ru material turned out to be quasi-

amorphous, only the peaks of Pt are present in the Ru@Pt diffractogram. The pattern of Pt-alone is also shown in Figure 2.

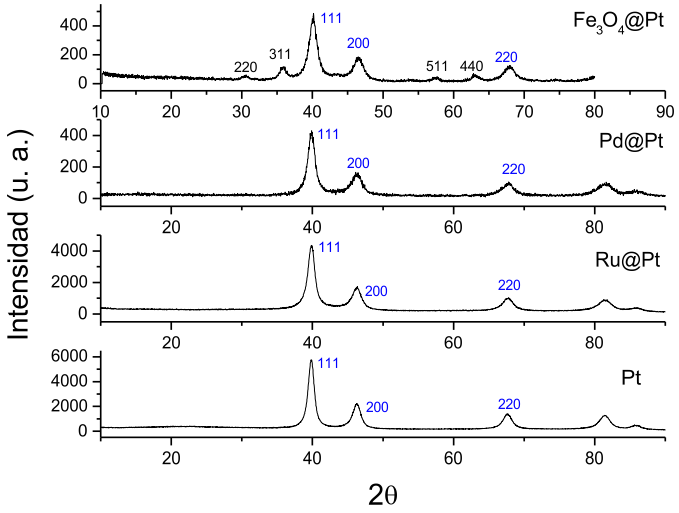

Figure 2. XRD patterns of the nanomaterials: Fe_3O_4@Pt, Pd@Pt, Ru@Pt and Pt-alone.

Figure 3 shows the CVs of the EOR at the four nanomaterials. The catalytic activity for the anodic reaction decreases in the order Ru@Pt > Fe_3O_4@Pt > Pt > Pd@Pt. In the positive potential scan, maximum peak current densities of 3.2 mA/cm^2 and 2.9 mA/cm^2 are obtained from Ru@Pt and Fe_3O_4@Pt, respectively. This means that the catalytic activity of Fe_3O_4@Pt is close to that of the Ru-based anode. The activity of the Fe_3O_4@Pt core-shell material is surprisingly high. To the best of our knowledge, this is the first time such nanostructure is evaluated as anode for the oxidation of organic molecules.

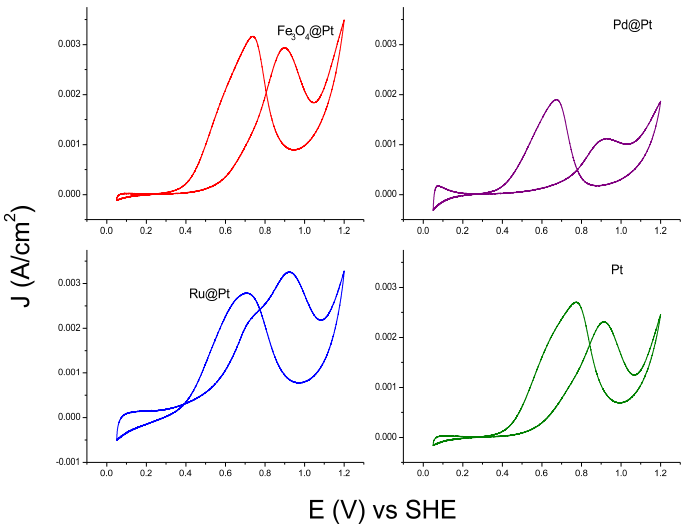

Figure 3. CVs of the EOR for Fe_3O_4@Pt, Pd@Pt, Ru@Pt and Pt-alone in N_2-saturated 0.5 M H_2SO_4 + 0.5 M C_2H_5OH solution. Scan rate: 20 mV/s.

Figure 4 shows the chronoamperometric measurements, recorded at 895 mV vs SHE during 600 s. Clearly, the Ru@Pt and Fe_3O_4@Pt catalysts show a more stable performance than the other two catalysts for the EOR. The behavior of those two materials is quite similar. After 600 s, the current density at Ru@Pt and Fe_3O_4@Pt is 1 mA/cm^2. Meanwhile, after such elapsed time, the current density is 0.8 and 0.4 mA/cm^2 for Pt-alone and Pd@Pt, respectively.

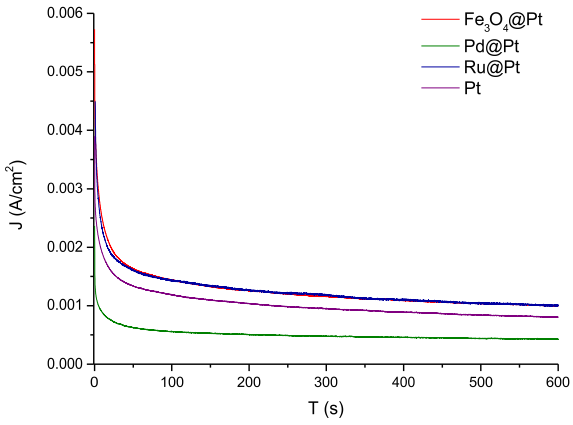

Figure 4. Chronoamperometric curves of the EOR at Fe_3O_4@Pt, Pd@Pt, Ru@Pt and Pt-alone, measured at 895 mV vs SHE and room temperature.

4. Conclusions

In this work we present a facile synthesis process to obtain M@Pt (with M = Fe_3O_4, Pd and Ru) core-shell nanostructures. The XRD patterns show the formation of the core materials and metallic Pt after one minute synthesis under UT stirring. The Ru@Pt and Fe_3O_4@Pt nanomaterials show the higher catalytic activity for the EOR. To the best of our knowledge, this is the first time that Fe_3O_4@Pt nanostructures are evaluated as anodes for the oxidation of organic molecules.

5. Akcnowledgements

The authors thank the Mexican National Council for Science and Technology (CONACYT) for financial support through grant 79870 and the Programa de Redes Temáticas.

6. References

[1] F. Vigier, C. Contanceau, A. Perrard, E. Belgsir, C. Lamy, J. Appl. Electrochem., 34, 439-446 (2004).
[2] C. Wan, C. Chen, Int. J. Hydrogen energy, 34, 9515-9522 (2009).
[3] R. Wang, H. Wang, B. Wei, W. Wang, Z. Lei, Int. J. Hydrogen Energy, 35, 10081-10086 (2010).
[4] C. Lamy, E. Belgsir, J.M. Leger, J. Appl. Electrochem., 31, 799-809 (2001).
[5] X. Yuan, H. Wang, PEM Fuel Cell Electrocatalysts and Catalyst Layers, Springer, Canada (2008).
[6] F. Kadirgan, S. Bayhan, T. Atilan, Int. J. Hydrogen Energy, 34, 4312-4320 (2009).
[7] Fuel Cells Catalysis: A surface Science Approach, Edited by Marc T. M. Koper, Wiley & Sons, New Jersey 2009.
[8] S. Heysiattalab, M. Shakeri, M. Safari, M. Keikha, J. Ind. Engineering Chemistry, 17, 727-729 (2011).
[9] T. Lopes, E. Antolini, E. Gonzalez, Int. J. Hydrogen Energy, 33, 5563-5570 (2008).
[10] J. Tayal, B. Rawat, S. Basu, Int. J. Hydrogen Energy, 37, 4597-4605 (2012).
[11] D. Kaplan, M. Alon, L. Burstein, E. Peled, J. Power Sources, 196, 1078-1083 (2011).
[12] H. Wang, R. Hang, H. Li, Q. Wang, J. Kang, Z. Lei, Int. J. Hydrogen Energy, 36, 839-848 (2011).
[13] L. Lai, G. Huang, X. Wang, J. Weng, Carbon, 49, 1581-1587 (2011).
[14] P. Ochal, J. Gomez, M. Tsypkin, F. Seland, S. Sunde, N. Muthuswamy, M. Rønning, D. Chen, S. Garcia, S. Alayoglu, B. Eichhorn, J. Electrochem. Soc., 655, 140-146 (2011).

Synthesis of Unsupported Pt-Based Electrocatalysts and Evaluation of their Catalytic Activity for the Ethylene Glycol Oxidation Reaction

Aldo Fabián Chávez Villanueva[1], Adriana M. Ramirez[1], G. Vargas Gutiérrez[2], F.J. Rodríguez Varela[2]
[1]Universidad de la Ciénega de Michoacán de Ocampo, Avenida Universidad 3000, Sahuayo, Michoacán, México, CP 59000.
[2]CINVESTAV Unidad Saltillo, Carr. Saltillo-Monterrey km. 13.5, Ramos Arizpe, Coahuila, CP 25900

ABSTRACT

Pt, Pt-Ru, Pt-CeO_2 and Pt-Ru-CeO_2 electrocatalysts were synthesized and evaluated as anodes for the ethylene glycol oxidation reaction (EGOR). The nanomaterials were prepared by slowly dropping the precursors in a $NaBH_4$ solution, in a reduction process of 10 min. The results from the electrochemical characterization of the anodes, carried out in 0.5 M H_2SO_4, showed that the Pt-Ru material possess a higher catalytic activity for the EGOR, compared to Pt-alone, Pt-CeO_2 and (Pt-Ru)-CeO_2. The nano-sized Pt-Ru anode demonstrated a high stability in accelerated potential cycling tests, with very low surface losses in the hydrogen adsorption/desorption region after 500 cycles.

1.-Introduction

Nanostructured materials present many interesting properties as catalysts for electrochemical devices such as Direct Alcohol Fuel Cells (DAFCs). This has been the reason why many researchers have generated a large interest in their study. However, although many systems are investigated, nowadays is necessary to study different Pt-based materials with specific catalytic properties for the type of fuel being used in DAFCs. Catalysts like Pt-Ru, Pt-CeO_2 or Pt-Ru- CeO_2 are of interest for DAFCs because of their high performance. The main objective of this research is to evaluate the performance of metallic nano-particles for the ethylene glycol oxidation reaction.

Cerium-modified Pt materials have shown good electrochemical behavior as anodes for DAFCS. Research has been carried out on structure, chemical properties, reduction behavior, stoichiometry, storage capacity and metal-cerium interactions [1-8]. It is also important to determine which of the materials with a Ce percentage may find application as environmental catalysts [4,6,9-15]. The presence of Ce in the crystalline structure has a positive effect, for example enhancing the storage and release of oxygen. This is crucial in several catalytic reactions such as the Oxygen Reduction Reaction (ORR) and the oxidation of organic molecules in fuel cells.

The metallic nano-particles Pt, Pt-Ru, Pt-CeO_2, Pt-Ru-CeO_2 were synthesized with sodium borohydride ($NaBH_4$). The materials were evaluated as anodes for the oxidation of $C_2H_6O_2$, via cyclic voltammetry (CV) and lineal scan voltammetry (LSV). The physicochemical characterization included EDAX and your crystal structures XRD.

2.-Experimental

The reagents used to obtain nanoparticles were $RuCl_3$ (Aldrich, 45.55% Ru), $H_2PtCl_6*6H_2O$ (Aldrich, 37.5% Pt base), and $CeN_3O_9*6H_2O$ (Aldrich, 99%), as metallic sources and $NaBH_4$ (Aldrich, solución 12% p/v in NaOH 14 M), as reducing agent. All reagents were used without further treatment. The synthesis was performed by slowly dropping the precursors in a $NaBH_4$ solution, in a reduction process of 10 min. The recovered powders were washed with excess water and dried in a furnace at eighty degrees. Figure 1 shows, a schematic diagram of the experimental procedure during the synthesis of nanoparticles. The molar ratio used for obtaining the powders is shown in Table 1.

The catalytic activity of the Pt-based materials for the EGOR was evaluated with the aid of a potentiostat (Voltalab) connected to a RDE instrument (Pine Inst.). CVs and LSVs were obtained in N_2-saturated 0.5 M H_2SO_4. The methods used to prepare catalytic inks and working electrodes has already been described with detail elsewhere [16].

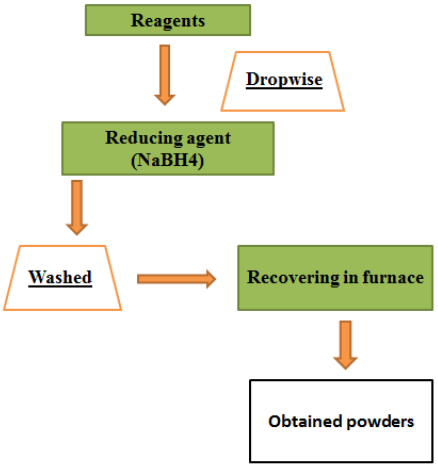

Figure 1. Schematic diagram showing the synthesis procedure of the nanomaterials.

Table 1.- Reagents molar ratio

Metallic materials	Reagents			Reducing agent
Salts precursor	$H_2PtCl_6*6H_2O$	$RuCl_3$	CeN3O9*6H2O	$NaBH_4$
Pt	0.000513 M			0.000075 M
Pt-Ru	0.001538 M	0.002950 M		0.001299 M
Pt-CeO2	0.001538 M		0.002141 M	0.000599 M
Pt-Ru-CeO2	0.001026 M	0.001967 M	0.001427 M	0.001115 M

3.-Results and discussion

Figure 2 shows the voltamperograms the four catalysts synthesized in this work. The CV of Pt depicts the typical characteristics of this metal. The CV of Pt-CeO_2 also shows a Pt-like shape. Meanwhile, the Pt-Ru and Pt-Ru-CeO2 anodes show less defined H_{ads} regions, probably due to the formation of a Pt-Ru alloy phase.

Figure 3 depicts the LSVs of the EGOR at the anodes studied here. The four catalysts demonstrate a degree of catalytic activity for this reaction. However, evaluating the peak current density in the positive going potential scan, it can be observed that the Pt-Ru anode delivers a higher current density (peak maximum of ca. 7 mA/cm^2) compared to the other three catalysts. This material also shows a less intense peak current density peak in the negative-going scan, indicating that smaller amounts of EG and/or intermediates remain at the catalytic surface, i.e., the oxidation of the molecule is more efficient at Pt-Ru. The catalytic activity for the EGOR decreases in the order Pt-Ru>Pt>Pt-CeO_2>Pt-Ru-CeO_2. Currently, we are investigating the catalysts by TEM to clarify their morphological characteristics and make a correlation with the catalytic activity toward the EGOR.

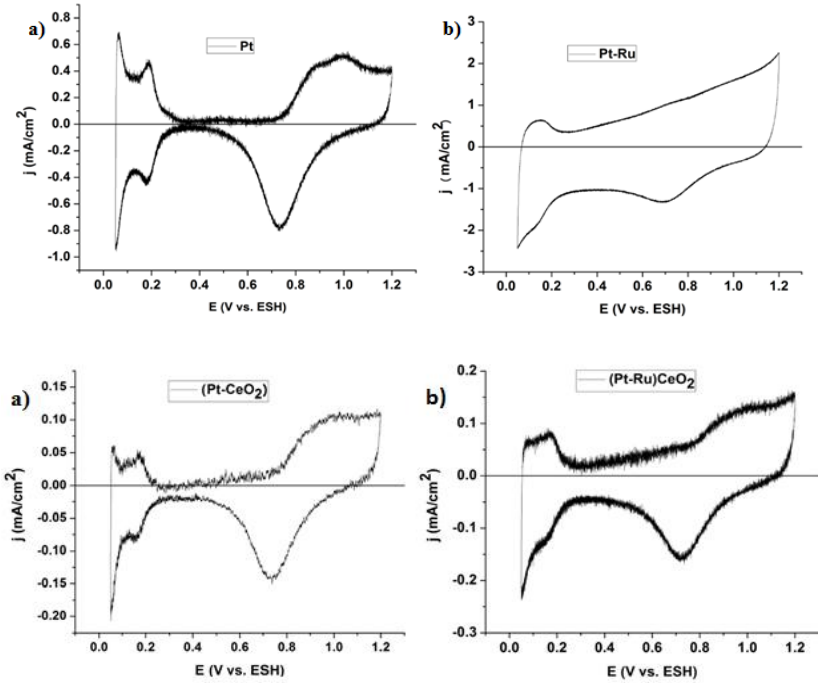

Figure 2.- CVs of Pt, Pt-Ru, Pt-CeO_2 and Pt-Ru-CeO_2. Scan rate 20mV/s.

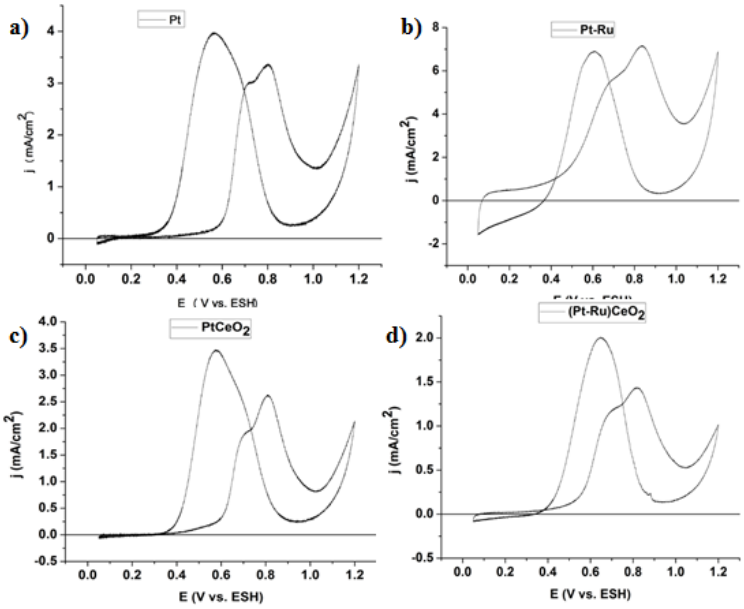

Figure 3. LSVs of the EGOR at Pt, Pt-Ru, Pt-CeO_2 and Pt-Ru-CeO_2. Scan rate 20mV/s.

4.-Conclusions

We synthesized and evaluated nanostructured catalysts for the EGOR. In acid medium, the catalytic activity of the anodes decreases in the order: Pt-Ru>Pt>Pt-CeO_2>Pt-Ru-CeO_2. Currently, we are investigating the catalysts by TEM to clarify their morphological characteristics and make a correlation with the catalytic activity toward the EGOR.

5.-Akcnowledgements

The authors thank the Mexican National Council for Science and Technology (CONACYT) for financial support through grant 79870 and the Programa de Redes Temáticas.

6.-References

[1] A. Troveralli, Catal. Rev. Sci. Eng., 38 (1996) 439.

[2] J. Kašpar, M.Graziani, and P.Fornasiero, "Handbook on the Physics and Chemistry of Rare Earths", K.A. Gschneidner, Jr. and L.Eyring, eds, Elsevier Science B.V., Amsterdam, vol. 29, Ch.184, (2000) pp. 159-267.

[3] G. Ranga Rao, Bull. Mater. Sci. 22 (1999) 89.

[4] G. Ranga Rao, J. Kašpar, S. Meriani, R.D. Monte and M. Graziani, Catal. Lett. 24 (1994) 107.

[5] P. Fornasiero, R. Di Monte, G. Ranga Rao, J. Kašpar, S. Meriani, A. Trovarelli and M. Graziani J. Catal., 151 (1995) 168.

[6] J. Kašpar, P. Fornasiero and N. Hickey, Catal. Today 77 (2003) 419.

[7] G. Ranga Rao, P. Fornasiero, R. Di Monte, J. Kašpar, G. Vlaic, G. Balducci, S. Meriani, G. Gubitosa, A. Cremona and M. Graziani, J. Catal. 162 (1996) 1.

[8] P. Fornasiero, G. Ranga Rao, J. Kašpar, F.L. Erario and M. Graziani, J. Catal. 175 (1998) 269.

[9] W. Liu and M. Flytzani- Stephanopoulos, Chem. Eng. J. 64 (1996) 283.

[10] Y. Li., Q. Fu and M. Flytzani-Stephanopoulos, Appl. Catal. B: Environ. 27 (2000) 179.

[11] A. Trovarelli, C. de Leitenburg, M. Boaro and G. Dolcetti Catal. Today, 50 (1999) 353.

[12] X. Wang and R. J. Gorte, Appl. Catal. A: Gen. 247 (2003) 157.

[13] J. A. Montoya, E. Romero-Pascual, C. Gimon, P. Del Angel and A. Monzón, Catal. Today 63 (2000) 71.

[14] N. Hickey, P. Fornasiero, J. Ka par, M. Graziani, G. Martra, S. Coluccia, S. Biella, L. Prati and M. Rossi, J. Catal. 209 (2002) 271.

[15] Imamura, S., Y. Okumura, T. Nishio, K. Utani and Y. Matsumura, Ind. Eng. Chem. Res. 37 (1998) 1136.

[16] D. Morales-Acosta, L.G. Arriaga, L. Alvarez-Contreras, S. Fraire Luna and F.J. Rodríguez Varela, Electrochemistry Communications, 11, 1414-1417 (2009).

9th International Symposium on New Materials and Nano-Materials for Electrochemical Systems
XII International Congress of the Mexican Hydrogen Society
Merida, Mexico, 2012

Integration of solar-hydrogen technologies for sustainable housing

A. Yunez Cano[1*], G. Contreras Puente[2], M. Tufiño Velázquez[2], D. Jiménez Olarte[2], P. González Arceo[1], R. González Huerta[1]

[1]ESIQIE-IPN, Laboratorio de Electrocatálisis, UPALM, CP 07738 México, D.F.
[2]ESFM-IPN, Departamento de Física, UPALM, CP 07738 México, D.F.

[*]E-mail: enigma_ayc@hotmail.com

Abstract

The continuous and accelerated growth of population has brought an increase in the energy demand for the production of goods and services. This has caused at the same time high cost environmental as well as economic troubles such as global warming and increase in electricity costs. These issues generated international actions to mitigate the consequences due to fossil fuels overexploitation; Mexico participates in these actions so it is promoting projects fostering environment care, such as the proposal described in this work, aimed to develop sustainable systems through the integration of technologies related to renewable energy sources.

In Mexico, greenhouse gas emissions are mainly due to the transport sector and electrical power consumption by industry. Regarding the last sector, electrical power consumption per household is around 33%. Electrical service users are classified according to power consumption as established by the Electricity Federal Commission, CFE. Lamps and fridges are the most used energy consuming households reaching around 50% of total consumption. These devices are commonly used in most houses during the day. TV and DVD's are other appliances used in most Mexican houses, representing a 25% of power consumption.

In this work a sustainable house was designed to be powered by a solar-hydrogen system. The whole project was divided in three stages; the first stage consists in setting up a photovoltaic system; in the second one, the integration of an electrolysis and hydrogen storage system to the solar system will be carried out. The third stage corresponds to the integration of a fuel cell device. We report the installation of a 1 kW PV system consisting of: two 540 W Si solar panels, controller, inverter and a set of batteries to supply power to basic services, such as lamps, fridge, TV, DVD and a laptop. We analyze the performance of the PV system regarding the power supply and consumption to the house.

Keywords: solar-hydrogen system, renewable energies sources, sustainable house.

1. Introduction

Nowadays the growing energy demand for the production of goods and services in the world and the need to produce it in a clean and sustainable way has generated in recent years a strong global interest in developing new technologies and materials. Extensive research to achieve the best approach to generate clean energy has been largely transformed from "scientific competence" to "scientific cooperation" to achieve social and environmental well-being, since the best way to generate sustainable energy is to harness the weather of each region and integrate key systems such as solar photovoltaic and other renewable energy sources such as hydrogen through fuel cells. [1] [2]

In the case of Mexico, the generation of greenhouse gas emissions is mainly due to the transport sector and the electrical power consumption by industry. However, the environment has also been badly damaged by the oil industry in different regions of the country. On the other hand, a factor of great importance in Mexico is the rapid increase in energy prices, being gasoline and electricity tariffs an important key factor to get a virtual stable economy in the country, but in the last 10 years it seems that actual economic instability in energy is jeopardizing national development. Among the principal electric power consumers in Mexico, household users represent 33% of total consumption, being the most used appliances like the refrigerator, TV, DVD player and interior lighting; based on this premise CFE has established a minimum power consumption average standard home in Mexico. [3] [4] [5]

This project is divided in three stages for its development, the first stage consists in installing a photovoltaic system whose power is according to the energy demand required to be covered. In this case a bimonthly energy demand of 150 kW·h was established so it can meet the basic energy needs of a CFE 01 rated house according to its average energy consumption. The second stage involves the integration of an electrolysis hydrogen production and storage system. The third and final stage is the integration of a fuel cell device to the photovoltaic-hydrogen system.

The implementation of renewable energy is currently growing in Mexico at a moderate pace, mainly due to lack of government support and ignorance on the benefits that can be obtained from its application for sustainable housing. On the other hand, some government programs encouraging investment in these technologies begin to appear, such as the INFONAVIT credit program called "Green mortgage" and the recent advantage of establishing a contract with CFE to interconnect these sustainable systems to the federal power grid. As these renewable energy systems supply electric power to the grid, they cause a reduction in the cost of current high electricity tariffs.

2. Experimental

3D Modeling

In order to project and visualize the scope of the sustainable housing system, a useful tool that we will use is the 3D digital modeling, so we worked on a preliminary design to define the necessary space and functionality of the structure, considering the house should support the weight of a 1 kW solar panels photovoltaic array and allow simulating the location of the other components of the photovoltaic system in this first stage.

.

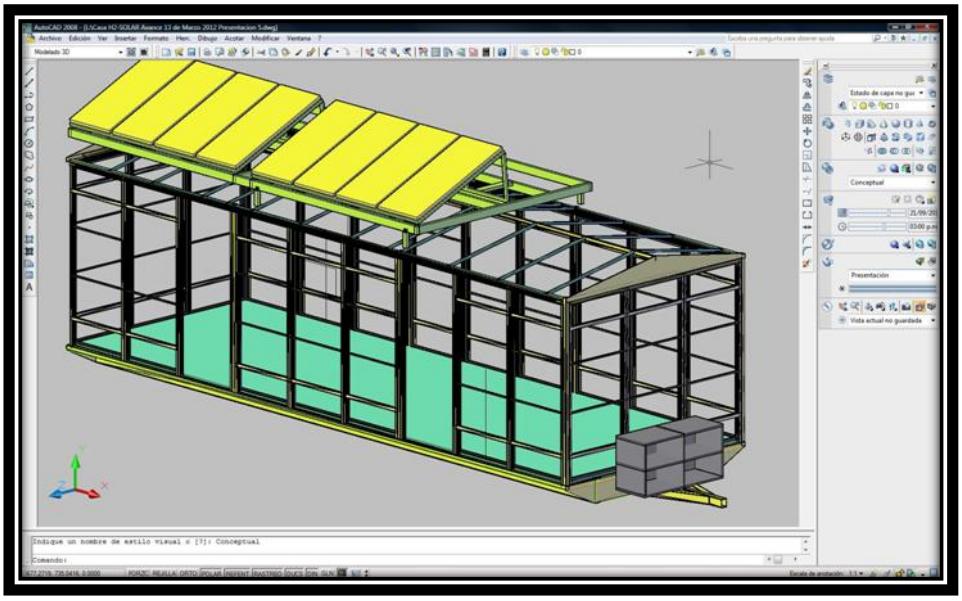

Figure 1. 3D Modeling of the Sustainable Housing

In order to create a functional design for the house, a mobile platform was considered so it could be used with the necessary flexibility, such as translating it to different locations for climate studies in different geographic locations or in didactic exhibitions for educational training. It was also thought that it should have a modular structure for performing subsequent modifications or adaptations and a simple and easy integration of friendly technologies to the environment, such as a solar water heater, rainwater collectors, electrochromatic windows, bioclimatic architecture and solar illumination among other technologies and materials.

The design was made with AutoCad software dimensioning the size of the structure to determine the areas of opportunity in the design. A prototype was developed which helped to define the real dimensions of the final model shown in this paper.

Dimensioning the Phtotovoltaic System

The capacity of the installed photovoltaic system (PVS) was calculated from the electric power demand based on the most commonly appliances used in a Mexican family typical house, establishing a baseline bimonthly consumption average of 150 kW·h. A conventional PV system was installed consisting of polycrystalline Si solar modules, a charge controller, a DC-AC electric inverter and a bank of batteries to obtain a fixed time interval of energy autonomy.

Due to the good average solar irradiance in our country and particularly in Mexico City, we considered 5 hours of effective sunlight per day. This factor shows that Mexico has an important solar potential to successfully implement the photovoltaic technology at homes. Most photovoltaic systems are mainly installed at the present time in public or private companies.

Photovoltaic modules for this stage were acquired of polycrystalline silicon, considering factors such as price, durability and efficiency, since the cost of investment is important for estimating the future savings and recovery cost. On the technical side an automatic charge controller was chosen to prevent that batteries suffer any damage due to overloading or unloading in excess due to the intermittency of solar radiation and the variable consumption of the energy stored in the bank batteries. [6] [7]

The selection of the inverter was considered for operating in isolated systems, such as the bank of batteries, and also to operate in an interconnected system to the grid, with the purpose that the investment may be lower and the return cost takes place in lower time delivering power to the federal electric grid, since in an isolated PVS the use of batteries corresponds approximately to 30% of total investment. The battery bank has the ability to provide 2 days of autonomy to the house, without exceeding the established daily consumption of 2.5 kW·h. The diagram of the PVS is shown in Figure 2.

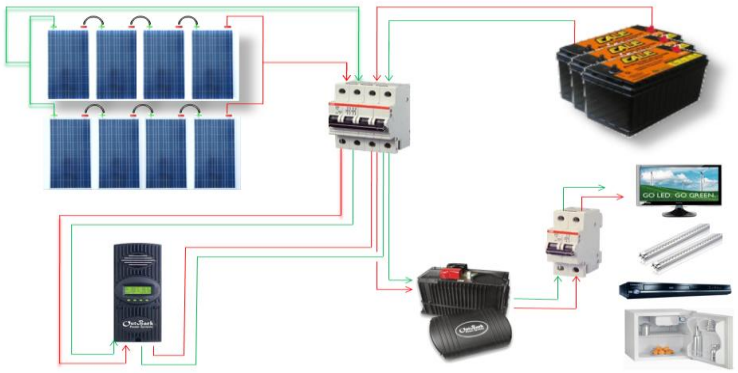

Figure 2. Photovoltaic System Diagram

3. Results and discussion

The photovoltaic system corresponding to the first stage of the sustainable housing project supplies the necessary electric energy making the house to become autonomous in energy for a certain time, covering the electricity demand established within the isolated system due to the use of the household appliances daily in its range of use as indicated above. Figure 3 shows a 3D digital modeling and photograph of the house with the solar panels installed in the roof of the house. On the other hand, the actual technical characteristics for working in the second stage are already established, which consists in the integration of the electrolyzer and hydrogen storage system.

Figure 3. Sustainable house developed at IPN with a 1 kW solar photovoltaic system powering the house. Solar panels installed in the roof are made of polycrystalline Si.

The sustainable housing project is intended to be used as a mobile testing laboratory for studying national and ecological technologies developed to produce clean energy, since it is projected to gradually replace each existing commercial component with devices developed in our labs. The commercial solar panels installed in the house with the technical data obtained to describe its performance for supplying energy to the house will be used as a reference such that we can compare with the performance of the devices we develop in our labs. The Solid State Physics Group of the Physics and Mathematics High Studies School of IPN (ESFM) is currently working on the development of thin film solar panels, with the aim to obtain energy conversion efficiencies values comparable to those of the commercial devices in order to substitute them in the sustainable housing and as a mean to foster a national industry for the production of solar panels.

In addition the School of Chemical Engineering and Extractive Industries of IPN (ESIQIE) in conjunction with the School of Electrical and Mechanical Engineering (ESIME) and the Center for Research and Advanced Studies of IPN (CINVESTAV) are developing prototypes of electrolyzer and PEM (Proton Exchange Membrane) fuel cell devices in order to be integrated and studied in fixed systems.

It is important to point out that other institutions are working on proposals for sustainable housing applications such as the construction of solar monitoring instruments, development of new materials to be used in these technologies, methods to reduce the cost or making affordable the use of PVS, economic impact studies to implement these technologies, and bioclimatic design of structures, among other topics.

4. Conclusions

This multidisciplinary project shows the feasibility of integrating renewable energy technologies based on photovoltaic and hydrogen devices for the development of sustainable housing, which could be located in urban or marginal rural areas. The project was divided in three stages and the first stage has been completed. The benefits of using solar energy has been demonstrated by supplying the necessary electric power to a CFE 01 rated house according to its bimonthly average energy consumption of 150 kW·h, allowing daily at least 5 hours of electric autonomy.

The short-and long term benefits lie in saving up to 100% of electricity consumption in the house, or at least in reducing the power consumption by harnessing a free and inexhaustible energy source as the sun. A direct impact is achieved due to the reduction of electricity consumption tariffs thus benefiting the citizens economy.

On the other hand, another important benefit can be obtained by compensating for the effect caused by the High Consumption Rate (DAC) established by CFE since the last couple of years, which generates electric rate costs greater than 200% of the standard tariff. The DAC applied to a user causes the CFE withdraw of the energy subsidy to the user, when he exceeds the electric energy consumption limit for a period of 12 consecutive months. The consumption limit is determined according to the contracted rate established by the user with CFE.

5. Akcnowledgements

Work supported by SIP-IPN Energy Research Network and ICYTDF.

6. References

[1] Rosa de Guadalupe González Huerta, Ernesto López Chávez, Blanca Velázquez Morales, “Hidrógeno: Introducción a la Energía Limpia”, Universidad Autónoma de la Ciudad de México. Primera Edición (2009).
[2] Libro de Ciencia y Tecnología N° 2 “Tecnologías Solar-Hidrógeno-Pilas de Combustible como fuentes de energía” Primera Edición, Tecnológico de Estudios Superiores de Ecatepec, México (2009) p. 235-266.
[3] Página Web Oficial “Cambio Climático - Fundamentos” Lunes, 09 de Agosto de 2010 19:47
Responsable de la información: Dirección General de Políticas para el Cambio Climático - SEMARNAT

http://www.cambioclimatico.gob.mx/index.php/es/fundamentos.html

[4] Jésica Lorena Escobar Delgadillo y Jesús Salvador Jiménez Rivera, "Crisis económica, crisis energética y libre mercado", Revista Digital Universitaria Vol. 10, No. 5 (Mayo 2009).

http://www.revista.unam.mx/vol.10/num5/art29/int29-2.htm

[5] "Estadísticas destacadas del Sector Energético", Sistema de Información Energética (Septiembre 2011).

[6] Sitio Web Oficial del "Instituto de Investigaciones Eléctricas".

http://www.iie.org.mx/proyectofotovoltaico/preguntas.php

[7] Arturo Morales Acevedo, "La Electricidad que viene del Sol: Una Fuente de Energía Limpia", CINVESTAV-IPN, 1ª Edición, México (2003) Págs. 106-108, 120.

Effects on Nafion® 117 Membrane Using Different Types of Strong Acids in Various Concentrations

L. Napoli[1, 2*], M. J. Lavorante[2, 3*], J. Franco[2], A. Sanguinetti[2], H. Fasoli[2, 3],

[1]Escuela Superior Técnica del Ejército, C1426AAA, Capital Federal, Argentina.
[2]Instituto de Investigaciones Científicas y Técnicas para la Defensa, B1603ALO, Villa Martelli, Provincia de Buenos Aires, Argentina.
[3]Pontificia Universidad Católica Argentina de los Buenos Aires, C1107AAZ, Capital Federal, Argentina.
*Tel: (005411) 4709-8100 int. 1472, lnapoli@citedef.gob.ar
*Tel: (005411) 4709-8100 int. 1472, mjlavorante@gmail.com

ABSTRACT

This work proposes a pre-treatment to Nafion® 117 membrane with different acids in various concentrations. The main goal of this study is to increase the membrane hydration, which is determined by the amount of water molecules it incorporates. It is well known that the membrane hydration directly affects its conductivity. Based on many studies that were published regarding this issue, we developed a treatment testing the acids proposed in the research works in order to find a difference between the acids and the effect of the concentrations. In addition, Perchloric acid was also studied. Our work was developed using five strong acids treatments -Nitric, Sulphuric, Perchloric, Phosphoric and Hydrochloric acid- in six different concentrations: -0.025 M, 0.05 M, 0.25 M, 0.5 M, 0.75 M and 1 M. Analyzing the results after an exhaustive study, the membrane shows a similar behaviour when it is treated with different strong acids, incorporating between 16 to 21 molecules of water depending on the concentration of the acid that was chosen. The effect of the different concentrations is remarkable, which leads to the conclusion that the best treatment is to use solutions 0.025 M and 0.05 M (twenty times more diluted than the most concentrated solution tested in the experience). Another effect to be taken into account when the Membrane Electrode Assembly (MEA) is joined in a following step, is the fact that after membrane hydration its size increases by 10 percent (average).

1. Introduction

Nafion membrane was developed in the 1960s and, nowadays, it is the most well known material of this type, consisting of perfluorinated polymer backbone and branches that end in sulfonic acid groups. Nafion acid groups and sorbed water are surrounded by a hydrophobic matrix of tetrafluoroethylene backbone and perfluorovinyl ether pendant side chains. Water sorption swells the hydrophilic domains providing paths for proton transport and water diffusion through hydrophobic domains [1].

Nafion membranes are widely used for Proton Exchange Membrane (PEM) fuel cells and water electrolyzers. The membrane performs two functions, as separator and as solid electrolyte in a variety of electrochemical cells with the main purpose of transporting cations across the cell junction, selectively. Over the last years the interest in Nafion has grown due to the good performance that it shows as a proton conducting membrane in fuel cells. This result takes the lead and is the first in studying proton conductivity, water management, hydratation stability at high temperatures and thermal stability [2].

Nafion membranes have been extensively characterized with respect to their structure, properties and mechanism of proton conduction. The proton conductivity of this material is strongly dependent on the presence of water and it can reach above 0,1 S cm-1 under fully hydrous conditions [3]. Therefore, it is appropriate to consider the existing relation between the membrane conductivity and the water content in the structure.

A recent study of water content considered the thermodynamic forces that affect the sorption of water in the Nafion membrane. The results showed the existence of a critical pore radius below which water is unstable and a critical length below which a pore cannot be filled. Another relevant result in this study is that in a saturated liquid enviroment much smaller pores are filled with liquid. This result is useful to understand the conditions in which Nafion absorbs much more water, which is in contact with saturated liquid as opposed to saturated vapor [4].

Many research works have explained different treatments to increase the content of water molecules in the structure of the membrane. Based on those publications and previous studies [5], a specific acid treatment was performed in order to activate the membrane and increase the amount of water molecules per sulfonic group.

For a better comprehension of this issue, it is important to study the morphology of the Nafion's structure. Naming four of those who proposed the structure of this membrane, there are Eisenberg [6], Gierke [7], Mauritz [8] and Yeager [9] models.

According to Gierke model, the membrane is a cluster type containing the aqueous ions imbedded in a continuous fluorocarbon phase. The clusters are interconnected by narrow channels which determine the transport properties of the ions and water. In the meantime, Hsu and Gierke had derived a

semiphenomenological expression for the evaluation of the diameters of the ionic clusters which vary with water content, equivalent weight and type of cation. Their theory also predicts that the short channels connecting two neighboring clusters are thermodynamically stable. On the other hand, Yeager's et al., studied and compared diffusion and water sorption of carboxylated and sulfonated perfluorinated membranes. Cation and water diffusion coefficients are very large in both materials. However, in the carboxylate membrane the diffusion coefficients are even larger and the water sorption is smaller compared to the Nation membrane. This is due to the different clustered morphology of these ion exchange membranes. These authors supposed that the intrusions of fluorocarbon is less frequent in the carboxylate membrane, and therefore, the phase separation is more complete compared to Nafion [10].

Perfluorosulfonic polymers are composed with an extremely high hydrophobicity of the perfluorinated backbone and an extremely high hydrophilicity of the sulfonic acid functional groups. In the presence of water, the sulfonic acid functional groups aggregate to form a hydrophilic domain. When this is hydrated, protonic charge layers by dissociation of the acidic functional groups, and proton conductance assisted by water dynamics occur. While the well connected hydrophilic domain is responsible for the transport of protons and water, the hydrophobic domain provides the polymer with the morphological stability and prevents the polymer from dissolving in water [11].

Even though many experiences considered various forces for convection including external pressure gradient, capillary pressure, osmotic pressures and elastic forces associaed with membrane deformation, a recent study was performed to confirm that the hydraulic permeability increases with the temperature due to both decreased water viscosity and increased hydrophilic volumen fraction. The relation between these parameters is established according to the ecuation 1.

$$Q_w = \frac{k_w}{\mu\, t_m} \Delta P \qquad (1)$$

Where Q_w meaning the water flux, k_w is the membrane permeability, μ is the water viscosity, t_m is the membrane thickness and ΔP is the hydraulic pressure difference.

The results of the study cited in the reference [1] showed that the membrane tested with the 1100 equivalent weight had a permeability circa 4 x 10^{-16} cm^2 at 23 °C and the membrane with equivalent weight of 1000 had a permeability about 40% greater than the previous one. Also, another determination led to the result that the water volume fraction changes by almost 10% while the hydraulic permeability increased by 50-80%. According to the authors, this difference suggests there may be structural changes to the hydrophilic domains with increased water sorption beyond simple volume expansion. The convection of water through Nafion can also serve as a probe to its structure. The hydrophilic domanis form a network through which water flows. The water flux depends on the size and density of the hydrophilic channels.

Another published observation is the mass loss when it is dried at room temperature in contact with the ambient air due to the water absorbed per sulfonic acid group which seems to be independent of the membrane thickness [13].

Enviromental conditions are relevant to make a right analysis. At ambient preasure the membrane dehydrates at temperatures above 100 ºC, resulting in a proton conductivity decay. The acid treatments were performed at 90 ºC and ambient preasure at each step.

It has been demostrated that the water content tends to be the same if the membrane is hydrated and it is also proved that the membrane can regain the water molecules in case it was intentionally dried as the example of the pretreatment when the Membrane Electrode Assembly (MEA) is joined.

Knowing the characteristics that the structure and the morphology provide, an exhaustive study was developed treating the proton exchange membrane with several acids in different concentrations evaluating the performance of each acid incorporating water molecules.

2. Experimental

The experience was developed using Nafion® 117, which means that the nominal thickness is 183 microns and the equivalent weight (EW) is 1100 considering that EW is the number of grams of dry Nafion per mole of sulfonic acid groups when the material is in the acid form.

The as-received Nafion® 117 (Du Pont) was cut into rectangular pieces and treated as follows. Firstly, they were weighted and measured considering this as the initial state without any treatment (zero step). Later, the first step was boiled in H_2O_2 3% for 1 hour [12]. Then the membranes were treated with acid for 3 hours. Five acids were tested in six different concentrations. It was brought under Nitric, Sulfuric, Phosphoric, Perchloric and Hydrochloric acid, 0.025 M, 0.05 M, 0.25 M, 0.50 M, 0.75 M and 1 M. Finally, the membranes were treated in destilled water for 3 hours. After each step, the membranes were cooled in destilled water at room temperature for 15 minutes before being weighted and measured.

According to quality statements, the study was performed by duplicate so 12 pieces of membrane were treated with each acid.

One last measurement is made at the end of the experience in order to check that the membrane hydration is mantained in destilled water, we weighted and measured the following day of finishing the treatment.

3. Results and discussion

Membrane treatment with H_2O_2 3% for 1 hour at 90 ºC is highly recommended to eliminate all the organic impurities as it is received. The result is evident when the membrane becomes colorless.

Besides this benefit, an analogous experience was performed treating the membrane with water at 90 ºC for 1 hour in order to compare the influence of H_2O_2 3% in the same conditions. This was the only difference in the procedure mantining the following steps equal for both acid treatments. We found that the initial treatment with H_2O_2 3% instead of water is remarkable in order to gain more molecules of waters during the entire proccess. The results are shown in Figure 1.

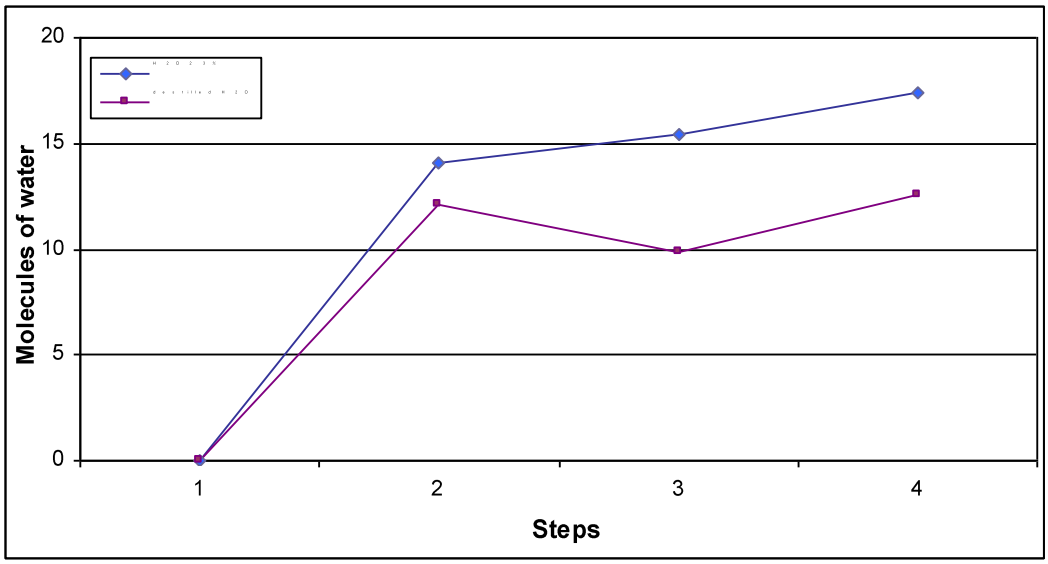

Figure 1. Importance of H_2O_2 3% in the membrane treatment. Treatment steps: 1. Membrane as-received, 2. H_20_2 3% (blue line) and destilled H_20 (purple line) + destilled H_2O 15 min, 3. HNO_3 0,25M (90 ºC for 3 hours) + destilled H_2O 15 min., 4. destilled H_2O (90 ºC for 3 hours) + destilled H_2O 15 min.

Continuing with the investigation, the membranes previously treated with H_2O_2 3% at 90ºC for 1 hour were studied according to the description given before. The results of the acids treatments are shown in the graphics below.

The following tables contain the quantity of water molecules obtained with different concentrations of the proposed acids considering the average (λ_a) value of two samples per acid concentration and the standard deviation (σ) of each measure in porcentual value.

Each table details the quantity of water molecules per sulfonic acid group obtained in the relevant steps of the procedure. These main steps are:

1. Zero
2. H_20_2 3% + destilled H_2O
3. Studied acid in different concentrations + destilled H_2O

4. Boiled H_2O + destilled H_2O

Note: Zero was ommited from the graphics to emphasize the results obtained in the following steps.

Nitric Acid

Table 1. Results obtained in the Nitric Acid treatment with different concentrations.

	HNO_3 0.025 M		HNO_3 0.05 M		HNO_3 0.25 M		HNO_3 0.5 M		HNO_3 0.75 M		HNO_3 1 M	
Steps	λ_a	σ	λ_a	σ	λ_a	σ	λ_a	Σ	λ_a	σ	λ_a	σ
1	0,000	0,00	0,000	0,00	0,000	0,00	0,000	0,00	0,000	0,00	0,000	0,00
2	17,108	0,86	14,708	0,15	14,048	1,74	15,300	0,47	15,683	0,35	15,653	0,40
3	18,613	0,57	18,220	0,57	17,238	0,93	15,489	0,45	16,401	0,46	15,984	0,11
4	16,972	0,21	18,566	0,24	18,080	2,06	17,748	0,01	19,806	0,39	19,131	0,11

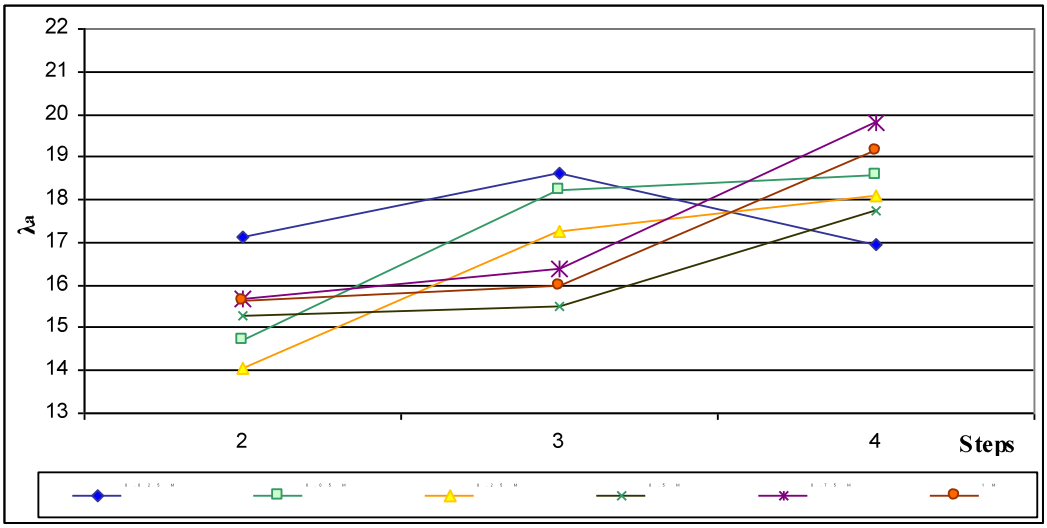

Figure 2. Treatment with HNO_3.

Between the six Nitric Acid concentrations tested during the first study, no significant difference was observed, even though a subtle increment of the water molecules can be noticed in the treatments with lower concentrations.

Sulfuric Acid

Table 2. Results obtained in the Sulfuric Acid treatment with different concentrations.

	H_2SO_4 0.025 M		H_2SO_4 0.05 M		H_2SO_4 0.25 M		H_2SO_4 0.5 M		H_2SO_4 0.75 M		H_2SO_4 1 M	
Steps	λ_a	σ	λ_a	σ	λ_a	σ	λ_a	σ	λ_a	σ	λ_a	σ
1	0,000	0,00	0,000	0,00	0,000	0,00	0,000	0,00	0,000	0,00	0,000	0,00
2	16,768	0,80	15,960	0,89	16,716	0,23	15,157	0,36	16,635	0,23	15,426	0,57
3	18,666	0,75	19,084	0,41	16,933	1,53	15,045	0,51	16,189	0,16	15,251	0,28
4	19,437	0,34	19,784	1,19	18,376	0,29	18,127	0,78	20,499	0,09	18,516	0,04

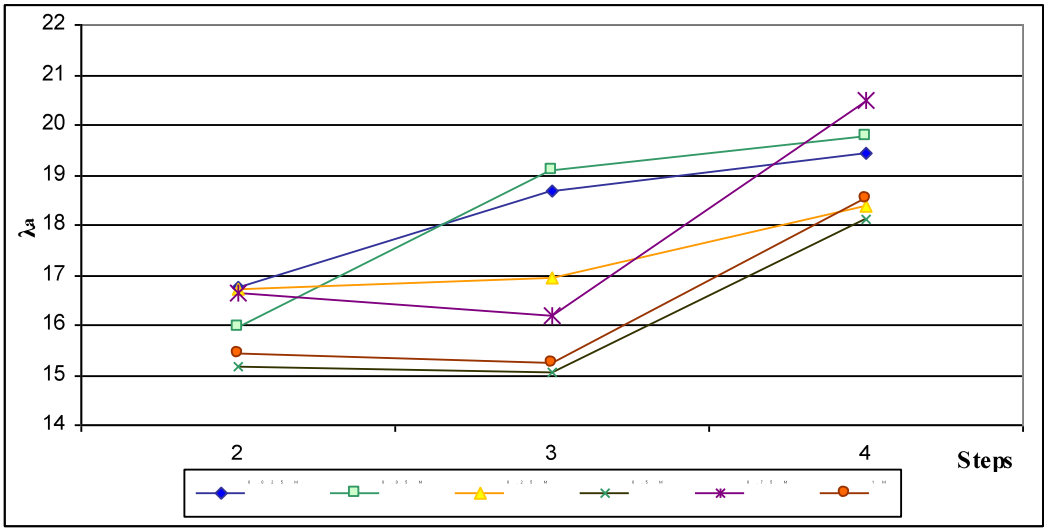

Figure 3. Treatment with H_2SO_4.

The results are similar to Nitric Acid treatment but what is remarkable is the fact that the membrane does not lose any molecules of water in step 3 when it is treated with Sulfuric Acid 0.025 M and 0.05 M.

Phosphoric Acid

Table 3. Results obtained in the Phosphoric Acid treatment with different concentrations.

	H_3PO_4 0.025 M		H_3PO_4 0.05 M		H_3PO_4 0.25 M		H_3PO_4 0.5 M		H_3PO_4 0.75 M		H_3PO_4 1 M	
Steps	λ_a	σ	λ_a	σ	λ_a	σ	λ_a	σ	λ_a	σ	λ_a	σ
1	0,000	0,00	0,000	0,00	0,000	0,00	0,000	0,00	0,000	0,00	0,000	0,00
2	15,870	0,34	17,121	0,48	18,231	0,80	15,876	0,37	16,781	0,66	17,001	0,37
3	17,415	0,49	19,469	0,63	20,564	0,11	18,635	0,46	19,508	0,39	19,951	0,04
4	19,248	0,18	19,966	0,72	21,170	0,06	20,739	0,17	20,198	0,09	21,006	0,14

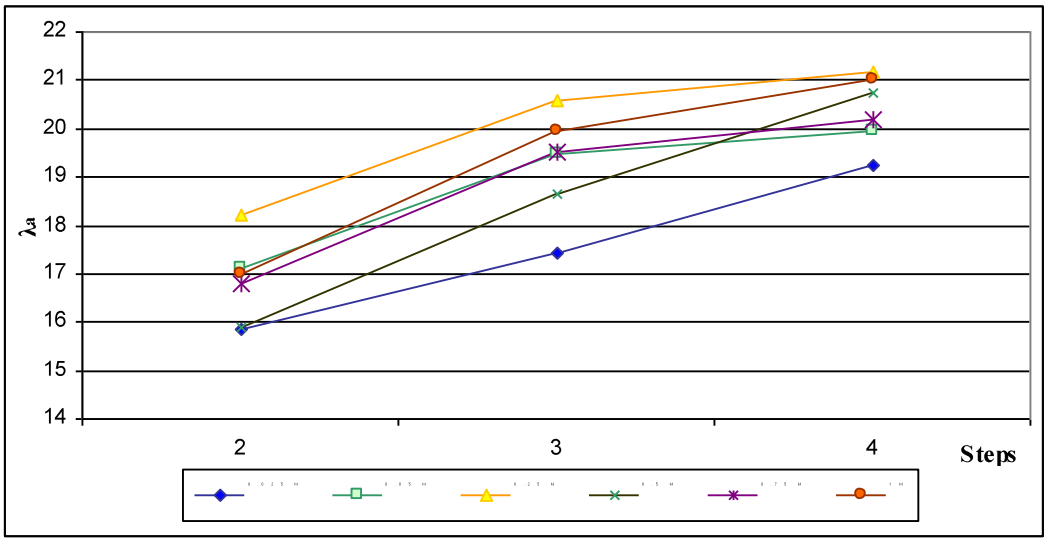

Figure 4. Treatment with H_3PO_4

Even though no result is remarkable comparing with the other acids treated up to now, a subtle improvement can be seen when the membrane is treated with Phosphoric Acid, λ_a is around 21 water molecules per sulfonic acid group.

Another observation to take into account is the fact that the membrane maintains the same tendency when treated with the six different concentrations and it does not lose any water molecules in step 3.

Perchloric Acid

Table 4. Results obtained in the Perchloric Acid treatment with different concentrations.

	$HClO_4$ 0.025 M		$HClO_4$ 0.05 M		$HClO_4$ 0.25 M		$HClO_4$ 0.5 M		$HClO_4$ 0.75 M		$HClO_4$ 1 M	
Steps	λ_a	σ	λ_a	σ	λ_a	σ	λ_a	σ	λ_a	σ	λ_a	σ
1	0,000	0,00	0,000	0,00	0,000	0,00	0,000	0,00	0,000	0,00	0,000	0,00
2	17,068	0,63	18,187	0,11	17,505	0,19	18,694	0,11	16,842	0,25	17,822	0,24
3	18,603	0,70	18,670	0,12	17,536	0,64	17,311	0,02	15,983	0,31	16,000	0,06
4	19,745	0,91	20,116	0,09	20,363	0,14	18,791	1,30	21,197	0,31	20,769	0,25

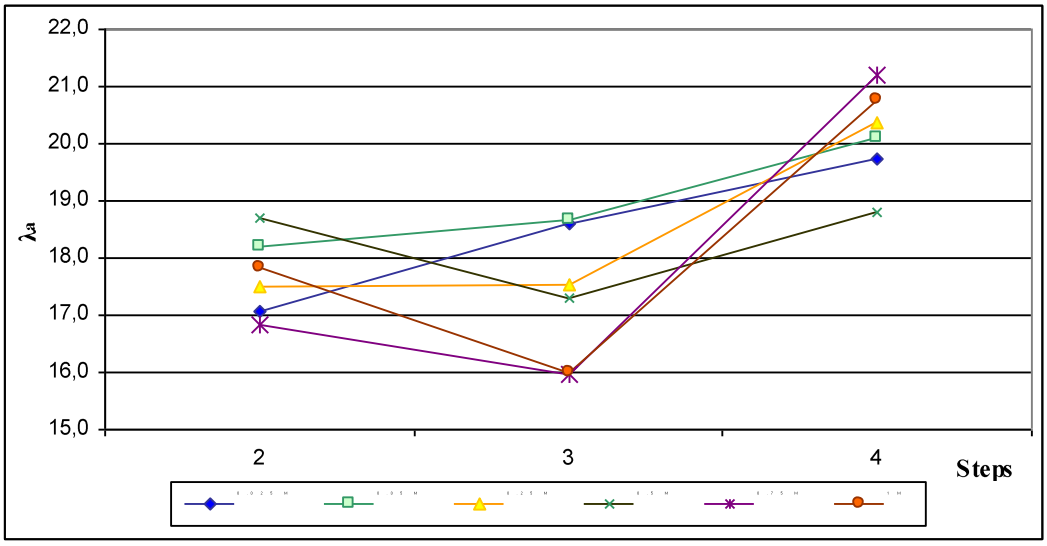

Figure 5. Treatment with $HClO_4$

Figure 5 shows the same tendecy observed with the Sulfuric Acid treatment where the membrane does not lose any water molecules when treated with Perchloric Acid 0.025 M and 0.05M.

Hydrochloric Acid

Table 5. Results obtained in the Hydrochloric Acid treatment with different concentrations.

	HCl 0.025 M		HCl 0.05 M		HCl 0.25 M		HCl 0.5 M		HCl 0.75 M		HCl 1 M	
Steps	λ_a	σ	λ_a	σ	λ_a	σ	λ_a	σ	λ_a	σ	λ_a	σ
1	0,000	0,00	0,000	0,00	0,000	0,00	0,000	0,00	0,000	0,00	0,000	0,00
2	16,842	0,01	16,186	0,59	16,088	0,13	18,556	0,48	18,523	0,24	17,692	0,15
3	19,409	0,13	19,972	0,81	17,562	0,69	17,849	0,17	17,403	0,04	17,056	0,02
4	21,168	0,07	19,949	0,48	19,911	0,33	20,756	0,31	21,185	0,04	21,890	0,13

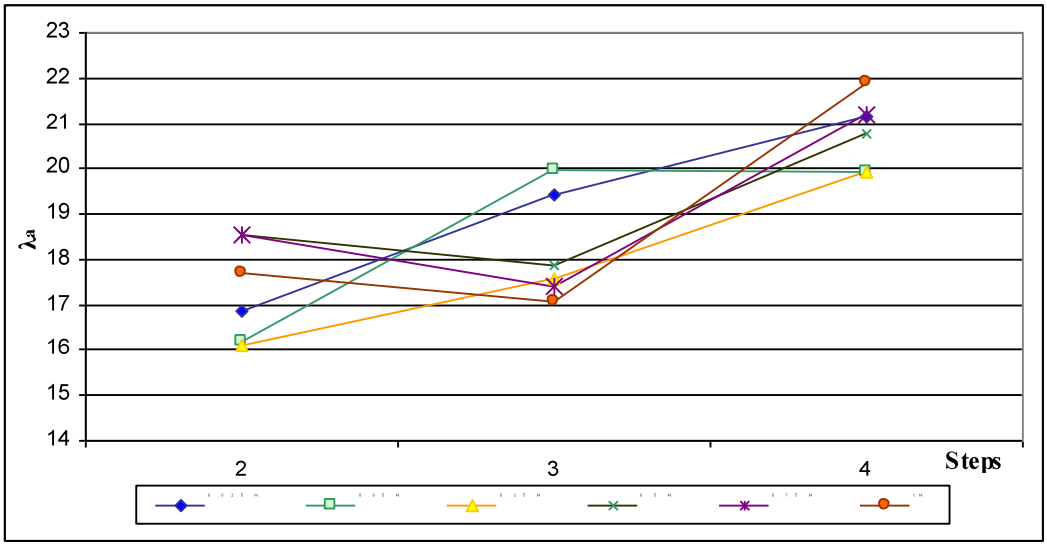

Figure 6. Treatment with HCl

The performance with Hydrochloric Acid is similar to the other acids so no difference between the strong acids tested in this study can be observed. Even though the results of the six different concentrations are similar, what is remarkable is the hydration stability when the membrane is treated with diluted solutions that does not lose water molecules due to the acid treatment at 90 ºC for 3 hours.

Size Analisys

The membrane hydration is visually noticeable because of the increment of its size in a vertical and horizontal way.

During the study, the increment of the size was measured and the results reflect that after membrane hydration its size increases by 10 percent (average). This effect must be taken into account when the Membrane Electrode Assemby (MEA) is joined.

4. Conclusions

The sulfonic acid group has an affinity for water and in contact with it, the sulfonic group dissociates facilitating the proton conductivity. On the other hand, the hydrophobic backbone opposes the increasing water content so an equilibrium state of water content is reached.

The membrane shows a similar behaviour when it is treated with different strong acids, incorporating between 16 to 21 molecules of water when it reaches equilibrium, depending on the concentration of the acid that was chosen and the stability of the temperature during the analysis. The effect of the different concentrations is remarkable regarding the hydration stability, which leads to the conclusion that the best treatments were performed with solutions 0.025 M and 0.05 M (twenty times more diluted than the most concentrated solution tested in the experience). This is shown in figures 7 and 8.

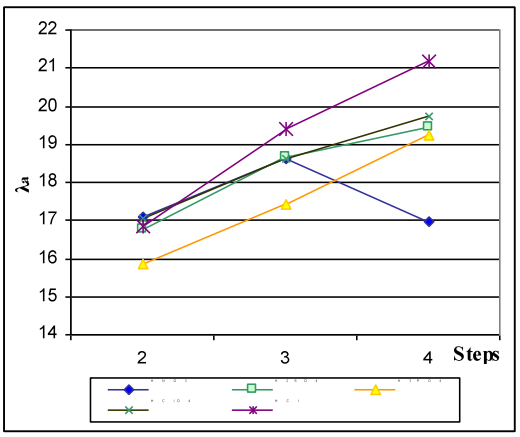

Figure 7. Comparing different acids 0.025 M

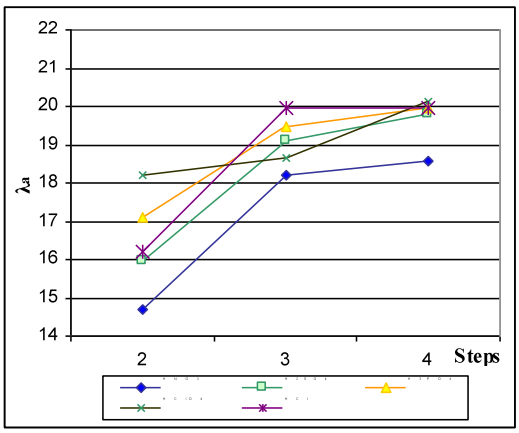

Figure 8. Comparing different acids 0.05 M

The intermolecular forces of the hydrophobic domains are affected in the same way by the different strongs acids studied in this experience. Therefore, it is allowed only to incorporate a certain amount of water molecules per sulfonic acid group and that result has a direct influence on the proton transport and water diffusion.

The effect that the hydraulic permeation increases with increasing temperature was proved.

One effect to be taken into account when the Membrane Electrode Assembly (MEA) is joined in a following step, it is the increasing size by 10 percent (average) when the membrane is hydrated.

An observation that required more study is the hydration stability when the membrane is treated with Perchloric Acid.

5. Akcnowledgements

María José Lavorante, co-author to this work, thanks YPF Foundation for granting her PhD scholaship.

6. References

[1] Q. Duan, H. Wang, J. Benziger, Transport of liquid water through Nafion Membranes. College of Material Science and Engineering, State Key Laboratory for Modification of Chemical Fibers and Polymer Materials, Donghua University, Shanghai, China and Chemical and Biological Engineering, Princeton University, Princeton, USA. Journal of Membrane Science, 2011.

[2] K. A. Mauritz and R. B. Moore. State of Understanding of Nafion. Chem. Rev. 2004, 104, 4535-4585. Department of Polymer Science, The University of Southern Mississippi, Hattiesburg, Mississippi.

[3] D. Aili, M. K. Hansen, C. Pan, Q. Li, E. Christensen, J. O. Jense, N. J. Bjerrum. Phosphoric acid doped membranes based on Nafion, PBI and their blends – Membrande preparation, characterization and steam electrolysis testing. Department of Chemistry, Kemitorvet 207, Technical University of Demark. International Journal of Hydrogen Energy 36 (2011).

[4] G. J. Elfring, H. Struchtrup. Thermodynamic considerations on the stability of water in Nafion. Institute for Integrated Energy Systems, Department of Mechanical Engineering, University of Victoria, PO Box 3055, STN CSC, Victoria, Canada. Journal of Membrane Science, 2007.

[5] M. J. Lavorante, B. Scalise, C. López, A. Sanguinetti, J. Franco, H. Fasoli. Study of the Nafion 117 hydration using different concentrarions of Sulfuric Acid, Escuela Superior Técnica del Ejército, General Manuel N. Savio, Pontificia Universidad Católica Argentina, Centro de Investigaciones Ciéntificas y Técnicas para la Defensa, HYFUSEN, Argentina, 2009.

[6] P. Choi, "Investigation of Thermodynamic and Transport Properties of Proton Exchange Membranes in Fuel Cell Applications" Worcester Polytechnic Institute, April 2004.

[7] L. Gierke, 152nd Meeting of the Electrochemical Society Extended Abstracts Atlanta, GA, Abstract Nº 438, 1977.

[8] K. Mauritz, C. Hora, A. Hopfinger, "Polym. Prep. Am. Chem. Soc. Div. Polym. Chem." 19, 1978, 324.

[9] H. Yeager, A. Steck, Journal Electrochem. Soc., 128, 1981, 1880-1884.

[10] C. Heitner-Wirguin, Recent advances in perfluorinated ionomer membranes: structure, properties and applications, Department of lnorganic and Analytical Chemistry ,The Hebrew University of Jerusalem. Jerusalem 91904, Israel, Journal Membrane Science 1996.

[11] K. D. Kreuer, On the development of proton conducting polymer membranes for hydrogen and methanol fuel cells. Max-Planck-Institut für Festkórperforschung, Heisenbergstr 1, D-70569 Stuttgart, Germany. Journal of Membrane Science 185 (2001) 29-39.

[12] M. Cappadonia, J. Wilhelm Erning, S. M. Seberi Niaki, U. Stimming, Conductance of Nafion 117 membranes as a function of temperature and water content, Institute of Energy Process Engineering (IEV), Research Centre Jülich (KFA), D-52425 Jülich, Germany. Solid State Ionics, 1995.

[13] P. W. Majsztrik, M. Barclay Satterfield, A. B. Bocarsly, J. B. Benziger, Water sorption, desorption and transport in Nafion membranes. Department of Chemical Engineering, Princeton University, Princeton, United States. Journal of Membrane Science, 2007.

Decentralized Energy Planning Using Multicriteria Methods

Juan Rojas Zerpa[1], José Yusta Loyo [2], Alberto Coronado Mendoza [3]

[1] PhD. Program: "Energy Efficiency and Renewable Energy" Campus Rio Ebro, Universidad de Zaragoza. María de Luna 3, 50018, Zaragoza, Spain.
[2] Professor Universidad de Zaragoza, Departamento de Ingeniería Eléctrica, Zaragoza, Spain.
[3] Professor Universidad Tecnológica de Nayarit, División Electromecánica Industrial, Tepic, Nayarit, México.

[1] Phone (0034) 675719954, juancarlosrojas4@yahoo.com
[2] Phone (0034) 976761922, jmyusta@unizar.es
[3] Phone (0052) 3112119800, alberto.coronado@utnay.edu.mx

ABSTRACT

Traditionally, the planning of rural electrification in the developing countries has taken into account technical and economic criteria. So far, the environmental and social aspects have been considered very little. Consequently, a coherent and appropriate power supply planning is required to facilitate the access to electricity. Multi-criteria Decision Making (MCDM) approaches emerge as well suited options for such purposes. This work applies Analytical Hierarchy Process (AHP) and a comprehensive VIKOR method for evaluate the best compromise solution that satisfies the electricity requirements from a rural-remote population located in the Venezuelan Andean region (35 houses, one school and a medical dispensary). The work considers 19 alternatives for electricity supply; the first nine alternatives are associated with Dispersed Decentralized Generation (DDG); other nine relates to Compact Decentralized Generation (CDG); and the latter alternative (in the comparative form) considers the network extension or Centralized Generation (CG). The criteria and sub-criteria weighting has been assigned through expert group assessment. The results indicate that DDG represents the best model for electricity supply, consisting on the combination of an integrated hybrid system with solar photovoltaic (SPV), small hydropower (SHP) and sustainable hydrogen fuel cell (FC).

Key words: Decentralized energy planning; Decentralized generation and multicriteria decision making; Power supply planning in rural and remote areas.

1. INTRODUCTION

Currently, 1600 million people worldwide have no access to electricity, of which 80% live in rural areas. The world's population and electricity demand will grow. If rural electrification does not increase, the number of people without access to electricity will remain almost unchanged [1]. According to the International Energy Agency (IEA) [2] in the last 15 years, the number of people without electricity has been reduced from 2000 million in 1990 to 1600 million in 2005, with China registering the fastest progress. Excluding China, the number of people without electricity has increased steadily over the last 15 years. Due to the constant growth of population, if the countries do not put in practical on new policies, it will continue existing 1400 million persons without access to the electricity in 2030.

The electrification of rural areas has gone through various stages or moments. Different factors, including political, economic, social and environmental concerns have influenced the shape, type, method and model to promote or facilitate the power supply.

The first formal development of energizing rural areas was realized using the model of urban areas [3]. Indeed, the extension of distribution networks has remained as the dominant model bring up electricity to rural and remote areas. Both technical and economic criteria [4] [5] have been the dominant features in growth of power systems to rural areas-and therefore, enables a considerable number of villages to benefit from the availability of energy. In contrast, centralized distribution in rural and remotes areas have shown some drawbacks as the partial or total blackout, the cost of energy, network's maintenance lack, social and environmental impacts, high costs of investment in new facilities, non-availability of enough financial resources and competition with new power technologies such as *distributed generation* (DG) [3] [6] [7].

The emergence of DG has brought a new vision of on-site generating power for applications as an affordable, secure and the minimal impact both social and environmentally (regarding the extension of distribution networks); such aspects should be taken into account in the planning of future power supply systems from rural and remote areas.

In general, the process of rural energy decision-making has neglected certain factors influencing rural electrification [8] (for example, considering of the population needs). Hence, there are important consideration on identifying a consistent and comprehensive energy planning in order to improve access to electricity taking into account the populations needs and the local environmental conditions. For this reason, this paper proposes a method of multicriterio decision that uses the combination of two techniques: Analytic Hierarchical Process (AHP) and VIKOR.

2. MULTICRITERIA METHODS FOR DECENTRALIZED ENERGY PLANNING

Most of problems are complex fundamentally due to the unknown aspects related to decision making process, as it is the consideration of vagueness and uncertainty. Although occasionally it is possible to solve them based on

experience or intuition, it has been proven several times to complex problems can lead to misguided solutions. For this reason, it is convenient to use models and methods to achieve a better quality decisions.

Rojas et al. [10] determined some considerations based in single criterion decision models, one-dimensional optimization using linear programming with applications to electricity supply in rural and remotes areas. The consideration of few criteria in the modeling of energy supply problems makes the context of planning unrealistic and very simplified. In contrast, energy planning problems are complex, and generally, require multiple decision-makers, criteria and restriction, which requires the use of more complete and robust methods. In this context, and given that the energy supply planning represent a multidimensional problem, its mathematical expression is of nature multicriterion-multiobjective or vice versa. Therefore, the multicriteria decision making (MCDM) emerge as well suited options for such purposes.

On the other hand, Alanne and Saari [7] explained that the choice of a distributed generation system from renewable sources is a good choice with regard to sustainable development throughout its life cycle. However, there are some implications of generation distributed in some aspects of sustainability. There on, Karger and Hennings [11] suggest the need for multicriteria methods for distributed generation decision making. Likewise, Pohekar and Ramachandran [12] consider that the Multicriteria methods are gaining popularity in sustainable energy management, since these techniques provide solutions to the problems involving multiple objectives; that may be conflicting or contradictory among them. Alarcon et al. [4] also explain that multicriteria methods are appropriate to solve multidimensional problems. In addition, Loken [13] proposes that the MCDM are suitable in situations of multiple decision-makers.

Based on these reviews, the MCDM methods are suitable for the treatment of problems that require the selection of a power supply systems under the sustainability consideration.

3. PROPOSED METHOD: AN INTEGRATION OF AHP – VIKOR

The decision-making problem intended to solve is: *given the need of electrical power in rural and remote areas of developing countries, a finite set of alternatives (discreet) associated with three modalities of power supply are presented, where several makers (multi-expert) must participate in the selection of the best alternative, taking into account different criteria or points of view in conflict (Multicriteria).*

Currently, there is a wide range of discrete multicriteria methods. Such diversity is the result of the incredible practical interest which these methods provide.

In reference to value measurement methods, the hierarchical analytical process (AHP), is one of the most popular MCDM methods. The ease to deal with complex problems, simplicity, transparency and a wide field of application has contributed to its widespread popularity.

Preference level methods are associated to certain features that favor its implementation such as their relative ease of management, flexibility, transparency and interactivity with decision makers, broad application and the speed to get a result. Of these methods, VIKOR, one of the most recent, in addition incorporates a concept of stability in the compromise solutions classification, which helps to improve the decisions quality.

3.1 Analytical Hierarchical Process (AHP)

The hierarchical analytical process was proposed by Thomas L. Saaty (1980, 1994, 1996 y 2000). AHP is a powerful tool that can be used to decompose a complex problem in a hierarchical model [14]. The purpose of the method is to allow that the decision-maker can structure a multicriteria problem in visual form, through the construction of a hierarchical model which basically contains three levels: goal or objective, criteria and alternatives [15]. Once built the hierarchical model, policy-makers carry out comparisons of pairs between these elements (criteria - sub-criteria and alternatives) and numeric values are attributed to the preferences expressed by them, delivering a synthesis through the aggregation of these partial judgments. This comparison is carried out using the Saaty scale, which is shown in table 1.

AHP enables decision making group by adding opinions, then take the geometric or arithmetic average of the opinions.

Table 1. Saaty scale

Value	Definition	Comment
1	Equally important	The criterion A is of equal importance that B
3	Moderate importance	The experience and the judgment favors slightly criterion A over B
5	High importance	The experience and the judgment are strongly favorable from criterion A over B
7	Very high importance	The criterion A is much more important than B
9	Extreme importance	The importance of the criterion A over B is indisputable
2,4,6,8	Intermediate values	

According to Saaty [16], once the corresponding trials in the matrix of comparisons have been introduced, the problem is reduced to the calculation of eigenvalues and eigenvectors, which represent the priorities and the consistency index of the process, respectively. Therefore, A is consistent if and only if the equation (1) is satisfied:

$$A * w = \lambda * w, \quad (1)$$

Where A represents the reciprocal matrix of paired comparisons (importance assessment of one criterion over another); λ, maximum eigenvalue of A; w, eigenvector of λ.

As a result, AHP calculates the consistency reason (CR), which is given by the equation 2.

$$CR = CI/RI, \quad (2)$$

Where CI is the consistency index of A; RI is the random consistency index (this value is taken from the table 2).

The consistency index is determined by the equation 3.

$$CI = (\lambda_{max} - n) / (n-1), \quad (3)$$

Where n corresponds to the number of items that are compared (criteria)

Table 2. Random consistency index

(n)	1	2	3	4	5	6	7	8	9	10	11	12	13	14
(RI)	0.00	0.00	0.58	0.90	1.12	1.24	1.32	1.41	1.45	1.49	1.51	1.54	1.56	1.57

A value less than 0.10 RC is considered to be acceptable; otherwise, it must ask the decision-maker to make their ratings again.

With regard to the applications of AHP, Herrar [17] presented a list of references which highlights the following areas: process of manufacturing, machinery selection, selection of technology parks, supply chain, selection and evaluation of suppliers, university management, assessment of companies, assessment of projects, food, etc. Other applications of AHP: management of water resources [18], allocation of resources [19], technologies selection for energy generation [13], energy planning from the transport sector [20], multicriteria renewable energy planning using an integrated fuzzy VIKOR and AHP methodology [21], etc.

The purpose of AHP in this research is related with the preference estimation of the different variables considered in the hierarchical structure levels of the decision tree, with the aim of obtaining absolute preferences of the criteria. Therefore, an expert group, with conflicting interests, have been consulted to facilitate the selection of the system power supply from a small town (village) located in a rural-remote area of the Venezuelan Andes. The expert groups have been subdivided in four categories: Academics (university professors, researchers, etc.); Companies and consulting agencies; Regulators or operators and Non-governmental organizations (integrated by environmental organizations and community organizations belonging to the village such as irrigation committee and the health-environment committee).

Once forming expert groups, individual preferences in a single collective valuation estimate is required. Therefore, in this work, the collective preference aggregation has been using the arithmetic mean weighted taking into account the interactive participation of all stakeholders.

3.2 Multicriteria optimization and compromise solution (VIKOR)

Opricovic [22] and Tzeng Opricovic [23] developed the VIKOR method for multicriteria optimization of complex systems, by determining a ranking of compromise solutions, the compromise solution and the weighting of stability interval [23]. VIKOR was proposed as a MCDM method to solve problems of discrete type [24] with conflicting and non-quantifiable criteria [23]. The multicriteria ranking index achieved is based on the particular measure of proximity to ideal solution [22]. Assuming that each alternative is evaluated according to each criterion function, the compromise ranking can be then performed by comparison of proximity measure to the ideal solution [23]. The multicriteria measure for compromise ranking is developed from the Lp-metric used as an aggregation function in compromise programming method (Yu [25] and Zeleny [26]):

$$Lp,\ j = \left\{ \sum_{i=1}^{n} [wi.(fi* - fij)/(fi* - fi^{-})]^{p} \right\}^{1/p}, \qquad (4)$$

$$1 \le p \le \infty;\ j = 1, 2, \ldots, J$$

Where $fi* = \max fij$ y $fi^{-} = \min fij$ if the ith function represents a benefit criterion.

The compromise solution would be accepted by decision makers since it provides the maximum group utility (represented by the minimum value of S) and a minimum individual regret of the opponents (represented by the minimum value of R).

VIKOR has been widely applied in the treatment of MCDM problems from various fields such as sustainable reconstruction after the earthquake [27], environmental policy associated with the quality of the air [28] and in comparison with other methods as Data Envelopment Analysis (DEA) [24]. More recently, VIKOR has been applied to design of experiments [29], water resources planning [30], selection of a web service [31], selection of raw materials distributor under a fuzzy environment [32] and in the selection of renewable energy project from Spanish energy system [33]. In this last application, VIKOR has been combined with AHP method, as in reference [21].

One of the limitations of VIKOR in its classical version is associated with numerical difficulties that have been detected in the final ranking of compromise solution. In this regard, Chang [34] has development the modified VIKOR for avoiding or rectifying these numerical difficulties. More recently, Jahan et al. [35] adapted the modified method using a new technique of standardization and it is also known as *comprehensive VIKOR. The main advantage of the comprehensive proposal over traditional VIKOR is that it covers all objectives in MCDM.* In addition, *the proposed model exceeds the critical problem of classical VIKOR* that was demonstrated by Huang et al. [36].

The steps required to implement the comprehensive VIKOR method is presented in figure 1.

3.2.1 Normalization of the input data

The standards proposed by Jahan et al. [35] must be made through the equation 5 and 6.

$$Aij = |(rij - Tj)| \text{ x } (-Aj)^{-1}, \quad (5)$$

$$Aj = rj\max - rj\min, \quad (6)$$

Where Aij represents the normalized value of the alternative i on criterion j; rij (i = 0 1, 2, 3,..., m and j = 1, 2, 3,..., n) correspond to the elements of the decision matrix (alternative i respect the criterion j); Tj represents the ideal value or target value of rij for all criterion j (T1, T2, T3, …., Tj, …., Tn); Aj is the difference between the minimum and maximum value of the criterion j; $rj\max$ is the maximum value on the criterion j; and $rj\min$, the minimum element in the criterion j.

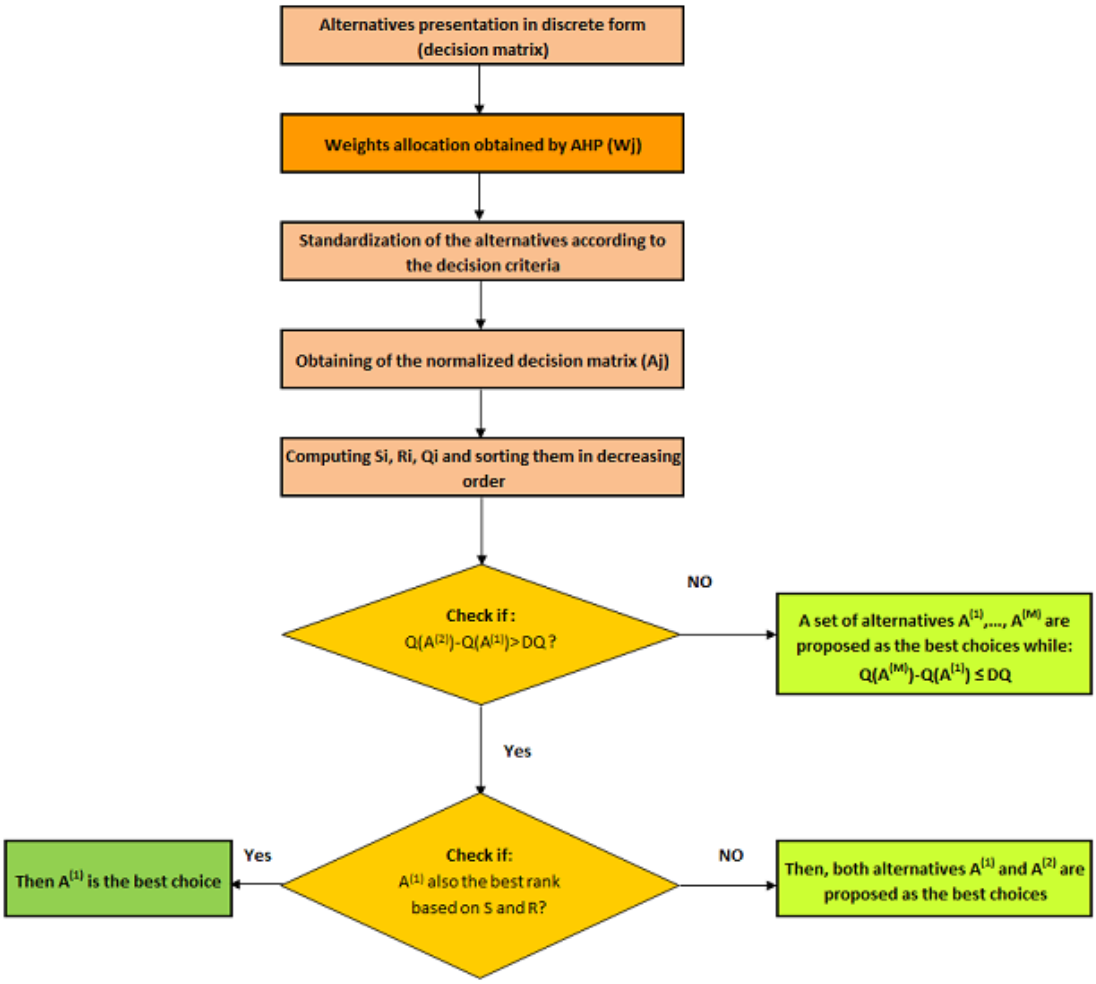

Figure 1. Flowchart of VIKOR comprehensive; adapted of Jahan et al. [35]

3.2.2 Calculation of Si, Ri and Qi

Jahan et al. [35] the values of Si, Ri can be calculated using equations 7 and 8; Qi, depending on the condition, can be calculated using the equation 9, 10 and 11:

$$Si = \sum_{i=1}^{n} wj \text{ x } (1\text{-}e^{\text{-Aij}}), \quad (7)$$

$$Ri = \max_{j} [wj \text{ x } (1\text{-}e^{\text{-Aij}})], \quad (8)$$

If $S^+ = S^-$ then:

$$Qi = (Ri - R^-)/(R^+ - R^-), \quad (9)$$

If $R^+ = R^-$ then:

$$Qi = (Si - S^-)/(S^+ - S^-), \quad (10)$$

Otherwise:

$$Qi = [(Si - S^-)/(S^+ - S^-)]v + [(Ri - R^-)/(R^+ - R^-)](1 + v), \quad (11)$$

Where Si represents the utility measure; Ri is the regret measure; Qi is the VIKOR value; $S^- = \text{Min } Si$; $S^- = \text{Max } Si$; $R^- = \text{Min } Ri$; $R^+ = \text{Max } Ri$; and υ represents the weight of the strategy associated with the maximum group utility, 1 - υ is the weight of the individual regret. The value of υ lies in the range between 0 and 1. A value of υ = 0.5 implies a consensus between both strategies. The results of Si, Ri and Qi are three ranking lists sorted in a decreasing way.

3.2.3 Verification of compromise ranking stability

The verification establishes a compromise solution for the alternative $A^{(1)}$ which is the best ranked by the measure Qi (minimum) if the following two conditions are satisfied:

C1. Acceptable advantage:

$$Q(A^{(2)}) - Q(A^{(1)}) \geq DQ, \quad (12)$$

$$DQ = 1 / (M-1), \quad (13)$$

Where $A^{(2)}$ is the alternative with second place in the ranking list given by Q; M is the alternatives number.

C2. Acceptable stability in the decision making:

The alternative $A^{(1)}$ should be the best ranked by S and/or R. Otherwise, a set of compromise solutions should be proposed if one of the conditions is not satisfied.

- Alternative $A^{(1)}$ and $A^{(2)}$ if only the C2 is not satisfied, or

- Alternatives $A^{(1)}$, $A^{(2)}$,..., $A^{(M)}$ if the C1 is not satisfied; where $A^{(M)}$ is determined by the following relation.

$$Q(A^{(M)}) - Q(A^{(1)}) \leq DQ, \quad (15)$$

3.3 Criteria for alternatives assessment

This assessment is developed on a decision tree scheme. As it is shown in figure 2, different criteria such as technical, economic, environmental and social features are proposed in order to the global goal associated with the selection of the best energy supply system to the study case in a Venezuelan rural-remote village. In the third level of hierarchy thirteen sub-criteria have been proposed. From a technical point of view, it contains sub-criteria as efficiency, non-served energy, long term supply security and reliability. Economic criteria also consist on net present cost and variable cost of operation and maintenance. Environmental criteria include the evaluation of CO_2 emissions, SO_2 emissions, NO_x emissions and the land use. Social criteria are associated to job creation, energy social acceptation and human development index (HDI). As is shown in figure 2 the fourth level of the hierarchy is organized as follows: dispersed decentralized generation (DDG), compact decentralized generation (CDG) and the extension of the public network or centralized generation (CG). In the last level of the hierarchy, specifically for the decentralized generation, five types of technologies such as solar photovoltaic (SPV), small wind (SWT), small hydro (SHP), internal combustion engines (ICE) and fuel cells (FC) have been considered; and for the alternative of network extension, the national energy production mix.

The dispersed decentralized generation shown in figure 3a implies the on-site generation of electric resource using one or several technologies (hybrid system) and a reserve subsystem (batteries), which must satisfy the energy requirements of housing and public institutions (school, medical module, etc.). For this modality, a street lighting system through solar street lamps has been proposed.

The CDG shown in figure 3b involves the integration of a set of generation and storage (batteries) technologies to supply electricity to the entire village. In turn, CDG consists on micro-grid deployment (on low voltage) to distribute electricity from the generation system to the different loading points of the village.

Finally, the CG involves the extension of a medium voltage network from national or regional interconnected system closer to the village. Then, the final distribution to the different loading points is achieved thanks to a low voltage network (see figure 3c).

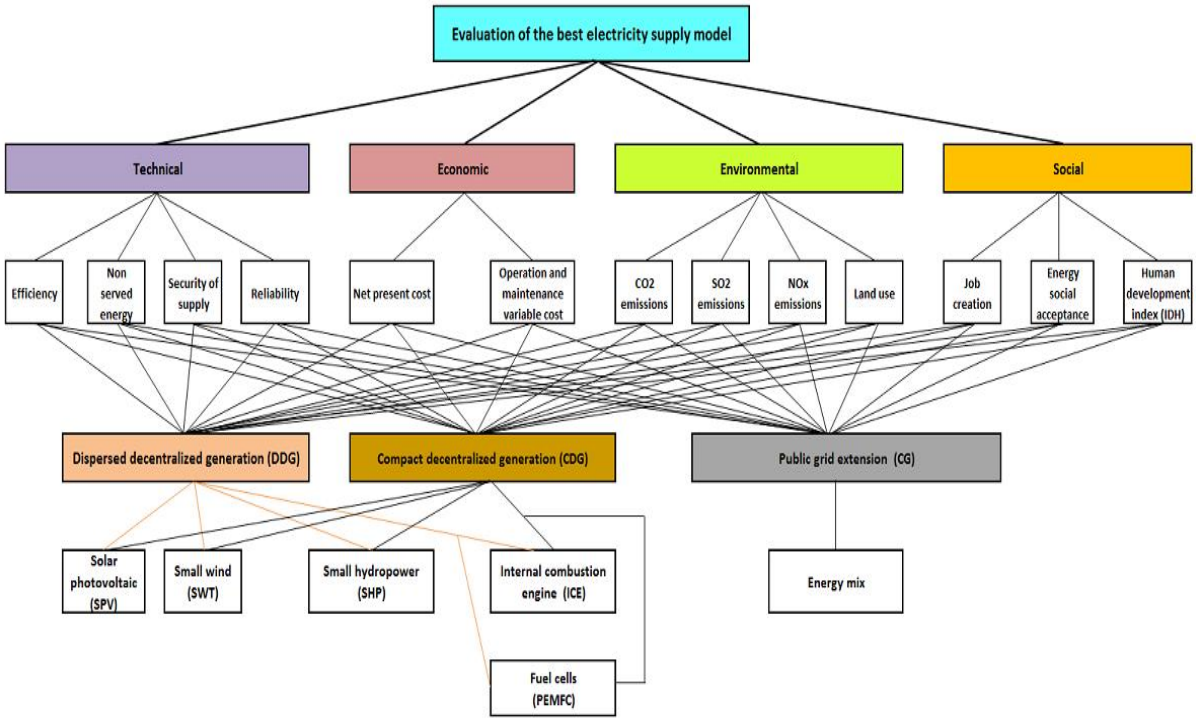

Figure 2. The hierarchical structure for the selection of the electricity supply model

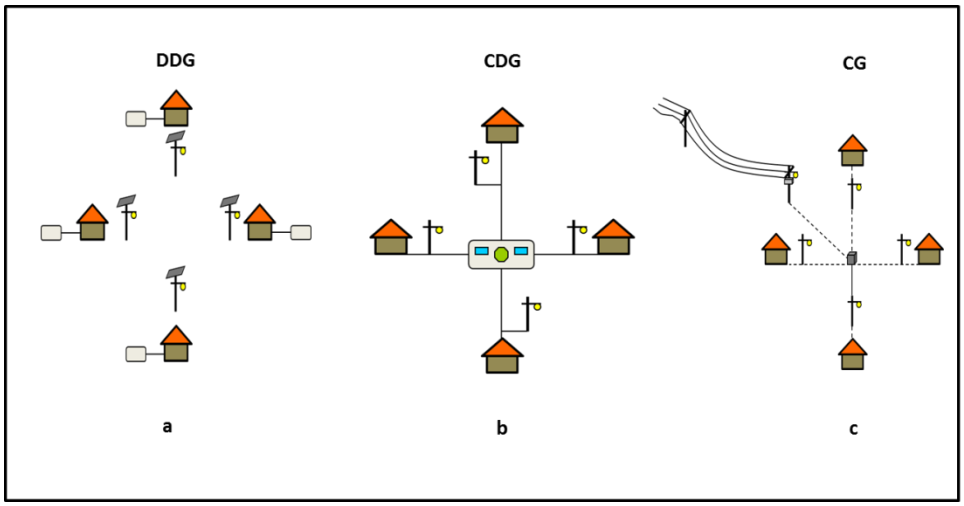

Figure 3. Power supply models

4. APPLICATION TO A VENEZUELAN RURAL-REMOTA VILLAGE

The methodology has been applied to a rural-remote people settled in a mountainous region of the Venezuelan Andes, at an altitude of 3400 meters above the sea level. The town was composed of a group of 35 household (216 people) distributed in a protected natural area (National Park) of 3.2 km^2. In addition to the houses, there is a health care centre and a primary school. Currently, the availability of energy of the population is very limited.

In this regard, a large part of the village uses candles, flashlight and kerosene for home lighting; another very small part uses the gasoline engine for lighting and other household appliances. The medical center and the school have no electrical supply and lighting system. The distance from the village to national electric networks is 25 km. The parameters used for the construction of the decision matrix are shown in table 3.

Table 3. Parameters used in the applied example

Parameters used in the applied example	Value	Parameters used in the applied example	Value
Population growth rate	0.5 % per year	River flow (average)	68 liter per second
Rate of growth in energy consumption	1.6 % per year	Cost reduction rate of solar modules	1.30% per year
Initial power consumption (includes housing and public services)	242 kWh per person	Cost reduction rate of fuel cells	1.27% per year
Fuel price (Gasoline; includes the distribution)	0.25 € per liter	Cost reduction rate of the batteries	1.73% per year
Hydrogen cost (H2-gas; includes the distribution)	5 € per kg	Cost reduction rate of wind turbines	0.10% per year
Discount rate	8 % per year	Cost reduction rate of ICE	0.12% per year
Inflation rate	3.5 % per year	CO2 emissions of solar energy (SPV)	2472.07 kg per kWp
Network investment cost (medium voltage)	10500 € per km	CO2 emissions of batteries	56.45 kg per kWh
Consideration of field factor	2.44	CO2 emissions of ICE (generator)	192.17 kg per kW
Technical losses (medium and low tension)	12%	CO2 emissions of fuel-ICE (gasoline)	3.15 kg per liter
Generation technical losses (DDG and CDG)	17%	CO2 emissions of fuel cells	50 kg per kW
Microgrid technical losses	10.14%	CO2 emissions of hydrogen energy (natural gas steam reforming with capture and	3.23 kg per kg-H2g
Average daily solar radiation per year	4.93 kWh per m²	useful life of the project (two periods of 20 year)	40 years

Alternatives considered for the village's electricity supply are shown in table 4. On these alternatives, HRES-ICE represents a hybrid system integrated by renewable energy technologies (SPV, SWT and SHP) supported by a gasoline generator (ICE); HRES-FC are alternative similar to the previous case but running with a fuel cells (support); HRES implies a power supply system working exclusively with renewable energy technologies; MCI, FC and SPV are associated with the exclusive use of every one of these technologies, respectively.

Table 4. Alternatives for power supply

Code	Alternatives	Code	Alternatives
DDG1	HRES -ICE	CDG11	HRES -ICE
DDG2	HRES -ICE	CDG12	HRES - FC
DDG3	HRES - FC	CDG13	HRES - FC
DDG4	HRES - FC	CDG14	HRES
DDG5	HRES	CDG15	HRES
DDG6	HRES	CDG16	ICE
DDG7	ICE	CDG17	FC
DDG8	FC	CDG18	SPV
DDG9	SPV	CG19	Grid extension
CDG10	HRES - ICE		

The sub-criteria proposed for decision making are shown in table 5.

Table 5. Sub-criteria used to evaluate the alternatives

Sub-criteria	Name	Unit
f1	Net present cost (NPC)	€
f2	Operation and maintenance variable cost (OMVC)	€ per year
f3	Emissions of CO2 (ECO2)	Tons per year
f4	Emissions of SO2 (ESO2)	kg per year
f5	Emissions of NOx (ENOx)	kg per year
f6	Land use (LU)	hectares
f7	Job creation (JC)	Jobs per year
f8	Human development index (HDI)	
f9	Energy social acceptance (ESA)	%
f10	Efficiency coefficient (EC)	%
f11	Energy not supplied (ENS)	kWh per year
f12	Security of supply in the long term (SSLT)	%
f13	Reliability of the technologies (RT)	%

Table 6 summarizes the results of the performance of each of the alternatives evaluated on the basis of decision sub-criteria. As you can be seen from this table, the multicriteria evaluation allows visualizing the alternatives performance under different points of view. As noted, when an alternative achieves better performance in one dimension (criterion) usually affect the next. For example, when an alternative is better from an environmental point of view (less impact), is more expensive economically.

Table 6. Decision matrix for the selection of the power supply system

	Economic criterion		Environmental criterion				Social criterion			Technical criterion			
Proposal	NPC	OMVC	ECO2	ESO2	ENOx	LU	JC	HDI	ESA	EC	ENS	SSLT	RT
SDG1	1337. 50	11.72	22.42	46.34	29.31	0.69	0.17	0.69	81.21	36.6	484.8	100.00	28.21
SDG2	1408.29	10.12	20.46	40.78	26.96	0.65	0.16	0.69	83.28	41.77	281.1	99.99	28.21
SDG3	1311.8	11.42	21.76	45.31	28.7	0.67	0.17	0.69	81.36	37.05	169.6	99.94	28.21
SDG4	1456.12	7.11	20.08	30.95	20.89	0.51	0.12	0.69	85.4	48.69	3.10	98.7	28.21
SDG5	1327.51	11.69	22.83	46.24	29.25	0.69	0.17	0.69	81.22	36.64	15.7	100.00	28.21
SDG6	1405.86	10.13	20.39	40.79	26.76	0.65	0.16	0.69	83.32	41.84	361.3	100.00	28.21
SDG7	2996.65	11.16	319.31	322.77	2307.52	1.23	0.11	0.69	33.91	30.26	3.30	39.25	30.09
SDG8	1921.96	11.63	45.74	110.52	46.47	0.32	0.10	0.69	56,00	40.08	10.00	48.18	51.97
SDG9	1679.18	17.61	31.01	66.03	36.98	0.79	0.23	0.69	71.43	12.28	356.4	100.00	28.06
CDG10	909.35	5.65	43.75	71.52	411.99	0.48	0.08	0.67	69.74	42.95	422.7	80.96	28.10
CDG11	1029.32	8.77	16.71	34.37	21.34	0.49	0.13	0.67	80.05	33.71	0.00	100.00	28.10
CDG12	1057.90	8.19	16.55	34.15	20.78	0.46	0.12	0.67	79.83	35.65	3.30	98.05	28.10
CDG13	1082.62	7.71	15.41	31.95	19.53	0.47	0.11	0.67	80.59	37.21	0.00	98.06	28.10
CDG14	1191.66	6.98	22.84	27.68	17.6	0.42	0.10	0.67	81.54	37.41	14.70	100.00	28.10
CDG15	1153.51	6.98	12.98	27.68	17.6	0.42	0.10	0.67	81.54	37.41	46.20	100.00	28.10
CDG16	1230.45	3.62	211.75	231.7	1781.22	0.72	0.02	0.67	14.29	39.67	340.00	7.48	31.85
CDG17	1649.58	5.39	35.26	90.68	34.55	0.03	0.02	0.67	45,00	59.90	0.10	11.22	75.25
CDG18	1358.56	13.22	23.99	49.56	27.75	0.59	0.17	0.67	71.43	12.28	0.00	100.00	27.82
CG19	1710.53	1.39	42.02	116.55	195.9	37.21	0.03	0.66	57.14	56.21	97.78	70.46	97.79

The weighting factors obtained by AHP taking into account the opinions of the expert panel (twelve experts) are shown in table 7.

Table 7. Summary of sub-criteria overall weight (resulting of AHP)

	Economic criterion		Environmental criterion				Social criterion			Technical criterion			
Sub-criteria	NPC	OMVC	ECO2	ESO2	ENOx	LU	JC	HDI	ESA	EC	ENS	SSLT	RT
Weight (Wi)	0.135	0.024	0.056	0.052	0.107	0.089	0.049	0.098	0.100	0.065	0.058	0.095	0.072

The implementation of the comprehensive VIKOR method to the set of power supply alternatives (table 6), and given the expert's preference weights (table 7), the ranking of compromise solutions is shown in table 8.

Ranking the alternatives by the comprehensive VIKOR method, an ordered list is obtained (for all values of υ equal to 0.5; consensus solution), where the alternative DDG4 (HRES-FC) is shown as the best solution (ranked by minimum Q). However, the C1 condition is not satisfied (unacceptable advantage) but C2 is true (stability in the decision-making process). Therefore, DDG4 is the best solution obtained by Q (VIKOR value), but not by S (utility measure) and R (regret measure). The compliance of C1 condition (acceptable advantage) requires the

grouping of more alternatives as final solution, i.e., DDG4, DDG5, DDG3 and DDG2 are good solutions by R and S.

Table 8. Values of Si, Ri, Qi and Ranking compromise for the applied example

Alternatives	Si	Ri	Qi (υ=0.5)	Ranking
DDG4	0,1209	0,0454	0,0000	1
DDG5	0,1315	0,0454	0,0171	2
DDG3	0,1449	0,0454	0,0387	3
DDG2	0,1510	0,0454	0,0487	4
DDG6	0,1557	0,0454	0,0563	5
DDG1	0,1669	0,0454	0,0743	6
CDG11	0,1647	0,0477	0,0999	7
CDG13	0,1673	0,0477	0,1041	8
CDG12	0,1683	0,0477	0,1057	9
CDG15	0,1726	0,0477	0,1126	10
CDG14	0,1730	0,0477	0,1133	11
DDG9	0,2018	0,0454	0,1315	12
CDG18	0,2090	0,0477	0,1715	13
CDG10	0,2438	0,0477	0,2277	14
DDG8	0,2380	0,0519	0,2710	15
CDG17	0,2607	0,0586	0,3918	16
CG19	0,2359	0,0619	0,3933	17
CDG16	0,4301	0,0632	0,7233	18
DDG7	0,4258	0,0853	0,9931	19

5. CONCLUSIONS

The selection of the best proposal of power supply under multiple criteria requires that different groups of experts are involved in the decision-making process. The inclusion of aspects of technical, economic, environmental and social makes the decision-making process more complex, but more consistent and appropriate to development local needs. The combination of two multicriteria techniques (as AHP for criteria's preference estimation and VIKOR for the proposal selection) makes that decision process is carried out in a coherent manner, transparent, participatory and understandable. This may allow designers, planners or decision-makers get better decisions, especially in case of multiple influence factor as rural and remote electricity supply from developing countries. The results of the applied example also demonstrate that dispersed decentralized generation is the best form of electrification for small rural and remote locations. Therefore, hybrid systems composed of renewable technologies, supported by a fuel cell (fed with sustainable hydrogen), are the most convenient solution. This work shows that the extension of the network is not always the most suitable solution for rural electrification.

6. ACKNOWLEDGEMENTS

Special thanks to Gran Mariscal de Ayacucho Foundation from Venezuela (FGMA) by providing specialized training of human resources abroad.

7. REFERENCES

[1] Alliance for Rural Electrification (ARE). Green light for renewable energy in developing countries, 2010.

[2] IEA, World Energy Outlook, 2006.

[3] Fernández L. Hacia un paradigma de electrificación rural descentralizada con sistemas fotovoltaicos. Tesis doctoral, Universidad Politécnica de Madrid, Escuela Técnica Superior de Ingenieros de Telecomunicación, Madrid-España, 2001.

[4] Alarcón A., Ault G. and Galloway S. Multi-objective planning of distributed energy resources: A review of the state of the art. Renewable and Sustainable Energy Reviews 2010. Article in Press.

[5] Mirasgedis and Diakoulaki D. Multicriteria analysis vs. externalities assessment for the comparative evaluation of electric generation systems. European Journal of Operational Research 1997; 102 (2): 364-379.

[6] Hiremath R., Kumar B., Balachandra P., Ravindranath N. and Raghunandan B. Decentralized renewable energy: Scope, relevance and applications in the Indian context. Energy for Sustainable Development 2009; 13: 3-9.

[7] Alanne K. and Saari A. Distributed energy generation and sustainable development. Renewable and Sustainable Energy Reviews 2006; 10: 539-58.

[8] Cherni J., Dayner I., Henao F., Jaramillo P and Smith R. Energy supply for sustainable rural livelihoods. A multicriteria decision support. Energy Policy 2007, 35 (1): 1493-1502.

[9] Ríos Insua S., Bielza C. y Mateos A. Fundamentos de los sistemas de ayuda a la decisión. De la edición RA-MA, Madrid-España, 2002.

[10] Rojas J., Yusta J and Carlos Ponce. Decentralized power planning: A review of mathematical models. XI International Hydrogen Congress. City of Cuernavaca- México, 2011.

[11] Bouffard F. and Kirschen D. Centralized and distributed electricity systems. Energy Policy 2008; 36: 4504-08.

[12] Pohekar S. and Ramachandran M. Application of multi-criteria decision making to sustainable energy planning – A review. Renewable and Sustainable Energy Review 2004; 8: 365 – 381.

[13] Loken E. Use of multicriterio decision analysis methods for energy planning problems. Renewable and Sustainable Energy Reviews 2007; 11: 1584-1595.

[14] Chatzimouratidis A. and Pilavachi P. Technological, economic and sustainability evaluation of power plants using the Analytic Hierarchy Process. Energy Policy 2009; 37: 778-787.

[15] Ávila R. El AHP (Proceso analítico Jerárquico) y su aplicación para determinar los usos de la tierra – El caso de Brasil. Proyecto regional "Información sobre tierras y aguas para un desarrollo agrícola sostenible" – FAO, Santiago de Chile-Chile, 2002.

[16] Saaty T. Decision Making for Leaders. RWS Publications, Pittsburgh, USA, 1992.

[17] Harrar A. Propuesta de aplicación de técnicas de decisión multicriterio en el desarrollo de alimentos funcionales en Venezuela. Tesis Doctoral Universidad Politécnica de Valencia, Valencia-España, 2010.

[18] Dong L., Fanxiang M. and Qiang F. Application of Analytic Hierarchy Process in Optimization election of Groundwater Artificial Recharge Methods in Sanjiang Plain. IEEE, 2009.

[19] Ramanathan R. and Ganesh L. Using AHP for resource allocation problems. European Journal of Operation Research 1995; 80: 410-417.

[20] Yedla S. and Shreshtha R. Multicriteria approach for selection of alternative option for environmentally sustainable transport system in Delhi. Transportation Research part A 2003; 37: 717–29.

[21] Kaya T. and Kahraman C. Multicriteria renewable energy planning using an integrated fuzzy VIKOR and AHP methodology: The case of Istanbul. Energy 2010; 35: 2517-2527.

[22] Opricovic S. Multicriteria optimization of civil engineering systems. Faculty of Civil Engineering, Belgrade-Yugoslavia, 1998.

[23] Opricovic S. and Tzeng G. Compromise solution by MCDM methods: A comparative analysis of VIKOR and TOPSIS. European Journal of Operational Research 2004; 156: 445-455.

[24] Opricovic S. and Tzeng G. A comparative analysis of the DEA-CCR model and the VIKOR method. Yugoslav Journal of Operation Research 2008; 2 (18): 187-203.

[25] Yu P. A Class of Solutions for Group Decision Problems. Management Science 1973; 19: 688-693, and Multicriteria decision making, J. L. Cochrane y M. Zeleny, pp. 262-301, University of South Carolina Press, Columbia-EEUU

[26] Zeleny M. Multiple Criteria Decision Making. Mc-Graw-Hill, New York-USA, 1982.

[27] Opricovic S. and Tzeng G. Multicriteria planning of post-earthquake sustainable reconstruction. The Journal of Computer-Aided Civil and Infrastructure Engineering 2002; 17 (3): 211–220.

[28] Tzeng G., Tsaur S., Laiw Y. and Opricovic S. Multicriteria analysis of environmental quality in Taipei: Public preferences and improvement strategies. Journal of Environmental Management 2002; 65 (2): 109–120.

[29] Tong L., Chen C. and Wang C. Optimization of multi-response processes using the VIKOR method. International Journal Adv. Manuf. Technol. 2007; 31: 1049-1057.

[30] Opricovic S. A compromise solution in water resources planning. Water Resource Management 2009; 23: 1549-1561.

[31] Khezrian1 M., Wan W., Ibrahim2 S. and Kalantari A. Service selection based on VIKOR Method. International Journal of Research and Reviews in Computer Science 2011; 5(2): 1182-1186.

[32] Amiri M., Ayasi S., Olfat L. and Moradi J. Group Decision Making Process for Supplier Selection with VIKOR under Fuzzy Circumstance Case Study: An Iranian Car Parts Supplier. International Bulletin of Business Administration 2011; 10: 62-75.

[33] San Cristobal J. Multi-criteria decision-making in the selection of a renewable energy project in Spain: The VIKOR method. Renewable Energy 2010; 36: 498-502.

[34] Chang C. A modified VIKOR method for multiple criteria analysis. Environmental Monitoring and Assessment 2010; 168:339-344.

[35] Jahan A., Mustapha F., Ismail M., Sapuan S. and Bahraminasab M. A comprehensive VIKOR method for material selection. Materials and Design 2011; 32: 1215-1221.

[36] Huang J., Tzeng G and Liu H. A revised VIKOR model for multiple criteria decision making – The perspective of regret theory. Cutting-Edge Research Topics on Multiple Criteria Decision Making 2009; 12 (7): 761-768.

9th International Symposium on New Materials and Nano-Materials for Electrochemical Systems
XII International Congress of the Mexican Hydrogen Society
Merida, Mexico, 2012

Synthesis and Characterization of Magnetic Barium Ferrite-Silica Nanocomposites

M.A. Aguilar-González[1], G. Mendoza Saurez[2], K.P. Padmasree[1*]

[1]Cinvestav-Saltillo, Carretera Saltillo-Monterrey Km.13, Ramos Arizpe, 25900, Coahuila, México
[2]Revision Military, Montreal, Quebec H2X1Y4, Canada.
*Tel: 8444389612, fax 8444389610, mail: padma512@yahoo.com

ABSTRACT

Hexagonal bariumferrite ($BaFe_{12}O_{19}$, BaM) has been studied intensively for many years due to their importance as permanent magnets, high density magnetic recording media and microwave devices. The magnetic and electromagnetic absorption properties of BaM can be improved by the partial substitution of nonmagnetic materials like SiO_2, Al_2O_3, ZrO_2, etc., to make composites. In this work, we prepared BaM-SiO_2 nanocomposites by using mechanical alloying in a planetary mill followed by heat treatment near to phase transition. Relationship of BaM and SiO_2 used were 40:60, 50:50, 6 0:40 and 70:30 % by volume. The magnetic properties and microstructure were characterized for different milling times and heat-treatments. Vibrating Sample Magnetometer (VSM), X-Ray Diffraction (XRD) and Scanning Electron Microscope (SEM) were used as the main characterization techniques to study as-milled and heat-treated powders. The results indicate that 15 h of milling were enough to avoid the generation of hematite phase and to get a good dispersion of barium ferrite particles in the ceramic matrix. For milling periods beyond 15 h, the XRD patterns showed the presence of hematite phase caused by the decomposition of BaM. The purpose of the annealing process was to refine the nanocomposite structure to obtain monodomains on the BaM grains and to modify the magnetic properties. The BaM-SiO_2 nanocomposites heat treated at 900°C showed that the magnetization (M_s) and coercivity (H_c) were enhanced with respect to lower BaM volume fractions. The agglomerate size observed through scanning electron microscopic analysis was around 150 nm with a good BaM dispersion into the SiO_2 matrix. The highest saturation magnetization of 43 emu/g is obtained for the composition $60BaFe_{12}O_{19}$-$40SiO_2$ heat treated at 900°C.

Keywords: Barium ferrite, Magnetic properties, Ball- milling

1. Introduction

Hexagonal barium ferrite ($BaFe_{12}O_{19}$), often denoted as M-type BaM, is used for numerous applications such as permanent magnets, particulate media for magnetic recording and microwave devices due to its excellent chemical and physical properties such as large magnetocrystalline anisotropy, high curie temperature, mechanical hardness, excellent chemical stability, relatively large saturation magnetization and corrosion resistivity [1]. The magnetic properties of these materials depend mostly on their grain size and phase purity which is very much depends on their preparation methods. Their magnetic properties arise from the interactions between metallic ions occupying particular positions relative to the oxygen ions in its crystalline structure. The magnetic properties of $BaFe_{12}O_{19}$ can be improved by elemental substitutions of Ba^{2+} or Fe^{3+} sites or both, or by doping or compositing with other materials [2,3]. The preparation method determines mainly the structural and magnetic properties. There exist many methods to synthesize barium ferrite and its composites including the traditional ceramic sintering route, sol-gel method, hydrothermal, chemical co-precipitation, sputtering techniques etc [4-8].

Mechanical milling is a solid state technique and is used extensively for the synthesis of a wide range of nanostructured materials and powder particle refinement through mechanical assisted reactions [9] and has also been used in the synthesis of magnetic powders [10]. Milling induces rigorous plastic deformation due to the gradual refinement of the internal structure of the powders to nanometer level, which affects the magnetic properties of magnetic materials. The magnetic and electromagnetic absorption properties of BaM can be improved by the partial substitution of nonmagnetic materials like SiO_2, Al_2O_3, ZrO_2 etc to make composites. In this work, we report synthesis and characterization studies of the different ratio of $BaFe_{12}O_{19}$-SiO_2 composites by high energy ball milling, and the effect of milling time and annealing temperature on the microstructure and magnetic properties of ceramic-BaM nanocomposites is discussed.

2. Experimental

Barium ferrite -silica nanocomposites were synthesized by mechanical alloying in a planetary mill. The raw materials consisted of BaM and SiO_2 powders of analytical grade reagent with a particle size of ~5 μm BaM and 1 μm SiO_2. Relationship of BaM and SiO_2 used were 40:60, 50:50, 60:40 and 70:30 % by volume. Stoichiometric mixtures of the above chemicals were placed in a zirconia containers together with 20mm diameter zirconia balls as milling media (ball to powder ass ratio =10:1). Dry mechanical milling was carried out in air in a planetary ball mill (RESTCH, model PM400) by using a rotating speed of 350rpm, followed by heat treatment near to phase transition. The milling were done for 30 hrs in steps of 5 hrs and the obtained powder after every 5 hrs were heat treated at different temperatures (500, 900,1000 and 1200° C). Phase evolution on milling and the heat treated sample powders were analyzed by using X-ray powder diffraction in Philips X'pert Diffractometer using Ni-filtered CuK_α

radiation (λ=1.5418Å) in the range of 2θ =20-80°. The morphological features of the particle were observed using a scanning electron microscope (SEM) Philips XL 30ESEM. The purpose of heat treatment was to refine the structure of the resulting nanocomposites and create mono-domains in the barium ferrite particles to modify the magnetic properties. The magnetic properties of the samples were measured at room temperature by using a vibrating sample magnetometer (Lakeshore model 7300/9300 VSM) with an applied field up to 1.3T.

3. Results and discussion

The structural evolution and phase formation of the composite after milling and heat treatment has been examined by X-ray diffraction. Figure 1 (a) shows the X-ray diffraction patterns of barium ferrite-silica composite samples milled for 5h and heat treated at 500°C. It shows the presence of only bariumferrite and silica phases. But compared to figure 1 (a), the X-ray diffraction of the same sample milled for 30 h and heated at 500°C (figure 1(b)) shows an increase in amorphization (broadening of the peak) and a decrease in the intensity of the peaks. In addition to that, the presence of hematite phase also observed after 30h of milling.

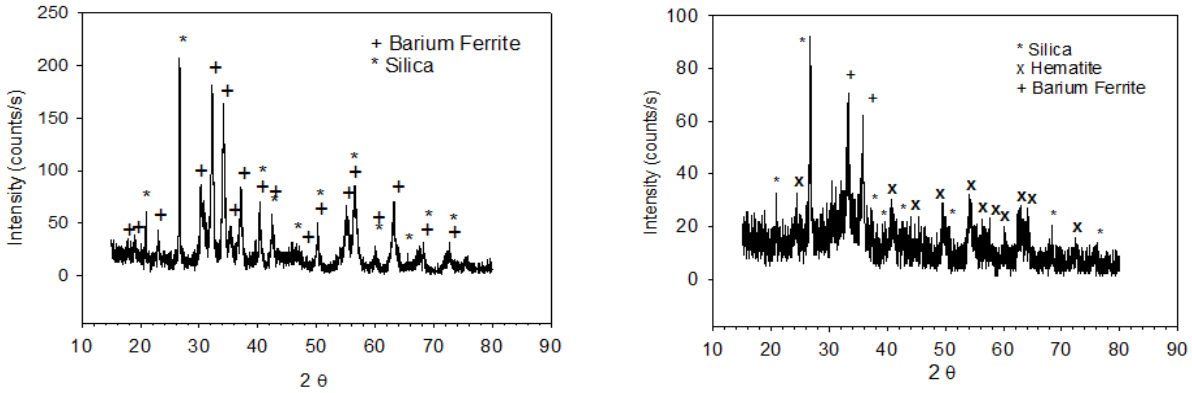

Figure1. X-ray diffraction patterns of 60%BaM-40%SiO_2 sample milled for 5h (a) and 30h (b) and heat treated at 500°C.

Figure 2 shows X-ray diffraction patterns of the samples milled for different hours and heat treated at different temperature of different compositions, (a) 30h milling for BaM-SiO_2 ratio 60:40 heat treated at 900°C (b) 30h milling for the ratio 50:50 at 900°C, (c) 15h milling for the ratio 60:40 at 900°C, (d) 15h milling for the ratio 60:40 at 1000°C and (e) 5h milling for the ratio 50:50 at 900°C. It shows as the milling time increases from 5h to 15h, the intensities of the diffraction pattern have diminished and peaks become broadened due to the refinement of the particles. The sample milled for 15h and heat treated at 1000°C (Figure 2 d) shows the major peaks of hematite phase. The sample of BaM-SiO_2 ratio 50:50 heat treated at 900°C also shows an increase amount diffraction peaks of hematite phase. From the figure 2, we can see from different compositional variation, milling time and heat treatment, the sample of BaM-SiO_2 ratio 60:40 milled for 15h and heat treated at 900°C shows the better structural

properties, though the same sample also exhibit a small quantity of hematite phase and in this case it doesn't have any negative effect as it occurs in very small quantities. The influence of volumetric concentration indicated that not always the great quantity of ferrite leads to better magnetic properties and it plays an important role in the degree of dispersion of the BaM in the ceramic matrix. The result shows that for BaM-SiO_2 samples of ratio 50:50 and 60:40, 900°C is enough to promote the structural rearrangement of Ba and Fe ions with short milling times and when the temperature increases to 1000°C leads to the partial decomposition of BaM to hematite phase.

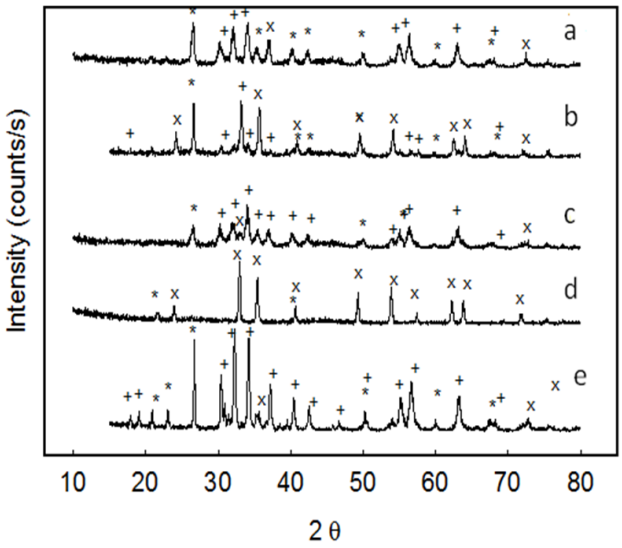

Figure 2. X-ray diffraction patterns of the samples milled for different hours and heat treated at different temperature for different compositions, (a) 30h milling for the ratio 60:40, heat treated at 900°C, (b) 30h milling for the ratio 50:50 at 900°C, (c) 15h milling for the ratio 60:40 at 900°C, (d)15h milling for the ratio 60:40 at 1000°C and (e) 5h milling for the ratio 50:50 at 900°C, (phases of silica (*), barium ferrite (+) and hematite (×))

To observe the distribution of phases and the dispersion of magnetic material in the ceramic host, samples were heat treated at 1200°C and analyzed by scanning electron microscopy in the secondary electron mode (a) and back scattering mode (b) and is shown in figure 3. From the figure we can see a two phase microstructure and also a good dispersion of a phase in another one. The back scattered electron mode gives us idea of compositions based on contrast and we can realize from the figure the existence of two phases. In this mode, the phase with lower atomic weight will appear more obscure, such as silica in the present case and consequently the clear phase will be of barium ferrite. The agglomerate size observed through scanning electron microscopic analysis was around 150 nm with a good BaM dispersion into the SiO_2 matrix.

(a) (b)

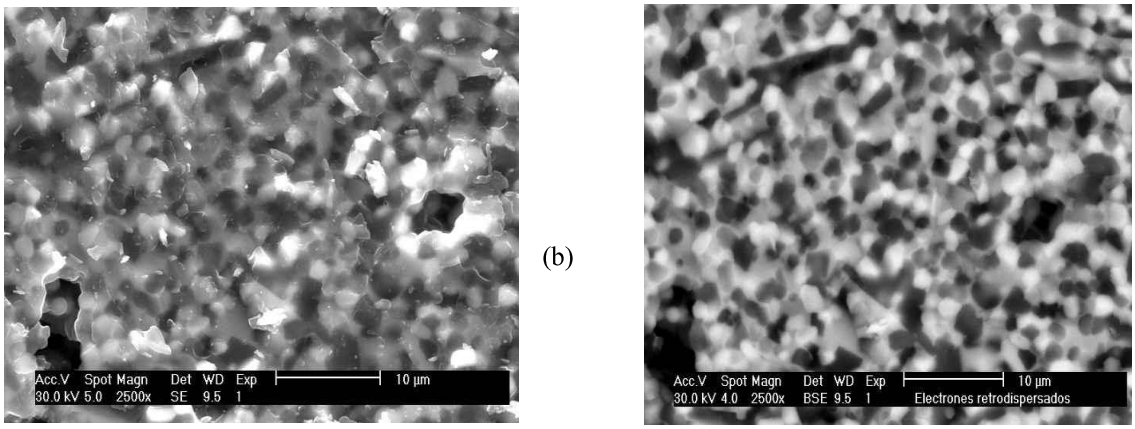

Figure.3 . Scanning electron micrographs of the 15h milled powder pressed and heat treated at 1200°C for the 60%BaM-40%SiO_2 sample (a) secondary electron and (b) back scattering mode.

Figure 4 shows the dependence of saturation magnetization (a) and coercivity (b) as a function of heat treatment temperature from 500 to 1000°C for the samples 60%BaM-SiO_2 and 40%BaM-SiO_2 with 15h of milling. Figure 4 shows the temperature treatment have an effect on the magnetization and coercivity of the material. Figure shows the sample 60%BaM-SiO_2 reached a saturation magnetization of 43emu/g at 900°C; however, for the sample 40%BaM-SiO_2 a maximum saturation magnetization of 33emu/g is obtained at the same temperature. In addition, as the annealing temperature is increased to 1000°C, a negative effect is seen on the magnetization as it reduces to 10emu/g in both samples. This is attributed to the formation of increase α-Fe_2O_3 phase with increase in annealing temperature

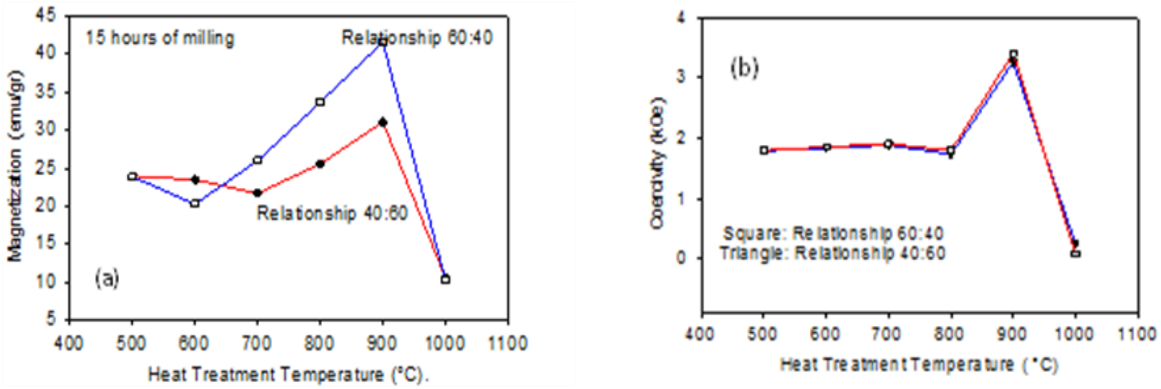

Figure 4. The dependence of saturation magnetization (a) and coercivity (b) as a function of heat treatment temperature for the samples 60%BaM-SiO_2 and 40%BaM-SiO_2 with 15h of milling.

to 1000°C as is also shown by the XRD spectrum of the samples heat treated at 1000°C. Figure 4(b) shows the dependence of coercivity as a function of different heat treatment temperatures. Coercivity also shows a similar trend as that of saturation magnetization. In the range 500-800°C that the samples presented an Hc values close to 2kOe. The sample heat treated at 900°C shows an increase in coercivity value of 3.5kOe for the ratio 60:40 and 3.4 kOe for the ratio 40:60. Both the samples show a value less than 0.5kOe for the samples treated at 1000°C.

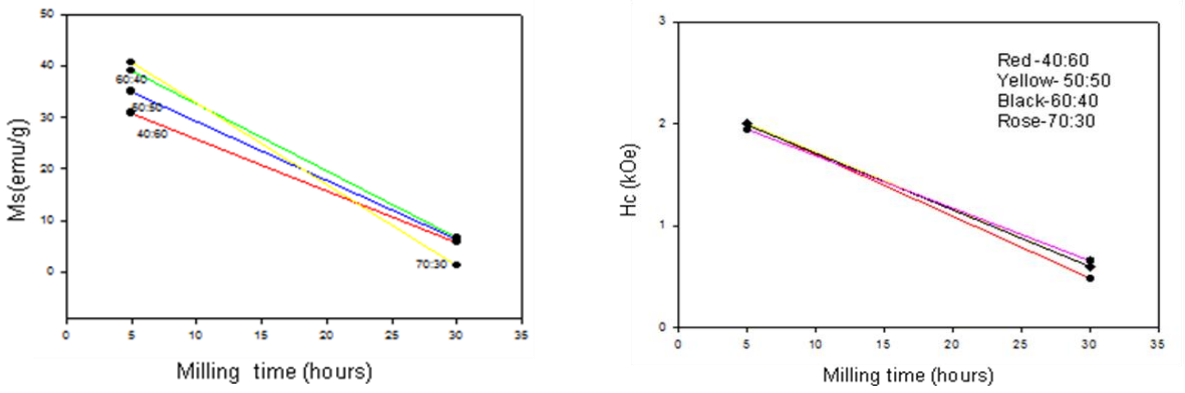

Figure 5. Effect of saturation magnetization Ms (a) and Coercivity (Hc) (b) as a function of milling time for different compositions treated at 500°C

The effect of magnetization and coercivity as a function of milling time for different compositions treated at 500°C is shown in Figure 5. It is noted that the system 70:30 has the highest value of magnetization for 5h milled sample (Figure 5(a)). The effect of increasing milling time reduces the magnetization of all samples due to the presence of α-Fe_2O_3 as well as the distortion of crystal lattice. The coercivity as a function of milling time (Figure 5 (b)) shows all the system have same value at 5h of milling and it decreases with milling time. The low value of coercivity at 30h of milling is due to presence of large number of defects in the network which does not disappear at 500°C. The milling clearly affects the distortion of the network for short and long milling hours and it is the combined action of the distortion and decomposition of BaM in to hematite (α-Fe_2O_3) and probably amorphous BaO. The latter could not be detected by X-ray, which suggests its not crystalline nature. Hematite is antiferromagnetic in nature; this means that it does not have a net magnetization. As its content increases with the time of milling the magnetization decreases due to the dissolution of ferrimagnetic phase (BaM). The coercive field strength does not depend on the presence of α-Fe_2O_3.

Figure 6 shows the saturation magentization and coercity as a function of milling time from 5 to 30 h for the samples 60%BaM-40%SiO_2 and 50%BaM-50%SiO_2 heat treated at 900°C. As we can see from the figure milling time have a strong influence on the magnetic properties. Figure shows an opposite trend for both factors, saturation magnetization decreases with milling time whereas coercivity increases. Maximum value of saturation magnetization is obtained for the BaM-SiO_2 ratio 60:40 (43emu/g), but for the ratio 50:50 at the same conditions saturation magnetization obtained is only 41emu/g. Also the higher coercivity is obtained for the sample with the ratio 60:40 (4.5kOe) but for the relation 50:50, the coercivity value is only 4.2kOe. The milling time causes an increase in coercivity because the particle size reduces with milling time and size is close to critical domain (mondomain) and is directly related to the increase in processing time. The values obtained for the samples milled for 15 h and subsequent heat treatment at 900°C are located in the values of 3.3kOe, which are acceptable for the purpose of magnetic recording.

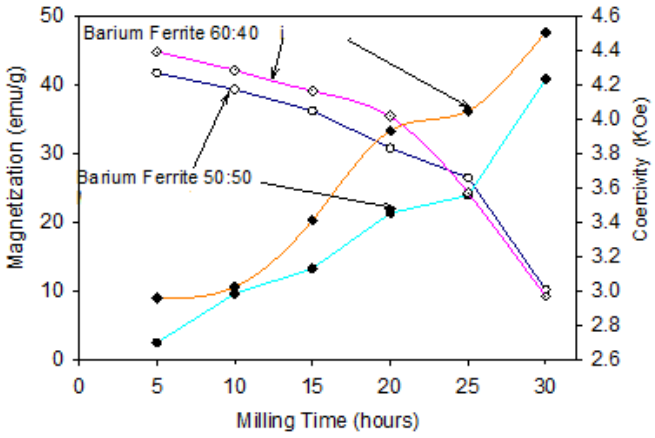

Figure 6. The saturation magnetization (□○) and coercivity (■●) as a function of milling time for the samples 60%BaM-40%SiO_2 and 50%BaM-50%SiO_2 heat treated at 900°C

Figure 7 shows the hysteresis loops for the sample 60%BaM-40%SiO_2 milled for 15h and heat treated at 700, 800, 900, 950 and 1000°C. The highest magnetization is obtained for the sample heat treated at 900 and 950°C. It was observed an increase in magnetization as the temperature increases from 700-950°C and afterwards a sharp drop at 1000°C, because the magnetic properties of the bariumferrite-silica nanocomposites changed significantly at 1000°C due to the presence of hematite (α-Fe_2O_3) phase. The coercivity also increased with heat treatment, as shown in the second quadrant of the hysteresis curve.

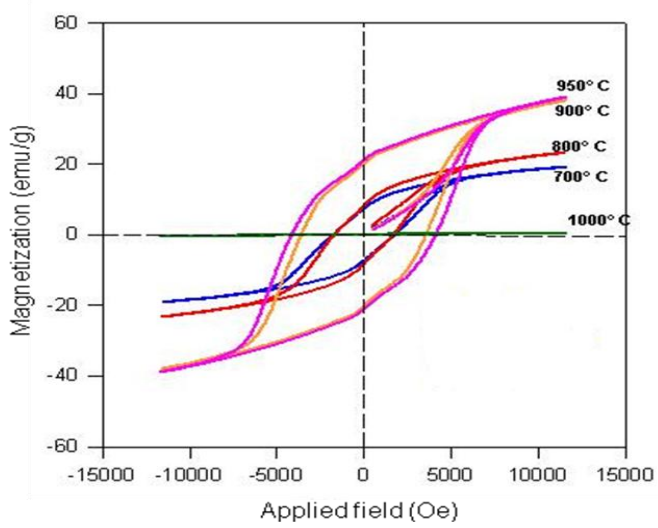

Figure 7. Hysteresis loops for the sample 60%BaM-40%SiO_2 milled for 15h and heat treated at 700,800,900,950 and 1000°C

4. Conclusions

In this work we synthesized barium ferrite and silica nanocomposite by high energy ball milling. The study was done with different compositional ratio of BaM and SiO_2, milling time and annealing temperature. X-ray diffraction study shows that the sample with compositional ratio 60%BaM-40%SiO2 with 15h of milling and 900°C heat treatment is enough for obtaining well dispersed phase of BaM on the ceramic matrix with better magnetic properties. The values obtained for the samples milled for 15 h and subsequent heat treatment at 900°C are located in the values of 3.3kOe, which are acceptable for the purpose of magnetic recording.

5. Acknowledgements

The support of CONACYT Mexico for this work is thankfully acknowledged.

6. References

[1] X. Liu, J. wang, L.M. Gan, S.C. Ng, J. Ding, J. Magn. Magn. Mater., 184, 344, (1998).

[2] H. Sozeri, I. Kucuk, H. Ozkan, J. Magn. Magn. Mater., 323, 1799, (2011).

[3] Wei Chen, Ji Zheng, Yan Li, J. alloys and Compounds, 513, 420, (2012).

[4] N.J. Schrtcliffe, S.Thompson, E.S. O'Keefe, S. Appleton, C.C. Perry, Mater. Res. Bull. 42, 281, (2007).

[5] Y. Liu, M.G.B. Drew, J. Wang, M. Zhang, Y. Liu, J. Magn. Magn. Mater. 322, 366, (2010).

[6] M.M. Rashad, M. Radwan,M.M. Hessien, J. Alloys Compod. 453, 304, (2008).

[7] L. Junliang, Z. Yanwei, G. Cuijing, Z. Wei, Y. Xiaowei, J. Eur. Ceram. Soc. 30, 993, (2010).

[8] M.H. Kim, D.S.Jung, Y.C. Kang, J.H.Choi, Ceram. Inter. 35, 1933, (2009).

[9] C. Suryanarayana, Prog. Mater. Sci. 46, 1, (2001).

[10] M. Zandrahimi, C. Delshad, M. Chermahini, M.H. Mirbeik, J.Magn. Magn. Mater. 232, 667 (2011).

Electrical Transport Studies of the Solid Electrolyte System xAgI-(95-x)[$2Ag_2O$-B_2O_3]-$5TeO_2$, where 45 ≤x≤65

D.H. Kothari[1], D.K. Kanchan[1], K.P. Padmasree[2*]

[1]Solid State Ionics Laboratory, Department of Physics, M. S. University of Baroda, Vadodara, India
[2]Cinvestav-Saltillo, Carretera Saltillo-Monterrey Km.13, Ramos Arizpe, 25900, Coahuila, México
*Tel: 8444389612, fax 8444389610, mail: padma512@yahoo.com

ABSTRACT

Superionic conducting glassy electrolyte materials with high ionic conductivity are of technological interest due to their potential applications in solid state batteries, capacitors, sensors, memory devices etc. An interesting class of superionic conductors is AgI doped silver borate glasses, which can accommodate AgI in a disordered phase without any evidence of crystallization. In this work, quaternary silverborotellurite glasses of the composition *x*AgI -(95 – *x*)[$2Ag_2O$-B_2O_3] -$5TeO_2$, where 45≤x≤65 in steps of 5 were synthesized by melt quenching technique. The synthesized samples were characterized by X-ray diffraction and Differential Scanning Calorimetry, to confirm the amorphous nature and glass transition. Ac conductivity measurements were carried out in the frequency range 1Hz to 32MHz by using Solartron 1260 impedance analyzer in the temperature range 303-473K. The present work explains the effect of AgI addition on the silver borotellurite glass and the obtained dc conductivity is found to increase with the addition of AgI and maximum conductivity is obtained for x=65 mole%. The frequency dependence of conductivity is found to obey Jonscher's Universal law. Impedance and dielectric analysis indicated the ionic motion in the system is responsible for the conductivity and relaxation effect. The cooperative motion due to strong coupling between the mobile Ag^+ ions are assumed to give rise to non-Debye type of relaxation.

Keywords: Glass, electrolyte, conductivity, dielectric

1. Introduction

Superionic conducting glassy electrolyte materials with high ionic conductivity are of technological interest due to their potential applications in solid state batteries, capacitors, sensors, memory devices etc [1]. Several studies on these materials have revealed that glasses need not necessarily be insulators, but can be super ionic conductors under certain circumstances [2]. These glasses have more advantages over crystalline materials because of their isotropic properties, ease of glass formation and change in composition. Considerable effort has been taken to the development of new Ag^+ ion conducting glasses, since the discovery of high ionic conductivity in $RbAg_4I_5$ system. Among the super ion conducting systems studied, AgI doped glasses are frequently investigated because it is easy to form glassy specimens having high ionic conductivity at room temperature. To optimize the transport properties of these systems various compositional variations of glass formers and modifiers were studied with the incorporation of alkali halides and metal halides as dopants, which is considered to be a predominant factor playing the role of enhancing the conductivity of conventional glasses to achieve the values of super ionic conductors. The introduction of glass modifier such as Ag_2O introduces ionic bonds usually associated with non-bridging oxygens (NBOs) along with modifying cations. The glass modifier Ag_2O leaves its oxygen and negative charges to the glass network and becomes rich in Ag^+ ions, and gains the capability to act as solvent for metal halide salts. Hence the mobility of Ag^+ ions in the iodide environment is considered to be higher and based on the fact that increase in the percentage of AgI in glass gives rise to higher conductivities.

Many studies have shown that the conductivities can be enhanced by mixing two different glass formers with different coordination polyhedrons [3]. However, such as mixture of glass formers has a tendency of phase separation at low modifier ratio; therefore the complete substitution of one network former by another is always possible. The most widely studied glass former for super ionic conducting glass is B_2O_3 and the structure and electrical properties of silver ion conducting borate based glass have been reported in the literature [4]. The glass structure consist of three co-ordianted trigonal BO_3 and four connected tetrahedral BO_4 boron atoms and these BO_4 atoms are produced by the modification at the expense of BO_3 units. The trigonal and tetrahedral conversion and formation of oxygen bridges by the oxide ion from the modifier reaches a maximum at the diborate composition. When the modifier concentration is increased further, the percentage of tetragonal boron decreases indicating a structural stability of tetrahedra in the presence of higher modifier oxide concentrations. Tellurium oxide is also a good network former and the interesting aspect of its structure is that when the environment is more ionic, the addition of modifier seems to favor the formation of trigonal pyramidal, TeO_3 (tp) units at the expense of trigonal bipyramidal TeO_4 (tbp) units. Tellurium appears to prefer these coordiantions; tp units form chains while tbp units show three dimensional networks. Also when TeO_2 added to the borate group, for example diborate which is quite ionic, TeO_2 prefers to form chains which interpenetrate the borate network. Tellurium oxide based glasses exhibit high dielectric constant and ionic conductivity with suitable modifications of the network and exhibit low glass

transition temperature, high thermal expansion co-efficient and are less hygroscopic in nature compared to phosphate and other oxide glasses which makes them suitable for many applications [5].

The ac conductivity measurements have been considered as an important tool for studying the ionic transport properties of these materials. Impedance spectroscopy is used widely to study the ionic conduction in solids and to avoid the polarization effects during the dc conductivity measurements. From the ac conductivity studies, the low frequency measurements gives useful insight into mobile ion diffusion and high frequency conductivity data helps us to study the short time phenomena due to local motion of mobile ions. The passage of electric current through a solid electrolyte is the result of several processes like ion movement through the bulk of the electrolyte, charge transfer across the electrode-electrolyte interface etc. Each of these processes usually has widely different relaxation times and therefore responds to the applied electric field at different frequency ranges. In the present study, we aim to investigate the glasses containing two glass formers B_2O_3 and TeO_2, by keeping the amount of TeO_2 as constant. In order to see the effect of dopant AgI on silver borotellurite glasses, we synthesized the composition xAgI -(95 – x)[$2Ag_2O$-B_2O_3] -5TeO_2, where 45 ≤x≤65 in steps of 5 by melt quenching technique.

2. Experimental

The glass samples of composition xAgI-(95– x)[$2Ag_2O$-B_2O_3]-5TeO_2, where 45 ≤x≤65 in steps of 5 were synthesized using the reagent grade chemicals AgI, Ag_2O, H_3BO_3 and TeO_2 by melt quenching technique. The chemicals were weighed according to their molecular weight percentage and mixed thoroughly in an agate mortar and pestle by wet grinding method and the mixtures of these materials were kept in an alumina crucible heated to a temperature range 800-1000K for 4 h. The resultant melt obtained was then quenched by pouring the melt immediately on a copper block kept at room temperature and pressed by another copper block. The glass nature of the samples was confirmed by X-ray diffraction and differential scanning calorimetric methods. The glass transition temperature of the amorphous sample was measured by differential scanning calorimeter at a heating rate of 10K/min, by TA instruments (Model MBSE-2910). The electrical conductivity measurements of the glasses were carried out from room temperature up to the glass transition temperature by complex impedance method by using Impedance Analyzer (Solartron 1260) in the frequency range of 10Hz to 32MHz. The samples of the appropriate shape (1mm thickness) were cut and coated with silver paint to serve as electrodes of the configuration Ag/electrolyte/Ag. The samples were kept in contact with two polished, cleaned and spring loaded copper electrodes.

3. Results and Discussion

The glassy nature of the synthesized samples was confirmed by XRD and DSC analysis. Figure 1 show the X-ray diffraction patterns for the composition 45 AgI - (50-x)[$2Ag_2O$-B_2O_3]-2TeO_2. It show a broad hallow thus suggesting their highly disordered nature. The diffractogram of all the samples of the series shows X-ray amorphous. In order to show that all these compositions were indeed glasses, they were analyzed by DSC technique.

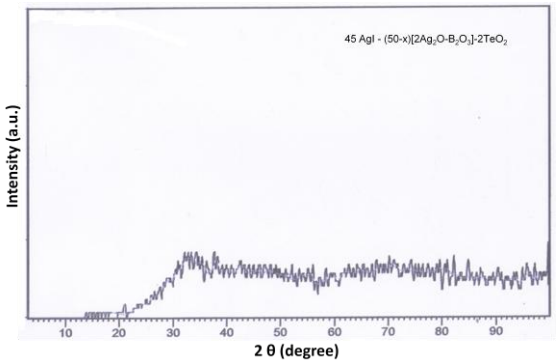

Figure 1. XRD pattern for the glass system 45 AgI - (50-x)[$2Ag_2O$-B_2O_3]-$2TeO_2$

and DSC spectra of all the composition exhibit a glass transition temperature. Figure 2 shows the DSC spectra for the glass system with x=60mole%. It shows an endothermic baseline shift corresponding to glass transition followed by exothermic peak due to crystallization of glassy phase.

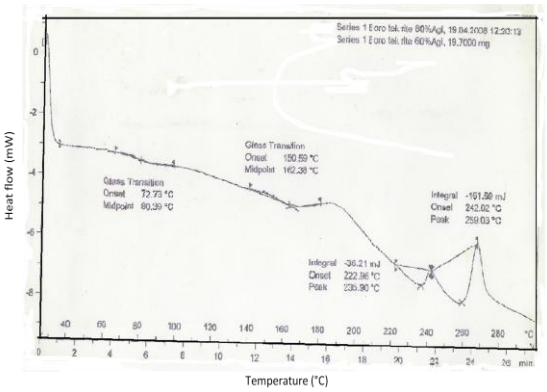

Figure 2. DSC scan for the sample with x=60 mole%

Complex impedance measurements were carried out to determine the electrical property of glasses over a range of temperature and frequencies. Figure 3 shows the impedance plot obtained for x =50mole% of AgI doped composition at different temperatures. Figure shows a depressed semicircle and with the increase in temperature, the intersection of the impedance plot on the real axis shifted towards the origin. That means the bulk resistance of the sample decreases with the increase in temperature which indicate a thermally activated conduction mechanism. The depressed semicircle arises from the distributed bulk relaxation due to ion migration in the glassy matrix. Bulk resistance values were determined from the real axis intercept at the low frequency side. The depressed semicircle in the impedance plot is characteristics of the parallel combination of capacitor and a resistor respectively, which are the bulk capacitance C_b and bulk resistance R_b of the material.

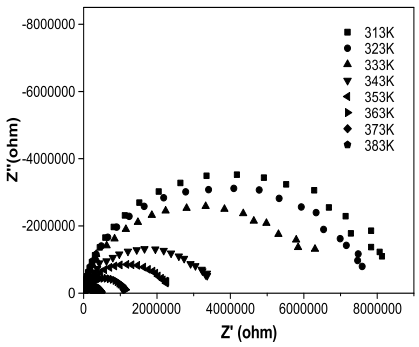

Figure 3. Complex impedance plot for the sample with x=30 mole% at different temperatures.

The real part of the ac conductivity is determined from the complex impedance data by using the relation

$$\sigma^{'} = (t / A)(Z^{'} /(Z^{'2} + Z^{"2})) \qquad (1)$$

where $Z^{'}$ and $Z^{''}$ are the real and imaginary part of the impedance respectively, t is the sample thickness and *A* is the area of the sample. Figure 4 shows the frequency dependence of conductivity at different temperatures for the sample with x=50mole% of AgI. It is observed from the figure that the conductivity increases gradually as the frequency increases. The frequency dependent behavior of conductivity is analyzed by the power law exponent.

$$\sigma'_{(\omega)} = \sigma_{dc} + A\omega^{n} \qquad (2)$$

Where $\sigma_{(\omega)}$ is the conductivity at a particular frequency, σ_{dc} is the dc conductivity of the sample or the conductivity at zero frequency, *A* is a constant at a particular temperature, ω (=2πf) is the angular frequency of the applied field and *n* is the power law exponent in the range $0<n<1$. According to Jonscher [6], a non-zero *n* in the dispersive region of conductivity is due to the energy stored in the short range collective motion of ions. The power law of ac behavior is observed in a wide range of system, Jonscher called it Universal behavior, since equation (2) is accepted universally for finding the sample dc conductivity, hopping rate, frequency dependence of conductivity etc. The frequency dependent conductivity plots at various temperatures show two distinct regions; an almost frequency independent plateau region at low frequencies and a dispersion at high frequencies. The frequency dependent of conductivity is the sum of dc conductivity due to the movement of free charges and the polarization conductivity due to the movement of the bound changes. The low conductivity value at low frequencies is related to the accumulation of the ions due to the slow periodic reversal of the electric field. In the high frequency region, the power law nature ($\sigma'_{(\omega)} \alpha \omega^{n}$) is observed and the conductivity sharply increases with the frequency. The power law variation has been widely investigated and the strong dispersion at low temperature in the high frequency region is attributed to many body effects [7].

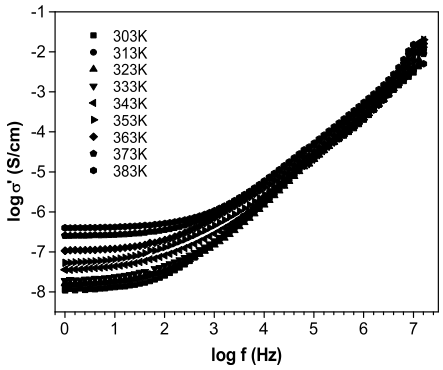

Figure 4. Frequency dependent conductivity at different temperatures for the composition x=50 mole%.

Figure 5 shows the plot of log σ versus 10^3/T for different compositions. The temperature variation of conductivity is found to obey the Arrhenius behavior.

$$\sigma_{dc} = \sigma_0 \exp(-E_a / kT) \qquad (3)$$

Where σ_0 is the conductivity pre-exponential factor, E_a is the activation energy, k is the Boltzmann's constant and T is the absolute temperature. The dc conductivity (σ_{dc}) is found to increase with temperature as well as with the concentration of AgI. The increase in conductivity with the dopant salt is mainly due to the increase in mobile ion concentration. The activation energy of conduction are measured from the slope of log σ_{dc} versus 10^3/T.

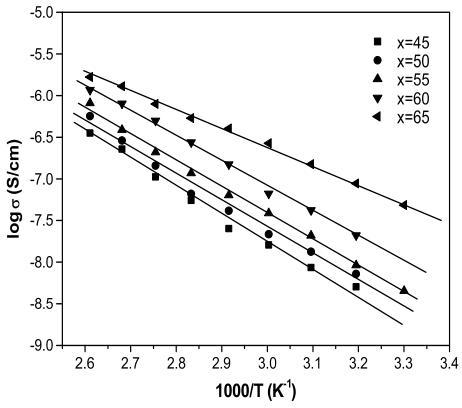

Figure 5. Arrhenius plot of dc conductivity as a function of the inverse of temperature for different compositions.

The observed variation of conductivity with the increase in AgI amount is due to the silver ions attached to I^- ions in the AgI clusters instead of Ag^+ attached to the borotellurite structural units which are more tightly bound. Figure 6 shows the dc conductivity and activation energy for all the samples of the present study. The dc conductivity is found to increase with the increase of AgI concentration and activation energy decreases the same.

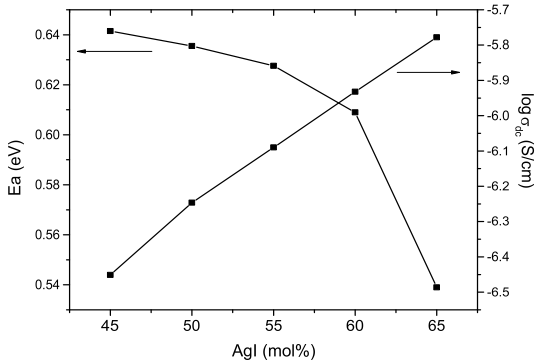

Figure 6. Variation of dc conductivity and activation energy with AgI content

Complex permittivity is related to the impedance data as, $\varepsilon^*=1/j\omega C_0 Z^* = \varepsilon' + j\varepsilon''$, where Z^* is the complex impedance, $\omega = 2\pi f$ is the angular frequency and C_0 is the vacuum capacitance of the cell. Frequency dependence of the real part of the permittivity (dielectric constantε') for x=65 mole% of AgI is shown in figure 7 at different temperatures. The observed high value of ε' at low frequency is due to the presence of large capacitance at the electrode electrolyte interface. The value of ε' is found to decrease with increase in frequency and saturates at higher frequencies. Dielectric constant ε' exhibits a dispersion which shifts to higher frequencies with increase in temperature. This is because at high temperature the jump frequency of mobile ion is large and it resonates with the frequency of the applied electric field. Since the conductivity in the solid electrolyte is visualized as a series of jumps by ions along the lattice sites. If all the sites are equivalent, the ions spend equal amount of time at each site during the conduction process. This is not the case when the sites are not equal. Thus, the charge carriers tend to pile up at high free energy barriers resulting in an increase of capacitance at low frequency. Thus, the variation of ε at lower frequencies is due to the long range diffusion of Ag^+ ions involving series of jumps over barriers of varying height. At higher frequencies, the periodic reversal of field takes place so rapidly that there are no excess ionic jumps in the field direction. The capacitive effect at the high free energy barrier site disappears at high frequencies and results in the low value of dielectric constant as shown in figure 7.

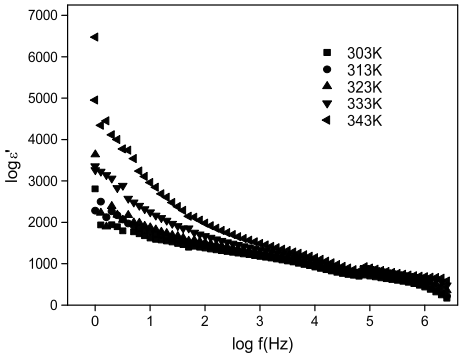

Figure 7. Frequency dependence of dielectric constant for the sample with x=65mole % at different temperatures.

Many studies on AgI based super ionic conductors agree with the conclusion that the insertion of metallic oxde Ag_2O as modifier disrupts the glassy network leading to the different structural arrangements of B_2O_3-TeO_2 glass network [8]. This change results in the formation of non-bridging oxygen and O-Ag partial co-valent bonding. The Ag^+ ions bonded to the NBOs have less freedom to move and are expected to be less mobile compared to Ag^+ ions in an iodine environment. Many structural studies revealed that the glass network is not strongly modified by the introduction of halide salt (AgI). Hence in the present system the increase of conductivity is explained by diffusion path model given by Minami [9]. According to the diffusion path model, a wide and shallow potential is formed by the interaction of Ag^+ ions with iodide ions while a narrow deep one is formed due to their interaction with oxide ions in the glassy structure. It is also suggested that the diffusion path is more easily formed in disordered structures than on an ordered one. In the present system, xAgI -(95–x)[$2Ag_2O$-B_2O_3] -5TeO_2 the concentration of AgI increases with the increase in dopant x, and the increase of conductivity can be explained in accordance with the conductivity expression, $\sigma=ne\mu$, where n is the number of charge carriers, e is the charge and μ is the mobility. Therefore, the increase in the number and mobility of charge carriers (Ag^+) with increase in dopant x in the present system follows the diffusion path model, where the increase of conductivity with dopant salt content in the glassy matrix is interpreted due to the increase of the concentration of the charge carriers Ag^+ attached to AgI and their mobility [10].

4. Conclusions

The present study deals with the synthesis of the glass system xAgI -(95–x)[$2Ag_2O$-B_2O_3] -5TeO_2 where 45≤x≤65 in steps of 5 by melt quenching technique and its electrical characterization. The composition with 65 mole% of AgI is found to exhibit the highest electrical conductivity. Frequency dependent conductivity study shows that the present system obeys Jonschers Universal response and the high frequency dispersion is attributed to many body interactions

between the conducting species. The variation of dielectric constant with frequency is attributed to ion diffusion and polarization occurring in the glass system.

5. Acknowledgement

The authors acknowledge with thanks the financial help rendered by the M.S. University of Baroda in the form of minor research project.

6. References

[1] S. Chandra, Super Ionic Solids: Principles and Applications, North Holland, Amsterdam, (1981).

[2] A.L. Laskar, S.Chandra, Super Ionic Solids and Solid Electrolytes: Recent Trends (1989).

[3] A. Magistrs, G.Chiodelli, Solid State Ionics, 9&10, 611 (1983).

[4] G. Chiodelli, GC Vigano, A.Magistris, M.Villa, Solid State Ionics, 37, 17 (1989).

[5] H. Yamamoto, N.Nasu, J. Mustoka, K. Kanira, J. Non-Cryst. Solids 170, 87 (1994).

[6]. A.K. Jonscher, Nature, 267, 673, (1977).

[7]. D.P. Almond, G.K. Ducan, A.R. West, Solid State Ionics 8,159, (1983).

[8]. P.S.S. Prasad and S. Radhakrishna, Solid State Ioncis 28/30, 814, (1988).

[9] T. Minami, J.Non-Crsyt.Solids, 73, 273 (1985).

[10] M.Venkateswarlu, K.N.Reddy, B.Rambabu, N. Satyanarayana, Solid State Ionics, 127, 177 (2000).

Structural and Magnetic Studies of Undoped and Strontium-Doped Lanthanum Manganite System

K.P. Padmasree*, A.I. Martínez, A.F. Fuentes

Cinvestav-Saltillo, Carretera Saltillo-Monterrey Km.13, Ramos Arizpe, 25900, Coahuila, México
*Tel: 8444389612, fax 8444389610, mail: padma512@yahoo.com

ABSTRACT

Lanthanum strontium manganite perovskites are the most studied cathode materials for solid oxide fuel cells. Lanthanum manganite and strontium doped lanthanum manganite belong to the perovskite oxide family. The larger rare earth ion (e.g., La) occupies the 12 coordinated A-sites and the transition metal ions (e.g., Mn) occupy the octahedral B sites. Both the electrical conductivity and catalytic activity of lanthanum manganite are enhanced considerably when lanthanum is substituted partially with strontium. In this work, the effect of Sr doping on the composition, $La_{1-x}Sr_xMnO_3$ (x=0, 0.1, 0.3, 0.5) has been studied. The perovskite oxides have been synthesized by the conventional ceramic route. The synthesized powders were characterized by X-ray diffraction, scanning electron microscopy. The magnetic studies were done by an alternating gradient magnetometer. The XRD patterns of all the samples clearly shows the formation of crystalline perovskite structure, however the LSM samples with x=0 and 0.1 shows a small amount of La_2O_3. The magnetic measurements of the samples were realized at room temperature and all samples displayed superparamagnetic properties with coercive fields near to zero. This behavior is originated from the surface spin disorder enhancement caused by decreasing particle size.

Keywords: Perovskite, cathode, lanthanum strontium manganite

1. Introduction

Solid oxide fuel cells (SOFCs) are the most efficient and environmentally friendly energy conversion technology to generate electricity from fuels as compared to the conventional thermal power generation plants [1]. However, there are many material problems to be solved due to the high temperature operation (~1000°C) of the SOFC system. The main factor limiting the performance of SOFC is the significant material limitations imposed by the cathode and the cathode leads because of the high corrosion effect of oxygen at high operating temperature. The cathode material has to meet some requirements like high electronic conductivity, thermal and chemical stability, and good compatibility with the solid electrolyte, sufficient porosity for the oxide ions to migrate, and good adherence at the surface of the electrolyte to work at high operating temperature in air or oxygen atmosphere. Some complex oxides in the perovskite family may satisfy the above mentioned requirements and has been widely studied in recent years for use as cathode materials for SOFCs [2].

Perovskite type oxides of the ABO_3 structure with trivalent rare earth in the A position and trivalent transition metal ions in the B position are p-type conductors. Lanthanum manganite ($LaMnO_{3\pm\delta}$) belongs to perovskite oxide family and can crystallize either with orthorhombic or rhombohedral symmetry depending on the value of δ, and it may depend on many factors like method of synthesis, thermal treatments etc. [3,4]. The larger rare earth ions (La) occupy the 12 coordinated A-sites and the transition metal ions (Mn) occupy the octahedral B-sites. The substitution of A-site cations by aliovalent cations forms oxygen vacancies and causes a change in the valence states in B-site cations so that charge neutrality can be maintained. As a result, the perovskite oxide shows substantial electronic conductivity as well as ionic conductivity at elevated temperatures. When lanthanum is substituted partially with strontium, the electrical conductivity and catalytic activity of lanthanum manganite can be considerably increased. Though lanthanum strontium manganite (LSM) as cathode material have proved to be a poor oxygen ion conductor, its electronic conductivity is high enough to make them the most investigated cathode materials for solid oxide fuel cells. With high electronic conductivity, LSM offers a high catalytic activity for oxygen reduction as well as chemical and thermal compatibility with the conventional yttria stabilized zirconia electrolyte at the operating temperature [5].

The perovskite $La_{1-x}Sr_xMnO_3$ exhibits a variety of magnetic phases, the end member x=0 is an antiferromagnetic insulator due to the superexchange between Mn^{3+} ions. The substitution of Sr in La sites of the $LaMnO_3$ phase leads to a ferromagnetic double exchange interaction, metallic conductivity and a large magnetoresistance [6]. Due to the mixed valence states of manganese ions, their spin states fluctuate between trivalent and quadruvalent states. In this study, conventional ceramic route was adopted for the synthesis of perovskite oxides and the analysis of crystal structure, magnetic and electrical properties of the synthesized samples were done by different techniques. Here we

report the effect of strontium substitution on lanthanum manganite on the crystal structure and magnetic properties of $La_{1-x}Sr_xMnO_3$ system, where (x=0, 0.1, 0.3,0.5).

2. Experimental procedure

Powders of $La_{1-x}Sr_xMnO_3$ (x=0, 0.1, 0.3, 0.5) were prepared by a high temperature solid state reaction by using the high purity (Aldrich 99.99%) oxides, La_2O_3, $Sr(NO_3)_2$ and MnO_2. The rare earth oxide, La_2O_3 was fired overnight at 800ºC before using, in order to decompose the hydroxides, carbonates and oxycarbonates present. The stoichiometric amounts of the starting materials were milled for 2 hrs after being thoroughly mixed in methanol. The obtained material was calcined at 1000°C in air for 12 hr. Then they were ground and calcined in air at 1200°C for 12 hr and ground again to obtain fine powders.

The crystal structure of the synthesized samples were done by X-ray diffraction (XRD) in a Philips X'Pert diffractometer using Ni filtered CuKα radiation (λ=1.5418A°) The chemical analysis and morphology of the synthesized powders and sintered pellets were done by JEOL-JSM-6300 Scanning Microscope. The specific surface area (S_{BET}) values were determined by BET method (Nova 2000, Quanta-Chrome). The average particle size (D_{BET}) was calculated assuming the presence of spherical particles, by means of the equation

$$D_{BET} = \frac{6}{S_{BET}\rho}$$

where ρ is the theoretical density of LSM (6.45 g/cm^{-3}). The magnetic properties were measured at room temperature in an alternating gradient magnetometer (AGM Micromag 2900) manufactured by Princeton Measurement Corporation.

3. Results and Discussions

The X-ray diffraction patterns of $La_{(1-x)}Sr_xMnO_3$ (where x=0,0.1,0.3 and 0.5) samples prepared by solid state reaction are shown in Fig.1. The XRD patterns of all the samples clearly shows the formation of crystalline perovskite structure, however the LSM samples with x=0 and 0.1 shows a small amount of La_2O_3 along with the rhombohedral phase. It is reported that in solid state reaction experiments, the presence of perovskite type phase in the first reaction step, but some of the La_2O_3 does not react and it takes very long firing times at high temperatures to have the La_2O_3 reacted completely with four or five intermediate grindings [7]. In our case, $LaMnO_3$ shows a rhombohedral phase and with the substitution of 10 and 30 mole% of Sr to $LaMnO_3$, the perovskite structure still shows a rhombohedral symmetry. When the strontium content increases upto to 50mole%, the perovskite structure adopts an orthorhombic symmetry. A slight shift of all peaks was observed in the direction of increasing diffraction

angles as the strontium doping level increased from x=0.1 to 0.5, and there is a significant broadening of the peak with increasing Sr content.

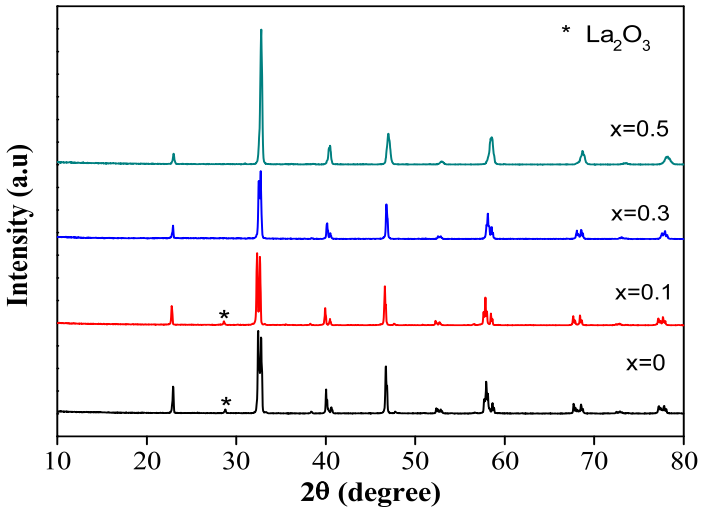

Figure 1. XRD patterns of the synthesized samples $La_{(1-x)}Sr_xMnO_3$, where x=0,0.1,0.3 and 0.5)

When La^{3+} is doped with lower valence cations like Sr^{2+}, leads to increase electronic disorder and changes in the oxidation state of the 3d transition metal and in the oxygen non-stoichiometry, which increases the concentration of Mn^{4+} in $LaMnO_3$, since the ionic radii of Sr^{2+} (1.44 A°) is slightly larger than La^{3+} (1.36A°) respectively. The crystallite size of all the samples were calculated by using the Scherrer equation by considering (204) peak at 2θ= 46.7° for the rhombohedral phase and (112) peak at 32.7° for the orthorhombic phase [8]. The crystallite sizes of all samples were found to be in the nanosize range and are shown in the Table 1.

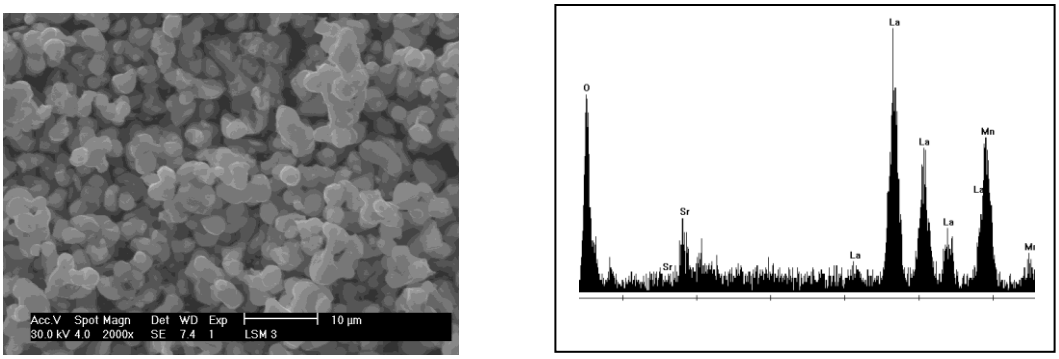

Figure 2. SEM micrographs and EDAX analysis of the synthesized sample with x=0.1

The morphology of the particles in ceramic materials is the consequence of the preparation method. Figure 2 shows the SEM and EDAX analysis of the LSM powders; it shows the formation of agglomerates of fine primary particles with porous structure. Table shows the values of crystallite size, surface area, pore volume, average particle size and pore size of the LSM powders synthesized by solid state method. Crystallite size is found to decrease with increase in Sr amount and an increase in specific surface area.

Table1. Average crystallite size (D_{XRD}), specific surface area (S_{BET}), pore volume (Vpore), average crystallite size (DBET) and pore size of the sample powders

Composition	Crystallite size (nm)	Surface area (S_{BET})(m^2/g)	Pore volume cc/g	Average particle size (D_{BET}) (μm)	Pore size (A°)
x=0	67.48	1.052	0.0025	0.88	31.69
x=0.1	77.87	0.601	0.0015	1.55	31.69
x=0.3	70.97	0.992	0.0034	0.94	31.69
x=0.5	59.18	2.027	0.0070	0.46	31.69

Scanning electron micrograph of the synthesized sample with x=0.5 sintered at 1500°C is shown in figure 3. The porous structure is also evident even if the sample sintered at 1500°C. With sintering the grains agglomerate and grow, the number of the open pores reduces, and the open pores are located at the multigrain boundaries.

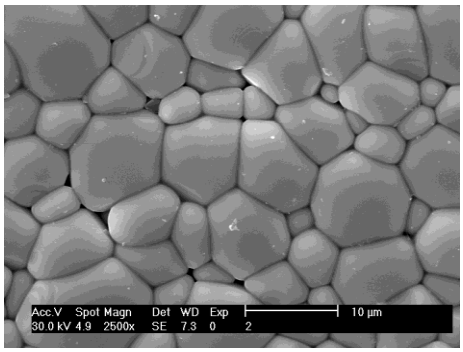

Figure 3. SEM micrographs of the sample with x=0.5 sintered at 1500°C

The magnetic properties of LSM samples are shown in figure 4. The magnetization hysteresis loop of LSM sample with x = 0.5 is displayed in figure 4(a), it can be observed that LSM samples exhibit superparamagnetic properties with both coercive field and remanent magnetization near to zero, this behavior is related with the nanostructured nature of the powders. In figure 4(b), the changes of saturation magnetization with x are shown, it is clear that Sr impurities plays an important role on the magnetic properties, although a non linear effect with concentration of x is observed. The non linear behavior can be due to the fact that the prepared powders are not pure and the quantification of additional oxide phases is hard to be determined. For future works, a more specific route for

formation of pure LSM powders have to be realized, this will help to have more realistic effect of Sr impurities on the magnetic properties of nanostructured LSM powders.

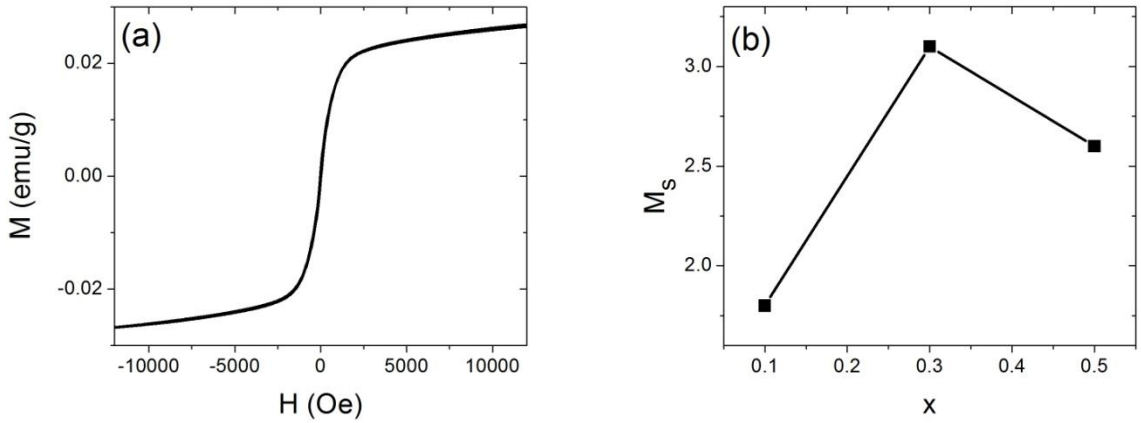

Figure 4. Magnetic properties of LSM samples. (a) Magnetization vs magnetic field for sample x= 0.5, (b) saturation magnetization (M_s) vs x.

4. Conclusions

Perovskite structured $La_{1-x}Sr_xMnO_3$ (x=0, 0.1, 0.3, 0.5) powders was prepared by the conventional solid state synthesis. The nanocrystallite sizes of the powders ranged between 59-77nm. Crystallite size is found to decrease with increase in Sr amount and specific surface area increases. LSM samples exhibit superparamagnetic properties with both coercive field and remanent magnetization near to zero, which can be related to the nanostructured nature of the powders.

5. Acknowledgements

The authors are responsible for Conacyt, Mexico for the financial support (Grant SEP-2007-CB-84267).

6. References

[1] S.C. Singhal, K. Kendall, High temperature solid oxide fuel cells: fundamentals, design and applications, Elsevier (2004).

[2] J.R. Smith, A.Chen, D. Gostovic, D. Hickey, D. Kundinger, KL Duncan, Solid State Ionics, 180, 90 (2009).

[3] S.P. Jiang, J.Mater Sci., 43, 6799 (2008).

[4] H. Yokokawa, N. Sakai, T. Horita, K. Yamaji, ME Brito, Mater Res Soc Bull., 30, 591, (2005).

[5] J. Mizusaki, Y. Yonemura, H. Kamata,, K. Ohyama, N.Mori, H.Takai, Solid State Ionics 132, 167 (2000).

[6] G. Srinivasan, D.Hana, Applied Physics Letters, 79, 641, (2001).

[7] J.A.M. van Roosmalen, P. van Vlaanderen, E.H.P. Cordfunke, J. Solid State Chem., 114, 516, (1995).

[8] R.V. Wandekar, B.N. Wani, S.R. Bharadwaj, Materials Letters, 59, 2799, (2005).

Bimetallic Materials Based on Ag for Cathode/Anode Electrode in a Glucose Microfluidic Fuel Cell

F. M. Cuevas Muñiz[1], M. Guerra-Balcázar[1], J. Ledesma García[1], L. G. Arriaga[2,*]

[1]División de Investigación y Posgrado, Facultad de Ingeniería, Universidad Autónoma de Querétaro
Cerro de las Campanas S/N, Querétaro, Qro. C.P. 76010

[2]Centro de Investigación y Desarrollo Tecnológico en Electroquímica, Parque Tecnológico Querétaro Sanfandila S/N
Pedro Escobedo, Qro. C.P. 76703
email: larriaga@cideteq.mx

ABSTRACT

The present work shows the results for bimetallic materials PtAg/C and AuAg/C as cathode and anode electrode respectively in a microfluidic fuel cell with glucose as fuel in basic media. The electrodes were prepared for chemical reduction according to a modification of the Burst method and were characterized by XRD and electrochemical techniques. The fuel cell was able to harvest 600 mW cm^{-2}. The PtAg/C exhibits a better performance respect the commercial Pt/C at high concentrations of glucose. Meanwhile AuAg/C also contributed to stability of the fuel cell during long times of operation.

1. Introduction

Microfluidic fuel cells or membraneless fuel cells operate without a membrane as physical barrier to separate the anode and cathode. This membraneless laminar flow-based fuel cell (LFFC) design eliminates PEM-related issues of fuel crossover, anode dry-out, and cathode flooding. A fuel with greater interest because of their low cost is the Glucose [1–3]. The glucose fuel cells, utilizes noble metal catalysts such as platinum and gold [4]. Yet, the use of these metal catalysts has the great disadvantages that are easily poisoned due to fuel crossover. In this context the use of bimetallic catalysts is a viable solution because these materials shows belter electrocatalytic activities compared to the monometallic materials [5, 6]. With the further advantage that reduce the amount of inordinately expensive precious metals.

In this work, PtAg/C and AuAg/C bimetallic catalysts were synthesized and evaluated for the oxygen reduction reaction ORR and glucose oxidation reaction respectively in order to reduce the self-poisoning of the electrocatalysts on the microfluidic fuel cell. These catalyts were used in an microfluidic fuel cell and were comparated with Pt/C and Au/C catalyst.

2. Experimental

The bimetallic catalysts AuAg and PtAg were prepared following a previously reported procedure [5, 6]. For AuAg, a mix aqueous solution of $HAuCl_4$ (J.T. Baker) with $AgNO_3$ (J.T. Baker) was employed. Meanwhile for PtAg an aqueous solution of $H_2Pt(NO_2)_2SO_4$ (Alfa Aesar) with $AgNO_3$ (J.T. Baker) was used. In both cases, the aqueous solution was put together with tetraoctyl-ammonium bromide (Fluka) in toluene, and later Dodecanethiol (Aldrich) was added, and finally the metals were reduced with $NaBH_4$ (Aldrich). The nanoparticles were supported in vulcan carbon XC-72 (Cabot).

Physicochemical characterization was performed with TEM was accomplished using a JEOL JEM2200Fs + Cs STEM, and the X-ray diffraction was obtained using a Bruker D8 Advance diffractometer operated at 30 mV and 30 mA. The electrochemical tests were performed in a potentiostat BioLogic VSP. A conventional three electrode cell was employed. Hg,HgO electrode was used as reference electrode. A carbon bar was used as counter electrode. As working electrode an ink with the nanomaterials was employed and deposited in a glassy carbon disk electrode. The materials were tested in basic media (KOH 0.3 M) with oxygen saturated for PtAg/C or glucose 10 mM for AuAg/C.

The fuel cell was reported previously [7]. In the walls of the microchannel, the catalysts were placed by spray technique. Two streams of KOH 0.3 M, one containing oxygen saturated was placed in the cathodic side and other

with glucose 100 mM was placed in the anodic side. Later discharge curves were performed at 5 mV s^{-1} since OCP to 0 mV.

3. Results and discussion

3.1 Synthesis and characterization of AuAg/C and PtAg/C

The TEM micrographs are showed on figure 1. The AuAg/C micrograph is showed in the figure 1a. The results indicate the formation of nanoparticles of AuAg/C of composition 83-16 according the EDS results. The size of nanoparticles is around 16 nm. The figure 1b shows the TEM micrograph of PtAg/C. The TEM analysis showed that the particle structure had a core–shell type with a platinum center coated with silver. The EDS analysis of the catalyst revealed the mean composition of PtAg/C to be 81% Pt and 19% Ag. The composition in both catalysts are in close agreement with that of the metallic precursors that were used. The mean particle size of the PtAg nanoparticles is approximately 7 nm.

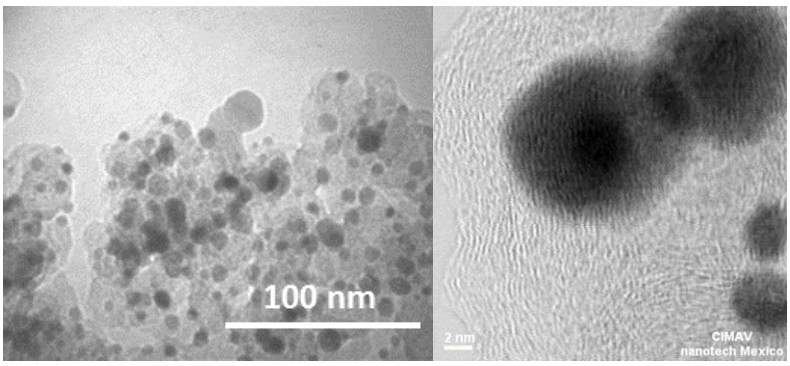

Figure 1. TEM micrograph of AuAg/C and PtAg/C catalysts.

The difractograms obtained were showed in figure 2. Crystalline planes of AuAg-based material are observed in Fig. 2a and located at 38.0°, 44.2°, 64.4°, 77.3° and 82°. The signals correspond to Au crystalline planes (1 1 1), (2 0 0), (2 2 0), (3 1 1) and (2 2 2). The value of lattice parameter is 4.089 Å and average particle size of 21 nm. The observed peaks are characteristic of a single face-centered-cubic (fcc) crystallographic structure of Au (JCPDS 04-0784). Variation of lattice parameter value suggests the presence of electronic interactions between outer electron shells of Ag and Au atoms, reducing the size of Ag atom [8]. This is an indicative of the formation of one phase in the material.

The figure 2b shows the X-ray diffraction pattern of PtAg/C, along with the characteristic peaks of a single fcc structure. The peaks located at 38°, 45°, 65°, 78° and 82° correspond to the same planes described above. The peak located at approximately 25° may be attributed to the graphite (0 0 2) crystalline plane of carbon. The lattice parameters calculated from this experimental data are 3.92 Å [9, 10]. The observed diffraction angles for the PtAg/C catalyst are located between those of the two pure metal elements Pt and Ag, suggesting the formation of alloy nanoparticles.

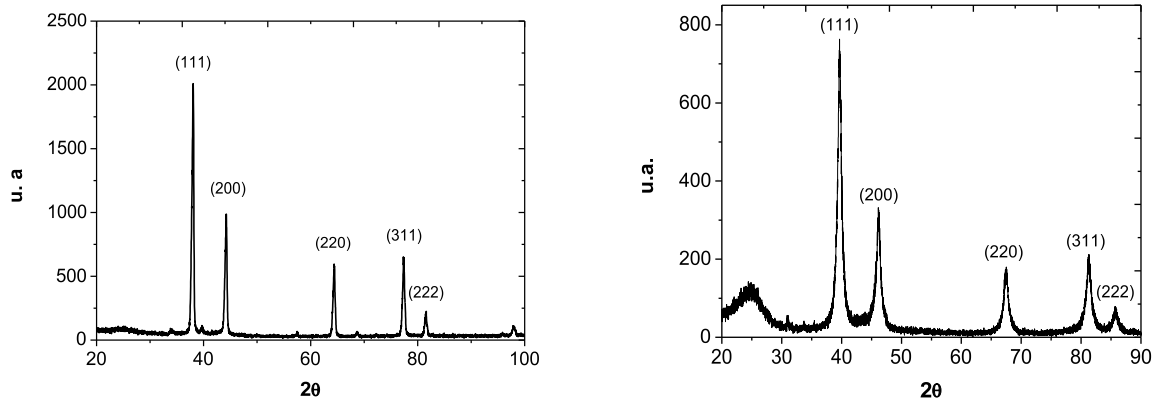

Figure 2. XRD patterns of (a) AuAg/C and (b) PtAg/C.

3.2 Electrochemical characterization

The voltametric profiles of (a) AuAg/C and (b) PtAg/C in basic media (KOH 0.3 M) and also Au/C, Ag/C y Pt/C for comparison are shown in the figure 3. For AuAg/C electrocatalyst are not observed the peaks corresponding to Ag oxides reduction, we can infer from this datum that that the bimetallic material are composed by a solid solution [11]. On the other hand the voltammetric profiles of PtAg/C, Pt/C and Ag/C electrodes in 0.3 M KOH under nitrogen atmosphere are compared. The Pt/C electrode shows the hydrogen adsorption and desorption to be located at 0.31 V vs. RHE. In the case of the Ag/C electrode, it is possible to observe an oxide peak around 1.1 V vs. RHE that corresponds to the formation of silver oxides. In the case of the PtAg/C catalyst, it sees a voltammetry similar to Pt/C, although both oxide and reduction peaks appear at 0.7 and 0.9 V vs. RHE, which is similar to the Ag/C catalyst [11].

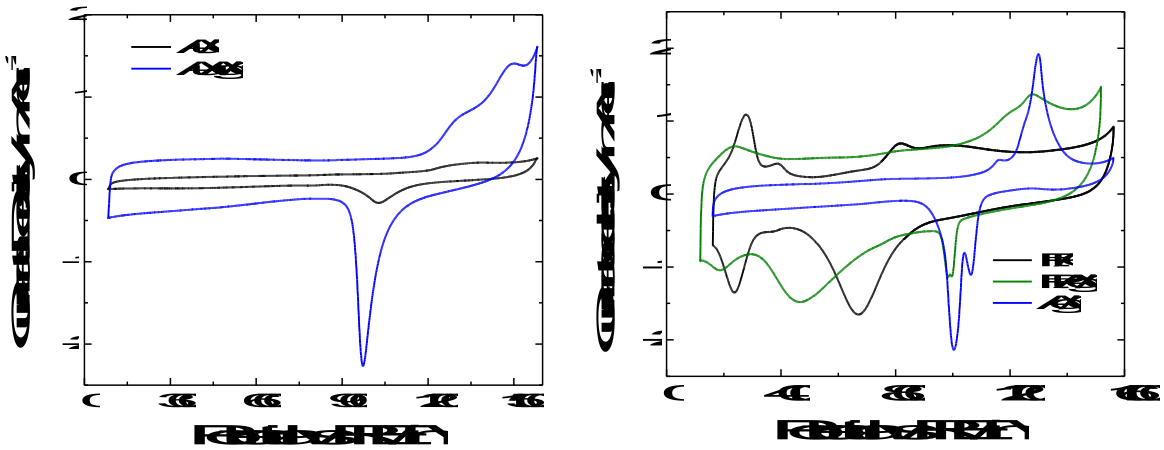

Figure 3. Voltammetric profile obtained in KOH 0.3 M at 20 mV s^{-1}

3.2.1 Glucose oxidation reaction

The response of AuAg/C for the glucose oxidation reaction was evaluated in presence of glucose 10 mM in basic media and compared to Au/C (figure 4). It is possible to observe a first signal in −225 and −380mV vs. RHE for Au/C and AuAg/C respectively, this process is related to the glucose oxidation to form gluconic acid [12, 13]. The AuAg/C electrocatalyst showed a negative shift ca. 150mV compared with Au/C for glucose electrooxidation. This observation point to that AuAg/C electrocatalyst favors the glucose electrooxidation as compared to Au/C. This behavior could be attributed to the interaction between bimetallic material and glucose. Yet, the mechanism of glucose oxidation involves adsorption of OH^- ions and this process is facilitated on Ag surfaces [14].

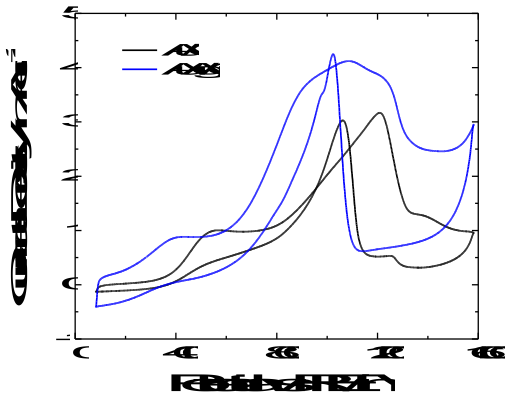

Figure 4. Cyclic voltammograms obtained on the Au/C and AuAg/C electrodes in 0.01M glucose + 0.3M KOH aqueous solution at 20mVs^{-1}.

3.2.2 Oxygen reduction reaction

To evaluate the catalytic activity of oxygen reduction reaction (ORR), polarization curves were obtained for the Ag/C, Pt/C and PtAg/C catalysts in 0.3 M KOH in an oxygen-saturated atmosphere using a rotatory disk electrode. The ORR curves for the PtAg/C, Pt/C and Ag/C catalysts are shown in Fig. 5 at 1600 rpm. The onset potential of the ORR is very similar for both Pt/C and PtAg/C (0.96 V vs. RHE), while the onset potential for Ag/C shows a negative shift of approximately 100 mV when compared with both Pt/C and PtAg/C. A higher current density is reached in the case of PtAg/C while using nearly 20% less loading than the Pt catalyst. These results show a better activity toward oxygen reduction reaction in an alkaline medium in the case of PtAg/C compared with Pt/C, which could be related to the synergistic relation between both metals as a bimetallic electrocatalyst.

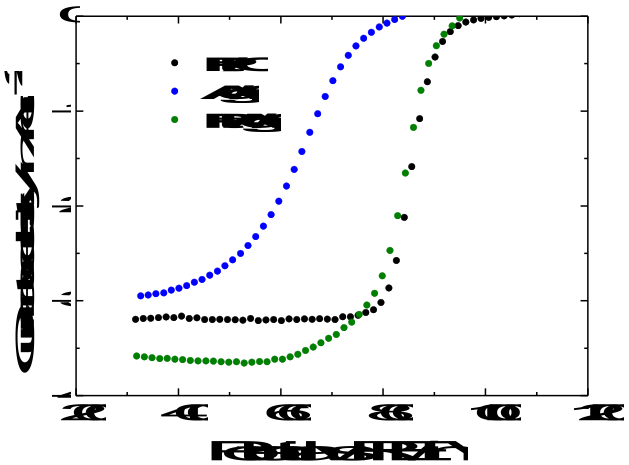

Figure 5. ORR polarization curves obtained in 0.3 M KOH under oxygen atmosphere.

3.4 Fuel cell tests

One fuel cell with PtAg/C (cathode) and AuAg/C (anode) was constructed and compared with a fuel cell with Pt/C (cathode) and Au/C (anode). The figure 6 show the performance of both cells with a solution of glucose 100 mM. The addition of silver allows a better performance at high concentrations of glucose. This result is attributed to tolerance to glucose for the cathode [6], and a better stability in the anodic side.

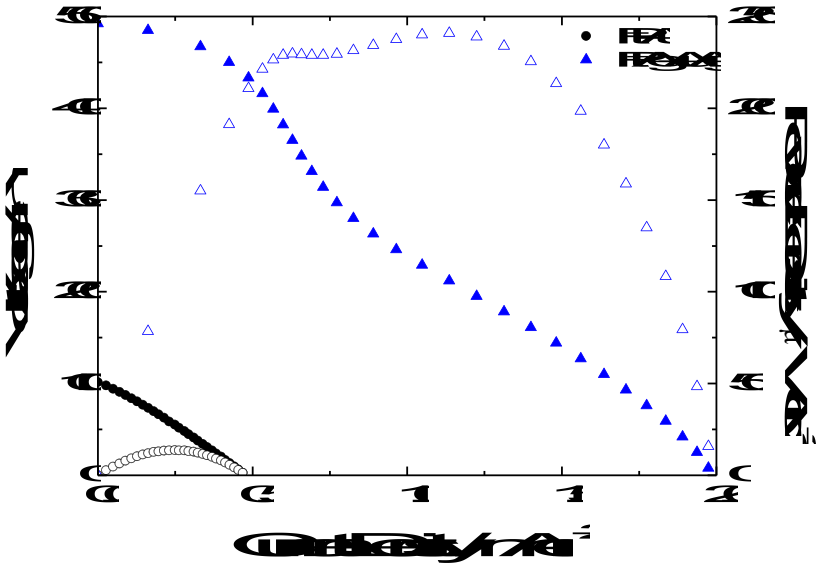

Figure 6. Discharge curves for monometallic and bimetallic microfluidic fuel cell.

4. Conclusions

The use of bimetallic alloy based in silver in catalysts for fuel cells can help the performance of this devices. In the case of glucose oxidation, the addition of silver reduce the potential of oxidation. For the oxygen reduction, the silver addition maintains the performance of the catalyst. Also the use of silver reduce the cost involved in the catalyst fabrication process.

5. Akcnowledgements

The authors to CONACYT for the economic support to this investigation.

6. References

[1]M. Guerra-Balcázar, D. Morales-Acosta, F. Castaneda, J. Ledesma-García, L.G. Arriaga, Electrochem. Commun. 12 (2010) 864.
[2] J. Ryu, H.-S. Kimb, H. Thomas, D. Lashmore, Biosens. Bioelectron. 25 (2010) 1603.
[3] C. Jin, I. Taniguchi, Mater. Lett. 61 (2007) 2365.
[4] A. Zebda, L. Renaud, M. Cretin, C. Innocent, F. Pichot, R. Ferrigno, S. Tingry, J. Power Sources 193 (2009) 602.
[5] F.M. Cuevas-Muñiz, M. Guerra-Balcázar, F. Castaneda, J. Ledesma-García, L.G. Arriaga, J. Power Sources 196 (2011) 5853.

[6] M. Guerra-Balcázar, F.M. Cuevas-Muñiz, L. Álvarez-Contreras, L.G. Arriaga, J. Ledesma-García, Journal of Power Sources 197 (2012) 121.

[7] M. Guerra-Balcázar, D. Morales-Acosta, F. Castaneda, J. Ledesma-García, L.G. Arriaga, Electrochem. Commun. 12 (2010) 864.

[8] N.N. Kariuki, J. Luo, M.M. Maye, S.A. Hassan, T. Menard, H.R. Naslund, Y. Lin, C. Wang, M.H. Engelhard, C.-J. Zhong, Langmuir 20 (2004) 11240.

[9] J.B. Xu, T.S. Zhao, Z.X. Liang, J. Phys. Chem. C 112 (2008) 17362.

[10] F.H.B. Lima, E.A. Ticianelli, Electrochim. Acta 49 (2004) 4091.

[11] M. Tominaga, T. Shimazoe, M. Nagashima, H. Kusuda, A. Kubo, Y. Kuwahara, I. Taniguchi, J. Electroanal. Chem. 590 (2006) 37.

[12] M. Tominaga, M. Nagashima, K. Nishiyama, I. Taniguchi, Electrochem. Commun. 9 (2007) 1892.

[13] M. Tominaga, M. Nagashima, K. Nishiyama, I. Taniguchi, Electrochem. Commun. 7 (2005) 189.

[14] V.A. Marichev, Electrochim. Acta 43 (1998) 2203.

Theoretic-Experimental Study of Pd-based Electrocatalysts for Fuel Cells

G. Ramos-Sánchez ǂ, R. Grande-Atzatzi, O. Solorza-Feria*, A. Vela

[1]Depto. Química, Centro de Investigación y de Estudios Avanzados del IPN,
Av. Instituto politécnico nacional No. 2506. Col. San Pedro Zacatenco 07360 México D.F.
*Tel: (+52) 55 57473715, ǂ mail: gramos@cinvestav.mx

ABSTRACT

The electrochemical oxygen reduction reaction (ORR) was analyzed by both theoretic and experimental methods, the objective of this project is to elucidate the factors controlling the observed activity and be able to design electrocatalysts ad hoc with high activity and stability. Three electrocatalysts were studied: Pd, PdNi and PdSe. For the theoretical study was used DFT as implemented in the deMon 2K software, oxygen adsorption was calculated in a four atoms cluster and then reduction steps were calculated. In this study we found that there are remarkable differences in the adsorption process for example: The oxygen adsorption energy is higher in PdNi followed by Pd and very low in PdSe, the preferred type of oxygen adsorption is bridge on Pd and PdNi however in PdSe the preferred adsorption is 1-hapticity on a single Pd atom. The experimental study demonstrate high activity towards the ORR when PdNi is used as catalyst, lesser for Pd and very low activity for PdSe, it was also demonstrated high hydrogen peroxide production on PdSe and low production on Pd and PdNi.

The theoretical and experimental results match very well correlating the Oxygen adsorption with the electrochemical acivity and the species formed during the simulation with the ORR mechanism.

1. Introduction

As electrochemical devices that directly convert fuels into electricity, fuel cells have some intrinsic properties that made them very attractive. Some of them are high energetic efficiency, no pollutants emission, noiselessly operation and modular capacity [1]. However, intensive research is needed to find better catalyst able to drive the normally slow Oxygen Reduction Reaction (ORR) kinetics [2].

Many approaches have been proposed in order to eliminate or decrease the use of platinum in fuel cells, platinum alloys or core shell compounds [3-4], palladium alloys or Pd/Pt core shell [5,6], Ru chalcogenides [7] and non-noble compounds [8,9] The challenge of produce new catalyst is difficult, it isn't easy to find a new material whit high catalytic activity, high selectivity, high stability and durability and for sure lower price [10].

It is undoubtedly that theoretic studies have helped to deeper understanding of the process occurring in fuel cells and also have served as start point for electrocatalyst synthesis [11-12]. Beyond the theoretical approach have been reported other studies in which the theoretical approach is carried out together with experimental studies [13-14].

In this work extensive electrochemical and first studies on theoretic Oxygen reduction in Pd, PdNi and PdSe, materials that has been proposed as catalyst for use in the cathode of low temperature fuel cells.

2. Experimental

2.1 Synthesis and physicochemical characterization

Pd and PdNi were synthesized by a widely reported reduction process [15]. Briefly 0.11 mmol $PdCl_2$ were dissolved in 100 ml THF and flurried during 24 h, after that 0.22 mmol $NaBH_4$ were quckly added and flurried during 0.5 h. The obtained powder was decanted washed with water and dried in N_2 atmosphere at 70 C during 6 h. The same procedure was used for the PdNi synthesis, except with the addition of 0.11 mmol $NiCl_2$ and double solvent amount. The PdSe compound was synthesized by the decomposition of a $Pd_x(CO)_y$ compound in the presence of Se at 230 C in 1,6 hexanediol. The obtained powder was decanted, washed thoroughly with ethyl-ether and dried.

The synthesized compounds were analyzed by Transmission Electron Microscopy (TEM) with a JEOLJEM 1200 EXM microscopy operated at 1200 kV and 70 μA. X-Ray diffraction (XRD) was used to analyze phases, an D8 Advance equipment from Brucker was used with CuKα (λ=0.154056 nm) from 30 to 90° in 2θ, the composition was analyzed with an Energy dispersive X-ray (EDX) Genesis 4000 equipment.

For the electrochemical experiments an ink with the catalytic material was prepared and deposited onto a 3mm diameter glassy carbon with Teflon® holder electrode. The ink was prepared by mixing 1 mg of the synthesized material and 1 mg of carbon Vulcan® then was added 6 μl of Nafion® at 5% (Aldrich) and 50 μl of isopropyl alcohol. The mixture was sonicated during 15 min, 2 μl of the resulted suspension was collocated on the exposed carbon surface of the electrode. For the experiments a classic three electrode array was used, the work electrode prepared as previously stated, a Pt mesh as counter-electrode, and a Hg/Hg_2SO_4/0.5 M H_2SO_4 reference electrode

(0.68 V vs NHE). H_2SO_4 0.5 M was used as electrolyte and during the experiments N_2, O_2 or CO was bubbled in the electrolyte.

2.2 Theoretic study

All the calculations were made with the functional density theory (DFT) and the lineal combination of Gaussian type orbitals to solve the Khon-Sham Equations as implemented in the demon 2k software version 2.4.4 [16]. The geometry optimization was done within the approximation of generalized gradient approximation (GGA) with the exchange-correlation functional of Perdew-Becke-Ernzerhoff (PBE) [17].

For the ORR simulation a metallic cluster was used as the catalyst and different intermediates of the ORR were induced to interact with the cluster (O_2, OH, OOH, H_2O_2 and H_2O). The analyzed clusters were Pd_4, Pd_2Ni_2, and Pd_2Se_2 in different electronic states. For H,O and Se the double ξ orbital with polarization functions base was used, for Pd the 18 electrons pseudopotential and quasirelativistic ECP|SD base from Stuttgart-Dresden was used, and for Ni the pseudopotential and non-relativistic base ECP|SD base was used. All optimizations were done without symmetry constrains unless otherwise stated.

3. Results and discussion

The structural parameters of the three compounds are resumed in Table 1. Images and spectra are available in the supplementary information.

Table 1. Structural parameters of Pd, PdSe and PdNi compounds.

Electrocatalyst	Particle size (TEM) / nm	Crystallite size / nm	Composition (EDX)
Pd	4	7	100
PdNi	4-10	9	37:62
PdSe	20	10	51:49

The obtained electrocatalyst powder show agglomeration because of the lack of support, however the formation of nanometric particles is evident by booth microscopic and diffraction experiments. The XRD diffractogram corresponds in the case of Pd and PdNi to the diffraction peaks of Pd fcc, in the case of PdNi those peaks are shifted towards more positive values in 2θ, indicating the formation of the PdNi alloy. For PdSe the XRD experiment revealed many intermetallic compounds with different stocquiometry that has been up to now impossible to identify or isolate. The calculated composition is very close to that expected for PdSe but very different in PdNi in which there is a high quantity of Ni in the alloy.

The electrochemical characterization showed specific current-potential behavior for every electrocatalyst. Cyclic voltammetry was performed in nitrogen saturated electrolyte (Fig 1), the voltage scan start in the open circuit

potential (~ 0.8 V) in anodic direction to 0V, followed by the cathodic scan up to 1.4 V. The voltagramm for Pd has been widely reported [18] in the figure 1 this behavior is observed, the hydrogen adsorption-desorption process (0-0.3V), the process of formation of oxides and de subsequent reduction in a peak at 0.6 V. The voltagramm of PdNi is very similar to that of Pd, however is remarkable that the peak reduction is shifted towards more postive potentials 0.7 V indicating an easier reduction process. For the PdSe electrocatalyst the voltagramm is very different, the hydrogen adsorption-desorption process is completely absent, the reduction of oxides is now shifted but to more negative potentials (0.52 V) indicating a more difficult reduction process.

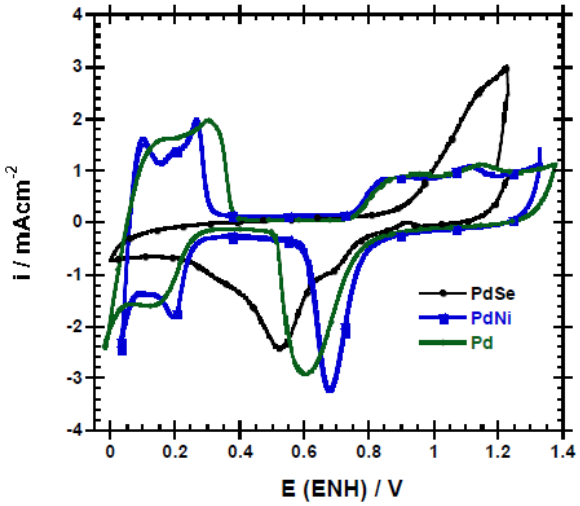

Figure 1. Cyclic voltagramm of Pd, PdNi and PdSe. ν=50 mVs^{-1} in H_2SO_4 0.5 M saturated with Nitrogen.

The kinetic of the ORR was studied by RDE experiments, this experiment was done in oxygen saturated electrolyte with electrode rotating from 100 to 2500 rpm and very slow voltage scan (ν=5 mVs^{-1}). The resulted data were corrected to eliminate the mass transfer process following the procedure described by Levich [19], in order to construct the Tafel plots for the electrocatalyst PdNi (Fig. 2a) and PdSe (Fig. 2b), booth figures compare the electrocatalyst with Pd in order to observe the differences.

The Tafel plots of PdNi indicate a more positive open circuit potential as well as higher current at the same potential on the other hand, for PdSe the open circuit potential is lesser positive and is needed a high overpotential to reach the same current density. In other words the catalytic activity is higher for PdNi and lower for PdSe in comparison with that presented by Pd. This result could be related also with position of the reduction of oxides in the cyclic voltammetry.

Rotating Ring disk electrode experiments showed a high hydrogen peroxide production on the PdSe electrocatalyst. In Pt and Pt-based electrocatalyst the peroxide production is very low <2%, which indicates that because of the

presence of Se, probably the oxygen adsorption is very weak, leading a very O-O bond which originates a high peroxide production as it has been probed in the oxygen reduction with gold electrodes [20].

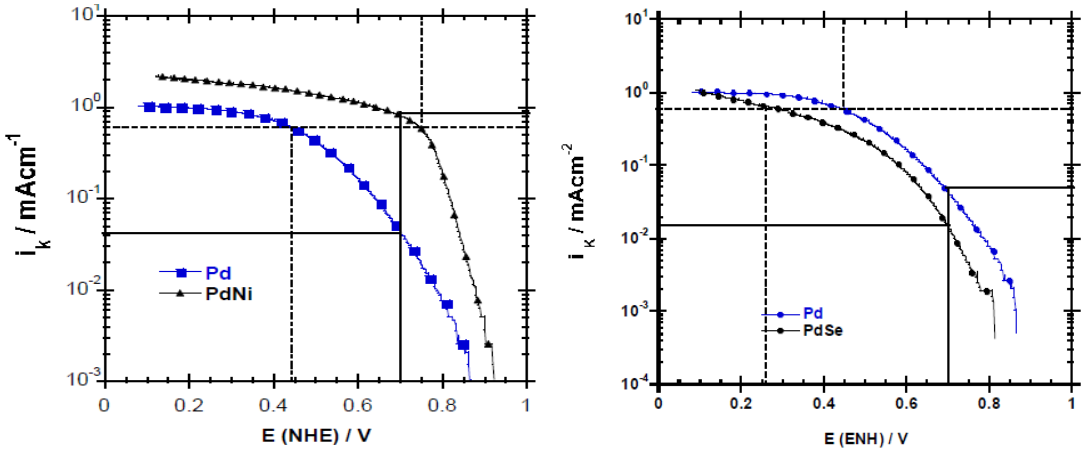

Figure 2. Mass transfer corrected Tafel plots for a) PdNi and b) PdSe. Plots made from de RDE experiments.

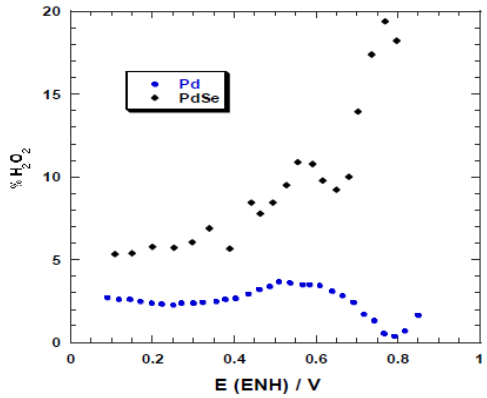

Figure 3. Hydrogen peroxide production versus potential, from RRDE experiments. Catalytic ink in the disc with voltage scan from ocp to 0V, ν=10 mVs^{-1}. Gold ring at 1.4 V, in H_2SO_4 0.5 M.

The electrochemical experiments have helped to the characterization and deeper understanding of the processes happening in the different electrocatalyst; however up to now it doesn't give any clue about the way to synthesis a better catalyst. This study up to now just give us the intrinsic properties of the catalysts, to give the next step we decided to study the ORR by theoretical methods.

The approach for the simulation of the solid is the cluster one. In table 2 we report the optimized clusters used for the simulation as well as some energetic and structural data. The optimization procedure consisted in find the lower energy structure for different conformations and multiplicities. It is easily observed that the PdNi cluster retains the

connectivity of the Pd cluster but enlarging the Pd-Pd bond length and shorting the PdNi bond length. The lowest energy structure corresponded to a multiplicity of 3 in the three cases.

Table 2. Clusters used for the ORR simulation. Blue balls Pd, green Ni and Se in yellow.

Electrocatalyst	ΔDis / kcalmol^{-1}	ε_{coh} / kcal mol^{-1}	HOMO-LUMO / kcalmol-1	Bond ength⁄ Å
	155.7	39.4	35	PdPd: 2.57 PdPd:2.63
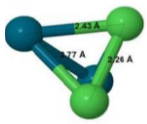	191.2	47.8	27.5	PdPd:2.77 NiNi:2.26 PdNi:2.43
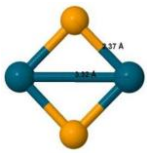	216.2	54.1	24.49	PdPd:3.32 SeSe:3.39 PdSe:2.37

Energetic data as dissociation energy (ΔDis) and cohesive energy (ε_{coh}) are calculated according to the procedure reported by Ahlrichs [21], those values the stability of the cluster, as the dissociation energy rises is more difficult to break the cluster away, the same applies for the cohesive energy. In this sense the new bimetallic clusters have higher stability which represents advantages for its use in the very reactive environment present in fuel cells. The HOMO-LUMO is reported because some authors [22] have speculated that this parameter is linearly related to the catalytic activity, speculation that is not observed in this study.

Once the lower energy clusters are obtained they are used for the adsorption of oxygen. Many structures are possible owed to the different adsorption sites, geometries and multiplicities, however the lower energy structure is searched and reported in table 3. The lowest energy structure suggests that that is the specie that is likely to exist, however other species could also be formed because they are minima in the process. A molecular dynamic study is needed and would complete the methodology proposed in this work.

For the oxygen adsorption the lowest structure corresponds to a bridge adsorption, the same is observed for the PdNi cluster; however, the oxygen is preferred bonded to the Ni atoms. In the PdSe cluster, in the other hand, the most stable adsorption site a single Pd atom single-coordinated to an oxygen atom. All structures correspond to a triplet, however the energetic differences are remarkable: a very low adsorption energy for oxygen on PdSe and high adsorption energy on the PdNi cluster. This trend was observed in the experimental studies which indicate that this parameter is related to the catalytic activity as it's been proposed by many authors [13, 23-24].

Table 3. Oxygen adsorption properties on Pd clusters. Pd in blue, Ni in green, Se in yellow and oxygen in red..

Adsorption geometry	Adsorption energy / kcal mol^{-1}	Bonde lenght / Å
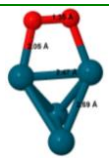	-31.04	PdPd: 2.47 OO: 1.35 PdO: 2.05
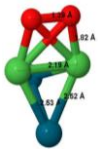	-48.7	NiNi: 2.19 OO:1.39 ONi:1.82 PdPd:2.53
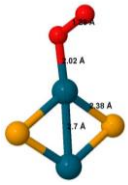	-22.6	PdPd:2.7 OO:1.28 PdO:2.02

The full optimization from oxygen to water or hydrogen peroxide was accomplished for every multiplicity and cluster; however of interest fundamental is the ORR mechanism. It was found that is possible to elucidate the preferred mechanism with the calculation of the stability of the specie (OOH) related to that of the (O)(OH) species. If the direct mechanism toward the formation of water is the main mechanism then the (O)(OH) species will be formed and will be more stable than (OOH); however if the peroxide production is the preferred mechanism, then the (OOH) will be preferentially formed. The electronic energy difference for those process in Pd is 12.43 $kcalmol^{-1}$, for PdNi this difference is 34.5 kcalmol-1, which indicates that there is a lesser probability for the formation of peroxide. On the other hand for PdSe, the only stable specie is (OOH) which indicates that the preferred mechanism is the formation of hydrogen peroxide which agrees well with the electrochemical characterization.

4. Conclusions.

In this work theoretical and experimental methods were utilized to study the Oxygen reduction reaction on different Pd-based compounds. The PdNi catalytic activity is higher than that of Pd, the measured kinetic current is an order of magnitude greater than that of Pd at 0.7V, and is related to the easiest oxide reduction observed by cyclic voltammetry, the molecular simulation reflects that the oxygen adsorption energy is greater and is responsible of the

measured kinetic. For PdSe in the opposite a lower catalytic activity is measured, this is attributed to the very weak oxygen adsorption energy, this weak adsorption process is also responsible for the formation of a high quantity of hydrogen peroxide.

More than the evident congruence between the theory and experiments, this work serves as start point for future studies. The theoretic methods now could be made previously to the synthesis and electrochemical characterization and then previously know the kinetic and mechanism by comparing the values of oxygen adsorption and (OOH) stability with other catalyst like Pd or Pt.

The theoretic model is simple, but correlate well with the experimental. However increasing the theory level and including factors like solvent interaction, cluster size and electrochemical potential will permit better and more quantitative comparison.

5. Acknowledgements

The support of CONACYT by means of doctoral fellowship to GRS is gratefully acknowledged. The financial support for this work was provided by CONACYT and ICyTDF.

6. References

[1] W. Vielstich. Handbook of Fuel Cells Fundamentals Technology and Applications V.2., Jhon Wiley & Sons, West Sussex (2003).

[2] S.M. Duron Torres Pilas de Combustible: principios y perspectivas. In: Gonzalez-Huerta RG, Lopez Chavez E, Velazquez Morales B, editores. Hidrogeno, Introduccion a la energia Limpia, Mexico: Universidad Autonoma de La Ciudad de Mexico; (2009)

[3] H. Zhu, X. Li, F. Wang. Int J Hydrogen Energy, 36, 9151 (2011).

[4] V.R. Stamenkovic, B.S. Mun,M. Arenz,K.J.J. Maryhoffer, C.A, Lucas, G. Wang, P.N. Ross , N.M. Markovic. Nature,6, 241 (2010):

[5] P. Mani, R. Srivastava, P. Strasser. J Power Sources, 196, 666 (2011).

[6] V.L. Nguyen, M. Ohtaki, T.D. Hien, J. Randy, M. Nogami. Elecytrochim Acta, 56, 9133 (2011).

[7] K. Suarez-Alcantara, O. Solorza-Feria O. J Power Source2, 192,165 (2009).

[8] L. Wang, L. Zhang, J. Zhang. Electrochem Acta 56, 5488 (2011).

[9] X. Li, G. Liu, B.N. Popov. J Power Sources 195, 6373 (2010)

[10] H.A. Gasteiger, S.S. Kocha, B. Sompalli, F.T. Wagner. Appl Catal B Environment 6, 9 (2005)

[11] Y. Suga. Chem Lett., 35,1406 (2006)

[12] A.B. Anderson, T.V. Albu. J Electrochem Soc., 147,4229 (2000)

[13] V. Stamenkovic V, B.S. Mun, K.J.J. Maryhofer, P.N. Ross, N.M. Markovic, J. Rossmeisl, J. Greeley,J.K. Norskov. Angewandte Chem., 45,2897 (2006).

[14] P. Rodriguez, N. Garcia-Araez, A. Koverga, S. Frank, M.T.M. Koper. *Langmuir* 26, 12425 (2010)

[15] G. Ramos-Sanchez, O. Solorza-Feria O. Int J Hydrogen Energy 35,12105 (2010)

[16] Koster AM, Calaminici P, Casida ME, Flores-Moreno R, Geudtner G, Goursot A, Heine T, Ipatov A, Janetzko F, Campo JMD, Patchkovskii S, Reveles JU, Salahub DR, Vela A, 2.3.1 ed. deMon developers: 2006.

[17] J. P. Perdew, K. Berke, M. Ernzerhof. Phys Rev Lett., 77,3865 (1996).

[18] J.J. Salvador-Pascual, S. Citalan-Cigarroa, O. Solorza-Feria. J Power Sources 172,229 (2007).

[19] L. Sung-Jai, P. Su-Il, L. Sang-Kwon , K. Suk-Joong. Isr J Chem., 48,215 (2008)

[20] G. Vazquez-Huerta, G. Ramos-Sanchez, A. Rodriguez-Castellanos, D. Meza-Calderon, R. Antano-Lopez, O. Solorza-Feria. J Electroanal Chem., 645, 35 (2010).

[21] P. Nava, M. Sierka, R. Ahlrichs, *Physical Chemistry Chemical Physics 5,3372 (*2003).

[22] T.J. Dhilip Kumar, C. Zhou, H. Cheng, R.C. Forrey, N. Balakrishnan. J chem. Phys., 128, 124704 (2008).

[23] Y. Wang, P. Balbuena. J Chem Theory Comput., 1,935 (2005).

[24] P.B. Balbuena, D. Altomare, N. Vadlamani, S. Bingi, L.A. Agapito. J Phys Chem A, 108,6378 (2004)

Hydrogen Generation in a Microbial Electrolysis Cell (MEC) using two configurations: Catalyzed by Platinum and Biocathode

Limberg Alejandro Gómez Roque [a*], Jorge A. Domínguez Maldonado [a], Liliana Alzate Gaviria [a]

[a] Unidad de Energía Renovable del Centro de Investigación Científica de Yucatán (CICY). C.43 No. 130 Col. Chuburná de Hidalgo
97200, Mérida, Yucatán, México.
[*] Tel. (999) 9428330 Ext. 321. mail: limbergberik@cicy.mx

ABSTRACT

Microbial Electrolysis Cells (MEC) are biological devices that offer a new way to produce hydrogen electrolyzing any type of organic matter by the action of electrochemically active microorganisms and an external potential (between 0.22 and 1 V). The MEC require a catalyst to form hydrogen, being platinum the most widely used in these devices. However, platinum is expensive and performance may decrease (poisoning) when it is exposed to compounds such as CO, CO_2 and sulfides. In the present study two types of catalysts were used: platinum (MEC Pt) and a biocathode using a technique that was allowed to reverse the reaction of hydrogenase enzymepresent in the electrochemically active microorganisms, so it was possible to convert a bioanode to biocathode hydrogen generator (MEC b). MEC Pt (0.5 mg/cm^2, 10% Pt / C) generated H_2 0.032 m^3 / m^3 of liquid reactor volume / day at a potential of 0.9 V and MEC b generated H_2 0.010 m^3 / m^3 liquid volume reactor / day at a potential of 1 V.

1. Introduction

The Microbial Electrolysis Cell (MEC) are a novel biological device which is capable of "electrolyser" any biodegradable substrate such as organic matter present in wastewater and convert it directly to hydrogen and CO_2 [1]. The electrolysis of organic matter in a CEM is achieved by a consortium of electrochemically active microorganisms which are capable of transferring electrons across its metabolism to an anode (called bioanode). In this way, electrons can be directed to a cathode through an external circuit, however, the electromotive force is not sufficient for this flow takes place, so it is necessary to apply an auxiliary potential through an power source. While the flow of electrons released from the anode to the cathode occurs, an equal number of protons produced during the metabolism of microorganisms permeate through a proton exchange membrane, reduced at the cathode in the presence of a catalyst to form molecular hydrogen (Figure 1). Thus, the microbial electrolysis can be carried out with potential applied between 0.22 V to 1 V [2].

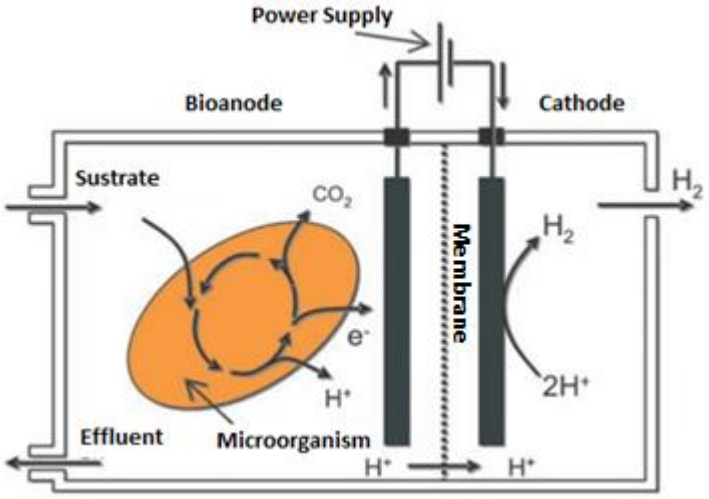

Figure 1. Schematic representation of hydrogen production by Microbial Electrolysis Cell [3].

One of the greatest challenges in the investigation of MEC systems is present in the cathode catalyst. MECs generally operate with platinum as a catalyst, since it has been proved very effective in other systems like the conventional fuel cell. However, the fuel cells operating at current densities around 10^3 to 10^4 A/m^2, which are greater than MEC (between 1 and 10 A/m^2) [4]. So, the production of current is too low to justify the use of expensives catalyst. Within this scenario, biocathodes are a viable option as they promise to be applied in the MECs with relatively inexpensive materials using electrochemically active microorganisms.

The strategy to achieve biologically cathodic reactions is mainly based on the reversibility of the hydrogenase enzyme [5]. The hydrogenase is widely distributed in anaerobic microorganisms. It produces hydrogen both irreversible and reversibly, depending on environmental conditions, being reversible only under strict anaerobiosis [6]. It is known that the reaction catalyzed by the hydrogenase is:

$$H_2 \leftrightarrow 2H^+ + 2e^- \quad (1)$$

In 2008, Rozendal et al. [4] developed a biocathode obtaining it from the electrochemical conversion of a graphite cloth bioanode with electrochemically active microorganisms (not identified yet). The procedure to form the biocathode was to change the polarity of bioanode, manipulating substrate conditions in the MEC to force microorganisms to generate cathodic currents.

The aim of this study is to develop a CEM system with anodic and cathodic reactions catalyzed by electrochemically active microorganisms and compare its performance with a platinum cathode MEC.

2. Experimental procedures.

The MECs were constructed of two polymethylmethacrylate chamber with a working volume of 0.57 L each, separated by a Nafion ® 117 membrane with an area of 22.2 cm^2 (Figure 2). The anode and cathode were made of graphite cloth with an area of 32 cm^2 (Figure 3) [7, 8, 9]. The cathode was prepared with 0.5 mg/cm^2 of platinum (10% Pt / C) and biocathode was obtained by reversing the polarity of an active bioanode [4].

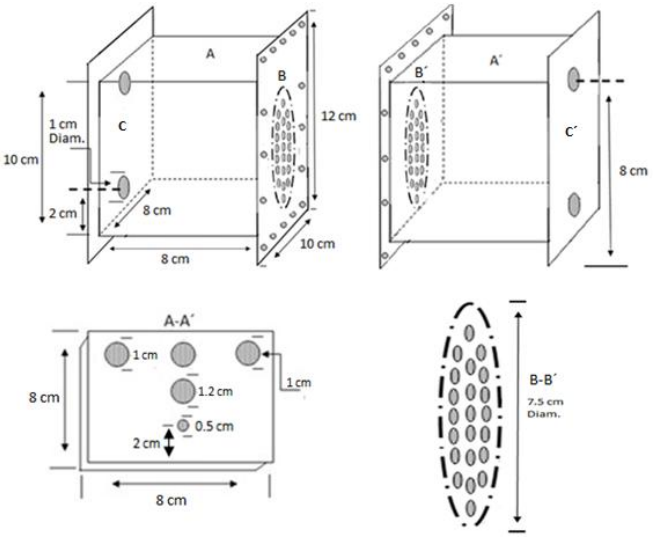

Figure 2. MEC scheme used in this study. (A-A ') Covers with 3 holes of 1 cm diameter each for sampling and gas output, 1 hole of 1.2 cm diameter to place the reference electrode and a 0.5 cm hole for the cable electrode outlet. (B-B ') Membrane support with an O-ring of 7.5 cm diameter. (C-C ') 2 holes of 1 cm diameter for input and output of nutrients.

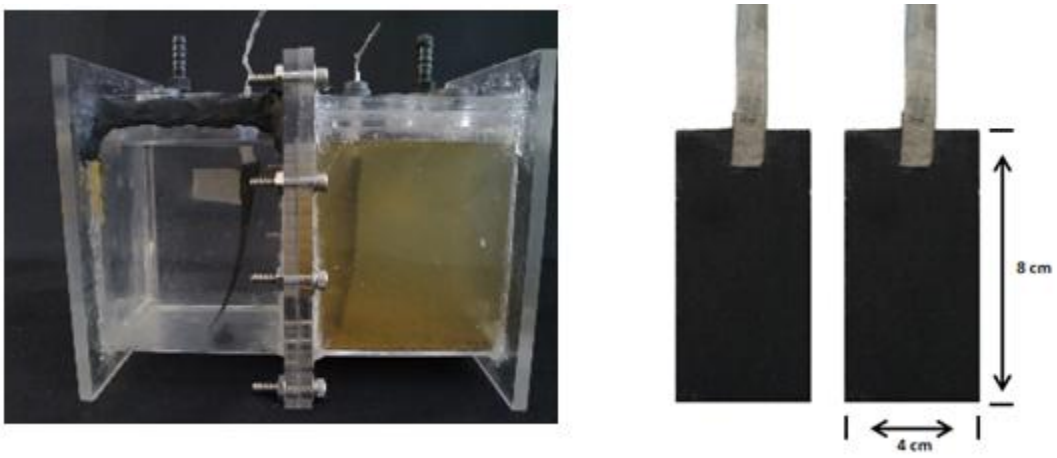

Figure 3. Photograph of the prototype of this study (left) and carbon cloth electrodes held by stainless steel mesh as wire (right).

The MECs had the following nomenclature and function. **CEM b:** Used for the formation of biocathode. It began with a conventional cathode (0.5 mg Pt/cm^2) and then was replaced by an active bioanode from CEM Reserve.**CEM Pt:** MEC formed with a Pt cathode (0.5 mg Pt / cm ^{2}) for comparative purposes to CEM b. **Control:** MEC

uninoculated and without catalyst**. CEM Reserva:** It was used to get a bioanode for CEM b during biocathode formation process.

2.1 Substrate and inoculum

The following nutrient medium was prepared for the anode chamber: 0.74 g / L KCl, 0.58 g / L NaCl, 0.68 g / L KH_2PO_4, 0.87 g / L K_2HPO_4, 0.28 g / L NH_4Cl, 0.1 g / L $MgSO_4 \cdot 7H_2O$ and 0.1g / L $CaCl_2 \cdot 2H_2O$. 12.14 mM of $NaCH_3COO$ was added as carbon source in CEM Pt anode chamber [4, 10], while in the cathode chamber was phosphate buffer at a concentration of 50mM. During the biocathode formation process in CEM b, $NaCH_3COO$ was replaced by 10 mM $NaHCO_3$. The inoculum used in the anode was 100 mL of a mixed microbial consortium described by Alzate et al. (2010) [11]. The pH in all MECs was maintained at 7.

2.2 Characterization and measurement of the gas generated

To measure the gas generated was used a flow meter (Ritter MilligasCounter ® MGC-1) (Figure 4).

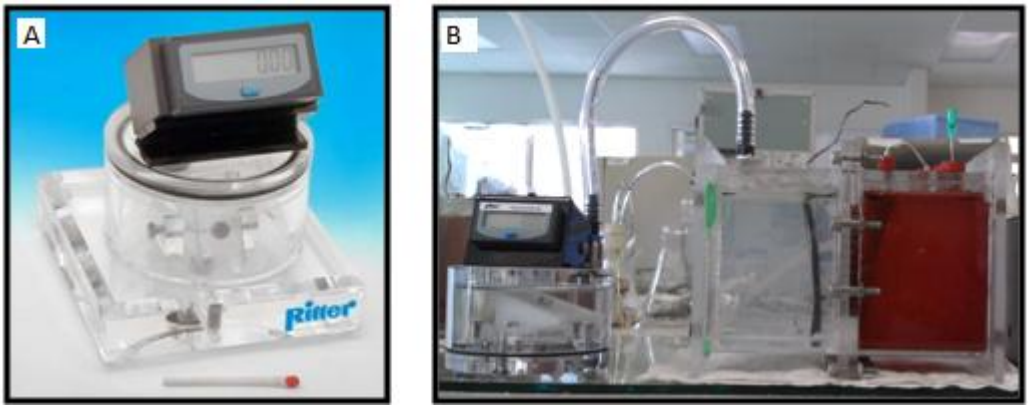

Figure 4. (A) MilligasCounter ® MGC-1 and (B) MilligasCounter ® coupled with CEM Pt.

For the gas characterization the samples were analyzed on a gas chromatograph Perkin Elmer Clarus 500 ® equipped with a thermal conductivity detector (TCD) using a Molsieve column (30 mx 0.53 mm packed) and nitrogen as carrier gas. The volume of H_2 in all the gas (Vt) was determined from [12]:

—— (2)

Where "$V_{E,t}$" (mL) is the expected volume of H_2 based on the load (C), "F" is the Faraday constant (96.485 C / mol), "C_t" is the Coulombs generated and V_M is the molar volume of gas (25.000 mL / mol at 28 ° C).

Cathodic hydrogen recovery (r_{Cat}) was calculated based on the volume ratio of hydrogen obtained experimentally (Vt) between the expected volume of hydrogen ($V_{E,t}$)

The hydrogen production rate (Q) was expressed in m^3 of H_2 generated / m^3 of liquid reactor volume / day ($m^3/m^3/d$) according to Logan et al. (2008) [13]:

(3)

Where "I_V" is the volumetric current density (A/m^3) based on the volume of reactor operation, "T" is the temperature (K) and "r_{Cat}" cathodic hydrogen recovery.

2.3 Electrochemical Analysis

The applied potential was carried out with a adjustable power supply from 0 to 5 V with intervals of 0.01 V (Instrumentation Department CICY, Merida, Yucatan, Mexico) and a potentiostat BioLogic ® SAS VSP 400.
Cyclic voltammetry and cronoamperometry was performed, also were obtained polarization curves and measurements of anodic potential. In all tests were used calomel reference electrode (+0.244 V vs SHE) and a platinum wire Premion ® 8 cm long and 0.5 mm thickness with a purity of 99.997% as auxiliary electrode. All potentials were expressed against the standard hydrogen electrode (SHE).

2.4 Startup and Operation

The MECs were fed every 24 hours with 100 ml of nutrient and carbon source, for CEM Pt was sodium acetate and for the CEM b sodium bicarbonate. Furthermore 0.9 V was applied in CEM Pt and 0.9 and 1 V in CEM b. The applied potentials of MECs were based on the polarization curves, by selecting those with higher current densities. The operating temperature for all MECs were 28 ± 2 ° C.

CEM Pt started with 12.14 mM of sodium acetate every 24 h and a potential of 0.9 V for 4 months. The air was displaced from the entire MEC with N_2 (Praxair, 99.999%) over 20 minutes and was completely sealed to maintain anaerobic conditions [14, 15, 16].

The CEM b started from 100 mL from the anode chamber of CEM Pt after 4 months of operation. CEM b operated for 3 months, 1 month for the biocathode formation and 2 months for operation as catalyzed by biocathode at 0.9 and 1 V. The H_2 supply was made by a metal hydride tank 20L (Udomi Fuel Cells ®) [4].

Reversing the polarity of bioanode in CEM b was as follows: **Stage 1**. Hydrogen was supplied to the chamber of bioanode (bioelectrode) at 40 mL / min for the adaptation of microorganisms to H_2 oxidation [17]. During this stage preliminary tests were performed by applying a potential of +0.34 V to the bioanode (vs. SHE) for one week and then changed to +0.1 V [4]. The carbon source was 12.14 mM sodium acetate every 24 h. **Stage 2**: When the current density was maintained constant, -0.2 V (vs. SHE) was applied on the bioelectrode and subsequently sodium acetate was removed from nutrient medium and replaced with 10 mM sodium bicarbonate every 24 h as inorganic carbon source [4.]. **Stage 3**: H_2 feeding was discontinued and then a linear sweep of -0.2 to - 0.8 volts at a rate of 0.025 mV /s was performed in order to observe the specific potential where the cathodic currents are generated. Finally, we applied the potential obtained from línear sweep to obtain the biocathode. At this point the original CEM b cathode was replaced by a bioanode from CEM Reserva. The feeding was 10 mM of sodium bicarbonate every 24 h [4]. A representative figure of the process is shown in Figure 5.

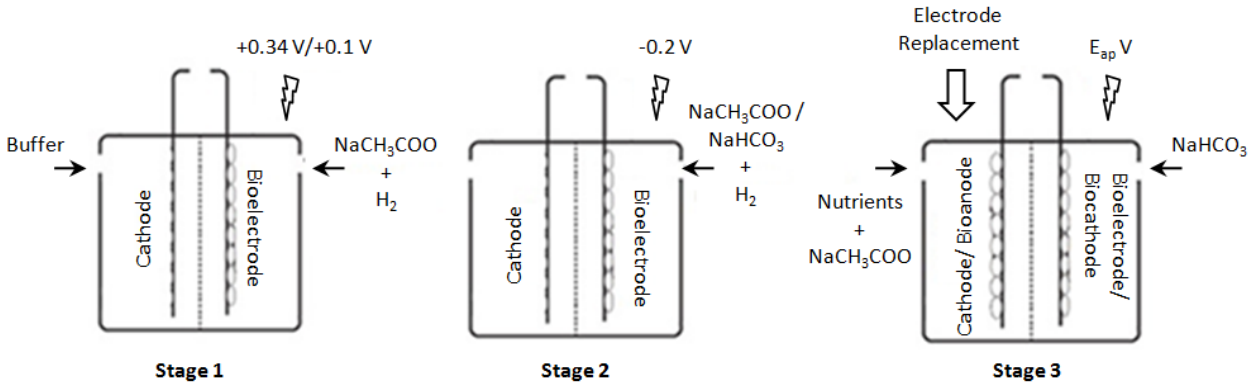

Figure 5. Process of biocathode creation in CEM b.

Once the CEM b catalyzed by biocathode was obtained, 0.9 V was applied to the whole MEC for one month and then increased to 1 V for another month. After that, we compared the current densities and volumes of hydrogen generated against to CEM Pt [10].

3. Results and discussion

The generation of H_2 in the CEM Pt at a potential of 0.9 V started at 24 hours, noticing the typical H_2 bubbling at the cathode. CEM Pt generated a current density of 2 A/m^2, yielding 27 mL H_2 / day (0032 m^3/m^3/d). The concentration of H_2 at the cathode was 38%, while the methane represented less than 1%.

The hydrogen generated experimentally accounted 52% of the total that may form in MEC per day (cathodic hydrogen recovery), while the rest (48%) was probably lost due to leaks in the system or by diffusion towards the anode through the membrane [2].

CEM Pt production was low compared with other platinum catalyzed MEC, like Cheng et al. (2007) with 1.1 m^3/m^3/d at 0.6 V [9] or Tartakovsky et al. (2009) with 6.32 m^3/m^3/d at 1 V [18]. This probably was due to leakage of gas or converting it to other undesirable gases such as CH_4 by methanogenic microorganisms [2]. This is reflected in the percentage recovery of hydrogen in the MEC cathode.

CEM b generated a current density of 0,032 A/m^2 producing 0.07 mL H_2/day, with concentration equal to CEM Pt, 38%. The CEM b performance was improved when the potential was increased to 1 V, the results are shown in Table 1.

Table 1. Results obteined in CEM b and CEM Pt.

MEC	Applied Potential (V)	Current Density (A/m^2)	V_t (mL/d)	$V_{E,t}$ (mL/d)	r_{Cat} (%)	Q (m^3/m^3/d)
CEM b	0.9	0.032	0.07	10.1	0.7	0
CEM b	1	0.53	11.05	18.4	60	0.010
CEM Pt	0.9	2	27	52	52	0.032

Table 1 shows that at a potential of 0.9 V applied for 24 h the current density in CEM b was 0.032 A/m^2. Compared with CEM Pt, the amount is 90% lower, as CEM Pt developed 2 A/m^2 at the end of the 24 h. Moreover, the current density obtained in CEM b at a potential of 1 V was 0.53 A/m^2, improving the density with respect to 0.9 V applied (0.032 A/m^2), but remained below of CEM Pt.

The CEM b at 1 V generated 11.05 mL H_2/day , corresponds to approximately 50% generated in CEM Pt that received 27 mL of H_2/day with similar cathodic hydrogen recovery (r_{Cat}), contrary to what happened in CEM b at 0.9V, that only generated 0.07 mL H_2/day, having a cathodic hydrogen recovery less than 1%.

CEM b compared with other studies, Jeremiasse et al. [10] generated 50 mL H_2/day (0.163 m^3/m^3/day) at 0.5 V in a MEC catalyzed by biocathode obtained from Rozendal et al. (2008) [4]. This value represents 94% higher compared with that produced in the CEM b at 1 V (based on Q, m^3 / m^3 / d). However, there were some differences in the way of starting MECs. In our study a MEC was initiated (CEM Reserve) especially to extract the bioanode and be able to use it on CEM b, while Jeremiasse et al. (2010) [10] inoculated the anode expecting 600 hours for stabilization, and subsequently inoculated the cathode with the MEC used by Rozendal et al. (2008) [4]. This methodology attributed improved stability of microorganisms in their study, generating higher current densities. However, in our study the decision to take a stable bioanode from another MEC became faster the CEM b startup.

About the Rozendal study[4], it´s important to mention that the anolyte was replaced by ferrocyanide to act as artificial electron donor, so in this way he could get more hydrogen production, 0.63 m^3/m^3/d at -0.7 V.
In Figure 6 shows a summary of the hydrogen generated in this study based on the production rate (Q), compared with the results obtained in CEM Pt and CEM b.

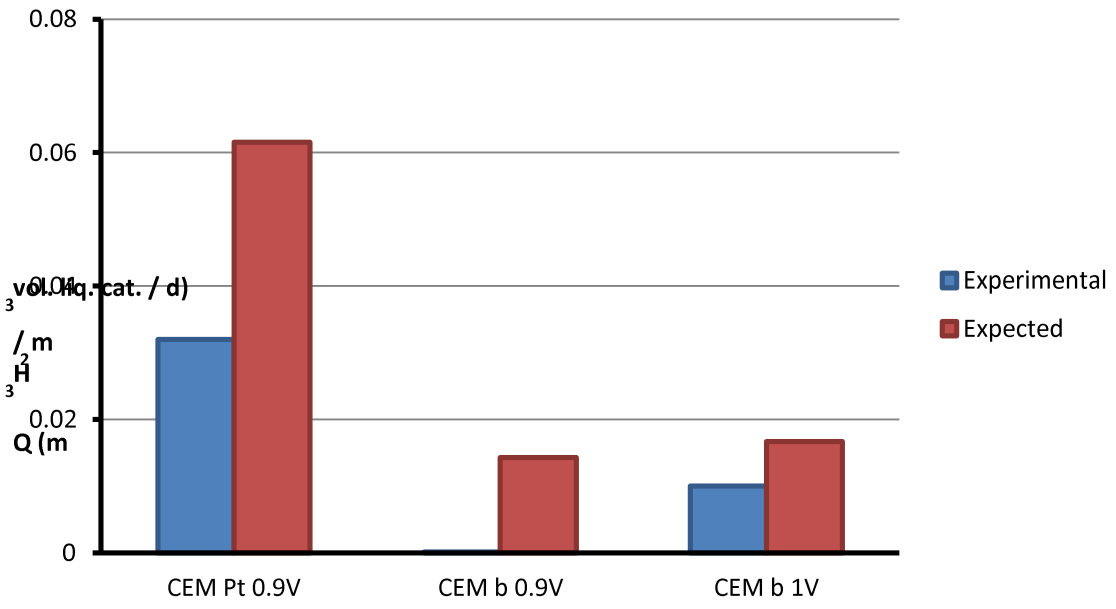

Figure 6. Results obtained in CEM Pt and CEM b.

4. Conclusions.

CEM Pt generated up to 0.032 m^3 H_2 / m^3 of reactor liquid volume / day at an applied potential of 0.9 V with a cathodic recovery rate of 52% due to leaks in the cathode chamber. The generation of H_2 in CEM Pt was low compared to other published works due to platinum poisoning by CO_2 and hydrogen sulfide.

CEM b produced 0.010 m^3 H_2 / m^3 of reactor liquid volume / day at 1 V with a cathodic recovery percentage of 60%. The low performance of CEM b was due to biocathode formation process. During the sweep for the reversal of bioelectrodo polarity, current densities were 50 times lower than that reported in the literature. Therefore, CEM b produced low hydrogen compared with CEM Pt.

5. Acknowledgements

This work was performed in the Scientific Research Center of Yucatan , centre of excellence for sustainable energy research in the southern of Mexico, with the support of the CONACYT studentship No. 236006.

6. References

[1] C. Song. Overview of Hydrogen Production Options for Hydrogen Energy Development, Fuel-Cell Fuel Processing and Mitigation of CO_2 Emissions. in Proc. 20th International Pittsburgh Coal Conference, (2003).

[2] R. Rozendal; H. V. M. Hamelers; G. J. W. Euverink; S. J. Metz and C. J. N. Buisman, Principle and perspectives of hydrogen production through biocatalyzed electrolysis *International Journal of Hydrogen Energy* 1632-1640, (2006).

[3] U. Schröder, From Wastewater to Hydrogen: Biorefineries Based on Microbial Fuel-Cell Technology, *ChemSusChem*, 4, 281-282, (2008).

[4] 5. R. Rozendal; A. W. Jeremiasse; H. V. M. Hamelers and C. J. N. Buisman, Hydrogen production with a microbial biocathode, *Environ. Sci. Technol.*, 629-634, (2008).

[5] P. M. Vignais and A. Colbeau, Molecular biology of microbial hydrogenases, *Curr. Issues Mol. Biol.*, 2, 159-188, (2004).

[6] P. M. Vignais; J.-P. Magnin and J. C. Willison, Increasing biohydrogen production by metabolic engineering, *International Journal of Hydrogen Energy*, 11, 1478-1483, (2006).

[7] J. Ditzig; H. Liu and B. E. Logan, Production of hydrogen from domestic wastewater using a bioelectrochemically assisted microbial reactor (BEAMR), *Int. J. Hydrogen Energy*, 13, 2296-2304, (2007).

[8] K.-J. Chae; M.-J. Choi; J. Lee; F. F. Ajayi and I. S. Kim, Biohydrogen production via biocatalyzed electrolysis in acetate-fed bioelectrochemical cells and microbial community analysis, *International Journal of Hydrogen Energy*, 19, 5184-5192, (2008).

[9] S. Cheng and B. E. Logan, Sustainable and efficient biohydrogen production via electrohydrogenesis, *Proceedings of the National Academy of Sciences*, 47, 18871-18873, (2007).

[10] A. W. Jeremiasse; H. V. M. Hamelers and C. J. N. Buisman, Microbial electrolysis cell with a microbial biocathode, *Bioelectrochemistry*, 1, 39-43, (2010).

[11] L. Alzate; K. González; I. Peraza; O. García; J. Domínguez; J. Vázquez; M. Tzec and B. Canto, Evaluación del desempeño e identificación de exoelectrógenos en dos tipos de celdas de combustible microbianas con diferente configuración en el ánodo, *Interciencia*, 1, 19-25, (2010).

[12] H. Hu; Y. Fan and H. Liu, Hydrogen production using single-chamber membrane-free microbial electrolysis cells, *Water Research*, 15, 4172-4178, (2008).

[13] B. E. Logan, *Microbial Fuel Cells*. 1 ed. 2008: Wiley-Interscience. 216.

[14] D. F. Call and B. E. Logan, Hydrogen production in a single chamber Microbial Electrolysis Cell lacking a membrane, *Environ. Sci. Technol*, 9, 3401–3406, (2008).

[15] R. C. Wagner; J. M. Regan; S.-E. Oh; Y. Zuo and B. E. Logan, Hydrogen and methane production from swine wastewater using microbial electrolysis cells, *Water Research*, 5, 1480-1488, (2009).

[16] A. Wang; W. Liu; N. Ren; J. Zhou and S. Cheng, Key factors affecting microbial anode potential in a microbial electrolysis cell for H2 production, *International Journal of Hydrogen Energy*, 24, 13481-13487, (2010).

[17] P. Parameswaran; C. I. Torres; H.-S. Lee; B. E. Rittmann and R. Krajmalnik-Brown, Hydrogen consumption in microbial electrochemical systems (MXCs): The role of homo-acetogenic bacteria, *Bioresource Technology*, 1, 263-271, (2011).

[18] B. Tartakovsky; M. F. Manuel; H. Wang and S. R. Guiot, High rate membrane-less microbial electrolysis cell for continuous hydrogen production, *International Journal of Hydrogen Energy*, 2, 672-677, (2009).

9th International Symposium on New Materials and Nano-Materials for Electrochemical Systems
XII International Congress of the Mexican Hydrogen Society
Merida, Mexico, 2012

Kinetic Study of Pt-$H_3PMo_{12}O_{40}$ for Methanol Electro-Oxidation

E. Fuentes-Quezada[1*], R. García-García[2], A. K. Cuentas-Gallegos[3], G. Orozco-Gamboa[1]

[1]Centro de Investigación y Desarrollo Tecnológico en Electroquímica, Parque Tecnológico Querétaro, Sanfandila, Pedro Escobedo, C. P. 76703 Querétaro, México.
[2]UTSJR, Av. Tecnológico, San Juan Del Rio, ZP 76800, Querétaro, México.
[3]Centro de Investigación en Energía-Universidad Nacional Autónoma de México, Privada Xochicalco S/N Col. Centro, AP 34, CP 62580 Temixco, Morelos, México

[*]Tel: +52 (442) 211 60 00, mail: efuentes@cideteq.mx

ABSTRACT

Composite materials based on 30% wt of Pt dispersed on Vulcan carbon XC-72, using 5% wt of Nafion® ionomer and phosphomolybdic acid ($H_3PMo_{12}O_{40}$) were prepared for their application as co-catalyst for methanol electro-oxidation. Different amounts of $H_3PMo_{12}O_{40}$ were incorporated in order to determine the optimum amount to form the electrocatalytic layer. Composite materials were characterized by X-ray diffraction (XRD), scanning electron microscopy (SEM), and Raman. The electrochemical characterization was carried out by cyclic voltammetry (CV) and impedance (EIS), using the composite materials over glassy carbon as working electrode, and solutions of 0.5M H_2SO_4 and 0.5M MeOH + 0.5M H_2SO_4 as electrolytes. Electrochemical results show that methanol oxidation is favored by the presence of $H_3PMo_{12}O_{40}$. Methanol electro-oxidation over-potential peak decreases around 150mV and a current increase of 50% is observed. These results open the opportunity to incorporate $H_3PMo_{12}O_{40}$ as part of the electrode-membrane assembly (MEA). However, this paper showed the first part, which was to determine the interaction between $H_3PMo_{12}O_{40}$ and Nafion. Further investigation will incorporate subsequently Pt into the composite for determine its kinetic parameters.

1 Introduction

Direct Methanol Fuel Cells (DMFCs) are part of the proposed technologies to achieve fewer emissions of gases such as CO_x, SO_x or NO_x that cause the greenhouse effect and related environmental problems. These devices use Pt as a catalyst, however, this metal is not abundant in the earth´s crust ($5x10^{-3}$ parts per million by weight). For this reason it is necessary to research new catalytic materials, which must be cheaper and have catalytic properties that allow a decrease in or the elimination of the Pt amount used and the achievement of the same or better activity on the reaction kinetics of electro-oxidation of methanol [1].

The polyoxometalates or heteropolyacids such as phosphomolybdic acid (PMo_{12}) are rigid inorganic metal-oxygen compounds that are very strong Bronsted acids. Well known as high proton conductors, they exhibit fast reversible multi-electron redox behavior under mild conditions, and good stability in most of their redox states, which makes them attractive for applications in devices for electrochemical energy storage, such as DMFCs. The structure of the heteropolyacid choice consists of nearly spherical Keggin anions $[PMo_{12}O_{40}]^{3-}$ of 12 A° diameter that are held together by an aqueous medium (Figure 1a). Keggin anion is illustrated in Figure 1b, and contains a phosphate group centered with four MoO_6 octahedral groups, each one sharing three edges. Each octahedron shares a pair of oxygen (O_p), and oxygen in phosphate group (O_{b2}) is bridged with other groups. Other Mo-oxygen bridges (O_{b1}) are shared by Mo atoms with bond length of ~1.65 A° to the terminal oxygen (O_t) to form poly-cations oxo-oxo-molybdenum $(Mo \equiv O_t)^{4+}$ [2].

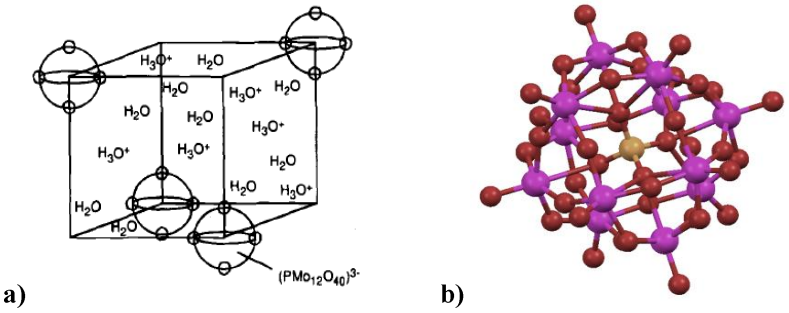

Figure 1.- Schematic representation of $H_3PMo_{12}O_{40}\bullet H_2O$ (a) and structure of Keggin anion $[PMo_{12}O_{40}]^{3-}$ (b).

A glassy carbon electrode was selected to be used as a substrate. Electron transfer kinetics is influenced significantly by pretreatment. This material could achieve negative potentials up to -1.0 V without significant evolution of hydrogen, common in aqueous media [3]. The potentiometric response of the carbon electrodes is influenced by the type and concentration of functional groups on the surface [4]. In other words, a carbon electrode that is immersed in an aqueous solution will acquire a potential, which will depend on the functional groups present on the carbon surface and their interaction with ions in solution. For this reason, it is known that carbon electrodes respond to redox

species in solution. The potentiometric response of carbon to ionic species in solution arises from the adsorption behavior of surface oxides. If the surface oxide has a quinone-type structure (C_xO), a positive electro kinetic potential is established by an equilibrium established between protons and anions (A^-) or cations (M^+) in solution:

(1)

A high acid concentration promotes the adsorption of protons in oxide-free sites (CxO) according to the following reaction:

(2)

In the above two reactions the anion is held in the diffuse double layer and is easily exchangeable with other anions in solution. The proton that attaches to the oxide group is strongly bound and must be neutralized by hydroxide, while the proton that is directly adsorbed on carbon is easily removed by washing with water. Studies of glassy carbon with Nafion coatings have been extensively reviewed by Natalya Yu [5]. These studies show that the Nafion acts as cation exchanger, so that negatively charged species do not show any reaction on the surface of glassy carbon. This implies that the sulfur (SO_3^-) groups of Nafion´s own negative ions electrostatically repel other species in solution. In other words, the polymer is expected to act as a molecular sieve separator. This implies that the PMo_{12} would be repelled by a Nafion layer into the bulk of the solution. However, the low charge density of these anions allows us to imply that the electrostatic repulsion would be of low intensity.

In this context, this paper attempts to explain the interactions between the co-catalyst (PMo_{12}) and Nafion® ionómero as the first step toward obtaining kinetic parameters of the compound after the incorporation of Pt as catalyst. The electrochemical characterization of composite Nafion/PMo_{12}/Pt are not showed, however, methanol oxidation is favored by the presence of $H_3PMo_{12}O_{40}$ and methanol electro-oxidation over-potential peak decreases around 150mV while a current increase of 50 % was observed.

2. Experiment

2.1. Composite GCE/Nafion and GCE/Nafion/PMo_{12} preparation

For preparation of the working electrode, 5 µL of Nafion ionomer (5 %wt) were place on the substrate surface (GCE/Nafion). Subsequently, in the case of the agglomerate Nafion/PMo_{12} this was prepared as follows: 4 mg of PMo_{12} was dissolved in 1 mL of ethanol, then 5 µL of this dilution was mixed with 5 µL of Nafion, sonicating the resultant agglomerate for 5 minutes. Then, using a micropipette, 5 µL of agglomerate was placed on freshly polished substrate allowed to dry for 10 minutes at room temperature.

2.2. Electrochemical characterization

Electrochemical characterization of the different composites was carried out with a Biologic (Mod. XX) potentiostat-galvanostat in a conventional three-electrode cell. As reference electrode, $Hg/Hg_2SO_4/K_2SO_4$ (640 mV vs NHE) was used, and as counter electrode, Pt wire thin coiled. As substrate we used a glassy carbon electrode (BAS brand) with a geometric area of 0.0707 cm^2. Before placing the composites on the electrode, it was polished with alumina of different particle sizes (0.3 and 0.05 microns), subsequently rinsed with distilled water and sonicated for 10 minutes in methanol in order to remove any residual alumina that had remained on the surface.

Voltammetric studies were evaluated in two different equimolar solutions, one of acid medium and another of neutral medium: 1 mM [$K_4Fe(CN)_6 \bullet 3H_2O$ / $K_3Fe(CN)_6$] (hereinafter $[Fe(CN)_6]^{3-/4-}$) + 0.1 M H_2SO_4, and 1 mM $[Fe(CN)_6]^{3-/4-}$ + 0.1M Na_2SO_4 both at room temperature (~ 25 °C), respectively. Before immersing the working electrode in the solutions, these were deoxygenated by bubbling N_2 gas (99.9% purity) for at least 10 minutes. It is important to clarify that all the voltammograms shown here are relative to the hydrogen electrode. The potential window considered for all experiments was 0.04 V to 1.04 V vs ENH, thus preventing the evolution of the medium in the form of H_2 and O_2 that could interfere with the reaction of interest.

3. Results and discussion

According to Noel and Anantharaman [6], the heat treatment of electrodes, which manufactures a glassy carbon, plays an important role in determining their surface properties. If an electrode is treated at high temperatures (from 600 to 3,000 °C), lower functional groups are formed on its surface and therefore, lower interactions with ions are present in solution. For our particular case, the work electrode that was used has two electrochemical signals very characteristic of this material, which are attributed to the quinone-hidroquinone pair as the inset showed in the Figure 1. This pair redox potential appears between 0.48 V and 0.60 V vs ENH.

In the same Figure 1, is shown the VC of the same work electrode (GCE), but now in the presence of the probe molecule $[Fe(CN)_6]^{3-/4-}$. The profile resembles that of $[Fe(CN)_6]^{3-/4-}$. However, potential peaks are shifted about 200 mV as reported in the literature [7], and which may be due to the acidic solution.

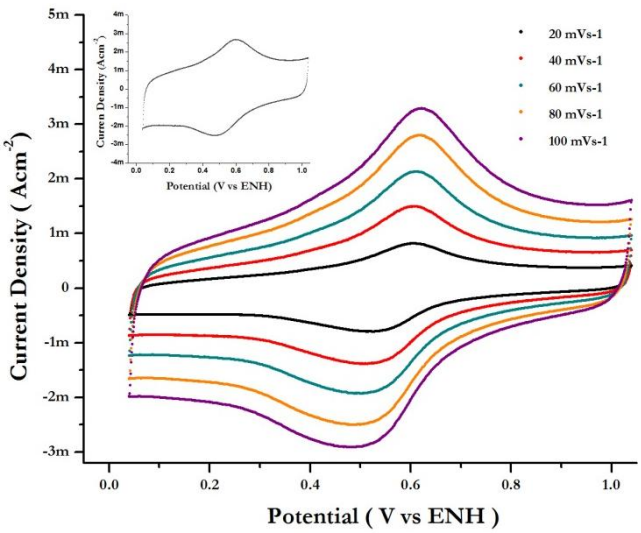

Figure 1. Cyclic voltammograms of the bare GC electrode in $[Fe(CN)_6]^{3-/4-}$ + 0.1M H_2SO_4 solution at different sweep rates, and inset: bare GCE in 0.1M H_2SO_4 solution only at sweep rate of 100 mVs^{-1}.

As shown in Table 1, the trend shows the potentials (lowest to highest sweep rate) is similar at the peak potential of the quinone-hydroquinone pair as was obtained in the Figure 1 inset, which indicates that the $[Fe(CN)_6]^{3-/4-}$ pair in the presence of H_2SO_4 competes with the redox couple displaying the glassy carbon. For other hand, the current density increased due to the presence of the $[Fe(CN)_6]^{3-/4-}$ pair, compared with Figure 1 inset.

Table 1. Potential of the anodic and cathodic peak of the GCE in 1mM $[Fe(CN)_6]^{3-/4-}$ + 0.1M H_2SO_4 at different sweep rates. $\mathbf{E_p}$ [=] mV; $\Delta E_p = E_{p,a}-E_{p,c}$ and $\boldsymbol{j_p}$ [=] mA cm^{-2}.

Scan Rate (mVs^{-1})	$E_{p,a}$	$j_{p,a}$	$E_{p,c}$	$j_{p,c}$	ΔE_p
20	606	0.816	525	-0.80	81
40	607	1.5	507	-1.39	100
60	612	2.13	499	-1.93	113
80	615	2.8	486	-2.50	129
100	**622**	**3.29**	**482**	**-2.92**	**140**

Furthermore, Figure 2a shows the cyclic voltammogram of glassy carbon electrode with Nafion agglomerate (GCE/Nafion) in the $[Fe(CN)_6]^{3-/4-}$ solution and displays the same peaks as in Figure 1, which are close to the potential of the quinone-hydroquinone pair (see Table 2). However, the current densities again decrease, which can be attributed to the presence of Nafion on the electrode.

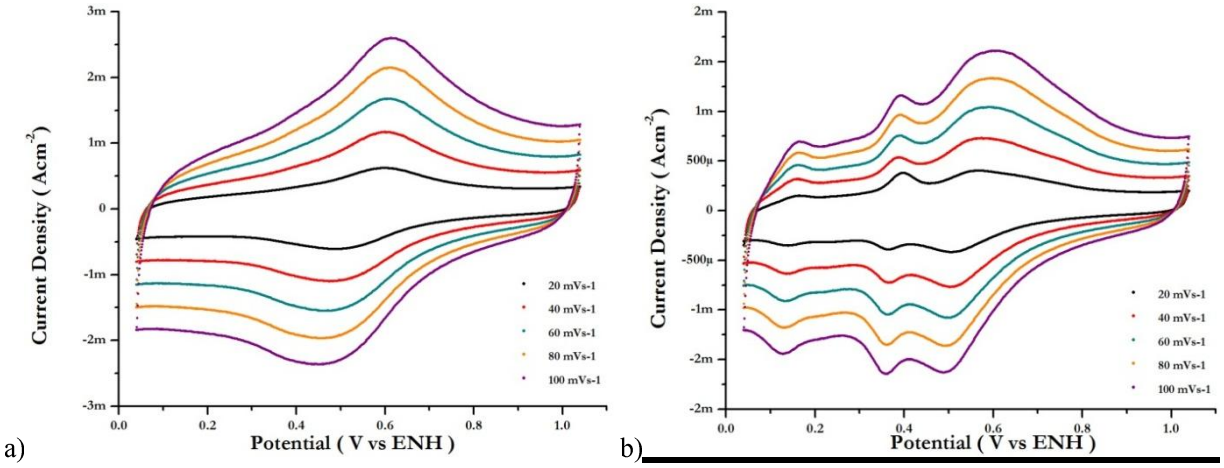

Figure 2. Cyclic voltammograms of the electrode GC/Nafion (a) and GCE/Nafion/PMo_{12} (b) in $[Fe(CN)_6]^{3-/4-}$ + 0.1M H_2SO_4 solution at different sweep rates.

It´s important to remember that the Nafion functions as a selective molecular sieve which only allows the passage of protons across their micelles, so that the $[Fe(CN)_6]^{3-/4-}$ pair is unable to reach the electrode surface to transfer its load. Therefore, no electrochemical responses are observed corresponding to the $[Fe(CN)_6]^{3-/4-}$ pair, attributing the peaks that appear to the quinone-hydroquinone pair. On the other hand, the currents shown in Table 1 are greater than those in Table 2, which is attributed to the fact that the $[Fe(CN)_6]^{3-/4-}$ pair in solution increases the capacitance of the electrode when not placed Nafion on the surface.

Table 2. Potential of the anodic and cathodic peak of the electrode GCE/Nafion in 1mM $[Fe(CN)_6]^{3-/4-}$ + 0.1M H_2SO_4 at different sweep rates. $\mathbf{E_p}$ [=] mV; $\Delta Ep=E_{p,a}-E_{p,c}$ and $\mathbf{I_p}$ [=] mA cm^{-2}.

Scan Rate (mVs^{-1})	$E_{p,a}$	$i_{p,a}$	$E_{p,c}$	$i_{p,c}$	ΔE_p
20	597	0.623	488	-0.611	109
40	600	1.17	482	-1.10	118
60	609	1.68	474	-1.55	135
80	612	2.15	460	-1.97	152
100	613	2.60	449	-2.37	164

Thus according to the values of ΔE with respect to the sweep rate of Table 1 and 2, both systems (GCE and GCE/Nafion) behave quasi reversibly and irreversible, respectively, since ΔE increases as the sweep rate in the range of 75 to 165 mV.

Figure 2b show the cyclic voltammogram of the GCE/Nafion/PMo_{12} where one can see the appearance of peaks, which are attributed to the oxidation states of PMo_{12} according to the following reactions [8]:

$$[PMo_{12}O_{40}]^{-3} + 2H^{+} + 2e^{-} = H_2[PMo_{12}O_{40}]^{-3} \quad (3)$$

$$H_2[PMo_{12}O_{40}]^{-3} + 2H^{+} + 2e^{-} = H_4[PMo_{12}O_{40}]^{-3} \quad (4)$$

$$H_4[PMo_{12}O_{40}]^{-3} + 2H^{+} + 2e^{-} = H_6[PMo_{12}O_{40}]^{-3} \quad (5)$$

In Table 3, it can be seen that the peak that arises from PMo_{12} overlaps with the peak corresponding to the quinone-hydroquinone pair reported above. In an acidic medium there is no signal corresponding to the $[Fe(CN)_6]^{3-/4-}$ pair. However, if can be seen very clearly that it corresponds to PMo_{12}. On the other hand, it is to be noted that the capacitance of the electrode containing Nafion/PMo_{12} is smaller that obtained with and without Nafion. Likewise, note that the current density of peaks in the direction of reduction are decreasing which is attributed to the different changes of oxidation states of PMo_{12}.

Table 3. Potential of the anodic and cathodic peak of the electrode GCE/Nafion/PMo_{12} in 1mM $[Fe(CN)_6]^{3-/4-}$ + 0.1M H_2SO_4 at different sweep rates. $\mathbf{E_p}$ [=] mV; $\Delta E_p = E_{p,a} - E_{p,c}$ and $\mathbf{I_p}$ [=] mA cm^{-2}.

	1st. Peak				2nd. Peak				3hr. Peak			
Scan Rate (mVs^{-1})	$E_{p,a1}$	$j_{p,a1}$	$E_{p,c1}$	$j_{p,c1}$	$E_{p,a2}$	$j_{p,a2}$	$E_{p,c2}$	$j_{p,c2}$	$E_{p,a3}$	$j_{p,a3}$	$E_{p,c3}$	$j_{p,c3}$
20	566	0.40	504	-0.42	398	0.38	364	-0.32	164	0.15	140	-0.35
40	575	0.73	503	-0.77	388	0.54	365	-0.73	158	0.32	143	-0.64
60	588	1.40	499	-1.08	390	0.76	363	-1.05	166	0.46	135	-0.91
80	601	1.33	500	-1.36	390	0.96	361	-1.35	165	0.58	129	-1.18
100	613	1.61	488	-1.63	393	1.16	358	-1.65	165	0.70	128	-1.44

Below are shown the results obtained based on the same methodology described above, but now in basic medium, for which 0.1M Na_2SO_4 solution was used as a supporting electrolyte. Figure 3 inset shows the VC glassy carbon electrode in the presence of the support electrolyte only. One can see that the quinone-hydroquinone peaks (seen in the first experiment, Figure 1) do not appear, which is attributed to the basic character of the supporting electrolyte. Recall that this redox couple is the result of a protonation of the functional groups found on the surface of the substrate.

Moreover, Figure 3 shows the cyclic voltammogram of the GCE immersed in the solution of the $[Fe(CN)_6]^{3-/4-}$ pair with the supporting electrolyte which is similar to that reported in Figure 1. However, both anode and cathode potential peaks are displaced. In accordance with the values of Table 4, at a scan rate of $20mVs^{-1}$, an anodic peak appears at a potential of 484 mV (basic medium). While in this acid environment a 606 mV peak appears, which

gives a displacement relative to each other of 122 mV, a difference which is maintained constant regardless of the sweep rate at which each of the VC's has been performed.

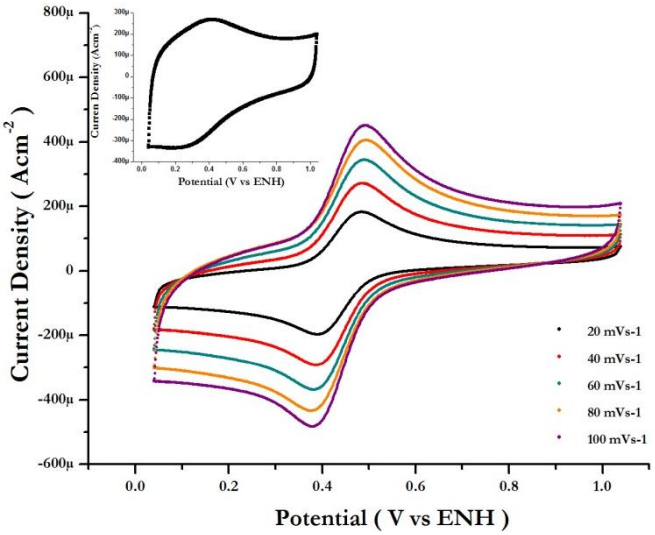

Figure 3. Cyclic voltammograms of the bare GC electrode in $[Fe(CN)_6]^{3-/4-}$ + 0.1M Na_2SO_4 solution at different sweep rates, and inset, bare GC electrode in 0.1M Na_2SO_4 solution only, sweep rate: 100 mVs^{-1}.

Table 4. Potential of the anodic and cathodic peak of the GC electrode in 1mM $[Fe(CN)_6]^{3-/4-}$ + 0.1M Na_2SO_4 at different sweep rates. $\mathbf{E_p}$ [=] mV; $\Delta E_p = E_{p,a} - E_{p,c}$ and $\mathbf{I_p}$ [=] mA cm^{-2}.

Scan Rate (mVs^{-1})	$E_{p,a}$	$j_{p,a}$	$E_{p,c}$	$j_{p,c}$	ΔE_p
20	484	0.183	391	-0.197	93
40	485	0.272	387	-0.292	98
60	490	0.344	383	-0.368	107
80	494	0.405	376	-0.434	118
100	493	0.451	378	-0.483	115

According to Figure 4a, by placing on the glassy carbon electrode a thin layer of Nafion does not allow the $[Fe(CN)_6]^{3-/4-}$ pair to approach the electrode surface to transfer electron. Therefore no signal in the voltammogram is seen. This behavior is consistent since, as a proton driver, the Nafion hinders the access of the $[Fe(CN)_6]^{3-/4-}$ pair. However, this behavior changed when the GC/Nafion/PMo_{12} electrode was immersed in the solution. Figure 4b show the voltammogram of the electrode mentioned above and suggests that the surface of the substrate is conducting an electronic transfer despite $[Fe(CN)_6]^{3-/4-}$ and PMo_{12} are negatively being charged. Table 5 summarizes the potential of anodic and cathodic peaks obtained from these voltammograms. As can be seen when comparing the peak potential of Table 4 and 5, there is a displacement of approximately 30 mV relative to each other. It can be said that the system of quasi-reversible steps is irreversible, as shown in Figure 4b.

One possible reason proposed to explain the above behaviors is the fact that the $[PMo_{12}O_{40}]^{3-}$ content in the agglomerate, by electrostatic repulsion between anion and sulfonic groups of the Nafion, increases the pore size through which the $[Fe(CN)_6]^{3-/4-}$ can access the electrode surface, so that, transferring the load gives rise to signals. However, the diffusion process is complicated, as voltammogram quasi-reversible to irreversible occurs.

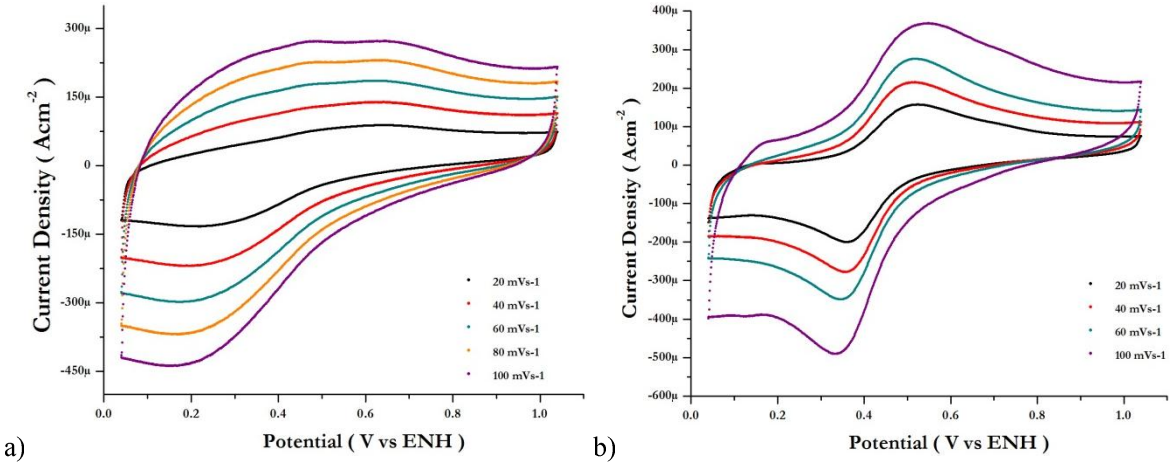

Figure 4. Cyclic voltammograms of the electrode GCE/Nafion (a) and GCE/Nafion/PMo_{12} (b) in $[Fe(CN)_6]^{3-/4-}$ + 0.1M Na_2SO_4 solution at different sweep rates.

Furthermore it is likely that the protons (H^+), which are part of $[PMo_{12}O_{40}]^{3-}$ like against load, neutralize sulfonic groups (SO_4^- of Nafion) such that charge density decreases sufficiently to allow the $[Fe(CN)_6]^{3-/4-}$ pair thus close enough to transfer its load.

Table 5. Potential of the anodic and cathodic peak of the electrode GCE/Nafion/PMo_{12} in 1mM $[Fe(CN)_6]^{3-/4-}$ + 0.1M Na_2SO_4 at different sweep rates. **Ep** [=] mV; ΔEp=Ep,a-Ep,c and **Ip** [=] mA cm^{-2}.

Scan Rate (mVs^{-1})	$E_{p,a}$	$j_{p,a}$	$E_{p,c}$	$j_{p,c}$	ΔE_p
20	524	0.157	361	-0.200	163
40	515	0.215	359	-0.278	156
60	519	0.276	346	-0.349	173
100	547	0.368	334	-0.491	213

4. Conclusions

In acid medium the GCE shows the quinone-hydroquinone pair is characteristic of materials regardless of the presence of a $[Fe(CN)_6]^{3-/4-}$ pair. This pair remains consistent even after placing the electrode surface on the Nafion ionómero. This makes it clear that the observed peaks correspond to the quinine-hydroquinone redox couple, as the

Nafion does not allow the $[Fe(CN)_6]^{3-/4-}$ to approach the electrode surface, only slightly increasing the capacitance of the electrode. The GC/Nafion/PMo_{12} electrode shows the characteristic signals of the latter compound corresponding to the change in oxidation state of Mo contained within the anion $[PMo_{12}O_{40}]^{3-}$ as a result of protonation.

Furthermore, in a neutral medium, CGE shows no peak characteristic of the pair corresponding to quinone-hydroquinone, which is attributed to the neutrality of the solution. In the presence of the $[Fe(CN)_6]^{3-/4-}$ pair the voltammogram shows only the presence of the characteristic peaks of the pair, which are displaced approximately 200 mV with respect to the results obtained in acidic medium. The GC/Nafion electrode does not show the $[Fe(CN)_6]^{3-/4-}$ peaks, attributed to the fact that Nafion only allows the passage of protons, but not the anion, and is repelled by electrostatic forces to the bulk of the solution. When placing the composite over the Nafion/PMo_{12} electrode, $[Fe(CN)_6]^{3-/4-}$ peaks reappear, which is attributed to the increase in the agglomerate PMo_{12}, by electrostatic repulsion with SO_4^-groups. The pore size of Nafion allows the $[Fe(CN)_6]^{3-/4-}$ pair sufficient to approach the electrode surface to transfer its load. Also, the H^+ that contains the PMo as counter ions helps to neutralize the negative charges of Nafion to reduce the repulsive forces between SO_4^- and the $[Fe(CN)_6]^{3-/4-}$ pair. This study was conducted as part of a project aimed at determining the kinetic parameters that were initially proposed. This opens the possibility of improving the electro-active area of MEA's used in methanol fuel cells.

5. Akcnowledgements

This work was performed under the auspices of the CONACYT (project number 102018). E. Fuentes and R. Garcia acknowledge CONACYT for scholarship support.

6. References

[1] F. Alcaide, G. Álvarez, P. L. Cabot, International Journal of Hydrogen Energy 36 (2011) 4432-4439.

[2] Atsuo Yamada, John B. Goodenough, J. Electrochem. Soc., Vol. 145, Num. 3, March 1998, 737 – 743.

[3] Christopher M. A. Brett, Electroanalysis 2001, 13, No. 3 pp. 212-218.

[4] K. Kinoshita, "Carbon, Electrochemical and Physicochemical Properties", John Wiley & Sons, New York (1988), Chapter 6.

[5] Natalya Yu. Stozhko, Natalya A. Malakhova. J. Solid State Electrochem. (2008) 12 1185-1204.

[6] M. Noel and P. N. Anantharaman, Surface and Coatings Technology, 28 (1986) 161 – 179

[7] Standar Potentials. Gyorgy Inzelt In: Scholz F, Pickett CJ Encyclopedia of electrochemistry, vol 7a. Wiley-VCH, Weinheim.

[8] Masahiro Sadakane and Eberhard Steckhan, Chem. Rev. 1998, 98, 219-237.

Thermodynamic Analysis of the Absorption Enhanced Autothermal Reforming of Ethanol

V. Collins-Martínez[§], M. A. Escobedo-Bretado[⌘], M. Meléndez-Zaragoza[§], J. S. Salinas-Gutiérrez[§], V. G. Guzmán-Velderrain[§], A. López-Ortiz[§*]

[⌘] Facultad de Ciencias Químicas, Universidad Juárez del Estado de Durango, Ave. Veterinaria s/n, Circuito Universitario, Durango 34120, México
[§] Departamento de Materiales Nanoestructurados, Centro de Investigación en Materiales Avanzados, S. C. Miguel de Cervantes 120, Chihuahua, Chih. 31109, México,
[*] Tel: 614 439 4815, Fax 614 439 1130, mail: alejandro.lopez@cimav.edu.mx

ABSTRACT

Thermodynamic analysis of the absorption enhanced autothermal reforming of ethanol using CaO as CO_2 absorbent was performed to determine favorable operating conditions to produce a high hydrogen ratio (HR, mols H_2-produced/EtOH-feed) and hydrogen concentration in gas product. Steam/Ethanol and oxygen/ethanol feed ratios were varied in order to find autothermal reaction conditions ($\Delta H \approx 0$) and carbon free operating regions. Equilibrium product compositions were studied from 300-900°C, steam to ethanol molar feed ratio (S/EtOH), oxygen to EtOH ratio (O_2/EtOH) and CaO as CO_2 absorbent at 1 atm. Carbon formation analysis used S/EtOH from 1.75-2.8, while for hydrogen production was varied from stoichiometric; 3:1 to 6.5:1, and O_2/ETOH from 0 to 1.0. Results indicate no carbon formation at S/EtOH $\geq$ stoichiometric. Conventional ethanol reforming at T = 600°C and S/EtOH = 6.5 resulted in a HR of 4.7 and a highly endothermic system. The introduction of O_2 (ATR) in the feed (O_2/EtOH = 0.88) produced a reduction in HR of 22% at autothermal conditions with no carbon formation, while the use of a CO_2 absorbent (CaO) combined with conventional reforming resulted in an increase in H_2 purity and HPR of about 21% with a still endothermic system. Whereas, the absorption enhanced autothermal reforming of ethanol using CaO, O_2/EtOH = 0.33, S/EtOH = 6.5 and 600°C, produced an autothermal system with 98% H_2 content and only a reduction of 9.8% in HR and with respect to the CO_2 absorption reforming without O_2 as a feed. Higher O_2/EtOH values than 0.33 produced a significant reduction in hydrogen content and purity at equilibrium.

Keywords: Absorption-Enhanced-Autothermal-Reforming, CO_2-absorbent, Thermodynamic Analysis

1. INTRODUCTION

Global warming is a central issue nowadays because its effects on the environment and human condition [1, 2]. Carbon dioxide (CO_2) is one of the main greenhouse gases, and CO_2 emissions are produced primarily from the use of fossil fuels for transportation (vehicles) and electricity generation (power plants). Due to this global warming danger and limited supply and rising demand for fossil fuels, alternative energy sources are at present being developed. A sustainable solution to today's energy needs must include the energy generation from renewable sources accompanied with a reduction in both pollution emissions and a large consumption of raw materials.

Hydrogen (H_2) is a promising energy vector due to the fact that it can be produced through environmentally friendly processes. For example, biomass and specifically agriculture wastes [3, 4], and water can react to produce hydrogen gas. Hydrogen is an important raw material used in the oil refinery industry and the manufacturing of various chemicals. As energy vector, hydrogen can efficiently be used to generate electricity through electrochemical reactions in fuel cells [5]. Different kinds of fuel cells have been developed, among these the most important are; proton-exchange-membrane fuel cells (PEMFC), solid-oxide fuel cells (SOFC), and molten carbonate fuel cells (MCFC) [5, 6], either for mobile or stationary applications. For hydrogen fuel cells to have a significant impact on reducing greenhouse gas emissions, the hydrogen needs to be produced from renewable sources such as sunlight, either directly or indirectly from biomass through photosynthesis. The use of hydrogen fuel cells in vehicles or in portable power plants will require lightweight H_2 storage or "on-board" reforming of hydrogen-containing compounds into H_2 [7].

Biomass candidates for H_2 production include; sugar, starch, oils, and crop wastes. The production of hydrogen from sugar by catalytic reaction has been demonstrated [8], but the process from glucose so far has shown only 50% selectivity to H_2 and reaction kinetics is extremely slow. Also, a fuel cell operating using sugars as raw materials has been demonstrated [9], but the obtained power densities are very low for practical use. Furthermore, biodiesel (the methyl ester of a vegetable oil) can be a good candidate for steam reforming to produce H_2 because the comparable fossil diesel can be reformed [10], although the higher cost of seed oil limits its economics.

On the other hand, ethanol is a very attractive raw material for hydrogen production because of its relatively high hydrogen content, availability, non-toxicity, and storage and handling safety. Furthermore, ethanol can be produced renewably by fermentation of biomass sources, such as energy plants, agroindustrial wastes, forestry residue materials, and organic fractions of municipal solid waste. Ethanol produced through these processes is called bioethanol [11].

Steam reforming of ethanol (SR) for hydrogen production based on the operation-mode can be very different, with important implications on the composition of the reformer effluent and the energy demand, necessary to generate the hydrogen-rich product. These operational modes are: steam-reforming, partial-oxidation and auto-thermal reforming. Steam-reforming is highly endothermic process:

$$CH_3CH_2OH + H_2O \Rightarrow CO + 4H_2 \qquad \Delta H_R^o = +298 \text{ kJ/mol} \qquad (1)$$

Complete steam-reforming (SR) operation is given by the following reaction

$$CH_3CH_2OH + 3H_2O \Rightarrow 2CO_2 + 6H_2 \qquad \Delta H_R^o = +347 \text{ kJ/mol} \qquad (2)$$

while the maximum hydrogen-yield of ethanol steam-reforming can be fixed by 6 moles of H_2/mole ethanol.

Partial-oxidation is the incomplete oxidation of the ethanol feed. This incomplete oxidation generates heat and decomposes the feed to smaller molecules as follows:

$$CH_3CH_2OH + 0.5O_2 \Rightarrow 2CO + 3H_2 \qquad \Delta H_R^o = +57 \text{ kJ mol}{-1} \qquad (3)$$

$$CH_3CH_2OH + O_2 \Rightarrow CO_2 + CO + 3H_2 \qquad \Delta H_R^o = -226 \text{ kJ mol}{-1} \qquad (4)$$

$$CH_3CH_2OH + 1.5O_2 \Rightarrow 2CO_2 + 3H_2 \qquad \Delta H_R^o = -509 \text{ kJ mol}{-1} \qquad (5)$$

As the oxygen content in the feed stream is increased, the ethanol is completely oxidized and the maximum heat output is achieved at the expense of an increase in carbon oxides (CO and CO_2) subproducts [12].

Auto-thermal reforming (ATR) is the combination of the above two processes (steam-reforming and partial-oxidation), in order to achieve a minimum energy input necessary to maintain the required reformer temperature. The total reaction of autothermal reforming of ethanol can be written as

$$CH_3CH_2OH + 2H_2O + 1.5O_2 \Rightarrow 2CO_2 + 5H_2 \qquad \Delta H_R^o = -50 \text{ kJ mol}{-1} \qquad (6)$$

This reaction indicates that the autothermal reforming not only attains thermally sustained operation, but also maximizes hydrogen production [13, 14].

The selection of operating conditions of a reformer is depending on various targets. In the case of the ATR operation the temperature is determined at conditions where the heat of the endothermic reforming is compensated with the heat of the exothermic partial oxidation so that the overall reaction heat is approximately null ($\Delta H \approx 0$). Another target of this process is a high hydrogen yield, combined with low carbon oxides (CO and CO_2) content. Maximum hydrogen efficiency and low carbon monoxide content is possible for steam reforming operation. However, steam-reforming is a highly endothermic process and therefore energy demanding. This energy has to be supplied into the system from external sources. In the case of a conventional reforming operation the heat needed to keep the reformer temperature is usually supplied through a furnace where a fossil fuel is burned (typically natural gas) and the fuel

demand is intensified during start-up-time. This is unacceptable if renewable hydrogen is to be produced. Therefore the partial-oxidation or auto-thermal operation is preferred as the process is exothermic.

It is inherent to the ATR reforming process that carbon monoxide is generated. The production of carbon monoxide needs to be avoided, as it is an inefficient by-product, which impacts the mass and size of the fuel processor (WGS). Furthermore, the production of carbon dioxide is also promoted under this operation scheme and both oxides represent two additional separate processes to obtain a high purity hydrogen product. On one hand, in a fuel processing system the reformer is followed by two water gas shift (WGS) reactors to reduce the carbon monoxide contents to the desired level. On the other hand, carbon dioxide is eliminated from the effluent stream of the WGS by an amine absorption process or a PSA unit to finally generate a high purity hydrogen stream, typically 99.9%. Even though there are some disadvantages of this operation mode ATR is considered to be the most energetically efficient and cost-effective reforming method [15, 16].

Another reforming operating mode, developed in the last decade deals with a modification of the conventional reforming process. This alternate processes was called the absorption enhanced reforming (AER). This AER process provides a promising alternative for a single step high purity hydrogen production [17]. The fundamental concept in which this process is based is the Le Chatellier's principle where the reforming equilibrium can be shifted towards the production of hydrogen when CO_2 is removed *in situ* within the reactor. Thus if the carbon dioxide generated during the steam reforming step is removed from the gas phase using a solid CO_2 absorbent such as CaO the hydrogen production will be enhanced. In the AER reactor a mixture of a CO_2 absorbent (for example CaO) and a reforming catalyst will theoretically produce a high purity hydrogen stream in one single step. The combination of the CO_2 absorption by CaO through the reaction:

$$CaO + CO_2(g) = CaCO_3 \quad \Delta H^\circ_{298} = -178.3 \text{ kJ/mol} \qquad (7)$$

and the steam reforming of ethanol lead to the following reaction

$$C_2H_6O(g) + 3H_2O(g) + 2CaO = 2CaCO_3 + 6H_2(g) \quad \Delta H^\circ_{298} = -185.3 \text{ kJ/mol} \qquad (8)$$

When comparing equation (2) with equation (8), it is evident that the use of a CO_2 absorbent changed from an endothermic steam reforming reaction to an exothermic reaction, which implies potential energy savings with the use of a solid CO_2 absorbent. However, this absorbent must be regenerated if a continuous process is desired and then the high endothermic reverse reaction (7) will eventually be required to be performed.

Thermodynamic analyses and experimental studies related to the use of simultaneous CO_2 removal using CaO as absorbent combined with the steam reforming of ethanol for hydrogen production has been reported by several authors [17, 18]. However, the balance between the high endothermic ethanol reforming reaction (2) and the high exothermic carbonation reaction (7) for autothermal operation ($\Delta H_R \approx 0$) requires temperatures of less than 380°C (S/EtOH = 6 and CaO/EtOH = 2.5 molar ratios). At these conditions the overall reaction rate is rather slow and consequently of not practical interest. At ethanol AER optimal operating temperatures (600-700ºC) hydrogen production is enhanced generating a high purity H_2 stream accompanied with a moderate endothermic overall heat of reaction. Therefore, there is a need of supplemental heat for the AER reactor to be able to operate at autothermal conditions where reaction temperatures (600-700ºC) are reported to generate sufficiently fast reactions kinetics [19].

From the above modes of reforming operations studied in the past is then convenient to take advantage of the AER process scheme, which presumably produce high hydrogen yield and content combined with a moderate endothermic reaction heat at temperatures of interest (600-700ºC) and the ATR process scheme that is able supply the necessary heat required for the AER process to operate in an autothermal mode ($\Delta H_R \approx 0$). Therefore, in the present thermodynamic study the combination of the ethanol reforming reaction (2), CO_2 absorption reaction by CaO (7) and ethanol partial oxidation reactions (3) to (5) are proposed as a renewable and energy efficient (autothermal operation) reforming mode of operation (AER-ATR) to produce a high H_2 content product gas in one single step.

Therefore, the objective of the present study is to perform a thermodynamic analysis of the AER-ATR process to determine carbon free and favorable operating conditions to produce a high purity hydrogen stream. The influence of steam-to-ethanol (S/EtOH) and oxygen-to-ethanol (O_2/EtOH) feed molar ratios and temperature on the product gas concentration were investigated at atmospheric conditions. These results were then compared to the ethanol steam reforming (EST) and AER reforming modes. Results will be compared with experimental (where available) and theoretical data generated and found in existing literature. Furthermore, it is expected that during the steam reforming of ethanol, carbon deposition over catalysts may be the main cause for deactivation, resulting in low durability and activity loss. Therefore, additionally a study of conditions where this carbon deposition is expected under the AER-ATR process was included and compared with current reforming operating modes. Hence, S/EtOH and O_2/EtOH feed ratios were varied in order to find autothermal reaction conditions ($\Delta H \approx 0$) and carbon free operating regions. Equilibrium product compositions were studied from 300-900°C and CaO was employed as CO_2 absorbent at 1 atm. Carbon formation analysis used S/EtOH from 1.75-2.8, while for hydrogen production was varied from stoichiometric; 3:1 to 6.5:1, and O_2/ETOH from 0 to 1.0.

2. SIMULATION CALCULATIONS

2.1 Gibbs Free Energy Minimization Technique

In a reaction system where many simultaneous reactions take place, equilibrium calculations can be performed through the Gibbs energy minimization approach (also called the non-stoichiometric method). In this technique the total free energy of the system consisting of an ideal gas phase and pure condensed phases, can be expressed as:

The technique is based in finding different values of n_i which minimizes the objective function (7) and are subjected to the constraints of the elemental mass balance:

where a_{ij} is the number of atoms of the j^{th} element in a mole of the i^{th} species. A_j is defined as the total number of atoms of the j^{th} element in the reaction mixture [20]. All calculations were performed through the use of the equilibrium module of the HSC chemistry software for windows [21]. HSC calculates the equilibrium composition of all possible combination of reactions that are able to take place within the thermodynamic system. These equilibrium calculations make use of the equilibrium composition module of the HSC program that is based on the Gibbs free energy minimization technique. The GIBBS program of this module finds the most stable phase combination and seeks the phase compositions where the Gibbs free energy of the system reaches its minimum (equation 9) at a fixed mass balance (a constraint minimization problem, equation 10), constant pressure and temperature.

In this non-stoichiometric approach every species in the system must be defined. The selection of feasible products should be based on previous experimental results found in the literature. For each system the possible species are specified based on reported experimental and thermodynamic analysis studies. In the steam reforming systems studied the species included were: ethanol, ethylene, ethane, acetone, acetaldehyde, acetic acid, C, CO, CH_4, CO_2, H_2, H_2O, CaO and $CaCO_3$. These were based on reported experimental species found in the literature [22-24].

3. RESULTS AND DISCUSSION

3.1 Thermodynamically Possible Products

During the equilibrium calculations the HSC program requires the input of all possible chemical species present in the system as reactants and products. For the steam reforming system the species considered at equilibrium were all gaseous and solid species already described in section 2.1 and those found in the current literature that appear when ethanol is converted along with other intermediate oxygenated hydrocarbons. Specifically, for the ethanol reforming system the additional intermediate species considered were: ethylene, ethane, acetaldehyde, acetic acid and acetone

[17, 18, 25-27]. In practice alcohol steam reforming reactions are under kinetic control, where suitable catalysts and supports are able to completely convert all the biofuel to avoid intermediate products. All this agrees well with the fact that only trace amounts (less than 1ppm) of these oxygenated intermediates were found in all the thermodynamic calculations performed and therefore these were not reported in the present study

3.2 Carbon Formation

Figure 1 show the effect of steam to ethanol (S/EtOH) molar ratios from 0-2.8 and temperature from 300-900ºC on the number of moles of carbon (graphite) produced / kmol of Ethanol feed (1Kmol) through the steam reforming (SR) and the absorption enhanced reforming of ethanol processes.

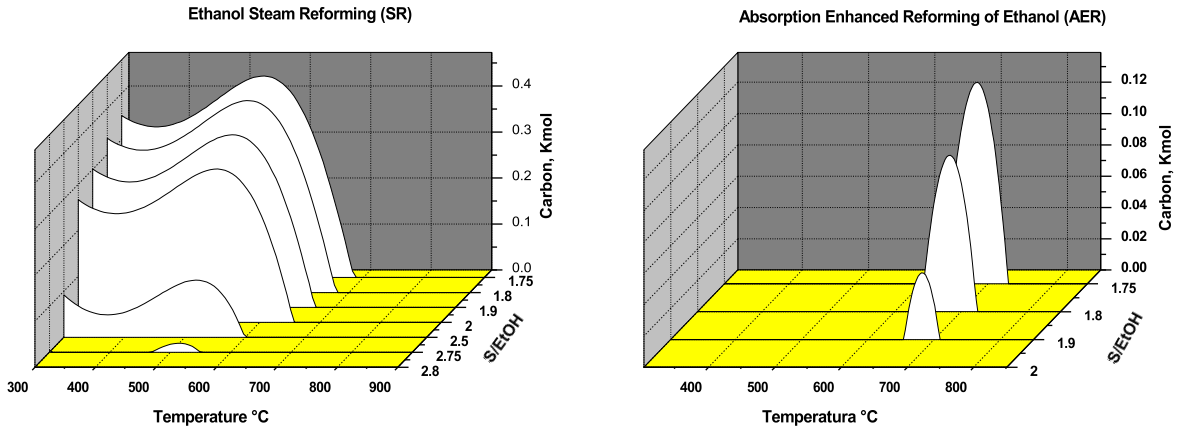

Figure 1. Carbon Formation for the SR and AER processes as a function of T and S/EtOH ratio

For the SR process 1 Kmol of ethanol was fed to the reaction system and the corresponding steam for each S/EtOH ratio, while for the AER system 2.5 Kmol of CaO was also fed along with steam and ethanol.

In these plots is evident that without the use of a CO_2 absorbent carbon formation is favored and its maximum is reached at lower temperatures ($T < 700°C$) than with the use of an absorbent ($600 < T < 750°C$) . The SR produced a maximum carbon formation of 0.43 kmol per mol of ethanol fed to the system at S/EtOH ratio of 1.75 and it is found at a temperature of 536°C. Greater temperatures and S/EtOH ratios will produce lower amounts of carbon and at S/EtOH ratio greater than 2.75 and temperatures higher will insure a carbon free operation under this system. Whereas, under the AER system carbon formation is only formed at high temperatures and in the range from 600-750ºC and from S/EtOH ratios from 0-1.9, with a maximum carbon formation of 0.128 Kmol/Kmol EtOH fed at a S/EtOH ratio of 1.75 and 686ºC. Higher S/EtOH ratios than 1.9 will ensure a carbon free operation under this reaction system. From Figure 1 it is clear that the use of a CO_2 absorbent inhibits carbon formation in about three orders of magnitude and smaller S/EtOH ratios can be used without the formation of carbon in the reaction system.

The behavior related to the lower carbon formation found with the use of a CO_2 absorbent (very low risk of carbon formation), is directly related to the reduction in CO content. Li [28] reported in his thermodynamic study, that graphite formation is suppressed with CO_2 absorption. According to this author, the Boudouard reaction:

$$2CO(g) = CO_2(g) + C(s) \qquad \Delta H°298 = -172.5 \text{ kJ/mol} \qquad (11)$$

is shifted towards the reverse Boudouard reaction because its equilibrium constant is related to the square of CO concentration.

Figure 2 presents results of equilibrium calculations for the ATR reforming mode of ethanol. In this plot the carbon formation in Kmol as a function of S/EtOH and temperature are presented using two different O_2 feed levels; O_2/EtOH ratios of 0.5 and 0.75, respectively.

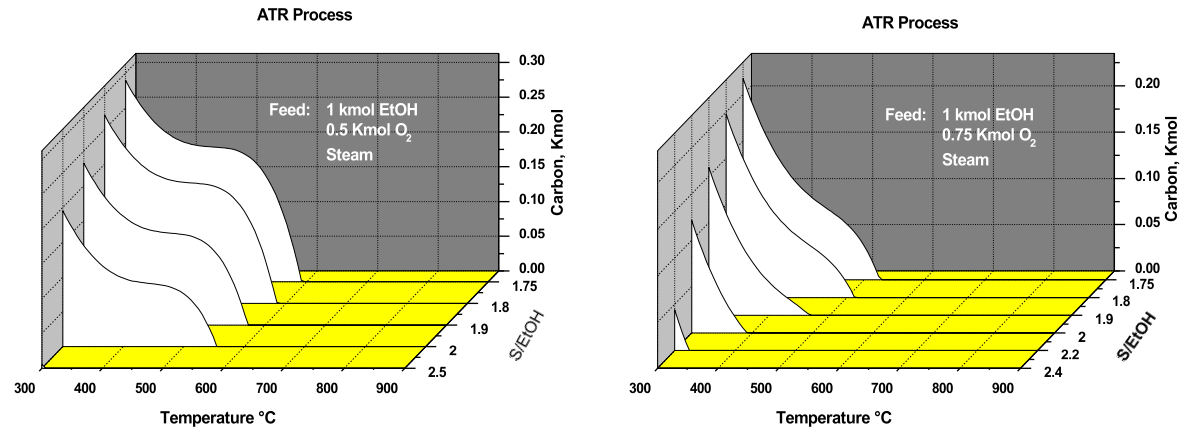

Figure 2. Carbon Formation for the ATR process at O_2/EtOH ratios of 0.5 and 0.75 as a function of T and S/EtOH ratios

From this Figure it can be seen that at O_2/EtOH = 0.5 carbon formation is predicted at a low temperature range of 300-600ºC and S/EtOH < 2 within the ATR system as high as 0.28 kmol at 300ºC. Greater temperatures from this region will prevent carbon to be formed in this reaction system. However, If the O_2 content is increased to a level of O_2/EtOH = 0.75 this will be traduced in a reduction of the carbon formation region accompanied with lower temperatures at higher S/EtOH ratios. Maximum temperature for carbon formation was reduced to 524ºC and S/EtOH = 1.75. This effect implies that at values of S/EtOH higher than 2.2 will ensure a carbon free operation. A further increase in the O_2 content for the ATR process can be seen in Figure 3, where the O_2 content in the feed is increased to a level of O_2/EtOH = 1.0. Here, the carbon formation region is additionally reduced with smaller regions for carbon deposition (T < 400°C) and as the S/EtOH is increased to values greater than 2.0 this will prevent carbon formation at all temperatures.

This behavior can be explained in terms of the following coke gasification reactions:

$$O_2 + C(s) = CO_2 \qquad \Delta H°298 = -393.48 \text{ kJ/mol} \qquad (12)$$

$$\tfrac{1}{2}\, O_2 + C(s) = CO \qquad \Delta H°298 = -110.70 \text{ kJ/mol} \qquad (13)$$

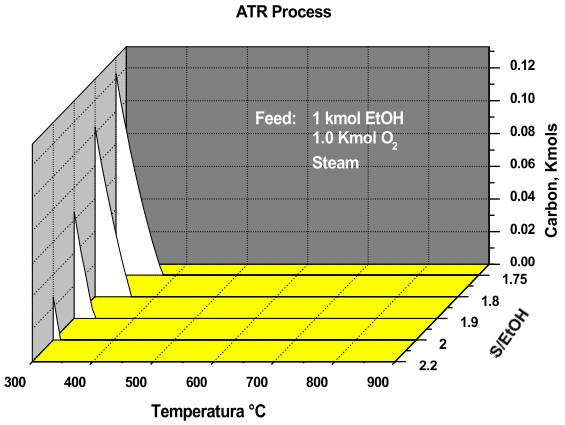

Figure 3. Carbon Formation for the ATR process at O_2/EtOH = 1.0 as a function of T and S/EtOH

The gasification equilibrium is also dependent on the steam to EtOH ratio and the temperature of the system. For instance, at S/EtOH ratios of 2 and greater, carbon is completely gasified at temperatures of 400°C and greater. This behavior can also be seen when the equilibrium content of carbon oxides are carefully examined. As the O_2 content in the feed is increased the equilibrium content of the carbon oxides (CO and CO_2) are also increased (not shown in Figures), which is consistent with the promotion of reaction (12) and (13). In reaction (12), oxygen fully gasifies carbon to CO_2 at an O_2/EtOH = 1.0 and, when there is insufficient oxygen O_2/EtOH < 0.5, gasification to CO is thermodynamically favorable at temperatures above 500°C. Nevertheless, carbon formation apart from reaction (11) can also be generated through the following reactions:

$$CH_4 = C(s) + 2H_2 \qquad \Delta H°298 = +73.84 \text{ kJ/mol} \qquad (14)$$

$$CO + H_2 = C(s) + H_2O \qquad \Delta H°298 = -130.8 \text{ kJ/mol} \qquad (15)$$

$$CO_2 + 2H_2 = C(s) + 2H_2O \qquad \Delta H°298 = -89.6 \text{ kJ/mol} \qquad (16)$$

Therefore, there is a complex network of reactions involved in the entire process. However the main fact is that O_2 content in the feed through the ATR process scheme produces a reduction in the carbon formation through gasification reactions (12) and (13).

Figure 4 shows the carbon formation as a function of S/EtOH and temperature for the AER-ATR reaction system at O_2/EtOH of 0.1 and 0.25, respectively. Feed to each system consisted in 1 kmol of ethanol, 2.5 kmol of CaO and the corresponding amount of steam for each S/EtOH ratio. For the case of O_2/EtOH = 0.1 the S/EtOH ratio was varied from 0 to 1.85, while for O_2/EtOH = 0.25 this changed from 0 to 1.6.

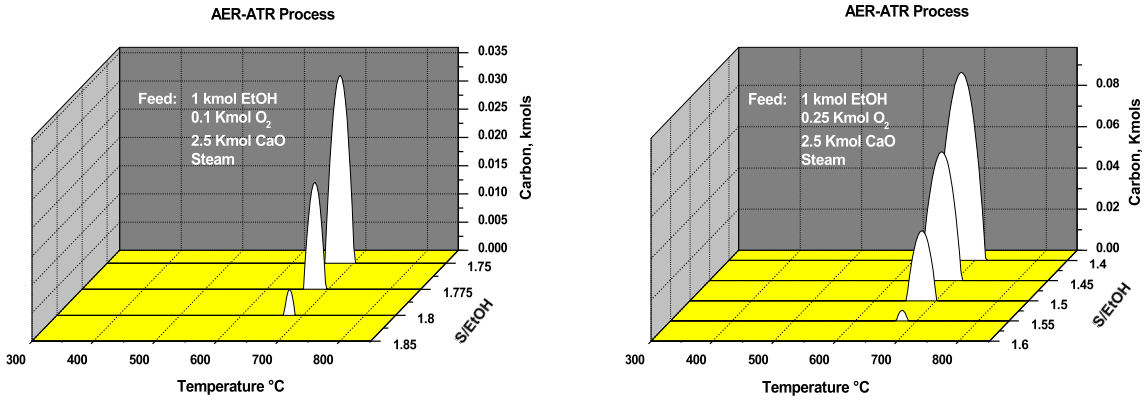

Figure 4. Carbon Formation for the AER-ATR process at O_2/EtOH = 0.1 and 0.25 as a function of T and S/EtOH

Here it can be seen that the effect of combining the AER and the ATR reforming modes resulted in carbon free regions located at lower S/EtOH ratios. For example at O_2/EtOH = 0.1 and 0.25 S/EtOH ratios as low as 1.85 and 1.6, can be operated without any carbon formation, respectively. However, one particular feature in Figure 4 is that carbon formation is now promoted at high temperatures (650 -800°C). This behavior can be explained in terms of reaction (14), where the production of CH_4 is favored at small S/EtOH ratios and then this is presumably converted to carbon. This behavior is even more enhanced as the S/EtOH is further reduced as can be seen in Figure 4.

Finally Figure 5 presents results at O_2/EtOH = 0.5 under the AER-ATR reforming mode. Here it can be seen that even though the amount of carbon is increased this is only at S/EtOH ratios of less than 1.2.

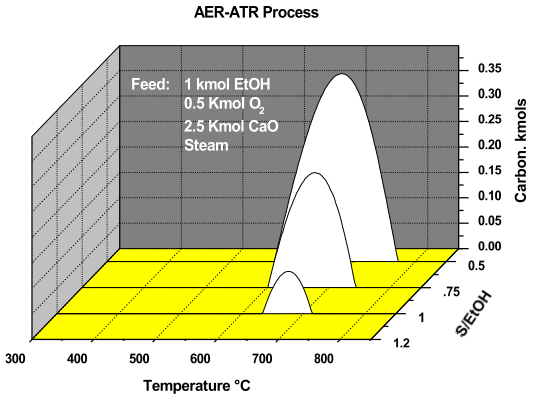

Figure 5. Carbon Formation for the AER-ATR process at O_2/EtOH = 0.5 and 0.25 as a function of T and S/EtOH

Here the increase in O_2 content within the absorption enhanced reforming of ethanol cased that the lower limit for carbon formation in terms of S/EtOH to be reduced. When comparing the SR, AER, ATR and AER-ATR it can be found that the amount of steam employed for the AER-ATR process is about half with respect to the S/EtOH ratio

needed to avoid carbon formation. Furthermore, in the case of the AER-ATR process, higher temperatures than 600°C are needed for carbon to be formed being these not typically found in a conventional reforming operation. Therefore, it can be concluded that in all the reforming operating modes (SR, AER, ATR and AER-ATR) greater than stoichiometric values will insure carbon free operation. In in terms of the order from higher to lower carbon formation is: SR > ATR > AER > AER-ATR.

3.3 Thermoneutral Condition

In an autothermal steam reforming process, oxygen supplies the necessary heat via oxidation reaction for the endothermic steam reforming; increasing oxygen to ethanol molar ratio (O_2/EtOH) decreases an external heat requirement. As a result, it is possible to operate the autothermal reformer without supplying external heat input by controlling appropriate oxygen feed ratios. This condition is referred as to a thermoneutral condition ($\Delta H \approx 0$). The operating temperature at which the external heat flow equals to zero is also known as an adiabatic temperature. Table 1 show the behavior of the adiabatic temperature and O_2/EtOH ratio at different S/EtOH ratios. Also in this table the different reforming modes are presented (SR, ATR, AER and AER-ATR) as well as the equilibrium dry molar composition of the gas product and the total kmols of hydrogen produced at each condition studied.

Table 1. Equilibrium Thermodynamic Results for the Autothermal Conditions for the Reforming Processes Studied

FEED, kmols		S/EtOH	Adiabatic T (ΔH = 0)	Product Composition % mol				H_2	FEED, kmols		S/EtOH	Adiabatic T (ΔH = 0)	Product Composition % mol				H_2
CaO	O_2	Molar Ratio	(°C)	H_2	CO	CO_2	CH_4	kmols	CaO	O_2	Molar Ratio	(°C)	H_2	CO	CO_2	CH_4	kmols
-	-	3	334	13.4	0.1	25.0	61.5	0.3	2.5	-	3	481	90.8	0.0	0.0	9.2	4.3
-	-	6.5	ΔH > 0	71.7	8.1	19.4	2.8	4.7	2.5	-	6.5	372	98.3	~ 0	~ 0	1.7	5.6
-	0.1	3	312	18.0	0.1	27.0	54.9	0.4	2.5	0.1	3	572	97.8	0.5	0.3	7.4	4.4
-	0.1	6.5	403	27.3	0.6	26.4	45.7	2.7	2.5	0.1	6.5	457	98.6	0.0	0.0	1.3	5.5
-	0.25	3	475	42.5	2.5	26.7	28.3	1.5	2.5	0.25	3	639	90.7	3.4	1.7	4.2	4.5
-	0.25	6.5	390	36.7	0.4	28.6	34.2	1.2	2.5	0.25	6.5	566	98.2	0.3	0.7	0.8	5.3
-	-	-	-	-	-	-	-	-	2.5	0.3	3	651	90.1	4.4	2.2	3.3	4.5
-	-	-	-	-	-	-	-	-	2.5	0.3	6.5	590	97.5	0.6	1.3	0.6	5.2
-	-	-	-	-	-	-	-	-	2.5	0.4	3	675	88.3	6.5	3.4	1.9	4.5
-	-	-	-	-	-	-	-	-	2.5	0.4	6.5	627	94.8	1.6	3.4	0.4	5.1
-	1	3	ΔH < 0	59.2	10.9	27.0	2.9	2.9	-	-	-	-	-	-	-	-	-
-	1	6.5	718	63.1	10.3	26.5	0.0	3.4	-	-	-	-	-	-	-	-	-

In this Table two levels of S/EtOH ratios were explored 3 (stoichiometric condition) and 6.5. Intermediate values were also calculated but only these were reported for simplicity reasons. Table 1 presents autothermal conditions for the SR process at S/EtOH = 3 an autothermal temperature of 334°C is found accompanied with a very poor hydrogen

production (0.3 kmol) and purity (13.4%). This was expected since the reaction system is very endothermic at stoichiometric conditions and this was the case for the S/EtOH = 6.5, since from a temperature range from 300-900 ºC an adiabatic temperature was not found even though the hydrogen content was increased ((4.7 kmols) and its purity (71.7%) with mayor impurities being CO and CO_2. In the same Table the ATR reforming mode was also explored in terms of the autothermal condition. Here, different O_2/EtOH ratios were studied; 0.1, 0.25, 0.375, 0.5, 0.75, 0.85 and 1.0. Generally, in terms of the adiabatic temperature as the S/EtOH ratio was increased the adiabatic temperature was reduced. These results imply that the net energy required from the reactions enlarges when the excess steam is fed to the reaction system. At O_2/EtOH = 0.1 and S/EtOH = 3.0 results in an adiabatic temperature of 312°C, which produce very small hydrogen product and purity furthermore, this condition is not kinetically feasible for practical purposes. Therefore, an increase in the O_2 content was explored and this was reflected in a gradual increase in the adiabatic temperature as well as in the hydrogen content and purity. For example at O_2/EtOH = 0.25 and 1.0 with S/EtOH = 6.5 temperatures of 390 and 718°C were found with hydrogen contents of 1.2 and 3.4 kmols, and H_2 purities of 42 and 63% respectively. As the oxygen content was increased the concentrations of carbon oxides (CO and CO_2) were also increased, since ethanol partial oxidation reactions (3) to (5) are promoted with higher oxygen content and temperatures. Methane concentrations decreased due to the enhancement of the methane reforming reaction at high temperatures. Therefore, even the autothermal condition produced lower hydrogen content with respect to the SR operating mode at expense of an adiabatic reactor operation. These results are consistent with studies performed by several authors in the literature [14, 19, 29, 30].

Also in Table 1 the AER process was evaluated in terms of the adiabatic conditions for a possible autothermal operation. In this Table 2.5 kmols of CaO were used at S/EtOH of 3 and 6.5and adiabatic temperatures were 481 and 372°C. These results generated hydrogen contents and purities of 4.3 and 5.6 kmols and 90.8 and 98.3%, respectively. Clearly, these are not the optimum thermodynamic operating conditions for a maximum hydrogen production that so far have been reported in the literature which are: A feed of 2.5 kmol CaO, S/EtOH = 6.5, 634°C, and 5.7 kmol of hydrogen being produced [31] . However these conditions are moderately endothermic with a ΔH_R = + 196.5 kJ/kmol. The values reported in Table 1 for the autothermal conditions under the AER process ar still at temperatures (372-481°C) where the ethanol reforming reaction are kinetically limited and the hydrogen content may necessarily be reduced (3.4 - 4.3 kmols of H_2) at the expense of an adiabatic operating temperature. Therefore, the need of additional heat to be supplied to the AER reactor is expected to be included in a possible continue operation of this process.

On the other hand, Table 1also presents results of the AER-ATR operating mode process proposed in the present work. Here, different O_2/EtOH ratios were studied; 0.1, 0.2, 0.25, 0.3, 0.35and 0.4. In terms of the adiabatic temperature here also as the S/EtOH ratio was increased the adiabatic temperature was reduced. At O_2/EtOH = 0.1 and S/EtOH = 3.0 results indicate an adiabatic temperature of 572°C, producing a hydrogen product and purity of 4.4

kmols and 97.8%, respectively. Major impurity of this product gas consisted of methane with 7.4% accompanied with fractional % of carbon oxides (CO and CO_2). As the S/EtOH increased to a value of 6.5, this even further enhanced the hydrogen production to 5.5 kmols and 98.6% with a consequent decrease in the adiabatic temperature to a value of 457°C. A further increase in the oxygen content to a O_2/EtOH = 0.3 and S/EtOH = 3.0 generated an adiabatic temperature of 651°C which is close to the typical reforming temperature of a catalytic autothermal steam reforming of ethanol reported by Deluga et al. [14]. They experimentally found that catalytic conversion of ethanol was only 40% at 400°C but rose to above 95% by 650°C. At 400°C, acetaldehyde and CH_4 selectivities were 16 and 14%, respectively, for a total selectivity to undesired minor products of about 30%. Both of these species decreased with increasing temperature and acetaldehyde fell to a negligible level by 650°C. In their studies, they concluded that ethanol conversion is much lower and minor products are more abundant at lower temperatures, indicating that catalyst temperatures above 600°C are needed for optimum performance.

A further increase in S/EtOH to 6.5 still at O_2/EtOH = 0.3 and using CaO as a CO_2 absorbent in the reaction system, generated a hydrogen product of 5.2 kmols and 97.5% purity with a consequent decrease in the adiabatic temperature to a value of 590°C. Again, mayor impurities were methane and carbon oxides. This adiabatic temperature value is close the desired catalytic operating temperatures experimentally found by Deluga et al. A further increase in oxygen content to a value of O_2/EtOH = 0.4 and S/etOH ratio of 6.5 generated an adiabatic temperature of 627°C accompanied with a reduction in the hydrogen content and purity of 5.1 kmols and 94.8%. This behavior can be explained in terms of an increase of the carbon oxides content (CO and CO_2) that presumably promote the ethanol partial oxidation reactions thus producing gaseous carbon species that eventually is traduced in a slight reduction in the hydrogen being produced. Therefore, it can be concluded that optimal operating conditions for high hydrogen production and purity in the AER-ATR process are given by an O_2/EtOH range of 0.3-0.4, S/EtOH = 6.5 and an adiabatic temperature range of 590-627°C.

4. CONCLUSIONS

Thermodynamic analysis of steam reforming of ethanol through SR, ATR, AER and AER-ATR reforming process schemes were carried out to determine favorable operating conditions to produce a high purity H_2 gas product. Results indicate no carbon formation at steam to ethanol ratios less than stoichiometric values (S/EtOH $\leq$ 3, stoichiometric) for the corresponding steam reforming reactions. In the SR process greater temperatures than 536°C and S/EtOH ratios greater than 2.75 will insure a carbon free operation under this system. Whereas, under the AER system carbon formation can be avoided with S/EtOH ratios greater than 1.9 and 686ºC combined with CaO as a solid CO_2 absorbent. The use of a CO_2 absorbent inhibits carbon formation in about three orders of magnitude with respect to the SR process. In the ATR process S/EtOH higher than 2.0 will ensure a carbon free operation at O_2 content in the feed in the order of O_2/EtOH = 1.0 and temperatures lower than 400°C at all reaction temperatures. In the case of the AER-ATR process at oxygen contents of about O_2/EtOH = 0.5, S/EtOH ratios greater than 1.2 are

needed in order to insure a carbon free operation at all temperatures studied. In all the reforming operating modes (SR, AER, ATR and AER-ATR) greater than stoichiometric values will insure carbon free operation. In terms of the order from higher to lower carbon formation is: SR > ATR > AER > AER-ATR. Finally, optimal operating conditions for high hydrogen production and purity in the AER-ATR process are given by an O_2/EtOH range of 0.3-0.4, S/EtOH = 6.5 and an adiabatic temperature range from 590-627°C.

5. REFERENCES

[1] Ogasawara T, De´bart A, Holzapfel M, Nova´k M, Bruce PG., J Am Chem Soc;128:1390-3 (2006).

[2] Zhou H, Flamant G, Gauthier D., Chem Eng Sci; 59:4205-15 (2004).

[3] Kalinci Y, Hepbasli A, Dincer I., Int J Hydrogen Energ., 34:8799-817 (2009).

[4] Guo XM, Trably E, Latrille E, Carre`re H, Steyer JP., Int J Hydrogen Energ., 35: 10660-73 (2010).

[5] Serra JM, Vert VB, Bu¨ chler O, Meulenberg WA, Buchkremer HP., Chem Mater., 20:3867-75 (2008).

[6] Saida T, Ogiwara N, Takasu Y, Sugimoto W. J Phys Chem C., 114:13390-6 (2010).

[7] G. W. Huber, J. W. Shabaker, J. A. Dumesic, Science 300: 2075(2003).

[8] R. D. Cortright, R. R. Davda, J. A. Dumesic, Nature 418: 964 (2002).

[9] D. Scott and B. Yann Liaw, Energy Environ. Sci., 2: 965-969 (2009).

[10] M. Slinn, K. Kendall, C. Mallon, J. Andrews, Bioresource Technol., 99: 5851–5858 (2008).

[11] X. Li, E. Mupondwa, S. Panigrahi, L. Tabil, S. Sokhansanj, M. Stumborg, Renew Sust Energ Rev., 16: 2954-2965 (2012).

[12] G. Rabenstein, V. Hacker, J Power Sources., 185: 1293–1304 (2008).

[13] J. R. Salge, G. A. Deluga, L. D. Schmidt, J Catal; 235: 69–78 (2005).

[14] G. A. Deluga, J. R. Salge, L. D. Schmidt, X. E. Verykios, Science; 303: 993–7 (2004).

[15] P.D. Vaidya, A.E. Rodrigues, Chem Eng J., 117: 39–49 (2006).

[16] A.N. Fatsikostas, X.E. Verykios, J Catal; 225: 439–452 (2004).

[17] E. Ochoa-Fernández, H. Berntsen, T. Zhao, L. Hi, E. A. Blekkan, D. Chen, "CO_2 Sorption Enhanced Steam Reforming of Ethanol", North American Catalysis Society 20th North American Meeting, June 17-22, Abstract P-S12-34B (2007).

[18] A. Lima da Silva, I. L. Müller, Int J Hydrogen Energ, 36: 2057-2075 (2011).

[19] G. A. Deluga, J. R. Salge, L. D. Schmidt, X. E. Verykios, Science, 303 13 (2004).

[20] S. Jarungthammachote, A. Dutta, Energy Convers. Manage, 49: 1345–1356 (2008).

[21] A. Roine, Chemical reaction and equilibrium software with extensive thermo-chemical database. Outokumpu HSC 6.0 Chemistry for windows 2010.

[22] M. Benito, J.L. Sanz, R. Isabel, R. Padilla, R. Arjona, L. Daza, J Power Sources, 151: 11-17 (2005).

[23] A. N. Fatsikostas, X. E. Verykios. J Catal, 225: 439-452 (2004).

[24] P. Biswas, D. Kunzru, Int J Hydrogen Energy, 32: 969-980 (2007).

[25] A. J. Akande, "Production of Hydrogen by Reforming of Crude Ethanol", Master of Science Thesis, University of Saskatchewan, Saskatoon, Saskatchewan, Canada (2005).

[26] M. Li, Int J Hydrogen Energy, 34: 9362-9372 (2009).

[27] B. Zhang, X. Tang, Y. Li, W. Cai, Y. Xu, W. Shen, Catal Commun, 7: 367-372 (2006).

[28] M. Li, Int J Hydrogen Energy, 34: 9362-9372 (2009).

[29] C. Graschinsky, P. Giunta, N. Amadeo, M. Laborde, Int J Hydrogen Energy, (2012), doi:10.1016/j.ijhydene.2012.01.182.

[30] S. Cavallaro b, V. Chiodo a, A. Vitaa, S. Freni, J Power Sources, 123: 10–16 (2003).

[31] M. A. Escobedo Bretado, M. D. Delgado Vigil, J. Salinas Gutiérrez, V. Collins-Martínez and A. López Ortiz Absorption Enhanced Reforming of Light Alcohols (Methanol and Ethanol) for the Production of Hydrogen: Thermodynamic Modeling, 11th International Hydrogen Congress Mexican Hydrogen Society, 11th International Hydrogen Congress Mexican Hydrogen Society, 20-23 September, 2011 City of Cuernavaca, Mexico.

Effect of Carbon Porosity on the Electrochemical Properties of Carbon/Polyaniline Supercapacitor Electrodes

M.A. Torre, C. del Río and E. Morales*

Instituto Ciencia y Tecnología de Polímeros (C.S.I.C.)
c/ Juan de la Cierva 3, 28006 Madrid, Spain
*Tel: 34 915622900, fax 34 915644853, mail: emorales@ictp.csic.es

ABSTRACT

Electrochemical supercapacitors have attracted great attention in power source applications, due to their high power density, high charge/discharge rate, good reversibility and long life. Activated carbons are the most frequently used electrode material, due to their high accessibility, non-toxicity, high chemical stability, good electrical conductivity, high surface area and low cost, but in practice the capacitance values are limited by the material microstructure. Several methods have been reported to increase the capacitance, such as the incorporation of functional groups at the surface, the development of nanostructured carbons and the synthesis of hybrid composites of carbon with conducting polymers or metal oxides. In this work we report on the synthesis and electrochemical characterization of carbon/polyaniline composites, synthesized by in-situ chemical oxidative polymerization in acid media of aniline monomer on the surface of two commercial activated carbons having different textural properties, and the effect of the carbon porosity on the electrochemical properties of the electrodes. Results obtained indicate that the BET specific surface of the composites decreases sharply due to the collapse of the porous structure (mainly the micropores) of the carbon by the polyaniline chains. Regarding capacitance values, C_{sp} increases on increasing polyaniline loading in the composite, however high polymer concentration lead to a decrease on capacitance when high current were applied, probably due to diffusion restrictions of the electrolyte to the carbon surface.

1. Introduction

Electrochemical capacitor devices, often called supercapacitors or ultracapacitors, have received significant attention in recent times due to their wide range of potential applications in hybrid electric vehicles, fuel cells, cellular phones, PDAs, etc [1-4]. Two types of mechanisms are associated with energy storage in a this kind of devices: one is the electric double-layer capacitor (EDLC), in which stored energy is accumulated by the separation of electronic and ionic charges at the interface between a high surface area electrode and an electrolyte solution; the other is the pseudocapacitor, in which the active species can be fast and reversibly oxidized and reduced at characteristic potentials. Carbon materials such as activated carbon fibers and powders, carbon aerogels, carbon nanotubes [5-8] etc, are commonly used as electrode materials for EDLC, displaying good stability, but the capacitance values are limited by the microstructures in the materials. Conducting polymers such as polyanilines (PANI's), polypyrroles (PPY's), polythiophenes (PT's), etc [9-11] and transition metal oxides such as RuO_2, NiO, MnO_2, etc [12-14], have been used for redox capacitors. These devices generally display high capacitance, however conducting polymer based devices usually exhibit poor stabilities during the charge/discharge process while the high price of metal oxide restricts their commercial use.

Composites of carbons having different morphologies and conducting polymers can fully combine advantages of double-layer capacitance of carbon materials and pseudo-capacitance of conducting polymer, providing materials with high specific capacitance and working voltage, but also excellent cycle stability [32-36]. In this work we report on the synthesis and electrochemical characterization of carbon/polyaniline composites, synthesized by in-situ chemical oxidative polymerization in acid media of aniline monomer on the surface of two commercial activated carbons having different textural properties, and the effect of the carbon porosity on the electrochemical properties of the electrodes.

2. Experimental

Two commercial activated carbons, mesoporous-rich (Monarch 1400C) and microporous-rich (BP2000) both obtained from Cabot, hereafter labeled as Meso-C and Micro-C were tested. Aniline monomer (Aldrich) was distilled prior to use and stored at 278K. Carbon/polyaniline composites were prepared by adsorption of aniline on the carbon surface followed by chemical polymerization. In a typical reaction, 2 g of carbon was added to 30 ml of an aqueous 1M HCl solution containing 0.5 g (5.37 mmol) of aniline. After stirring for 30 min, 30 ml of an aqueous 1 M HCl solution containing 1.227 g (5.37 mmol) of ammonium peroxodisulfate (Aldrich) was added dropwise at 273 K and stirring continued for 3 h. The resulting composites were filtered and washed with deionized water up to neutral pH, then dried dried at 313 K over P_2O_5 for 72h. The mass loading of PANI in the composite was evaluated by microanalysis (LECO CHNS- 932).

Porosity of the composites was analyzed by N_2 adsorption at 77K (Micromeritics ASAP 2010). The apparent specific surface area was determined from the N_2-adsorption isotherm using the BET equation [15]. The pore volume (V_{total}) was calculated by applying the Dubinin–Radushkevich (DR) equation to the N_2-adsorption isotherms [16]. The

microporous surface area was obtained from the equation: S_{mic} ($m^2.g^{-1}$) = $2000V_{N2}$ ($cm^3\ g^{-1}$)/L_0 (nm), where L_0 represents the average micropore width [17]. Additionally, the analysis of the adsorption isotherm by a classical comparison plot based on the reference N_2 adsorption for a non-porous carbon (Vulcan 3G carbon) provided information on the mesopore area S_{meso}. Pore size distribution was calculated by means of the Kruk–Jaroniec–Sayari method [19] applied to the adsorption branch. The electrochemical performance of the composites was analyzed in symmetric two-electrode Swagelok™-type cells by both cyclic voltammetry and constant current galvanostatic charge–discharge using a Solartron 1480 multichanel potentiostat–galvanostat equipment. The electrodes (12 mm in diameter and ca. 1 mm height), were obtaining by pressing (500 Kg) a homogeneous mixture of the composite (70 wt.%), polyvinylidene fluoride binder (20 wt.%) and carbon black (Super P, 10 wt.%). Glassy microfibre paper discs (Whatman BS45) were used as separator and aqueous 2 M H_2SO_4 solution as electrolyte. Two stainless steel (A20 alloy) rods acted as current collectors.

3. Results and discussion

Table 1 shows composite composition obtained from microanalysis tests (N determination, average of three measurements). A small decrease on the PANI content in the composites regarding to the theoretical one was detected in all cases.

Table 1. Carbon/PANI composites composition

Sample	PANI Nominal content wt%	PANI Real content wt%
Meso-C/PANI1	20.0	18.6
Meso-C/PANI2	33.3	25.7
Meso-C/PANI3	50	39.0
Meso-C/PANI4	60	46.0
Micro-C/PANI1	20	16.1
Micro-C/PANI2	33.3	24.3
Micro-C/PANI3	50	35.1
Micro-C/PANI4	60	43.1

Figures 1 show the N_2 adsorption–desorption isotherms corresponding to both carbons, polyaniline and the synthesized carbon/PANI composites. In terms of shape, the isotherm of both carbons can be classified as type IV according to the IUPAC, a hysteresis loop being observed on both isotherms in the range of ca. 0.6–1.0 P/P_0 for the Meso-C sample and 0.85-1.0 for the Micro-C carbon.

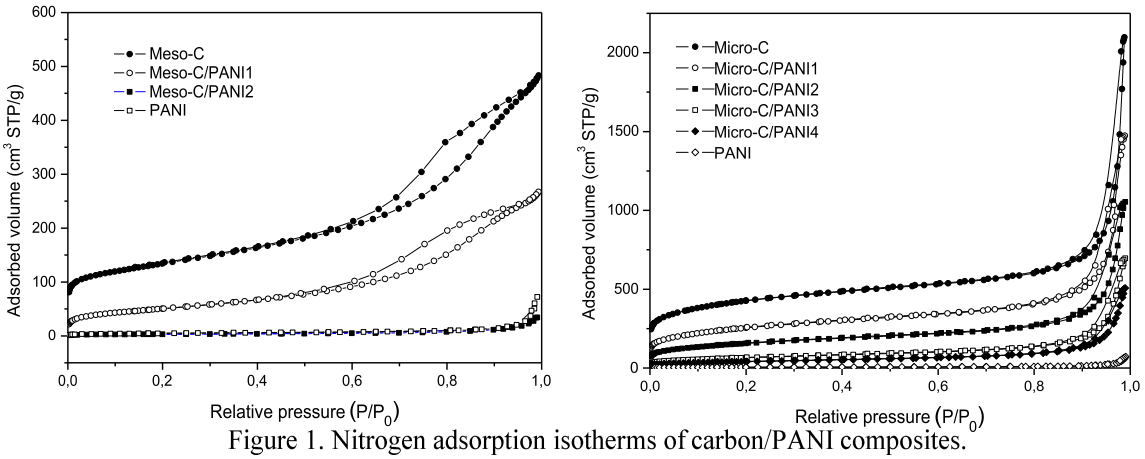

Figure 1. Nitrogen adsorption isotherms of carbon/PANI composites.

The textural characteristics of the samples calculated from nitrogen adsorption–desorption isotherms are listed in Table 2. Results indicate that the pore structure of the composites depends strongly on PANI $_{concentration}$, the BET surface area decreasing from 471 m^2g^{-1} calculated for the Meso-C to 4.7 m^2g^{-1} for the composite with a 46 wt% PANI loading, due to the partial covering or filling of the pore structure of the carbon by the polymer, the mesoporous structure of the carbon was maintained after PANI loading up to 20 wt%. The total pore volume also decreases when increasing PANI concentration, mesopore and micropore structure being practically disappear for high PANI loadings.

Table 2. Textural properties of carbon/PANI composites

Sample	S_{BET} (m^2g^{-1})	V_{total} (cm^3g^{-1})	V_{mic} (cm^3g^{-1})	V_{mes} (cm^3g^{-1})	S_{mic} (m^2g^{-1})
Meso-C	471	0,75	0,18	0,57	254
MESO-C/PANI1	183	0,41	0,07	0,31	28,9
MESO-C/PANI2	20,2	0,08	0,01	0,01	1,77
MESO-C/PANI3	12,2	0,04	-	-	1,80
MESO-C/PANI4	4,7	0,02	-	-	1,04
Micro-C	1510	3,24	0,57	2,68	700
Micro-C/PANI1	930	2,28	0,32	1,96	320
Micro-C/PANI2	566	1,63	0,20	1,43	171
Micro-C/PANI3	237	1,08	0,08	0,99	47,3
Micro-C/PANI4	145	0,78	0,05	0,73	24,0
PANI	16,7	0,10	0,01	0,09	0,03

Similar effect was observed for Micro-C/PANI samples, but in this case the hysteresis, associated to the mesoporous pore structure was detected in all cased, independently of PANI concentration in the composite. Pore-size distribution of the samples, calculated by applying the Kruk-Jaroniec-Sayari to the adsorption branch of the isotherms, is shown in Figure 2. Meso-C carbon has a broad pore size distribution, with a maximum centered at 11.8 nm. Regarding the composites, the sample with the lower loading of PANI show a profile similar to that of the carbon, with a maximum centered at 11.2 nm: increasing PANI loadings lead to a decrease on the pore size to 7.3 nm for the Meso-C/PANI2 sample, no pore being detected for higher PANI concentration. Regarding Micro-C-based composites, the pore size distribution graph indicate the presence of macropores (pore diameter >50 nm) in all samples, the volume decreases on increasing PANI concentration in the composite.

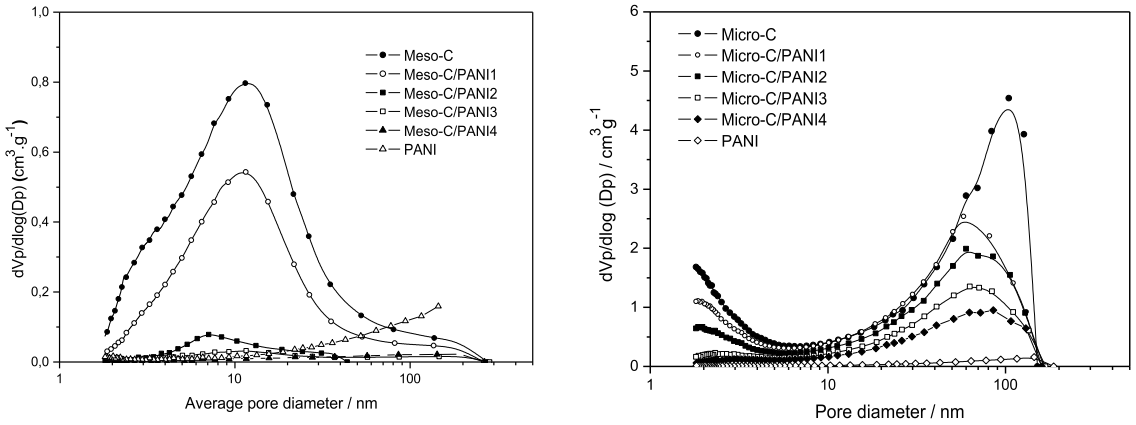

Figure 2. Pore-size distribution calculated for carbon/PANI composites.

Figure 3 shows the cyclic voltammograms of symmetric supercapacitors based on the Meso and Micro-C/PANI composites under study recorded at a scan rate of 10 $mV.s^{-1}$. Carbon-based devices cyclic voltammograms show the expected rectangular shape associated to EDLC behaviour, while deviations from this behaviour were detected for all composites, where two redox oxidation and reduction peaks were observed, associated to the pseudocapacitive contribution of the polymer.

Figure 4 show the variation of the specific capacitance, calculated from constant current galvanostatic charge/discharge test vs. the applied current density. The larger values of C_{sp} were obtained for the PANI device, but the value decrease sharply on increasing the applied current due to restrictions on the diffusion of the electrolyte. Carbon/PANI composites show specific capacitance values that, at low applied current are higher than that of the pristine carbon, but again due to electrolyte diffusion restrictions decrease on increasing the applied current density up to been lower than the carbon. This effect was observed in both Meso and Micro-C derived composites.

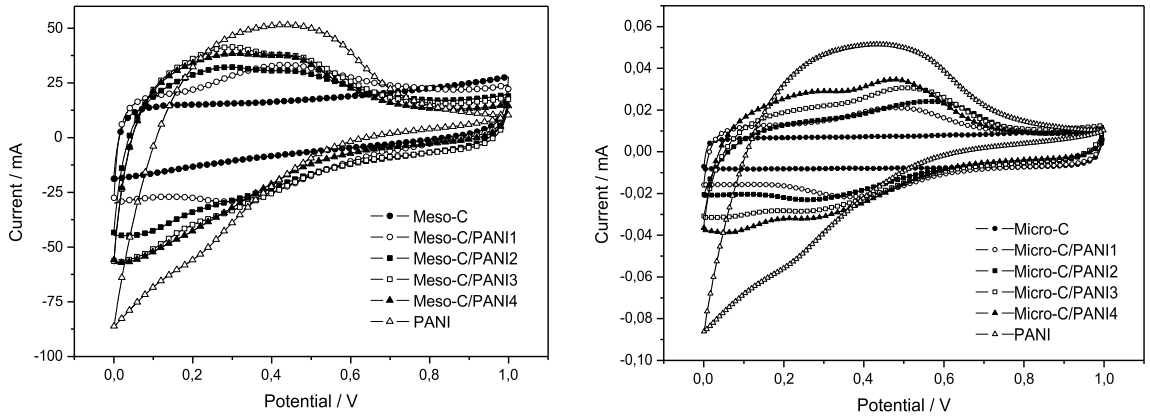

Figure 3. CV's of symmetric supercapacitors based on Meso and Micro-C/PANI composites measured at a scan rate of 10 mV.s^{-1}. Potential window 0-1 V.

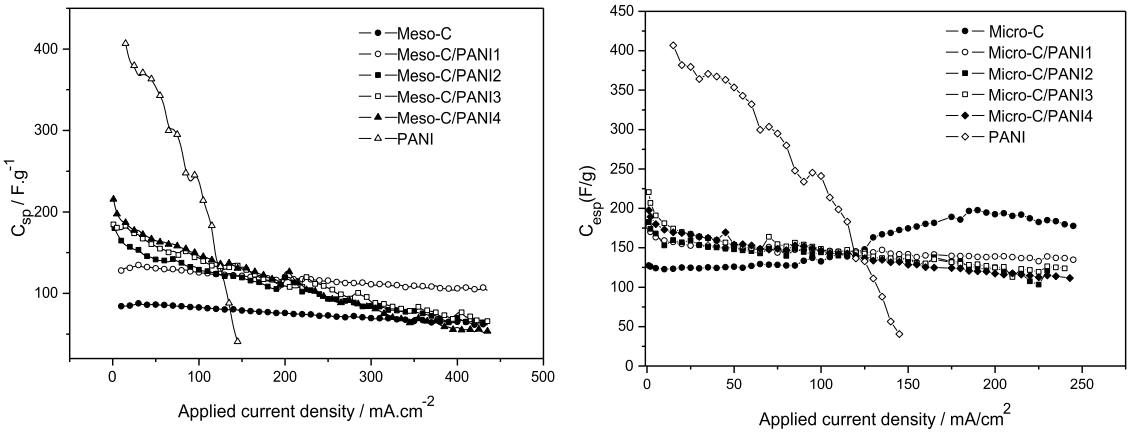

Figure 3. Discharge specific capacitance vs. applied current density of Meso C and Micro-C/PANI based symmetric supercapacitors. Potential window 0-1 V.

The best results were obtained for the Meso-C/PANI composite with the lower polyaniline loading (20 wt %), were the specific capacitance is 70% higher than that of the Meso-C carbon through all the range of applied current densities tested. Looking at the results obtained can be postulated that for carbon/PANI composites, the best electrochemical properties, in terms of specific capacitance, will be obtained when using carbons with a mesoporous structure and low polyaniline loadings. The diffusion of the electrolyte to the carbon surface, and so the EDLC contribution to the energy storage mechanism, is restricted in the presence of micropores, that can be easily collapse by the polymer, or when using high polymer loadings in the composite.

4. Conclusions

Meso and microporous carbon/polyaniline composites have been synthesized by the in-situ oxidative polymerization of aniline monomer on the surface of the carbon particles. Textural analysis indicate that composites porous structure depends strongly on the PANI content, S_{BET} and pore volume decreasing on increasing PANI concentration. Regarding supercapacitor performance, the best results, in terms of specific capacitance, were obtained for the Meso-C/PANI composite, the specific capacitance been 70% higher than that of the Meso-C carbon through all the range of applied current densities tested. The results obtained suggest that, for carbon/PANI composites, the best specific capacitance will be obtained when using carbons with a mesoporous structure and low polyaniline loadings. The diffusion of the electrolyte to the carbon surface, and do, the EDLC contribution to the energy storage mechanism, is restricted in the presence of micropores that can be easily collapse by the polymer or when using high polymer loadings in the composite.

5. Acknowledgements

Financial support by the Spanish Ministry of Science and Innovation Project ENE2007-62791/ALT is gratefully acknowledged. M.A. Torre thanks for a contract associated with that project.

6. References

[1] A.F. Burke, T.C. Murphy, in Proceedings of the Materials Research Society Symposium on Materials for Energy Storage and Conversion: Batteries, Capacitors and Fuel Cells, Eds. D.H. Goughtly, B. Vyas, T. Takamura, J.R. Huff, Pittsburgh, USA (1995).

[2] S. Sarangapani, B.V. Tilak, C.P. Chen, J. Electrochem. Soc., 143, 3791 (1996).

[3] C. Arbizzani, M. Mastragostino, B. Scosati, Handbook of Organic Conductive Molecules and Polymers vol. 4, H.S. Nalwa Ed, Wiley, Chichester, UK, (1997).

[4] B.E. Conway, Electrochemical Supercapacitors, Kluwer Academic/Plenum, New York, USA, (1999).

[5] K. Babel, K. Jurewicz, J. Phys. Chem. Solids, 65, 275 (2004).

[6] A.B. Fuertes, G. Lota, T.A. Centeno, E. Frackowiak, Electrochim. Acta, 50, 2799 (2005).

[7] J. Li, X.Y. Wang, Q.H. Huang, S. Gamboa, P.J. Sebastian, J. Power Sources, 158, 784 (2006).

[8] E. Frackowiak, K. Jurewicz, S. Delpeux, F. Beguin, J. Power Sources, 97-8, 822 (2001).

[9] H.H. Zhou, H. Chen, S.L. Luo, G.W. Lu, W.Z. Wei, Y.F. Kuang, J. Solid State Electrochem., 9, 574 (2005).

[10] L.-Z. Fan, J. Maier, Electrochem. Commun. 8, 937 (2006).

[11] A. Laforgue, P. Simon, C. Sarrazin, J.-F. Fauvarque, J. Power Sources 80, 142 (1999).

[12] J.H. Jang, A. Kato, K. Machida, K. Naoi, J. Electrochem. Soc., 153, A321 (2006).

[13] Y.G. Wang, Y.Y. Xia, Electrochim. Acta, 51, 3223 (2006).

[14] R.N. Reddy, R.G. Reddy, J. Power Sources, 124, 330 (2003).

[15] S. Brunauer, P. Emmet, E. Teller, J. American Chemical Soc., 60, 309 (1938).

[16] M.M. Dubinin, Progress in Surface and Membrane Science vol. 9, D.A. Cadenhead Ed., , Academic Press, London, UK (1975).

[17] H.F. Stoeckli, Porosity in Carbons, J.W. Patrick Ed., Edward Arnold, London, UK (1995).

[18] J.A. Fernández, T. Morishita, M. Toyoda, M. Inagaki, F. Stoeckli, T.A. Centeno, J. Power Sources, 175, 675 (2008).

[19] M. Jaroniec, A. Safari, Langmuir, 13, 6267 (1997).

[20] K.S.W. Sing, D.H. Everrett, R.A.W. Haul, L. Moscow, R.A. Pierotti, J. Rouquerol, T. Siemieniewska, Pure Appl. Chem. 57, 603 (1985).

Carbon-Supported Copper Phthalocyanine (Cupc/C) as a Novel Cathode Catalyst for Polymer Electrolyte Membrane Fuel Cells --- Effect of Nafion Ionomer as for Alkaline Electrolyte

Lei Ding[1,2], Xianfeng Dai[1], Samir Ibrahim[2], Yuyu Liu[2*], Jinli Qiao[1*]

[1]College of Environmental Science and Engineering, Donghua University,
2999 Ren'min North Road, Shanghai 201620, P. R. China
[2]Lab of Urban and Regional Environmental Systems, Graduate School of Environmental Studies,
Tohoku University, Aramaki, aza Aoba 6-6-11,
Aoba-ku Sendai 980-8579, Japan

ABSTRACT

Carbon-supported copper phthalocyanine (CuPc/C) nanoclusters, as a novel suitable cathode catalyst in polymer electrolyte membrane fuel cells have been synthesized via a combined solvent-impregnation and milling procedure along with the high temperature treatment. For optimizing the electrocatalytic activity of the catalyst obtained, the electrode with a variety of Nafion ionomer contents in the catalyst layer was screened by cyclic voltammetry (CV) and linear sweep voltammetry (LSV) employing a rotating disk electrode (RDE) technique to investigate the effect of Nafion ionomer as for alkaline electrolyte. For comparative purposes, electrode with various contents of available anion-ionomer was also investigated. The results revealed that the content of Nafion ionomer can affect the ORR activity of the CuPc/C catalyst and an optimal content of Nafion ionomer was around 3.5×10^1 μg cm^{-2}, which corresponds well with the electrode prepared using available anion-ionomer. Under which, the electrode prepared using Nafion ionomer can produce a comparable performance to that of using available anion-ionomer, giving an on-set potential at 0.1 V with a half-wave potential of -0.03 V. Furthermore, Koutechy-Levich analysis showed that the value of electron transfer number is in a range of 3.40 to 3.74 when electrode with Nafion ionomer contents changing from 2.5×10^1 to 1.6×10^2 μg cm^{-2}. The membrane electrode assembly (MEA) fabricated with CuPc/C cathode catalyst with a loading of 3.6 mg cm^{-2} and, a Nafion membrane immersed in 3M KOH for 48 hours, reached an initial power density of 3.8 mW cm^{-2} at room temperature.

1. Introduction

It is commonly believed that fuel cells are promising power sources for offering clean and high energy conversion efficiency technology. For obtaining the high catalytic performances, platinum (Pt) supported on carbon black is normally used as the best electrocatalyst for both the anode and the cathode, particular to Nafion®-based proton-exchange membrane fuel cells (PEMFCs). However, the widespread commercialization of the fuel cell technology has been hindered so much because of the high cost of Pt and its scarcity. This becomes more serious particular to high loading requirements on the cathode for the oxygen reduction reaction (ORR) due to the sluggish kinetics of Pt (~ 300 mV overpotential loss) [1]. Alternatively, the use of alkaline media in fuel cell applications presents many advantages, both in electrocatalytic activity and in materials stability over acidic media, which can provide more choices for suitable Pt alternatives [2-6].

With respect to non-platinum catalysts, Metal-N_4 macrocycles after heat-treatment, such as Fe- and Co-centered phthalocyanine complexes, are considered to be the most promising non-precious metal catalysts due to their high conjugate structure and relatively good chemical stability [7-10]. Comparatively, little are concerned for other metal centered phthalocyanines, this is because that in strong acidic conditions such as in PEM fuel cells, the catalysts that show high ORR catalytic activity, and at the same time, high stability are strongly desired. However, little progress is achieved because of trade-off relations between these parameters [11,12]. Recent studies indicate that pH could affect the ORR activity of MPcs, which suggests that other metal centered phthalocyanines such as Ni-, Mn- and Cu-centered phthalocyanines, might be more appropriately used in alkaline solutions [13].

As is known to all, electrode preparing is a necessary step in the electrocatalytic activity study of the catalysts for the ORR, particular to the polymer electrolyte membrane fuel cells. Among which, a polymer binder is essential to bind discrete catalyst particles to form a porous catalyst layer that facilitates the transfer of ions, electrons and reactants. In recent years, more and more polymer materials have been used as a binder for preparing MEAs for alkaline membrane fuel cells [14-16]. Bunazawa et al. [17] investigated an anion ionomer solution (labeled as A3) as a binder for alkaline direct methanol fuel cell and, studied the effect of anion ionomer content in the anode and cathode catalyst layers. The results suggested that MEA with 45.4% mass ionomer content showes the highest performance at both anode and cathode electrodes. Zhao et al. [18] used A3 ionomer and polytetrafluoroethylene (PTFE) as the binder in anode catalyst layer for alkaline direct ethanol fuel cells. They found that the PTFE binder yields better performance than does the A3 binder. Unfortunately, up to now, no alkaline binder can completely realize the commercialization like Nafion® binder in PEMFC. Hence, it is difficult to choose a suitable binder used for alkaline electrolyte. Generally, in the process of the preparation of the electrode, the thickness of the binder coated on the electrode layer is very thin. Therefore, using Nafion® ionomer as the binder may be good choice if it has no significant effect on the O_2 reduction rate.

In view of these facts, in this work, the possibility of constituting new electrocatalysts using carbon-supported

copper phthalocyanine (CuPc) complexes are pursued for the ORR after heat-treatment at high temperatures. We focus on the feasibility by applying Nafion® ionomer as a binder for electrochemical measurements in alkaline solution. Emphasis is made on the effect of Nafion® content on the catalyst layer, whether Nafion® ionomer could affect more or less the ORR activity and how much is the optimal content for catalyst ink preparation. Further more, the preliminary fuel cell test using the conventional hot-pressing MEAs with a Nafion membrane immersed in KOH solution and, carbon supported CuPc as cathode catalyst was also carried out.

2. Experimental

2.1 Materials and catalyst preparation

Copper phthalocyanine was purchased from Sigma Aldrich with 97% purity and used as received. Carbon support (Vulcan XC-72) was purchased from Cobat Corporation. Carbon-supported copper phthalocyanine catalysts were prepared using milling method combined with a heat-treated procedure. Briefly, a mixture of 40 mg CuPc and 60 mg carbon black in 10ml methanol was prepared and carefully milled for about 2 hours in a mortar, then vacuum dried at 40^{o}C for another 1 hour to remove the methanol. The resulting powders were placed in a crystal boat, and pyrolyzed at 800^{o}C for 120 minutes at the rate of 5^{o}C min^{-1} in a flowing nitrogen atmosphere. The catalyst as-prepared is thus designated as CuPc/C.

2.2 Physical characterization

The crystal-phase X-ray diffraction (XRD) patterns were collected on a Philips PW3830 X-ray diffractometer using Cu-kα radiation (λ = 0.15406 nm). The current was 40 mA and the voltage was 40 KV. The intensity data were collected at 25^{o}C in the 2θ range from 5° to 90°with a scan rate of 1.20^{o} min^{-1}.

2.3 Electrochemical measurements

Electrochemical evaluation was carried out in a standard three compartment electrochemical cell in 0.1 mol L^{-1} KOH at room temperature. A pre-cleaned rotating disk electrode (RDE) (Glassy carbon electrode with a diameter of 6.0 mm corresponding to a geometric surface area of 0.283 cm^{2}, purchased from Pine Instruments) was used as the working electrode. A Pt wire and a saturated calomel electrode (SCE) were used as the counter and reference electrode, respectively. All measured potentials were converted into the values referring to a standard hydrogen electrode (SHE).

The catalyst ink for RDE measurements was prepared by blending 4 mg of the catalyst and 2 mL of methanol/Nafion® solution which was ultrasonically dispersed for 10 minutes to form a suspension. 10 μL of this suspension was then pipetted onto the surface of GC electrode and then dried at room temperature. For investigating the effect of Nafion content on the catalyst layer, methanol/Nafion® solution with different scales (70:1, 50:1, 30:1 and 10:1 in mass) were used to form catalyst inks. The Nafion® loadings were 2.5 × 10^{1}, 3.5 × 10^{1}, 5.7 × 10^{1} and 1.6 × 10^{2} μg cm^{-2}, respectively.

Initially, cyclic voltammograms (CVs) were carried out by scanning the disk potential from -0.3 to 0.6 V to measure the surface behavior of the catalyst in N_2-saturated 0.1 M KOH solution. For ORR measurements, the solution was then bubbled by pure O_2 to form an O_2-saturated in 0.1 M KOH solution. A CV was recorded in O_2-saturated electrolyte with the scan rate of 50 mV s^{-1}. For more quantitative measurements of ORR activity, linear sweep voltammetry (LSV) was conducted on the catalyst-coated RDE in the potential range between -0.7 and 0.2V in O_2-saturated 0.1 M KOH solution at desired rotating rates. In order to ensure a steady state in each point of the curve, a slow sweeping rate of 5 mV s^{-1} was applied.

2.4 Single cell tests

The cell configuration: H_2 | Pt/C | Nafion-OH^- | CuPc/C | O_2, was used in a single cell of PEMFC. The fabrication of MEAs was prepared by following steps: (i) The standard anode ink was prepared by mixing 40% Pt/C (Johnson Matthey) with a solution of 5 wt% Nafion® (DuPont) and isopropanol, and then sonicated for 4 h, where the ratio of Pt/C catalyst to Nafion® was 3:1. the catalyst ink was sprayed onto carbon papers (Toray TGP-H-090) to deposit a catalyst layer with a Pt loading of 0.5 mg (Pt) cm^{-2}. (ii) For cathode with non-platinum catalyst, the catalyst inks were prepared by mixing 40% CuPc/C with a solution of 5 wt% Nafion® and isopropanol, and then sonicated for 4 h, where the ratio of CuPc/C catalyst to Nafion® was also 3:1. Similar to the anode fabrication, the catalyst ink was sprayed onto carbon papers to deposit a catalyst layer with a CuPc loading of 3.6 mg cm^{-2}. (iii) Nafion-OH^- membrane was prepared using a Nafion® membrane with a size of 4 × 4 cm immersed in 3 M KOH for 48 hours. The Nafion solution was also used for the corresponding binders for both of the anode and the cathode. The Nafion®-OH^- membrane was sandwiched with two same pieces of carbon papers coated with catalyst and binder, and then were hot-pressed at a pressure of 10 MPa at 75 °C for 3 min.

Scheme 1 shows the working mechanism of polymer electrolyte membrane fuel cell. The MEAs with an active area of 4 cm^2 was inserted into a fuel cell hardware which consisted of graphite block with machined serpentine flow channel and copper current collector (Scheme 1 (B)). Pure hydrogen and oxygen were supplied to enter the anode and cathode channels at a flux of 100 and 60 ml min^{-1}, respectively, through a humidifier maintained at 25°C under ambient pressure. Polarization curves were obtained using a fuel cell evaluation system (GE/FC1-100).

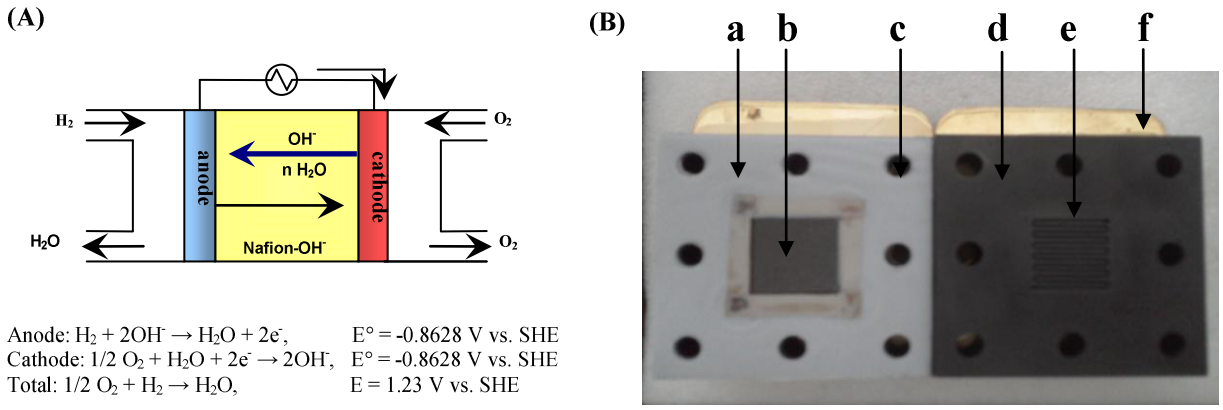

Anode: $H_2 + 2OH^- \rightarrow H_2O + 2e^-$, $E° = -0.8628$ V vs. SHE
Cathode: $1/2\ O_2 + H_2O + 2e^- \rightarrow 2OH^-$, $E° = -0.8628$ V vs. SHE
Total: $1/2\ O_2 + H_2 \rightarrow H_2O$, $E = 1.23$ V vs. SHE

Scheme 1. (A) working mechanism of polymer electrolyte membrane fuel cell; (B) photograph of polymer electrolyte membrane fuel cell showing silicon sheets (a), MEA (b), screw hole (c), graphite block (d), gas channel and (e) and current collector (f).

3. Results and discussion

3.1 physical characterization

Figure 1 shows the XRD patterns of the CuPc/C catalysts synthesized at different heat-treatment temperatures. The first large broad peak located at about $2\theta = 25^o$ was observed for all the XRD patterns, which is attributed to the diffraction of carbon. From Figure 1, it can be seen that CuPc/C without heat-treatment showed some quite strong diffraction peaks due to the crystalline nature of CuPc. However, these peaks disappeared after heat-treatment at 600°C. For catalyst sample heat-treated at 800°C, two new small diffraction peaks centered at 43.3° and 50.4° were clearly observed, indicating that part of the CuPc on the carbon support may have decomposed, forming the new Cu-N_x-C compositions. According to literature [19-21], these two diffraction peaks may correspond to the characteristic diffraction peaks of metallic Cu. When catalyst sample was further heat-treated at 900°C, the shape of these peaks becomes strong and narrow, indicating the growth of metallic Cu cluster particles after decomposition of the CuPc structure. Since the porosity of the catalyst may be blocked by metallic Cu which are not active for the ORR, the heat-treatment temperature for CuPc/C synthesis should not be higher than 800°C in order to obtain the high electrocatalytic activity. Thus, for a more detailed analysis of the effect of Nafion® ionomer, the CuPc/C heat-treated at 800°C was chosen for further study.

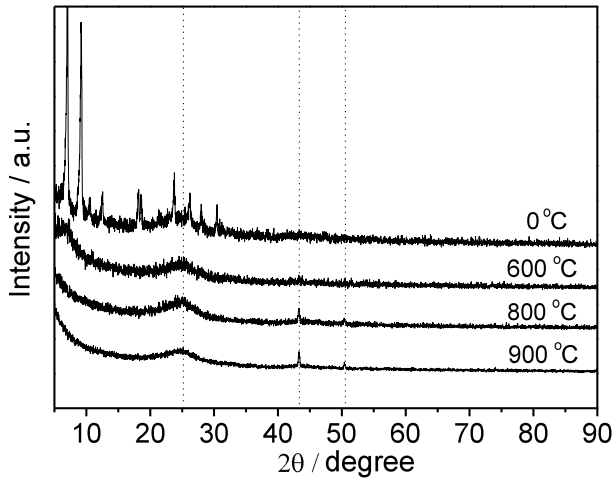

Figure 1. X-ray diffraction spectra of the CuPc/C catalysts before and after heat-treatment at 600, 800 and 900°C, respectively.

3.2 Electrochemical activity of CuPc/C catalyst towards ORR

Figure 2 shows CVs for the ORR on the CuPc/C electrode prepared with different Nafion® ionomer contents in the catalyst layer, measured in O_2-saturated 0.1 M KOH solution (where the CuPc/C catalyst loading on GC electrode was fixed of 140 μg cm^{-2}). It can be seen that CVs of CuPc/C electrode prepared with Nafion® contents of 2.5×10^1 and 3.5×10^1 μg cm^{-2} show the same oxygen reduction peak position (-0.06 V), but the latter gives 25% higher current density than the former. When Nafion® contents were increased to 5.7×10^1 and 1.6×10^2 μg cm^{-2}, the oxygen reduction peaks were at -0.1 and -0.12 V, respectively. Both are lower than that of CuPc/C electrode prepared with Nafion® contents of 2.5×10^1 and 3.5×10^1 μg cm^{-2}. Also, the peak current densities of CuPc/C electrode prepared with Nafion® contents of 5.7×10^1 and 1.6×10^2 μg cm^{-2} are both smaller than the values observed for CuPc/C catalyst with 3.5×10^1 μg cm^{-2} Nafion® content. The above results indicate that the optimal Nafion® ionomer content in the catalyst layer should be around 3.5×10^1 μg cm^{-2}.

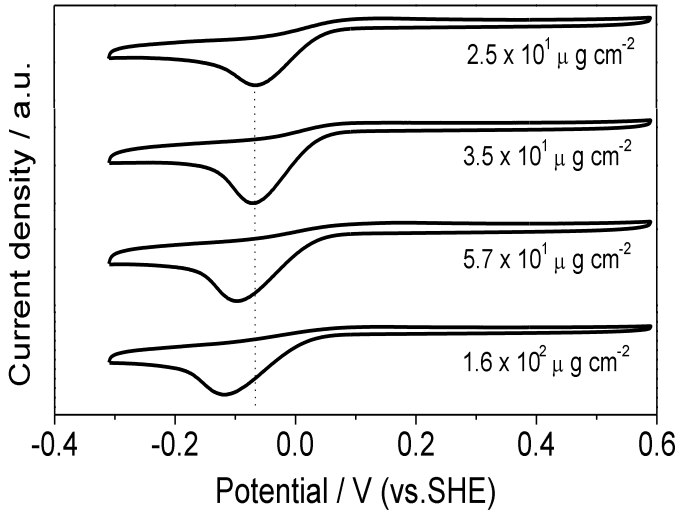

Figure 2. The cyclic voltammogram curves recorded in O_2-saturated 0.1 M KOH solution for the CuPc/C electrode coated with different Nafion® ionomer contents. Scan rate: 50 mV s^{-1}.

For further clarifying the effect of Nafion® ionomer content on the ORR activity, LSV was conducted on CuPc/C electrodes with different Nafion® contents in an O_2-saturated 0.1 M KOH solution (Figure 3). For a better comparison, the LSV curves of CuPc/C electrode prepared with available anion-ionomer are also depicted in the same figure. Acorrding to rotating disk theory, the overall measured current density (i) of the oxygen reduction at each electrode potential (E), shown in Figure 3, can be expressed as being dependent on the kinetic current density (i_k) and the diffusion-limited current density (i_d). The relationship between these current densities can be expressed by the following equation [22].

$$i_k = \frac{ij_d}{j + i_d} \tag{1}$$

Several important kinetic parameters for ORR on CuPc/C electrodes prepared with Nafion® ionomer and available anion-ionomer are summarized in Table 1. It can be seen that for CuPc/C electrode prepared with different contents of Nafion® ionomer, the onset potentials increase with decreasing Nafion® loading. Comparatively, for CuPc/C electrode prepared with different contents of available anion-ionomer, the onset potentials have no significant change with decreasing available anion-ionomer loading, and all are little higher than those of prepared with Nafion® ionom-

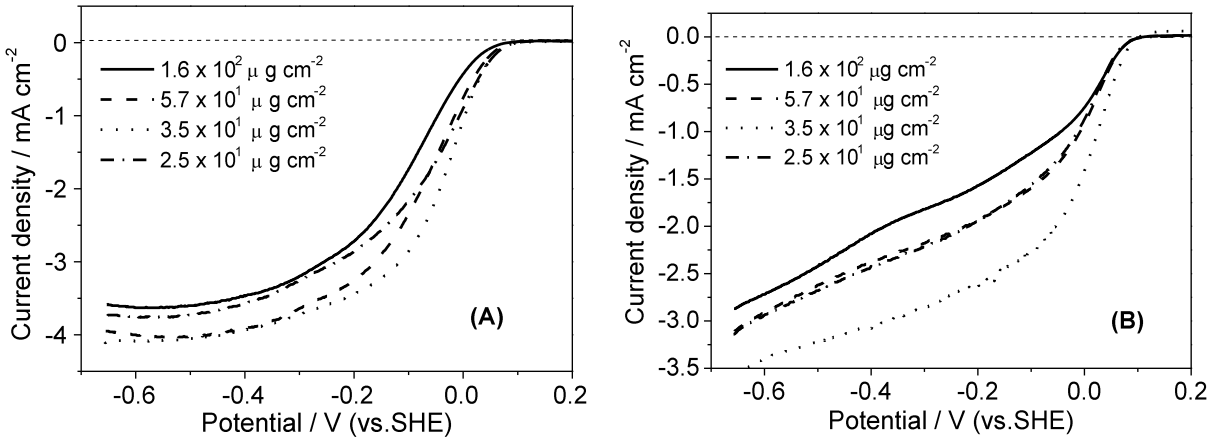

Figure 3. Polarization curves for the ORR on the CuPc/C catalysts, measured in O_2-saturated 0.1 M KOH at room temperature. (A) Nafion® solution for the catalyst ink preparation; (B) anion-ionomer for catalyst prepartion. Scan rate: 50 mV s^{-1}. Electrode rotation rate: 1500 rpm.

Table 1. Comparison of several kinetic parameters for ORR on CuPc/C electrode prepared with different contents of Nafion® ionomer and available anion-ionomer (potential versus SHE)

Binder loading (μg cm^{-2})		Onset Potential (V) [a]	$\Delta E_{1/2}$ (V) [a]	i_k at 0.05 V (mA cm^{-2}) [a]	Potential (V) at 0.1 mA cm^{-2} [a]
1.6×10^2	Nafion® ionomer	0.08	-0.105	1.40	0.045
	anion-ionomer	0.11	-	0.32	0.074
5.7×10^1	Nafion® ionomer	0.09	-0.06	3.90	0.061
	anion-ionomer	0.11	0.00	0.33	0.073
3.5×10^1	Nafion® ionomer	0.10	-0.03	4.50	0.066
	anion-ionomer	0.11	0.02	0.65	0.085
2.5×10^1	Nafion® ionomer	0.10	-0.06	2.90	0.068
	anion-ionomer	0.11	0.00	0.29	0.070

a) rpm 1500

er. Similarly, the half wave potential shows the positive shift from -0.06 to -0.03 V for Nafion® content changing from 2.5×10^1 to 3.5×10^1 μg cm^{-2}, but starts to fall with further increasing the content of Nafion® ionomer (Figure 3A). These observations indicate that the content of Nafion® ionomer can affect the ORR activity of the CuPc/C catalyst and, the optimal content of Nafion® ionomer is about 3.5×10^1 μg cm^{-2}. It should be mentioned that the optimal content of available anion-ionomer in CuPc/C electrode is also about 3.5×10^1 μg cm^{-2}, which leads to a highest half wave potential. However, all of catalysts prepared here have no well-defined diffusion-limiting current plateau (Figure 3B), suggesting that the distribution of active sites on these catalysts is less uniform and oxygen diffusion rate is slower in the available anion-ionomer layer.

When Nafion® ionomer is used as a binder, the proton exchange Nafion® ionomer would be converted into the potassium exchange Nafion® ionomer when the coated electrode was measured in KOH solution. For ORR in alkaline solution, the reaction can be written as:

$$O_2 + 2H_2O + 4e^- \Rightarrow 4OH^-$$

The cation-exchange membrane with fully impregnated by K^+ ion in KOH solution should have a blocking effect for fast OH^- removal. For these reasons, the onset potentials and half wave potentials of CuPc/C electrode prepared with Nafion® ionomer are lower to some extent than those of CuPc/C electrode prepared with available anion-ionomer. However, the kinetic current densities, i_k at 0.05V for the ORR on the CuPc/C electrodes coated with Nafion® ionomer are all much higher than those with available anion-ionomer (Table 1). At the same time, at a defined current density of 0.1 mA cm^{-2}, the overpotentials of the CuPc/C electrode prepared with Nafion® ionomer are all lower than 0.068 V, while, when coated with available anion-ionomer, the overpotentials of the CuPc/C electrodes are all higher than 0.07 V. Hence, it is reasonable to conclude that CuPc/C still shows very good catalytic activity for the ORR by applying Nafion® ionomer as a binder.

3.3 Rotating disk electrode studies of O_2 reduction

The kinetics of the ORR on GC electrodes coated with different content of Nafion® ionomer were measured at different electrode rotating rates using RDE technique. Figure 4 shows typical RDE curves at various rotation rates for the ORR on carbon-supported CuPc electrodes coated with Nafion® loading of 3.5×10^1 μg cm^{-2} in O_2-saturated 0.1 M KOH. It can be seen that the ORR limiting currents for CuPc/C catalyst prominently increased with the rotating rate, along with the onset potential for the ORR unchanged on the same catalyst. The number of electrons tr-

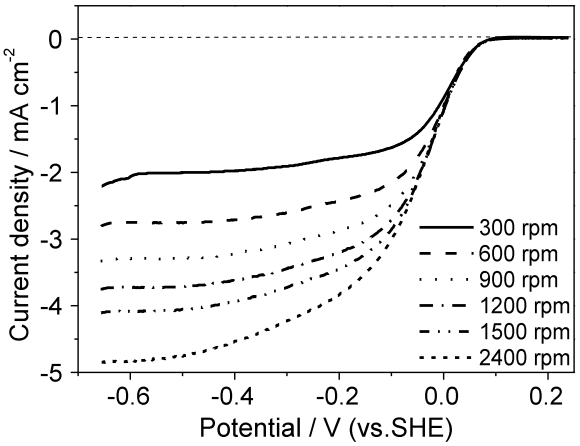

Figure 4. RDE polarization curves at different rotation rates for oxygen reduction on CuPc/C electrode prepared with Nafion® ionomer content of 3.5×10^1 μg cm^{-2} in 0.1 M KOH solution. Scan rate: 5 mV s^{-1}.

ansferred per O_2 molecule (n) was calculated from the Koutecky-Levich （K-L） equation [23]:

$$\frac{1}{j}=\frac{1}{j_k}+\frac{1}{j}+\frac{1}{j_d}=\frac{1}{j_k}+\frac{1}{j}+\frac{1}{0.62nFC_{O_2}D_{O_2}^{2/3}\nu^{-1/6}\omega^{1/2}} \quad (2)$$

Where j is the measured current density at -0.6 V, j_k is the activation controlled current density, j_f is the effect of Nafion® ionomer inside the catalyst layer on the measured current density, which may be negotiable if the equivalent Nafion® ionomer thickness is much small ($j_f \rightarrow \infty$), j_d is the O_2 diffusion limiting current density, n is the number of electrons transferred per oxygen molecule, F is Faraday constant, $C_{O2}$is the concentration of dissolved oxygen in the solution, D_{O2} is the diffusion coefficient of O_2 in the solution, ν is the kinetic viscosity, and ω is the electrode rotating rate in rpm. The plot of $\frac{1}{j}$ vs. $\omega^{-1/2}$ according to Equation (2) can give a slope of $(0.62nFC_{O_2}D_{O_2}^{2/3}\nu^{-1/6})^{-1}$, from which the electron transfer number (n) can be estimated if other parameters are known. Figure 5 shows the Koutecky-Levich plots for the ORR at the potential of -0.6 V on the CuPc/C electrode

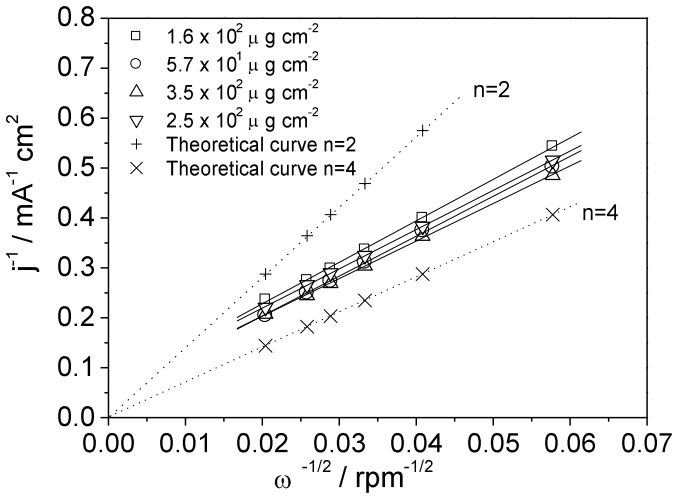

Figure 5. Koutecky-Levich plots for the ORR on CuPc/C electrode coated with different contents of Nafion® ionomer at -0.6 V *vs.* SHE

prepared with different contents of Nafion® ionomer derived from the data in Figure 4. The plots for the two-eletron and four-eletron transfer processes of the ORR are also shown in Figure 5. It can be seen clearly that the K-L slopes of CuPc/C electrode coated with different contents of Nafion® ionomer are all close to that of four-eletron transfer reaction. Based on these slopes, we can calculate the electron transfer number and found that the it changes with increasing the content of Nafion® ionomer: 3.40 for 1.6×10^2 μg cm^{-2}, 3.52 for 5.7×10^1 μg cm^{-2}, 3.74 for 3.5×10^1 μg cm^{-2} and 3.58 for 2.5×10^1 μg cm^{-2}. These results indicate that content of Nafion® ionomer can affect not only the ORR activity of the CuPc/C catalyst but also the ORR electron transfer number. At a lower Nafion® loading (2.5 ×

10^1 and 3.5×10^1 μg cm^{-2}), the value of electron transfer number is bigger than that at a high Nafion® loading (5.7×10^1 and 1.6×10^2 μg cm^{-2}), which is attributed to difference of Nafion® thicknesses in the catalyst layer.

3.3 Single-cell performance

Finally, to further study the effect of Nafion® ionomer as for alkaline electrolyte, electrical test in a real H_2/O_2 single-cell was performed based on a Nafion® membrane rinsed with 3 M KOH for about 48 hours. Figure 6 shows the fuel cell polarization curve and power density profile obtained using pure O_2 as the oxidants and pure H_2 as the fuel at room temperature, a humidifier maintained at 25°C under ambient pressure. As shown in Figure 6, the open-circuit voltage around 0.75 V can be observed, which is lower than 1.0 V found for fuel cells with Co- and Fe-centered phthalocyanines as cathode catalysts [24]. The maximum power density at ambient temperature of Nafion®-OH^- membranes reached 3.8 mW cm^{-2}. Although the power density is still very low in comparison with reported in the literature [24], this initial value indicates the promising application of Nafion®-OH^- membranes and Copper phthalocyanines for alkaline fuel cell. Considering the initial value in this paper, future work has then to be focused on the optimizaiton of the experimental conditions in order to further improve the fuel cell performance.

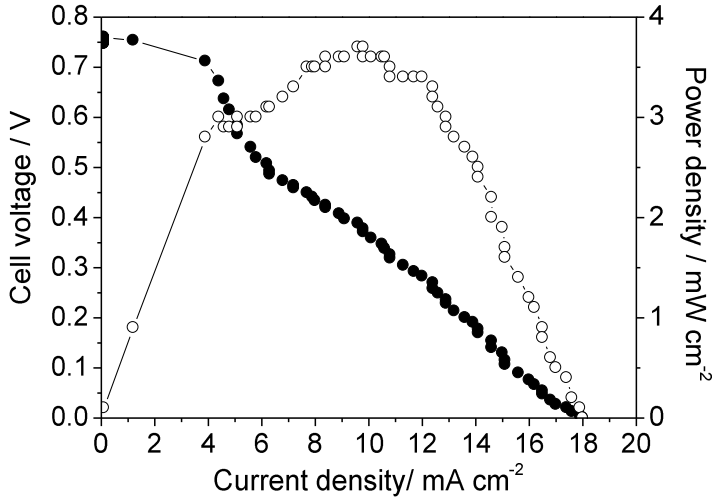

Figure 6. PEMFC performance of MEAs with CuPc/C based cathodes using Nafion®-OH^- membrane

4. Conclusions

This paper is focused attention on the Nafion® binder for electrocatalytic measurements and single-cell tests for an alkaline fuel cell. Electrochemical techniques such as CV, LSV and RDE were used to investigate the effect of the Nafion® ionomer content in the CuPc/C-based catalyst layer on the ORR. The results indicate that the electrocatalytic activity varies with the Nafion® loading and, the best performance is obtained from the CuPc/C electrode coated with 3.5×10^1 μg cm^{-2}, which is in a well agreement with the one studied using available anion-ionomer. An onset potential of 0.1 V and a half wave potential of -0.03 V are achieved in alkaline electrolyte. Besides the ORR kinetic rate, the ORR electro transfer number was also increased from 3.40 to 3.74 with decreased the content of Nafion®

ionomer from 1.6×10^2 to 3.5×10^1 μg cm^{-2}. An initial power density of 3.8 mW cm^{-2} was obtained with a Nafion® membrane rinsed with 3 M KOH for about 48 hours. As discussed in this paper, it is expected that an improved ORR activity could be achieved when changing the Nafion® ionomer to an anion ionomer. However, at the present, the anion ionomer is not so common used as Nafion® ionomer and, it's difficult to get. Our work demonstrated that in the process of alkaline fuel cell study, it's reasonable by applying Nafion® ionomer as substitute for anion ionomer considering that CuPc/C catalyst still shows promising catalytic activity for the ORR when Nafion ionomer is used as a binder.

5. Akcnowledgements

We give our thanks to the financial support from the National Natural Science Foundation of China (21173039), Specialized Research Fund for the Doctoral Program of Higher Education, SRFD (20110075110001), Environmental Protection Engineering Center for Pollution Treatment and Control in Textile Industry, China (20110927) and the Shanghai Leading Academic Discipline Project (B604) Fund.

6. References

[1] H. R. Colón-Mercado and B. N. Popov, J. Power Sources, 155, 253 (2006).
[2] C. J. Song, L. Zhang and J. J. Zhang, J. Electroanal. Chem., 293, 587 (2006).
[3] L. Xu, J. L. Qiao, L. DING, L. Y. HO, L. L. Liu and H. J. Wang, Acta Phys Chin Sin, 2251, 27 (2011).
[4] K. Gong, F. Du, Z. Xia, M. Durstock and L. Dai, Science, 323, 760 (2009).
[5] J. H. Kim, A. Ishihara, S. Mitsushima, N. Kamiya and K. I. Ota, Electrochim. Acta, 52, 2492 (2007).
[6] K. Lee, A. Ishihara, S. Mitsushima, N. Kamiya and K. I. Ota, Electrochim. Acta, 49, 3479 (2004).
[7] M. Lefevre and J. P. Dodelet, Electrochim. Acta, 48, 2749 (2003).
[8] R. Baker, D. P. Willkinson and J. Zhang, Electrochim. Acta, 53, 6906 (2008).
[9] R. Cheng, H. Li, D. Chu and G. Wang, J. Phys. Chem. C, 113, 20689 (2009).
[10]Y. Nabae, S. Moriya, K. Matsubayashi, S. M. Lyth, M. Malon, L. Wu, N. M. Islam, Y. Koshigoe, S. Kuroki, M. Kakimoto, S. Miyata and J. I. Ozaki, Carbon, 48, 2613 (2010).
[11] Y. Lu and R. G. Reddy, Electrochim. Acta, 52, 2562 (2007).
[12] J. Ozaki, S. Tanifuji, N. Kimura, A. Furuichi, and A. Oya, Carbon Japan, 44, 1298 (2006).
[13] N. Sehlotho, and T. Nyokong, J. Electroanal.Chem. South africa, 595, 161 (2006).
[14] E. H. Yu and K. Scott, J. Power Sources, 137, 248 (2004).
[15] C. Coutanceau, L. Demarconnay, C. Lamy and J. M. Léger, J. Power Sources, 156, 14 (2006).
[16] K. Scott, E. Yu, G. Vlachogiannopoulos, M. Shivare and N. Duteanu, J. Power Sources, 175, 452 (2008).
[17] H. Bunazawa and Y. Yamazaki, J. Power Sources, 182, 48 (2008).
[18] Y. S. Li, T. S. Zhao and Z. X. Liang, J. Power Sources, 190, 223 (2009).

[19] H. Zhu, X. Li and F. Wang, Int J Hydrogen Energy, 36, 9151 (2011).

[20] A. Sakar and A. Manthiram, J. Phys. Chem. C, 114, 4725 (2010).

[21] R. Wang, H. Li, H. Feng, H. Wang and Z. Lei, J. Power Sources, 195, 1099 (2010).

[22] C. V. Rao and B. Viswanathan, J. Phys. Chem. C, 111, 16538 (2007).

[23] A. J. Bard and L. R. Faulkner, Electrochemical Methods, Fundamentals and Applications, 2nd ed., John Wiley & Sons, Inc., N. Y., (2000).

[24]I. Kruusenberg, L. Matisen, Q. Shah, A. M. Kannan and K. Tammeveski, Int J Hydrogen Energy, 37, 4406 (2012).

Electrochemical Behavior of Nanostructured Nickel Phthalocyanine (NiPc/C) for Oxygen Reduction Reaction in Alkaline Media

Lei Ding[1], Jinli Qiao[1*], Hui Li[2], Haijiang Wang[2*]

[1]College of Environmental Science and Engineering, Donghua University,
2999 Ren'min North Road, Shanghai 201620, P. R. China
[2]Institute for Fuel Cell Innovation National Research Council Canada, 4250
Wesbrook Mall Vancouver, BC, Canada V6T1W5

ABSTRACT

Carbon-supported nickel phthalocyanine (NiPc/C) nanoparticle catalysts have been synthesized by a simple solvent-impregnation and milling procedure, then heat-treated at 600, 700, 800 and 900°C to optimize their activity for the oxygen reduction reaction (ORR). The electrocatalytic activity and electron transfer mechanism of NiPc/C catalysts were demonstrated in oxygen-saturated alkaline electrolyte by cyclic voltammetry (CV), linear sweep voltammetry (LSV) as well as rotating disk electrode (RDE) technologies, respectively. The results show that the heat-treatment temperature has a remarkable impact on the ORR activity of NiPc/C. In particularly, an onset potential of 0.05 V and a half-wave potential of -0.15 V are achieved in 0.1 M KOH after the catalyst was heat-treated at 800°C. In addition to an increase in ORR kinetics the number of electrons transferred for ORR also increased from 2.2 to 2.8 with increasing heat-treatment temperature from 600 to 800°C. To understand the heat-treatment effect, X-ray diffraction (XRD), transmission electron microscopy (TEM), thermogravimetric analysis (TGA) and X-ray photoelectron spectroscopy (XPS) were used to identify the catalyst structure and composition. XPS analysis clearly shows that after the sample was heat treated at 800°C, pyridinic-N and graphitic-N were observed. Both of these species might be assigned to sites catalytically active towards the ORR leading to activity enhancement.

1. Introduction

Proton-exchange membrane (PEM) fuel cells as efficient energy conversion devices, have been considered one of the most promising clean powder sources [1,2]. However, despite over a century of study and decades of intensive research, the cost of PEMFCs still inhibits its large scale commercialization. Recently, alkaline fuel cells (AFC) have appeared to be the most promising power source on a cost basis [3-5]. This kind of fuel cell uses an alkaline electrolyte, where the oxygen reduction reaction (ORR) is much faster than in the acidic media of an acidic PEM fuel cells. The faster ORR kinetics in alkaline media makes it possible to use non-Pt catalysts to achieve desirable kinetics for ORR and the high stability of the electrode material afforded. In addition, the use of non-Pt catalysts can effectively reduce the cost of the fuel cell system [6,7].

Due to the advantages associated with alkaline fuel cell systems, significant interests have been evoked on the development of non-Pt catalysts including various transition metals and macrocyclic complexes [8,9]. Among these catalysts, heat-treated metal-N4 macrocycles (MN4), such as phthalocyanine (MPc) complexes and porphyrins, have been considered the most promising ORR catalysts because of their conjugated structure and good chemical stability [10-13].

For pyrolyzed transition metal macrocycle catalysts, it has been reported that four ingredients are required to make well-performing ORR catalysts that exhibit both ORR catalytic activity and stability: transition metal, nitrogen coordinators on these catalysts, carbon support and the process of pyrolysis [14]. With respect to transition metal, macrocycles with different transition metals may display diverse activities, and the electrocatalytic activity of various transition metals follows the order of: $Fe^{2+} > Co^{2+} > Mn^{2+} > Ni^{2+}$, Cu^{2+} [15]. Co- and Fe-centered phthalocyanines are thus popular non-noble metal catalysts that have attracted significant efforts due to their reasonable activity and remarkable selectivity towards ORR in both acidic and alkaline electrolytes [16-20]. Nevertheless, little attention has been given to other metal centered phthalocyanines in the past decades because of the fact that, in strong acidic conditions, such as in PEM fuel cell operating conditions, both activity and stability are much more difficult to achieve. For example, Jun-ichi *et al* [21] reported a procedure to prepare the ORR catalysts using Li- and Mg-phthalocyanines as nitrogen doping agents, but their ORR activities are still lower than those of Co- and Fe-centered phthalocyanines. Most recently, Tebello *et al* [22] measured the ORR activity of several types of Mn-phthalocyanine complexes tetra-substituted with different peripheral ligands. By changing the pH value of solution from 1-12, they found that the electron transfer number per oxygen molecule in the overall reduction process was $2e^-$ in acidic or slightly alkaline media, but $4e^-$ in alkaline media.

In view of these facts, we speculated that other metal centered phthalocyanines could show high catalytic activity towards ORR when changing the electrolyte from acidic to alkaline. In this work, carbon-supported nickel pthalocyanines (NiPc/C) as a typical target was studied as cathode catalyst after heat-treatment. Both electrochemical measurements and physical characterization were performed to study its electrocatalytic activity and its structure and morphology. In case of electrochemical measurements, CV and LSV techniques were employed to investigate the

electrocatalytic activity of NiPc/C heat-treated at different temperatures. RDE theory was used to clarify the ORR mechanisms of NiPc/C with increasing the heat-treatment temperature. With respect to physical characterization, TEM and XRD and TG were conducted to determine the structure and morphology of NiPc/C at different temperatures. In addition, XPS was used to detect surface structure changes and shed some light on the nature of the active centers of the catalyst.

2. Experimental

2.1 Materials and catalyst preparation

Nickel phthalocyanine (NiPc) was purchased from Sigma-Aldrich with 97% purity and used as received without further purifications. Carbon Black (Vulcan XC-72, 254 $m^2\ g^{-1}$) was purchased from Cobat Corporation and used as support for all catalysts. In order to disperse the catalysts on the surface of carbon black, 0.4 g NiPc and 0.6 g Vulcan XC-72 were mixed with 100 ml ethanol under constant milling in a mortar for about 2 hrs to obtain a uniform mixture. This mixture was then dried in vacuum at 40°C for about 1 hr to remove ethanol. After drying, the resulting powder was divided into four parts and heat-treated at 600, 700, 800 and 900°C for 120 min under N_2 atmosphere, respectively. For convenience, the catalysts heat-treated at different temperatures were denoted as NiPc/C-600, -700, -800, and -900, respectively. H_2Pc/C as a reference was also synthesized using the same procedure.

2.2 Physical characterization

TG analyses were carried out on a NETZSCH simultaneous thermal analyzer TG 209. Catalysts samples of about 10 mg were loaded into an alumina pan, and then heated from 25 to 900°C at a rate of $10^oC\ min^{-1}$. All measurements were conducted under nitrogen. The vacant alumina pan was used as a referece throughout the whole experiment.

The crystal-phase XRD patterns were collected on a Philips PW3830 X-ray diffractometer using Cu-kα radiation (λ = 0.15406 nm). The current was 40 mA and the voltage was 40 kV. The intensity data were collected at 25°C in the 2θ range from 5°to 90°with a scan rate of $1.20^o\ min^{-1}$.

TEM analyses were performed on a high-resolution Hitachi JEM-2100F operating at 200 kV to obtain information of the average particle size and the size distribution of the catalysts prepared.

XPS analysis was conducted using a Kratos AXIS Ultra ^{DLD} electron spectrometer to determine the surface composition with Al K X-ray anode source (hν=1486.6 eV) at 250 W and 14.0 kV.

2.3 Electrochemical measurements

Electrochemical measurements were conducted through CV and LSV techniques using a potentiostat CHI 760 electrochemical analyzer. A conventional three-compartment electrochemical cell was employed for all electrochemical tests, in which a saturated calomel electrode (SCE) was used as the reference electrode and a platinum foil was used as the counter electrode. A rotating disk electrode (RDE) made of glassy carbon (GC) electrode with a diameter of 6.0 mm (corresponding to a geometric surface area of 0.283 cm^2, Pine, 5908Triangle Drive, Raleigh, NC)

was used as the working electrode, on which a layer of the studied catalysts was casted. The working electrode was coated with catalysts using the following steps: 4 mg of the NiPc/C catalyst was suspended in 2 mL of methanol/Nafion® solution (50:1 in mass) to form a catalyst ink, which was ultrasonically dispersed for 10 min. Then, 10 µL of the suspension was pipetted onto the surface of the GC electrode and then dried at room temperature for testing. The catalyst loading of each electrode was 70.6 µg cm^{-2}. All measured potentials were converted into the values referring to a standard hydrogen electrode (SHE).

RDE measurements were performed in 0.1 M KOH solution at room temperature. For every test, CV was first carried out by scanning the disk potential from -0.3 to 0.6 V at a scan rate of 50 mV s^{-1} to examine the surface behavior of the catalyst in N_2-saturated 0.1 M KOH solution. Then O_2 was bubbled into the solution to form an O_2-saturated solution for ORR measurement. For more quantitative measurements of ORR activity of the catalysts, LSV was performed in the potential range between -0.7 and 0.2 V in O_2-saturated 0.1 M KOH solution at desired rotating rates. In order to ensure a steady state at each point of the LSV curves, a slow sweeping rate of 5 mV s^{-1} was applied.

3. Results and discussion

3.1 Electrochemical activity of NiPc/C catalysts towards ORR

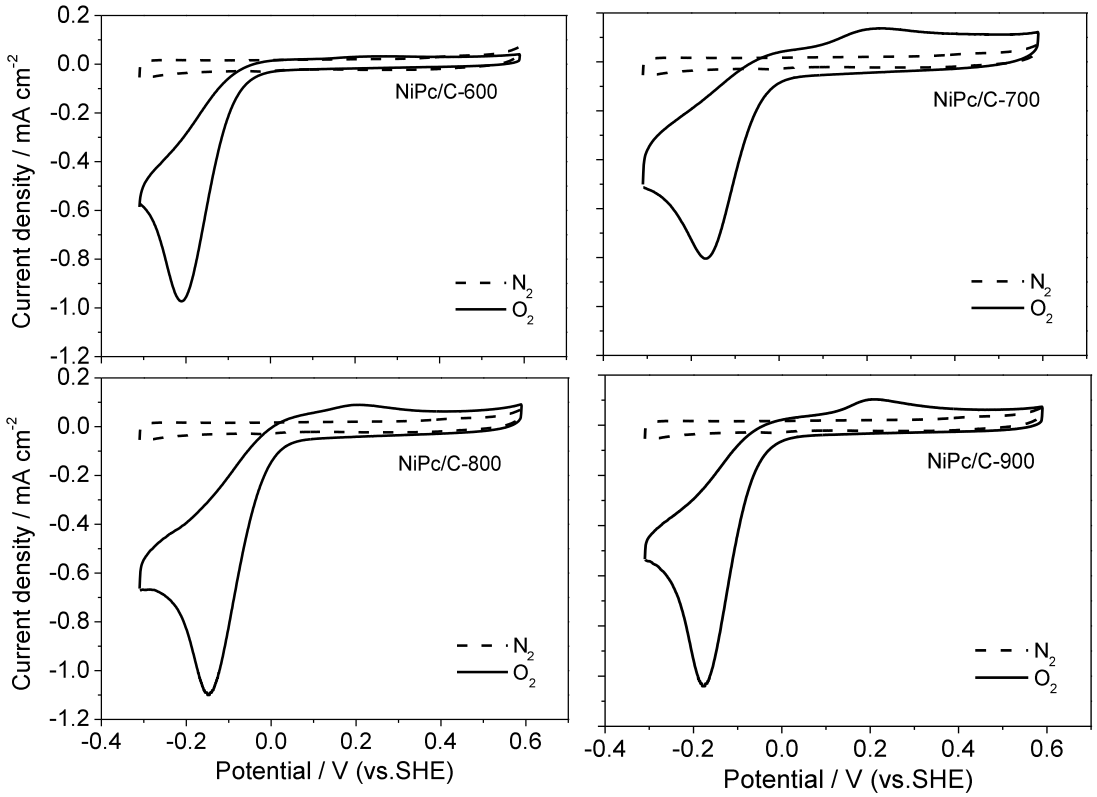

Figure 1. Cyclic voltammograms of the NiPc/C catalysts heat-treated at different temperatures in N_2-saturated and O_2-saturated 0.1 M KOH at room temperature. Scan rate: 50 mV s^{-1},

Although the catalyzed ORR mechanisms of MPc catalysts are still not fully understood, there has been a general agreement in the literature that heat-treatment can effectively improve the electrocatalytic activity of the catalysts. In order to pursue the best catalytic performance for ORR, the influence of heat-treatment on the catalytic activity of NiPc/C catalysts was investigated by CV and LSV. Figure 1 shows the CV curves of N_2-saturated and O_2-saturated 0.1 M KOH solution obtained with the GC electrode coated with NiPc/C catalysts. It can be seen that there is no reduction peaks of oxygen at the NiPc/C catalyst electrodes in N_2-saturated 0.1 M KOH solution. However, clear reduction peaks are observed in O_2-saturated 0.1 M KOH solution for all NiPc/C catalysts after heat-treatment at various temperatures: -0.21 V for NiPc/C-600, -0.17 V for NiPc/C-700, -0.15 V for NiPc/C-800 and -0.17 V for NiPc/C-900, respectively. In addition, the ORR peak current density changes with increasing the heat-treatment temperature and reaches a maximum value at 800°C. Among all the curves in Figure 1, there is no peak attributed to the Ni $^{3+}/^{2+}$ redox, which indicates that the element nickel is in some other state, rather than nickel ions adsorbed on the carbon surface.

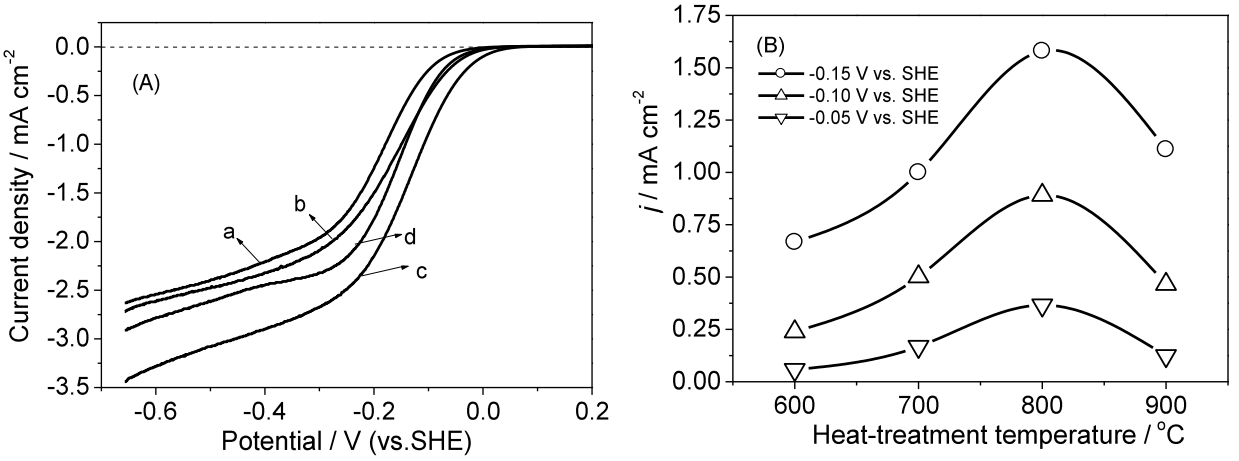

Figure 2. (A) Current-voltage curves for ORR catalyzed by NiPc/C catalysts heat-treated at (a) 600°C, (b) 700°C, (c) 800°C and (d) 900°C measured in O_2-saturated 0.1 M KOH at the scan rate 5 mV s^{-1}. Electrode rotating rate: 1500 rpm. (B) Current densities at -0.05, -0.10 and -0.15 V vs. SHE as a function of catalyst heat-treatment temperature with data obtained from (A).

In order to investigate the eletrocatalytic activity of NiPc/C catalysts for the ORR after heat-treatment at different temperatures, LSV was carried out using RDE coated with NiPc/C catalysts heat-treated at 600, 700, 800 and 900°C, respectively, and the polarization curves obtained are shown in Figure 2(A). It can be seen that for catalyst samples heat-treated at 600, 700 and 900°C, the onset potentials for the ORR are all located near 0.03 V, which are lower than that of the sample heat-treated at 800°C (near 0.05 V). The same trend can also be observed in the half-wave potentials

of the catalysts, which are: NiPc/C-800 (-0.15 V) > NiPc/C-700 ≈ NiPc/C-900 (-0.17 V) > NiPc/C-600 (-0.21 V), suggesting that ~800°C may be the optimal temperature in obtaining the most active electrocatalyst for ORR.

To further verify the heat-treatment temperature effect on the ORR activity, the current densities at -0.15, -0.10 and -0.05 V are plotted as the function of temperatures and, the results are shown in Figure 2(B). As can be seen, the current density increases significantly with increasing the heat-treatment temperature from 600°C to 800°C. Above 800°C, the current density decreases again and shows the lowest value when the heat-treatment temperature for the catalyst synthesis is at 900°C. The phenomenon clearly indicates that below 800°C, more ORR active sites in the NiPc/C catalyst could be produced. While, when temperature is high enough such as at 900°C, a portion of the active sites may be damaged to form other structures such as metallic nickel or nickel carbide, which are less active for ORR. These will be discussed throughly below. According to the curves shown in Figure 2(B), we can conclude that the optimal heat-treatment temperature is around 800°C. Therefore, in the subsequent study the NiPc/C obtained at 800°C was selected as the target catalyst.

3.2 Kinetic study of the ORR catalyzed by heat-treatment NiPc/C

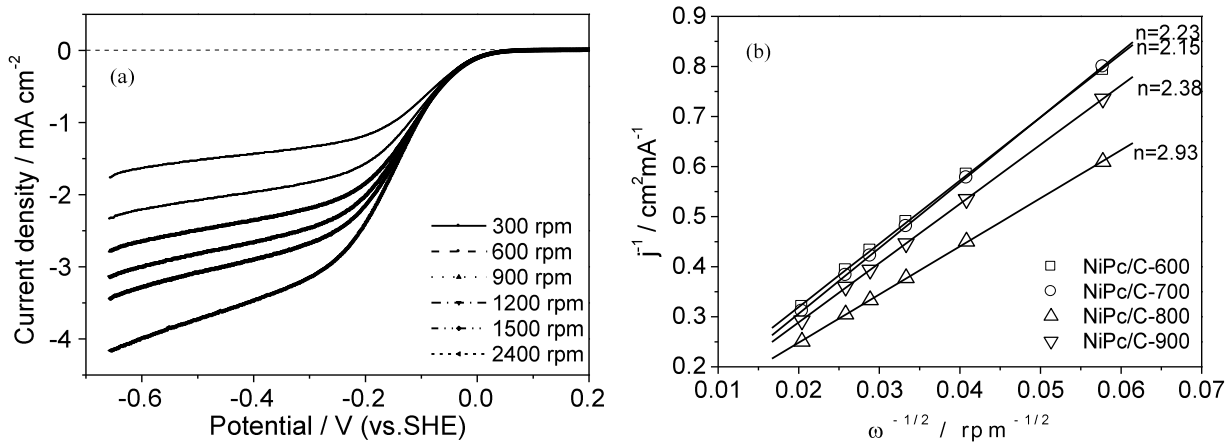

Figure 3 (a) Current-voltage curves at various electrode rotating rates obtained with NiPc/C-800 catalyst in O_2-saturated 0.1 M KOH at the scan rate 5 mV s^{-1}. (b) Koutecky-Levich plots for the ORR at –0.6 V vs. SHE from the current-voltage curves recorded at the same conditions as those in Figure 3(a) using catalysts obtained at various heat-treatment temperatures.

In order to further explore the kinetics of ORR catalyzed by NiPc/C in alkaline media, LSV data obtained at various rotation rates were processed using the Koutecky-Levich (K-L) equations[23]:

$$i_k = i \cdot i_d/(i_d - i) \text{ ----------(1)}$$

$$i_d = B\omega^{1/2} \text{----------(2)}$$

$$B = 0.2nFSCo_2Do_2^{2/3}v^{-1/6} \text{ --------(3)}$$

Where B is the Levich slope, ω is the rotation rate, n is the electron transfer number per oxygen molecule, F is Faraday constant, S the electrode geometric surface area, C_O is the concentration of oxygen, D_O is the diffusion coefficient of O_2 in the electrolyte, v is the kinetic viscosity and the constant 0.2 is adopted when rotation speed is expressed in revolutions per minute. Figure 3(a) shows the polarization curves at various rotation rates for ORR on the GC electrode coated with NiPc/C-800 in O_2-saturated 0.1 M KOH solution as a typical candidate. It can be seen that the limiting current for ORR increases with the rotation rate, while the onset potential of the catalyst for ORR remains unchanged. Figure 3(b) shows Koutecky-Leivich plots at -0.6 V, which indicates the estimation of overall electron number (n) transferred per oxygen molecule. For a better comparison, Koutecky-Leivich plots of NiPc/C catalysts heat-treated at other temperatures are also depicted in Figure 3(b). From the slopes of the Koutecky-Leivich plots, the electron transfer numbers per oxygen molecule in the overall reduction process can be calculated, and it was found that it changes with increasing the heat-treatment temperature: 2.23 for NiPc/C-600, 2.15 for NiPc/C-700, 2.93 for NiPc/C-800 and 2.38 for NiPc/C-900. These data suggest that the ORR catalyzed on NiPc/C-600, NiPc/C-700 and NiPc/C-900 electrodes is mainly a $2e^-$ reduction process leading to a large amount of H_2O_2. However, For NiPc/C-800 electrode, the electron transfer number is 2.93, which lies between the $2e^-$ and $4e^-$ reduction process, suggesting a great affect on the decreasing of H_2O_2 by heat-treatment at 800°C.

3.3 Studies on the acitve site structures of the NiPc/C catalysts

Figure 4 shows the TG and DTG curves for H_2Pc/C and NiPc/C, respectively. As shown in Figure 4(a), H_2Pc/C shows only one major peak at 550°C with a weight loss of about 30 wt%, indicative of the decompsition of H_2Pc [19]. In the case of NiPc/C, situations are different. The DTG curve of NiPc/C shows three peaks at around 150, 560 and 760°C (Figure 4(b)). Corresponding to DTG, there are three steps on the curve of TG: (1) the first step starts at 130°C to reach a plateau near 250°C with a weight loss of about 7.5 wt%. In this stage, NiPc has a stable molecular structure and a small amount of weight is lost due to volatilization of absolute ethanol and water molecules. (2) the second step starts at 500°C and ends at 610°C with 10.5 wt% weight loss which may corresponds to the release of NiPc/C on the carbon surface. (3) the decomposition of NiPc/C chelate happens at a temperature above 610°C. The catalytic activities of NiPc/C-700, NiPc/C-800 and NiPc/C-900 are all much higher than that of NiPc/C-600, which indicates that catalytic active sites are probably formed at the third step. Furthermore, the total mass loss of NiPc/C is smaller than that of H_2Pc/C by about 12%. This implies that Ni species prevents phthalocyanine from thermal decomposition and leads to higher nitrogen content which are helpful to form more ORR activity sites.

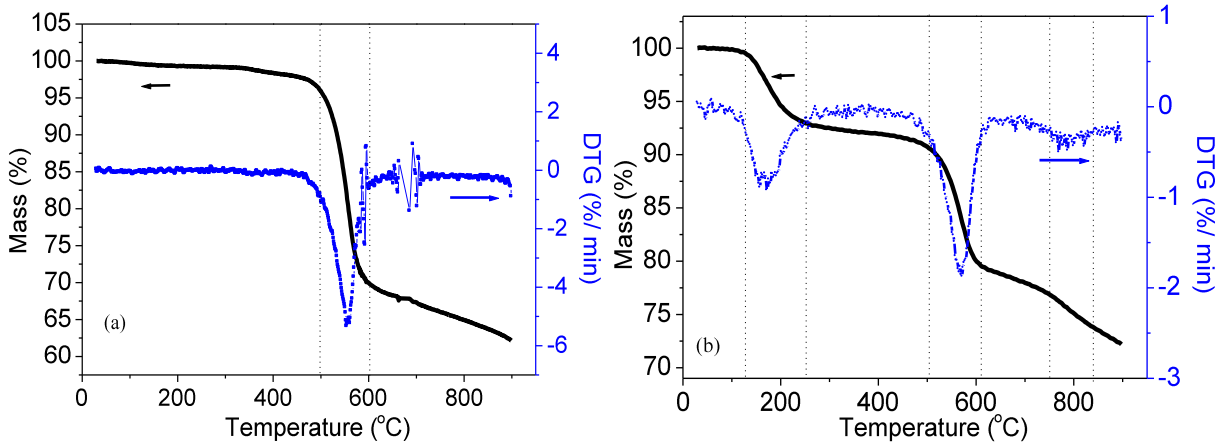

Figure 4. TG/DTG curves of (a) H_2Pc/C and (b) NiPc/C, respectively

XRD analyses were conducted to obtain crystallographic information on the NiPc/C catalysts. Figure 5 shows the XRD patterns of NiPc/C catalysts after heat-treatment at 600, 700, 800 and 900°C, respectively. The first large broad peak located at about $2\theta = 25^{o}$ in all the XRD patterns can be assigned to the strong graphite character of the Vulcan XC-72. It can also be clearly seen that NiPc/C-600 shows only one and broad peak at 44.5°, which is assigned to the Ni (111) peak. However, when heat-treatment temperature is increased from 700 to 900°C, two new diffraction peaks at 51.8° and 76.3°, respectively, appeared, indicating the occurrence of the decomposition of NiPc/C structure during the heat-treatment process and the aggregating of the metallic nickel. These two peaks centered at 51.8° and 76.3° are corresponding to the Ni (200) peak and Ni (220) peak, and these two peaks become sharpened with the increase in heat-treatment temperature, which suggests that Ni clusters grow at higher pyrolyzing temperature.

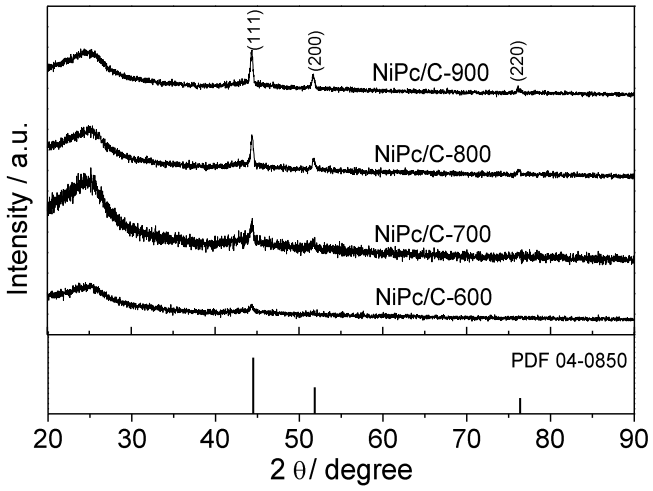

Figure 5. XRD patterns of NiPc/C catalysts heat-treated at 600, 700, 800 and 900°C, respectively.

Another confirmation of the presence of metallic Ni in the NiPc/C catalysts heat-treated at different temperatures can be seen from Figure 6, in which TEM images of the NiPc/C obtained at 600, 700, 800 and 900°C heat-treatment are illustrated. As seen in Figure 6a, no clear metal particles appear for the catalyst heat-treated at 600°C except for some aggregates with an average particle size of 50 nm on the carbon support surface. When the catalyst is heat-treated at 700°C, the aggregate size decreases, and a smaller size of the particle cluster is observed with an average size of about 30 nm (Figure 6b). It is worth to mention that the TEM images of the NiPc/C catalyst samples heat-treated at 600 and 700°C give no conspicuous indication of metallic Ni aggregation, however, the TEM image of the samples heat-treated at 800 and 900°C clearly show the metallic Ni aggregation (Figure 6c and 6d). For example, some black dots with an average size of about 25 nm can be observed in the NiPc/C sample heat-treated at 800°C, and the NiPc/C after heat-treatment at 900°C shows a heavily agglomerated material of nano-sized particles (with an average particle size of 60 nm). The NiPc/C is in a highly crystalline phase (the Ni crystallites growth) after high-temperature treatment. These results suggest that heat-treatment can decompose the NiPc/C to metallic Ni, which then agglomerates into large particles when the heat-treatment temperature is increased. This result is in agreement with the observation from the XRD analysis in Figure 5. Generally, metallic Ni is not active for the ORR. Hence, to prevent the formation of metallic Ni in the catalyst, the heat-treatment should be conducted not at a too high temperature. As shown in Figure 2, NiPc/C catalyst sample heat-treated at 800°C shows the best ORR activity, indicating that a lot of active sites may be formed at this temperature, although some small metallic Ni particles are observed. In order to gain some information on active sites of the catalysts as-prepared, the surface characterization of NiPc/C catalysts after heat-treatment at 800°C was carried out by XPS.

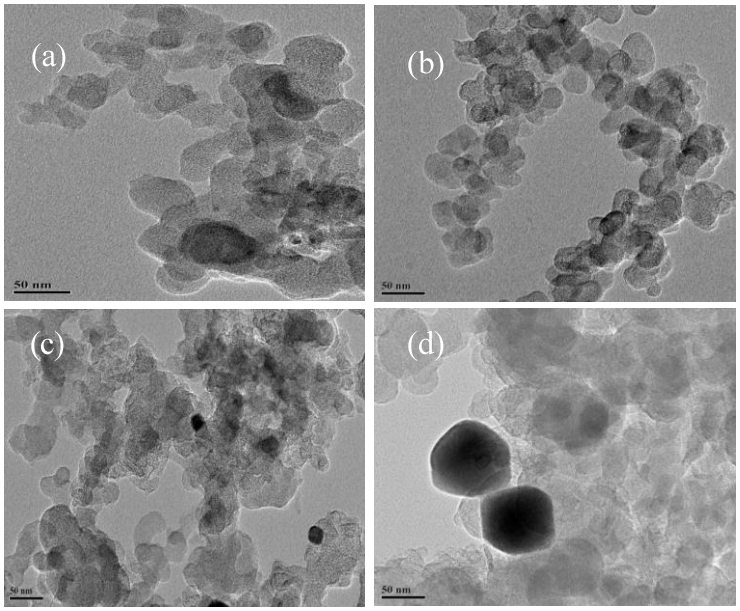

Figure 6. TEM images for NiPc/C catalyst heat-treated at (a) 600°C, (b) 700°C, (c) 800°C and (d) 900°C, respectively.

Figure 7 shows the N 1s spectral region for NiPc/C-800, where the N signal is divided into four bands, marked N_I, N_{II}, N_{III}, and N_{IV}, respectively. The N_I band at lower binding energy of 398.8 eV could be assigned to pyridinic-N, the N_{II} band at 399.9 eV and the N_{III} band at 401.2 eV may be related to pyrrolic-N and graphitc-N, respectively. Finally, the broader N_{IV} band at 404.3 eV could be attributed to N-O bonds (pyridine-N-oxide) [24-26]. According to literatures, pyridine-N and graphitic-N are believed to play important roles in determining the electrocatalytic ORR activity and stability of macrocycles, while pyridine-N-oxide seems useless in improving the activity [27,28]. In the case of NiPc/C-800, it can be clearly seen that both pyridinic-N and graphitic-N are the major bands in this sample forming the ORR active sites, although pyridine-N-oxide can be observed also. Sidik *et al.* [29] once observed that graphitic-N could catalyze the ORR through a $4e^-$ pathway. That is why we observed the high ORR activity catalyzed by NiPc/C-800 catalyst. This study may at least partially explain the results that the electron transfer number of NiPc/C-800 is higher than NiPc/C catalysts heat-treated at other temperatures. Therefore, it can be concluded that both pyridinic-N and graphitic-N bonded by Ni ions should be mainly responsible for the enhanced ORR activity in this work.

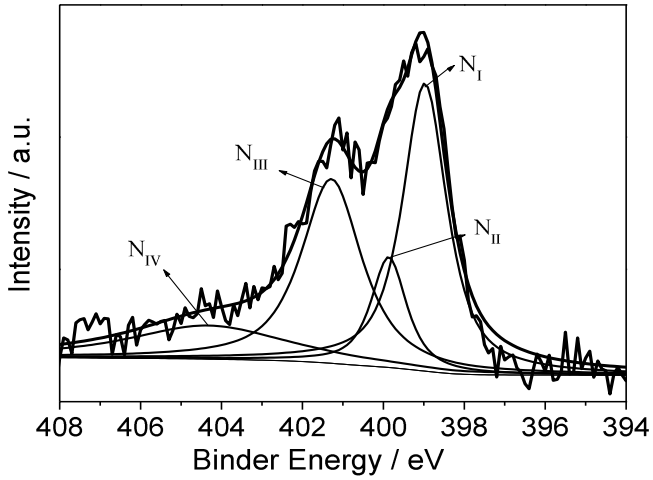

Figure 7. XPS spectra in the N 1s region for the NiPc/C catalysts heat-treated at 800°C.

4. Conclusions

In conclusion, carbon-supported NiPc/C catalyst as an novel cahode catalyst for ORR has been succefussly prepared by solvent-impregnation along with the high-temperature treatment. A significant influence of the heat-treatment was found on the catalytic activity of the NiPc/C catalysts for ORR. The catalyst heat-treated at 800 °C displayed significantly improved activity through RDE and CV measurements in oxygen-saturated alkaline electrolyte at room temperature. The number of electrons transferred during the ORR varies with increasing the heat-treatment

temperature: 2.23 at 600°C, 2.15 at 700°C, 2.93 at 800°C and 2.38 at 900°C. XRD and TEM clearly confirm that the depositions of nanometallic Ni with different sizes are produced with heat-treatment temperature, which are not active for ORR. XPS analysis reveals that both pyridinic-N and graphitic-N should be the active sites responsible for the enhanced ORR activity. Here, the catalytic activity of NiPc/C is still low in comparison with reported Co- and Fe-centered phthalocyanines [17]. However, these initial results are promising for the application in alkaline fuel cells. It is believed that by further optimizaiton of the experimental conditions, such as using other synthetic method, modification with metal or nitrogen precursers, both the catalytic activity and the selectivity of NiPc/C could be improved further.

5. Akcnowledgements

We give our thanks to the financial support from the National Natural Science Foundation of China (21173039), Specialized Research Fund for the Doctoral Program of Higher Education, SRFD (20110075110001), the Opening Foundation of Zhejing Provincial Top Key Discipline and the Shanghai Leading Academic Discipline Project (B604) Fund.

6. References

[1] S. Sharma, A. Ganguly, P. Papalonstantinou, X. Miao, M. Li, J. L. Hutchison, M. Delichatsios and S. Ukleja, J. Phys. Chem. C, 114, 19459 (2010).

[2] B. Wang, J. Power Source, 152, 1 (2005).

[3] N. Wagner, M. Schulze and E. Gülzow, J. Power Source, 127, 264 (2004).

[4] C. Coutanceau, L. Demarconnay and J.−M. Léger, J. Power Source, 156, 14 (2006).

[5] M. Zhiani, H. A. Gasteiger, M. Piana and S. Catanorchi. Int. J. Hydrog. Energy, 36, 5110 (2011).

[6] H. Schulenburg, S. Stankov, V. Schünemann, J. Radnik, I. Dorbant, S. Fiechter, P. Bogdanoff and H. Tributsch, J. Phys. Chem. B, 107, 9034 (2003).

[7] L. Jiang, A. Hsu, D. Chu and R. Chen, J. Electrochem. Soc., 156, B370 (2009).

[8] S. Lj. Gojković, S. Gupta and R. F. Savinell, J. Electroanal. Chem., 462, 63 (1999).

[9] C. Song, L. Zhang and J. Zhang, J. Electroanal. Chem., 587, 293 (2006).

[10] M. Lefèvre and J. P. Dodelet, Electrochim. Acta, 48, 2749 (2003).

[11] R. Baker, D. P. Wilkinson and J. Zhang. Electrochim. Acta, 53, 6906 (2008).

[12] G. Lalande, G. Tamizhmani, R. Côté, L. Dignard-Bailey, M. L. Trudeau, R. Schulz, D. Guay and J. P. Dodelet, J. Electrochem. Soc., 142, 1162 (1995).

[13] G. Faubert, G. Lalande, R. Côté, D. Guay, J. P. Dodelet, L.T. Weng, P. Bertrand and G. Dénès, Electrochim. Acta, 41, 1689 (1996).

[14] M. Lefèvre, E. Proietti, F. Jaouen and J. P. Dodelet, Science, 324, 71 (2009).

[15] Y. Lu and R. G. Reddy. Electrochim. Acta, 52, 2562 (2007).

[16] I. Kruusenberg, L. Matisen, Q. Shah, A. M. Kannan and K. Tammeverski, Int. J. Hydrogen. Energy, 37, 4406 (2012).

[17] R. Chen, H. Li, D. Chu and G. Wang, J. Phys. Chem. C, 113, 20689 (2009).

[18] V. Bambagioni, C. Bianchini, J. Filippi, A. Lavacchi, W. Oberhauser, A. Marchionni, S. Moneti, F. Vizza, R. Psaro, V. Dal Santo, A. Gallo, S. Recchia and L. Sordelli, J. Power Source, 196, 2519 (2011).

[19] Y. Nabae, S. Moriya, K. Matsubayashi, S. M. Lyth, M. Malon, L. Wu, N. M. Islam, Y. Koshigoe, S. Kuroki, M. Kakimoto, S. Miyata and J. Ozaki, Carbon, 48, 2613 (2010).

[20] C. W. B. Bezerra, L. Zhang, K. Lee, H. Liu, A. L. B. Marques, E. P. Marques, H. Wang and J. Zhang, Electrochim. Acta, 53, 4937 (2008).

[21] J. Ozaki, S. Tanifuji, N. Kimura, A. Furuichi and A. Oya, Carbon, 44, 1298 (2006).

[22] N. Sehlotho and T. Nyokong, J. Electroanal. Chem., 595, 161 (2006).

[23] A. J. Bard and L. R. Faulkner, Electrochemical Methods, Fundamentals and Applications, 2nd ed., John Wiley & Sons, Inc., N. Y., (2000).

[24] P. Wang, Z. Ma, Z. Zhao and L. Jia, J. Electroanal. Chem., 611, 87 (2007).

[25] A. Velázquez-Palenzuela A, L. Zhang, L. Wang, P. L. Cabot, E. Brillas, K. Tsay and J. Zhang, J. Phys. Chem. C, 115, 12929 (2011).

[26] G. Liu, X. Li, P. Ganesan and N. B. Popov, Electrochim. Acta, 55, 2853 (2010).

[27] X. Li, G. Liu and N. B. Popov, J. Power Source, 195, 6373 (2010).

[28] K. Lee, L. Zhang, H. Liu, R. Hui, Z. Shi and J. Zhang, Electrochim. Acta, 54, 4704 (2009).

[29] A. R. Sidik, B. A. Anderson, P. N. Subramanian, P. S. Kumaraguru and N. B. Popov, J. Phys. Chem. C, 110, 1787 (2006).

Carbon-Supported Copper Phthalocyanine (CuPc/C) as a Novel Cathode Catalyst for Polymer Electrolyte Membrane Fuel Cells --- Effect of Nafion Ionomer as for Alkaline Electrolyte

Lei Ding[1,2], Xianfeng Dai[1], Samir Ibrahim[2], Yuyu Liu[2*], Jinli Qiao[1*]

[1]College of Environmental Science and Engineering, Donghua University,
2999 Ren'min North Road, Shanghai 201620, P. R. China
[2]Lab of Urban and Regional Environmental Systems, Graduate School of Environmental Studies,
Tohoku University, Aramaki, aza Aoba 6-6-11,
Aoba-ku Sendai 980-8579, Japan

ABSTRACT

Carbon-supported copper phthalocyanine (CuPc/C) nanoclusters, as a novel suitable cathode catalyst in polymer electrolyte membrane fuel cells have been synthesized via a combined solvent-impregnation and milling procedure along with the high temperature treatment. For optimizing the electrocatalytic activity of the catalyst obtained, the electrode with a variety of Nafion ionomer contents in the catalyst layer was screened by cyclic voltammetry (CV) and linear sweep voltammetry (LSV) employing a rotating disk electrode (RDE) technique to investigate the effect of Nafion ionomer as for alkaline electrolyte. For comparative purposes, electrode with various contents of available anion-ionomer was also investigated. The results revealed that the content of Nafion ionomer can affect the ORR activity of the CuPc/C catalyst and an optimal content of Nafion ionomer was around 3.5×10^1 μg cm^{-2}, which corresponds well with the electrode prepared using available anion-ionomer. Under which, the electrode prepared using Nafion ionomer can produce a comparable performance to that of using available anion-ionomer, giving an on-set potential at 0.1 V with a half-wave potential of -0.03 V. Furthermore, Koutechy-Levich analysis showed that the value of electron transfer number is in a range of 3.40 to 3.74 when electrode with Nafion ionomer contents changing from 2.5×10^1 to 1.6×10^2 μg cm^{-2}. The membrane electrode assembly (MEA) fabricated with CuPc/C cathode catalyst with a loading of 3.6 mg cm^{-2} and, a Nafion membrane immersed in 3M KOH for 48 hours, reached an initial power density of 3.8 mW cm^{-2} at room temperature.

1. Introduction

It is commonly believed that fuel cells are promising power sources for offering clean and high energy conversion efficiency technology. For obtaining the high catalytic performances, platinum (Pt) supported on carbon black is normally used as the best electrocatalyst for both the anode and the cathode, particular to Nafion®-based proton-exchange membrane fuel cells (PEMFCs). However, the widespread commercialization of the fuel cell technology has been hindered so much because of the high cost of Pt and its scarcity. This becomes more serious particular to high loading requirements on the cathode for the oxygen reduction reaction (ORR) due to the sluggish kinetics of Pt (~ 300 mV overpotential loss) [1]. Alternatively, the use of alkaline media in fuel cell applications presents many advantages, both in electrocatalytic activity and in materials stability over acidic media, which can provide more choices for suitable Pt alternatives [2-6].

With respect to non-platinum catalysts, Metal-N_4 macrocycles after heat-treatment, such as Fe- and Co-centered phthalocyanine complexes, are considered to be the most promising non-precious metal catalysts due to their high conjugate structure and relatively good chemical stability [7-10]. Comparatively, little are concerned for other metal centered phthalocyanines, this is because that in strong acidic conditions such as in PEM fuel cells, the catalysts that show high ORR catalytic activity, and at the same time, high stability are strongly desired. However, little progress is achieved because of trade-off relations between these parameters [11,12]. Recent studies indicate that pH could affect the ORR activity of MPcs, which suggests that other metal centered phthalocyanines such as Ni-, Mn- and Cu-centered phthalocyanines, might be more appropriately used in alkaline solutions [13].

As is known to all, electrode preparing is a necessary step in the electrocatalytic activity study of the catalysts for the ORR, particular to the polymer electrolyte membrane fuel cells. Among which, a polymer binder is essential to bind discrete catalyst particles to form a porous catalyst layer that facilitates the transfer of ions, electrons and reactants. In recent years, more and more polymer materials have been used as a binder for preparing MEAs for alkaline membrane fuel cells [14-16]. Bunazawa et al. [17] investigated an anion ionomer solution (labeled as A3) as a binder for alkaline direct methanol fuel cell and, studied the effect of anion ionomer content in the anode and cathode catalyst layers. The results suggested that MEA with 45.4% mass ionomer content showes the highest performance at both anode and cathode electrodes. Zhao et al. [18] used A3 ionomer and polytetrafluoroethylene (PTFE) as the binder in anode catalyst layer for alkaline direct ethanol fuel cells. They found that the PTFE binder yields better performance than does the A3 binder. Unfortunately, up to now, no alkaline binder can completely realize the commercialization like Nafion® binder in PEMFC. Hence, it is difficult to choose a suitable binder used for alkaline electrolyte. Generally, in the process of the preparation of the electrode, the thickness of the binder coated on the electrode layer is very thin. Therefore, using Nafion® ionomer as the binder may be good choice if it has no significant effect on the O_2 reduction rate.

In view of these facts, in this work, the possibility of constituting new electrocatalysts using carbon-supported copper phthalocyanine (CuPc) complexes are pursued for the ORR after heat-treatment at high temperatures. We

focus on the feasibility by applying Nafion® ionomer as a binder for electrochemical measurements in alkaline solution. Emphasis is made on the effect of Nafion® content on the catalyst layer, whether Nafion® ionomer could affect more or less the ORR activity and how much is the optimal content for catalyst ink preparation. Further more, the preliminary fuel cell test using the conventional hot-pressing MEAs with a Nafion membrane immersed in KOH solution and, carbon supported CuPc as cathode catalyst was also carried out.

2. Experimental

2.1 Materials and catalyst preparation

Copper phthalocyanine was purchased from Sigma Aldrich with 97% purity and used as received. Carbon support (Vulcan XC-72) was purchased from Cobat Corporation. Carbon-supported copper phthalocyanine catalysts were prepared using milling method combined with a heat-treated procedure. Briefly, a mixture of 40 mg CuPc and 60 mg carbon black in 10ml methanol was prepared and carefully milled for about 2 hours in a mortar, then vacuum dried at 40^{o}C for another 1 hour to remove the methanol. The resulting powders were placed in a crystal boat, and pyrolyzed at 800^{o}C for 120 minutes at the rate of 5^{o}C min^{-1} in a flowing nitrogen atmosphere. The catalyst as-prepared is thus designated as CuPc/C.

2.2 Physical characterization

The crystal-phase X-ray diffraction (XRD) patterns were collected on a Philips PW3830 X-ray diffractometer using Cu-kα radiation (λ = 0.15406 nm). The current was 40 mA and the voltage was 40 KV. The intensity data were collected at 25^{o}C in the 2θ range from 5° to 90°with a scan rate of 1.20^{o} min^{-1}.

2.3 Electrochemical measurements

Electrochemical evaluation was carried out in a standard three compartment electrochemical cell in 0.1 mol L^{-1} KOH at room temperature. A pre-cleaned rotating disk electrode (RDE) (Glassy carbon electrode with a diameter of 6.0 mm corresponding to a geometric surface area of 0.283 cm^{2}, purchased from Pine Instruments) was used as the working electrode. A Pt wire and a saturated calomel electrode (SCE) were used as the counter and reference electrode, respectively. All measured potentials were converted into the values referring to a standard hydrogen electrode (SHE).

The catalyst ink for RDE measurements was prepared by blending 4 mg of the catalyst and 2 mL of methanol/Nafion® solution which was ultrasonically dispersed for 10 minutes to form a suspension. 10 μL of this suspension was then pipetted onto the surface of GC electrode and then dried at room temperature. For investigating the effect of Nafion content on the catalyst layer, methanol/Nafion® solution with different scales (70:1, 50:1, 30:1 and 10:1 in mass) were used to form catalyst inks. The Nafion® loadings were 2.5×10^{1}, 3.5×10^{1}, 5.7×10^{1} and 1.6×10^{2} μg cm^{-2}, respectively.

Initially, cyclic voltammograms (CVs) were carried out by scanning the disk potential from -0.3 to 0.6 V to measure the surface behavior of the catalyst in N_2-saturated 0.1 M KOH solution. For ORR measurements, the

solution was then bubbled by pure O_2 to form an O_2-saturated in 0.1 M KOH solution. A CV was recorded in O_2-saturated electrolyte with the scan rate of 50 mV s^{-1}. For more quantitative measurements of ORR activity, linear sweep voltammetry (LSV) was conducted on the catalyst-coated RDE in the potential range between -0.7 and 0.2V in O_2-saturated 0.1 M KOH solution at desired rotating rates. In order to ensure a steady state in each point of the curve, a slow sweeping rate of 5 mV s^{-1} was applied.

2.4 Single cell tests

The cell configuration: H_2 | Pt/C | Nafion-OH^- | CuPc/C | O_2, was used in a single cell of PEMFC. The fabrication of MEAs was prepared by following steps: (i) The standard anode ink was prepared by mixing 40% Pt/C (Johnson Matthey) with a solution of 5 wt% Nafion® (DuPont) and isopropanol, and then sonicated for 4 h, where the ratio of Pt/C catalyst to Nafion® was 3:1. the catalyst ink was sprayed onto carbon papers (Toray TGP-H-090) to deposit a catalyst layer with a Pt loading of 0.5 mg (Pt) cm^{-2}. (ii) For cathode with non-platinum catalyst, the catalyst inks were prepared by mixing 40% CuPc/C with a solution of 5 wt% Nafion® and isopropanol, and then sonicated for 4 h, where the ratio of CuPc/C catalyst to Nafion® was also 3:1. Similar to the anode fabrication, the catalyst ink was sprayed onto carbon papers to deposit a catalyst layer with a CuPc loading of 3.6 mg cm^{-2}. (iii) Nafion-OH^- membrane was prepared using a Nafion® membrane with a size of 4 × 4 cm immersed in 3 M KOH for 48 hours. The Nafion solution was also used for the corresponding binders for both of the anode and the cathode. The Nafion®-OH^- membrane was sandwiched with two same pieces of carbon papers coated with catalyst and binder, and then were hot-pressed at a pressure of 10 MPa at 75 °C for 3 min.

Scheme 1 shows the working mechanism of polymer electrolyte membrane fuel cell. The MEAs with an active area of 4 cm^2 was inserted into a fuel cell hardware which consisted of graphite block with machined serpentine flow channel and copper current collector (Scheme 1 (B)). Pure hydrogen and oxygen were supplied to enter the anode and cathode channels at a flux of 100 and 60 ml min^{-1}, respectively, through a humidifier maintained at 25°C under ambient pressure. Polarization curves were obtained using a fuel cell evaluation system (GE/FC1-100).

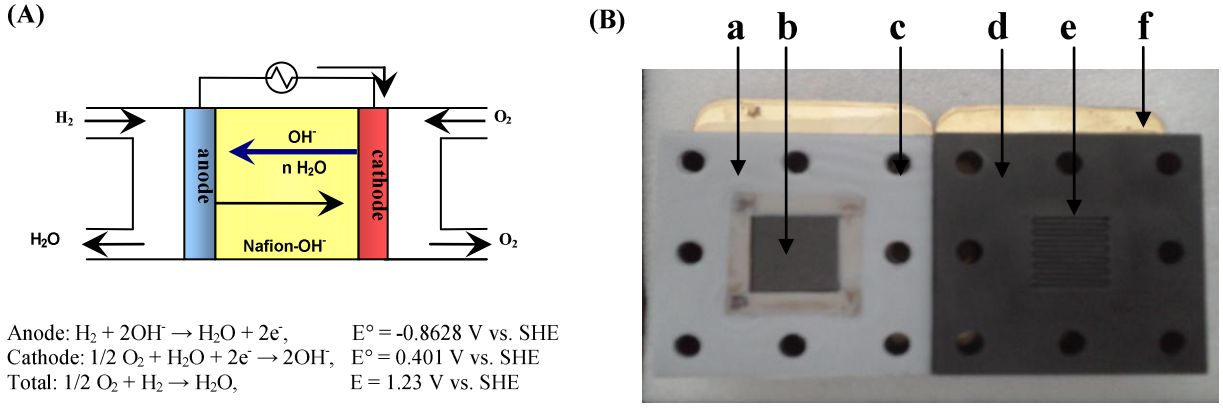

Anode: $H_2 + 2OH^- \rightarrow H_2O + 2e^-$, $E° = -0.8628$ V vs. SHE
Cathode: $1/2\ O_2 + H_2O + 2e^- \rightarrow 2OH^-$, $E° = 0.401$ V vs. SHE
Total: $1/2\ O_2 + H_2 \rightarrow H_2O$, $E = 1.23$ V vs. SHE

Scheme 1. (A) working mechanism of polymer electrolyte membrane fuel cell;
(B) photograph of polymer electrolyte membrane fuel cell showing silicon sheets (a), MEA (b),

screw hole (c), graphite block (d), gas channel and (e) and current collector (f).

3. Results and discussion

3.1 physical characterization

Figure 1 shows the XRD patterns of the CuPc/C catalysts synthesized at different heat-treatment temperatures. The first large broad peak located at about $2\theta = 25^{o}$ was observed for all the XRD patterns, which is attributed to the diffraction of carbon. From Figure 1, it can be seen that CuPc/C without heat-treatment showed some quite strong diffraction peaks due to the crystalline nature of CuPc. However, these peaks disappeared after heat-treatment at 600°C. For catalyst sample heat-treated at 800°C, two new small diffraction peaks centered at 43.3° and 50.4° were clearly observed, indicating that part of the CuPc on the carbon support may have decomposed, forming the new Cu-N_x-C compositions. According to literature [19-21], these two diffraction peaks may correspond to the characteristic diffraction peaks of metallic Cu. When catalyst sample was further heat-treated at 900°C, the shape of these peaks becomes strong and narrow, indicating the growth of metallic Cu cluster particles after decomposition of the CuPc structure. Since the porosity of the catalyst may be blocked by metallic Cu which are not active for the ORR, the heat-treatment temperature for CuPc/C synthesis should not be higher than 800°C in order to obtain the high electrocatalytic activity. Thus, for a more detailed analysis of the effect of Nafion® ionomer, the CuPc/C heat-treated at 800°C was chosen for further study.

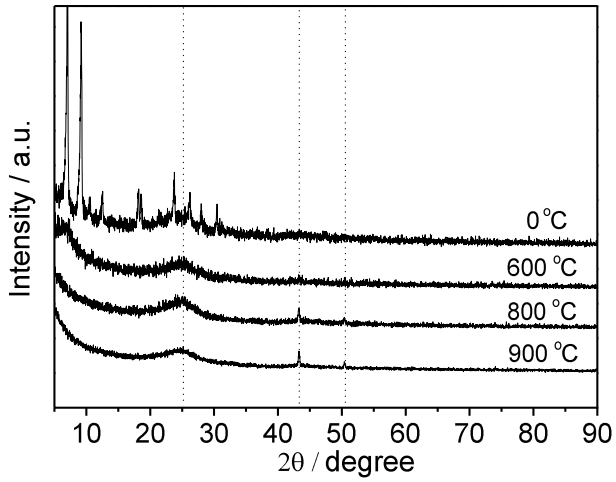

Figure 1. X-ray diffraction spectra of the CuPc/C catalysts before and after heat-treatment at 600, 800 and 900°C, respectively.

3.2 Electrochemical activity of CuPc/C catalyst towards ORR

Figure 2 shows CVs for the ORR on the CuPc/C electrode prepared with different Nafion® ionomer contents in the catalyst layer, measured in O_2-saturated 0.1 M KOH solution (where the CuPc/C catalyst loading on GC electrode was fixed of 140 μg cm^{-2}). It can be seen that CVs of CuPc/C electrode prepared with Nafion® contents of 2.5×10^{1} and 3.5×10^{1} μg cm^{-2} show the same oxygen reduction peak position (-0.06 V), but the latter gives 25% higher

current density than the former. When Nafion® contents were increased to 5.7×10^{1} and 1.6×10^{2} μg cm^{-2}, the oxygen reduction peaks were at -0.1 and -0.12 V, respectively. Both are lower than that of CuPc/C electrode prepared with Nafion® contents of 2.5×10^{1} and 3.5×10^{1} μg cm^{-2}. Also, the peak current densities of CuPc/C electrode prepared with Nafion® contents of 5.7×10^{1} and 1.6×10^{2} μg cm^{-2} are both smaller than the values observed for CuPc/C catalyst with 3.5×10^{1} μg cm^{-2} Nafion® content. The above results indicate that the optimal Nafion® ionomer content in the catalyst layer should be around 3.5×10^{1} μg cm^{-2}.

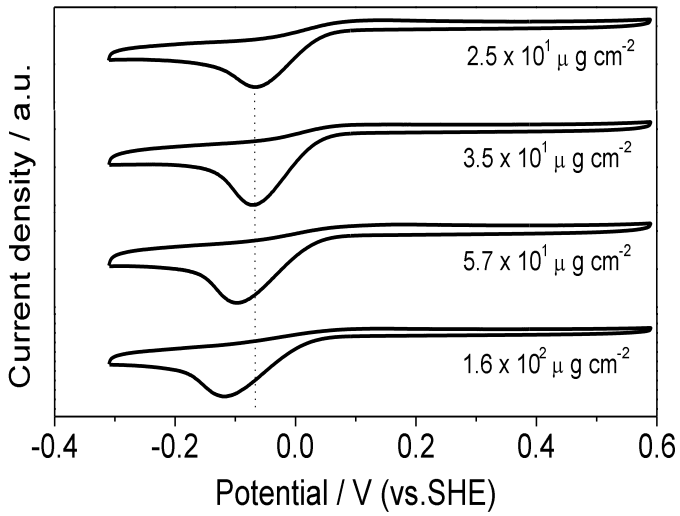

Figure 2. The cyclic voltammogram curves recorded in O_2-saturated 0.1 M KOH solution for the CuPc/C electrode coated with different Nafion® ionomer contents. Scan rate: 50 mV s^{-1}.

For further clarifying the effect of Nafion® ionomer content on the ORR activity, LSV was conducted on CuPc/C electrodes with different Nafion® contents in an O_2-saturated 0.1 M KOH solution (Figure 3). For a better comparison, the LSV curves of CuPc/C electrode prepared with available anion-ionomer are also depicted in the same figure. Acorrding to rotating disk theory, the overall measured current density (i) of the oxygen reduction at each electrode potential (E), shown in Figure 3, can be expressed as being dependent on the kinetic current density (i_k) and the diffusion-limited current density (i_d). The relationship between these current densities can be expressed by the following equation [22].

$$i_k = \frac{ij_d}{j + i_d} \tag{1}$$

Several important kinetic parameters for ORR on CuPc/C electrodes prepared with Nafion® ionomer and available anion-ionomer are summarized in Table 1. It can be seen that for CuPc/C electrode prepared with different contents of Nafion® ionomer, the onset potentials increase with decreasing Nafion® loading. Comparatively, for CuPc/C electrode prepared with different contents of available anion-ionomer, the onset potentials have no significant change with decreasing available anion-ionomer loading, and all are little higher than those of prepared with Nafion® ionom-

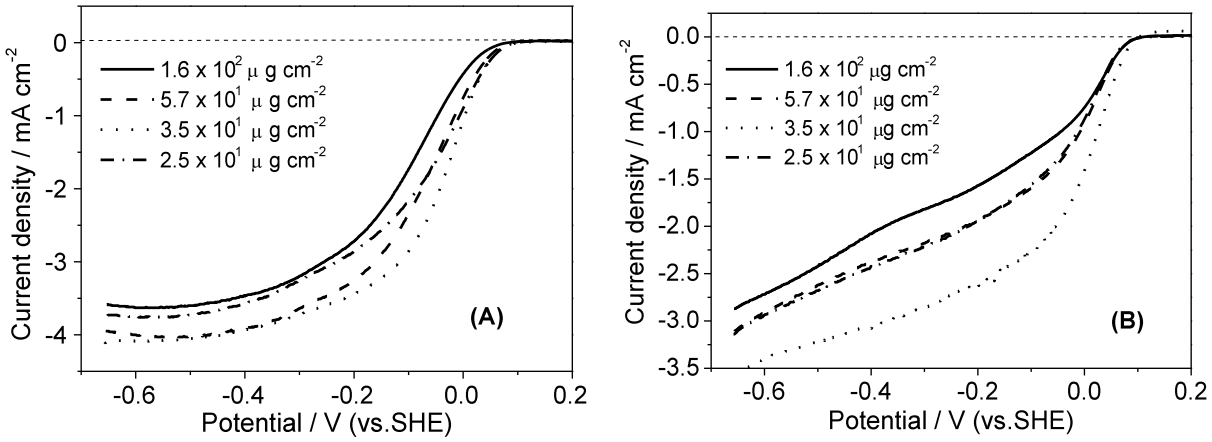

Figure 3. Polarization curves for the ORR on the CuPc/C catalysts, measured in O_2-saturated 0.1 M KOH at room temperature. (A) Nafion® solution for the catalyst ink preparation; (B) anion-ionomer for catalyst prepartion. Scan rate: 50 mV s^{-1}. Electrode rotation rate: 1500 rpm.

Table 1. Comparison of several kinetic parameters for ORR on CuPc/C electrode prepared with different contents of Nafion® ionomer and available anion-ionomer (potential versus SHE)

Binder loading (μg cm^{-2})		Onset Potential (V) [a]	$\Delta E_{1/2}$ (V) [a]	i_k at 0.05 V (mA cm^{-2}) [a]	Potential (V) at 0.1 mA cm^{-2} [a]
1.6×10^2	Nafion® ionomer	0.08	-0.105	1.40	0.045
	anion-ionomer	0.11	-	0.32	0.074
5.7×10^1	Nafion® ionomer	0.09	-0.06	3.90	0.061
	anion-ionomer	0.11	0.00	0.33	0.073
3.5×10^1	Nafion® ionomer	0.10	-0.03	4.50	0.066
	anion-ionomer	0.11	0.02	0.65	0.085
2.5×10^1	Nafion® ionomer	0.10	-0.06	2.90	0.068
	anion-ionomer	0.11	0.00	0.29	0.070

a) rpm 1500

er. Similarly, the half wave potential shows the positive shift from -0.06 to -0.03 V for Nafion® content changing from 2.5×10^1 to 3.5×10^1 μg cm^{-2}, but starts to fall with further increasing the content of Nafion® ionomer (Figure 3A). These observations indicate that the content of Nafion® ionomer can affect the ORR activity of the CuPc/C catalyst and, the optimal content of Nafion® ionomer is about 3.5×10^1 μg cm^{-2}. It should be mentioned that the optimal content of available anion-ionomer in CuPc/C electrode is also about 3.5×10^1 μg cm^{-2}, which leads to a highest half wave potential. However, all of catalysts prepared here have no well-defined diffusion-limiting current plateau (Figure 3B), suggesting that the distribution of active sites on these catalysts is less uniform and oxygen diffusion rate is slower in the available anion-ionomer layer.

When Nafion® ionomer is used as a binder, the proton exchange Nafion® ionomer would be converted into the potassium exchange Nafion® ionomer when the coated electrode was measured in KOH solution. For ORR in alkaline solution, the reaction can be written as:

$$O_2 + 2H_2O + 4e^- \Rightarrow 4OH^-$$

The cation-exchange membrane with fully impregnated by K^+ ion in KOH solution should have a blocking effect for fast OH^- removal. For these reasons, the onset potentials and half wave potentials of CuPc/C electrode prepared with Nafion® ionomer are lower to some extent than those of CuPc/C electrode prepared with available anion-ionomer. However, the kinetic current densities, i_k at 0.05V for the ORR on the CuPc/C electrodes coated with Nafion® ionomer are all much higher than those with available anion-ionomer (Table 1). At the same time, at a defined current density of 0.1 mA cm^{-2}, the overpotentials of the CuPc/C electrode prepared with Nafion® ionomer are all lower than 0.068 V, while, when coated with available anion-ionomer, the overpotentials of the CuPc/C electrodes are all higher than 0.07 V. Hence, it is reasonable to conclude that CuPc/C still shows very good catalytic activity for the ORR by applying Nafion® ionomer as a binder.

3.3 Rotating disk electrode studies of O_2 reduction

The kinetics of the ORR on GC electrodes coated with different content of Nafion® ionomer were measured at different electrode rotating rates using RDE technique. Figure 4 shows typical RDE curves at various rotation rates for the ORR on carbon-supported CuPc electrodes coated with Nafion® loading of 3.5×10^1 μg cm^{-2} in O_2-saturated 0.1 M KOH. It can be seen that the ORR limiting currents for CuPc/C catalyst prominently increased with the rotating rate, along with the onset potential for the ORR unchanged on the same catalyst. The number of electrons tr-

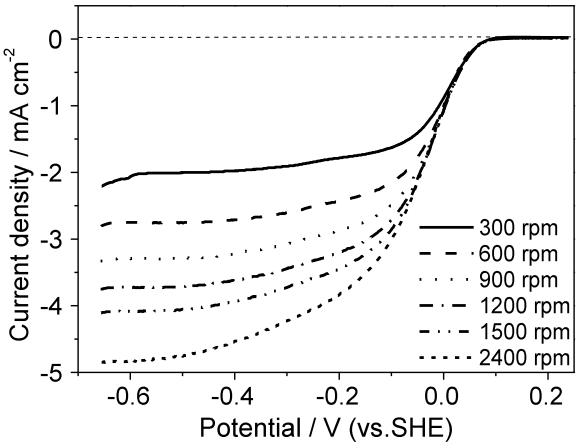

Figure 4. RDE polarization curves at different rotation rates for oxygen reduction on CuPc/C electrode prepared with Nafion® ionomer content of 3.5×10^1 μg cm^{-2} in 0.1 M KOH solution. Scan rate: 5 mV s^{-1}.

ansferred per O_2 molecule (n) was calculated from the Koutecky-Levich （K-L） equation [23]:

$$\frac{1}{j}=\frac{1}{j_k}+\frac{1}{j}+\frac{1}{j_d}=\frac{1}{j_k}+\frac{1}{j}+\frac{1}{0.62nFC_{O_2}D_{O_2}^{2/3}\nu^{-1/6}\omega^{1/2}} \quad (2)$$

Where j is the measured current density at -0.6 V, j_k is the activation controlled current density, j_f is the effect of Nafion® ionomer inside the catalyst layer on the measured current density, which may be negotiable if the equivalent Nafion® ionomer thickness is much small ($j_f \rightarrow \infty$), j_d is the O_2 diffusion limiting current density, n is the number of electrons transferred per oxygen molecule, F is Faraday constant, $C_{O2}$is the concentration of dissolved oxygen in the solution, D_{O2} is the diffusion coefficient of O_2 in the solution, ν is the kinetic viscosity, and ω is the electrode rotating rate in rpm. The plot of $\frac{1}{j}$ vs. $\omega^{-1/2}$ according to Equation (2) can give a slope of $(0.62nFC_{O_2}D_{O_2}^{2/3}\nu^{-1/6})^{-1}$, from which the electron transfer number (n) can be estimated if other parameters are known. Figure 5 shows the Koutecky-Levich plots for the ORR at the potential of -0.6 V on the CuPc/C electrode

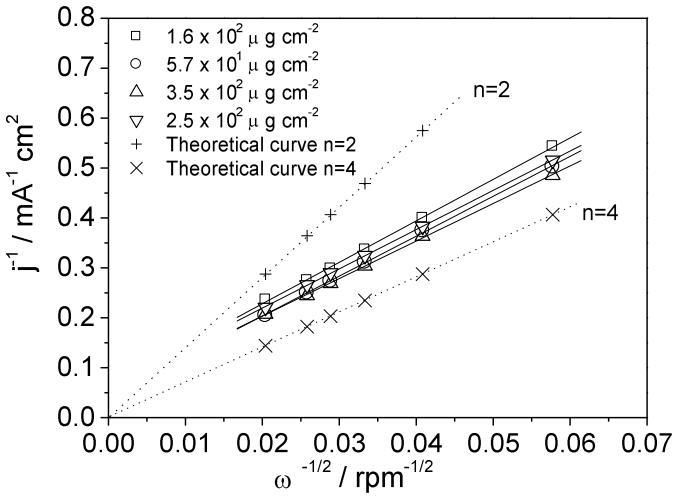

Figure 5. Koutecky-Levich plots for the ORR on CuPc/C electrode coated with different contents of Nafion® ionomer at -0.6 V *vs.* SHE

prepared with different contents of Nafion® ionomer derived from the data in Figure 4. The plots for the two-eletron and four-eletron transfer processes of the ORR are also shown in Figure 5. It can be seen clearly that the K-L slopes of CuPc/C electrode coated with different contents of Nafion® ionomer are all close to that of four-eletron transfer reaction. Based on these slopes, we can calculate the electron transfer number and found that the it changes with increasing the content of Nafion® ionomer: 3.40 for 1.6×10^2 μg cm^{-2}, 3.52 for 5.7×10^1 μg cm^{-2}, 3.74 for 3.5×10^1 μg cm^{-2} and 3.58 for 2.5×10^1 μg cm^{-2}. These results indicate that content of Nafion® ionomer can affect not only the ORR activity of the CuPc/C catalyst but also the ORR electron transfer number. At a lower Nafion® loading (2.5 ×

10^1 and 3.5×10^1 μg cm^{-2}), the value of electron transfer number is bigger than that at a high Nafion® loading (5.7×10^1 and 1.6×10^2 μg cm^{-2}), which is attributed to difference of Nafion® thicknesses in the catalyst layer.

3.3 Single-cell performance

Finally, to further study the effect of Nafion® ionomer as for alkaline electrolyte, electrical test in a real H_2/O_2 single-cell was performed based on a Nafion® membrane rinsed with 3 M KOH for about 48 hours. Figure 6 shows the fuel cell polarization curve and power density profile obtained using pure O_2 as the oxidants and pure H_2 as the fuel at room temperature, a humidifier maintained at 25°C under ambient pressure. As shown in Figure 6, the open-circuit voltage around 0.75 V can be observed, which is lower than 1.0 V found for fuel cells with Co- and Fe-centered phthalocyanines as cathode catalysts [24]. The maximum power density at ambient temperature of Nafion®-OH^- membranes reached 3.8 mW cm^{-2}. Although the power density is still very low in comparison with reported in the literature [24], this initial value indicates the promising application of Nafion®-OH^- membranes and Copper phthalocyanines for alkaline fuel cell. Considering the initial value in this paper, future work has then to be focused on the optimizaiton of the experimental conditions in order to further improve the fuel cell performance.

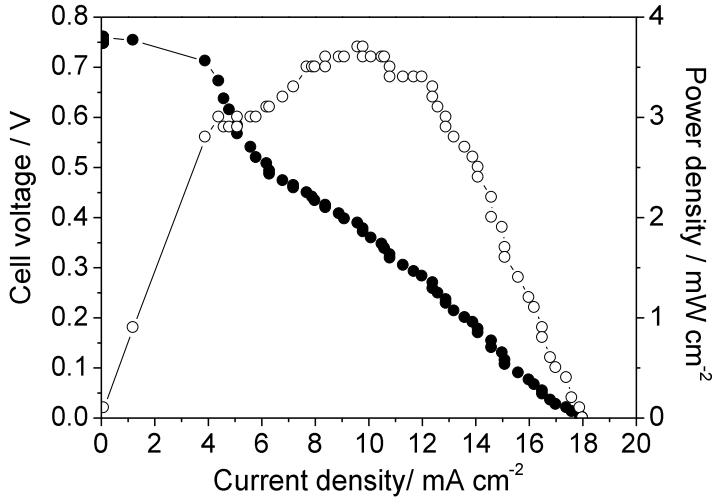

Figure 6. PEMFC performance of MEAs with CuPc/C based cathodes using Nafion®-OH^- membrane

4. Conclusions

This paper is focused attention on the Nafion® binder for electrocatalytic measurements and single-cell tests for an alkaline fuel cell. Electrochemical techniques such as CV, LSV and RDE were used to investigate the effect of the Nafion® ionomer content in the CuPc/C-based catalyst layer on the ORR. The results indicate that the electrocatalytic activity varies with the Nafion® loading and, the best performance is obtained from the CuPc/C electrode coated with 3.5×10^1 μg cm^{-2}, which is in a well agreement with the one studied using available anion-ionomer. An onset potential of 0.1 V and a half wave potential of -0.03 V are achieved in alkaline electrolyte. Besides the ORR kinetic rate, the ORR electro transfer number was also increased from 3.40 to 3.74 with decreased the content of Nafion®

ionomer from 1.6×10^2 to 3.5×10^1 μg cm^{-2}. An initial power density of 3.8 mW cm^{-2} was obtained with a Nafion® membrane rinsed with 3 M KOH for about 48 hours. As discussed in this paper, it is expected that an improved ORR activity could be achieved when changing the Nafion® ionomer to an anion ionomer. However, at the present, the anion ionomer is not so common used as Nafion® ionomer and, it's difficult to get. Our work demonstrated that in the process of alkaline fuel cell study, it's reasonable by applying Nafion® ionomer as substitute for anion ionomer considering that CuPc/C catalyst still shows promising catalytic activity for the ORR when Nafion ionomer is used as a binder.

5. Akcnowledgements

We give our thanks to the financial support from the National Natural Science Foundation of China (21173039), Specialized Research Fund for the Doctoral Program of Higher Education, SRFD (20110075110001), Environmental Protection Engineering Center for Pollution Treatment and Control in Textile Industry, China (20110927) and the Shanghai Leading Academic Discipline Project (B604) Fund.

6. References

[1] H. R. Colón-Mercado and B. N. Popov, J. Power Sources, 155, 253 (2006).
[2] C. J. Song, L. Zhang and J. J. Zhang, J. Electroanal. Chem., 293, 587 (2006).
[3] L. Xu, J. L. Qiao, L. DING, L. Y. HO, L. L. Liu and H. J. Wang, Acta Phys Chin Sin, 2251, 27 (2011).
[4] K. Gong, F. Du, Z. Xia, M. Durstock and L. Dai, Science, 323, 760 (2009).
[5] J. H. Kim, A. Ishihara, S. Mitsushima, N. Kamiya and K. I. Ota, Electrochim. Acta, 52, 2492 (2007).
[6] K. Lee, A. Ishihara, S. Mitsushima, N. Kamiya and K. I. Ota, Electrochim. Acta, 49, 3479 (2004).
[7] M. Lefevre and J. P. Dodelet, Electrochim. Acta, 48, 2749 (2003).
[8] R. Baker, D. P. Willkinson and J. Zhang, Electrochim. Acta, 53, 6906 (2008).
[9] R. Cheng, H. Li, D. Chu and G. Wang, J. Phys. Chem. C, 113, 20689 (2009).
[10]Y. Nabae, S. Moriya, K. Matsubayashi, S. M. Lyth, M. Malon, L. Wu, N. M. Islam, Y. Koshigoe, S. Kuroki, M. Kakimoto, S. Miyata and J. I. Ozaki, Carbon, 48, 2613 (2010).
[11] Y. Lu and R. G. Reddy, Electrochim. Acta, 52, 2562 (2007).
[12] J. Ozaki, S. Tanifuji, N. Kimura, A. Furuichi, and A. Oya, Carbon Japan, 44, 1298 (2006).
[13] N. Sehlotho, and T. Nyokong, J. Electroanal.Chem. South africa, 595, 161 (2006).
[14] E. H. Yu and K. Scott, J. Power Sources, 137, 248 (2004).
[15] C. Coutanceau, L. Demarconnay, C. Lamy and J. M. Léger, J. Power Sources, 156, 14 (2006).
[16] K. Scott, E. Yu, G. Vlachogiannopoulos, M. Shivare and N. Duteanu, J. Power Sources, 175, 452 (2008).
[17] H. Bunazawa and Y. Yamazaki, J. Power Sources, 182, 48 (2008).
[18] Y. S. Li, T. S. Zhao and Z. X. Liang, J. Power Sources, 190, 223 (2009).

[19] H. Zhu, X. Li and F. Wang, Int J Hydrogen Energy, 36, 9151 (2011).

[20] A. Sakar and A. Manthiram, J. Phys. Chem. C, 114, 4725 (2010).

[21] R. Wang, H. Li, H. Feng, H. Wang and Z. Lei, J. Power Sources, 195, 1099 (2010).

[22] C. V. Rao and B. Viswanathan, J. Phys. Chem. C, 111, 16538 (2007).

[23] A. J. Bard and L. R. Faulkner, Electrochemical Methods, Fundamentals and Applications, 2nd ed., John Wiley & Sons, Inc., N. Y., (2000).

[24]I. Kruusenberg, L. Matisen, Q. Shah, A. M. Kannan and K. Tammeveski, Int J Hydrogen Energy, 37, 4406 (2012).

9th International Symposium on New Materials and Nano-Materials for Electrochemical Systems
XII International Congress of the Mexican Hydrogen Society
Merida, Mexico, 2012

Scooter's Electric Motor Characterization and the Sizing of a PEMFC Power Plant Required for its Operation

A. J. Torres-Guerrero[1], F. Loyola-Morales[2,*], U. Cano-Castillo[2], S. A. Serna-Barquera[1]

[1]Centro de Investigación en Ingeniería y Ciencias Aplicadas, Av. Universidad 1001, Col. Chamilpa, Cuernavaca, Morelos, 62209, México.

[2]Instituto de Investigaciones Eléctricas, Reforma 113, Col. Palmira, Cuernavaca, Morelos, 62490, México.

[*]Tel: +52 7773623811, ext. 7798, Fax (777) 362-3881, ext. 7781, mail: felix.loyola@iie.org.mx

ABSTRACT

The development of power plant prototypes based on PEMFC´s for a particular application has important technical and economical impacts on the practical implementation of this technology. In this study, the characterization of an electric motor of an E-Z rider model Scooter was performed aiming at determining the load and therefore, the power demand required under specific operating conditions: no-load, with load and during sudden full stop breaking due to overload conditions. The characterization was performed under two operating modes, i.e. low and high speed modes. Results show that the minimum power required for the low speed, no load operation is 48 W, while maximum power reaches 84 W for operation at high speed with load. Also, maximum power during sudden breaking was limited to 84 W as the Scooter's control system allows for a maximum consumption of 7A at 12V.

The second part of the work presents the methodology used for dimensioning a fuel cell stack that will provide the power for the motor to fulfill load requirements. Simple calculations are based on polarization curves of a 90.5 W fuel cell stack. Accordingly, a 50cm^2 area and 20 cell stack can provide 84W of power plus a 20% extra power for auxiliaries required in the power system. To maintain higher efficiencies in the conversion of hydrogen while meeting power requirements, it was established that 0.615V per cell at an operating current density of 0.16A/cm^2 fuel cell stack is adequate for the application.

Keywords: Scooter, PEMFC dimension, electric motor characterization.

1.- Introduction

During the last years PEMFC´s have outstood from other types of fuel cells due to their advanced technology development [1], as well as their flexibility to accommodate many different applications , from portable devices such as mobile phones to stationary applications [2,3]. On the other hand the increase in number of personal vehicles and therefore the increase of pollutant gas emissions from transport activities [4], as well as the constant increase of fossil fuel costs [10], is taking our society to search for newer and better mobility concept alternatives.

In México there are more than 32 million vehicles registered for use on the roads [11], most of them used in big cities which concentrates their use in urban areas causing large traffic jams aggravating the problem [4], resulting also in waste of time and an excessive consumption of fuels. Individual transport alternatives, such as bicycles, motorcycles and scooters offer advantages over more conventional means of transport. Among those benefits we can mention shorter transfer times, less space on the roads, an increase in potential alternative routes and most importantly less power required [5,6]. Using PEMFC technology on this transportation alternatives represent an additional advantage, by eliminating completely the harmful emissions including green-house gases [6,7].

Implementing PEMFC technology as power generators, using hydrogen as a fuel, still represents opportunities to overcome technical engineering challenges [8], that could help improve the extensive use of this technology.

In this work, the electrical characterization of a scooter E-Z rider model electric motor was realized in order to evaluate current demand under some load conditions. Also, a methodology for designing a PEMFC stack for this particular application was carried out. Results for both activities are presented.

2.- Methodology

2.1.- Scooter's electric motor characterization

The characterization of the engine consisted in determining the current consumed by this under different load conditions. To do this, an array consisting of electric motor, Hall-type sensor, power supply, data logger, processor and power source was joined. Prior to the characterization of the engine, the Hall sensor calibration was carried out by a circuit similar to that described above, in which the scooter was replaced by an electronic variable load. The following sections describe the experimental approach of these activities.

2.1.1.- Sensor Hall-type calibration (Hawkeye® H970HCB DC current sensor)

The calibration test consisted in feed a known current to an electronic load (electronic Load of Heliocentris EL 100) (see figure 1a). When a current is passing through the Hall sensor, it generates a voltage signal associated with it (product of magnetic field strength and the current that is flowing) that is read by the data acquisition system

(PCS10/K8047 Velleman Instruments) and sent to the processor. The data sample consisted of 11 current values between 0 and 6 A, of which the data logger read a total of 1024 values. From this data (V, voltage signal) and the current consumed by the load, a linear regression was used to generate continuous function of the type I = mV + b.

2.1.2.- Current consumption test of the Scooter´s electric motor

This test consisted in determine the amount of current demanded by the engine for its two modes of operation (low and high speed) and under the following conditions:

- Without load
- With load (a person of 80 kg)
- Sudden braking of the motor (overload)

For the test were connected to the motor scooter two 6V batteries in series (see Figure 1b). The motor power cord was passed through the Hall sensor for measuring the current consumed, the voltage signal emitted by the Hall sensor was sent to the data processor via the data acquisition system.
The continuous function determined in the Hall sensor calibration was used to calculate the amount of current consumed by the motor, this as a function of the voltage generated by the sensor.

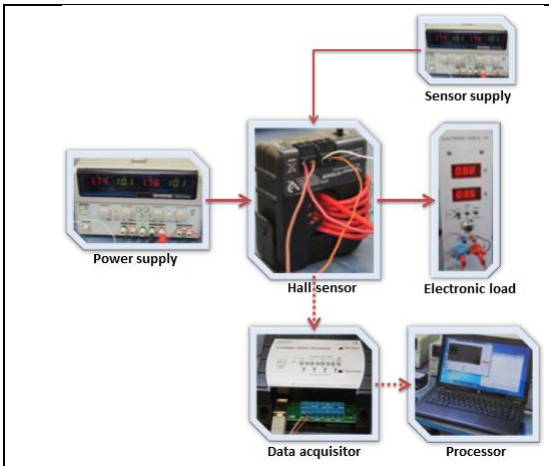

Figure 1a. Connection diagram for the electrical arrangement for calibration of Hall sensor.

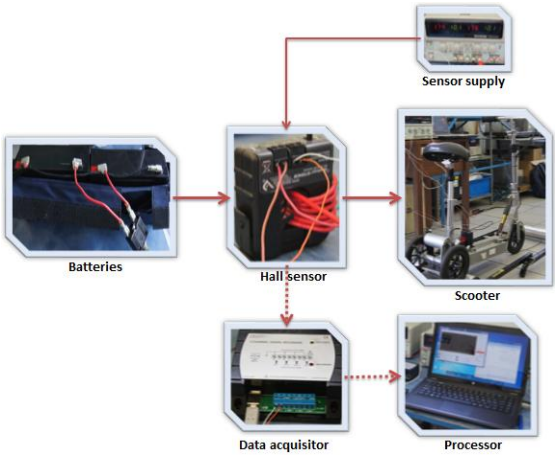

Figure 1b. Connection diagram for the electrical arrangement for the scooter´s electrical motor characterization.

2.2.- Stack fuel cell´s dimension

2.2.1.- Polarization curve

Initial information on designing a fuel cell stack is the steady state polarization curve, which can be a theoretical initial curve or an experimental curve. This curve describes the fuel cell stack performance in particular, it represents the voltage-current density (*V vs i*). An experimental polarization curve is the most reliable information to perform the size design [9], as it represents the actual performance of a system accounting for all implicit voltage loses. Nevertheless, not having an experimental set of data should not be a barrier to determine a fuel cell stack capacity, as the theoretical polarization curve calculation is very useful and reasonably accurate if other experimental information is taken in consideration:

$$E_{FC} = E_{r,T,P} - \frac{RT}{\alpha F} ln\left(\frac{i+i_{loss}}{i_0}\right) - \frac{RT}{nF} ln\left(\frac{i_L}{i_L - i}\right) - iR_i \qquad \text{Ec. 1}$$

where:

E_{FC}, is the cell potential (V)
$E_{r,T,P}$, is the reversible potential at given temperature and press (V)
R, is the constant gases ($8.314\ J\ mol^{-1}\ K^{-1}$)
T, is the temperature (K)
α, is the charger transfer coefficient
n, is electrons number involved
F, is the Faraday´s constant (96,485 $C\ mol^{-1}$)
i, is the current density ($A\ cm^{-2}$)
i_{loss}, are the current losses ($A\ cm^{-2}$)
i_0, is the reference exchange current density ($A\ cm^{-2}$)
i_L, is the limit current density ($A\ cm^{-2}$)
R_i, is the internal resistance (Ohm cm^2)

2.2.2.- Dimensioning method

In this section the sequence of calculations to determine the fuel cell stack capacity is shown. The methodology starts with the maximum current and voltage demanded by the load, 12 V and 7 A, with a total maximum power of 84 W, for this case. These data and the experimental or theoretical polarization curve data should also be considered, these

are shown on table 1a and 1b, respectively. In this work the polarization curve data points were obtained from a 20 cell fuel cell stack of 25 cm^2 of geometrical active area, as well as other theoretical data using equation with data shown on table 2. Internal resistance (*Ri*) and limit current density (*i*) were obtained experimentally. On the other hand, the charge transfer coefficient (α) was used to fit the experimental data to the theoretical curve.

Table 1. Polarization curve data

a) Experimental data

*V*c, (V)	Current density (A/cm^2)
0.7573	0.04632
0.725	0.05952
0.67095	0.09948
0.633	0.13948
0.615	0.15964
0.585	0.19956
0.55395	0.23968
0.52615	0.27968
0.5	0.3198
0.489	0.3398
0.4793	0.36
0.466	0.37992
0.4517	0.39992
0.39245	0.43996
0.34865	0.46
0.3267	0.465

b) Theoretical data adjusted to the experimental curve

*V*c (V)	Current density (A/cm^2)
0.883	0.001
0.773	0.025
0.733	0.050
0.703	0.074
0.679	0.098
0.657	0.123
0.637	0.147
0.618	0.172
0.600	0.196
0.582	0.220
0.565	0.245
0.548	0.269
0.531	0.293
0.515	0.318
0.498	0.342
0.480	0.367
0.462	0.391
0.443	0.415
0.420	0.440
0.360	0.464

Table 2 Equation 1 parameters.

Polarization curve parameter [units]	Value
$E_{r,T,P}$ [V], (60°C y a 1 atm)	1.191
R [J mol^{-1} K^{-1}]	8.314
T [K]	333.15
α	0.645
n	2
F [C mol^{-1}]	96,485
i_{loss} [A cm^{-2}]	0.002
i_0 [A cm^{-2}]	3X10^{-6}
i_L [A cm^{-2}]	0.465
R_i [Ohm cm^2]	0.455

This information is used as follows:

a) Cell's efficiency calculation

The cell's efficiency (ŋ), defined as the relation between the energy obtained in form of electricity and the hydrogen energy consumed, is given by:

$$ŋ = \frac{W_{el}}{W_{H2}} \quad \text{Ec. 2}$$

The electricity produced is the product between of voltage and current:

$$W_{el} = I * V \quad \text{Ec. 3}$$

where I is the current in Amperes and V is the cell's voltage in Volts. The hydrogen energy is according to Faraday's law, proportional to the current:

$$N_{H2} = \frac{I}{nF} \quad \text{Ec. 4}$$

where N_{H2} is in *mols*$^{-1}$, and

$$W_{H2} = \Delta H \frac{I}{nF} \quad \text{Ec. 5}$$

where, W_{H2} is the energy contained in hydrogen and ΔH is the water formation heat, from molecular hydrogen and oxygen:

Liquid water formation: $\Delta H_{H2O\ liq} = -286\ kJ/mol$, then $\Delta H/nF = 1.482$V.
Vapor water formation: $\Delta H_{H2O\ vap} = -241\ kJ/mol$, then $\Delta H/nF = 1.254$V.

Combining equations 2 and 5, the cell's efficiency is directly proportional to the cell's voltage:

$$\eta_{H2O\ liq} = \frac{V_C}{1.482} \qquad \text{Ec. 6}$$

or

$$\eta_{H2O\ vap} = \frac{V_C}{1.254} \qquad \text{Ec. 7}$$

It should be noted that in equations 6 and 7 the sign has been ignored as it does not affect the efficiency estimate.

b) Fuel cell stack voltage

The fuel cell stack (V_{CC}) is determined by the cell voltage (V_C) and the number of cells (N_C) in the stack, (equation 8). Increasing the number of cells also increases the voltage drop due to ohmic resistance. In this work such resistance is not included. Nevertheless, for this work 8 values for N_C were used. Once N_C is known the voltage can be determined (V_{CC}):

$$V_{CC} = \sum_{i=1}^{N_C} V_i = \overline{V_C} \cdot N_C \qquad \text{Ec. 8}$$

c) Cell stack current estimation

The fuel cell stack power (W_{CC}) is an operating parameter associated to the application load and is estimated:

$$W_{CC} = V_{CC} \cdot I_{CC} \qquad \text{Ec. 9}$$

From the equation above, we can obtain the cell current (I_{CC}):

$$I_{CC} = \frac{W_{CC}}{V_{CC}} \qquad \text{Ec. 10}$$

Once W_{CC} is determined a safety factor can be considered to account for auxiliaries or transient specifications so that the cell will have the capacity to provide energy for control, balance of plant (BOP) and even losses during power conditioning. This factor normally is between 20 and 30 % but it is up to the designer to choose the final factor.

d) Cell's geometrical area

I_{CC} is also defined as the product of current density times the active area:

$$I_{CC} = i \cdot A_C \qquad \text{Ec. 11}$$

From this A_C, can be calculated:

$$A_C = \frac{I_{CC}}{i} \qquad \text{Ec. 12}$$

e) Recalculation of data for graphical representation

From equations 7, 8, 10 and 12, cell efficiency ($\eta_{H2O\ vap}$), cell stack voltage (V_{CC}), total fuel cell stack current (I_{CC}) cell's active area (A_C), were calculated for each operating point of the cell's polarization curve (V_C, i) and for each case of number of cells proposed for a cell stack (N_C). Once sets of data are obtained, plots of $V_C\ vs.\ i$, V_C *vs. Power density* and *Cell efficiency vs. Power density*, as well as A_C vs. V_C, , are built using visual tools ("graphical" design).

f) Design criteria and restrictions

Estimation of V_{CC}, I_{CC} or A_C, for the 8 proposed cases for N_C and combined with 20 points from the polarization curve (table 1b) give a range of 160 possibilities of fuel cell stacks, each with particular features of V_{CC}, I_{CC}, A_C and N_C. Each stack can fulfill the required power but not all will fulfill restrictions related to the target efficiency, the geometrical active area and nominal current and voltage:

I. Cell efficiency: the recommended range is between 45 and 60%. 60 % would be for cases where there are no restrictions for the stack size of the volume provided for it in the particular application. 45 % can be used for the case where these restrictions are tight.
II. A valid restriction that the designer or technical expert can define is the size of the maximum geometrical active area for the stack.

III. If mechanical and structural limitations are light for the stack integration, values of V_{CC} and I_{CC} for the selected case, are recommended to be near the required values for the load, which will allow better efficiencies for power electronics conversion.

IV. An additional restriction can be the establishment of a particular work efficiency.

3.- Results and analysis

3.1.- Scooter´s electrical motor characterization

3.1.1.- Hall sensor calibration

In figure 2a current load values and their corresponding voltage values measured by a Hall sensor. The correlation of measured values showed that there exist a direct relation with a slope and a Y intercept of -0.68 y 7.33, respectively. Figure 3b shows a comparison between experimental values and those calculated with the line equation obtained. Such figure shows a good fit of the experimental data equal or larger than 1.5 A and up to 6 A.

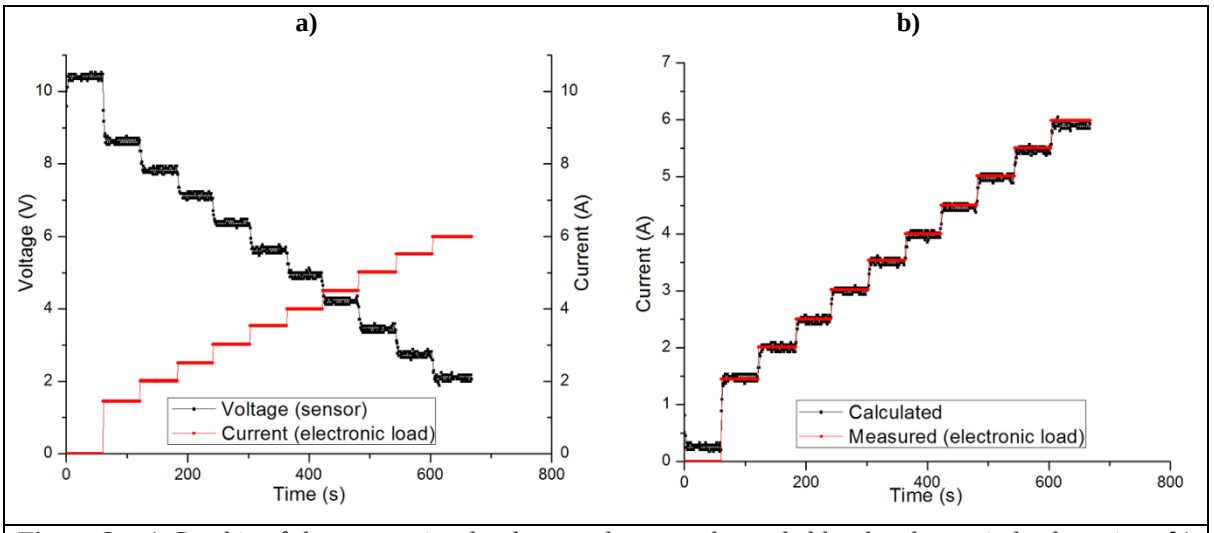

Figure 2. a) Graphic of the sensor signal voltage and current demanded by the electronic load vs. time. **b)** Comparison of the calculated current values by the equation vs. the experimental ones.

3.1.2.- Current consumption test of the scooter's electrical motor

The test for determining power consumption consisted in make work the scooter in the two modes of operation and loading conditions, figure 3 shows the result of this test. The baseline (a) corresponds to the on-state of the scooter but without power demand; the nonzero value read in the graph is due to the deviation of 0.28 A that the equation showed for current values below 1.5 A (figure 2b). The first peak (b) corresponds to the current demand on the low-speed mode and unloaded, in this state the scooter consumes 3.7 A. The test at this same speed but with load, showed a demand for 7 A (peak c). The peak b' and d represents the sudden braking test at low speed; corresponding b' to the current demand without stopping (3.7 A) and d to the demand with sudden braking (7 A). As shown, the load demand in both the test with load and sudden braking the motor´s current consumption is 7 A, apparently the electric circuit of the scooter is limiting the maximum current consumption.

For testing power consumption at high speed, it was found that the demand for no-load current is 4.13 A (peak e), only slightly higher than that consumed in low speed. On the other hand, the test under load showed a demand of 7 A (peak f) and during sudden braking the demand was also 7 A, thus confirming that the electrical control circuit of the scooter is controlling the maximum current. This result indicates that in the sizing process of the stack should be considered as operating nominal current 7 A. Considering also the batteries used as a source gave a voltage of 12 V, then we have that the stack in design process should be able to provide an output of 84 watts plus a percentage for auxiliary systems (BOP) and a factor design safety.

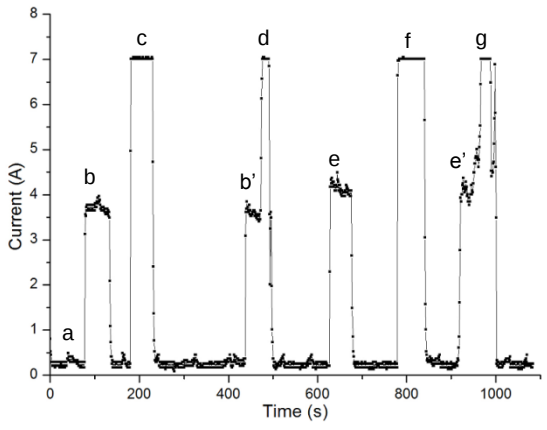

Figure 3. Scooter current consumption at different loads conditions

3.2.- Stack fuel cell´s dimension

3.2.1.- Polarization curve

As discussed in section 2.2.2, the initial information in the design of a stack are the data from an experimental polarization curve or theoretical. In order to show that both the use of experimental and theoretical data is completely valid, figure 4 shows graphs of the polarization curve data presented in tables 1a and 1b, experimental and theoretical, respectively. In this, one can observe the similar trend between the two data sets.

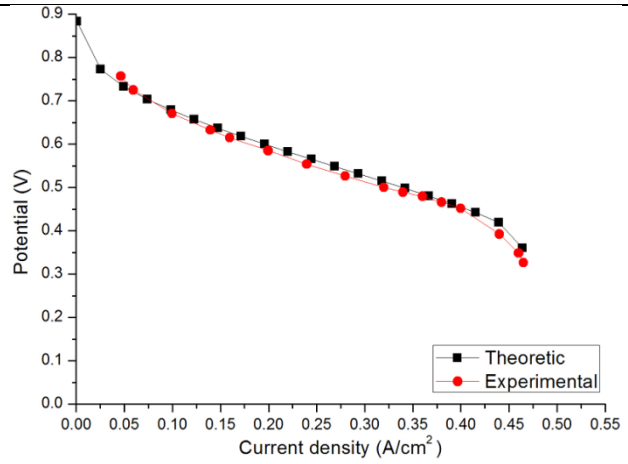

Figure 4. Adjust of the theoretical polarization curve to the experimental one.

3.2.2.- Graphical dimensioning of the fuel cell´s stack

The results obtained in the characterization of the motor scooter was our input information on the sizing process:

I. Current required: 7A
II. Voltage required: 12V
III. Power required: 84 W

The following Nc values were proposed as case studies:

Cases	Nc: Number of cells
Caso 1	5
Caso 2	10
Caso 3	15
Caso 4	20
Caso 5	25
Caso 6	30
Caso 7	35
Caso 8	40

From the value of power required, we calculated the nominal power of the stack given an additional 20%: 100.8 W. Using this value, Nc, and data of polarization curve in the equations 7, 8, 10 and 12, allowed the calculation of the cell efficiency, (ŋ_(H2O vap)), stack voltage (*V*cc), stack total current (*I*cc), and the geometric active area of the cell (*A*c). As mentioned in the experimental section 2.2.2, the combination of *N*c and the 20 points of the polarization curve resulted in 160 possible cases of stack; all of them meet the required rated power of 100.8 W by combining the values *V*dc and *I*cc. From this range of possible stacks, we applied the "Restriction I", related to the cell efficiency interval recommended (used fuel efficiency): 45 to 60%, which represented in the graph Voltage, efficiency Vs. Power density (Figure 5a), can be seen that the efficiency range is equivalent to voltage range between 0.55 and 0.75 V. The representation of this interval voltage on the polarization curve can be seen in Figure 5b.

a)

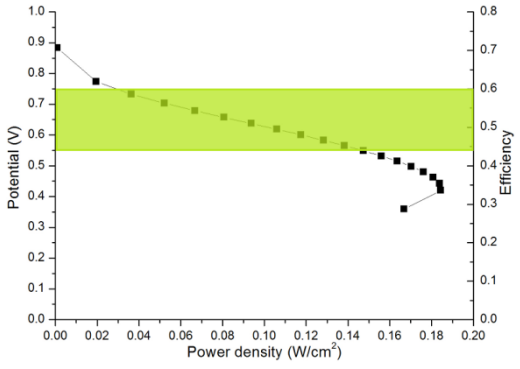

Figure 5a. Visual representation of the recommended efficiency interval in the graphic: *potential, Efficiency vs. Power density.*

b)

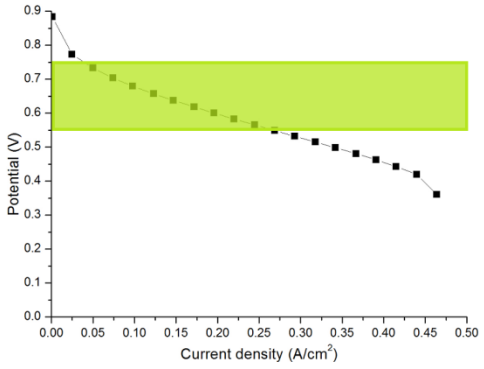

Figure 5b. Visual representation of the recommended efficiency interval in the polarization curve.

The application of this restriction decreases the number of possible stacks to 72. Additionally, in applying the "Restriction II" related to the maximum active area, which in our case is 100 cm^2, limited by the space for the stack on the scooter, the number of cases decreased to 54. In figure 6, the aplication of both restrictions can be observed.

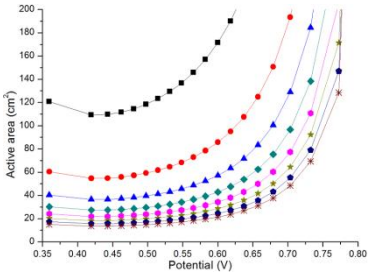

Figure 6a. Graphic representation of the range of initial cases of stack.

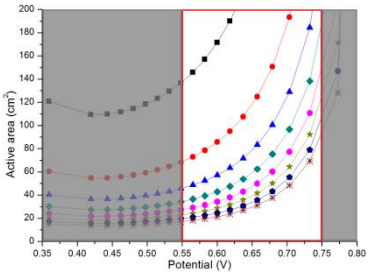

Figure 6b. Application of the restriction I: efficiency interval recommended.

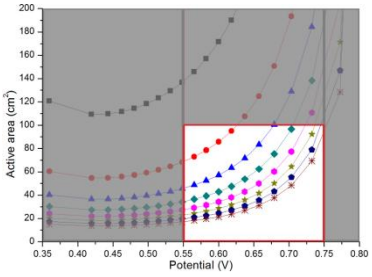

Figure 6c. Application of the restriction II: Maximum geometrical active area.

The 54 cases resulting from applying the restrictions I and II are already cases that could function properly, however, choose any of them, would transfer to the power electronics team the work of adjust the voltage and current required by the scooter. In our case, seeking to have the highest efficiencies in the stages of voltage regulation, the restriction III was applied, in which we stated that the output of the stack may have 7 ± 2 A y 12 ± 2 V. Values falling in these ranges have been highlighted in the tables 5 and 6. Of these, only 7 cases of stack meet both conditions, all in the "Case 4", corresponding to stacks of 20 cells. If after these seven cases apply the "Restriction IV", establishing a fuel usage efficiency of 50%, for example, we have the characteristics of the stack that meets this criterion is between two values:

Geometric active area:	48-54 cm^2
Stack nominal Voltage:	12.37-12.75 V
Stack nominal current:	7.91-8.15 A
Cell's number:	20

With this we finish the stack sizing process

Table 4. Geometrical active area values (*A*c) after applying the restrictions I and II.

	STACK ACTIVE AREA							
Efficiency	CASE 1	CASE 2	CASE3	CASE 4	CASE 5	CASE 6	CASE 7	CASE 8
0.584						92	79	69
0.561				97	77	64	55	48
0.542			100	75	60	50	43	38
0.524			83	62	50	42	36	31
0.508			72	54	43	36	31	27
0.493		95	63	48	38	32	27	24
0.479		86	57	43	34	29	24	21
0.464		79	52	39	31	26	22	20
0.451		73	49	36	29	24	21	18

Table 5. Stack voltage values (*V*cc) after applying the restrictions I and II..

	STACK VOLTAGE							
Efficiency	CASE 1	CASE 2	CASE 3	CASE 4	CASE 5	CASE 6	CASE 7	CASE 8
0.584						21.977	25.640	29.303
0.561				14.069	17.586	21.103	24.620	28.137
0.542			10.186	13.581	16.976	20.372	23.767	27.162
0.524			9.860	13.146	16.433	19.719	23.006	26.293
0.508			9.558	12.745	15.931	19.117	22.303	25.489
0.493		6.183	9.274	12.365	15.457	18.548	21.639	24.731
0.479		6.001	9.001	12.002	15.002	18.003	21.003	24.004
0.464		5.825	8.737	11.649	14.562	17.474	20.386	23.299
0.451		5.652	8.479	11.305	14.131	16.957	19.784	22.610

Table 6. Stack current (*I*cc) values after applying the restrictions I and II.

	STACK TOTAL CURRENT							
Efficiency	CASE 1	CASE 2	CASE 3	CASE 4	CASE 5	CASE 6	CASE 7	CASE 8
0.584						4.587	3.931	3.440
0.561				7.165	5.732	4.777	4.094	3.582
0.542			9.896	7.422	5.938	4.948	4.241	3.711
0.524			10.223	7.668	6.134	5.112	4.381	3.834
0.508			10.546	7.909	6.327	5.273	4.520	3.955
0.493		16.304	10.869	8.152	6.521	5.435	4.658	4.076
0.479		16.798	11.198	8.399	6.719	5.599	4.799	4.199
0.464		17.306	11.537	8.653	6.922	5.769	4.944	4.326
0.451		17.833	11.889	8.916	7.133	5.944	5.095	4.458

4.- CONCLUSIONS

The characterization of the electric motor scooter showed that power consumption is between 3.7 A for the condition "without load" and 7 A for the terms "with load" and "motor suddenly stopping." This result indicated that 7 A is the maximum current allowed by the electrical control of the scooter.

The application of the restrictions I and II of the proposed methodology allowed to identify the possible dimensions of the stack in design, this, in terms of ranges of total voltage, current, total geometric active area and number of cells. This range of options can be reduced to one, if we apply restrictions as the III and IV.

According to the proposed methodology and restrictions, the recommended stack size to supply the power required by the scooter is 20 cells with active area between 48 and 54 cm^2, rated operating voltage between 12.4 and 12.8 V and rated current between 7.9 and 8.2 A.

5.- ACKNOWLEDGMENTS

Authors express their gratitude to the Instituto de Investigaciones Eléctricas for the financial support in the development of this work (Project 14261). Allan Josue Torres Guerrero thanks CONACYT-México for financial support through grant No. 253751.

6.- BIBLIOGRAPHY

[1] A. Dicks and J. Larminie. (2003). *Fuel Cell Systems Explained*, 2nd Edition. England: John Wiley.

[2] N. Sammes. (2006). *Fuel Cell Technology, Reaching Towards Commercialization*. England: Springer.

[3] R. G. González, E. López, B. Velázquez. (2009). *Hidrógeno: introducción a la energía limpia*, pp. 127-136, 1ª Edición. México: UACM

[4] A. Lozano, V. Torres and J.P. Antún. (2003). *Tráfico vehicular en zona urbanas*. Revista Ciencias.(México), 70, 34-45.

[5] S. Harper, S. Pettitt, C. Goble. *XPMI an eXtensible Personal Mobility Interface (A Semantic Web of Mobility Devices)*. In Proceedings of the First International Semantic Web Conference (ISWC2002), June 2002.

[6] F.J. Rodríguez, O. Solorza and E. Hernández. (2011). *Celdas de combustible*, pp. 80-96. México.

[7] R. Beneito, J. Vilaplana and S Gisbert, *Int. J. of Hydrogen Energy*, 32, 1554, (2007).

[8] R. G. González, E. López, B. Velázquez(2009). *Hidrógeno: introducción a la energía limpia*, pp. 89-104, 1ª Edición. México: UACM.

[9] F. Barbir. (2005). *PEM Fuel Cells: Theory and Practice*, edited by Richard C. Dorf. USA: Elsevier.

[10] Consultar: http://www.ri.pemex.com/files/dcpe/petro/epublico_esp.pdf

[11] Consultar: http://www.inegi.org.mx/lib/olap/consulta/general_ver4/MDXQueryDatos.asp?proy=vmrc_vehiculos

Nanostructured Ferrite as Photocatalysts for H_2 Generation from Water Splitting and Sunlight

Mercedes Yudith Ortega-López, Jesús Manuel Salinas-Gutiérrez, Alejandro López-Ortiz, Virginia Collins-Martínez*

Centro de Investigación en Materiales Avanzados S. C., Laboratorio Nacional de Nanotecnología, Depto. de Materiales Nanoestructurados, Miguel de Cervantes 120, C. P. 31109, Chihuahua, Chih. México.
*Tel: +52 614 436 1129, Fax: +52 614 439 1130: e-mail: virginia.collins@cimav.edu.mx

ABSTRACT

Materials with higher efficiency and activated under the sunlight spectrum (band gap energy from 1.5 to 3.0eV) are today´s trends in newer photocatalysts for the hydrogen generation. The aim of the present study is to investigate alternative semiconductor materials to titanium dioxide for the generation of hydrogen with band gap energy values lower than that of TiO_2 (<3.2eV). Examples of these are some transition metal ferrites such as $CuFe_2O_4$, $CoFe_2O_4$ and $NiFe_2O_4$. These ferrites were prepared by co-precipitation and heat treatment. Characterization was performed by XRD, BET, SEM, TEM and UV-Vis spectroscopy. Photocatalytic activity evaluation of the materials for hydrogen generation from water splitting under visible light was followed by gas chromatography. Results indicate that these materials showed corresponding spinel crystalline phases and nanometer particle sizes. Photocatalytic evaluation of these ferrites under visible light showed H_2 yields up to 10.8 mmoles/g_{cat}. These yields compared with those reported in the literature indicate that these materials can be considered as promising photocatalysts for hydrogen generation.

Keywords: Ferrites, Nanoparticles, Photocatalytic activity, Water splitting

1. INTRODUCTION

The adverse environmental impact and the near depletion of fossil fuels, which are currently the preferred energy sources, represent the main motivations in seeking alternative energy sources from renewables. In this context, solar energy as an infinite resource [1] and the production of hydrogen as an energy carrier [2], are a clear option to clean, economical and sustainable energy generation through the use of fuel cells. In this context the hydrogen production from solar energy [3] and through the process of photocatalytic water-splitting represents a feasible clean energy alternative.

Within hydrogen production from photocatalytic water-splitting it is important to consider three main factors [3]: first, solar energy must be efficiently absorbed to generate pairs of electrons and holes for the dissociation of water, second, H_2 and O_2 recombination must proceed in order to reform the water molecule again and third, possible undesirable reactions may take place (corrosive reactions).

For the photocatalytic process to occur some conditions are needed to obtain a viable process. Since 1972, when Fujishima and Honda once successfully used by the first time TiO_2 photo-anodes in the evolution of hydrogen, while the use of semiconductor oxides has been considered a promising path for a sustainable hydrogen production [4]. From this fundamental study, an important amount of research has focused in finding alternate semiconductors to TiO_2 Degussa P25 (material usually used as a reference photocatalyst) with equal or better activity towards the hydrogen production under the UV or visible light irradiation. One of the main disadvantages that TiO_2 presents is that the energy needed for its activation is found under the UV light spectrum (~3.2 eV). Therefore, it is a reasonable strategy to explore other materials capable to be activated under the visible light spectrum and that present equal or better efficiencies towards the hydrogen production through the water splitting process.

One example of such materials is the ferrites, which have been considered as a novel option in photocatalytic processes.

Dentro de este grupo de materiales las ferritas han sido estudiadas como una opción novedosa como fotocalizador. Entre sus principales características se encuentran sus excelentes propiedades magnéticas, alta conductividad electrónica, alta estabilidad térmica, su efectiva actividad catalítica [5] , su resistencia a la corrosión [3] y sobre todo un ancho de banda prohibida que se encuentra dentro del espectro de luz visible (1.4 eV) [1]. Among their main features are their excellent magnetic properties, high electronic conductivity, high thermal stability, their effective catalytic activity [5], its corrosion resistance [3] and mostly a forbidden band gap energy within the range of visible light (1.4 eV) [1]. Therefore, the objective of the present research is aimed on the synthesis, characterization and

photocatalytic evaluation of ferrite nanoparticles towards the hydrogen production using methanol as sacrificial reagent under visible light irradiation.

2. EXPERIMENTAL

2.1. Synthesis

$CuFe_2O_4$, $CoFe_2O_4$ and $NiFe_2O_4$ were prepared by the method of chemical co-precipitation using the corresponding metal nitrate solutions and NaOH as a precipitating agent followed by a thermal treatment (see Figure 1). Stoichiometric amounts of nano-hydrated ferric nitrate, 2.5 hydrated copper nitrate and hexa-hydrated cobalt and nickel nitrates were used to prepare the corresponding nitrate solutions [6]. Using a peristaltic pump, these nitrates were slowly added at a rate of 5 ml/min to the precipitating agent solution (NaOH). The reacting mixture was kept under constant stirring and a basic pH of 13 using NaOH under constant stirring. This basic pH was required to influence the precipitation reaction rate of the complex, since a highly alkaline medium generates smaller (precipitate) size particles [6]. In order to obtain a nanoparticulate crystalline material the resulting solution was dried and exposed to a low temperature thermal treatment at 250°C for 6 hours, followed by 1 hour at 350°C. This precipitate was the allowed to cool to room temperature. Finally, the product was washed with distilled water and ethyl alcohol to eliminate any residue, then filtered and dried at 80°C by 4 hours to follow its characterization and photocatalytic evaluation.

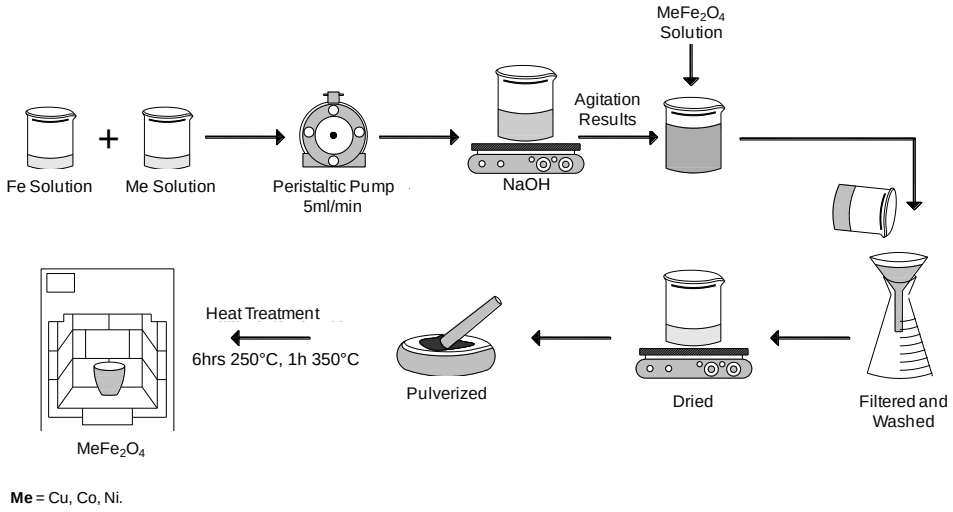

Figure 1. Procedure for the synthesis of $CuFe_2O_4$, $CoFe_2O_4$ and $NiFe_2O_4$ nanoparticles through co-precipitation.

2.2. Powder Characterization

Samples crystalline phase was determined by X-ray diffraction (XRD) using a PANalytical diffractometer model X'Pert PRO equipped with a X'Celerator detector. From the X-ray diffraction patterns information and through the use of the Scherrer equation, the crystal size of the materials was calculated. The specific surface area of the materials was estimated by N_2 physisorption using the BET technique on an Autosorb-1, Gas Sorption System (Quantachrome Corporation). The homogeneity in chemical composition of the samples was determined through dispersive X-ray spectroscopy (EDS) mapping using a detector coupled to a scanning electron microscope model 5800-LV Jeol JSM brand. The particle size of the materials and their morphology was determined by transmission electron microscopy (TEM) using a Philips CM-200. The light absorption spectrum of the materials was obtained through UV-visible spectroscopy (UV/Vis) by a Perkin Elmer spectrophotometer model Lambda 10 equipped with integrating sphere.

2.3. Photocatalytic Evaluation

Figure 2 shows a scheme of the experimental system employed for the photocatalytic evaluation of the materials, which consists of a photoreactor, artificial lighting and data collection analysis equipment. The photoreactor was built using a quartz tube with a 5 and 19 cm diameter and length, respectively where a suspension of each nanoparticle material ($CuFe_2O_4$, $CoFe_2O_4$ y $NiFe_2O_4$) was placed. Two aluminum flanges bolted together by threaded rods were used to close the tube and its sealing was achieved through neoprene o-rings. The radiation source used was a white light artificial mercurial lamp of 120 W, GE. Concentration of initial reagents and changes in gas phase composition within the photoreactor during the course of the experiments was determined by gas chromatography (GC) using a Clarus 500, Perkin Elmer, equipped with thermal conductivity (TCD) and flame ionization (FID) detectors arranged in series. The sampling of the gas was performed through a septum sampling port located on one side of the photoreactor and transferred to the GC by hand injection using a 1 ml special syringe for gases.

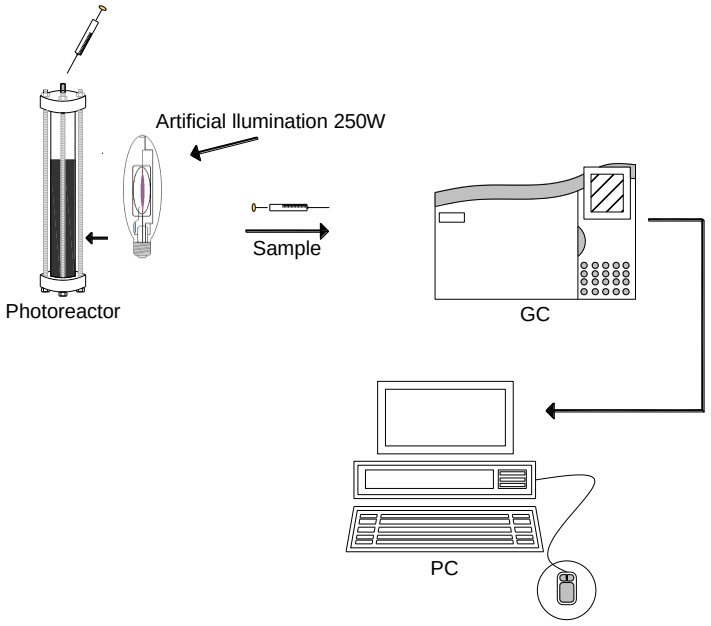

Figure 2. Experimental setup system for the photocatalytic evaluation of the nanomaterials.

The photoreactor was hermetically sealed and checked for leaks. The photocatalytic suspension consisted of a mixture of distilled water and ethanol as a sacrificial reagent (50:1 molar ratio) and 200 mg of photocatalyst, which was artificially, irradiated using a visible light lamp. Prior to the photocatalytic evaluation the reactor was covered to prevent it from light exposure and was subjected to constant stirring for 15 minutes in order to achieve good homogenization of the suspension in the photoreactor. The initial concentration of gases was evaluated by gas sampling of the gas phase within the photoreactor and analyzed by GC. Then the mercury lamp was turned on and a gap of seven inches was left between the lamp and the photoreactor reactor wall. Sampling was performed manually every hour to complete twenty two hours of irradiation. Analysis of the initial gas phase concentration and of changes in gas composition inside the reactor was performed by means of gas chromatography (GC, Perkin Elmer Clarus 500), compounds separation used a Carboxen 100 packed column coupled with a thermal conductivity detector (TCD). Product identification was achieved by determining the elution time with respect to pure reagent concentrations and the quantification was performed using calibration curves.

3. RESULTS AND DICUSSION

3.1. X-ray Diffraction (XRD)

Figure 3 presents results of XRD characterization for samples $CuFe_2O_4$, $CoFe_2O_4$ and $NiFe_2O_4$

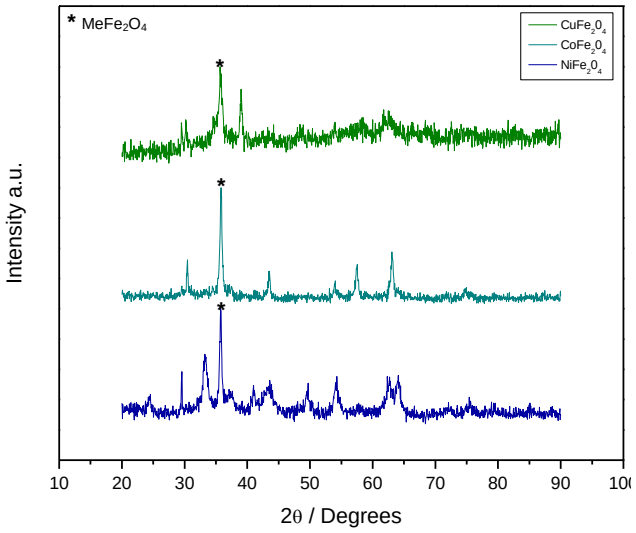

Figure 3. XRD patterns of the ferrites studied in the present research study.

For the copper ferrite sample CuO and $CuFe_2O_4$ phases were found in the XRD diffractogram, while for the case of the cobalt ferrite sample only the $CoFe_2O_4$ phase was present and in the particular case of sample nickel ferrite two phases were found; Fe_2O_3 and $NiFe_2O_4$. Haihua, et al 2009 [3] reported a diffraction pattern with the same phases as those for sample $CuFe_2O_4$. Whereas, the cobalt ferrite diffraction pattern is consistent with the one reported by Hua, et al, 2008 [7].

3.2. Scanning Electron Microscopy (SEM)

Figure 4 shows SEM images of samples $CuFe_2O_4$, $CoFe_2O_4$ and $NiFe_2O_4$. In this Figure it can be observed that in all cases it can be observed agglomerated particles with irregular morphologies (spherical, flake-like or needle), which are in the order of nanometers. Here it can be concluded that a careful control of the nitrate addition during the precipitation process has a significant effect in obtaining nano-sized particles as can be seen in the SEM images [6].

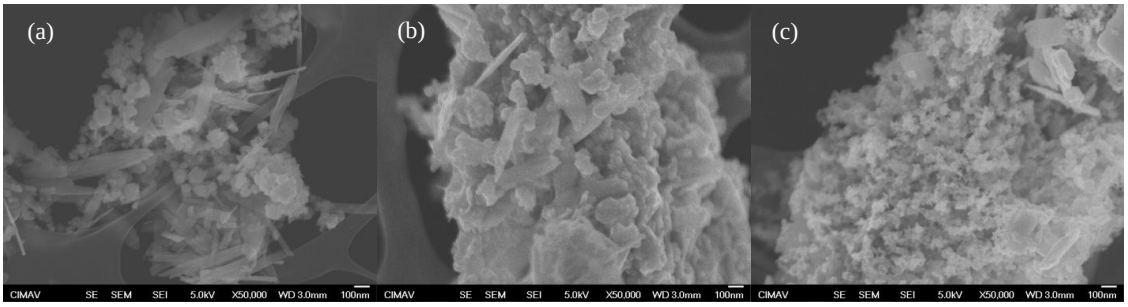

Figure 4. SEM Images of (a) $CuFe_2O_4$, (b) $CoFe_2O_4$ and (c) $NiFe_2O_4$.

3.3. Transmission Electron Microscopy (TEM)

Morphology for the case of sample $CuFe_2O_4$ (see Figure 5a) is composed by agglomerate particles of irregular shapes with sizes varying between 15 and 30 nm, the same morphology was reported by Haihua, et al 2009 [3] for copper ferrites. While, for cobalt (b) and nickel (c) ferrites it can be observed sizes of around 25 nm. Here also, very similar particle sizes were reported by Hua et al, 2008 [7] for both kind of samples.

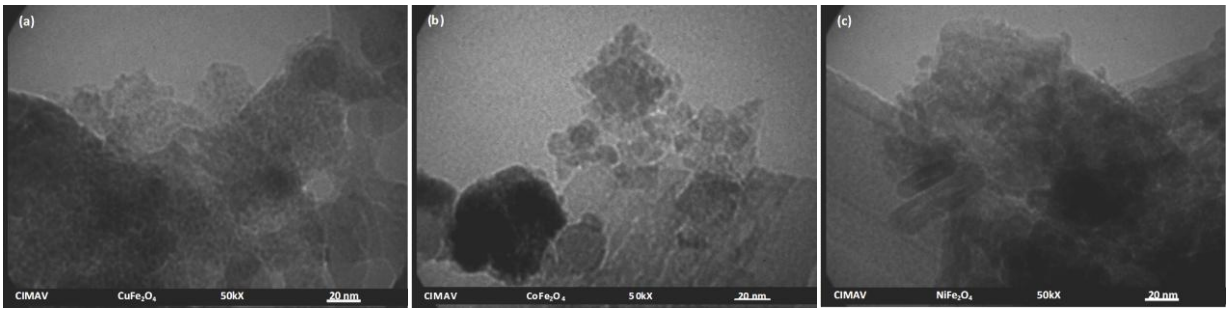

Figure 5. TEM images at 50kX for samples (a) $CuFe_2O_4$, (b) $CoFe_2O_4$ and (c) $NiFe_2O_4$.

3.4. BET Surface Area

It is well known that surface area is directly influenced by the particle size and at the same time closely related to the method of synthesis being employed. The specific surface areas of the photocatalysts were 32, 21 and 24 m^2/g for samples $CuFe_2O_4$, $CoFe_2O_4$ and $NiFe_2O_4$, respectively.

Figure 6 shows the BET adsorption isotherms obtained for the synthesized samples in the present research. The above reported values of surface area can be explained in terms of the shapes of these isotherms. For the case of

sample $CuFe_2O_4$ the presence of hysteresis and a type IV is an indication of a porous material, while samples $CoFe_2O_4$ and $NiFe_2O_4$ present type III isotherms with negligible hysteresis and consequently porosity.

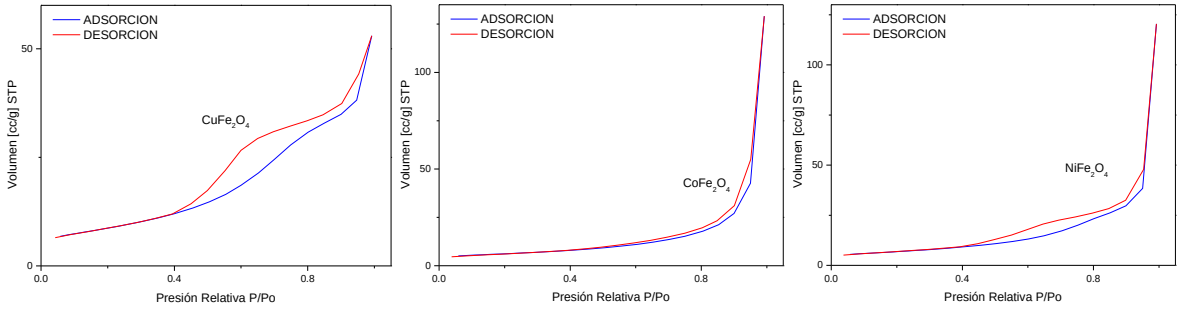

Figure 6. BET adsorption Isotherms for samples (a) $CuFe_2O_4$, (b) $CoFe_2O_4$ and (c) $NiFe_2O_4$.

3.5. UV/Vis Spectroscopy

UV/Vis diffuse reflectance spectra for samples of $CuFe_2O4$, $NiFe_2O_4$ $CoFe_2O_4$ and are presented in Figure 7. Here, the edge energy of the forbidden band can be calculated from the reflectance data by the Kubelka-Munk function.

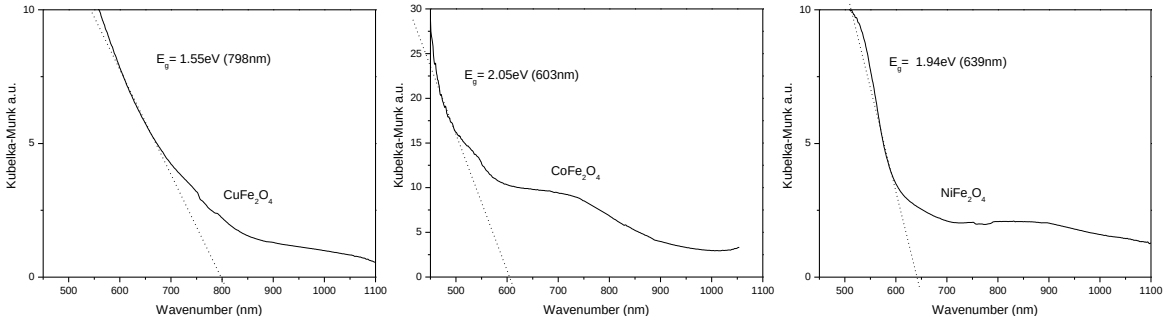

Figure 7. UV/Vis diffuse reflectance spectra from samples (a) $CuFe_2O_4$, (b) $CoFe_2O_4$ and (c) $NiFe_2O_4$.

From this Figure it can be observed that UV/Vis spectra for all samples fall within the visible light range. The band gap energy value for samples $CuFe_2O_4$, $CoFe_2O_4$ and $NiFe_2O_4$ were 1.55, 2.05 and 1.94 eV, respectively. Therefore, it can be concluded that these materials presumably work as photocatalysts within the visible light spectrum. These values are consistent with the ones reported in the literature. For example, a value of 1.42 eV is reported for $CuFe_2O_4$ by Kezzim, et al 2011 [1], a band gap of ~ 1.5 eV for $CoFe_2O_4$ reported by Limei, et al 2011 [8], while a value of 2.19 eV for $NiFe_2O_4$ is reported by Erik, et al 2012 [9].

3.6. Photocatalytic Activity

Photocatalytic evaluation of the synthesized materials was carried out by follow up of the hydrogen production by gas chromatography.

Figure 8 show results from the photocatalytic evaluation of the synthesized materials. In this Figure, the hydrogen evolution in micro-mols per gram of catalyst ($\mu m/g_{cat}$) as a function of time is plotted for each tested photocatalyst. Here it can be seen that the superior performance of the ferrites with respect to TiO_2 (P25) is evident.

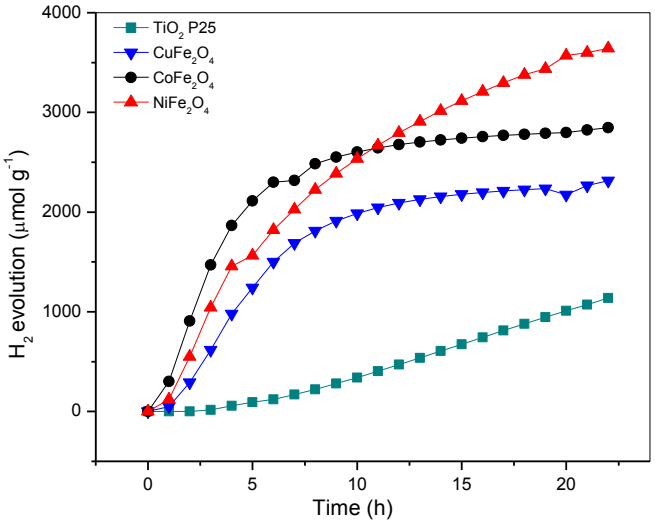

Figure 8. Hydrogen evolution profile for the synthesized materials as a function of time.

Otherwise, Table 1 show values of hydrogen evolution in micro-mols per gram of catalyst ($\mu m/g_{cat}$) after a total of 22 hours of reaction taken from results presented in Figure 8 and these are compared to TiO_2 (P25). The order from higher to lower hydrogen production was: $NiFe_2O_4$ > $CoFe_2O_4$ > $CuFe_2O_4$, which values were well above the obtained, for reference TiO_2 (P25). This behavior can be attributed to the fact that the ferrites are materials whose characteristics meet the conditions for carrying out the electron-hole pair reaction needed for good photocatalytic activity [9,10].

Table I. Hydrogen generation (%) as a function of time after 22 hours of irradiation

Material	H_2 Evolution @ 22 h ($\mu m/g_{cat}$)
TiO_2 (P25)	1138
$CuFe_2O_4$	2315
$CoFe_2O_4$	2846
$NiFe_2O_4$	3643

4. CONCLUSIONS

$CuFe_2O_4$, $NiFe_2O_4$ and $CoFe_2O_4$ nanoparticles were synthesized by a chemical co-precipitation method followed by heat treatment and tested for hydrogen production, demonstrating that the present synthesis technique is a simple, inexpensive and reproducible. For samples of $NiFe_2O_4$ and $CuFe_2O_4$ the dominant crystal structure is that of a spinel $MeFe_2O_4$ (Me = Cu, Ni) accompanied with formation of Fe_2O_3 and CuO, respectively. For the case of the $CoFe_2O_4$ sample the crystallographic structure of spinel $CoFe_2O_4$ is the only crystallographic phase present in the sample. SEM results indicate that in all cases nanoparticles were obtained with a wide variety of nanoscale morphologies ranging from spherical to flakes or needles. Photocatalytic evaluation towards hydrogen production resulted in a superior behavior of nickel, cobalt and copper ferrites compared to results obtained for reference TiO_2 (P25) photocatalyst. The order from higher to lower hydrogen production was: $NiFe_2O_4$ > $CoFe_2O_4$ > $CuFe_2O_4$. The good photocatalytic activity of the synthesized samples is related to the inherent properties of these materials, demonstrating that meet necessary conditions to carry out the electron-hole pair reaction required for good photocatalytic activity.

ACKNOWLEDGEMENTS

The authors are grateful to M Sc. Enrique Torres, M Sc. Karla Campos, Eng. Wilber Antunez, M Sc. Raul Ochoa and Eng. Luis de la Torre for their help on XRD, SEM, TEM, BET and UV-Vis spectroscopy characterization, respectively. Also to CIMAV, S. C and CONACYT for their financial assistance.

REFERENCES

[1]A. Kezzim, N. Nasrallah, A. Abdi, M. Tari,Visible light induced hydrogen on the novel hetero-system $CuFe_2O_4/TiO_2$; Energy Conversion and Management 52 (2011) 2800–2806. 2800–2806.

[2]N. Shimoda , K. Faungnawakij, R. Kikuchi, T. Fukunaga, K. Eguchi, Catalytic performance enhancement by heat treatment of $CuFe_2O_4$ spinel and g-alumina composite catalysts for steam reforming of dimethyl ether; Applied Catalysis A: General 365 (2009) 71–78.

[3]Haihua Yang, Jianhui Yan, Zhouguang Lu, Xiang Cheng, Yougen Tang, Photocatalytic activity evaluation of tetragonal $CuFe_2O_4$ nanoparticles for the H_2 evolution under visible light irradiation; Journal of Alloys and Compounds 476 (2009) 715–719.

[4]Zhonghai Zhang, Md. Faruk Hossain, Takakazu Takahashi, Photoelectrochemical water splitting on highly smooth and ordered TiO_2 nanotube arrays for hydrogen generation; International Journal of Hydrogen Energy 35, 16 (2010) 8528–8535.

[5]N.M. Deraz, Production and characterization of pure and doped copper ferrite nanoparticles/Pyrolysis; J. Anal. Appl. 82 (2008) 212–222.

[6]M.Y. Ortega-López, J.M. Salinas-Gutiérrez, V. Guzmán-Velderrain, A López-Ortiz, V. Collins-Martínez, Alternate Semiconductor Materials to TiO_2 as Photocatalysts for the Degradation of Organic Compounds (2012).

[7]Chaoquan Hua, Zhenghong Gaoa, Xiaorui Yangb, One-pot low temperature synthesis of MFe_2O_4 (M ¼ Co, Ni, Zn) superparamagnetic nanocrystals; Journal of Magnetism and Magnetic Materials 320 (2008) L70–L73.

[8]Xue Limei, Zhang Fenghua, Chen Bin, Bai Xuefeng, Preparation of Light-Driven Spinel Nanoparticles $CoAl_2O_4$, $MgFe_2O_4$ and $CoFe_2O_4$ and Their Photocatalytic Reduction of Carbon Dioxide; ISBN: 978-0-7695-4350-5 (2011).

[9]Erik Casbeer, Virender K. Sharma, Xiang-Zhong Li, Review: Synthesis and photocatalytic activity of ferrites under visible light: A review; Separation and Purification Technology 87 (2012) 1–14.

[10]Hong Deng, Hongyu Chen, He Li, Synthesis of crystal MFe_2O_4 (M = Mg, Cu, Ni) microspheres; Materials Chemistry and Physics 101 (2007) 509–513.